RAL-86-046

Science and Engineering Research Council
Rutherford Appleton Laboratory
CHILTON, DIDCOT, OXON, OX11 0QX

Science and Engineering Research Council Central Laser Facility

Annual Report to the Laser Facility Committee 1986

Laser Division
Rutherford Appleton Laboratory

RAL-86-046

Science and Engineering
Research Council

SCIENCE AND ENGINEERING RESEARCH COUNCIL
CENTRAL LASER FACILITY
ANNUAL REPORT TO THE LASER FACILITY COMMITTEE

PREFACE

M H Key

Research and facility development work carried out at or in association with the Central Laser Facility (CLF) in the year ended 31 March 1986 is reported.

The CLF is funded by the Science Board of SERC and its Subject Committees and operated by the Laser Division of the Rutherford Appleton Laboratory, primarily as a user facility providing access to advanced lasers for UK University and Polytechnic research workers. The competitive peer review system governing access to the facilities and the CLF's organisation and funding are briefly outlined in the Introduction to Part I of the report.

Part I then gives technical details of the year's work at the CLF. It is a compilation of contributions from users of the facilities describing their research results, from CLF staff reporting facility development work and from theorists whose work is connected with research at the CLF. The report concentrates on scientificially or technically interesting material and does not attempt to give a catalogue of all scheduled work. Rapid production has been aimed at in order to distribute useful information to the scientific community prior to publications appearing in the scientific literature.

The high power Nd:glass laser, VULCAN, and KrF laser, SPRITE, are the major installations at the CLF and their scientific applications are discussed in Section A. A range of smaller lasers provided for use either at the CLF or in users' home laboratories constitute the new Laser Support Facility and its multidisciplinary research work is presented in Section B, while Section C covers laser research and development by in-house staff and Section D presents the year's publications. No classified work is done by CLF staff. All work is published in the literature with the exception that the laser facility may be used for up to 10% of available time for contract work where the customer may choose to have commercial confidentiality.

The Laser Division of RAL also undertakes some R&D work aimed at developing commercially useful applications of UV lasers in the manufacture of microcircuits by UV lithography. The programme is funded by the Engineering Board of the SERC and by the Department of Trade and Industry. Patents and exploitation agreements with UK companies are the major objectives and this restricts what can be included in the report on the project given in Part II.

The year's work has several highlights. New facilities for X-ray laser research using VULCAN were brought into operation in October, after a year's delay due to earlier funding problems. The new facilities give the CLF an internationally unique capability and led to immediate important results in which 50-fold XUV laser amplification was demonstrated on the CVI Balmer α transition at 18.2nm. Very attractive opportunities for the development of a range of XUV lasers are now in prospect for next year.

The SPRITE KrF laser facility, used for scheduled experiments for the first time, is the most powerful KrF laser available anywhere for target irradiation, and many interesting results were obtained.

A particularly important development this year has been the expansion of our provision of small lasers for multi-disciplinary science, with extra funds provided by the Subject Committees of the Science Board, and the reorganisation of the activity into the new Laser Support Facility. The varied work of the LSF now includes advanced studies of DNA repair processes in molecular biology and picosecond measurements in photosynthesis, in addition to a wide range of photochemistry.

I will conclude this preface by expressing my appreciation of the work of the staff of the CLF who have shown dedication and enthusiasm in carrying out a considerably expanded programme despite some staff shortages. The CLF is now providing services to a 150-strong user community with, at any one time, five user groups working in parallel at RAL and several groups using loan equipment throughout the UK, with considerable international collaboration in the scheduled programme.

Prospects for the future depend on the outcome of a major review in 1987 and on a new (Phase II) plan for the development of the CLF to be considered by the Science Board in 1987/88.

CONTENTS

PART I

INTRODUCTION

P T Rumsby (RAL)

The Central Laser Facility (CLF) is funded by the Science Board of the Science and Engineering Research Council and in the year covered by this report, April 1985 to April 1986, its allocation was £3.2 M.

The Science Board has provided the Facility for research whose major themes are:

- A High Density Plasma Physics
- B High Intensity Laser Plasma Interactions
- C Energy Transport in Laser Produced Plasmas
- D Laser Driven Implosions
- E X-Ray Lasers
- F Other Applications of Laser Produced Plasmas (eg as X-Ray sources)
- G Applications of Short Pulse Frequency Tunable Lasers

The programme is managed by the Laser Facility Committee (LFC) whose membership is given in Table 1. The LFC delegates responsibility to the Rutherford Appleton Laboratory for the operation of the Facility.

The Laser Division of RAL used 56 man years of effort, 54 of which were deployed in the organisational structure shown in Table 2 and a further 2 man years used as support in other RAL Divisions. Staff costs and overheads used 42% of the allocation while facility operations and minor development costs used another 42%. The remaining 16% of the total allocation was spent on the Phase 1 programme of capital facility development.

The major facilities provided by the CLF and a brief indication of their principal scientific applications is given in Table 3.

The Nd glass laser VULCAN is the major facility and about 50% of resources was used to support its programme of research by UK Universities.

The high power UV gas laser SPRITE has now been developed to the point that at least 50% of its time is used to provide UV and X-ray source facilities for University work. About 16% of total operating resources were committed to this work.

Multidisciplinary scientific applications of excimer lasers and excimer pumped dye lasers by UK Universities has been catered for by the Laser Support Facility (using 25% of resources). This also operates a picosecond laser system for photobiological applications at the CLF and a laser loan scheme for University based experiments.

A target prepararion service (6%) and a small group giving theoretical support by maintaining computer codes (3%) support all CLF activities.

Use of the CLF by UK Universities is free of charge to those successful in a peer review process. Research grants of typically three years duration covering expenditure in University Laboratories and research assistants' salaries may be obtained from the LFC by application to SERC. LFC Grant holders are entitled to bid for time on the CLF's lasers through a procedure described below.

A few percent of the time may also be allocated to bids for short trial experiments from University researchers working in the Science Board area who do not hold LFC grants.

The SERC encourages use of the CLF by industry or other organisations on the basis of payment for the full cost of laser time. Such use is limited to not more than 10% of available laser time.

International collaboration in the research programme is particularly welcomed, either through collaborative participation in approved experiments of UK University groups or through agreements negotiated with the CLF and SERC.

Selection and scheduling of University experiments using the VULCAN glass laser and SPRITE UV laser is via proposals to one of 4 informal specialist scientific groups which anyone may join. Each has a University Chairman and an RAL secretary (Table 4). Each group

discusses the experimental proposals and makes modifications, improvements and collaborative suggestions. More formal proposals based on these discussions are then submitted to an expert panel which places scientific priorities on the proposals. This panel is chaired by the Scientific Programme Chairman and its secretary is the Scientific Programme Coordinator. Its members include the five Scientific Group Chairman, the Chairman of the High Power Laser Scheduling Committee (HPLSC) and a representative of the LFC. A draft schedule which includes as many of the high priority proposals as possible (typically <50% of proposals), is then prepared, discussed and modified at a meeting of the more formal High Power Laser Scientific Programme and Scheduling Committee (HPLSPSC). All University staff members involved in the programme have voting rights, together with the group secretaries and programme coordinator. The Committee is chaired by the Division Head of Laser Division and is formally advisory to him.

Scheduling of Laser Support Facility lasers is performed in a different way. The LFC has delegated LSF Management duties to a panel whose membership is given in Table 5. Selection of experiments requiring loan pool lasers or use of the lasers based at the CLF is carried out by this panel and scheduling is performed by an ad hoc committee of users chaired by the Laser Division Head.

Scheduled experiments are supported by the operating budget of the CLF which covers travel and subsistence costs for University users and minor engineering work and other costs of experiments.

The experimental programme is linked to theoretical work in Universities which is supported by grants from the LFC and coordinated by the Theory and Computation Scientific group (Table 4).

There is a large and diverse community of University researchers participating in the programme. They number about 150 staff and research students. Most are physicists and chemists, but recently there has been a rapid growth of participation from biologists.

TABLE 1

Membership of the Laser Facility Committee 1985/86

Professor G J Pert (Chairman)
Dept of Applied Physics
University of Hull

Dr J E Allen
Department of Engineering
Science
University of Oxford

Dr E H Evans
School of Sciences
Preston Polytechnic

Professor M G Haines
Imperial College of
Science and Technology
London

Dr T A Hall
Department of Physics
University of Essex

Dr M H R Hutchinson
Imperial College of
Science and Technology
London

Dr T A King
Schuster Lab
University of Manchester

Dr C L S Lewis
Department of Pure and
Applied Physics
The Queen's University of
Belfast

Professor D Phillips
Department of Chemistry
Royal Institution of Great Britain

Professor J P Simons
Department of Chemistry
University of Nottingham

Dr M Vaughan
Procurement Executive
Royal Signals & Radar Est, MOD,
Gt Malvern

TABLE 2

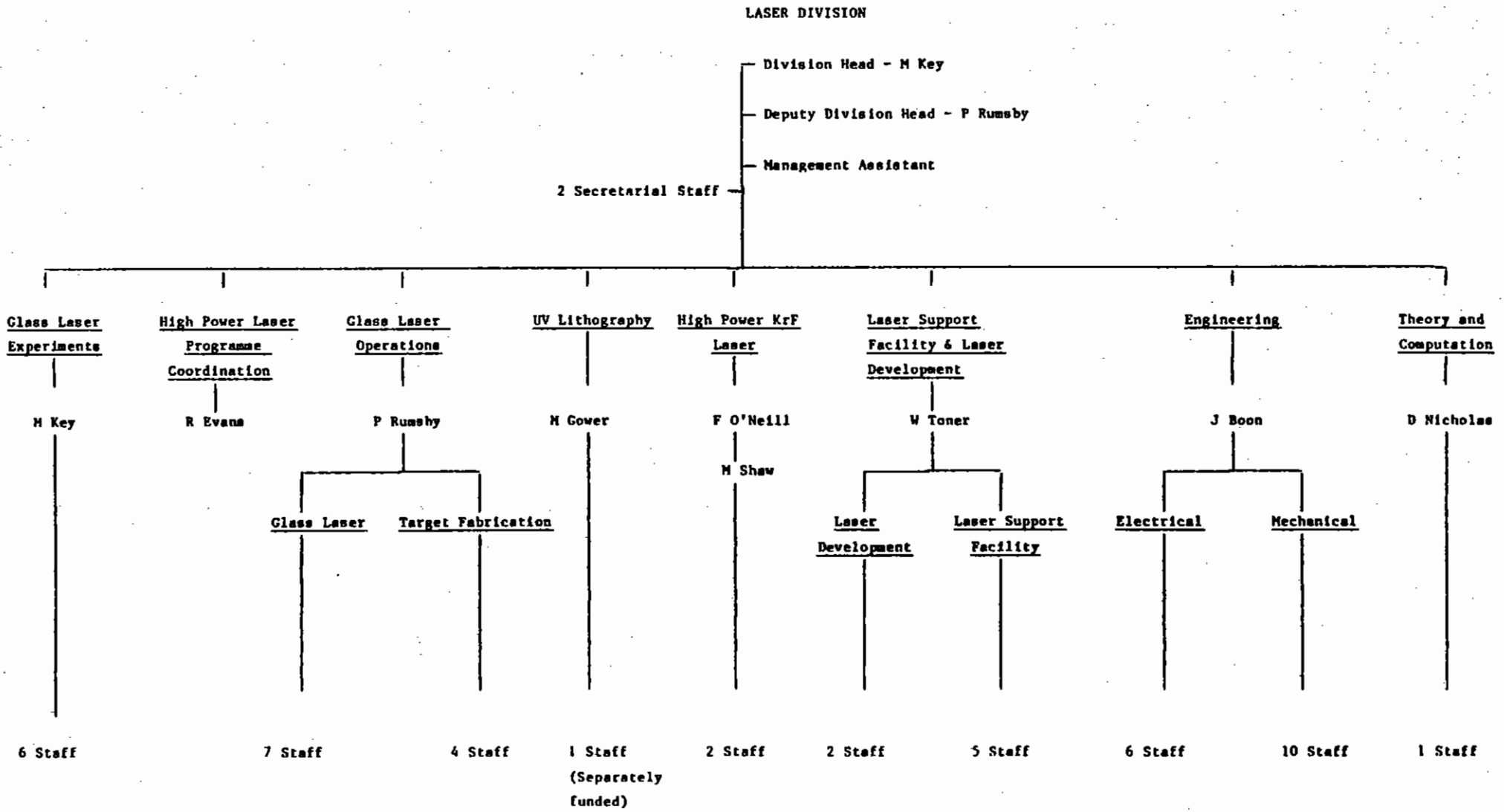
LASER DIVISION
Division Head - M Key
Deputy Division Head - P Rumsby
Management Assistant
2 Secretarial Staff
Glass Laser Experiments
M Key
6 Staff
High Power Laser Programme Coordination
R Evans
Glass Laser Operations
P Rumsby
Glass Laser
7 Staff
Target Fabrication
4 Staff
UV Lithography
M Gower
1 Staff (Separately funded)
High Power KrF Laser
F O'Neill
M Shaw
2 Staff
Laser Support Facility & Laser Development
W Toner
Laser Development
2 Staff
Laser Support Facility
5 Staff
Engineering
J Boon
Electrical
6 Staff
Mechanical
10 Staff
Theory and Computation
D Nicholas
1 Staff

TABLE 3

Nd glass Laser facility	Laser Support Facility	High power KrF laser facility
VULCAN	LSF	SPRITE
Plasma Physics Applications of intense X-ray and particle sources X-ray laser Research	Photo chemistry Photo biology Materials processing Non linear optics Plasma diagnostics Tunable VUV source Laser loan pool	Facility utilizing the high X-ray brightness of UV laser produced plasmas
Target Preparation Service Theoretical support service		

TABLE 4

Groups of the HPLSPSC	Chairman	Secretary
Laser plasma Interaction and Energy transport	Dr A E Dangor	Dr R G Evans
Laser Driven Compression and dense plasmas	Dr T A Hall	Dr A J Cole
XUV lasers and applications of laser produced plasmas	Dr C L S Lewis	S Rose
Theory and Computation	Dr R A Cairns	Dr D Nicholas
Facility Development	Dr P T Rumsby	Mr J E Boon
Scientific programme coordinator	R G Evans	

TABLE 5

Laser Support Facility Panel

Professor J P Simons - Chairman
Nottingham University

Professor R E Hester for Chemistry Committee
York University

Dr P B Davies for Chemistry Committee
Cambridge University

Dr C W Wharton for Biological Sciences Committee
Birmingham University

Dr C Webb for Physics Committee
Oxford University

Dr H Evans for Laser Facility Committee
Preston Polytechnic

SECTION A HIGH POWER LASER SCIENTIFIC PROGRAMME

A HIGH POWER LASERS SCIENTIFIC PROGRAMME

Introduction

This section of the CLF Annual Report describes the scientific results from the VULCAN Nd glass laser and the SPRITE KrF laser facilities. This is the first time that results from SPRITE are included in this chapter and reflects the emergence of SPRITE as a scheduled facility, at least for a portion of the year.

Out of 52 experimental proposals, 29 were actually scheduled. The major improvement in the experimental facilities was the introduction of Target Area East with its sophisticated line focus optics for X-ray laser research. Significant results in this area have already emerged with the measurement of a reproducible gain on the 182Å carbon recombination line.

A large body of work is described on the application of laser plasmas as X-ray sources, following preliminary results last year. It is in this area that SPRITE has made its initial contributions, the short laser wavelength being particularly suitable for X-ray generation.

Thermonuclear reaction products (alpha particles) have proved to be a very useful diagnostic probe and have been used to diagnose implosion symmetry and Rayleigh Taylor instability in accelerated foils. The twelve beam spherical irradiation facility has been used to continue the study of laser driven implosions and of thermal energy transport.

The first attempt at generating "beat waves" was less successful than anticipated due to strong Raman scattering in atmospheric nitrogen. This effect may have unexpected 'spin off' in generating an effectively broad band laser source for laser fusion purposes.

Editor: R G Evans

A1.1 BEAT WAVE EXPERIMENTS

A K L D Bradshaw, A E Dangor, A Dyson, T Garvey, I Mitchell (Imperial College), A Cole, R G Evans C Danson, C B Edwards (RAL)

A1.1.1 Introduction

The resonant beating of two laser beams, frequencies ω_0, ω_1 in a plasma whose natural frequency $\omega_p = \omega_0 - \omega_1$ will drive a large amplitude electrostatic wave with wavenumber $k_p = k_0 - k_1$. For parallel propagating pump waves the phase velocity of the longitudinal beat wave is approximately c and it has been proposed that this mechanism has potential as a particle accelerator for high energy physics research. The fast beat wave has been observed in experiments at UCLA (A1.1) and at INRS Quebec (A1.2), both experiments using the CO_2 rotational bands at 9.6 μm and 10.6 μm. Since the phase velocity of the beat wave is characterised by a Lorentz factor $\gamma = (1 - {}^{v_{ph}^2}/_{c^2})^{-\frac{1}{2}} \approx {}^{\omega_o}/_{\omega_p}$, the beat wave produced in these experiments is not really fast enough for high energy acceleration.

Within the bandwidth of the neodymium glass laser it is possible to amplify two lines at 1.053 μm (YLF) and 1.064 μm (YAG). The laser development necessary to provide 80 Joules at each of these wavelengths is described in Section C1.2. This gives a Lorentz factor $\gamma = 100$ and a resonant density of $n_e = 1.1 \times 10^{17}$ cm^{-3} which is a convenient density to operate the Imperial College Z-pinch in hydrogen. The planned experiment should have demonstrated a beat wave at a phase velocity which is more relevant to high energy physics than the earlier CO_2 laser experiments.

A1.1.2 Experimental Arrangement

The layout of the Z-pinch, 1.05 and 1.06 μm pump beams, and diagnostic equipment is shown in Fig A1.1. The two laser beams are focussed into the pinch discharge by a 3 metre focal length lens giving a focal spot size measured on the equivalent plane camera of about 400 μm diameter. The existing beam is attenuated by wedged uncoated mirrors and

focussed into a 30 cm Bentham spectrometer, the emerging spectrally dispersed light is imaged onto the entrance slit of an S1 Imacon 675 streak camera. This diagnostic channel, referred to as the 'cascade' channel monitors the development of spectral sidebands on the pump light caused by forward Raman scattering of the pump light from the beat wave. The sideband amplitude is a measure of the intensity of the beat wave if the interaction length is also known. To assist in detecting weak sidebands the 1.053 and 1.064 μm pump lines can be masked off by a neutral density 2.0 filter strip on the slit of the streak camera.

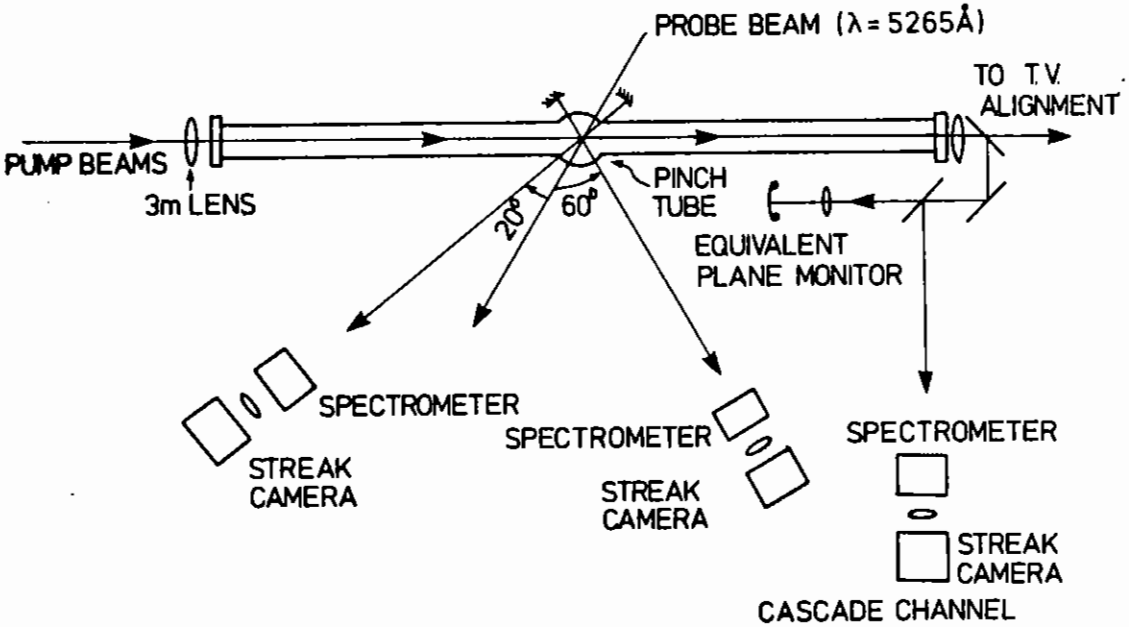

Fig A1.1 Experimental layout for the beat wave experiment.

A portion of the transmitted light is fed to a TV alignment monitor, to a calorimeter, and an equivalent focal plane camera.

The plasma density and temperature are measured by Thomson scattering of a 0.53 μm probe laser beam. Scattering angles of 20^0 and 160^0 (using a mirror behind the scattering volume) give high and low α scattering respectively while scattering at 60^0 and 120^0 measures the Raman and Brillouin plasma waves excited by the infra-red pumps. These two scattering channels feed combinations of spectrometer and streak camera similar to the cascade channel but using S20 streak cameras. The Imacon 500 streak camera on the Raman/Brillouin channel was provided by CERN as part of their collaboration in the experiment.

A1.1.3 Two Frequency Results

The planned use of the cascade channel to measure the beat wave amplitude was made impossible by the unexpected near coincidence of the beat frequency of the 1.064 and 1.053 μm pump waves (98.2 cm^{-1}) with the S(11) rotational line of nitrogen at 99 cm^{-1}. The simultaneous propagation of both laser frequencies through an air path of ~ 30 metres gives rise to extremely strong Raman scattering and gives the spectrum shown in Figure A1.2. Two Stokes lines and two anti-Stokes lines can be seen on the originals. The temporal development of each of the stronger lines is shown in Figure A1.3. Whilst of no use for the generation of beat waves this spectrum is of some interest in laser fusion as an approximate broad band laser source which would be expected to reduce the problems of laser plasma instabilities.

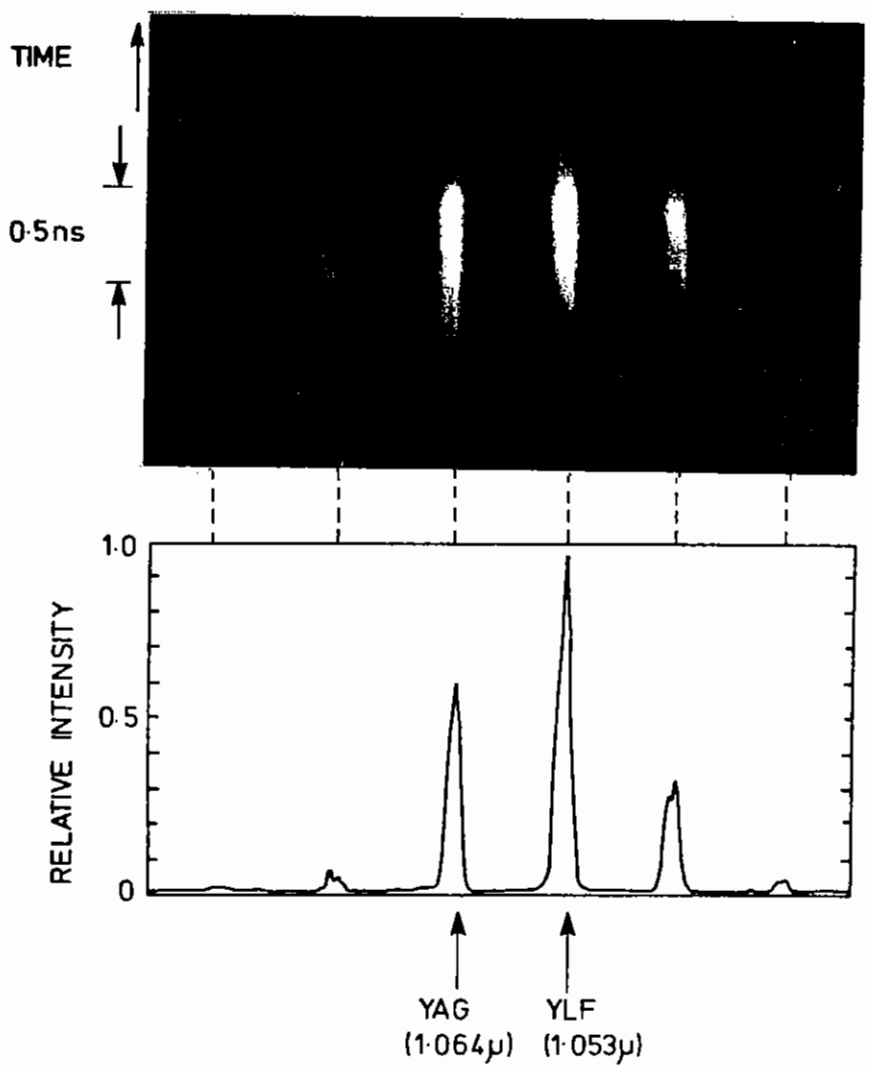

Fig A1.2 A time resolved spectrum of the infra-red pump lasers due to atmospheric Raman scattering. The lower trace is corrected for film characteristic and spectral sensitivity variations.

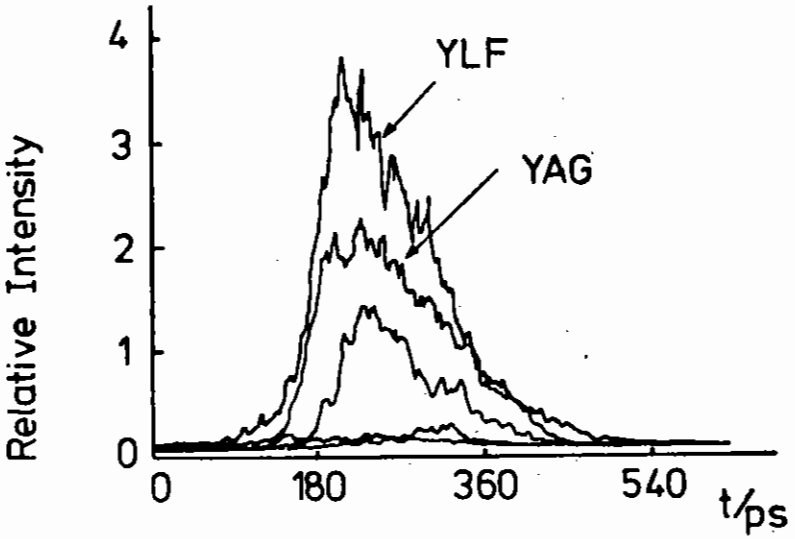

Fig A1.3 Temporal scans of the intensity of YLF and YAG pump beams and the Raman scattered sidebands.

These sidebands were not observed at the output of the laser disc amplifiers and were a consequence of the air propagation path.

The extremely strong sideband generation requires that the two frequencies be present simultaneously in the same volume of air. If the two laser oscillators are deliberately desynchronised then only very weak spontaneous Raman scattering can be seen (Fig A1.4).

A 'quick fix' to attempt to minimise the effect of the nitrogen Raman scattering is shown in Fig A1.5. A small Michelson interferometer is introduced into the beam paths just before the 3 metre focussing lens. The time delay between the two arms of the Michelson is set to be the same as the deliberate desynchronisation of the laser oscillators. In the pinch discharge this means that the first (1.064 μm) pulse from one

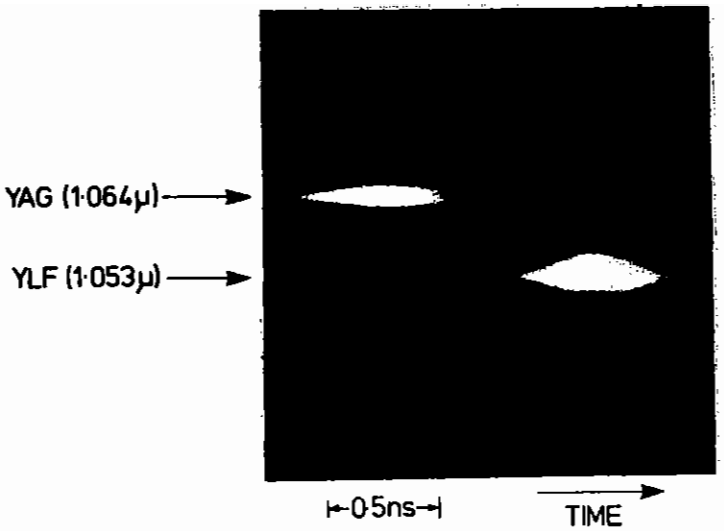

Fig A1.4 A time resolved spectrum with deliberately desynchronised YLF and YAG beams.

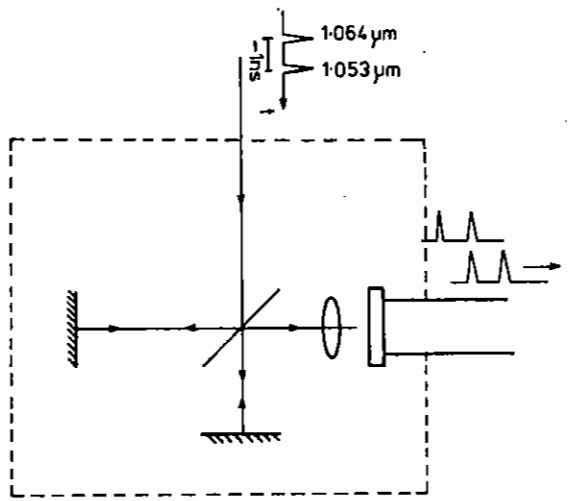

Fig A1.5 The Michelson interferometer used to recombine the desynchronised YLF and YAG beams. The dotted line represents a perspex box flushed with Argon.

arm and the second (1.053 μm) pulse from the second arm will be coincident. To further minimise the air region in which both wavelengths are synchronous the Michelson arrangement was enclosed in a perspex box which was continuously flushed with argon.

Unfortunately, the S(11) line of nitrogen is pressure broadened at STP and does not become Doppler dominated until the pressure falls below 0.5 Torr. This implies that the residual gas within the evacuated pinch vessel still contributes significantly to the rotational scattering. This can be reduced in future by improved vacuum pumping.

With the Michelson in place and filled with argon the level of rotational Raman scattering (see Fig A1.6) is very substantially

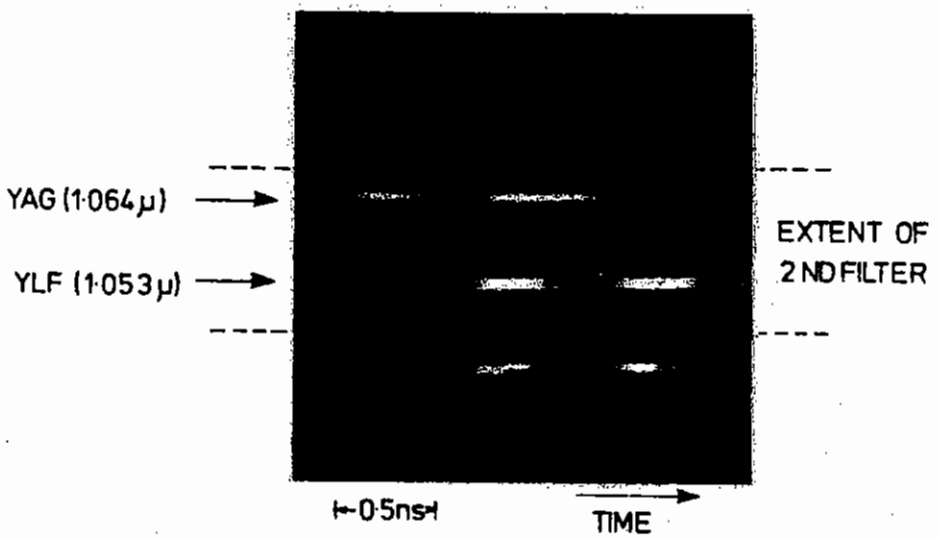

Fig A1.6 A time resolved spectrum obtained with the Michelson interferometer in place. The central region of the spectrum containing YLF and YAG lines is attenuated by a neutral density ND2.0 filter.

reduced compared with Fig A1.2 but is still large enough to compete with the expected beat wave signal. The introduction of the Michelson arrangement results in only one quarter of the laser energy being effective in driving the beat wave, reducing the expected electric field of the beat wave by the same factor, and the relative plasma sideband intensity by a factor of sixteen. Exactly at resonance the plasma beat wave might just have been detectable, but the expected high Q of the resonance made it impossible to find the small off resonant signal and use this to tune in the plasma density.

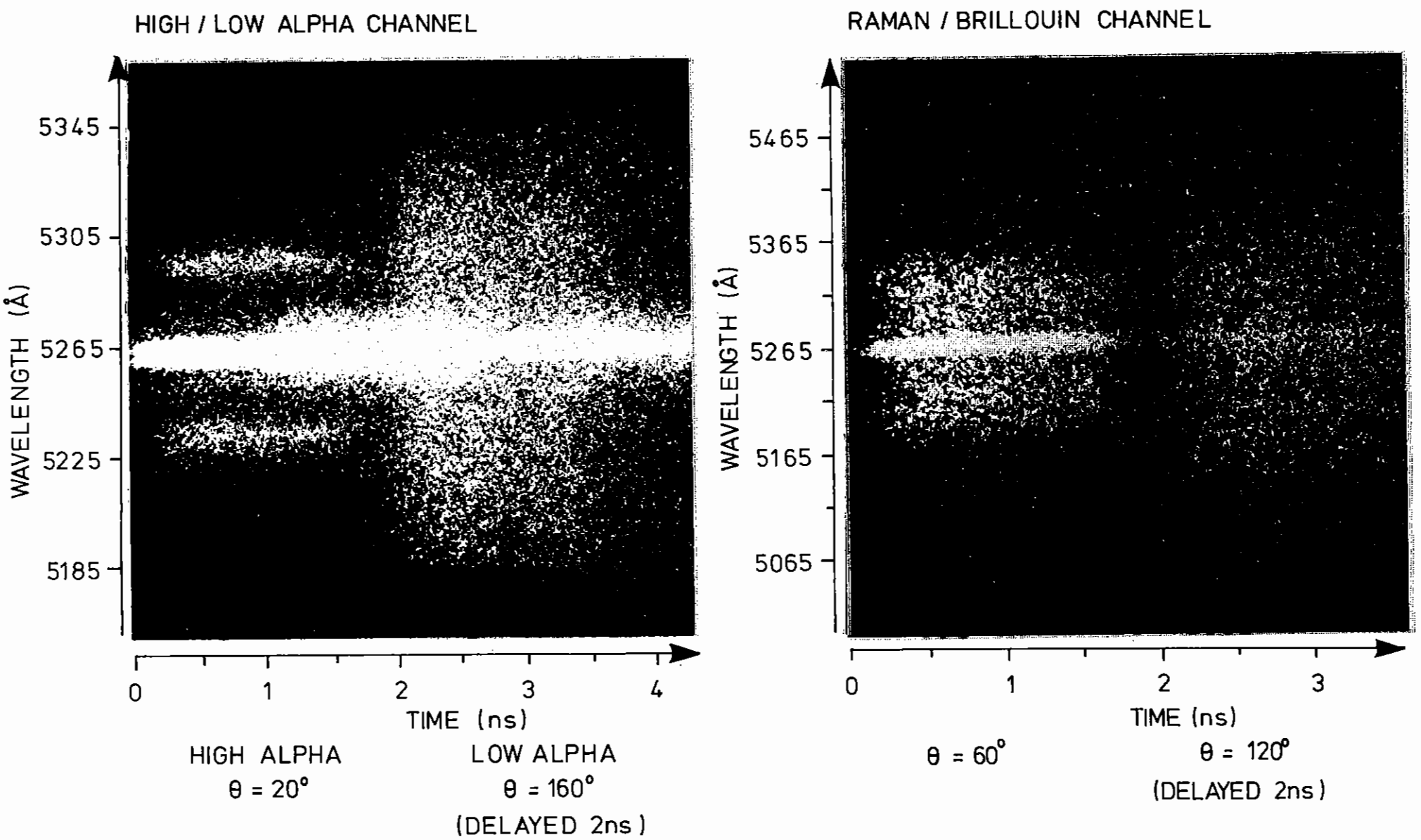

Fig A1.7 Time resolved Thomson scattering at four different angles obtained from a multiphoton ionised plasma.

A1.1.4 Single Frequency Multiphoton Ionisation Results

One of the long term problems of beat wave experiments is that a long path length of very homogeneous plasma is required, uniform to better than 1%. This is beyond the capability of plasma discharges and pinches and it has been suggested that the lasers used to drive the beat wave could produce the required ionisation in a neutral gas by multiphoton absorption. For this part of the experiment the Z-pinch discharge was disabled and the 0.53 μm 'probe' beam was used both to produce the ionisation in the hydrogen gas and as a Thomson scattering probe beam. This meant that no spatial uniformity measurements could be made.

Gas filled pressures in the range 0.5 Torr to 4.0 Torr were set on a Vacustat mercury gauge and the range of laser energies was from 1J to 40J in a 1 nsec pulse as measured after passing through the pinch vessel. The focal spot of the 1 metre focussing lens used for the 0.53 μm beam was estimated to 150 μm diameter since it was only just possible to obscure the focus with a microballoon of this size.

Typical Thomson scattering results from the High/Low alpha and Raman/Brillouin channels are shown in Fig A1.7. Data from all available scattering angles are fitted simultaneously to theoretically predicted profiles, allowing for film response, spectral sensitivity variations and the spectrometer slit function. Ideally the high alpha (20^0) channel would give density directly with only a small temperature correction but for the parameters of this experiment the scattering α was not large enough and the computer curve fitting was needed. An example of the curve fitting procedure is shown in Fig A1.8.

It is apparent from Fig A1.7 that there is little or no change in density or temperature during the laser pulse and this is borne out by the curve fitting procedures. The densities and temperatures quoted are measured about 300 ps into the pulse but apply to the whole of the 1 nsec scattering pulse duration.

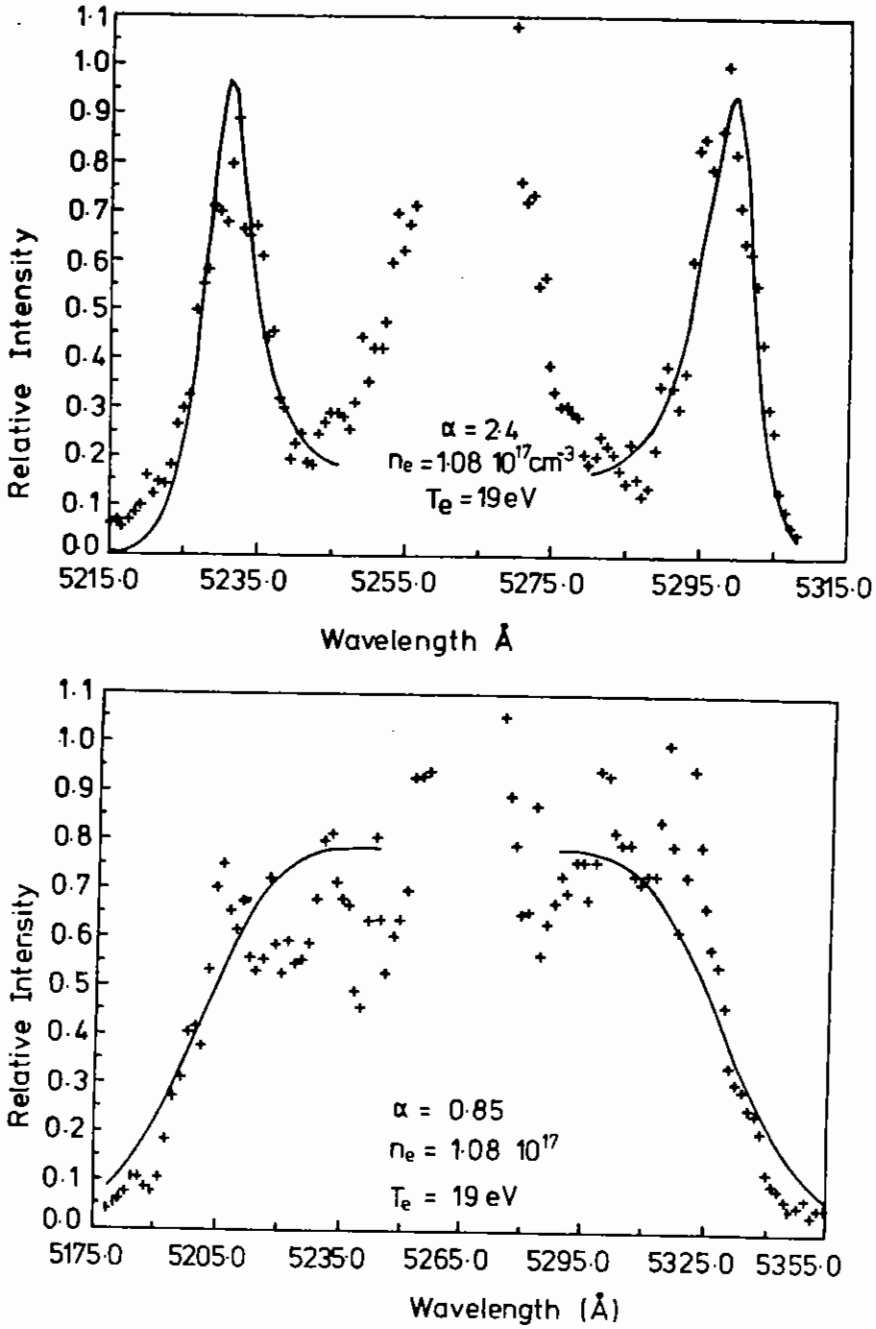

Fig A1.8 Intensity corrected Thomson scattering profile from (a) the 20 degree, high alpha channel and (b) the 60 degree channel, together with the computer generated best fit curve.

The reduced data for electron temperature are shown in Fig A1.9. The temperature increases with laser irradiance up to about

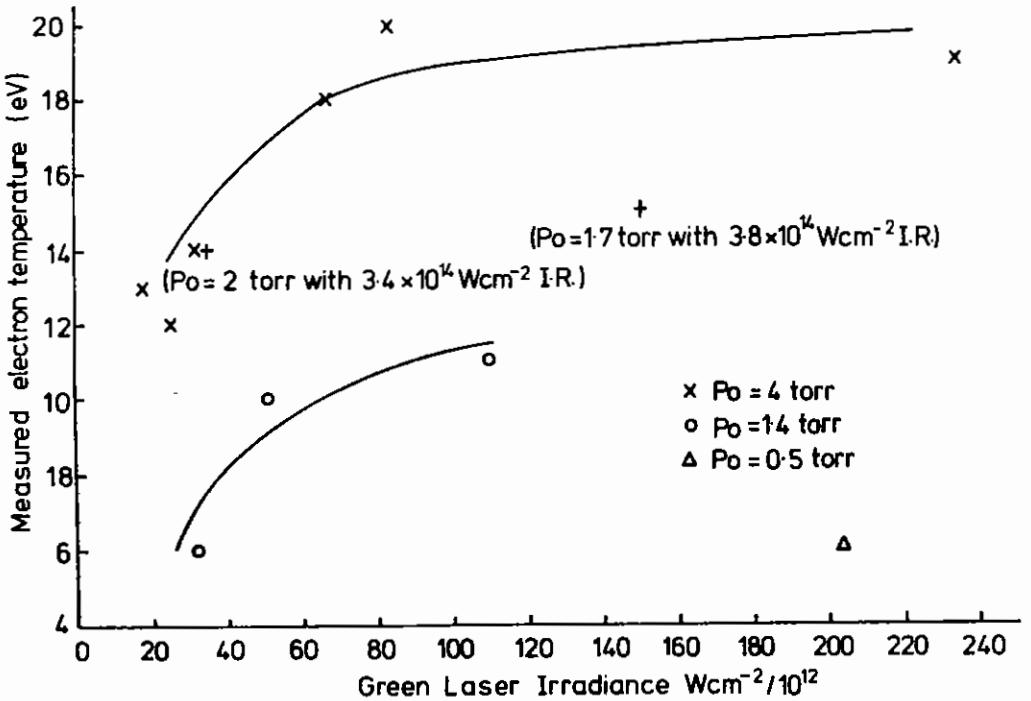

Fig A1.9 Variation of electron temperature with laser irradiance at three gas fill pressures: Δ 0.5 torr; O 1.4 torr; X 4.0 torr. Two points are included (+) with both infra-red and green laser beams heating the plasma.

0.5×10^{14} W cm^{-2} but thereafter remains constant. The temperature is markedly dependent on the fill density, going from 6 eV at 0.5 Torr to 20 eV at 4.0 Torr. This behaviour is consistent with the strong field modification of inverse bremsstrahlung absorption. When the oscillating velocity of the electron in the electromagnetic field of the laser $v_{osc} = \frac{eE}{m\omega}$ becomes comparable to the thermal velocity $v_e = \sqrt{kT/m}$, the effective collision frequency is modified and becomes approximately $\nu_{eff} = \nu_o \left(\frac{v_e^2}{v_e^2 + v_{osc}^2}\right)^{3/2}$. Since this asymptotically behaves as v_{os} it will ultimately fall off as the

irradiance is increased. On the other hand the absorption is proportional to the square of the density while the heat capacity is only linear in the density, giving higher temperatures at higher density.

The measured electron density does not depend on laser energy, the lower limit on laser energy was set by the reduced level of scattered light rather than the absence of ionisation. The density as a function of fill pressure is shown in Fig A1.10 and shows that the density is

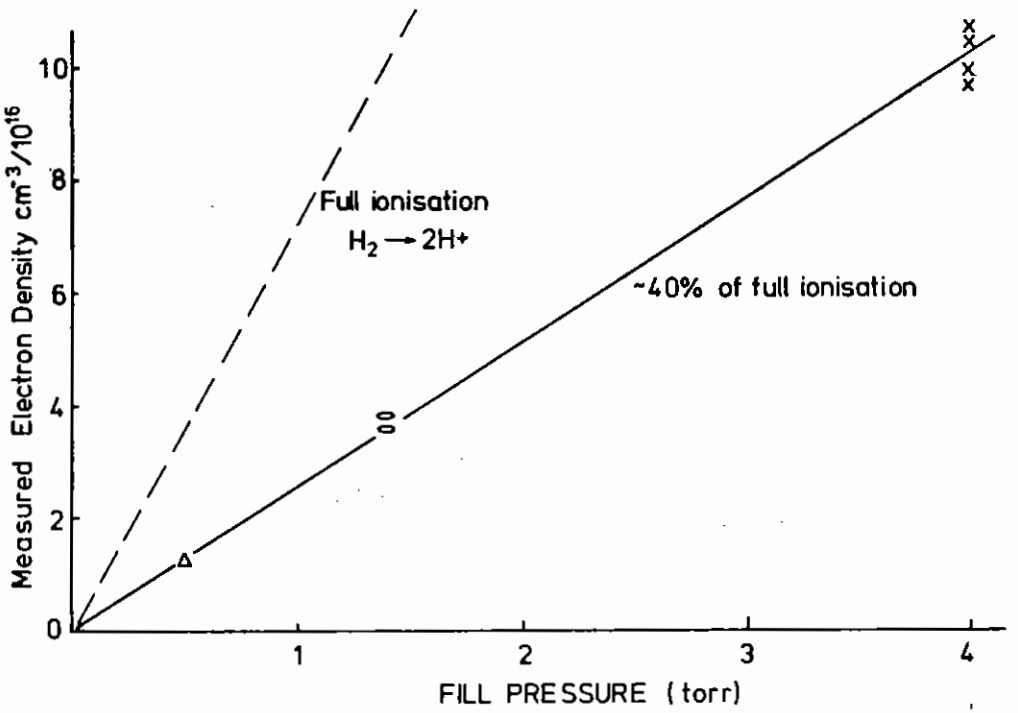

Fig A1.10 Variation of measured electron density with gas fill pressure. The ionisation fraction is measured with respect to the nominal gas fill pressure.

proportional to the fill pressure, but corresponds to only 40% of what would be expected from total ionisation of the H_2 molecules. Bearing in mind the inaccuracies of the pressure gauge and the measurement of the spectral dispersion of the spectrometer/streak camera this result is consistent with the formation of the hydrogen molecular ion H_2^+.

There is considerable evidence to suggest that this cannot be the case since at a temperature of 20 eV and density of 10^{17} cm^{-3} the collisional ionisation rate for $e + H_2^+ \rightarrow H^+ + H^+ + 2e$ is about 1.6×10^9 s^{-1}. There should then be a marked change in electron density during the 1 nsec scattering period, but none is observed. Experimental data on multiphoton ionisation of molecular hydrogen (A1.3) (λ = 6943 Å) shows an ionisation rate of 10^6 s^{-1} at 2.10^{11} W cm^{-2} (with a ruby laser) and a rate scaling as I^7. This gives a rate of 10^{13} s^{-1} at 2.10^{12} W cm^{-2} so the multiphoton ionisation will occur very early in the laser pulse. The rates for a laser wavelength of 5265 Å would almost certainly be substantially greater than for the ruby laser. At 2.10^{11} W cm^{-2} about 10% of the observed ions were H^+ rather than H_2^+ and this fraction should increase rapidly with increasing intensity.

All the background information leads to the conclusion that the hydrogen must be fully ionised, and to reconcile this with measured values we must assume that there is an error in measuring the pressure in the focal region. The vacuum gauge is "upstream" relative to the focus and the pumping port, and could possibly give rise to the necessary pressure differential.

A1.2 12 BEAM THERMAL TRANSPORT EXPERIMENT AT 1.05 μm IN SPECTRAL GEOMETRY

S D Tabatabaei, O Willi, D K Bradley, D J Bassett (I C),
A J Cole, E Turcu (RAL)

1.2.1 Introduction

The transport of thermal energy by electron heat conduction in laser produced plasmas has attracted a great deal of experimental and theoretical study. Energy transport from the hot corona to the relatively cool ablation front is essential in generating the high pressures needed for laser fusion but the temperature gradients are so steep that the Spitzer diffusion theory breaks down.

This section described a comprehensive series of experimental measurements of observable quantities which depend on the heat flow, ie ablation rate, temperature, density profiles, and in the case of non-uniformily irradiated targets, magnetic fields. The experiments are performed in spherical geometry and for the most part with uniform illumination from the CLF 12 beam system. This is to produce an essentially 1D spherically symmetric plasma for comparison with hydrodynamic models. The experiment was performed by a collaboration between Imperial College, Lawrence Livermore National Laboratory, USA, the Los Alamos Laboratory, USA and staff of the RAL.

A1.2.2 Experimental Arrangements

A variety of diagnostic equipment was set up as listed below and shown in Figures A1.11 and A1.12.

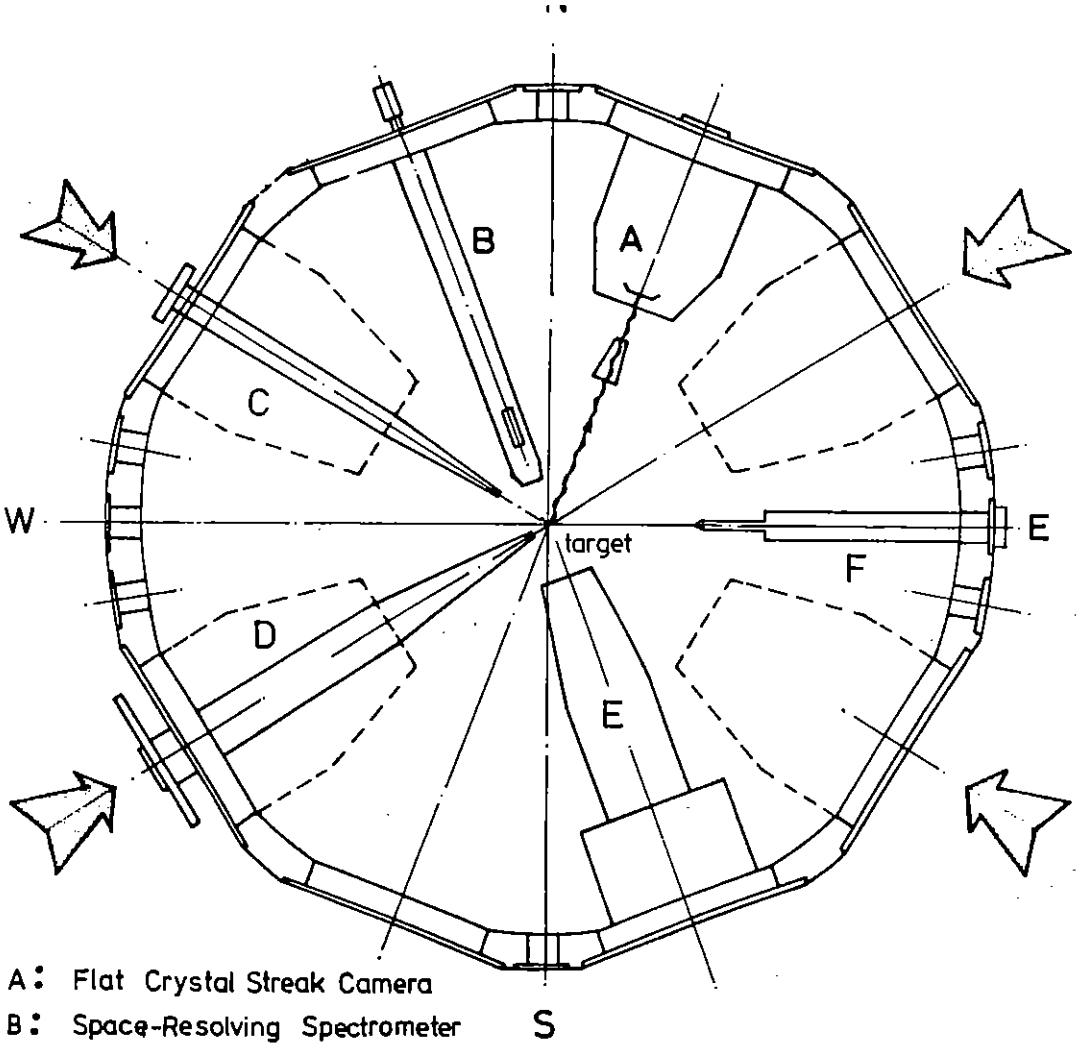

A: Flat Crystal Streak Camera
B: Space-Resolving Spectrometer
C: Static low-mag pinhole Camera
D: Active high-mag pinhole Camera
E: X-ray diode array
F: Los Alamos passive 6-pinhole camera

Fig A1.11 Diagnostic equipment for the twelve beam thermal transport experiment.

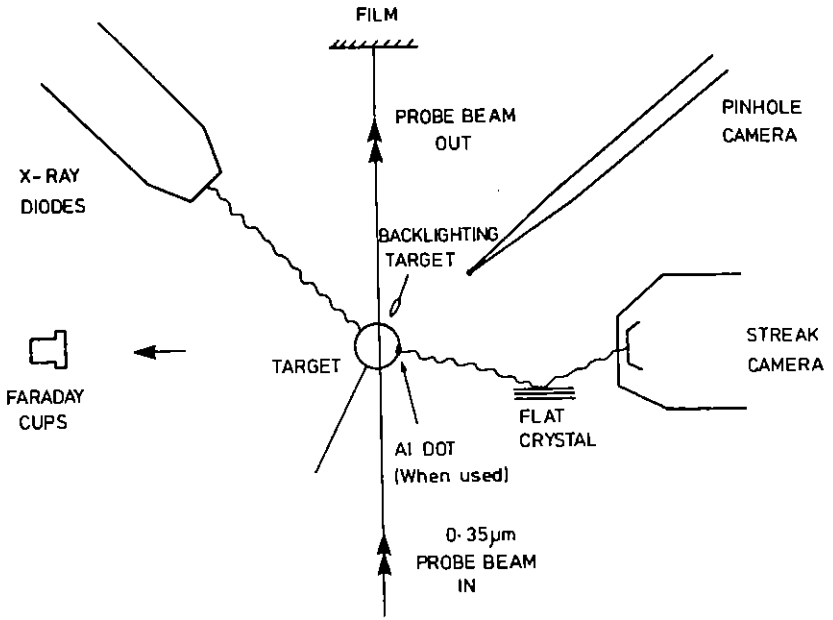

Fig A1.12 Arrangement of the probe beam, backlighting target and Aluminium tracer dots.

1) Time resolved x-ray spectroscopy of line and continuum emission from plasma was used to obtain data for burnthrough and temperature profile measurements. Various flat crystals were used to obtain the required dispersion and spectral range. A separate laser beam with very short pulse duration (~ 100 ps) was used to generate an x-ray time fiducial from a thin gold layer placed near the main target, see Figure A1.13.

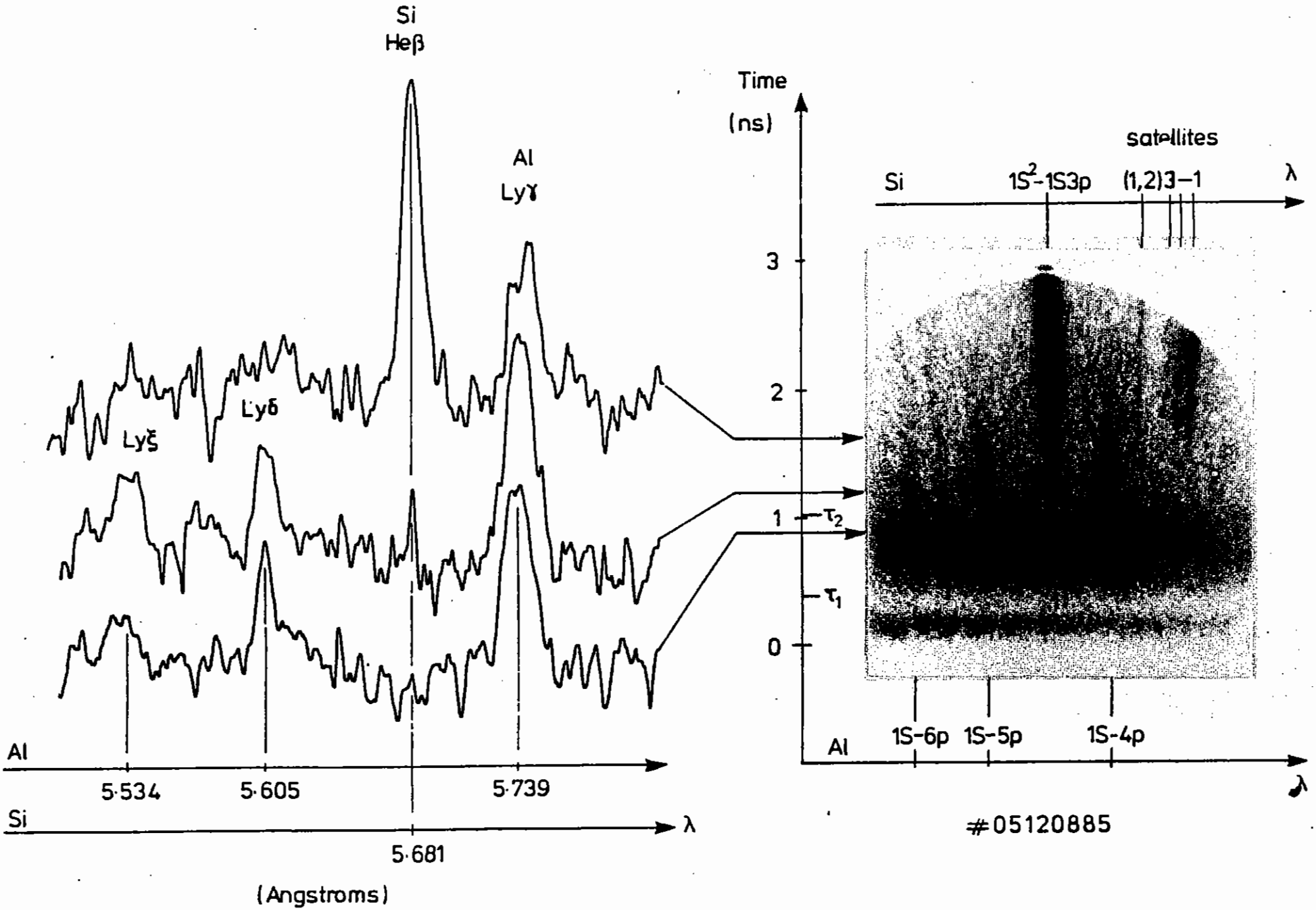

Fig A1.14 Time resolved Al and Si line emissions from a multilayered spherical target irradiated uniformly by twelve beams in a 4 nsec pulse.

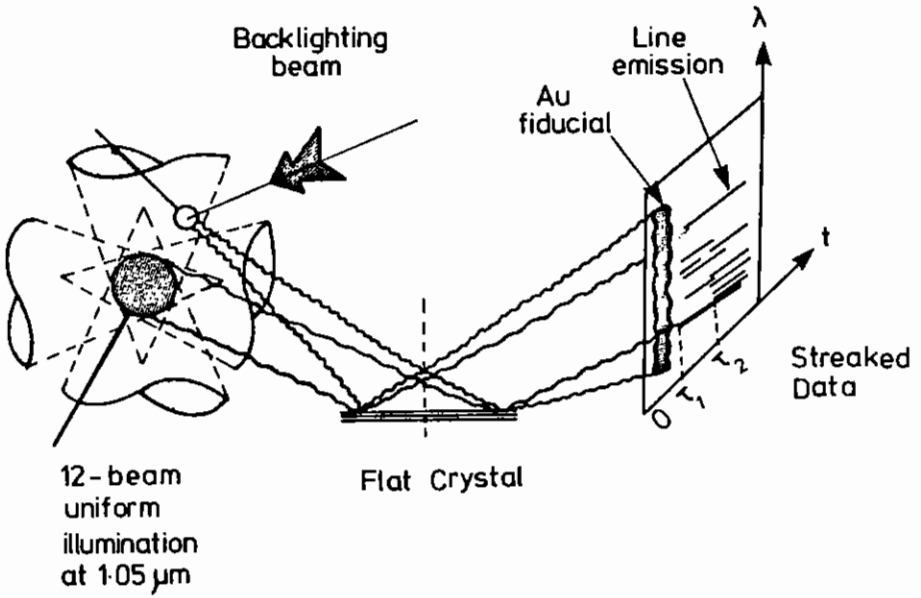

Fig A1.13 The X-ray timing fiducial using the Gold backlighting target.

2) An optical probe was used to measure the density profile of the underdense plasma ($n_e \leq n_c$) by interferometric technique using a 40 ps 0.35 μm laser beam. This interferometric technique was elaborated later on in the course of the experiment to a novel 4-frame interferometer each separated by 350 ps in time giving a time history of the target blow-off conditions.

3) The magnetic field generated in the plasma under non-uniform irradiation was measured by Faraday rotation with a 30 ps, 0.62 μm Faraday rotation probe beam, probing densities as high as 0.6 n_c.

4) A seven-channel Si PIN diode array with different filters covering an energy range of 2.8 - 25 Kev was used to measure the hot electron temperature from the x-ray continuum slope.

5) Faraday cups, placed at different locations inside the target chamber, were used to measure the ion velocity distribution.

6) A high-magnification active pinhole camera was used to monitor the focussing condition on every shot. This together with a low-magnification passive pinhole camera placed in the opposite hemisphere of the target chamber provided a complete coverage of the focal spot sizes of all twelve beams irradiating the target. The latter camera was designed and made at Los Alamos Laboratory and was equipped with a 6-pinhole array of the same sizes but filtered differently for different x-ray energies. Another static pinhole camera of magnification 7 was placed in the same hemisphere as the active pinhole camera but closer to the streak camera to obtain images of the target when dot-targets were used, as these dots faced the streak camera only, see Fig A1.12.

7) An array of five ion calorimeters was used to measure the absorbed irradiance by the target. They were placed around the inside of the target chamber viewing the plasma at various angles. The calorimeters consisted of pairs of tantalum discs, one exposed to the plasma (collecting x-rays and scattered light) and the other exposed to the scattered light only.

A1.2.3 Targets

The targets used throughout this work were composite layered types, consisting of solid glass spheres of average diameter equal to 160 μm doped with calcium and coated with variable layers of CH ranging from 0.1 μm to 4 μm, a thin layer of aluminium of thicknesses 0.025, 0.05 and 0.1 μm and finally a thin CH overcoat layer of varying thickness ranging from 0.06 μm up to 2.5 μm. In some cases larger glass spheres of 220 and 360 μm diameter were used to increase the density scale length. Single aluminium and silicon dots were also deposited on some of the targets. A1.2.4 Measurements Made

A1.2.4 (a) The mass ablation rate

Time-resolved spectroscopy of the x-ray emission from the different emitting layers was used to measure the mass ablation rate of spherical targets.

The dispersing crystal used was a flat TlAP crystal (2d = 25.75Å) in Bragg geometry. In order to reference the onset of x-ray emission to the arrival of the laser pulse at the target surface, a short pulse beam synchronized with the main pulse was used to burn a thin layer of gold deposited on a plastic disc placed 2 mm away from the main target. The x-ray emission from the M-band of this gold backlighter produced a time fiducial on the x-ray streak record, see Fig A1.13. The mass ablation rate was then estimated by taking the delay τ_1 between the gold and aluminium emission as the time needed to ablate the first plastic layer and the delay τ_2 between the Aℓ and Si lines as the time needed to ablate the Aℓ and the inner plastic layer which separated these two elements.

The specific mass ablation rate $\dot{M}_s$ was calculation from (A1.4):

$$\dot{M}_s = \frac{P}{C\tau_b}$$

where, P is the area density of the initial plastic layer or initial aluminium and plastic layers, τ_b is the burn-through time for the layer(s) concerned and C is a correction factor close to unity which allows for the time variation of the ablation rate due to the shape of the pulse (A1.5). The time resolved line emission data from different elements and their measured delay time for laser pulse lengths 0.1, 1.5 and 4 nanosecond are presented in Figs A1.14, A1.15 and A1.16. The preliminary analysis of the mass ablation rate together with shot specifications for some of the data shots is presented in Table A1.1.

A1.2.4 (b) Temperature Gradient

Time-resolved x-ray line emission from low-Z and medium-Z elements was used to determine the steepness of the temperature profile of the heat front. The estimated effective radiating temperatures for local thermodynamic equilibrium conditions at a density slightly above critical are, 200 - 350 ev for aluminium, 250 - 400 ev for silicon and 500 - 700 ev for calcium in the glass core. Thus an aluminium line at 1.87 Kev ($1s^2 - 1s3p$) probes temperature contours near 350 ev, while using Si and Ca lines at 2.2 Kev ($1s^2 - 1s3p$) and 3.9 Kev ($1s^2 - 1s2p$), probe higher temperatures nearing ~ 400 ev and ~ 700 ev respectively (A1.6, A1.7).

The difference between the time of emission of these lines corresponding to the low-Z and medium-Z elements is thus a measure of the steepness of the heat front.

The data presented in Fig A1.14 represents one of the data shots where Ca-Heα ($1s^2$–$1s2p$) at 6.35Å in second-order is clearly seen. The measured delay between the Si-Heβ ($1s^2$–$1s3p$) was ~ 150 ps from the streaked data, for uniformly illuminated target with a nominal pulse length of 1.5 ns. The Ca-Heα in second order was obtained by

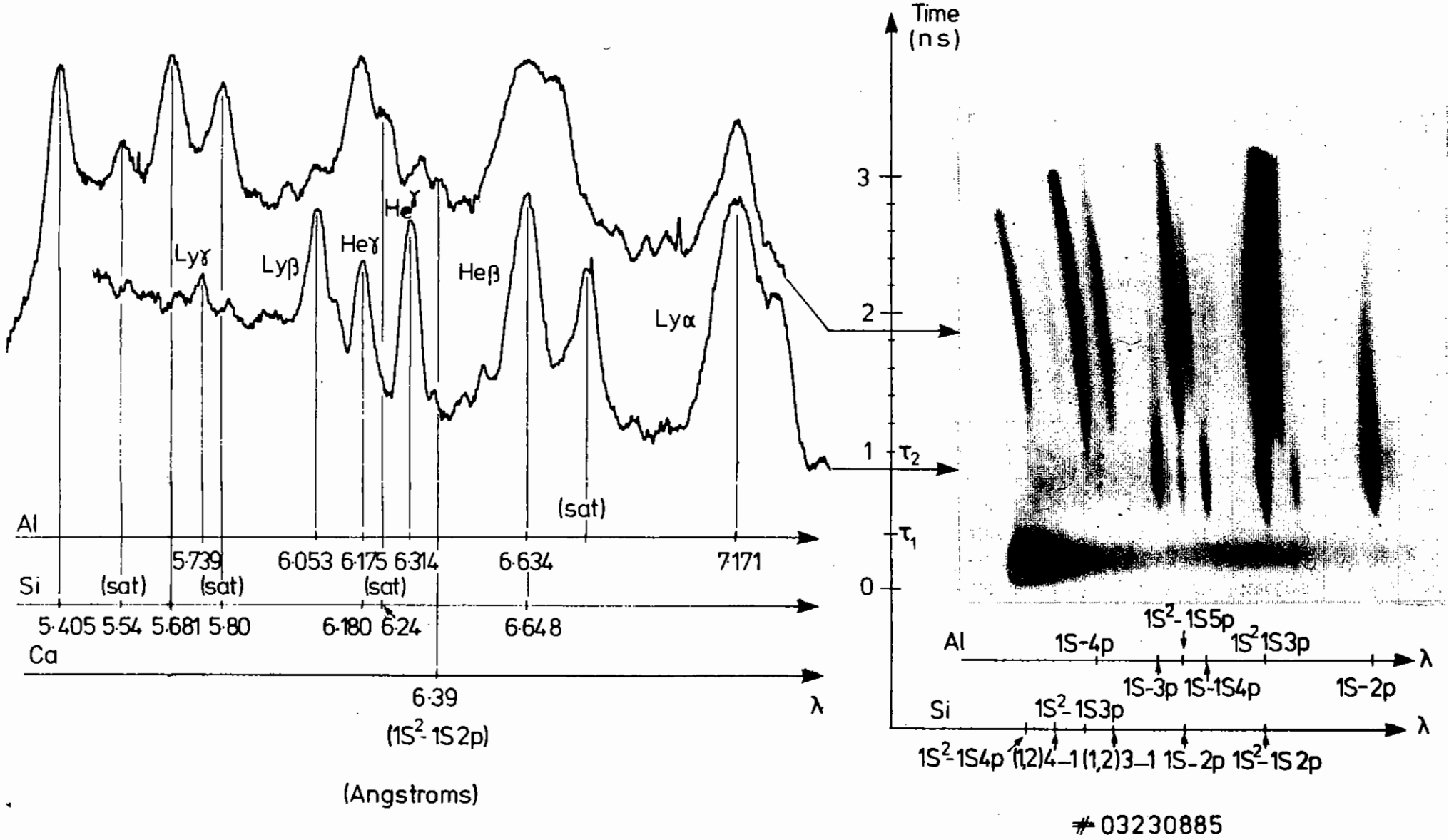

Fig A1.15 Time resolved Al, Si and Ca line emissions from a multilayered spherical target irradiated uniformly by twelve beams in a 1.5 nsec pulse.

TABLE A1.1 Typical target and laser conditions of some of the data shots analyzed together with their measured mass ablation rates

	laser parameters						target parameters									
								Inner		Middle		Outer				
number	shot number	no of beams	average energy per beam	I inc per beam	pulse length	focussing condition	type	material	thickness	material	thickness	material	thickness	glass core diam.	R overall	
Units	- - -	- - -	J	Wcm^{-2}	ns	- - -			μm		μm		μm	μm	μm	$gcm^{-2}\ s^{-1}$
1	08090885	12	141	2.8×10^{13}	4	obsc.	layer	CH	1.5	Aℓ	0.05	CH	1.1	171.5	88.4	1.22×10^{5}
2	05120885	12	95.5	2.3×10^{13}	4	obsc.	layer	CH	0.8	Aℓ	0.1	CH	1.1	157.6	80.8	1.13×10^{5}
3	13140885	12	29	2.3×10^{13}	1.5	obsc.	layer	CH	1.35	Aℓ	0.1	CH	0.79	158.1	81.3	-
4	04190885	12	64.4	1.7×10^{14}	1.5	v. tight	layer	CH	1.36	Aℓ	0.1	CH	1.56	153.5	79.8	2.02×10^{5}
5	06	12	106.3	3.0×10^{14}	1.5	v. tight	layer	CH	1.35	Aℓ	0.1	CH	0.96	145.7	75.3	4.0×10^{5}
6	03200885	12	113.3	6.5×10^{13}	1.5	obsc.	layer	CH	0.6	Aℓ	0.1	CH	1.5	165.0	84.7	0.1×10^{5}
7	07	12	124.3	7.3×10^{13}	1.5	obsc.	layer	CH	0.6	Aℓ	0.1	CH	0.8	165.0	84.0	1.43×10^{5}
8	08220885	12	12.4	2.7×10^{14}	0.1	tight	layer	Kc	0.1	Aℓ	0.1	CH	0.1	162.7	81.7	-
9	10	12	18.3	1.8×10^{14}	0.1	tight	layer	Kc	0.1	Aℓ	0.1	CH	0.1	159.8	80.2	-
10	12	12	10	1×10^{14}	0.1	obsc.	layer	CH	0.1	Aℓ	0.05	CH	0.06	156.9	78.7	-
11	03230885	12	26.8	1.9×10^{13}	1.5	obsc.	layer	CH	0.74	Aℓ	0.06	CH	0.4	151.8	77	1.67×10^{5}
12	16	12	971	5.2×10^{13}	1.5	obsc.	layer	CH	4	Aℓ	0.025	CH	0.6	166.0	87.6	

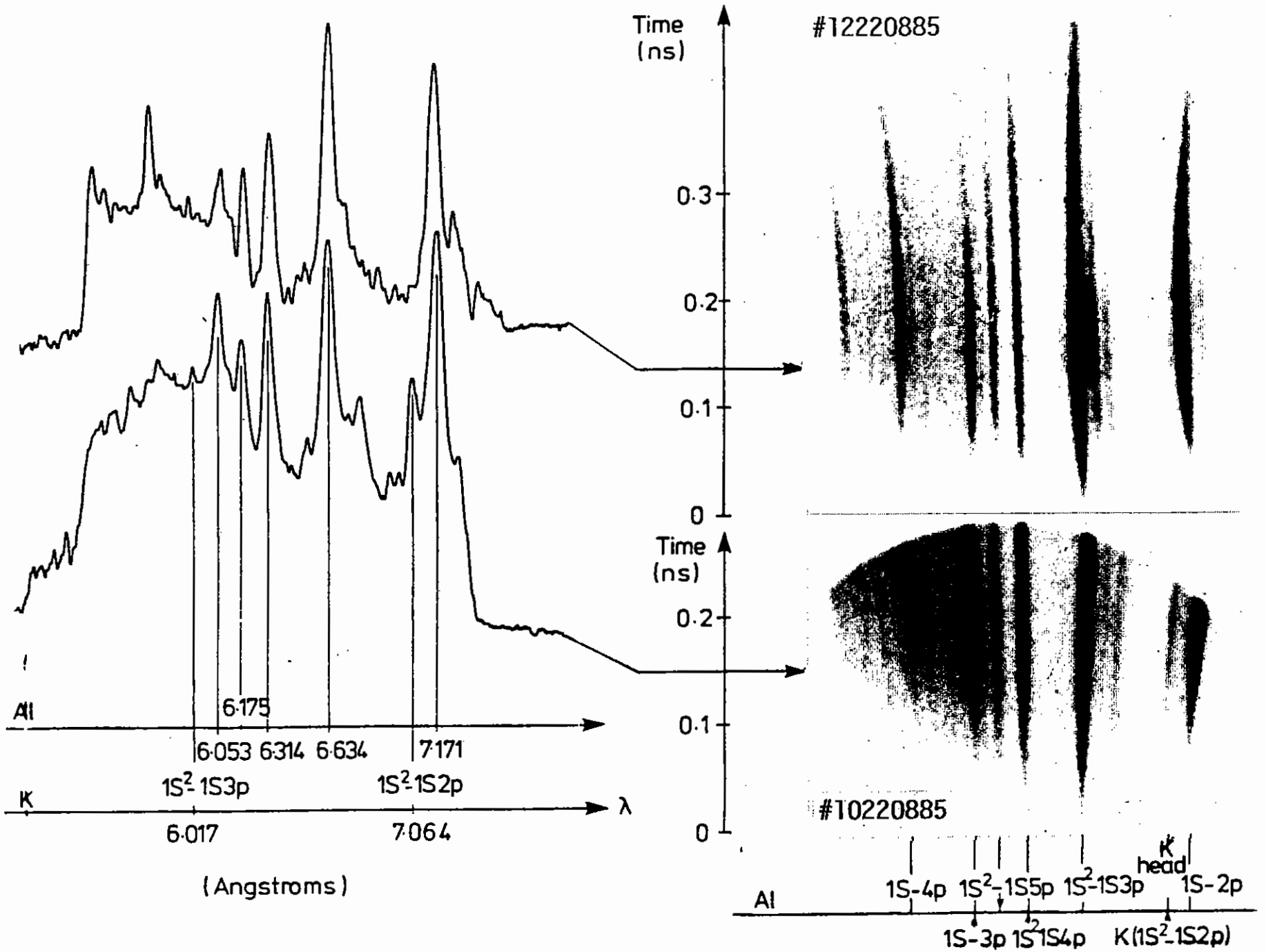

Fig A1.16 Time resolved Aℓ, Si and K line emission from a multilayered spherical target irradiated uniformly by twelve 0.1 nsec pulses.

attenuating the bright Aℓ and Si lines by choosing a suitable filter thickness which would transmit most of the Ca line intensity at 3.18Å. A more rigorous analysis involving the inclusion of the film response in the measurements is in progress. The rise time between the effective temperatures of silicon and calcium is thus a small fraction of the burnthrough time interval given by the streaked data. This indicates a relatively steep heat front. This measurement is yet to be compared with a non-LTE calculation.

The scale length of the heat front was experimentally measured by irradiating a target with a thin layer of 0.1 μm thick KCℓ deposited between the Aℓ layer and the glass sphere. The time of K-Heα emission (recorded in second order) gave an estimate of this scale length, see Fig A1.15.

A1.2.4 (c) The Electron Temperature (Te)

Time resolved x-ray spectroscopy was used to measure the electron temperature (T_e) from the slope of the aluminium recombination continuum emitted by the aluminium plasma in the Corona (A1.8). The slope was obtained by microdensitometer scans along the spectrum at different times. The dispersing crystal used was the same flat TℓAP crystal which was used for mass ablation rate measurements. To measure the slope of the recombination continuum accurately, the reflectivity of the crystal within the spectral region concerned must be known. Thus an accurate calibration of the crystal was necessary and is being carried out at LLNL.

A1.2.4 (d) Hot Electron Temperature (T_H)

A seven-channel Si PIN diode array with different filters covering 2.8 - 25 KeV energy range was used to record the integrated x-ray emission from the target plasma. The choice of the filters used (see Table A1.2) gave the thermal and hot-electron temperatures from the

TABLE A1.2. Table of K-edge filters used in the x-ray diodes.

no.	element	Area Density		K-edge
		needed	used	
units		mg cm^{-2}	mg cm^{-2}	KeV
1	PVC	4.6	4.0	2.82
2	Ti	12.2	11.3	4.97
3	Fe	18	19.6	7.87
4	Ni	21	22.3	8.9
5	RbBr	42	45.1	13.47 15.20
6	Y	57	57.0	17.04
7	mo	71	76.5	20.0
8	Ag	102	105.5	25.5

x-ray continuum slope. On average, for an incident irradiance of about 1 x 10^{15} Wcm^{-2}, under uniform illumination with a 1.5 ns pulse, T_H and T_{th} were measured to be ~ 6.0 Kev and ~ 1.6 Kev respectively.

A1.2.4 (e) Density Measurements Using Stark Broadening

Time-resolved x-ray emission from high principal quantum number aluminium Lyman lines was obtained to measure the electron density, n_e, from Stark broadening of these lines (A1.9) as emitted from thin layers or dots. The streak camera used was equipped with a high-dispersion flat PET crystal (2d = 8.742Å) with a dispersion of ~ 15 mÅ/mm at the centre of the spectral range considered.

The aluminium line used was Aℓ Lyγ (1s-4p) at 5.739Å. The complete analysis of these data is still in progress.

A1.2.4 (f) Ion Velocity

An array of five Faraday-cups, placed in different parts of the target chamber, was used to measure the velocity amd relative mass of the ion flow (A1.10, A1.11). The cups were placed normal to the target chamber walls a distance of r = 47 cm away from the target, viewing different parts of the target. The peak ion velocity, V_p, was estimated from:

$$V_p = \frac{r}{\Delta t}$$

where r is the cup-plasma distance and Δt is the delay time of the peak of the Faraday-cup current. V_p was typically 4.6 x 10^7 cm s^{-1}.

A1.2.5 Conclusions

This experiment has generated a large amount of data which is still being analysed. On the basis of data already available we can say that:

a) New data has been obtained on the heat from propagation and ablation processes as a function of laser pulse length.

The ablation rate in the transient regime (100psec) is greater than in the steady state regime (1nsec).

b) The heat front into the solid is "steep" as evidenced by the relative turn on of different X-ray lines. This contradicts data from other laboratories suggesting that a low temperature "foot" precedes the heat front, but is in better agreement with the Fokker Planck modelling.

When more data is analysed we will be able to compare the measured ablation rate with theoretical models and assess the effects of non-uniform illumination and magnetic field generation on electron energy transport.

References:

A1.1 C E Clayton, C Joshi, C Darrow and D Umstadter, Phys Rev Lett 54, 21 2343 (1985).

A1.2 F Martin, P Brodeur, F Laroche, H Pepin, P Lavigne, N A Ebrabin, Paper presented at the 1985 APS Plasma Physics Meeting.

A1.3 G S Voronov, G A Delone, N B Delone, O V Kudrevatova Soviet Phys JETP Letters vol 2 No 8 p 237 (1965).

A1.4 M H Key, C L S Lewis, J G Lunney, A Moore, and J M Ward, Phys. Rev. Lett. 44 (1980) 1669.

A1.5 Annual Report to the Laser Facility Committee 1981, RL-81-040, T J Goldsack et al, pp. 4.13.

A1.6 Laboratory for Laser Energetics, University of Rochester, Rochester. NY 14623, Report No. 136 (1982) B Yaakobi et al.

A1.7 J D Kilkenny et al, Phys. Rev. Lett 53 (1984) 2563.

A1.8 Annual Report to the Laser Facility Committee 1985, RAL-85-047, S D Tabatabaei, B J MacGowan, PP A1.21.

A1.9 H R Griem, Plas, a Spectroscopy, McGraw Hill (1964)

A1.10 A Raven, P T Rumsby, and J Watson, Rev. Sci. Instrum, 51 (1980) 351.

A1.11 M H Key et al, Phys. Fluids, 26 (1983) 2011.

pages

A2 DYNAMICS AND COMPRESSION OF LASER DRIVEN TARGETS

Editor: A J Cole

A2 DYNAMICS AND COMPRESSION OF LASER DRIVEN TARGETS

A2.1 TWELVE BEAM COMPRESSION EXPERIMENTS

J Corbett, C L Lewis, Queens University Belfast
A Cole, M H Key, RAL

Following the successful twelve beam compression of low aspect ratio (~8) plastic shells [A2.1] a systematic investigation of the performance of higher aspect ratio (up to 20) targets was undertaken. The purpose of the experiment was to study implosion symmetry and peak density as a function of absorbed power, irradiation uniformity, shell size and wall thickness and to attempt to quantify the extent of effects such as irradiation non-uniformity and shell decompression by comparison with the results of the one dimensional hydrodynamic code MEDUSA. The main diagnostic used was conventional extended source backlighting [A2.2]. A 0.53 μm backlight beam was used rather than the 1.06 μm used previously, to enhance source brightness, with the result that the backlight source was less uniform than before.

This experiment was carried out in the twelve beam target chamber of TAW using the same geometrical arrangement and essentially the same diagnostics as described in Section A2.2 of last years annual report [A2.1]. The initial beam timing was achieved by observing the visible reflections on low power laser shots from a target placed in the centre of the chamber, using an optical streak camera, and beam arrival times had a total spread of less than 20ps. The delay between the driver and backlight pulses was initially set to zero and thereafter monitored using another optical streak camera and varied by an optical path adjustment. The beam surface positioning accuracy was also improved to become, under surface focus conditions, 5-7% of the target diameter. Maximum green energies of 300J were achieved in a pulse which was approximately gaussian with a FWHM of 800ps. More accurate energy absorption measurements were made with calibrated plasma calorimeters and the revised absorption vs d/r curve is shown in Fig A2.1. All compression shots were carried out with d/r = +10 giving 30% absorption and maximum absorbed energies of 70J (taking into account losses in the optics). Beam balance, which is achieved by first optimally tuning the

frequency-doubling crystals and then adjusting half wave plates to match the energies to the lowest, was impeded by 'teething troubles' in the newly commissioned switchyard and was at best 10%, typically worse.

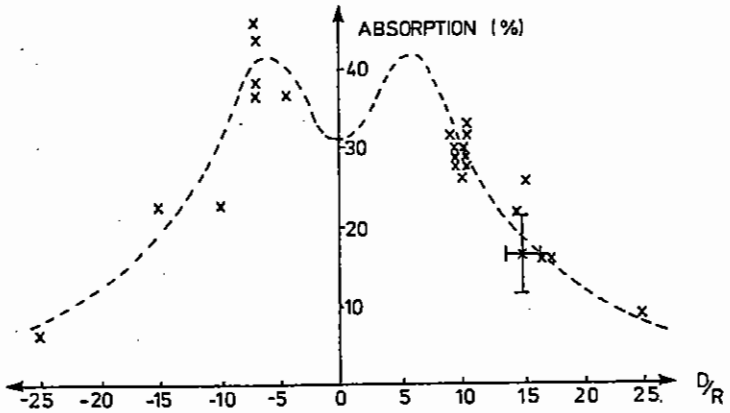

Fig A2.1 Percentage of incident laser energy absorbed as a function of d/r.

The targets used were hollow polymer shells with diameters 140-200μm and aspect ratios 7-20, mounted on 7μm carbon fibres. The backlight targets were 275/550 μm Cu/Au lollipop-type foils 3-13 μm thick. The active pinhole camera's pinhole limited resolution was > 6μm. The filtering was chosen to give a transmission peak for the Au M shell centred at 2.4 Kev with duration < 100ps or the Cu L shell emission centred at 1.2 Kev with duration < 200ps.

Table A2.1 summarizes the useful results from this experiment. In most of these shots the lack of uniformity of the backlight source was such

that transmission profiles could not be obtained from microdensitometer traces and the shell boundary measurements indicated are obtained by direct measurements from the negatives. In many shots this is subjective as the distribution of mass is not in a homogeeous shell/sphere but indicates localized variations in implosion velocity. This was more apparent for higher aspect ratio shells. Fig A2.2 shows the shots in the table plotted along with a normalized MEDUSA-generated

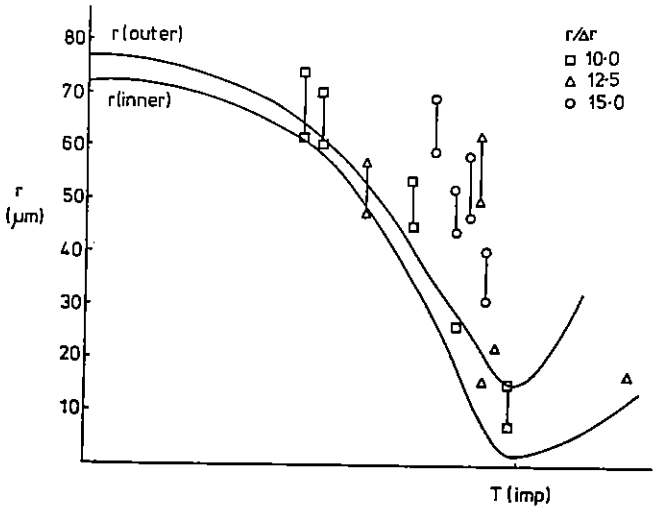

Fig A2.2 Normalised MEDUSA generated implosion trajectories of shell inner and outer boundaries (for an aspect ratio 15.0 shell). Also shown boundary positions at probe times for aspect ratio 10.0 (0), 12.5 (Δ) and 15.0 (0) shells. All probe times shown as fractions of the implosion time.

implosion trajectory giving a semi-quantitative comparison between code and results. Due to the poor uniformity of illumination, we observed on many of the radiographs, taken at around 50% of the implosion time (T(imp)), absorption features associated with the shell indicating jets of material directed inwards. Also, core emission features on a 10 μm scale length were observed but not always geometrically centred, see

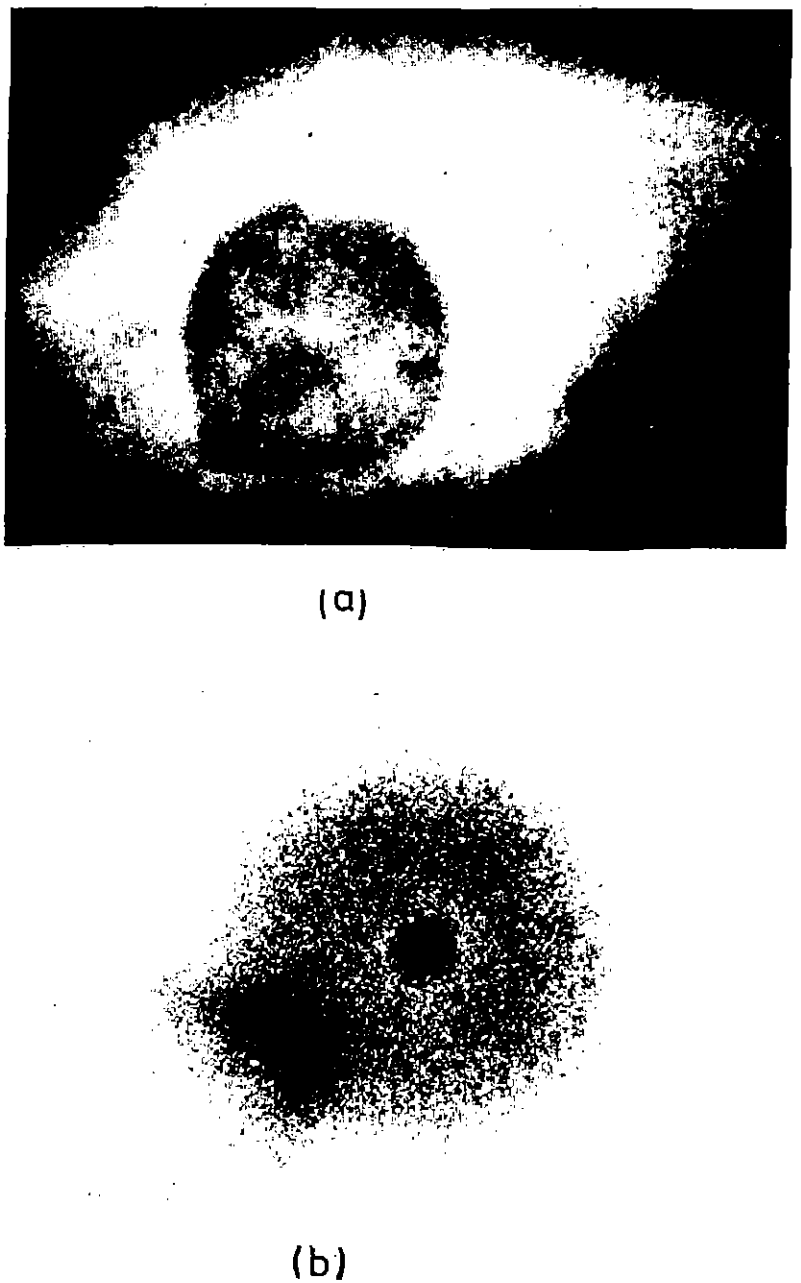

Fig A2.3 (a) 29/10/85 3 (See table A2.1 for details). (b) Typical standard pinhole picture of an aspect ratio 12.5 target irradiance 2.0×10^{14} Wcm^{-2} showing shell self emission.

TABLE A2.1

SHOT No	r (μm)	r/dr	I (Wcm^{-2})	B/ℓ	INNER WALL (μm)	OUTER WALL (μm)	T(pr) (ps)	T(pr) T(imp)	r(expt) r(MED)
25/10 ∓6	80.65	10.7	1.43 $x10^{14}$	Cu	61.0	72.5	200	0.50	1.04
25/10 ∓8	76.25	9.9	1.43 $x10^{14}$	Cu	59.0	68.0	400	0.54	1.11
1/11 ∓1	78.8	9.5	2.48 $x10^{14}$	Cu	12.2	21.5	600	0.94	1.20
23/10 ∓8	74.8	12.5	2.7 $x10^{14}$	Cu		17.0	800	1.26	0.33
23/10 ∓10	75.0	12.5	1.57 $x10^{14}$	Cu		43.0	600	0.92	1.83
23/10 ∓11	76.05	12.5	1.87 $x10^{14}$	Cu	50.0	62.5	400	0.91	1.17
23/10 ∓13	77.5	12.5	1.33 $x10^{14}$	Cu	59.0	68.0	200	0.64	1.01
31/10 ∓12	80.0	12.9	2.6 $x10^{14}$	Au		16.25	400	0.91	0.77
31/10 ∓14	73.35	12.2	1.67 $x10^{14}$	Au		24.5	600	0.95	1.53
24/10 ∓2	75.9	15.0	1.87 $x10^{14}$	Cu	59.0	68.0	200	0.80	1.92
24/10 ∓3	74.0	14.9	1.7 $x10^{14}$	Cu	46.5	58.0	400	0.88	1.84
28/10 ∓3	78.45	15.0	1.33 $x10^{14}$	Cu	31.5	39.5	600	0.92	1.50
29/10 ∓3	76.6	15.6	1.27 $x10^{14}$	Cu	44.0	51.0	400	0.85	1.67
29/10 ∓8	89.0	9.5	2.33 $x10^{14}$	Cu	52.50	60.0	400	0.75	1.26
29/10 ∓9	88.65	10.6	2.13 $x10^{14}$	Au		29.0	600	0.86	0.87
30/10 ∓15	91.6	14.5	0.97 $x10^{14}$	Au		23.0	600	0.78	0.49
30/10 ∓17	91.0	14.5	1.63 $x10^{14}$	Au		23.0	400		

Fig A2.3(a) and A2.3(b). On some shots the core feature appeared elongated or even consisted of two distinct features. Radiographs taken closer to peak compression indicated more spherical distributions of shell material whose spatial scale length closely matched the central non-emitting region observed on standard pinhole pictures - Fig A2.3(b). In fact the inner boundary of the self emission observed on these time integrated pinhole pictures tends to indicate the minimum size of the bulk of the compressed material although the self emission zones within this region are of a much smaller spatial extent. It may be conjectured that these small emission zones are generated by the coalescense of the jets of material travelling faster than the bulk of the shell material and emit their radiation before peak compression. The brightness of the emission tends to increase with both shell aspect ratio and irradiance. Analysis of the self emission spectra was complicated by the presence of bright emission from the glue with which the microballoons are attached to their support stalks. Future experiments (time and space resolved X ray emission and absorption spectroscopy) will investigate this core emission.

The smallest absorption features observed indicated bulk shell compression to a radius of around 15 μm from typically 75 μm ie a factor of 5 in radius indicating densities of around $15gcm^{-3}$. The presence of the even smaller self emission features within this volume might suggest, on the basis of opacity considerations, that these were formed earlier in time when the bulk of the material was in shell form. This experiment has by no means been definitive and further study of the compression of high aspect ratio shells is required.

A2.2 THERMONUCLEAR PARTICLE SPECTROSCOPIC MEASUREMENTS OF IMPLOSIONS DRIVEN BY 0.53μm RADIATION

P M Evans, A P Fews, University of Bristol
W T Toner, A Cole, RAL

A2.2.1

In previous experiments with 6-beam geometry (A2.3) we have shown that measurements of the residual ranges of α-particles and protons emitted from ablatively driven implosions are capable of giving information about the compression at the time of thermonuclear particle emission and its uniformity both globally and locally. We are now attempting to extend this work to make a more complete study of implosion dynamics in 12-beam symmetry. In this section we report on track measurement automation, the development of a monte-carlo tracking programme to aid in the interpretation of the data and on a 12-beam implosion series at RAL. Data from a six beam experiment using .26 μm radiation at Ecole Polytechnique are reported in A2.3.

A2.2.2 Track measurement

As all our previous experiments have been severely limited by the small number of tracks which can be measured manually, the major part of the effort in the past year has been devoted to completing the development of a fully automated image analysis and measuring system at Bristol (A2.4,A2.5). CR-39 plates can now be scanned at 4 image frames per second ($10cm^2$ per hour) and the dimensions and position of each etch pit are recorded so that the energy of each particle may be individually determined. The etch pit recognition algorithms give good discrimination against artifacts. An important by-product of the improved statistical precision has been the identification of systematics affecting energy calibration. For example, it has been found that although tracks recorded in vacuo have the same calibration as those recorded at atmospheric pressure, it is important not to etch the plastic immediately after their return to atmospheric pressure but to wait until an equilibrium has been established. If the plates are

etched immediately they must be individually calibrated.

A2.2.3 Monte Carlo

The width of the observed particle energy distribution depends on the source temperature, the time dependence of the compression, energy loss straggling in source and detector and also on a number of geometrical effects such as the effective source size in relation to the diameter of the shell in which the bulk of the energy loss takes place. Preliminary results from a monte-carlo Medusa post-processor code showing the time dependence of the α-particle residual energy distribution are shown in fig A2.4. Hot matter stopping power corrections have still to be included in the code.

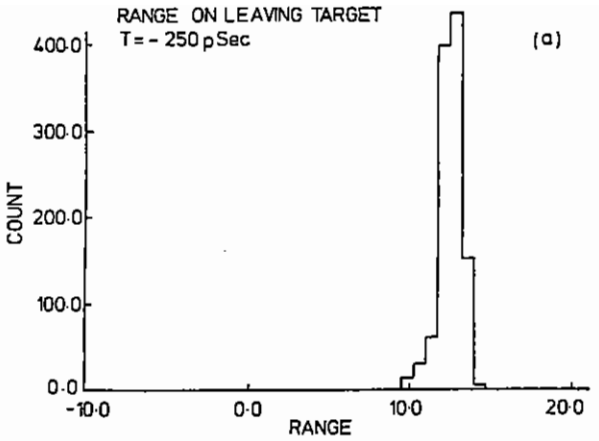

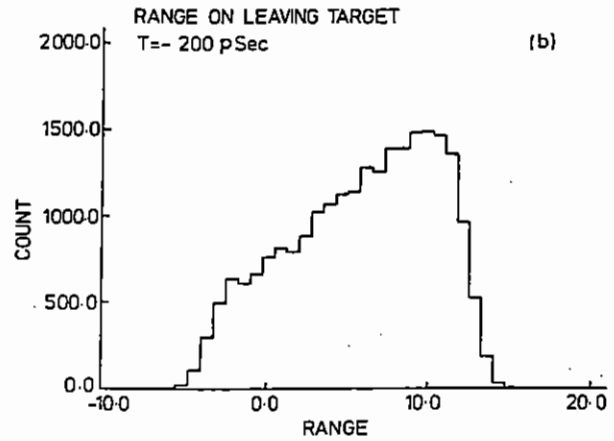

Fig A2.4 Simulation showing the ranges of DT α particles on leaving the target at times: (a) 250psec (b) 200psec and (c) 150psec before the peak of the laser pulse. Hot matter stopping power modifications have not been included.

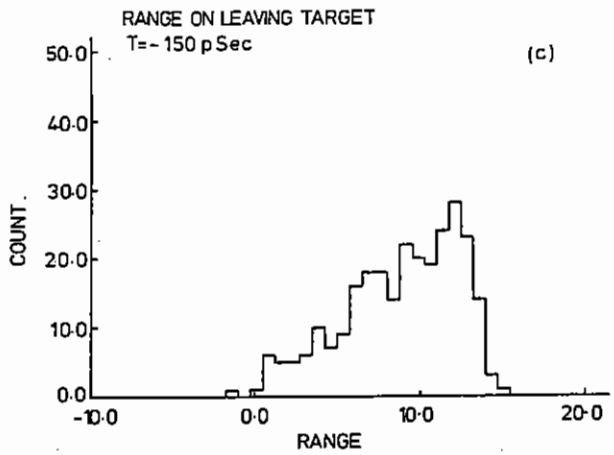

Fig A2.4 Simulation showing the ranges of DT α particles on leaving the target at times: (a) 250psec (b) 200psec and (c) 150psec before the peak of the laser pulse. Hot matter stopping power modifications have not been included.

A2.2.4 12-beam compression experiment

The CR-39 plates are cut out of sheet material as regular pentagons each containing a central hole for the passage of the laser beam and twelve of these plates can be mounted on a dodecahedral frame to cover about 80% of 4Π if no other diagnostics are used.

A first optimised 12-beam experiment using 0.8 nSec pulses of .53μm irradiation was carried out in November 1985. Pointing accuracy was verified to be at the level of 9μm RMS on a 150μm diameter target by using two diametrically opposed pinhole cameras to view surface focus test targets. 12 beam timing was checked at the ±5 psec level. Beam

balance, though poor on some shots was maintained at ± 5% for a substantial part of the data. Each D-T target used had its Tritium content checked by counting X-rays produced by the β particles in the shell walls. Some targets were placed in the chamber, subjected to the full alignment procedure and exposed to full laser shots on which the pulse switchout was disabled and then removed and recounted. There was found to be no loss of gas fill.

Neutron yields and target parameters are given in Table A2.2. Yields measured with the standard RAL plasic scintillator system were in good agreement with CR-39 measured yields from thin walled targets where all the α-particles would be expected to escape. The yields from targets of similar dimensions to those irradiated in the earlier 6-beam ablative experiment were a factor of 20 below those observed previously and scaled only slowly with energy per unit mass whereas a very steep dependence was expected and had been seen in previous experiments. Since the major objective of the experiment was the study of proton spectra from relatively thick walled targets and this would require high yields, most of the run was devoted to the exhaustive checks described above and full CR-39 coverage was not used in order to observe pinhole images of the implosions. No evidence of any gross asymmetry was seen in the pinhole pictures.

One possible, but untested, explanation of the low yields would be a difference in pulse rise-time from experiment to experiment. Thermonuclear particle production in these implosions is thought to be predominantly due to the first shock, whose strength would depend on the shape of the pulse at early times.
The α-particle range distribution from shot 4/5/12/85 is shown in figure A2.5. The distribution of energy loss is noticeably wider than was observed in the six-beam experiments and some particles have lost almost no energy in leaving the target. This may indicate shell breakup.

Table A2.2

Shot Number	Incident Green Energy (μm)	Target diameter (μm)	Target wall thickness (μm)	Neutron Counter Yield
5/12/11/85	263	121.3	1.0	4.6×10^{4}
5/19/11/85	289	124	1.06	1.7×10^{5}
8/19/11/85	427	142	1.6	8.2×10^{4}
13/9/11/85	322	138	2.0	4.2×10^{14}
1/20/11/85	288	138	2.1	7.2×10^{4}
2/20/11/85	334	133	2.1	3.6×10^{4}
7/20/11/85	281	131	1.2	9×10^{4}
9/20/11/85	255	133	1.2	1.2×10^{5}
12/20/11/85	378	128	1.1	2.3×10^{5}
2/21/11/85	240	138	1.1	4.8×10^{4}
11/21/11/85	248	137	1.3	2.6×10^{4}
8/22/11/85	164	126	1.1	1.2×10^{4}
10/22/11/85	245	128	1.1	1.1×10^{4}
1/27/11/85	309	121	1.3	3×10^{4}
4/ 5/12/85	284	254	1.2	4.7×10^{5}
6/ 5/12/85	278	224	1.0	4×10^{5}
8/ 5/12/85	312	229	1.4	1×10^{5}
10/ 5/12/85	399	148	1.6	2.4×10^{4}
12/ 5/12/85	392	130	1.2	2.5×10^{4}
15/ 5/12/85	451	231	2.1	1.5×10^{4}
16/ 5/12/85	423	221	2.6	1.2×10^{4}
20/ 5/12/85	409	222	1.6	1.1×10^{5}
24/ 5/12/85	252	132	1.2	4.6×10^{4}
25/ 5/12/85	389	134	2.4	1.2×10^{4}
28/ 5/12/85	416	129	2.0	9×10^{3}
2/ 6/12/85	215	136	1.5	7×10^{3}

(Energy on target is 78% of the figure quoted)

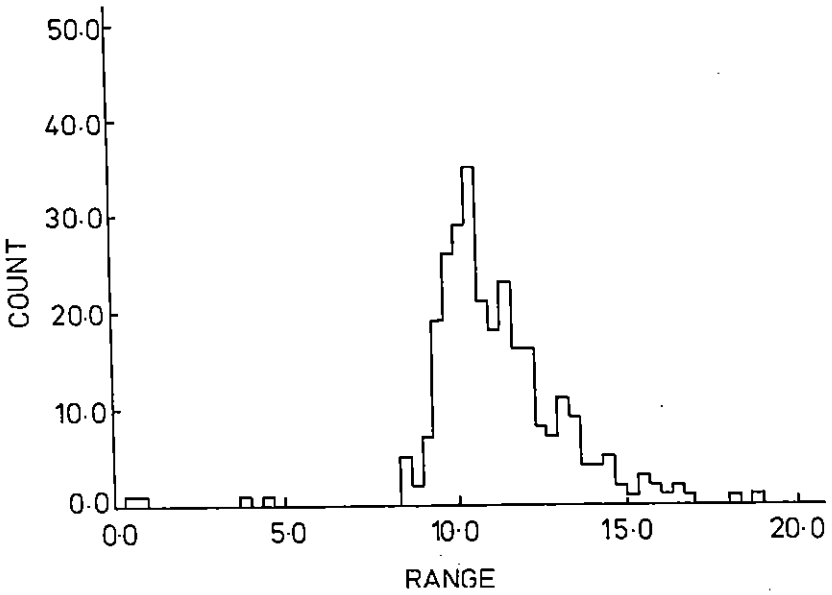

Fig A2.5 Preliminary range histogram for DT α particles produced from a 1.2μm wall thickness and 254μm diameter target.

A2.3 THERMONUCLEAR PARTICLE SPECTROSCOPY OF ABLATIVE IMPLOSIONS DRIVEN BY 0.26μm LIGHT

P M Evans and A P Fews, University of Bristol
E Fabre, D Bruneau, and A Michard, Ecole Polytechnique, Palaiseau
J Briand, University of Toulouse

A collaborative experiment has been perfomed at Ecole Polytechnique, Palaiseau to investigate implosions, using spectroscopy of the emitted thermonuclear particles. The techniques used were developed at Bristol University for use at the CLF and are based on measurements of etched nuclear particle tracks in CR-39 plastic detector [A2.6].

The targets used were 10, 20 and 40 bar DT filled glass walled microballoons varying between 90 and 230 μm in diameter and 1 to 3.5 μm in wall thickness. The 20 bar targets were supplied by RAL. The targets were imploded with the 6 beam, 0.26 μm wavelength laser at Ecole Polytechnique (A2.7), (A2.8). The laser energies on target were between 70 and 140 J with a pulse length of 0.5 μs. CR.39 plastic detectors were placed at distances of between 30 and 87 mm.

The data were analysed using the automated system described in the previous section (A2.2).

Results have been obtained from both DT α particle and DD proton reaction products. Figs A2.6 and A2.7 show α-particle ρR spectra, expressed in terms of the α particle range loss in the target, in units of CR-39 equivalent thickness. Details of these ρR spectra are discussed below. Fig A2.8 shows a similar proton range loss spectrum from the DD reaction.

One of the principal effects on the width of these distributions is the Doppler motion of the centre of mass of the reacting particles. The width of the distributions may thus be used to predict the temperature of the reacting ions. Fig A2.9 shows a graph of the temperature deduced in this way plotted against the measured DT α-yield. Each point corresponds to a separate shot. The points can be seen to fall into two groups. The first group have range distributions of the type shown in Fig A2.6 with a small spread in range, but may have a non Gaussian tail going to either low or high range loss. The measured α yields exhibit a typical $(\text{temperature})^{\frac{5+1}{2}}$ relationship, with deduced temperatures in the range 600e eV to 2 keV, which were the expected temperatures for the implosion parameters used. Proton range spectra were obtained on two of the shots in this group and yield the same temperature as the α distributions. As the effect of energy loss non uniformities on the proton spectra is five times smaller relative to the doppler broadening than in the case of the α spectra, this confirms that these α distributions are dominated by doppler broadening. The second group of data have much broader range loss distributions such as shown in Fig A2.7, with correspondingly much higher deduced

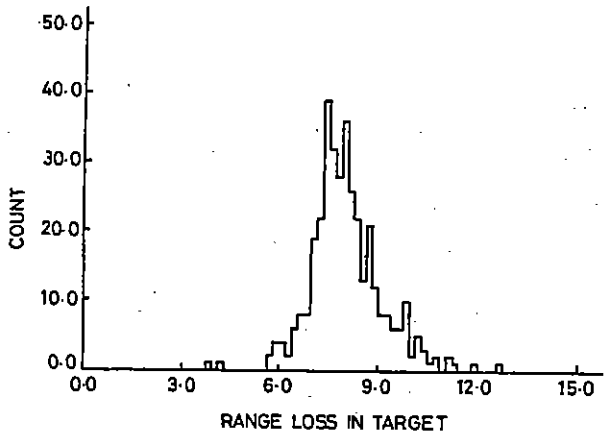

Fig A2.6 α-particle range loss spectrum in units of CR-39 equivalent thickness. $T_i = \pm$ is deduced from the width. This shot comes from the first group (see text).

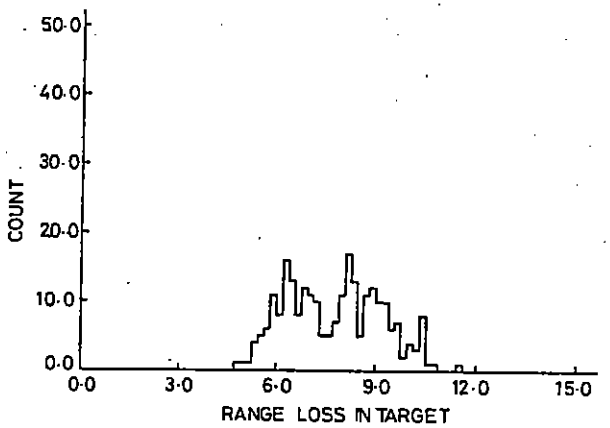

Fig A2.7 α-particle range loss spectrum in units of CR-39 equivalent thickness. The T_i deduced from the width is $\pm$ which is unrealistic. This shot comes from the second group.

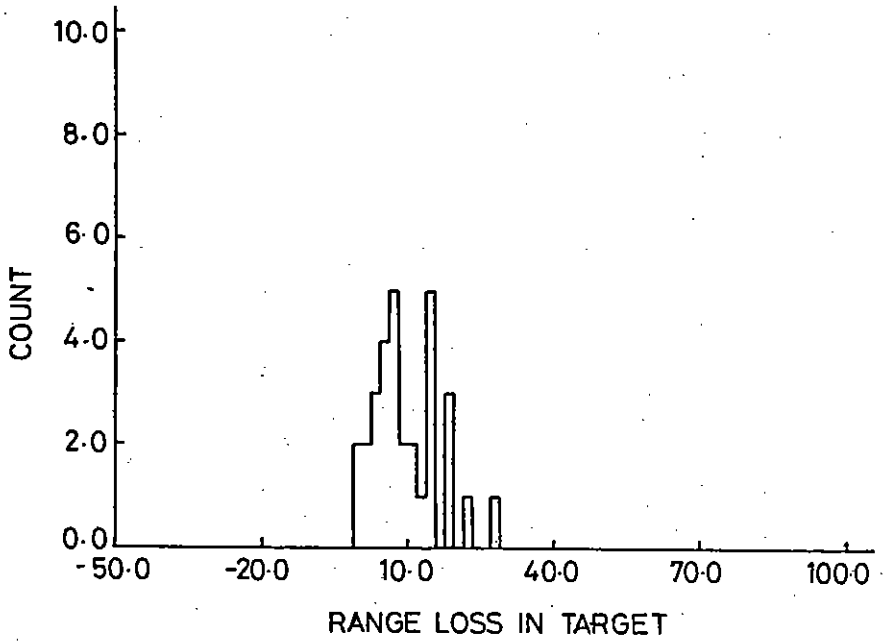

Fig A2.8 Proton range loss spectrum in units of CR-39 equivalent thickness. $T_i = \pm$ is deduced from the width. This shot comes from the first group (see text).

temperatures, between 3 -10 keV. Since these temperatures are unlikely to have been achieved, other broadening mechanisms, for example uneven compression of the target or thermonuclear particle generation in several bursts at different times must presumably be responsible for producing the observed distribution widths. The range loss distributions in this group (eg Fig A2.7) show no sharp features within the data. Unfortunately there are no proton range loss distributions for this group of shots. Further analysis of this data is in progress.

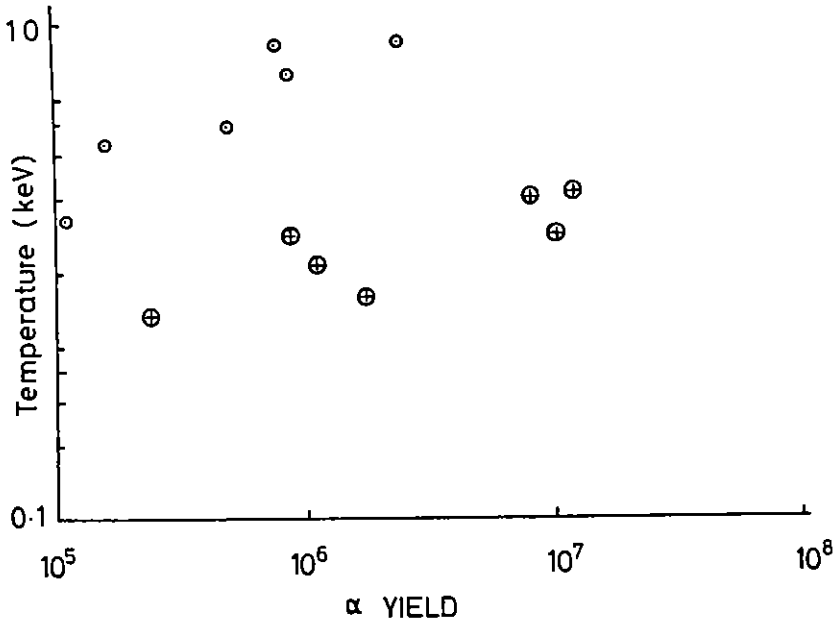

Fig A2.9 T_i deduced from ρR distributions versus normalised DT α yield. The normalisation factor is $\rho_o^2 R_o^4$.

References

A2.1 Rutherford Appleton Laboratory Annual Report to the Laser Facility Committee RAL-85-047 (1985) Section A2.2.

A2.2 Rutherford Appleton Laboratory Annual Report to the Laser Facility Committee RAL-084-049 (1984) Section A2.2.4.

A2.3 A P Fews et al Annual Report to the Laser Facility Committee RAL-84-049 (1984) A2.27.

A2.4 A P Fews et al Annual Report to the Laser Facility Committee RAL-85-047 (1985) A6.45.

A2.5 A P Fews "Fully Automated Image Analysis of Alpha Particle and Proton Etched Tracks in CR-39" Proceedings of the 13th International Conference on Solid State Nuclear Track Detectors, Rome, (1985) (In Press).

A2.6 A P Fews "Thermonuclear Track Spectroscopy using CR-39 Detectors" Proceedings of the 2nd International Workshop on Atomic Physics for Ion Fusion (1985) (In Press).

A2.7 GRECO Rapport D'Activite, CNRS (1981).

A2.8 E Fabre, 17th European Conference on Laser Interaction with Matter, Rome, (Nov 1985).

pages

A3 DENSE PLASMAS AND PLASMA RADIATION PHYSICS

Editor: A J Cole

A3 DENSE PLASMAS AND PLASMA RADIATION PHYSICS

A3.1 ION CORRELATION EXPERIMENTS IN HIGH DENSITY PLASMAS

T A Hall, R W Eason, C Jackson, B Shiwai (Essex University) and
S J Rose (RAL)

A3.1.1 Introduction

A colliding shock technique [A3.1] was used to create aluminium plasmas with high values of the ion coupling parameter. The value of Γ predicted by the MEDUSA computer code is typically 10–20. Under these conditions the ion motions become strongly correlated and there is a preferred ion pair separation.

In these experiments this close range order is observed using the EXAFS technique [A3.2]. The normal EXAFS spectrum of aluminium is well known and shows modulation in the x-ray absorption above the K edge (and the L and M edges). These modulations typically have a depth of up to about 10% and a periodicity in energy of approximately 26eV (for the fundamental period). As a result of compression, the position, depth of modulation and periodicity will change.

Finite temperature effects will tend to reduce the modulation depth of the EXAFS spectrum due to the thermal motions of the ions about this mean position.

A3.1.2 Experiment

The targets in these experiments were a planar sandwich of 2μ of aluminium covered on both sides by 3–10μ of N parylene. Figure A3.1 shows a schematic layout of the experiment. Two beams of the VULCAN laser were directed onto opposite sides of these targets driving shock waves in towards the central aluminium layer. These shocks collide in the aluminium producing a uniform compression of the aluminium layer for about 100 psec. The laser pulses driving the shock were 500 psec duration, .53μ wavelength and 20–30J energy in each beam. The beams were focussed to a uniform spot of 0.5 mm diameter resulting in an

irradiance of approximately 2 x 10^{13} Wcm^{-2}. At these irradiances the shocks collide very near to the peak of the laser pulse. The low irradiance and the plastic coating reduce the target x-ray emission to

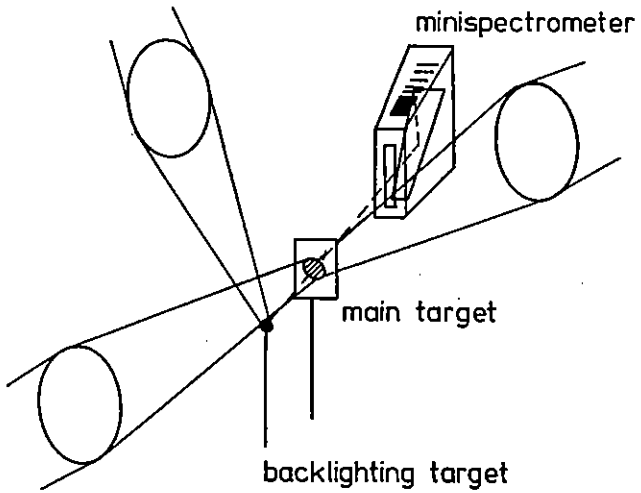

A3.1 Experimental arrangement showing long pulse compression beams and short pulse backlighting beams.

an insignificant level. The targets were probed using x-rays from a subsidiary high Z target placed about 3 mm from the main target.

Time resolution was obtained using a short pulse (100psec) of .53μ light to produce these x-rays. The EXAFS spectra observed in these experiments were associated with the aluminium K edge and it is necessary to record the absorption spectrum for several hundred electron volts x-ray energy above the K edge. A convenient dispersing crystal for this spectral range is ADP and measurements on uncompressed aluminium using this crystal and a bismuth backlighting

source have already been conducted [A3.3]. Unfortunately, the ADP crystals that were available were found to have much lower reflectivities than those used previously and produced inadequate exposures on the Kodak DEF film used in the minispectrometers. Increasing the irradiance on the bismuth target did not increase the soft x-ray yield from the target but resulted in more intense hard x-rays. These harder x-rays increased the background exposure levels on the film by causing fluorescence in the spectrometer and by high order reflectivity from the crystal.

A TlAP crystal has much higher relectivity than ADP and the dispersion in the 6-9A region is much lower, so that much higher film exposures were found to be possible. Unfortunately, the second order reflectivity of TlAP is also high, and the second order bismuth spectrum was found to have features similar to EXAFS modulation. Since these features occur in a similar region on the film to the first order EXAFS, the interpretation of the results proved very difficult. Several other backlighting sources were tested: the ideal requirements were that it should have a bright quasi-continuum in the 6-9A region and low level emission without spectral features in the 3-4.5A region. Of the sources tried, uranium appeared to have the best characteristics: there are two fairly weak broad features in the second order spectrum but these are not easily confused with the EXAFS spectrum.

The normal filtering in front of the minispectrometer consisted of 25μ of beryllium. Some discrimination against the second order can be obtained using a pure silicon filter but such a filter was not available. An alternative technique that was adopted was to place a further 125μ of beryllium over half the aperture to the mini spectrometer so that the first order was absorbed. Thus the first and second order spectra were recorded side by side on the same film. Since the second order spectrum is at a relatively low level it can be subtracted numerically afterwards.

EXAFS spectra were obtained for various relative delays between the main drive pulse and the backlighting pulse.

Figure A3.2 shows two spectra obtained in this way. One spectrum was obtained with the backlighting pulse coming early with respect to the main drive pulse and effectively shows the EXAFS spectrum of uncompressed aluminium. The second spectrum was taken near to peak compression: in this case the features are spread out in energy and less well defined indicating both compresion and heating. Interpretation of the data is still in progress and this will be carried out initially using data on phase shifts and scattering amplitudes for uncompressed aluminium. These parameters will not, however, give the correct interpretation. Recent work by Albers [A3.4] on the EXAFS of compressed aluminium should lead to the correct parameters and a collaborative programme is being arranged.

A3.2 ABSORPTION SPECTROSCOPY IN IMPLOSION EXPERIMENTS

C Chenais Popovics (Ecole Polytechnique, Palaiseau, France)
P Norreys (Royal Holloway College, London)
A Cole, S Rose, M Key (RAL)

A3.2.1 Introduction

Absorption spectroscopy has been demonstrated to be an interesting diagnostic of microballoon implosions [A3.5]. The diagnostic allows a measure of the density and temperature of the coolest part of the imploded shell. Absorption features in X-ray spectra have been observed on glass shells, the inside of the shell being the emitter and the cooler compressed part being the absorber [A3.6]. They have also been seen in colliding shock experiments with chlorine absorption of Bismuth emission [A3.7]. They have only recently been used as a quantitative diagnostic of implosions driven by 10.6μm laser radiation [A3.5].

A3.2.2 Temperature and density diagnostic

An intermediate Z element can absorb in different ways: if its temperature is low (~50eV), its K absorption edge can be shifted by density effects [A3.8]; if it is hot enough to be ionized to between fluorine-like and helium ion stages (100-300eV), each ion stage absorbs on a K_α line. These lines are close to each other and lie on the red side of the He_α line of the absorber (ie Lyman α resonance transition of the helium like ion).

To observe such absorptions in a microballoon implosion, the target has to be carefully chosen: its core must emit a continuum spectrum around the absorber He_α line. Moreover, the absorber must be buried in the shell at a depth to match the cool dense part of the shell at peak compression.

When conditions are reached to have K_α absorption lines, the line integrated absorption gives a measurement of the ρΔr achieved in the shell, where ρ is the density and Δr the thickness of the compressed absorbing layer. The ionic composition can be deduced from the relative strengths of the different absorption lines. The use of a model describing the ionisation of the plasma enables electronic temperature determination. Time resolution of the spectra is useful to ensure that the different species absorb at the same time and not successively during the temperature rise or decay.

A3.2.3 Experimental set up

We used twelve beam irradiation at 0.53μm wavelength with a 400ps FWHM pulse. The illumination parameter d/R was kept between 6 and 10, (d is the distance between target centre and focus position and R is the radius of the target). The absorbed laser intensity was between 10^{14} and 3×10^{14} W/cm^2.

The targets were 60μm diameter, 1μm thick glass microballoons filled with 10 Bar of Neon. A 0.9μm layer of chlorine parylene (CH_2Cl_2) was coated on the microballoon. A layer of plastic of variable thickness

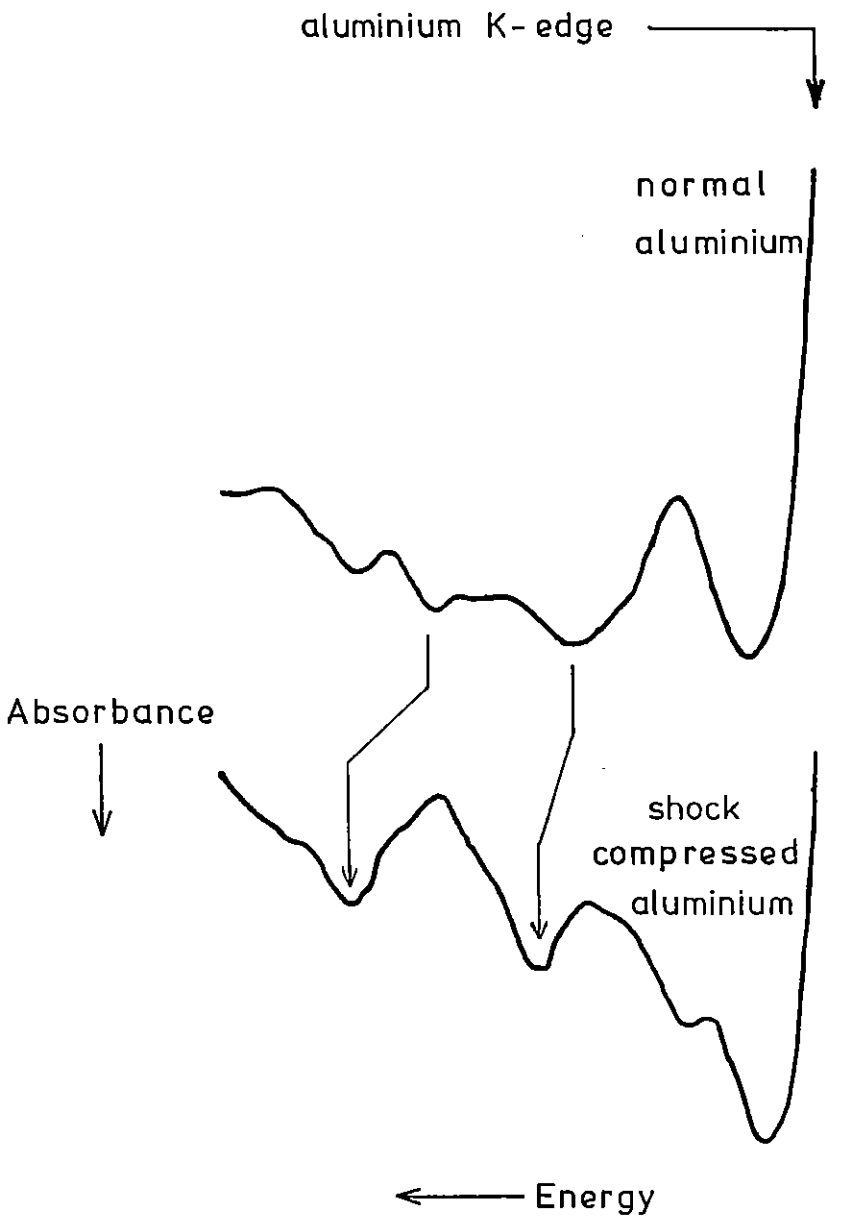

A3.2 EXAFS spectra of normal uncompressed aluminium (upper trace) and shock compressed aluminium. The absorption peaks are spread out in energy in the lower trace indicating a compression of the material.

was coated on top (1 to 5μm thick).

A pinhole camera with 25μm Be filter and mylar attenuators was set up to check the core emission. The X-ray spectrum was recorded in the region around 4.5Å by a time resolved spectrometer consisting of a flat PET crystal in front of a streak camera. A space resolving, time integrated spectrometer was also set up at the same wavelength range. The spectrometers were set to record recombination continuum emitted by the compressed gas and hot inner surface layer of the silicon shell, absorbed by the chlorinated layer.

A3.2.4 Experimental Results

Figure A3.3(a) shows a time resolved spectrum obtained for a target overcoated with 1.1μm of plastic. The brighter lines are the intercombination and resonance lines of helium like chlorine ions and associated dielectronic satellites. We kept the intensity high enough to see the absorption features, which causes the resonance lines to saturate the detector. These lines last for the whole interaction duration. The limit of the series of H-like silicon lines (n=5 and 6) and the recombination continuum are clearly seen. An impurity Heα sulfur line is prominant on the silicon continuum, at 4.73Å. Two weak absorption features appear on the long wavelength side of the chlorine satellites.

Figure A3.4 shows a densitometer trace of the same shot, traced at the time when the continuum is maximum. Absorption features appear to be very weak. They correspond to B-like and Be-like ion stages. The Li-like and He-like absorption lines are coincident with the resonance and intercombination lines and do not appear. From densitometer tracings, it appears that the absorption lines have a sightly shorter duration than the silicon continuum emitted by the hot core of the implosion which lasts 300ps.

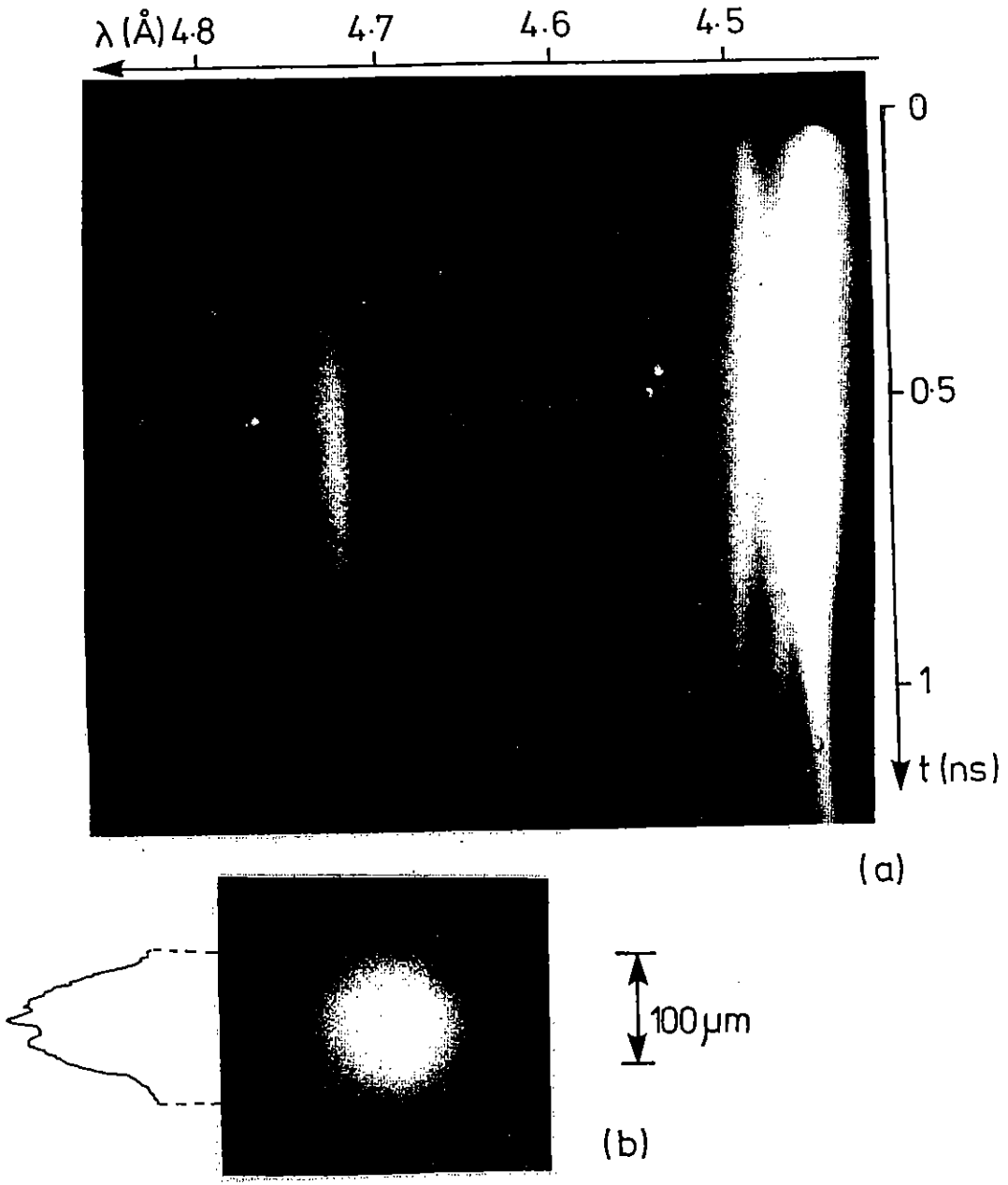

A3.3 (a) Time resolved spectrum in the range 4-5Å.
(b) Pinhole picture showing a bright core of about 10μm diameter.

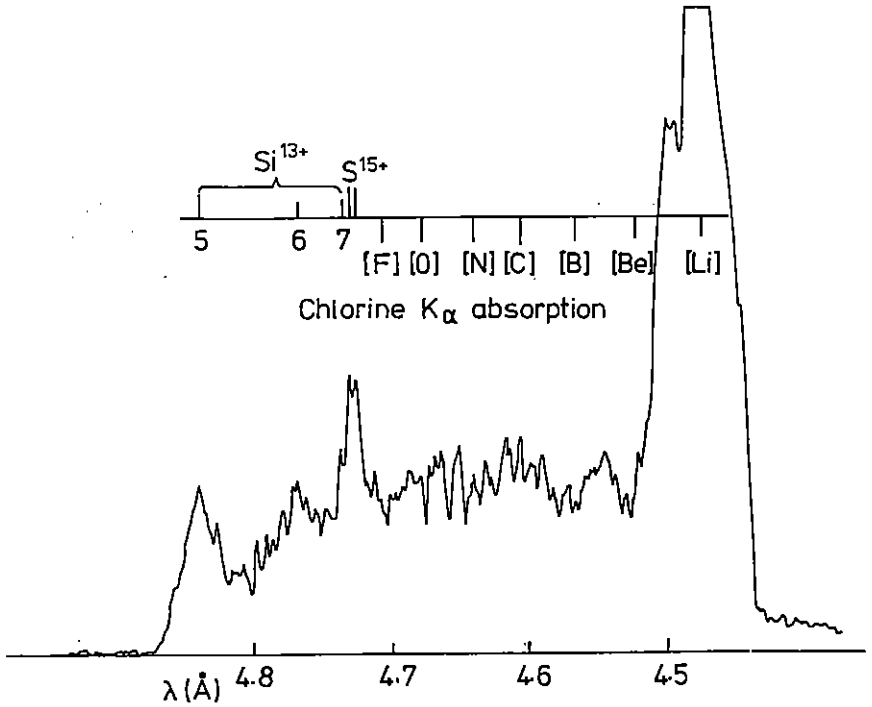

A3.4 Densitometer trace of figure A3.3(a) at maximum emissivity of the silicium recombination continuum showing absorption features.

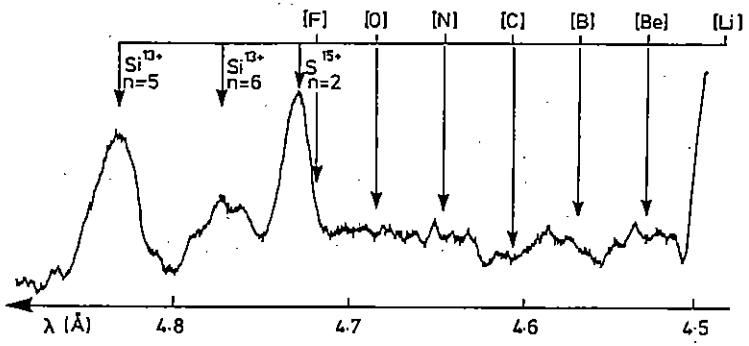

A3.5 Densitometer trace of the time integrated spectrum obtained on the same shots as figure A3.4.

Figure A3.5 is a densitometer trace of the time integrated spectrum obtained on the same shot. There are very weak absorption features similar to the time resolved ones. However, one absorption is at the C like ion position which was not observed on the time resolved spectrum. This could be explained assuming that the C like ion stage is less populated than higher ionic stages but last longer.

Figure A3.3(b) shows a pinhole picture of same shot. It exhibits a bright core of 10μm diameter. This picture demonstrates that the target is imploding. The time behaviour of the silicon spectrum proves that the implosion time is close to the laser pulse maximum and that its duration is not much shorter than the laser pulse duration. This is characteristic of a compression with higher laser intensity than optimum. The duration of the emission and the weakness of the

absorption structures suggest that the targets are not well matched for the absorption diagnostic.

The chlorine resonance line is emitted very early and lasts for the whole interaction. This indicates that the chlorine layer is not buried deep enough in the target and is at least partly ablated. The weak absorption features demonstrate that the chlorine layer is not totally ablated or at least lies in the heat front region. Indeed, these absorption and emission chlorine structures show the presence of B-like, Be-like and He-like ions. As the heat front is a very thin region, Be-like and B-like ions must be well populated to absorb. This would imply a temperature of about 250 to 350eV according to population models [A3.5, A3.9].

A3.2.5 Code Simulations

We have run hydrodynamic simulations with the 1 dimensional code MEDUSA [A3.10] in order to improve the understanding of the experimental results. The simulations are run with laser conditions corresponding to the experiment. We included transport radiation and used a flux limit. Figures A3.6 and A3.7 show the density and temperature profiles obtained in two simulations. As in the experiment the target is a 120μm diameter glass shell 1μm thick, overcoated with 0.9μm of chlorinated parylene. The overcoating of plastic is 6.3μm in the case of figure A3.6 and 1.1μm in the case of figure A3.7. Density and

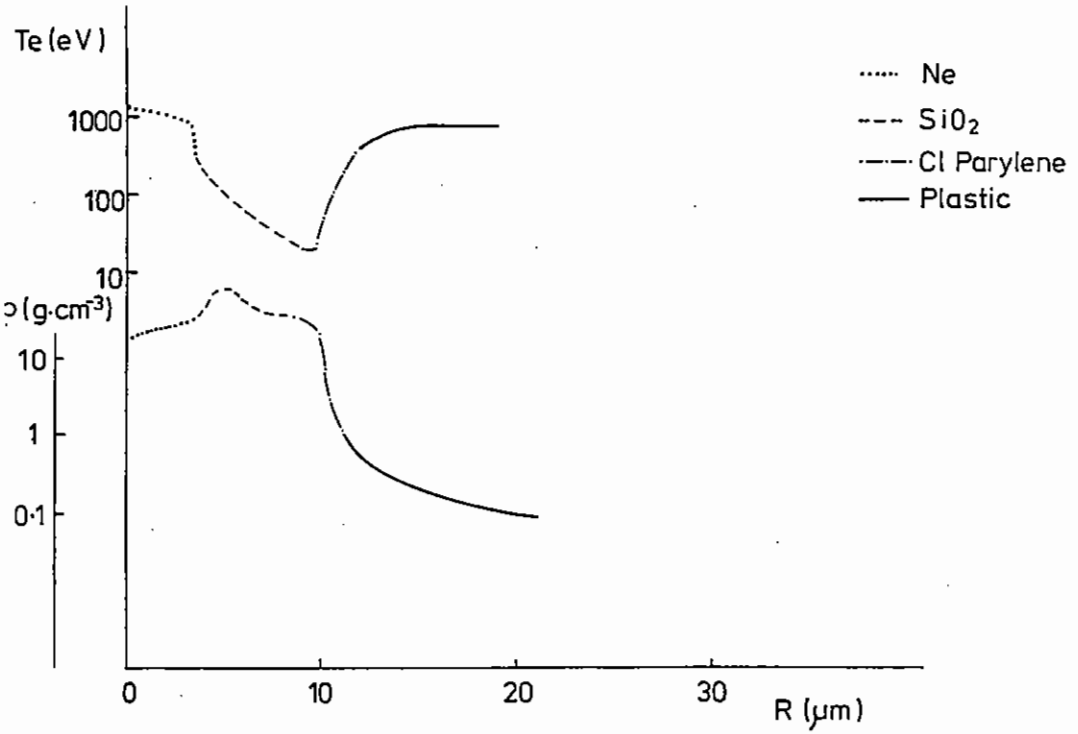

A3.6 Density and electronic temperature obtained at peak compression in a Medusa simulation. The plastic overcoating is 5μm.

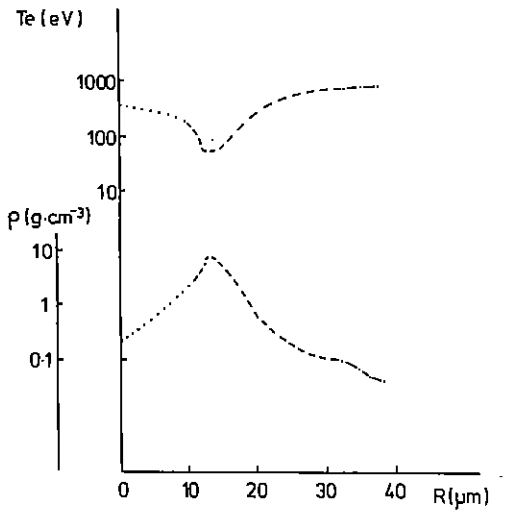

A3.7 Density and electronic temperatures obtained at peak compression in a Medusa simulation. The plastic overcoating is 1.1μm, as in the experiment. At peak compression, the plastic cells are out of the spatial range of the graph.

temperature profiles are traced at the maximum of the laser pulse and at the maximum compression. Figure A3.6 shows what we expected to have, ie, a chlorine plastic layer lying in the foot of the thermal front. However for these conditions, the experiment showed no bright core on the pinhole pictures and therefore no absorption features on the spectra. The gas and glass may have remained too cold to emit. We had to go to thinner plastic layers to obtain the bright core but this led to only weak absorption features. Figure A3.7 which is a plot under these last conditions shows a plastic layer completely ablated and overestimates the temperature of the chlorine layer. It does not fit the experimental data as the silicon has a temperature too low to emit at the time when chlorine could absorb. Comparison of experiment and simulations suggest that the glass shell was too thick for the chlorine layer to be in the compressed region. For the intensity used it should have been more suitable to use 0.5 to 0.8μm thick glass shells, which was technically not possible.

A3.2.6 Conclusion

These very preliminary experiments give us useful information for selecting the right targets for diagnosing the implosion by absorption

spectroscopy. However, for ablation at 0.53μm, in contrast to earlier work at 10.6μm, very thin layers must be used if the velocity is to be high enough to produce a strongly emitting core. The aspect ratio r/Δr of the target determines the implosion velocity for a given irradiance, and the total power and energy of the laser pulse limit the target radius and therefore the layer thickness. A better scheme than the one used here could be to use the inner gas as an emitter, and put the absorber on a very thin substrate. It is planned to try this approach in future experiments.

References

A3.1 J D Hares, D K Bradley, A J Rankin and S J Rose, Annual Report to the LFC A3.2.1 RAL 84-049 1984.

A3.2 D E Sayers, E A Stern and F W Lytle Phys Rev Lett 27, 1204 1971.

A3.3 R W Eason, D K Bradley, J D Kilkenny and G N Greaves J Phys C 17, 5067, 1984.

A3.4 R C Albers private communications but for similar work on compressed copper see: R C Albers, A K McMahan and J E Muller, Phys Rev B 31, 6, 3435, 1985.

A3.5 A Hauer, D Cowan, B Yaakobi, O Barnouin and R Epstein, submitted to Phys Rev A, Report LA-UR-85-3914.

A3.6 B J MacGowan, J D Kilkenny, M H Key, P T Rumsby, W T Toner, A P Fews, and D L Henshaw, Opt Commun 48, 256, (1983).

A3.7 D K Bradley, J D Hares and J D Kilkenny, Annual Report to the Laser Facility Committee, Rutherford Appleton Laboratory Report, RL-83-043, p5-6 (1983).

A3.8 S J Rose, Annual Report to the Laser Facility Committee, Rutherford Appleton Laboratory Report, RL-85-047, pA3.3 (1985).

A3.9 R M More, Atomic Physics in Inertial Confinement Fusion, Applied atomic collision Physics vol II, Academic Press, and UCRL Report 84991, (1981).

A3.10 S J Rose and R G Evans, Radiation Transport in MEDUSA, Rutherford Appleton Laboratory Report RL-83-040, (1983).

A4 XUV AND X-RAY LASERS AND OTHER APPLICATIONS OF LASER-PRODUCED PLASMA SOURCES

Editors: F O'Neill and S J Rose

A4 XUV AND X-RAY LASERS AND OTHER APPLICATIONS OF LASER-PRODUCED PLASMA SOURCES

A4.1 INTRODUCTION

F O'Neill and S Rose (RAL)

In the past year the Sprite KrF laser has for the first time been used for scheduled user experiments. This followed the very successful trial experiments which were reported in last year's report.

Using X-ray sources generated by the Sprite and VULCAN lasers there has been considerable progress in the X-ray microscopy applications and clear X-ray contact images of a number of biological specimens have been recorded in X-ray resist. A start has been made on the first use of X-ray microscopy for truly biological investigations.

This year has seen considerable activity using the VULCAN laser system in the field of XUV-lasers, culminating in a successful demonstration of amplified spontaneous emission at 182 Å using the carbon recombination scheme.

The topics above are discussed in Sections A4.2 - A4.5. In addition, a novel method of overcoming the problems of refraction in XUV and X-ray laser systems is described in Section A4.6 and further very interesting developments and applications in the reflEXAFS technique are shown in Section A4.7.

A4.2 LASER X-RAY MICROSCOPY USING SPRITE AND VULCAN

A4.2.1 Introduction to the Techniques

R W Eason (Essex University)

From very early in the 20th Century, the possibility of using low energy (soft) X-rays to examine biological, and other, material has often been discussed (A4.1, A4.2). While optical or electron microscopy are currently the standard tools for biologists, there are

considerable benefits to imaging with X-rays as opposed to visible light or electrons. As the wavelength of X-rays is much shorter than for visible light, higher resolution can be achieved. For electron microscopy, the specimen to be viewed must also undergo careful preparation, for example sectioning and staining, so that there is every chance of introducing artefacts. Furthermore electron microscopy (excluding transmission work) is limited to looking at surface features of the specimen and the interaction between the electron beam and the specimen may also result in damage. The necessity for operating in vacuum with electron microscopy also requires that the specimen be dehydrated.

All of these problems can in principle be overcome by using X-rays. As the dominant attenuation process for X-rays is photoabsorption rather than scattering, relatively thick samples (up to several μm) can be viewed. Due to the inherent variation in the absorption cross section for X-rays between different elements there is also the possibility for natural contrast, without the need for staining (A4.3). This situation is depicted in figure A4.1 which shows that between the oxygen and carbon K-absorption edges, at 2.3nm and 4.4nm respectively, protein shows marked contrast in water, due to ≈ 10 times greater X-ray absorption by carbon (protein). This allows the specimen to be viewed therefore in its natural water/nutrient environment.

The main attraction of using X-rays however is the possibility of imaging specimens while they are still living. If the exposure is sufficiently short, then the image can be recorded before any structural damage has time to occur, even though the actual X-ray dose may ultimately prove fatal. This requirement can readily be met by a laser-produced plasma X-ray source. By focusing the laser pulse onto suitable target materials, a plasma is formed which emits strongly throughout the soft X-ray region. It is also easy to arrange for the emitted wavelengths to fall within the all-important 'water-window' region of 2.3nm and 4.4 nm (see Fig A4.1).

In this section A4.2, we report the work that has been carried out on both Vulcan and SPRITE in the last year. The work follows on from the initial studies performed in July 1984, and reported in the 1985 Annual

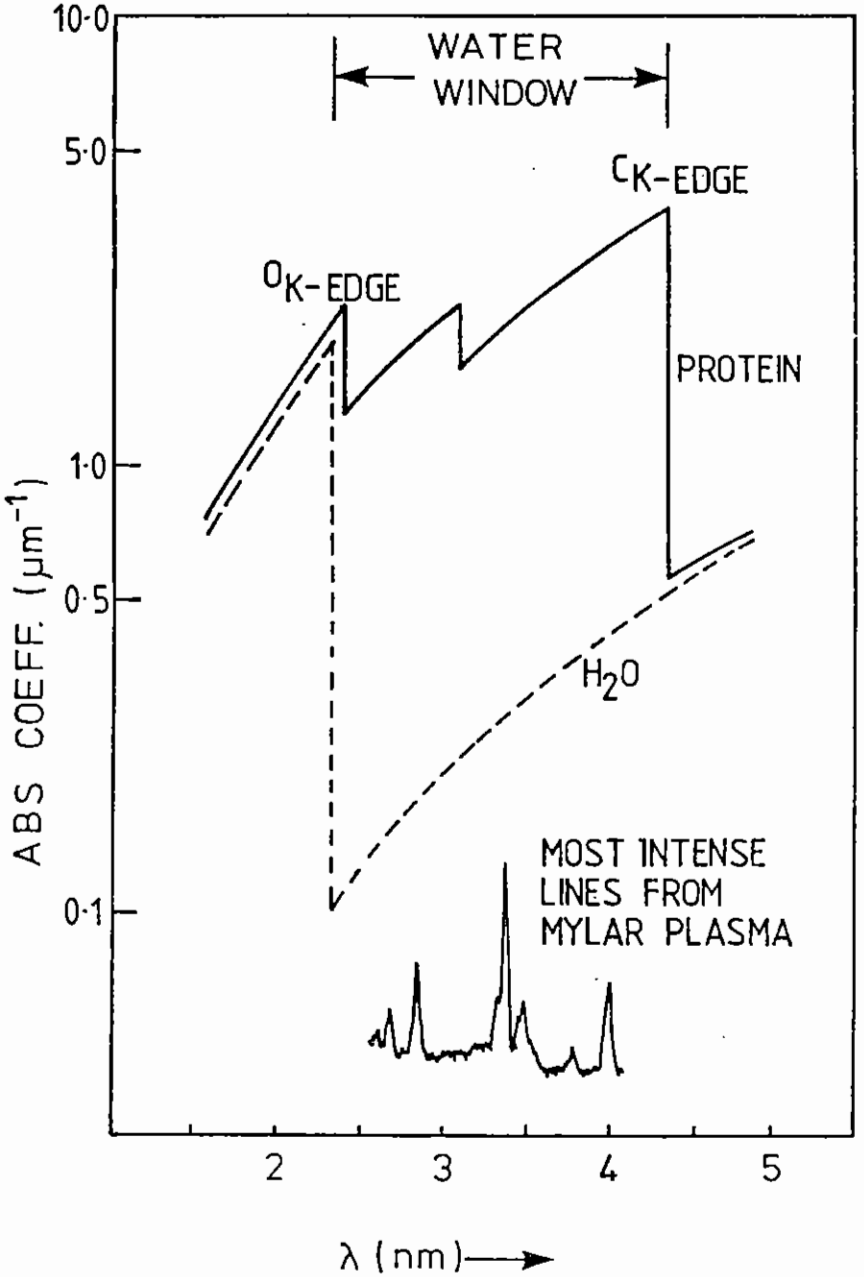

Fig A4.1 The "water window" spectral region showing the difference in X-ray absoprtion coefficient between protein (carbon) and water (oxygen).

Report to the Laser Facility Committee (A4.4).

The contact imaging process is conceptually very simple. In a manner entirely analagous to contact printing in optical photography, the specimen is placed on top of the recording medium, and exposed to X-rays. The technique, developed many years ago (A4.5) has since been extensively developed to include the use of X-ray resists (X-ray sensitive polymers) as the recording medium (A4.6). After exposure, the latent image in the resist is chemically developed, to yield a relief pattern corresponding to a 2-dimensional map of integrated mass absorption coefficient in the specimen.

For imaging live specimens, the situation is more complicated. To maintain the specimen in its normal atmospheric/nutrient environment, a 'wet-cell' is used. The wet-cell is placed inside a vacuum chamber some few mm or cms away from the laser plasma source. The vacuum is required to avoid laser induced gas breakdown, which would prevent laser light from reaching the target, and also to allow efficient X-ray transmission to the wet-cell. A thin (~ 100nm) 1 mm^2 Si_3N_4 window is used on the wet cell to maintain the required atmospheric pressure difference. The Si_3N_4 is deposited by CVD onto a silicon wafer, which is then back-etched, leaving a clear Si_3N_4 film, supported at its four edges. This material is very strong, and due to the low Z elements used, only attenuates X-rays in the water-window region by ≈ 20%. A spring or plunger is included in the cell design, to keep the resist-coated silicon wafer in close contact with the specimen. This is important since the resolution achievable is dependent on the sample to resist distance, and also the thickness of the resist itself. In practice if the combined distance is 1μm, diffraction effects will limit the resolution to ≈ 50nm. A schematic diagram of a wet cell is shown in Fig A4.2.

Resist materials that are sensitive to irradiation by electron beams are also sensitive to X-rays (A4.7), so that resists that have been developed for use in microcircuit technology are also suitable for X-ray microscopy. There is a strong correlation between the sensitivities of resists to electron beam and X-ray radiation (A4.7). Typical materials used include poly-methylmethacrylate, PMMA, or

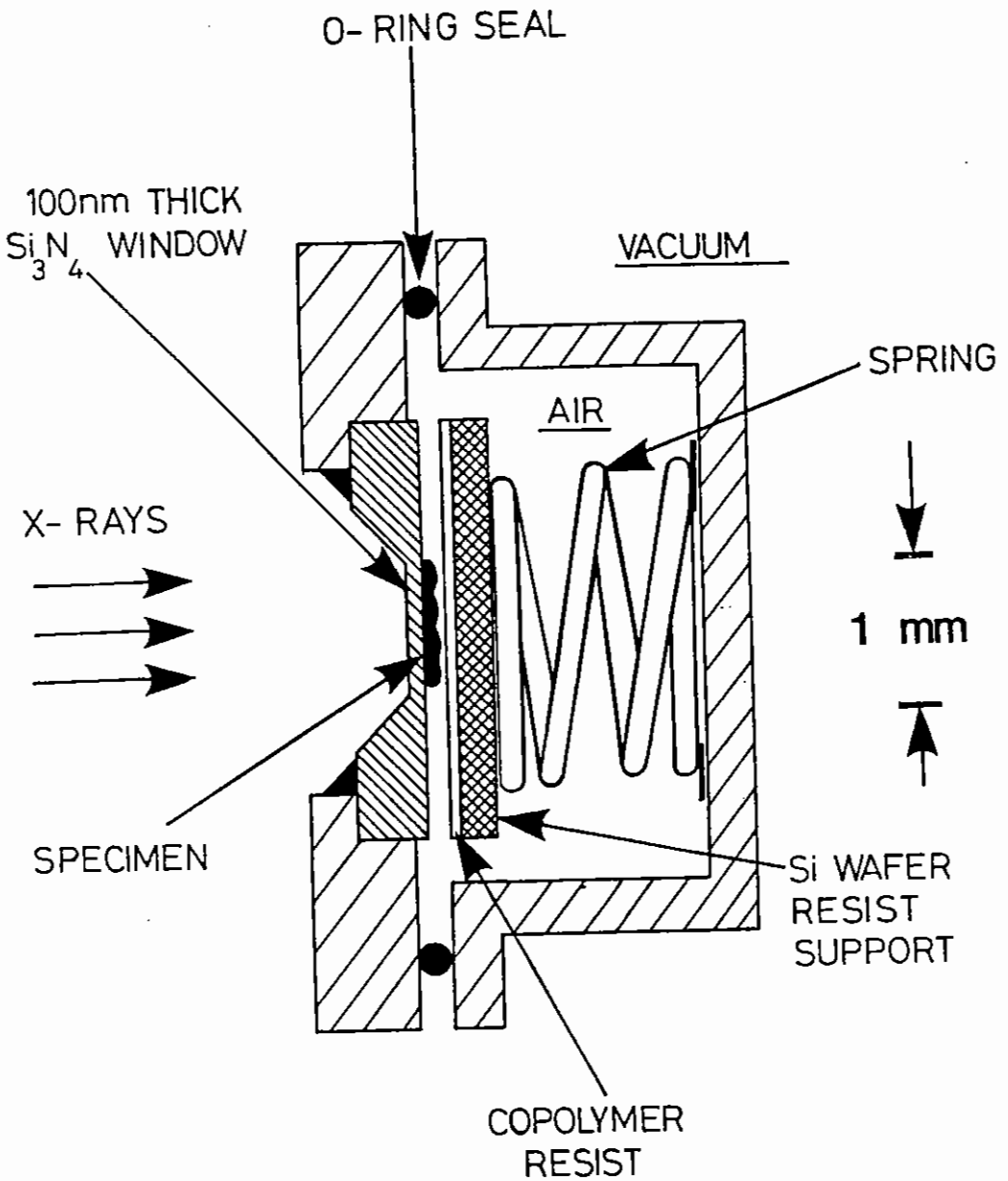

Fig A4.2 Schematic diagram of wet cell holder.

copolymers such as glycidyl methacrylate and ethyl acrylate, P(GMA-EA). The resist material used in most experiments described in this paper was a slightly different copolymer, P(MMA-MA), which is one of the more sensitive (fastest) positive resists presently available. The first laser experiments used a different terpolymer resist (C4.4). For a positive resist, the exposed areas are rendered more soluble in a developer. In terms of energy required per unit area, P(MMA-MA) is some three times more sensitive than PMMA (C4.8).

After exposure the resists were developed for a short time in a suitable solvent mixture. For P(MMA-MA) resists the development procedure was typically 1-2 minutes in a 1:1 mixture of methyl isobutyl ketone (MIBK) and isopropyl alcohol (IPA) or for a more aggressive development up to 5 mins in ethyl cellusolve acetate (ECA). One method that was used to ensure optimum development involved exposing several specimens at the same time. Trial development of one or more resists allowed the optimum development procedure to be established so that this could be used on the remaining resists. In extreme cases, these control samples were obtained by dividing a single resist into multiple pieces.

For viewing the developed resist, optical, and scanning electron microscopes were used. In some cases a transmission electron microscope (TEM) was also used for viewing resists that had been spun onto Si_3N_4 windows. These 100 nm thick windows, identical to those used for the wet-cell work are also reasonably electron transparent, hence the possibility of viewing in a TEM. An alternative method involves floating resists off carbon coated support glass wafers (A4.9). A Normarski interference optial microscope was also routinely used to monitor the progress of the development. Results obtained using both methods are shown in subsequent sections.

A4.2.2 Source Characteristics on Sprite and VULCAN

R W Eason (Essex University), P C Cheng, R Feder (IBM Yorktown),
A G Michette (Kings College), R J Rosser (SUNY, Stoneybrook),
F O'Neill, Y Owadano, I C E Turcu (RAL).

In the past, the development of all forms of soft X-ray microscopy has been hampered by the lack of sources intense enough to allow images to be obtained in reasonable times, and by the lack of suitably sensitive detectors. Over the past decade or so the problem of the X-ray source has been improved by the development of dedicated synchrotron radiation facilities (A4.10).

Contact X-ray microscopy has given interesting results at several synchrotron sources (A4.6, A4.11) and, with the commissioning of undulator beam lines due on several synchrotrons in the near future (A4.12) thus increasing the brightness by more than an order of magnitude, will continue to do so. However, the exposure times necessary using synchrotron radiation are still much too long for obtaining images of living specimens. For example, contact images obtained recently of erythrocytes and blood platelets required a 20s exposure time, using the SERC Daresbury Laboratory Synchrotron radiation source (A4.11). While this may seem short in comparison with the first experiments of this kind which took 16 hours and 15 minutes respectively (A4.6) it is still much too long for recording images of living material.

Alternative sources such as gas-puff z-pinches, which generate 100ns X-ray pulses have also recently been used (A4.13) but there are limitations here in terms of the minimum distance possible between source and specimen. Debris problems can also occur, whereby energetic material from the plasma hits the window/resist surface, damaging the surface quality.

The laser-produced plasma source used for the experiments reported here has numerous advantages over other sources. Using the VULCAN laser at the CLF, X-ray exposure times of 1ns (or less) are routine. There is also great flexibility in choosing the X-ray wavelengths used for

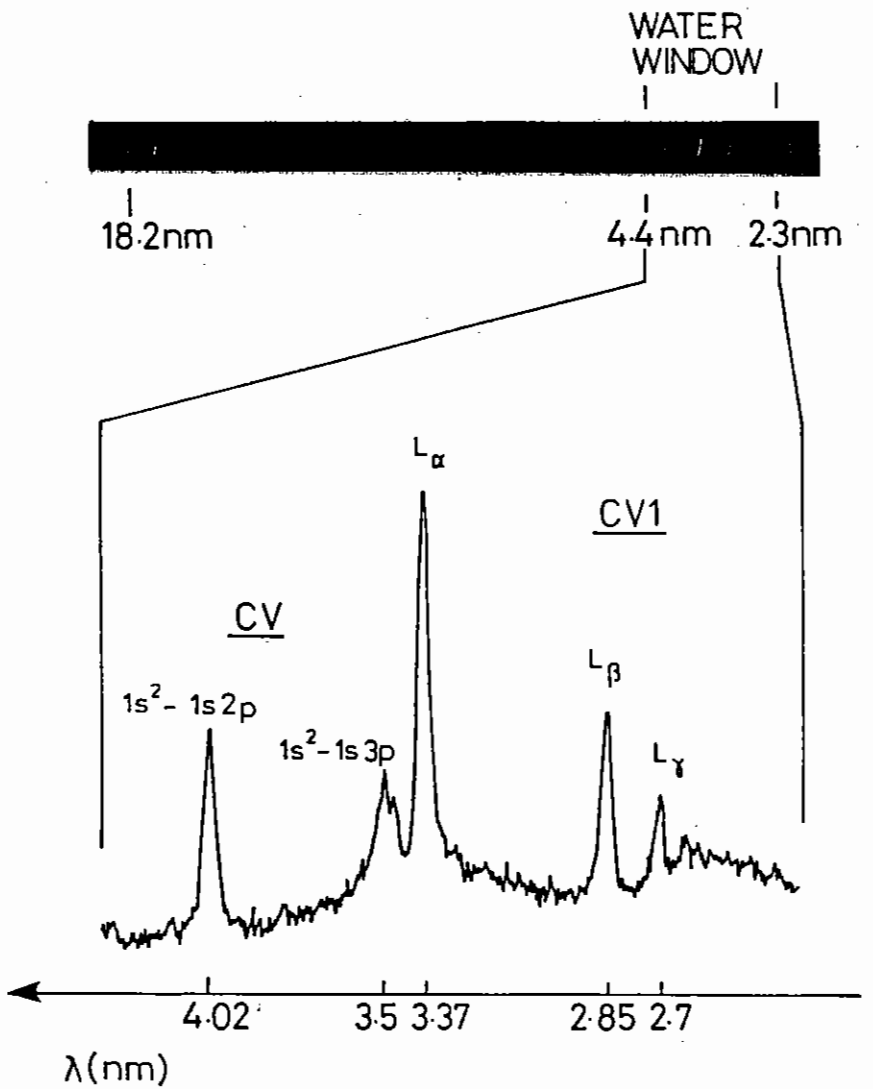

Fig A4.3 A typical X-ray spectrum (upper) recorded using a grazing incidence grating spectrograph. The water window region is indicated and an expanded microdensitometer trace is shown of this region of the film (lower). The X-ray line emission is produced from Hydrogen-like (CVI) and Helium-like (CV) ions.

exposure. By a suitable choice of target material (ie Z) and laser irradiance (W cm^{-2}), it is possible to arrange for certain emission lines to contain a large percentage of the X-ray energy. Some target materials can also emit quasi-continua, spanning some 2-3 nm which can straddle the water-window region. The experiments here predominantly used targets containing carbon, ie mylar or graphite. For the earlier VULCAN exposures (A4.14), the fundamental laser wavelength of 1.053μm was frequency doubled to 0.526μm to achieve a greater conversion efficiency to X-rays. Approximately 30-40J, 1ns laser pulses were focussed to 200-300μm spot sizes onto graphite targets. This corresponds to a laser irradiance of ~ 6 x 10^{13}W cm^{-2}. The resultant plasma showed strong line emission features at 3.37nm and 4.03nm, corresponding to CVI (H-like) and CV (He-like) ions. The intensity ratio of these lines could be varied by altering the laser irradiance, thus changing the effective plasma temperature.

For most recent work using Sprite operating at its fundamental 0.249μm wavelength, laser energies on target were typically 80 - 100 J in 50ns, of which approximately 50% was contained in a spot size of ~ 75μm diameter. The corresponding peak laser irradiance was 5 x 10^{13} W cm^{-2}. The X-ray pulse duration was measured to be ~ 35 ns (FWHM), shorter than the 50 ns incident laser pulse. Measurement of the integrated X-ray energy over 2π steradians from 250μm thick Mylar foil targets indicated that ~ 740 mJ fell inside the water-window spectral region. Spectra taken of the X-ray emission in this region revealed that of the 740 mJ X-ray energy, approximately 50% is due to line emission and 50% is from continuum radiation. The X-ray flux incident on the Si_3N_4 window of the sample holder which was positioned 50 mm from the plasma at ~ 30^0-40^0 to the target normal was estimated to be 10 mJ (± 5 mJ) cm^{-2}. A typical spectrum recorded on Sprite using a compact grating spectrograph is shown in figure A4.3. The water window spectral region is indicated, and this has been traced using a microdensitometer, and reproduced on an expanded scale. The line emission from hydrogen-like carbon (CVI) is seen to be particularly strong. Space resolved spectral measurements taken with the same spectrograph shows the soft X-ray source diameter to be ~ 200 μm (Fig A4.4).

To quantify the X-ray emission, calibrated X-ray photodiodes were used

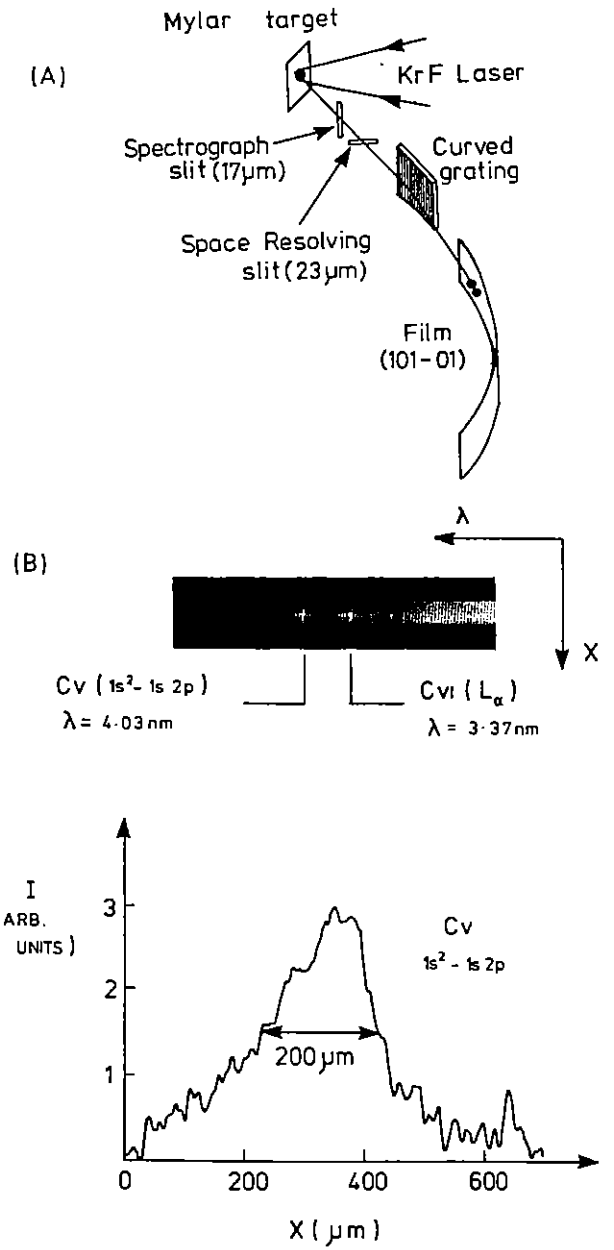

Fig A4.4 (a) Experimental arrangement used for recording space resolved spectral measurements.

(b) Space resolved spectrum from plasma using Mylar foil target.

to determine the absolute X-ray energy content in certain spectral regions. By choosing a suitable combination of filters it is possible to simulate, for example, a diode response predominantly in the water window region. Measurements were taken with several such diode and filter combinations placed at various angles with respect to the target normal. These results are shown in figure A4.5 for the two spectral regions $\lambda < 2.3$nm and $2.3\text{nm} < \lambda < 4.4$nm. It is clear that in this latter region there is a very strong angular dependence to the X-ray emission. The angles that the specimen chambers were positioned at experimentally ($\sim 30^0 - 40^0$) therefore do not appear optimum for receiving the maximum X-ray flux.

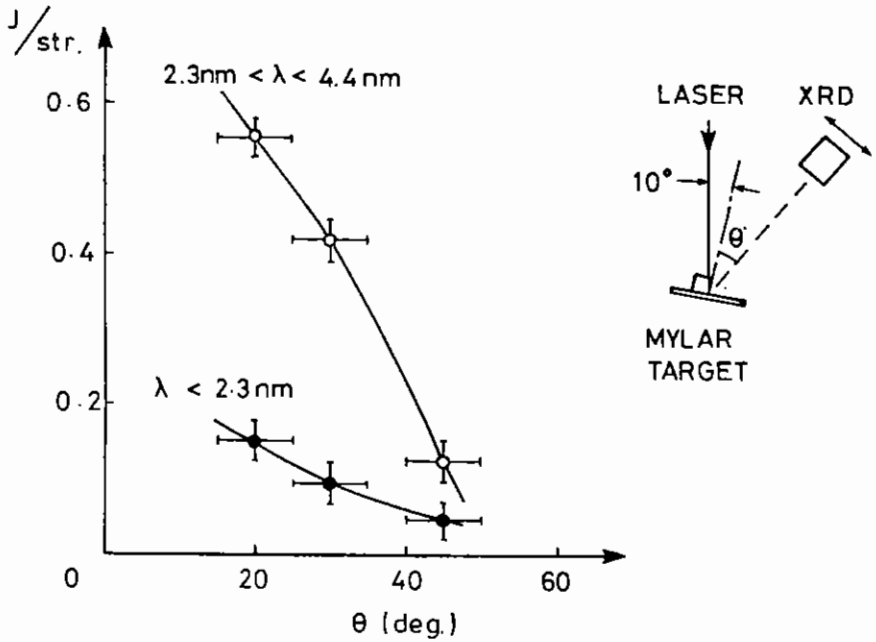

Fig A4.5 Angular dependence of absolute X-ray emission for the two wavelength regions; $\lambda < 2.3$nm and $2.3\text{nm} < \lambda < 4.4$nm. Target=250μm thickness of Mylar foil.

A4.2.3 X-ray Images of Foxglove Epidermal

A D Stead (Royal Holloway and Bedford New College),
A G Michette (Kings College)

One of the more striking contact x-ray images obtained in this past year is that of an epidermal hair from the corolla of a foxglove (Digitalis purpurea L.CV.Foxy), recorded using Sprite. The hair was removed from a fresh flower immediately before exposure and was not prepared in any way. The exact specimen thickness is unknown - the hairs are typically 10-20 μm thick - but the one imaged was probably flattened in the specimen holder. Scanning electron micrographs of the developed x-ray image after coating with 10 nm of Au:Pd are shown in Figures A4.6c and A4.6d. The cell is from the distal region of the hair and the cytoplasm is seen to be arranged in long strands. This arrangement is not observed in the chemically fixed, dehydrated and embedded material used for transmission electron microscope imaging of biological material (Figures A4.6a, a cell from the middle of the trichome in tangential longitudinal section, and A4.6b, a basal cell in transverse section), although similar strands can sometimes be seen in the larger and more transparent cells at the base of each hair by light microscopy (Figures A4.6e and A4.6f). This suggests that the TEM image of this material may not represent the arrangement of the cytoplasm in the living tissue.

A4.2.4 Fibroblasts

P C Cheng, R Feder (IBM, Yorktown), R W Eason (Essex), A G Michette (Kings College), R J Rosser (SUNY, Stoneybrook).

The human fibroblasts used in this study were exposed on Sprite and were grown on the surface of 100 nm thick Formvar films which were supported by nickel index-grids. The cells were cultured in Eagle's medium (10% fetal calf serum and antibiotics) under 5% CO_2 at 37^0C. The cells were then fixed in 1% glutaraldehyde, dehydrated in an ascending series of EtOH and critical-point dried. Fibroblasts have been used as standard test materials in various X-ray imaging experiments (A4.16). The advantages of using cultured fibroblasts are

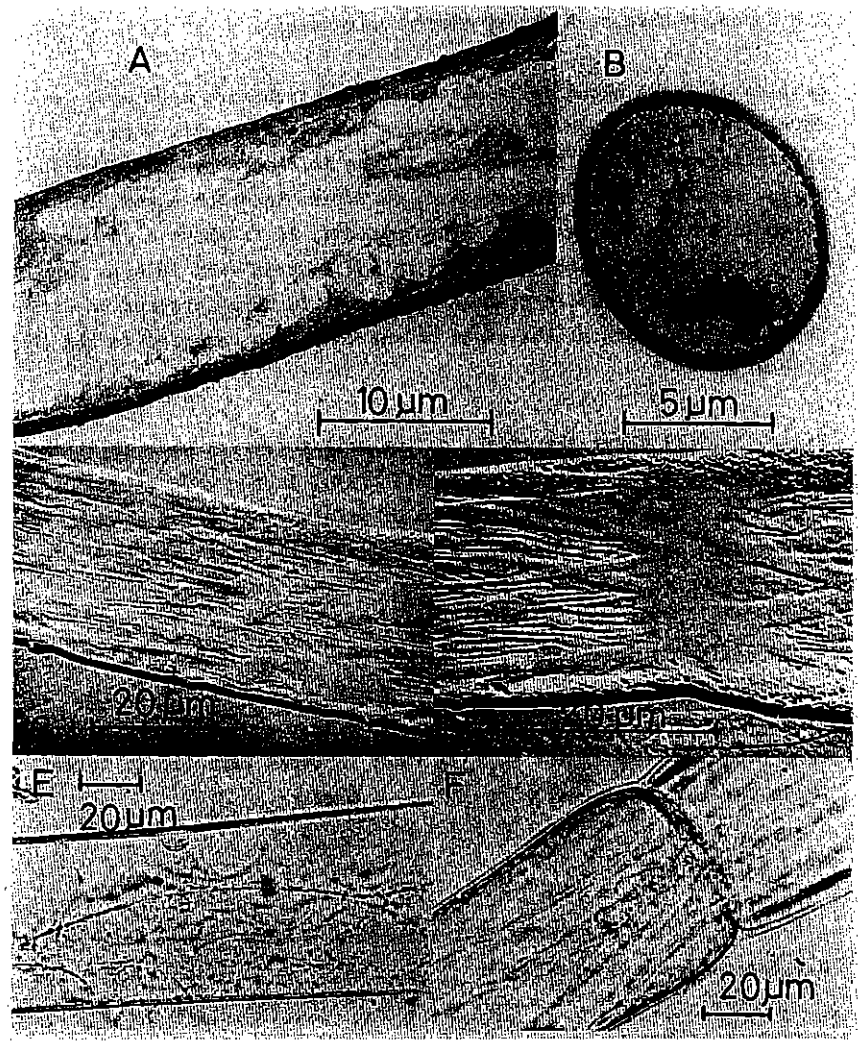

Fig A4.6 Images of epidermal hairs from the corolla of a foxglove.

not only that their ultrastructures have been extensively studied, but also that the cell thickness can be controlled by varying the type of cultured substrates and type of coatings on the substratum (ie polylysine coating can cause the cell to spread out on the substratum). Because the fibroblast is relatively thin and flat, a good contact between specimen and resist can also be achived. The P(MMA-MA) X-ray resist used in this study was supported on the surface of a 100 nm thick Si_3N_4 window and the resulting X-ray contact images were viewed by using a TEM. Two layers of Si_3N_4 films, each 100 nm thick, were placed in front of the specimen as filters and protecting films. These Si_3N_4 films not only cut off UV radiation from the source, but were also found to be essential to prevent breaking of the Si_3N_4 window which supports the X-ray resist during exposure. The TEM-magnified contact images shown in this section are the first series ever obtained from a pulsed X-ray source. Figure A4.7 shows the X-ray image of a human fibroblast.

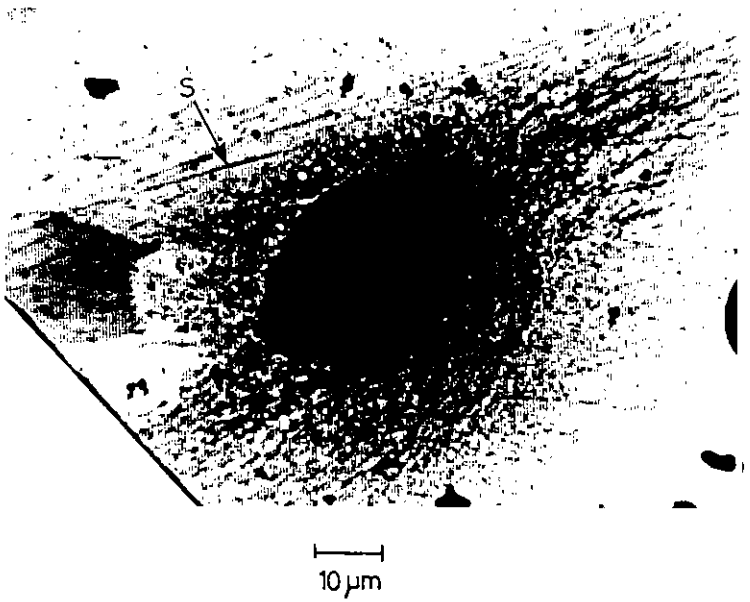

Fig A4.7 TEM-magnified X-ray contact image of human fibroblast. The image shows nuclei with X-ray dense nucleoli. Stress fibre bundles (S) are readily visible in the cytoplasm.

The nucleus with pronounced nucleoli is evident. The nucleoli appear to be X-ray dense structures. In the cytoplasm, stress fiber bundles are clearly visible. The TEM-magnified contact image provides higher resolution that those images obtained by using an SEM. However, due to the relative insensitivity of detecting small changes in resist profile heights by conventional TEM and SEM, and the potential artifacts introduced by prolonged development of the resist in the developer, one can only fully explore the resolution of the X-ray resist by using resists which have been shallowly developed and surface shadowing techniques (A4.17).

A4.2.5 Red Blood Cells

R W Eason, M Clague, R Cherry (Essex University).

Samples of fresh blood cells obtained by venipuncture were used here to investigate the change in shape of the cells that occurs when particular toxins are introduced. Figure A4.8(a) shows the developed resist surface for an exposure made on Vulcan in which a red blood cell image is seen. The shape is rather curious, as it shows a rim around the circumference of the cell. It is not certain what this is due to, but possibly results from the different in X-ray absorption between the integrated path at the edges of the cell when compared to the middle.

Figure A4.8(b) shows the effect on the cell structure when melittin is introduced. Melittin, a cytolytic toxin, is the main component of bee venom. The pictures illustrate transformation of the normal erythrocyte biconcave disc shape to the spiculated structure characteristics of an echinocyte upon addition of toxin.

Blood cells are particularly good specimens to study by this technique, as their natural size and shape is well suited to the dimensions of the grid structures (1.5 μm deep photoresist) which have been put onto some of the Si_3N_4 windows in these experiments to act as wells for the specimens.

A4.2.6 Flagellae

A G Michette, M E J Holwill, N R Sylvester, J Adam (Kings College), R W Eason (Essex University)

A scanning electron micrograph of the x-ray image of Crithidia oncopelti, with flagellae, is shown in Figure A4.9. This specimen was prepared as for electron microscopy, and the image is similar to those of specimens similarly fixed and viewed directly by scanning electron microscopy.

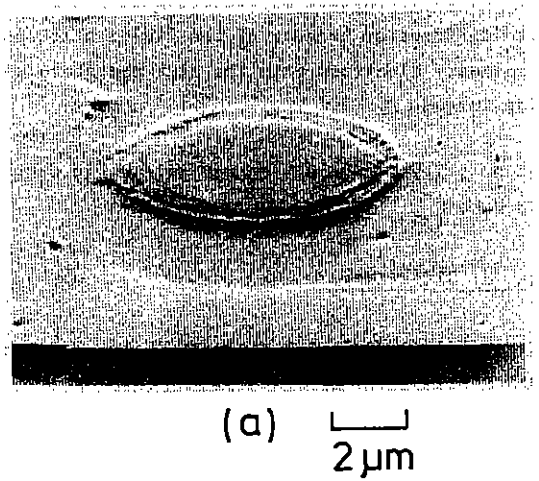

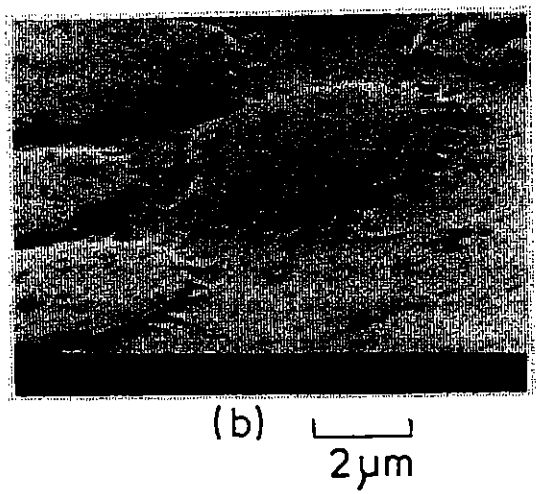

A4.8 Replicas of in vivo red blood cell (a) and cells plus melittin (b). Blood obtained by venipunture, washed 3 times in buffer containing 141 mM NaCl, 2 mM $MgCl_2$, 5 mM KCL, 5 mM glucose, 1 mM EDTA and 10 mM Tris. pH 7.5 at room temp. Sample 5% haematocrit in same buffer. Melittin prepared from crude bee venom, by extensive gel filtration. Low phospholipase activity. Melittin added to produce ~ 10% release of haemoglobin from red bloodcells.

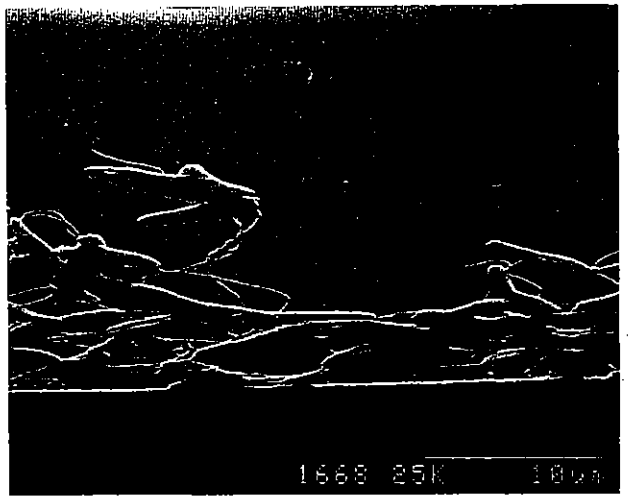

Fig A4.9 X-ray images of Crithidia oncopelti showing flagellae. Average flagella length is 17μm and diameter 0.1μm.

A4.2.7 Lead Contaminated Earthworm Tissue

S Richards (Keele University), A Rush (SERC).

A preliminary investigation into the use of the VULCAN and Sprite laser facilities at the Rutherford Appleton Laboratory to image thin sectioned, lead contaminated chloragogeous tissue of the earthworm Dendrolavena rubida has been made.

A number of serial sections were cut (~ 600Å thick), mounted on microscope grids, and studied using a Transmission Electron Microscope (TEM) and the resultant images photographed. These sections were then exposed on the Synchrotron Radiation Source at Daresbury Laboratory. The resultant 1:1 images were studied using a Scanning Election Microscope (SEM). The same sections were then exposed on the Sprite laser and the 1:1 images in the resist analysed using an SEM.

The images produced by all three methods were compared and it was established that both SRS and laser techniques did give information on biological structure that could be readily understood. However, this information was not uniform throughout the sample and the image was blurred and indistinct in certain areas. There is little doubt that both techniques are useful and complimentary but further research and stricter controls on method, both on recording and developing, are necessary before full recognition of the technique can be established.

The resolution achieved at the moment is ~ 1000Å but this could be reduced to ~ 250Å if the following criteria were adopted.

1. The resist to be characterized before running to ensure optimum development time - resist has a limited shelf life (3 - 6 months), and varies from batch to batch.

2. The developer strength to be monitored frequently (at least once an hour) to ensure mixture ratio is maintained - there is a differential evaporation of the constituents.

3. The resist to be post baked after development when it is still "soft" to evaporate remaining solvent - this temperature must be carefully controlled to avoid deforming the resist.

4. Gold deposition to be kept to a minimum so that a good image in the SEM is obtained. It must be thick enough, however, to avoid resist 'bubbling'.

5. The SEM voltage to be kept as low as possible to reduce possibility of "burn" and "bubbling". Where areas of special interest require higher voltages for increased definition, exposure should be kept to a minimum.

Further increases in definition may be obtained but resolution is reduced due to diffraction because of the finite thickness of the sample and secondary electrons from the high absorbers within the specimen being imaged.

A4.3 SCALING OF X-RAY MICROSCOPY SOURCE BRIGHTNESS WITH LASER ENERGY ON SPRITE AND VULCAN

A4.3.1 Vulcan Nd: Glass Laser

R W Eason (Essex University), A G Michette (Kings College), R J Rosser (SUNY, Stoneybrook).

For the work performed so far, the laser energy available has exceeded that required for adequate exposures by a large amount. While this enables the exposures to be recorded at large source-to-resist distances, thus minimising debris problems, one question that needs to be answered is how large a laser is needed for this work? There is clearly a great deal of scope here as all of the parameters such as source to specimen distance, angle between specimen and target normal, laser irradiance, resist material, and development procedure can be altered to attempt optimum exposure. We now know that for the experiments conducted so far this optimum was almost certainly not achieved, so the question remains how much energy is required from the laser to achieve a single-shot exposure.

One method of answering this is to adopt an empirical approach, and progressively decrease the laser energy until an inadequate exposure level is reached. This had been done, using the Vulcan laser, where a series of five 1ns, 0.53μm shots of progressively decreasing energy were used (A4.18). To maintain the laser irradiance approximately constant, the spot size was reduced accordingly, while moving the resist nearer to the plasma source to ensure approximately constant incident X-ray flux. To simulate an environmental chamber, the resist was placed behind a Si_3N_4 window for each shot.

Green Laser Energy E_L(J)	Spot diameter d(um)	Irradiance $= \frac{E_L}{\pi d^2 \tau}$(WCM^{-2}) τ = pulselength = 1 ns	Source to sample separation ℓ (mm)	Relative Flux incident at sample $= E_L/\ell^2$	Type and time of development
34.2	600	1.2×10^{13}	60	0.57	1:1 MIBK 1 min
34.0	450	2.1×10^{13}	45	1.0	1:1 MIBK 1 min
14.4	300	2.0×10^{13}	30	0.95	1:1 MIBK 1 min
2.0	100	2.5×10^{13}	10	1.2	1:1 MIBK 1 min
0.5	70	1.3×10^{13}	7	0.6	ECA 5 mins.

TABLE 1

The results of these shots are summarised in table A4.1. Although all five shots produced exposures, the first four (those with energy > 2J) yielded visible images after ~ 1 min. development in 1:1 MIBK. The fifth required 5 mins. in ECA, before any pattern became visible. As the 1 min. in 1:1 MIBK developer has been found to be a good gauge of adequate exposure, this fifth shot was judged inadequate.

Further tests using a Nd:glass laser capable of producing up to 3 Joules in 2 ns, have again produced positive results (A4.19). At the 1 J level it is at present uncertain that adequate exposures can be achieved although some positive results have recently been achieved using a 0.6J, 25 ns KrF laser (A4.20 and Section C of this Annual report). Several moderately priced lasers are capable of this level of output, for example KrF excimer lasers, or small ruby or glass systems, so that it is important to answer this question. Experiments are

currently under way at several different institutions (Essex, King's College and RAL) to find a lower limit to the laser energy and irradiance conditions needed for single-shot exposures.

A4.3.2 Work on the Sprite KrF Laser

Y Al-Hadithi, R W Eason (Essex University), A G Michette, C Hills, A M Rogoyski (Kings College), F O'Neill, U Zammit, I C E Turcu (RAL).

Work on the Sprite laser has concentrated on characterising the X-ray emission from carbon, tungsten and gold targets at a range of energies between 0.3J and 122 J using an NO_2 absorption cell to vary the energy (A4.21). A passive absorption cell (to contain a gas which absorbs at the wavelength of the laser) is inserted into the laser beam to achieve this. Fig A4.10 shows a calibration curve for the NO_2 cell attenuation of the Sprite laser beam. The energy of the beam incident on the cell was approximately 110J. The windows of the cell were uncoated and there was some aperturing of the beam and hence a great deal of attenuation (about 35%) occurred even with the pressure of the NO_2 close to zero. As the pressure was increased, the transmission varied as $\alpha e^{-\beta\gamma}$ (γ = pressure in cell, α,β = constant).

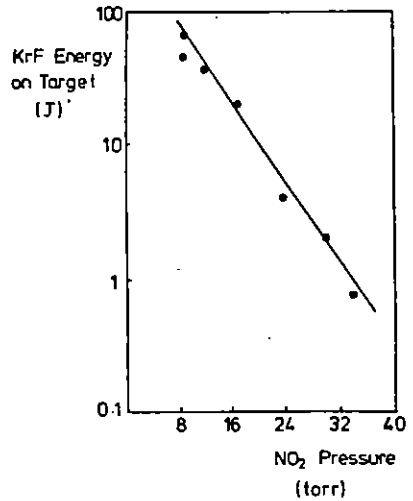

Fig A4.10 Calibration of NO_2 absorber cell.

A soft X-ray diode was used to measure quantitatively the integrated X-ray emission from carbon, tungsten and gold targets into the water window region of the spectrum. An X-ray filter was placed in front of the XRD to give a response mainly in the 2.3 - 4.4 nm range. Figure A4.11 shows the angular characteristics of the X-ray emission from a carbon rod target for an incident laser energy ~ 100 J. The X-ray emission from these massive targets should be compared with the emission from 250 μm thick Mylar foil targets shown in Fig A4.5. The massive target gives much more X-rays due to the fact that the laser pulse was burning through the thin Mylar target. This also explains why the X-ray pulse from Mylar was shorter than the laser pulse. Using massive Graphite targets the X-ray pulse has the same duration as the laser pulse ie ~ 60ns.

From curves like that shown in Fig A4.11 we can integrate the total X-ray emission into all angles from the target. In Fig A4.12 we plot the variation of total X-ray yield with laser energy on target for graphite and tungsten targets. The peak conversion efficiency from laser light to X-rays is seen to be extremely high being > 10% for carbon and > 50% for tungsten. These numbers do however depend critically on the exact calibration of the X-ray diode and filters. These items are now being calibrated on the synchrotron radiation source at Daresbury Laboratory in order to make the data in Fig A4.12 more accurate.

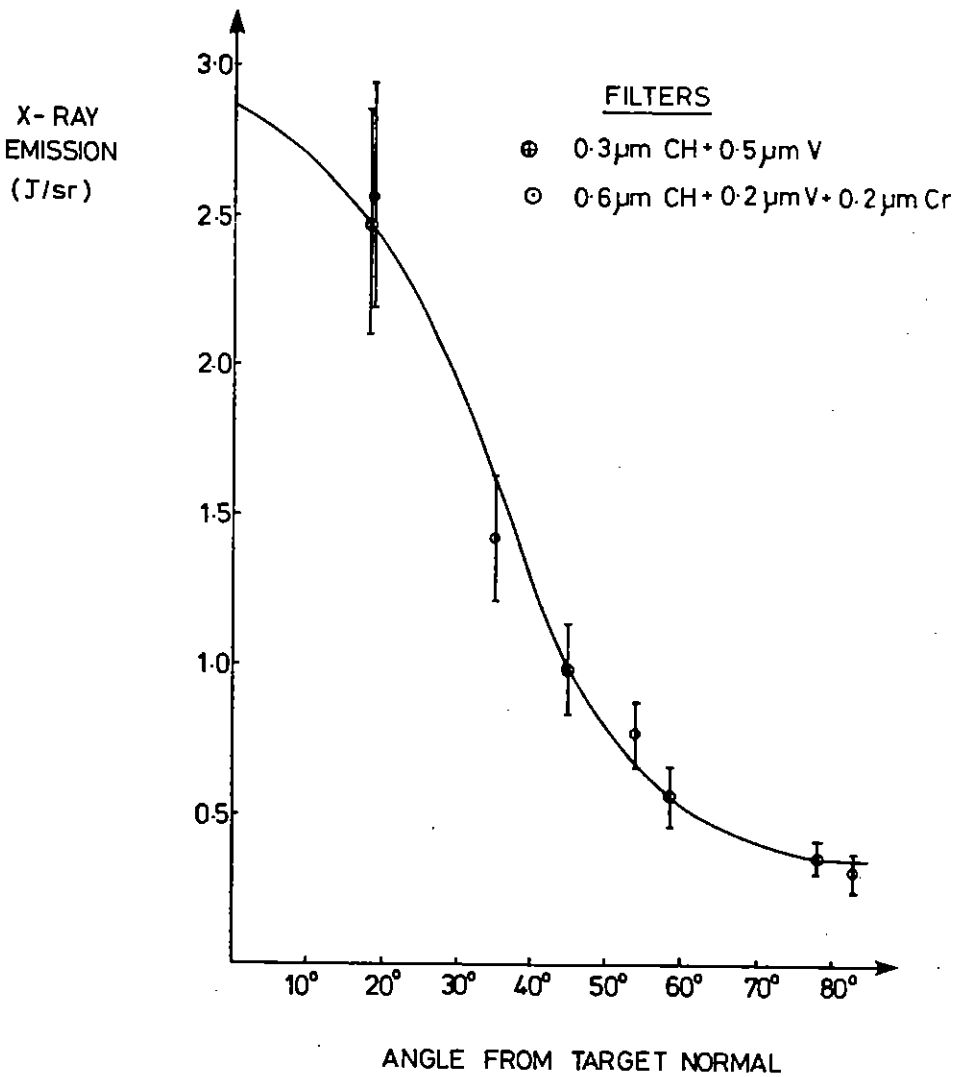

Fig A4.11 Angular dependence of X-ray emission in water window from massive graphite target.

Using carbon based targets, X-ray emitting plasmas were produced whose spectra were recorded in the wavelength range ~ 20Å - 230Å, using a grazing incidence grating Rocket spectrograph. Spot sizes on target were in the range 50 μm - 100μm, and the laser energy varied between 0.3J and 122J. The spectroscopic data is shown in Fig A4.13, for a range of energies from 2J upwards. Below 2J, no exposure was visible under single shot conditions. X-ray spectra have been recorded using multiple shots from a 0.6J KrF laser and these are described in Section C6 and in reference A4.20. The spectra with Sprite were recorded on Kodak 101-01 X-ray film, with the spectrometer at ~ 48^0 to the incident laser direction.

Further analysis is in progress to correlate the data in Fig A4.13 with the measurements recorded using filtered X-ray diodes (Figs A4.11 and A4.12), which viewed the water-window spectral region alone. Deductions about spectral energy in lines versus continuum should be possible, and an absolute limit concerning minimum laser energy needed will be determined.

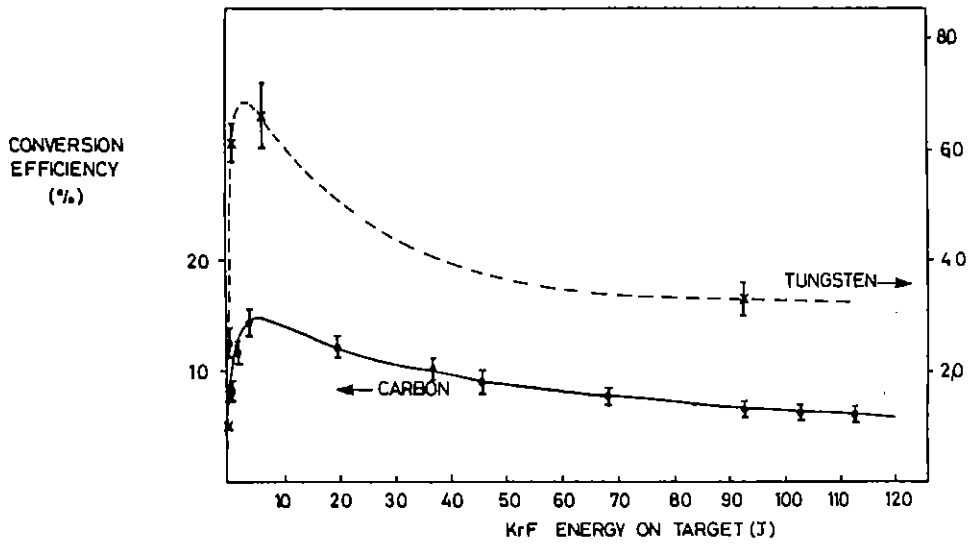

Fig A4.12 Conversion efficiency of KrF laser light to X-rays in the water window into 2π steradians.

A4.4 X-RAY SOURCE CHARACTERISTICS AT 1.7nm > λ > 0.4 nm ON SPRITE

M J Lamb, P McCavana, E Robertson (QUB) and I C E Turcu (RAL)

A4.4.1 Introduction

The first target experiments using the KrF SPRITE laser were reported in last years Annual Report (A4.4) and included the first observation of X-ray line emission from He-like and H-like ion species in a KrF laser-produced plasma (A4.22). We report here on the observation of a number of K, L, and M-shell x-ray spectra in the wavelength range 0.4 - 1.7 nm from a variety of targets irradiated by the Sprite laser.

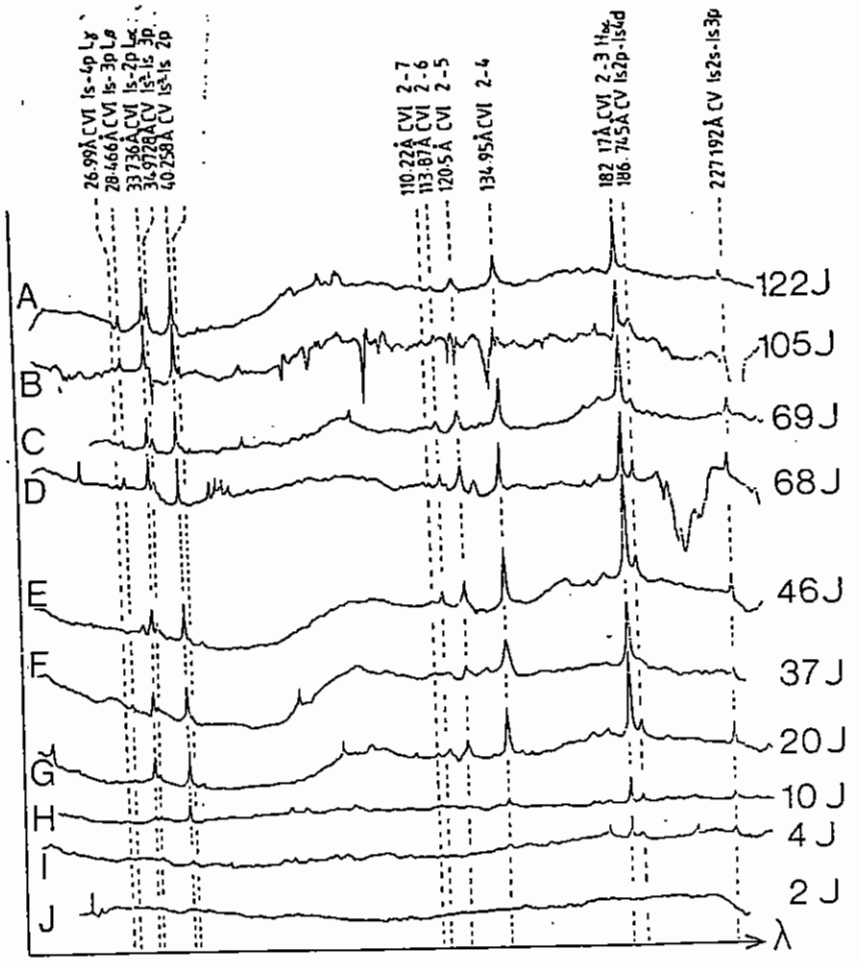

Fig A4.13 X-ray spectrum from carbon targets as a function of KrF laser energy.

The spectra obtained consist of K-shell emission from F, Na, Mg, Al, Si and Cl, L-shell emission from Cu, Zn, Br and Y, and M-shell emission from Yb, Ta and W.

A4.4.2 Experimental

The convergent output beam from the Sprite KrF laser (140 J maximum energy at a wavelength of 249 nm in a 50 ns pulse) was focussed by a 1.2 m focal length fused silica lens to a spot size of ~ 150 microns giving an irradiance of 1.5×10^{13} W cm^{-2}. The focussed beam was incident normally on to the surface of a flat target (either massive or > 100 micron thick foil) placed at the centre of an evacuated target chamber.

Two space-resolving miniature crystal spectrometers, two pinhole cameras and a silicon PIN diode recorded the X-ray emission from the resultant plasma. We will concentrate here on the data from the X-ray spectrometers. These viewed the plasma symmetrically at an angle of 45^0 to the laser axis. Spatial resolution was provided by a 50 micron wide entrance slit. The spectrometers were positioned 2 - 3 cm from the plasma. At closer distances the target debris destroyed the entrance slit despite the presence of various protective filters of beryllium, aluminium and mylar. Even at 3 cm these filters needed frequent replacement.

Two spectrometers were used to provide extended spectral coverage. Each spectrometer contained a different Bragg crystal chosen from PET (2d = .874 nm), ADP (2d = 1.065 nm), Beryl (2d = 1.595 nm) and TlAP (2d = 2.575 nm). The particular pair of crystals used for a specific target was chosen to record the appropriate spectral region and provided a degree of spectral overlap allowing cross calibration of the crystals. The X-ray film used was Kodak DEF which has been extensively calibrated (A4.23).

Single shot space-resolved spectra were recorded from targets of PTFE (fluorine), NaCl (sodium), magnesium, aluminium, silicon, Saran (chlorine), copper, zinc, KBr (bromine), yttrium, ytterbium, tantalum and tungsten.

A4.4.3 Results and Discussion

Figures A4.14 and A4.15 show the series of K-shell spectra obtained. In the case of the fluorine spectrum, recorded off TlAP, the vertical scale is in relative exposure units the original data having been processed to account for filter absorption, film response and contributions from second order continuum. The trace for magnesium is a composite of two spectra recorded simultaneously off Beryl (for wavelengths > 0.8 nm) and ADP. The data has been normalised to the intensity of the strong satellite to the He_{beta} line to account for the different crystal reflectivities. The vertical scale however is effectively relative photographic density as in the case of the remaining spectra illustrated.

In the fluorine spectrum both the H-like and He-like resonance series lines can be seen clearly, the dominant feature being the L_{alpha} line. The continuum radiation shown in the figure is due to recombination into the He-like ion. A weak contribution due to recombination into the H-like ion is also present on the original, but not shown here, and indicated the presence of fully-stripped ion in the plasma.

As we go through the iso-electronic sequence from sodium to silicon the He-like resonance series and associated continuum become the dominant features. The relative brightness of the He-like to H-like resonance lines shows a systematic increase indicating a shift in the ionisation balance in the plasmas away from fully-stripped and H-like ions. In the case of sodium the L_{alpha} and He_{alpha} lines have approximately equal brightness whilst for silicon the He_{alpha} line is eight times brighter. In the extreme case of chlorine the only spectral features are the He_{alpha} line and its associated satellites around 0.44 nm. Chlorine therefore represents the limit for exciting K-shell spectra with the current Sprite laser configuration.

The plasma temperature has been calculated from the slope of the recombination continuum in the case of Mg (495 eV), Al (400 and 450 eV), and Si (270 eV). These values are comparable with those

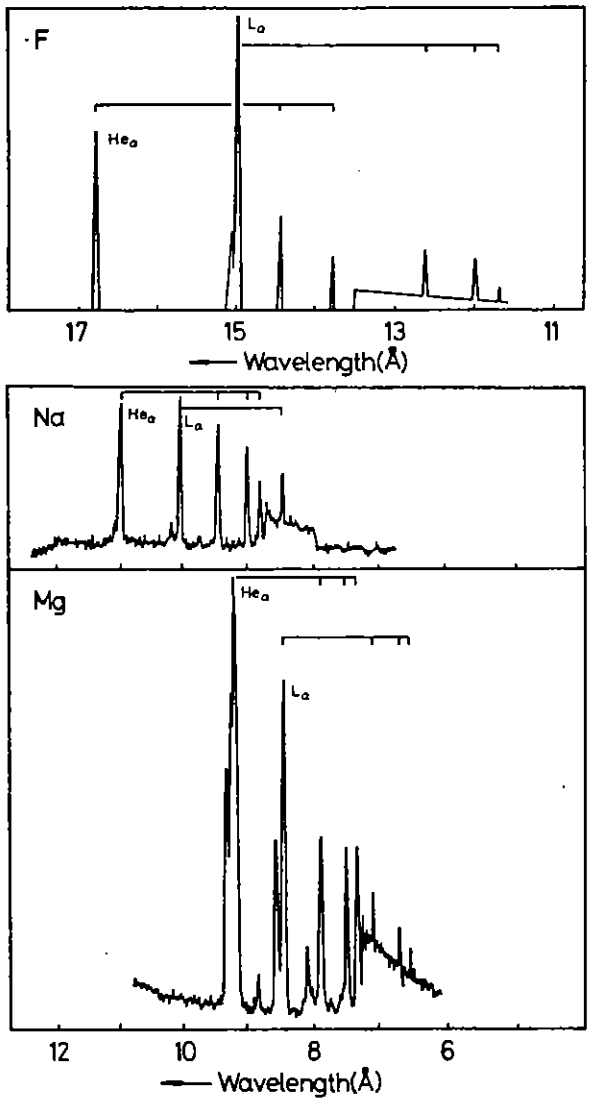

Fig A4.14 K-shell spectra of F, Na and Mg recorded on Sprite.

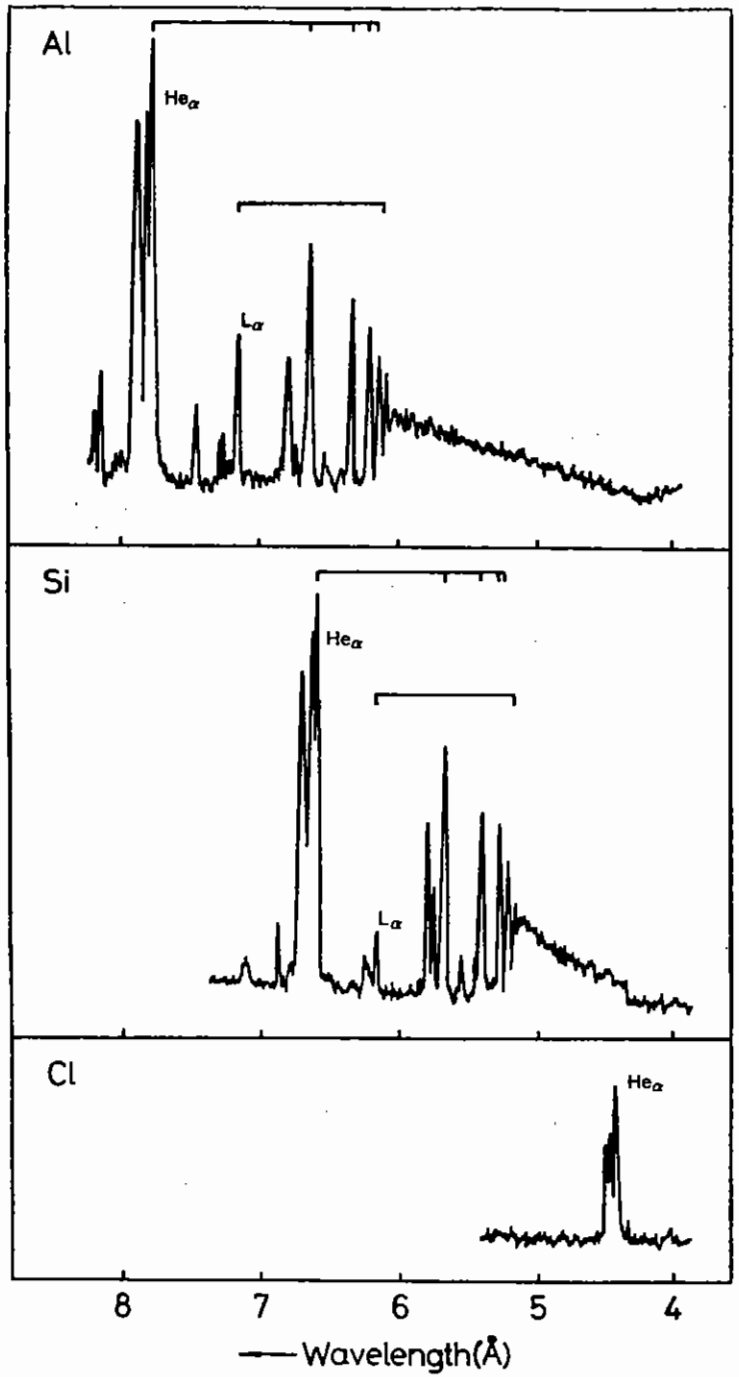

Fig A4.15 K-shell spectra of Al, Si and Cl recorded on Sprite.

estimated from collisional-radiative calculations of the ionisation balance (A4.24).

Spectra of the M-shell emitters ytterbium, tantalum and tungsten are shown in Fig A4.16. The emission here is due to 4p-3d, and 4f-3d transitions in Co- and Ni-like ions (A4.25). The recorded spectra show a systematic reduction in brightness for higher Z.

Figure A4.17 shows an example of one of the L-shell spectra obtained, that of bromine, showing 3-2 and 4-2 transitions in Ne-like ions, L-shell spectra were also obtained for copper, zinc and yttrium. All of the spectra recorded require further analysis.

A4.5 EXPERIMENTAL STUDY OF XUV LASER SCHEMES

G J Pert, Hull; R Corbett, C L S Lewis, C Reagan, S Sadaat, QUB; G P Kiehn, R Smith, O Willi, IC; J E Boon, C Brown, A R Damerell, R G Evans, P Gottfeldt, C J Hooker, M H Key, D A Pepler, S J Rose, I N Ross, P T Rumsby, RAL; A Carillon, P Jaegle, G Jamelot, A Klisnick, University of Paris, Orsay; T Tomie, Electrotechnical Lab, Japan; C Chenais-Popovics, Ecole Polytechnique

A4.5.1 Introduction

New facilities for focussing the six beams of the Vulcan laser to six line foci 7 mm long and 25 μm wide, enabling irradiation of XUV laser targets of length up to 21 mm, were completed in September 1985 (Section A6.2), together with a new time resolving XUV spectrograph of high sensitivity (Section A5.1). The new facilities were specifically designed to exploit the available power of the Vulcan laser in the best way possible for XUV laser studies.

Several XUV laser schemes studied at the CLF and elsewhere have now reached a stage of development giving experimental evidence of amplification with gain coefficients 'g' in the range of 1 to 10 cm^{-1}. The possibility of producing plasma lengths 'ℓ' upto 2 cm with the CLF's new facilities therefore allows the experimental study of XUV gain using the exponential behaviour of the intensity of XUV laser lines with increasing length of plasma. The output intensity I is,

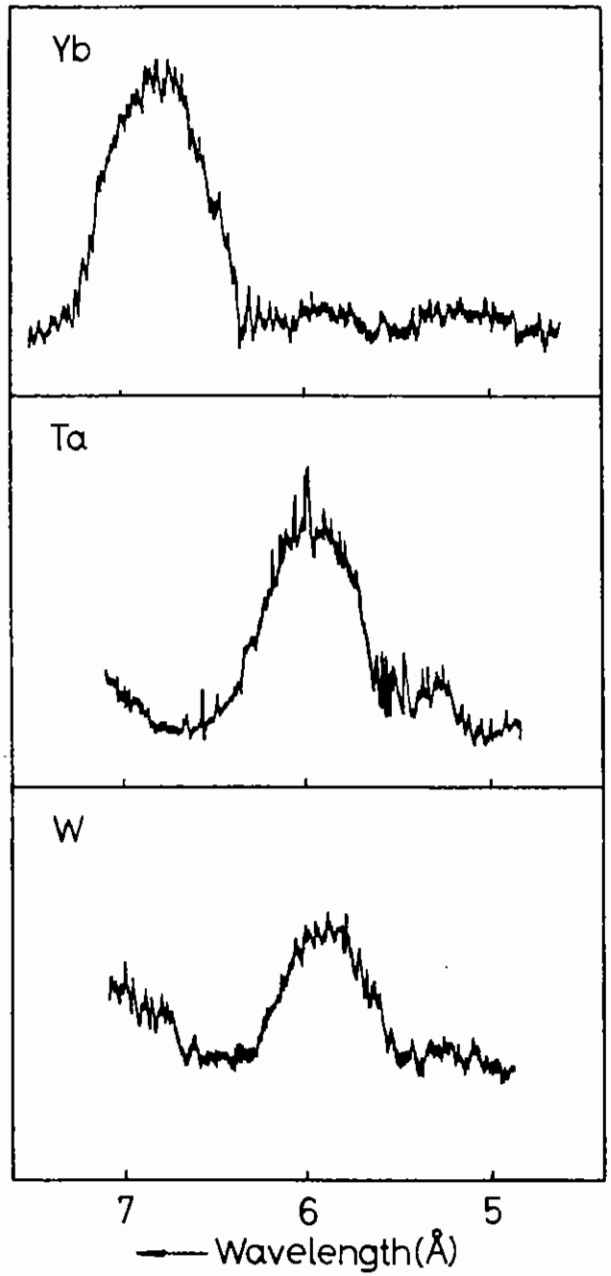

Fig A4.16 M-shell spectral of Yb, Ta and W recorded on Sprite.

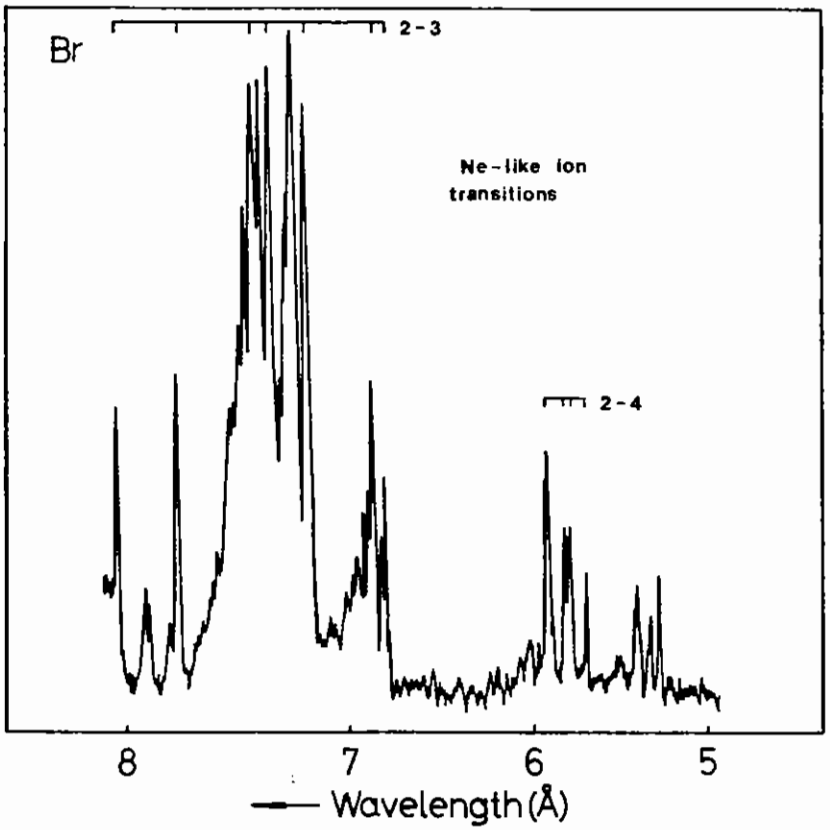

Fig A4.17 Example of L-shell spectrum (Br) recorded on Sprite.

$$I = \exp(g\ell) - 1$$

and unambiguous observation of the exponential form of the function becomes possible for $g\ell$ values greater than about 2.

The initial experiment planned for the new facilities was a rapid survey (three weeks in November 1985) of the most promising laser schemes, designed to address the practical problems in recording the necessary time resolved XUV spectra and related data.

The initial study included:

- Recombination pumping in the CVI Balmer spectrum using carbon-fibre targets
- Recombination pumping in CVI, N VII and O VIII Balmer spectra from thin polymer film targets.
- Recombination pumping in the Li-like Aℓ XI spectrum from planar targets of Aℓ.
- Electron collisional pumping of neon-like 3p - 3s transitions in Se XXV

The most interesting results in the initial survey were obtained with carbon fibre targets and a follow up three week experiment in February 1986 was used to investigate this system in more detail.

The outcome of the carbon fibre study was a striking demonstration of exponentially increasing intensity of the 18.2 nm Balmer α transition in CVI. The experiment is discussed in Section A4.5.2. Encouraging preliminary data from the other systems are presented in Sections A4.5.3, A4.5.4 and A4.5.5.

A4.5.2 Carbon-fibre recombination scheme

A4.5.2 (i) Theoretical Background.

Extensive theoretical modelling underlies the use of laser irradiated carbon fibres to produce population inversion and amplification on the CVI Balmer α transition at 18.2 nm (A4.26). Most of the detailed calculations (and previous experiment with plasma lengths less than 2 mm (A4.27)) have involved use of a prepulse and about a 200 psec main pulse to produce the plasma. Optimisation of gain required rather thin fibres (< 5 μm diameter) which presents problems for work with lengths up to 2 cm. Introduction of a prepulse is also an experimental difficulty.

A reappraisal of the optimisation of gain for partial burn through of the fibre targets led to the conclusion that thicker fibres could be used with shorter laser pulses and with no prepulse, to create essentially the same plasma mass and energy content as before. (Section A5.3.5). On this basis it was concluded that 7 μm diameter fibres irradiated with 70 psec pulses at $\lambda = 0.53$ μm would give the optimum energy content of the ablated plasma, and a gain coefficient of about 8 cm^{-1}, when 4J cm^{-1} was absorbed and the plasma mass was 10^{-7} gcm^{-1}, corresponding to ablation of only a small fraction of the fibre mass. The initial experimental study was aimed at recording the variation of the intensity of CVI Balmer lines with plasma length for the above parameters.

A4.5.2 (ii) Experimental System

The experimental set up is shown in Figure A4.18. The six line foci were used in pairs to irradiate 7, 14 or 21 mm lengths of fibre. Targets were introduced into the chamber via an airlock mechanism and were aligned using a novel split field microscope system (section C5.3) viewing along the two axes illustrated in Figure A4.18. The targets were positioned with a few micron spatial accuracy and an angular accuracy of about 10^{-3} rad. The line foci were aligned on the fibre using a CW Ar-Ion laser operating at 528.7 nm to simulate the 526.5 nm 2nd harmonic wavelength of the Vulcan laser operating with an YLF

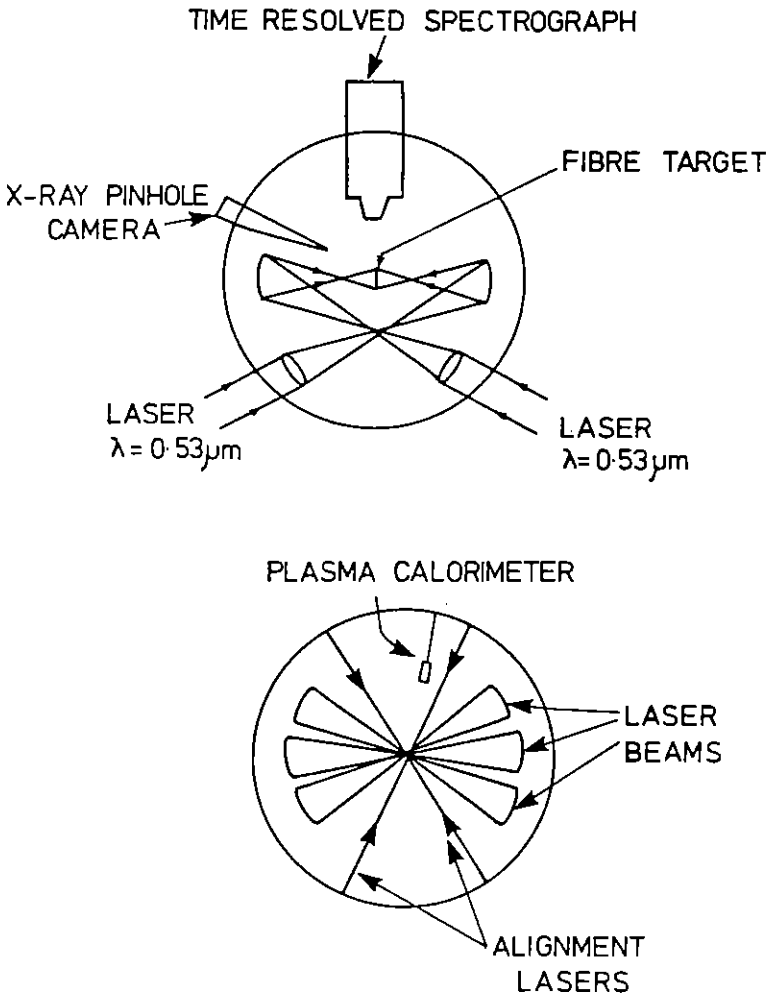

Fig A4.18 Experimental arrangement.

crystal oscillator. Observation of the 'Foucault' shadows, in the beams transmitted past the fibre, were used to optimise the focussing of the beams on the fibre target. Motorized 3-axis micrometer drives on each lens and mirror pair used to produce the line foci enabled precise control. Diagnostics for the experiment were a novel flat field grazing incidence spectrometer viewing along the fibre axis (described in Section C5.1), two linear arrays of plasma calorimeters measuring the well collimated plasma flow perpendicular to the fibre axis, Faraday cups recording ion flow velocity and two X-ray pinhole cameras recording X-ray images of the irradiated fibres.

A4.5.2 (iii) X-ray Images and Plasma Energy

Measurements of the irradiated lengths of the fibres were made from X-ray images recorded on two pinhole cameras, one active with a phosphor screen/intensifier assembly, the other recording directly onto DEF X-ray film. These viewed the targets at angles of 70^0 to the fibre axis. The active pinhole camera had a pinhole size of 80 μm, and was filtered with 0.8 microns of aluminium; this had a significant transmission in the region of the CVI resonance lines (7% at 30 Å). The passive pinhole camera had a 25 μm pinhole and was unfiltered. The overall magnifications onto film (allowing for projection angles and intensifier demagnification) were 1.57 and 1.06 for the active and passive cameras respectively.

Figure A4.19 shows an active pinhole camera picture of a 12 mm length of irradiated fibre, of original diameter 7 μm.

Measurements of the laser energy absorbed by the plasma were obtained from a plasma calorimeter array which was placed 176 mm from the target at an angle of 30^0 below the horizontal on the west side of the target chamber. Each element of the array consisted of 25 micron diameter constantan/chromel thermocouple wires spot welded to a 10 μm thick piece of tantalum foil, 3 mm by 3 mm. Each channel of the array comprised two such elements connected in different mode, with one element being screened from the plasma by a transparent cover, so that scattered light was subtracted out of the overall signal. The output

from each channel was amplified and recorded on the main computer. The distribution of plasma energy in the direction parallel to the fibre axis is shown for shot 4 of 26.2.86 in Figure A4.20. The distribution is sharply peaked, with a FWHM of 1.6 cm, indicating that the divergence of the plasma blowoff was 9×10^{-2} rad.

The total plasma energy E was estimated by integrating under the angular distribution profile, and assuming that the azimuthal distribution was cylindrical (this may lead to an underestimate of the absorbed energy if the azimuthal distribution is peaked in the direction towards the laser beams). A value for E/L, the coupled energy per unit length of fibre, was then obtained by dividing by the irradiated fibre length as measured from the X-ray pinhole camera photographs. For the distribution shown in Figure A4.20 this gives E/L = 2.8 J/cm, with L = 10.7 mm.

The relative intensities of the active pinhole camera images were calculated, taking a weighted average over the length of the image. The values obtained are plotted against the corresponding values of E/L in Figure A4.21. This relationship between image intensity and E/L enabled an estimate of the variation in the local value of E/L along the fibre from X-ray images such as that in Figure A4.19. Typical values were ± 50% RMS.

Estimates of the time-integrated electron temperatures were made by recording the X-ray intensities transmitted through 15, 30 and 45 micron thicknesses of beryllium. These thicknesses were sufficient to cut out line radiation, thus giving values for the relative intensities of the continuum emmision over different wavelength ranges, from which the time-integrated electron temperature can be estimated. Spatial resolution of 1 mm along the fibre length was obtained by placing a 1 mm slit in front of the filters. The images were recorded using a phosphor plate/intensifier assembly. A typical image is shown in Figure A4.22, where the distinct regions reveal that there was some degree of non-uniformity along the fibre length. The temperature estimated for the hotter region is about 250 eV.

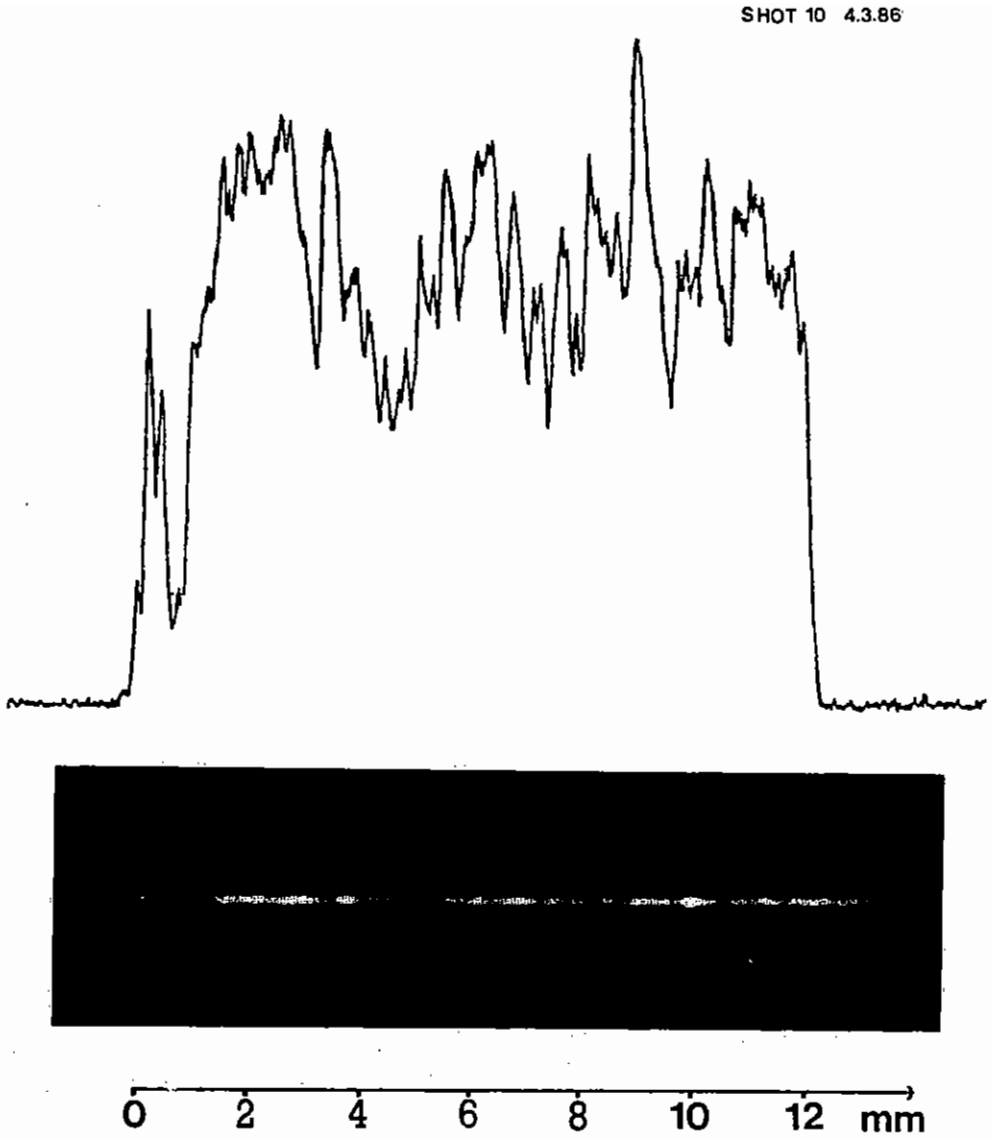

Fig A4.19 Active pinhole camera picture of 12mm fibre.

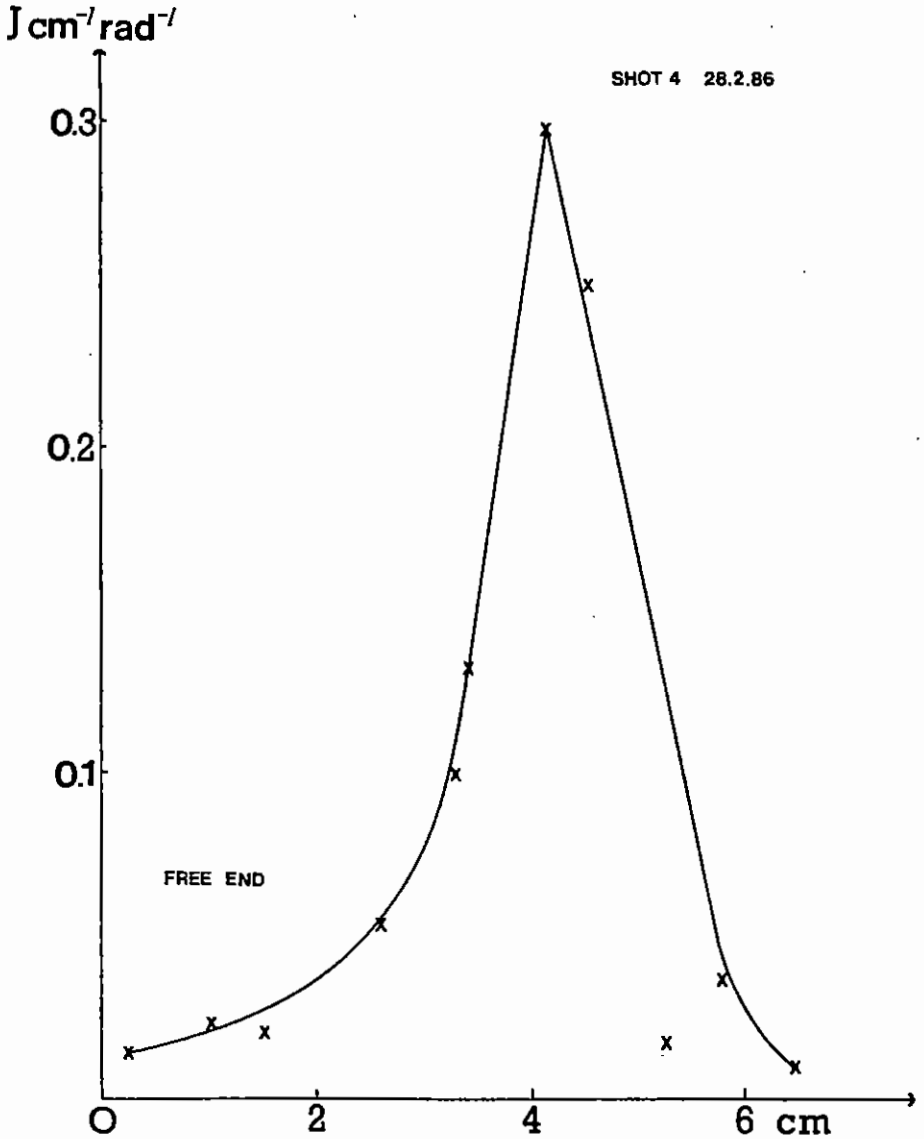

Fig A4.20 Plasma calorimeter readings for shot 4 of 26.2.86.

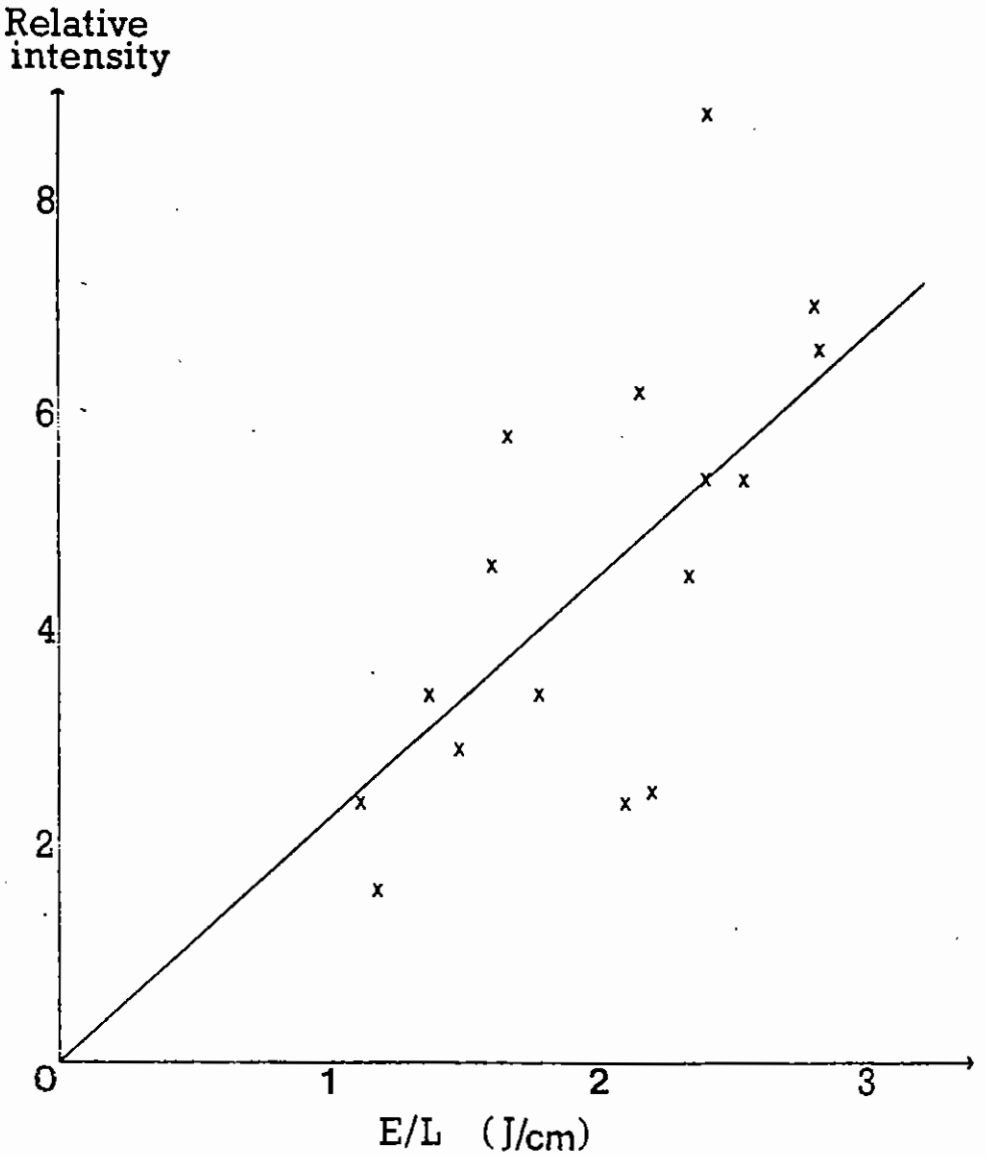

Fig A4.21 Correlation between brightness of actoive pinhole camera image and absorbed energy per unit length of fibre.

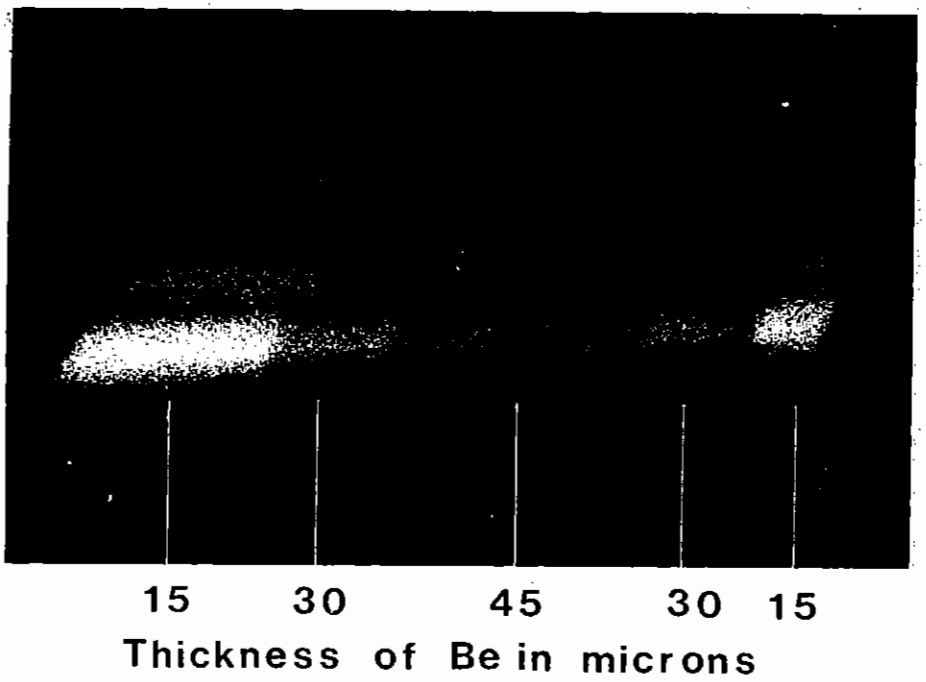

Fig A4.22 Continuum radiation transmitted through Be filters, used to estimate time-integrated electron temperature.

A4.5.2 (iv) XUV Spectra

The new instrument for time resolved XUV spectrometry described in Section C5.1 was used to record the CVI Balmer spectrum along the axis of the targets. The streak rate was 130 psec/mm and the streak covered a 3.75 nsec period. A 2 mm streak slit gave a time resolution of 260 psec. The spectral resolution was determined by the transverse dimension of the plasma, the system having no spectral slit. As the plasma expanded the source size increased so the spectral resolution varied from about 0.5 to 1 Å over the 3.75 nsec streak period. The intensity profile of the spectral line was a one-dimensional integrated spatial profile of the emission perpendicular to the fibre axis.

The principal experiment in February 1986 involved recording spectra from carbon fibres, which were attached to a support at one end and free at the other, with the irradiated length being varied from 1.5 mm to 11 mm. The laser beams were used in opposed pairs so that data for lengths up to 7 mm were obtained using two beams and for lengths upto 11 mm using four beams. The beams were masked to vary the irradiated length and care was taken to ensure that irradiation was as uniform as possible up to the free end of the fibre. Over 60 shots were recorded and the resulting spectra were analysed by densitometry at various times after the laser pulse.

Figure A4.23 show a spectrum obtained for a fibre length of 1.3 mm and Figure A4.24 shows a densitometer tracing 650 psec after irradiation. The Balmer spectrum lines are prominent but their relative intensities are influenced by instrumental factors. Balmer α is relatively suppressed because of reduced transmission of its longer wavelength through the thin-film filters and photocathode substrate of the instrument. Balmer β is enhanced because of both its greater transmission and some underlying 4th order CVI L α intensity (estimated at about 50% from spectra in which the 1st order was suppressed by filters to show the underlying higher order emission. Balmer γ is free of underlying higher order emission). Balmer δ has a 30% contribution from 4th order CVI L β.

Figure A4.25 and 4.26 present the corresponding information from an irradiated length of 12.1 mm. There is an obvious increase in Balmer α intensity relative to the other lines.

The streak records allow the temporal evolution of the C VI Balmer series to be obtained. Figure A4.27 shows the temporal evolution of the short fibre shot and Figure A4.28 shows that of the long fibre shot. A similar temporal appearance exists for all the Balmer series in the short fibre records. However, in the long fibre record a distinctive change in the temporal evolution of Balmer α is noted compared to the other Balmer transitions. This different appearance is consistent with the onset of amplification in the Balmer α transition resulting in a modified, peaked temporal history.

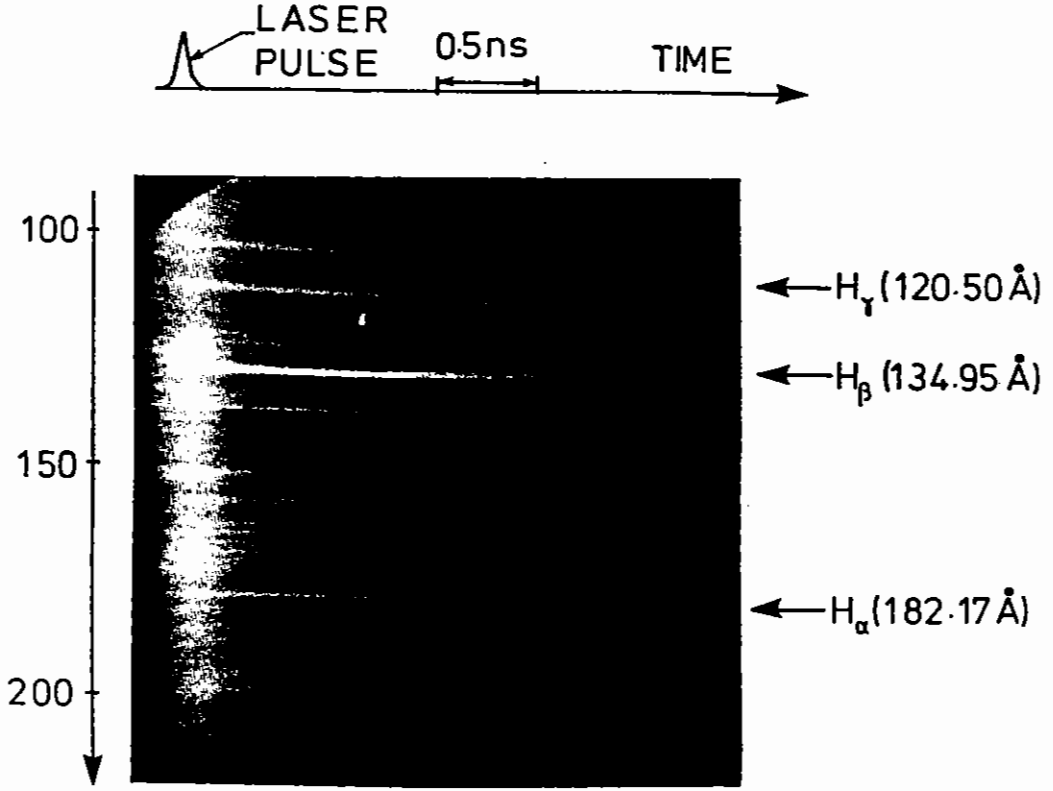

Fig A4.23 Streak record of a short, 1.3mm, carbon fibre shot.

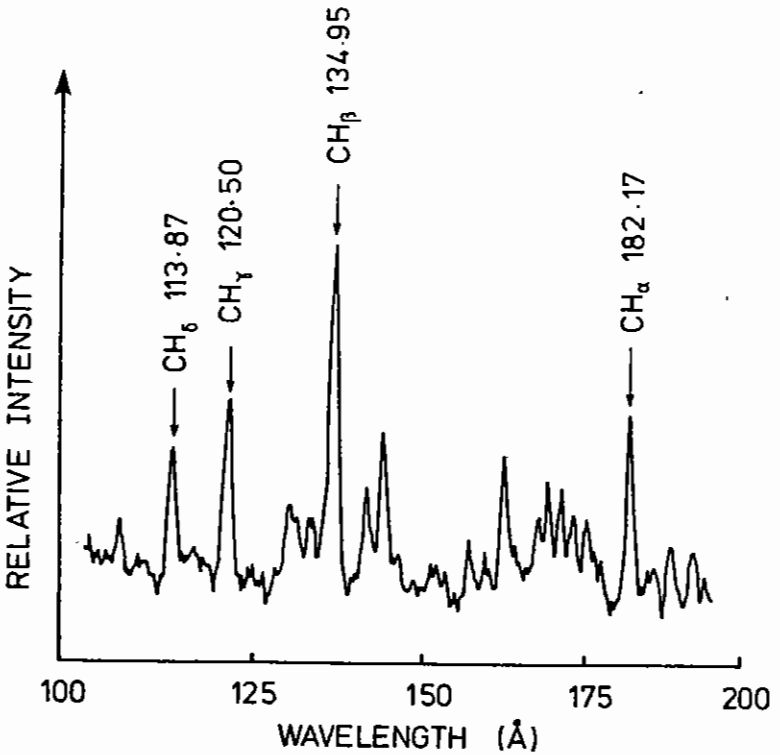

Fig A4.24 Microdensitometer trace of the short carbon fibre shot presented in Figure A4.23, taken 650 psec after laser pulse.

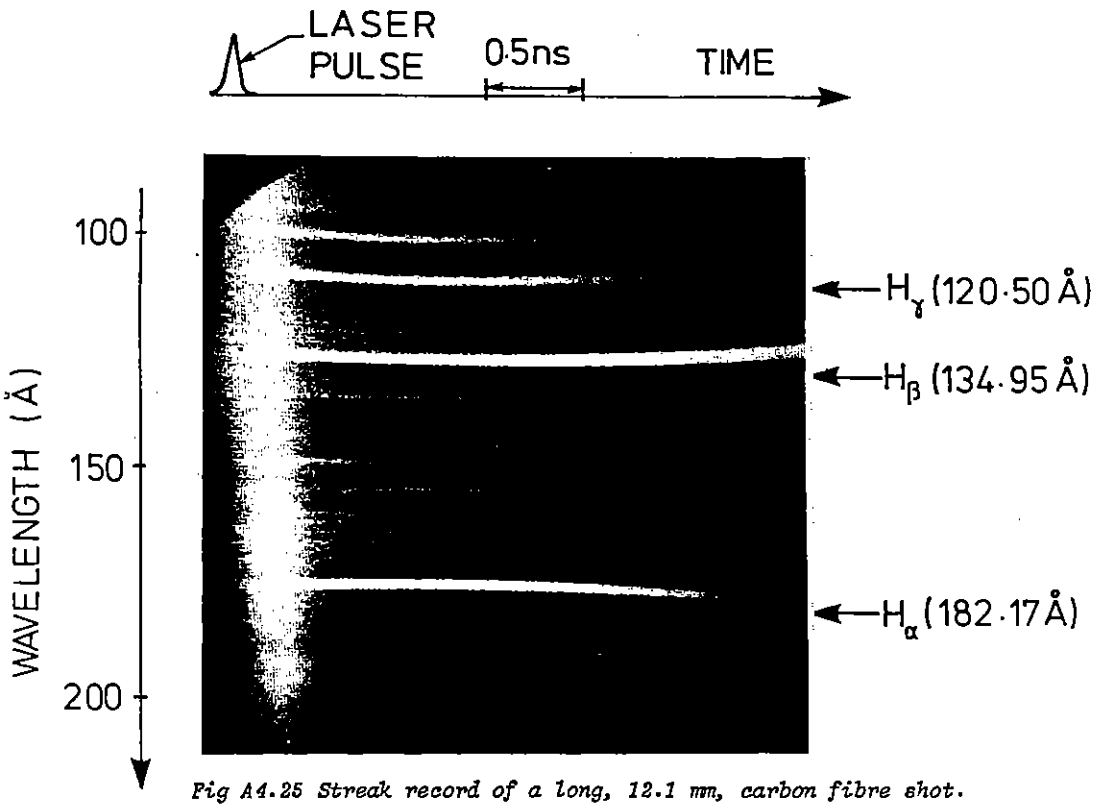

Fig A4.25 Streak record of a long, 12.1 mm, carbon fibre shot.

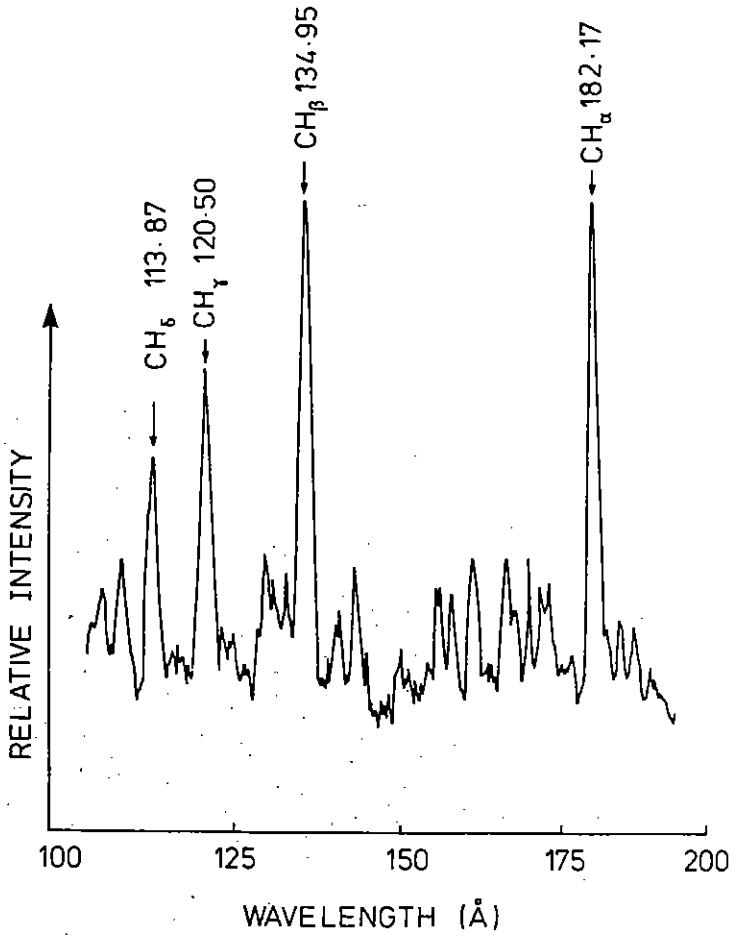

Fig A4.26 Microdensitometer trace of the long carbon fibre shot presented in Figure A4.25, taken 650 psec after laser pulse.

The strongest evidence for amplification is shown by plotting the length dependence of the C VI Balmer line intensities. C V transitions and the higher C VI Balmer transitions exhibit a linear growth of intensity with length, as expected for an optically thin plasma. Figure A4.29 shows the line intensity of H_γ vs length at a time of 650 ps after the input laser pulse as an example of linear growth. However, a clear exponential growth of line intensity with length is observed on the Balmer α transition. Figure A4.30 gives the exponential dependence of the Balmer α line with length, at t = 650 ps after the input laser pulse. This graph demonstrates the expected scaling of exp (gℓ)-1 expected for amplified spontaneous emission. The data can be best fitted by a gain coefficients of between 3.5 and 4 cm^{-1}. This implies single transit amplification by a factor of 50 or a gℓ value of 4.

During the initial survey run in November 85, the axial spectrograph recorded time resolved spectra which showed intense narrow features super-imposed on the C VI Balmer α and Balmer β transitions. The features began approximately 350 ps after the start of the laser pulse and lasted for ~ 1 ns. A typical streak record is shown in Figure A4.31. The subsequent experiment carried out in February 1986 on C-fibres did not reproduce these intense features. It is not currently known whether they are instrumental in origin or represent a spatially localised region of amplified spontaneous emission which is expected and would be resolved by the XUV spectrometer.

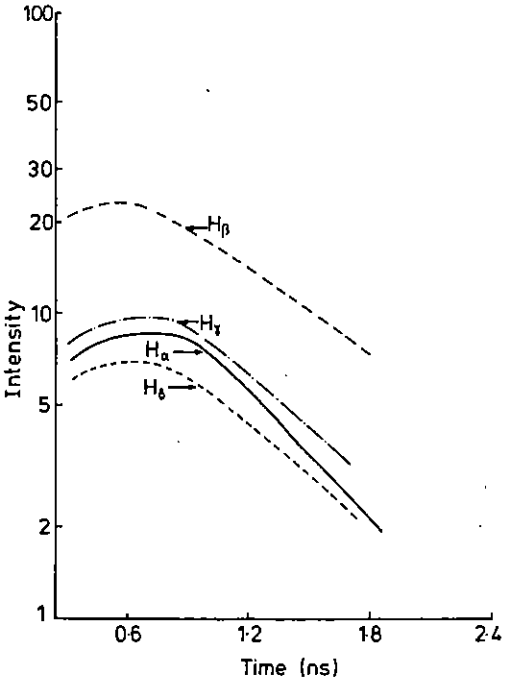

Fig A4.27 Temporal evolution of the CVI Balmer transitions from the short, 1.3 mm, carbon fibre shot.

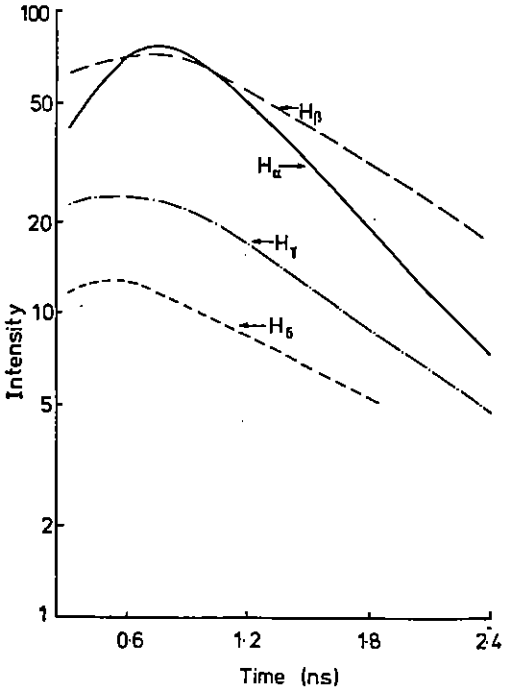

Fig A4.28 Temporal evolution of the CVI Balmer transitions from the long, 12.1 mm, carbon fibre shot.

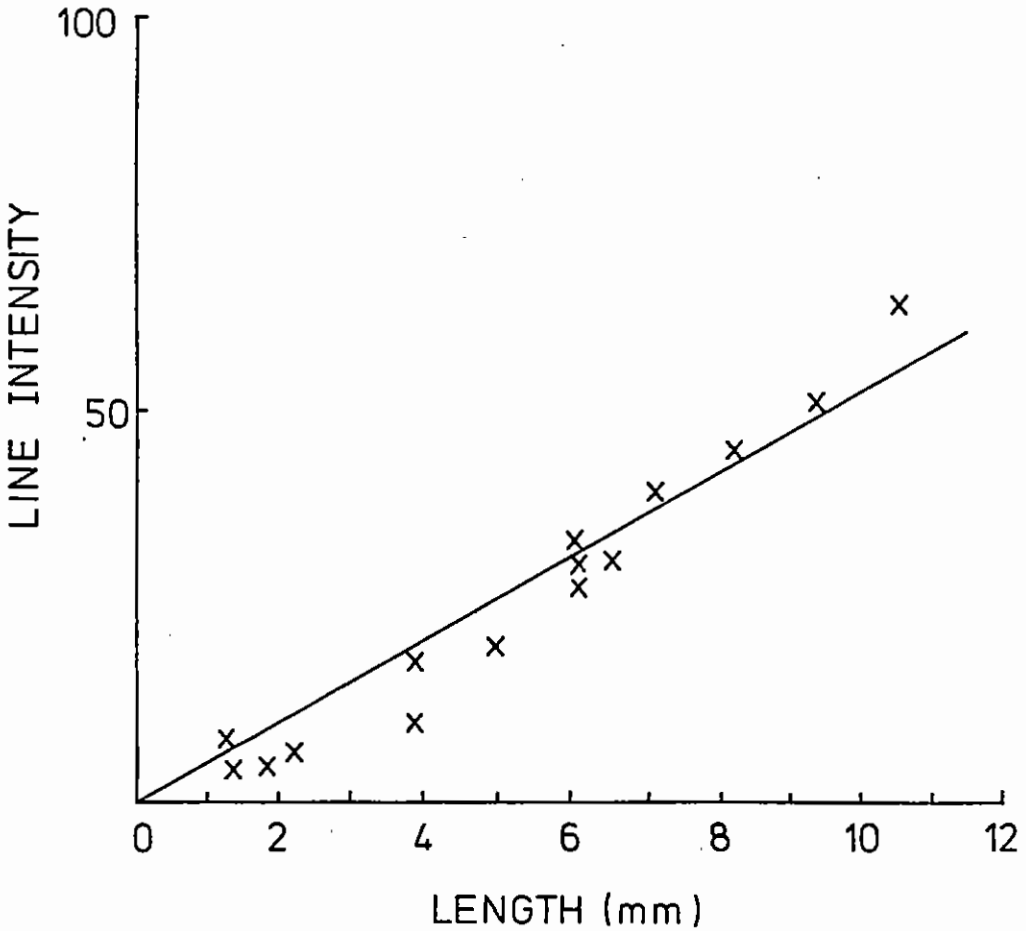

Fig A4.29 H_γ line intensity vs plasma length.

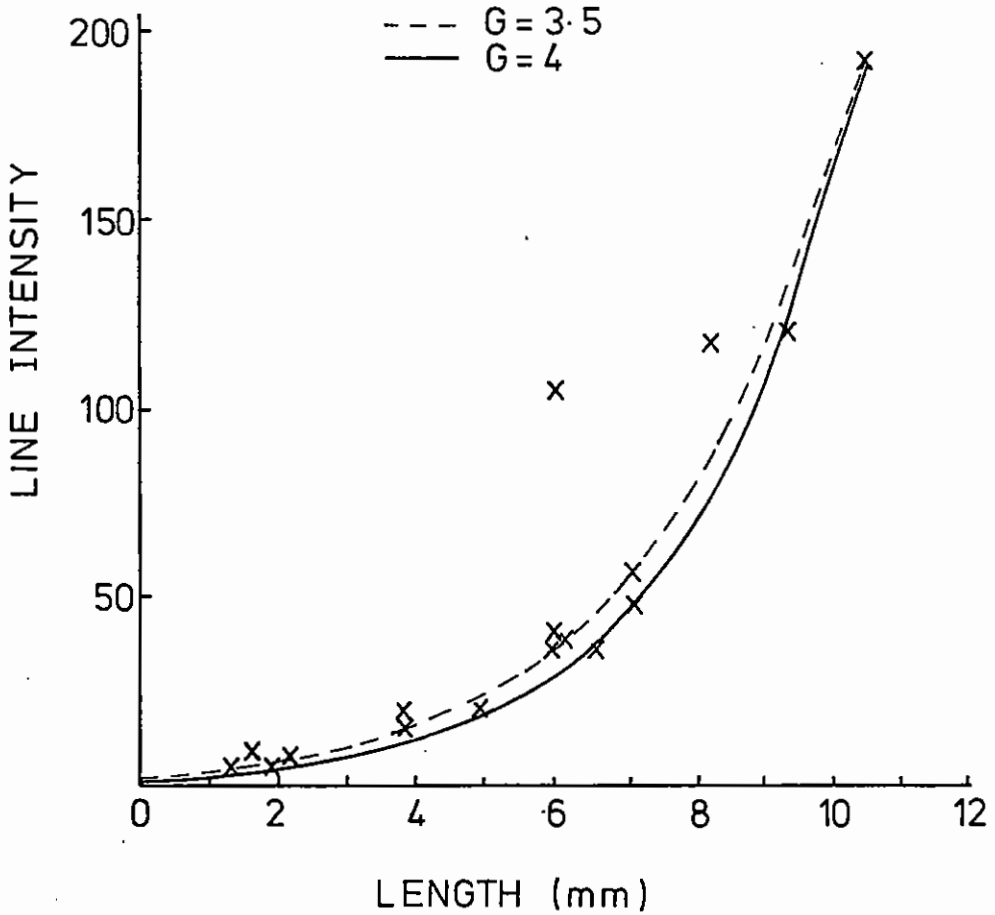

Fig A4.30 Balmer α line intensity vs plasma length.

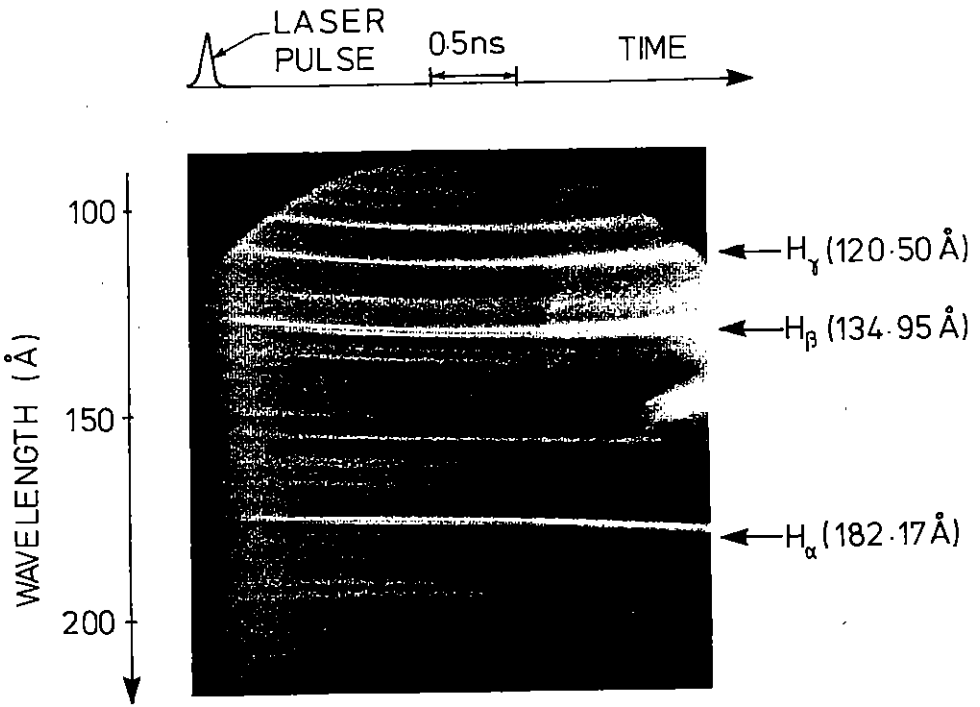

Fig A4.31 Streak record from a carbon fibre shot showing intense narrow features on CVI Balmer α and β transitions.

A4.5.2 (v) Discussion

These results give unambiguous evidence of strong amplification of the 18.2nm Balmer α transition in C^{5+}. Only the recent Se^{24+} laser experiment carried out with the Nova laser facility in the USA has shown a similar exponential variation of intensity with length (A4.28).

The new experiment owes much to the new line focus system and time resolving XUV diagnostics which give a strong basis for future work on a wide range of XUV laser schemes. Improved understanding of the scaling behaviour of the CVI laser scheme, which led us to the choice of better target and irradiation parameters, will be helpful in further development of this laser towards saturated laser amplification (gl > 15, Reference A4.29). Particularly attractive factors are the

laser energy required in the plasma only (3J cm^{-1}) relative to the more than 100x greater energy per unit length required for the Se^{24+} scheme. The relative insensitivity to refraction for the C^{5+} laser is also significant. Gain occurs at $n_e \sim 10^{19}$ cm^{-3}, in comparison with 10^{21} cm^{-3} in Se^{24}, so that refraction is 100x greater in the latter.

Wavelength scaling of the recombination scheme is an attractive possibility since isoelectric scaling gives $\lambda \sim Z^{-2}$ and there are reasonable prospects for recombination laser action at wavelengths below the important carbon K absorption edge needed for the study of biological materials.

A4.5.3 Thin Polymer Foil Targets

Thin polymer foil targets were used to investigate recombination pumping of the Balmer α transition in C VI, N VII and O VIII. 1000 Å thick foils consisting of H, C, N and O were irradiated with a 25 μm wide by up to 2.5 cm long line focus with an energy of 100 J in 70 ps. The use of these targets allows the Balmer alpha transitions in C, N and O to be simultaneously examined and enables isoelectronic scaling of the potential lasing transition to be investigated. A preliminary experiment has been performed and a typical streak record is shown in Figure A4.32 with Figure A4.33 giving a microdensitometer trace of this streak taken at 1 ns after the peak of the input laser pulse.

The hydrogen like transitions in C, N and O can clearly be seen. Analysis is being carried out on the preliminary data set and a more thorough experiment is planned for the future.

A4.5.4 Lithium-like Aluminium Recombination Scheme

After the successful demonstration of lasing in Li-like Aℓ with gain of up to ~ 3 cm^{-1} at ~ 103 Å by Jaégle et al, a collaborative experiment was performed by a joint French/UK team at RAL. The experiment was part of the November 1985 commissioning run and consequently was of a survey nature. Aluminium strips 100 μm wide and 2 cm long coated on plastic plates were irradiated with 7GW/cm in single sided illumination with 3 ns pulses. Figure A4.34 shows a streak record and Figure

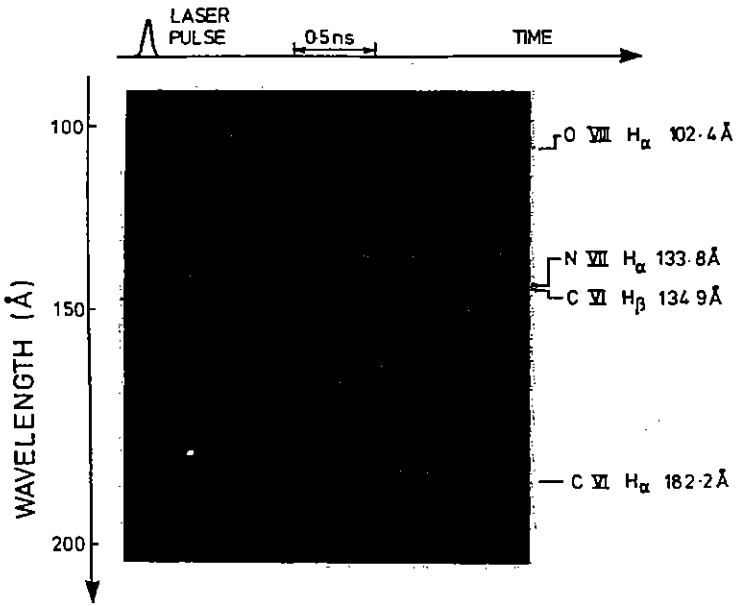

Fig A4.32 Typical streak record from a thin polymer foil shot.

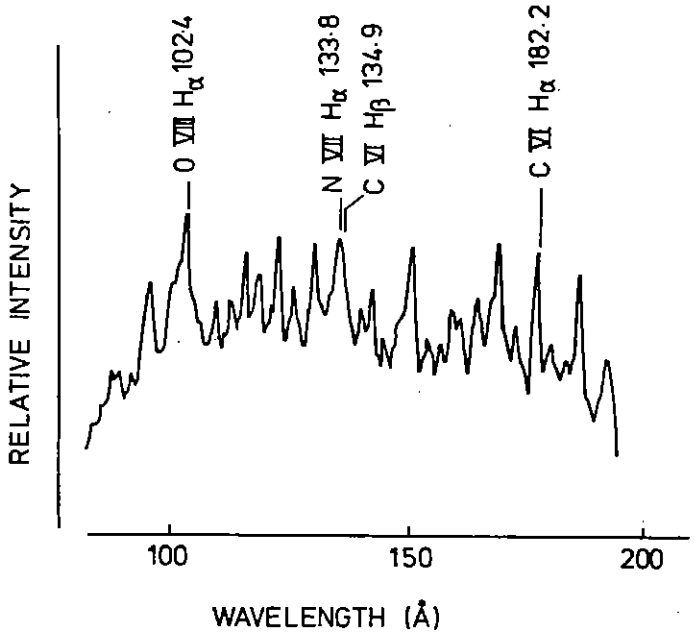

Fig A4.33 Microdensitometer trace of the polymer foil streak record in Figure A4.32 taken 1 nsec after the laser pulse.

A4.35 shows a microdensitometer trace taken at t = 1 ns after the input laser pulse. The potential laser operates on the 5f-3d line whose spectral location is shown in Figure A4.35, while evidence of production of the Al^{10+} ion can be sought from observation of the 15.4nm 4f-3d transition which is also shown.

Further collaboration will be maintained through the joint discussion of the current data and possible future experiments.

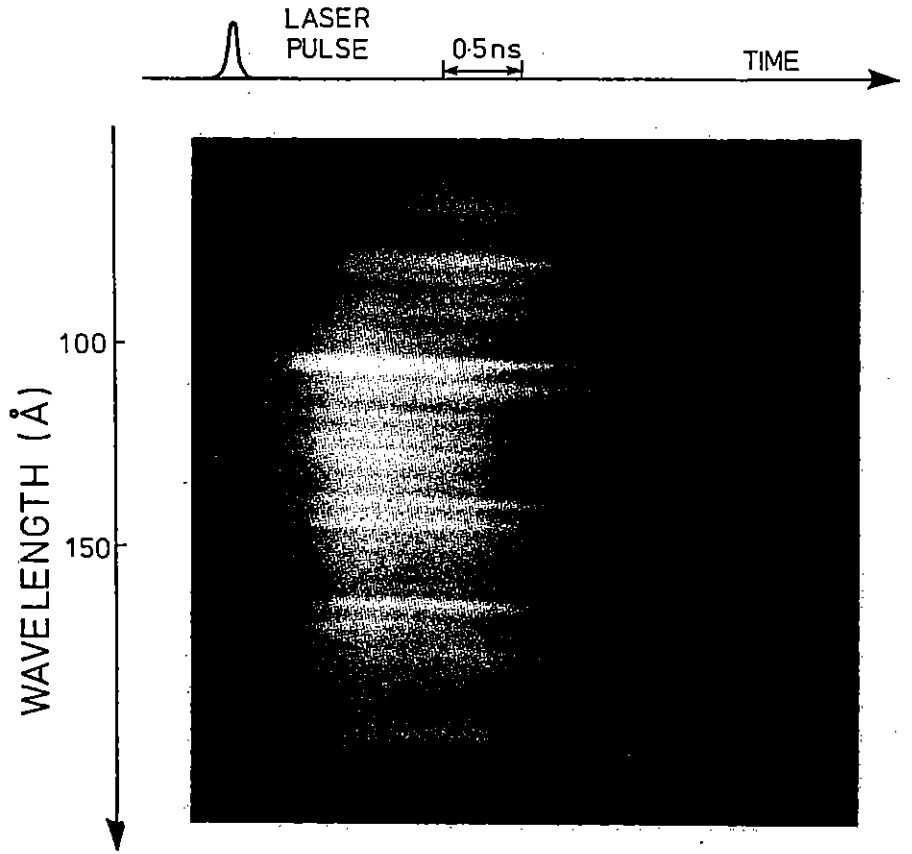

Fig A4.34 Typical streak record of a planar aluminium shot.

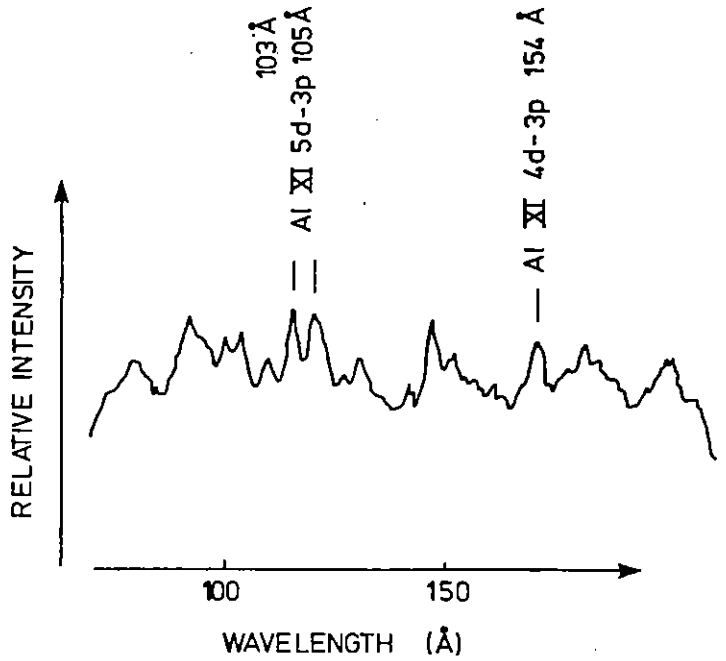

Fig A4.35 Microdensitometer trace of the aluminium streak record in

A4.5.5 3p - 3s Transitions in Se^{24+}

A small number of shots were taken on Se foil targets composed of a 50 μm wide by 750Å deep by 1.4 cm long Se strip coated on 1000Å formvar foils. Laser energies of approximately 300 J in 700 ps at 0.53μm were directed onto the target in double-sided irradiation. This experiment was performed to examine the electron collision pumping of a population inversion in Ne-like Se at 206Å and 209Å.

Figure A4.36 shows a streak record and Figure A4.37 gives a microdensitometer trace taken at 1 ns after the input laser pulse. The sharp fall in intensity at 17.2nm is due to the L absorption edge of an Al filter and gives an absolute wavelength reference. Na-like Se transitions at 20.1 and 23.9nm are identified and have been seen in

other spectroscopic studies. The Se^{24+} J = 2-1 transitions at 20.6 and 20.9nm are expected to be located at the points indicated but are not seen. The strong lines nearby have not been positively identified. The complexity of the highly ionised Se spectrum and the source size limited instrumental spectral resolution made it difficult to precisely identify the Se transitions. Further work must be done to fully explore this scheme.

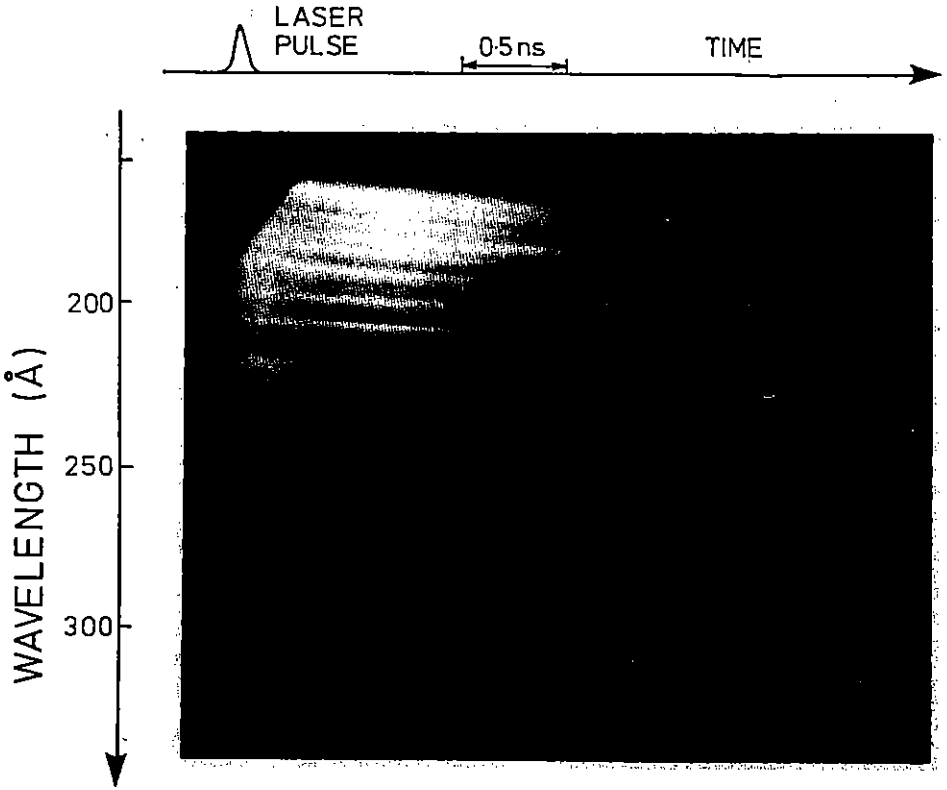

Fig A4.36 Typical streak record of a selenium shot.

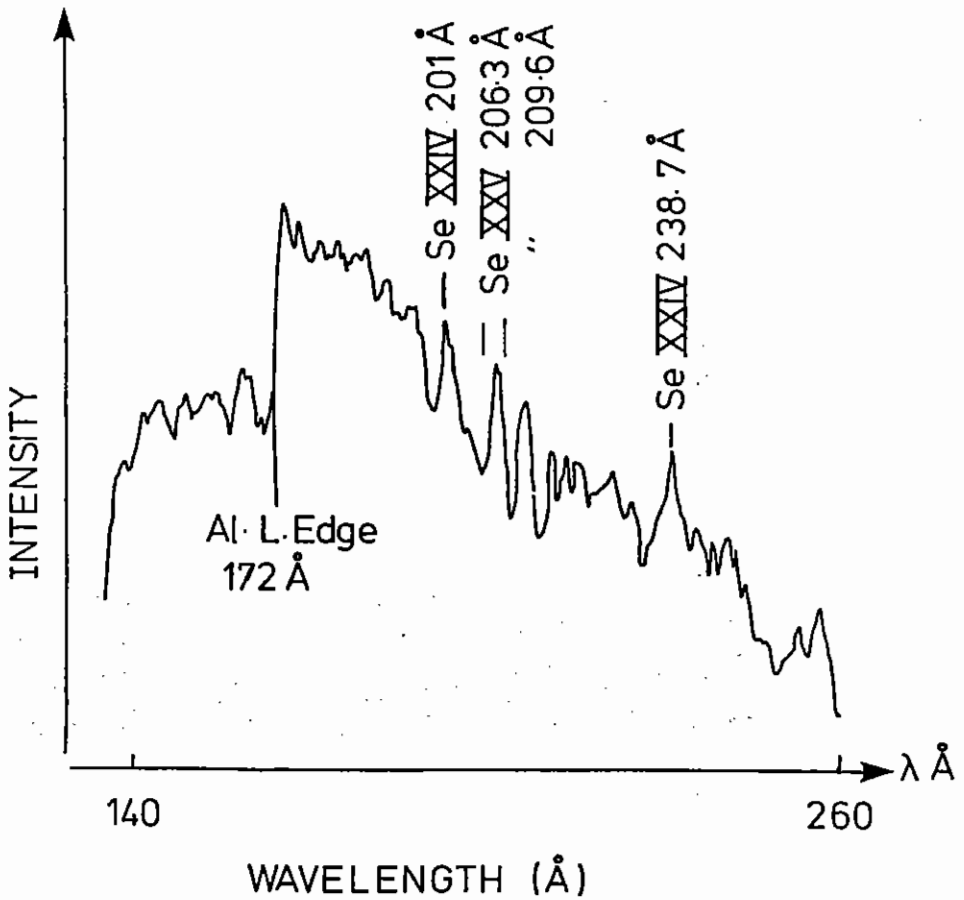

Fig A4.37 Microdensitometer trace of the selenium streak record in Figure A4.36 taken 1 nsec after the laser pulse.

A4.6 WAVEGUIDING IN SOFT X-RAY LASER EXPERIMENTS

J G Lunney (Dublin)

Amplified spontaneous emission at 206.3 Å and 209.6 Å has recently been observed in a laser produced plasma (A4.28, A4.30). Gain coefficients of 5.5 cm^{-1} were measured on $2p^53p - 2p^53s$ transitions in neon-like selenium. The plasma was prepared by double-sided laser irradiation of 1500 Å thick Formvar substrate coated with 750 Å of selenium on one side. A line focus with dimensions 0.02 x 1.12 cm was used, and the laser irradiance was 5×10^{13} W/cm^2. This thin foil substrate was chosen since it will explode nearly symmetrically and give a region of plasma where the density gradients are sufficiently small to avoid refraction of the soft X-rays out of the region of gain. By choosing to use such a thin foil target the electron density obtained in the region of gain is $\sim 3 \times 10^{20}$ cm^{-3}, which is substantially lower than the value of 10^{22} cm^{-3} at which it is predicted (A4.31) that this laser scheme should have maximum gain. This letter described a technique to compensate for refraction in soft X-ray laser experiments which uses laser produced plasmas on thick targets where the plasma density falls off rapidly with distance away from the target. In this way it should be possible to carry out experiments on these laser schemes at the electron densities at which the gain is maximised.

The technique will be illustrated using the calculation of Vinogradov and Shylaptsev (A4.32) for the soft X-ray laser gain that can be obtained in neon-like iron in a laser produced plasma. Figure A4.38 shows the electron density and temperature profiles which were obtained for the laser irradiation of an iron target at 3×10^{12} W cm^{-2}. To simulate the 2-dimensional hydrodynamics of a 50 μm wide line focus the plasma expansion from a cylindrical target with an initial radius of 50 μm was modelled. For distances from target < 50 μm the plasma parameters are nearly the same as would be found in the laser irradiation of an infinite flat target. The region of interest lies

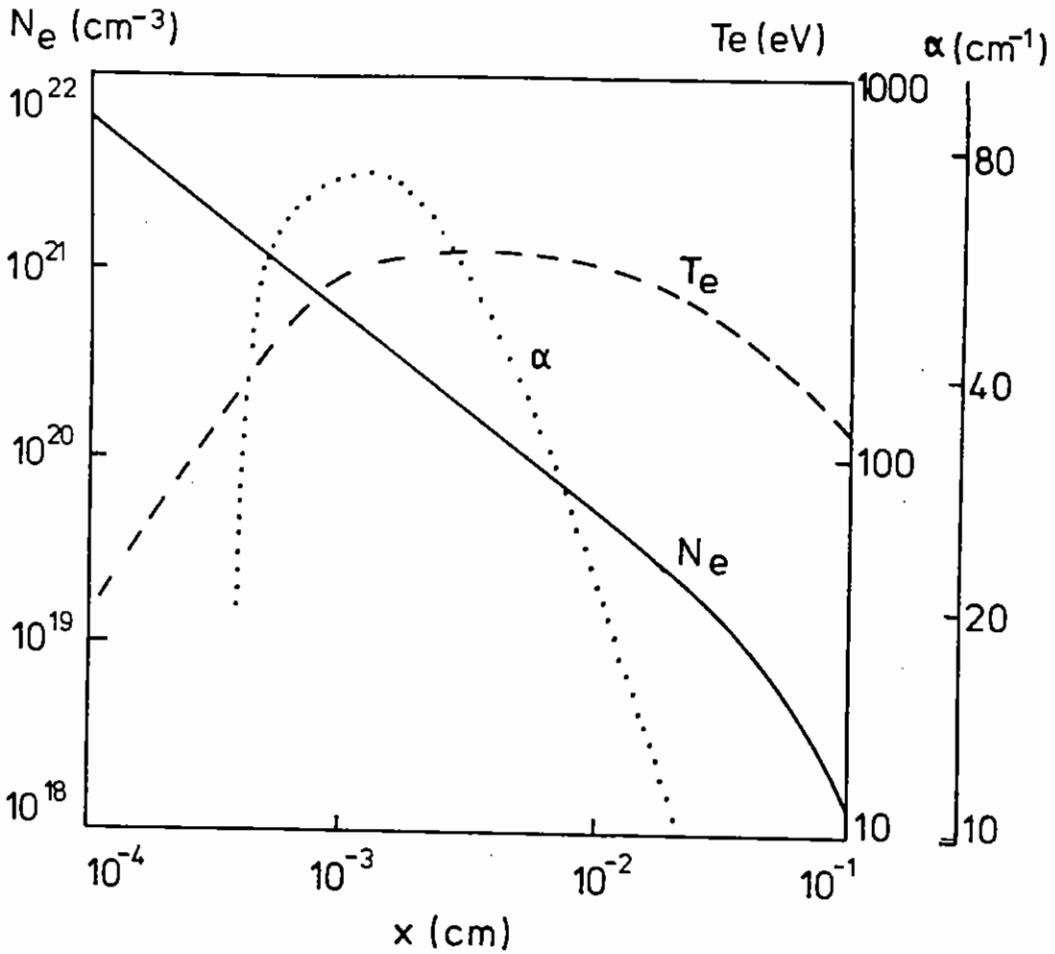

Fig A4.38 Electron density and temperature profiles obtained for the laser irradiation of a 50 μm radius, cylindrical iron target at 3 x 10^{12} W cm^{-2}. Also shown is the calculated gain coefficient on the 250 Å, 3p - 3s transition in neon-like iron (From Ref A4.32).

between 7.5 μm and 18.5 μm from the target, and for the purposes of this paper the target surface and the surfaces of constant electron density will be regarded as planar. Also shown in Figure A4.38 is the calculated gain coefficient on the 250 Å, 3p - 3s transition in neon-like iron.

The gain coefficient has a maximum value of 75 cm^{-1} at 12 μm from the target surface. At that surface the electron density, N_e, is 4.7 x 10^{20} cm^{-3} and the electron density gradient is 3.9 x 10^{23} cm^{-4}. The free electron contribution to the refractive index, n, is given by

$$n^2 = \left(1 - \frac{N_e}{N_c}\right) \qquad (1)$$

where N_c is the critical density for the laser wavelength and is given by

$$N_c = 1.1 \times 10^{29}\ \lambda^{-2}\ \text{cm}^{-3} \qquad (2)$$

where λ is in Å. For a wavelength of 250 Å the critical density, N_c, is 1.8 x 10^{24} cm^{-3}. No attempt has been made here to include the bound-bound and bound-free contributions to the refractive index. The free-free contribution is expected to predominate, but a detailed analysis of a particular experiment should consider these other contributions. Choosing a coordinate system where x is distance measured normal to plane of maximum gain towards the target surface and z is distance measured along that plane, then

$$\frac{dn}{dx} = -\frac{1}{2N_c}\frac{dN_e}{dx} \quad \text{for } \frac{N_e}{N_c} \ll 1 \qquad (3)$$

A ray of light propagating in the z direction at x = 0 will have a trajectory

$$x = \frac{1}{2}\, z^2 \frac{1}{n_o}\frac{dn}{dx} \quad \text{for } \frac{dx}{dz} \ll 1 \qquad (4)$$

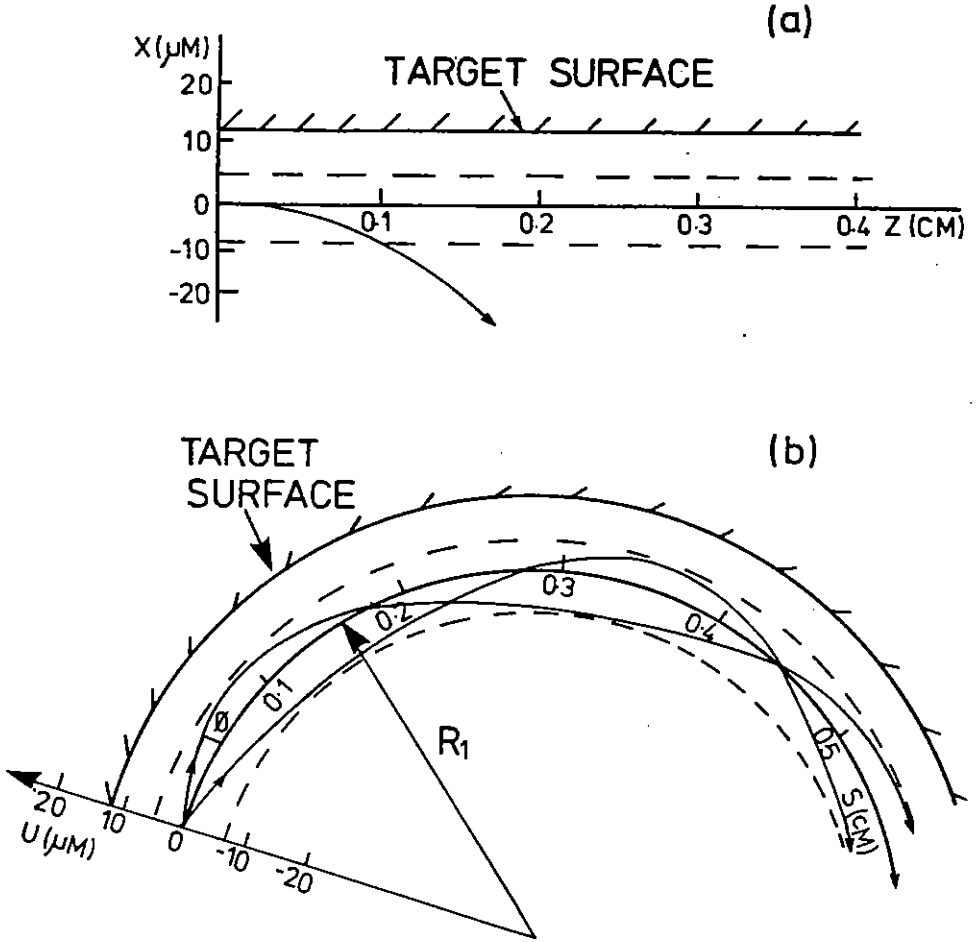

Fig A4.39 (a) Refraction of a ray at 250 Å out of the region of gain (between dashed lines).

(b) Waveguiding within region of gain for a cylindrical target with radius of curvature, R_1 = 9.3 cms. The u-coordinate is increased by a factor of 40 and the radius of curvature decreased by a factor of 40.

where n_o is the value of n at x = 0. In other words the ray trajectory is an arc of a circle of curvature $\frac{1}{R} = -\frac{1}{n_o}\frac{dn}{dx}$.

Key (A4.29) has pointed out that a gain length product, $\alpha\ell = 14$ is required for a mirrorless soft X-ray laser to reach gain saturation. Thus, the region of plasma where the gain is greater than ~ 13/14 of the maximum value will have approximately the same cross-section as the saturated laser output. For the plasma shown in Figure A4.38 the gain has a maximum value of 75 cm^{-1} at 12 μm from the target surface and falls to 70 cm^{-1} at 7.5 μm and 18.5 μm. At the plane of maximum gain x = 0, $\frac{dn}{dx} = 0.11$ cm^{-1} so the radius of curvature of a ray propagating

at x = 0 in the z-direction will be 9.3 cms. Assuming for the moment a constant refractive index gradient $\frac{dn}{dx} = 0.11$ cm^{-1} such a ray will bend away from the target surface and reach the plane at x = -6.5 μm for z = 0.11 cms, thus leaving the region of high gain as shown in Figure A4.39(a). For $\alpha = 75$ cm^{-1} the path length required to reach gain saturation is ~ 0.2 cms.

Hagelstein (A4.33) has proposed a method of overcoming the problems caused by plasma refraction in soft X-ray laser schemes using thick targets. He has suggested that by alternately propagating the laser beam through plasmas expanding in opposite directions it should be possible to bend the beam first to the left and then to the right, and so forth, in such a way as to keep it within the regions of gain.

This paper proposes that the problem of plasma refraction can be overcome by bending the target surface to form a cylindrical surface of the same radius of curvature as the refracted soft X-ray laser beam. The radius of curvature of the target will be chosen to match the curvature caused by refraction in the region where the gain is maximised. A ray propagating tangential to the cylinder will follow the curve of the cylinder and so stay in the region of maximum gain. The laser produced plasma can be formed using a line focus on a cylindrically concave surface.

For the density profile shown in Figure A4.38, it can be shown that rays making a small angle with the tangent to the cylindrical surface will be guided around the cylindrical surface in a manner analagous to a whispering-gallery. This light-guiding action can be analysed using the coordinate system shown in Figure A4.39(b). The variables s and u are introduced to measure, respectively, position along and normal to the cylindrical surface of radius R_1, where the gain is maximum. Over the region of interest the variation of electron density is closely approximated by the quadratic functions

$$N_e = 4.7 \times 10^{20} + 3.9 \times 10^{23}\, u + 5.6 \times 10^{26}\, u^2,\ 0 \leq u \leq 4.5\ \mu m \qquad (5)$$

$$N_e = 4.7 \times 10^{20} + 3.9 \times 10^{23}\, u + 2.2 \times 10^{26}\, u^2,\ 0 \geq u \geq -6.5\ \mu m \qquad (6)$$

The refractive index is then given by the equations:

$$n^2 \doteq 1 - 2.6 \times 10^{-4} - 0.22\, u - 310\, u^2,\ 0 \leq u \leq 4.5\ \mu m \qquad (7)$$

$$n^2 \doteq 1 - 2.6 \times 10^{-4} - 0.22\, u - 120\, u^2,\ 0 \geq u \geq -6.5\ \mu m \qquad (8)$$

If the refractive index is of the form

$$n^2 = n_o^2 - \alpha\, \xi - \beta\, u^2$$

and $\frac{2n_o^2}{R_1} = \alpha$ then using the methods described in Ref. A4.34 it can readily be shown that trajectory of paraxial rays crossing the u = 0 surface at angle ϕ is given by

$$u = \frac{\phi\, n_o}{\sqrt{\beta}} \sin\left(\frac{s\sqrt{\beta}}{n_o}\right) \qquad (9)$$

A ray propagating towards the target surface returns to the surface u = 0 after a distance s = 0.18 cms, while a ray propagating away from the target will return at s = 0.28 cms. The waveguiding action of the plasma is illustrated in Figure A4.39(b). A ray crossing the surface

u = 0 at an angle $\phi = 7 \times 10^{-3}$ rads will have maximum and minimum u values of 4 μm and −6.4 μm, and will thus stay within the region where the gain coefficient is $> 70\ cm^{-1}$. The advantages of using a curved target can be clearly seen by comparing Figure 4.39(a) and Figure A4.39(b). For the plasma under consideration here a path length in the high gain region greater than 0.11 cm can only be achieved using the curved target. It can also be seen from Figure A4.39(b) that the waveguiding will lead to laser emission into a divergence angle that may be substantially larger than the angle subtended by the width of the gain region over its length. This will lead to a corresponding increase in total laser output.

If the viability of this laser scheme is to be assesed using current flat-field laser focussing optics then it will be necessary to measure, or model, the change of electron density gradient caused by the variation of laser focussing conditions along the cylindrical surface.

Bending the target surface to form a toroidal surface will give waveguiding in the plane orthogonal to the case described above. This is illustrated in Figure A4.40 which shows a toroidal target surface curved to radii R_1 = 9.3 cms and R_2 = 200 μm. Waveguiding of this type may be a useful way of overcoming the deleterious refraction that will be caused by a decrease in the electron density towards the edges of the line focus. For $y \ll 200\ \mu m$ the separation of the y − s surface and the surface of maximum gain is $\frac{y^2}{2R_2}$. Thus, the variation of refractive index along the y direction can be obtained by substituting $u = \frac{y^2}{2R_2}$ in equation (7) to give

$$n^2 = 1 - 2.6 \times 10^{-4} - 5.5\, y^2 - 1.9 \times 10^5\, y^4 \qquad (10)$$

For $y \leq 25\ \mu m$ the y^4 term can be neglected so the ray trajectories are approximately sinusoidal as illustrated in Figure A4.40. A ray crossing s-axis at s = 0 making an angle $\Psi = 5.5 \times 10^{-3}$ rads with that axis will reach a maximum y value of ≈ 23 μm at s ≈ 0.67 cm. The waveguiding period of rays in the y − s surface is much longer than the period of rays in the v − s plane, and for plasma length < 0.5 cm the weak guiding of rays on the y − s surface will not have any significant

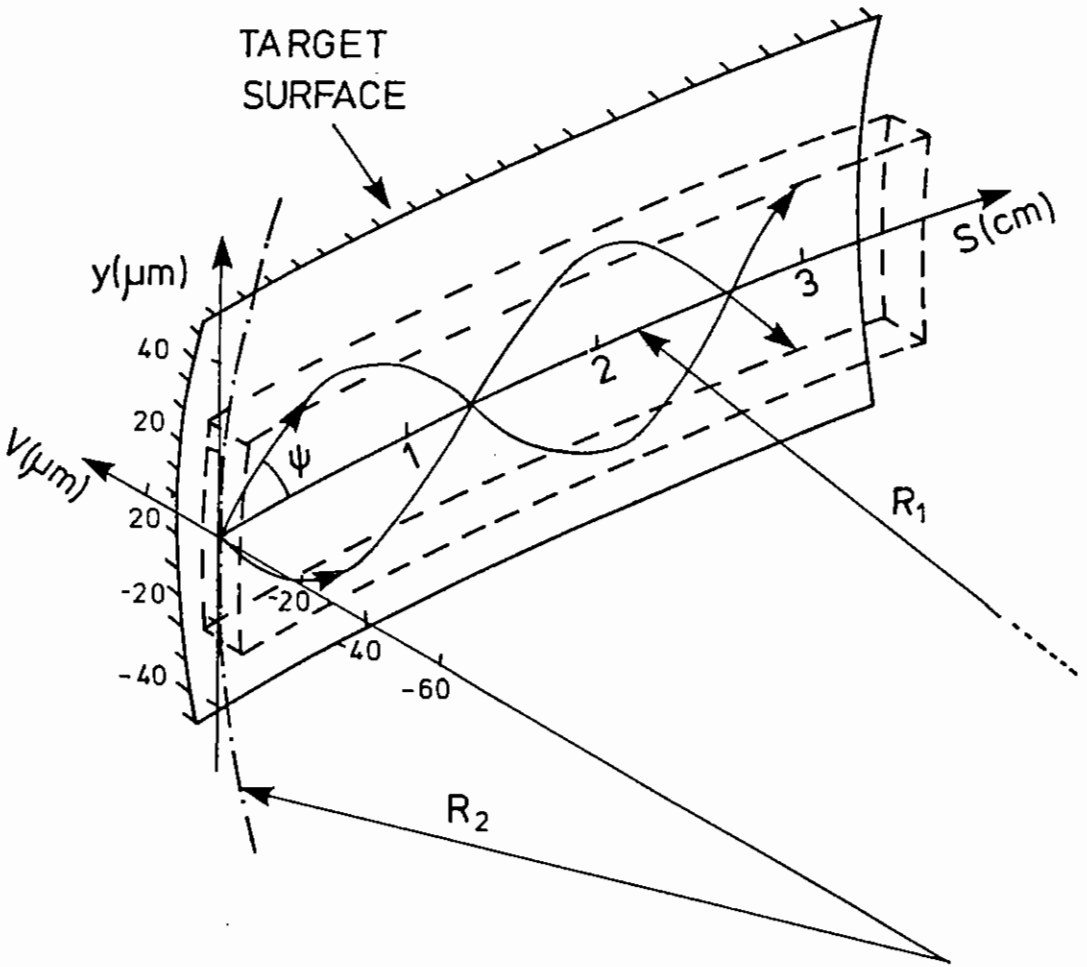

Figure A4.40
Waveguiding of rays in the y - s surface for a toroidal target with R_1 = 9.3 cms and R_2 = 200 μm. The radius of curvature R_2 and the v and y coordinates are increased by a factor of 200.

effect on the laser output in the scheme considered here. However, if the gain coefficient is much lower and the length of the plasma much greater, then a toroidal target may give an improvement in performance over a cylindrical one. The small radius of curvature of the toroidal surface in the v - y plane suggests that such a target surface may have to be formed by machining a channel of 200 μm radius on a cylindrical surface.

In conclusion, it seems that in soft X-ray laser experiments using laser produced plasmas where the electron density gradients cause refraction of the soft X-rays out of the region of gain, bending of the target to a cylindrical or toroidal surface can overcome this refraction problem. For the toroidal case this paper only considered the waveguiding on two orthogonal sections of the gain region. A complete description of the waveguiding can be obtained using numerical ray tracing techniques.

A4.7 TIME-RESOLVED METAL SILICIDE FORMATION USING GRAZING INCIDENCE X-RAY SPECTROSCOPY

A J Rankin, D K Bradley (Imperial College), R W Eason (University of Essex), U Zammit (University of Rome), P M G Allen, J L Brebner (University College Cardiff)

A4.7.1 Introduction

An initial trial experiment early last year (A4.4) demonstrated the feasibility of using grazing incidence X-ray spectroscopy to diagnose changes in surface structure of metal silicides to depths of ≈ 30Å.

The subsequent study described here is a more ambitious and sophisticated experiment incorporating features of high quality sample preparation, improved annealing beam uniformity and the use of a purpose built high precision experimental rig.

The main objective of the experiment was to diagnose the evolution and formation of a metal silicide using a 2 beam 'pump' and 'probe' scheme. An annealing beam initiates the formation of the silicide while a

second beam provides an X-ray source to spectroscopically diagnose the surface structure at various time delays in the range 0-300 nsec after the anneal. A nickel silicide system has been selected for these studies due to the commercial availability of high quality silicon slices and the current interest in the semiconductor device field in refractory metal silicides (A4.35). As in the previous experiment single crystal silicon samples are used with overcoated layers of ≈ 100A of nickel. A highly uniform annealing beam is applied to heat the surface causing silicide compounds of different stoichiometry to be formed at different depths in the sample.

The diagnosis of the silicide formation was envisaged to be possible in two ways, firstly the recording of reflEXAFS Spectra identifying the compound stoichiometry and secondly the existence and height of the silicon 'K' absorption edge. In this experiment the former technique has shown to be unreliable with the EXAFS spectra proving difficult to record. A more accurate method has shown to be the dependence of the critical angle of reflection with electron density which allows the compound stoichiometry to be uniquely identified from shot to shot. This technique however demands very accurate alignment which, with the use of a high precision experimental rig has been achieved with the results described here.

A4.7.2 Experimental

The experimental arrangement, shown in Figure A4.41, utilises three 0.53 μm beams of 1n sec FWHM pulse duration. The first beam is used to produce an X-ray source by irradiating a wedged steel rod coated with ~ 5 μm of Bismuth. The second and third beams form the annealing pulse, each of which originates from a 3 x 3 array of 25 mm square mirrors. This intensity smoothing scheme is similar to that used previously (A4.4) except that enhanced uniformity has been achieved by combining two separate annealing beams to form the 20 nsec annealing pulse.

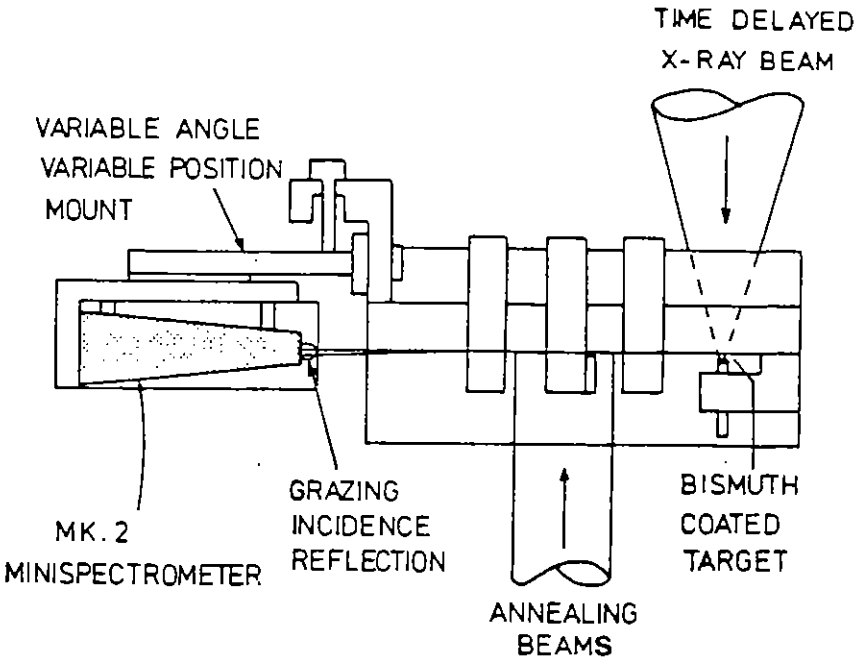

Fig A4.41 Experimental arrangement to perform grazing incidence X-ray spectroscopy of laser annealed nickel coated silicon samples. The X-ray beam is delayed with respect to the annealing beam in the range 0-280nsec.

An optical streak camera monitored the temporal profile of the annealing pulse allowing accurate tailoring of the profile by empirical adjustment of the individual mirror separations. The power density of the annealing pulse was measured on each shot using a fraction of the beam relayed to a calibrated GENTEC calorimeter. The spatial uniformity of the annealing beam was recorded on several shots by replacing the silicon sample with ILFORD HP5 fast recording film.

The grazing incidence geometry allows X-rays, emitted from the bismuth rod to be reflected off the surface of the sample at angles of reflection between 0.5^0 and 2.0^0. A mark II minispectrometer equipped with an ADP crystal then records the spectrum as a function of angle of incidence. A direct X-ray block was positioned such that a small fraction of the direct X-rays is recorded on the film, thus giving a reference spectrum of the source on each shot.

The samples themselves were 1 cm silicon squares prepared by flash annealing the silicon to 800^{0}C and then depositing coatings of nickel in the range 100Å - 200Å at a pressure of 10^{-6} Torr. The thickness of these samples has been measured by optical ellipsometry measurements in an E.S.C.A. Laboratory.

In order to investigate the evolution of the silicide formation process, the delay between the X-ray source and the annealing beam was varied in the range 0-280 nsec maintaining the annealing beam energy density at a constant value of ~ 500 mJ cm^{-2}.

A4.7.3 Results

The annealing pulse temporal and spatial profiles are shown in Figure A4.42(a) and A4.42(b) together with their respective densitometer tracings A4.42(c) and A4.42(d). The annealing beam uniformity is estimated at < 5% in the central 1 cm^2 where the sample was located.

The Spectra recorded have been processed by a digitising microdensitometer and colour enhanced to reveal the dependence of the angle of reflection with wavelength. In this report it is not possible to reproduce these colour images, however the main features are still discernable. Figure A4.43 shows a number of different spectra recorded at different delay times after the annealing pulse. Shot A is a pure silicon sample showing the characteristic 'K' absorption edge spectral feature. Shot B shows a sample coated with ≈ 100 Å of nickel which has not been laser annealed, the edge is clearly absent confirming the penetration depth of the X-ray is less than 100Å. Higher angles of incidence are present in Shot B relative to Shot A due to the presence of nickel on the surface of the sample which because of its greater density has a higher value of critical angle of reflection.

Shots C, D and E are of identical samples annealed at approximately the same annealing beam energy density ≈ 500 mJ cm^{-2}. In Shot C the delay between the annealing beam and X-ray beam is 280 nsec, by this time a high concentraction of silicon atoms are present in the surface layers of the sample and the characteristic silicon edge is quite clear. In

Shot D the delay is only 23.2 nsec and the 'K' edge feature is only just visible, the height of the silicon edge is much lower comensurate with the reduced concentration of silicon atoms in the silicides which are present. Additionally the range of critical angles of reflection which are present, reduce as the delay reduces since the silicides containing high silicon atom concentrations are not formed at early times.

Shot E is at a delay of 13 nsec, the silicon edge is now not visible suggesting the concentration of silicon atoms in the surface compounds has reduced to a very low value. The angles of incidence also confirm a very high concentration of nickel in the surface layer compounds.

This only qualitative description of these results show some very exciting features which are being carefully investigated. Only when all the spectra have been deconvolved with the individual direct spectra (source function) will accurate comparison and microdensitometers be meaningful.

To interpret these results accurately it is essential to identify the compounds formed and how the stochiometry changes with depth into the sample.

This is being performed using both optical ellipsometry and S.I.M.S. analysis techniques. Provisional results from the latter approach suggest the presence of very unusual compound formation which has caused considerable attention from workers in the surface science community.

A4.7.4 Conclusions

From the preliminary analysis of this work it would seem that the timescale of the formation of nickel silicide at an annealing flux of ~ 500 mJ cm^{-2} begins at 20 nsec after the start of the laser anneal. Grazing incidence x-ray spectroscopy, if performed with very high precision has shown itself to be a useful diagnostic in monitoring the formation of metal silicide compounds.

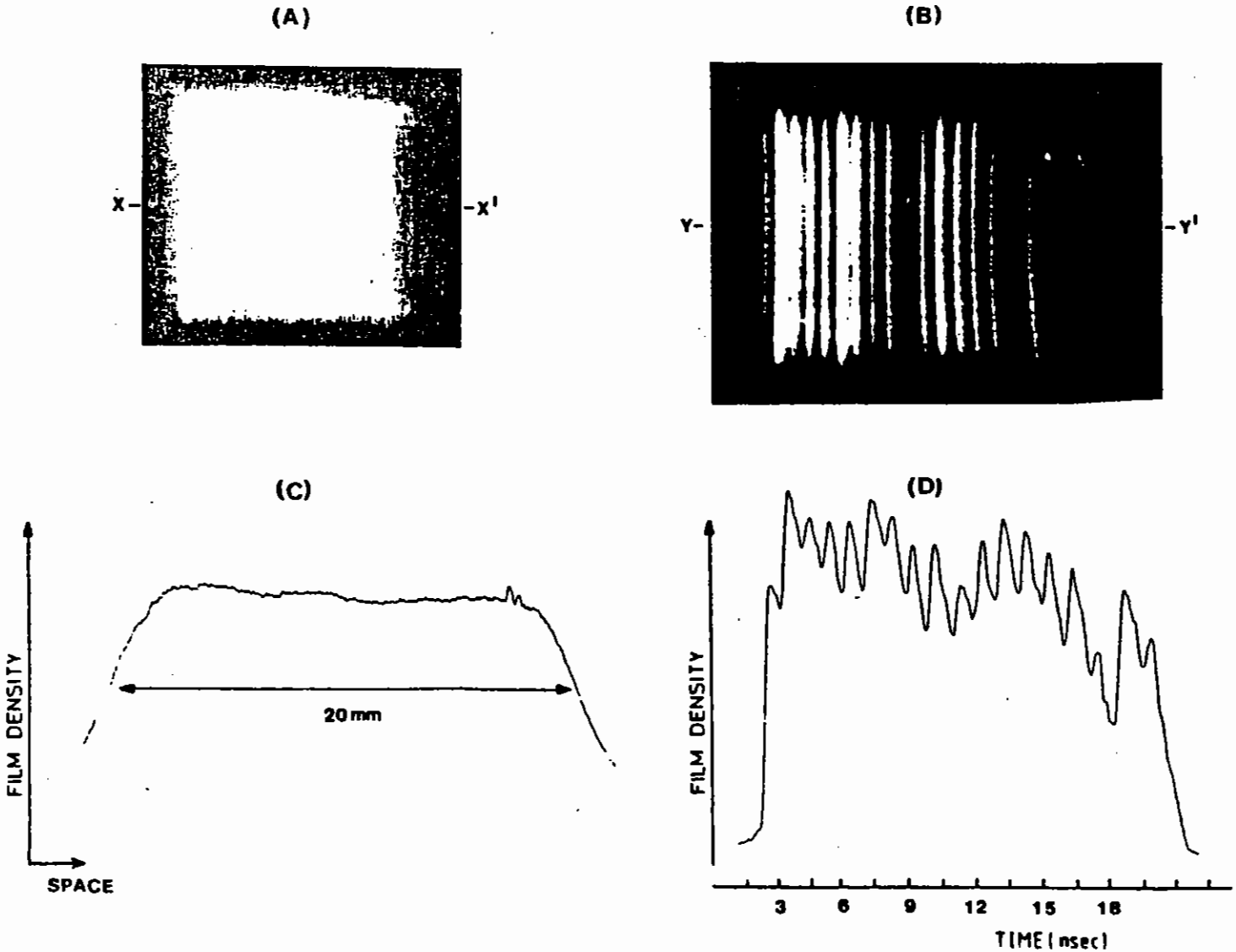

Fig A4.42 Spatial and temporal uniformity records (a) and (c) together with microdensitometer tracings (b) scan XX^1 (d) scan YY^1 for the laser annealing pulse.

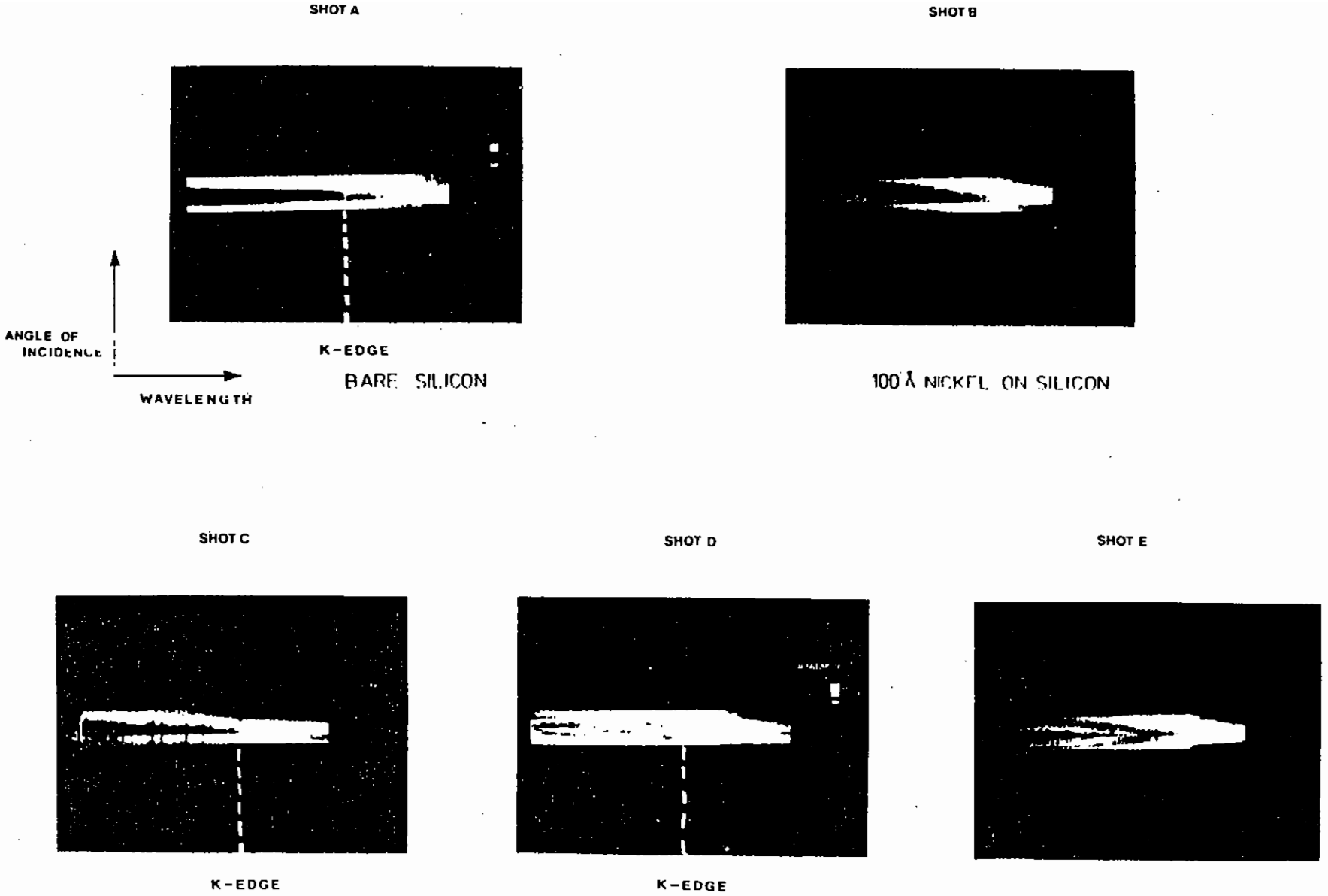

Fig A4.43 Angle resolved X-ray spectra showing the temporal evolution of nickel silicide formation, Shot A: bare silicon, Shot B: 100Å nickel on silicon, Shot C-E 100Å nickel on silicon laser annealed (~ 500mJcm^{-2}) at different delay times with respect to the annealing pulse. Shot C: 280nsec, Shot D: 23nsec and Shot E: 13nsec.

REFERENCES

A4.1 P Goby, C R Acad Sci Paris 156, 686 (1913)

A4.2 G Schmahl and D Rudolph, X-ray microscopy, Springer series in Optical Sciences 43 (1984)

A4.3 H Wolter, Ann Phys 10, 94 (1952)

A4.4 Annual Report to the Laser Facility Committee 1985, Rutherford Appleton Laboratory Report No RAL-85-047.

A4.5 V E Cosslett, W C Nixon, Nature 168, 24 (1951)

A4.6 R Feder, E Spiller, J Topalian, A N Broers, W Gudat, B J Panessa, Z A Zadunaisky, J Sedat, Science 197, 259 (1977)

A4.7 C G Wilson, 'Organic Resist Materials - Theory and Chemistry' in Introduction to Microlithography, ed L F Thompson, C G Willson M J Bowden. A C S Symposium Series 219 87-159 (1983)

A4.8 R P Haelbich, J P Silverman, J M Warlaumont, Nucl Instrum and Meth Phys Res 222, 291 (1984)

A4.9 P C Cheng, H B Peng, R Feder, J W McGowan in Electron Microscopy (10th Int Electron Microscpy Proc), 1, p461 (1982)

A4.10 Synchrotron Radiation Research, ed H Winick and S Doniach, Plenum Press (1980)

A4.11 A D Rush, SERC Daresbury Laboratory, private communication

A4.12 M W Poole, I H Munro, D G Taylor, R P Walker, Nucl Instrum and Meth Phys Res 208, 143 (1983)

A4.13 R Feder, V Banton, D Sayre, J Costa, M Baldini, B Kim, Science 227, 63 (1984)

A4.14 R J Rosser, K G Baldwin, R Feder, D Bassett, A J Cole, R W Eason, J. Microscopy 138, 311 (1985)

A4.15 A D Stead and J C Duckett, Ann Bot 46, 549 (1980).

A4.16 P C Cheng, K H Tan, J Wm McGowan, R Feder, H B Peng and D M Shinozaki: eds. G Schmahl and D Rudolph (Springer-Verlag, Berlin, 1984), p285

A4.17 P C Cheng, R Feder, J Wm McGowan, K H Tan and D Shinozaki, Proceeding of 43rd Annual Meeting of Electron Microscopy Society of America, 602-605 (1985).

A4.18 R J Rosser, G Kiehn, P C Cheng, R W Eason, R Feder, A Michette (In preparation).

A4.19 R J Rosser, R Feder, A Ng, P Celliers, submitted to J Microscopy, Sept. (1985)

A4.20 F O'Neill, Y Owadano. I C E Turcu, A G Michette, C Hills and A M Rogoyski, Proc. 3rd Topical Meeting on Short Wavelength Coherent Radiation: Generation and Applications, Monterey, March (1986).

A4.21 E Armandillo, A K Kearsley and C E Webb, J. Phys. E: Sci Instrum 15, 177 (1982)

A4.22 Y Matsumoto, M J Shaw, F O'Neill, J P Partanen, M H Key, R Eason, I N Ross, E M Hodgson, and Y Sakagami. 'X-ray emission from KrF laser-produced Al plasmas', Appl Phys Lett 46, 28 (1985).

A4.23 P D Rockett et al, Appl. Opts, 24, 2536 (1983)

A4.24 C Chenais-Popovics, (private communication)

A4.25 V A Boiko, A Ya Faenov and S A Pikuz. X-ray spectroscopy of multiply-charged ions from laser plasmas, J Quant Spectrosc Radiat Transfer, 19, 11 (1978).

A4.26 G J Pert, J Phys B:Atom Molec Phys, 9, 3301, (1976), 12, 2067, (1979).

A4.27 G J Pert et al, in "Laser Techniques in the Extreme UV" Eds Harris SE and Lucatorts T B, A.I.P. (1984).

A4.28 D L Matthews, P L Hagelstein, M D Rosen, M J Eckart, N M Ceglio, A U Hazi, H Medecki, B J MacGowan, J E Trebes, B L Whitten, E M Campbell, C W Hatcher, A M Hawryluk, R L Kauffman, L D Pleasance, G Rambach, J H Scofield, G Stone and T A Weaver, Phys Rev Lett, 54, 110, (1985).

A4.29 M H Key, Nature, 316, 314 (1985).

A4.30 M D Rosen, P L Hagelstein, D L Matthews, E M Campbell, A U Hazi, B L Whitten, B MacGowan, R E Turner, R W Lee, G Charatis, Gar. E Busch, C L Shepard and P D Rockett, Phys Rev Lett, 54, 106 (1985).

A4.31 U Feldman, J F Seely and A K Bhatia, J App Phys, 56, 2475, (1984).

A4.32 A V Vinogradov and N Shlyaptsev, Sov J Quantam Electron, 13, 1511 (1983).

A4.33 P L Hagelstein, Plasma Physics, 25, 1345, (1983).

A4.34 E W Marchand, "Gradient Index Optics", Academic Press, New York (1978).

A4.35 J Ottaviani, J Vac Sci Tech, 16, 5, (1979).

A5 THEORY AND COMPUTATION

Editor: D J Nicholas

A5 THEORY AND COMPUTATION

A5.1 INTRODUCTION

R A Cairns (St Andrews) and D J Nicholas (RAL)

For the sake of clarity, this years theory section is again in two parts, section A5.2 on Classical Plasma physics and hydrodynamics and A5.3 on Atomic Physics. Current contributions show a conserted effort being made on plasma instabilities; the ongoing work on Raman and Brillouin moving towards more realistic models and growing effort on the basic understanding of plasma jets and the role of magnetic fields in transport through the inclusion of Hall and Nernst terms in transport and an increasing discussion of the Weibel instability. Detailed modelling of the filamentation instability has also been made in support of currently proposed experiments.

In atomic physics the major effort has been directed to the support of the XUV laser experiment, here the work has been considerably enhanced by some detailed calculations using R matrix techniques, on energy levels and line strength in Ne-like selenium. There is also a broadening of interest into strong field and quantum well effects in dense plasma and solid state physics.

A5.2 CLASSICAL PLASMA PHYSICS

A5.2.1 Stimulated Raman Scattering in the presence of Filamentation

H C Barr, T J M Boyd and G A Coutts (University College of North Wales, Bangor)

The importance of stimulated Raman scattering (SRS) from the extensive underdense coronas characteristic of contemporary laser fusion experiments has been recognised for some time (A5.1). While the observations confirm some of the characteristics of Raman emission there are features which do not readily conform to the predictions of the standard treatment of the instability in a linear density profile. If we are to understand the details of the various Raman observations it is important to model the plasma realistically and in particular to take account of the possible effects of other instabilities taking

place concurrently (A5.2). Here we focus attention on ways in which SRS may be affected by filamentation. Filamentary structures are present in many target plasmas, these structures being localized on a spatial scale finer than that associated with non-uniformities in the incident beam (A5.3). There is some indirect evidence that filamentation can affect the Raman emission (A5.4). We would expect on the one hand that the enhanced intensity of radiation within the filament might lead to correspondingly enhanced Raman growth while on the other the denisty modulation resulting from filamentation is likely to restrict the development of the Raman instability through its effect on the plasma wave, since phase matching is only satisified locally. Experiments in which filamentation has been observed provide some information about the width and perhaps the length of filaments but none about details such as depth or shape. In this work we adopt a model which is readily amenable to analysis and yet able to account fully for both the plasma inhomogeneity (without recourse to assumptions of weak inhomogeneity, a local approximation or to WKB analysis) and the kinetics (Landau damping).

The filament is modelled by an electron plasma whose zero-order electron density is

$$n_o(Y) = n_o\ (1 + \varepsilon \cos 2Ky) \qquad (1)$$

and so is assumed to have a slab geometry with a wavelength $\lambda = \pi/K$ and prescribed depth 2ℓ relative to the mean background density n_o. The laser, frequency ω_o and vacuum wavelength $\lambda_o = 2\pi/k_o$, is incident along the filament in the x direction. The Vlasov equation with the ponderomotive force of the beating light waves included has been adapted to describe driven plasma waves in the presence of the profile given by (1). The light waves are adequately treated using fluid theory and incorporating (1).

The propoagation of plasma waves parallel to a sinusoidal density gradient has been considered by others, the propagation characteristics being described by the Mathieu equation (A5.5). The propagation of light waves polarized perpendicular to the density gradient (s-polarized) is similarly described. Plasma waves propagating

obliquely to the density gradient satisify a closely related equation. We assume that incident and scattered waves are both s-polarized. The propagation of all three waves may then be described in wavenumber space by the difference equation

$$(a - \kappa_n^2)E_n = q\,(\Theta_n E_{n-1} + \Theta_{n+1}E_{n+1}) \qquad (2)$$

where $\underset{\sim}{k}_n = \underset{\sim}{k} + 2n\underset{\sim}{K}$, $\underset{\sim}{K} = K\underset{\sim}{y}$, $\underset{\sim}{\kappa}_n = \underset{\sim}{k}_n/K$ and $E_n = E(\underset{\sim}{k}_n)$ is the electric field of the wave in question. For light waves $a = (\omega^2 - \omega_p^2)/K^2c^2$, $q = \epsilon\,\omega_p^2/2K^2c^2$, $\Theta_n = 1$ and ω_p is the plasma frequency corresponding to the mean density n_o. For plasma waves $a = (\omega^2 - \omega_p^2)/3K^2V_T^2$, $q = \epsilon/6K^2\lambda_D^2$ and $\Theta_n = \underset{\sim}{k}_n \cdot \underset{\sim}{k}_{n+1}$ is a geometric factor. Treating the plasma waves kinetically requires the replacement of $(\omega^2 - \omega_p^2 - 3k^2V_T^2)/\omega_p^2$ by $-[1 + 1/\chi(\underset{\sim}{k},\omega)]$ where χ is the usual electron susceptibility for a homogeneous Maxwellian plasma.

For a given $\underset{\sim}{k}$, the periodic solutions of (2) yields an indefinite but discrete set of eigenvalues $a = a_N$ (N=0,1,2,....). The crucial quantity determining the nature of the solution is the coupling parameter q. When q is small, the wave can adjust its wavenumber to compensate changes in density and hence propagates at every density present ie between $\omega_{\pm}^2 = \omega_p^2\,(1 \pm \epsilon)$. When q is large this compensation is no longer possible and the wave is evanescent at higher densities. The wave then becomes trapped within the filament. In addition coupling into shorter wavelength modes implied by (2) gives rise to enhanced Landau damping which can be the dominant effect for sufficiently deep filaments. Just what large or small q means must be seen in relation to the particular eigenstate $a_N(q)$. Higher N corresponding to higher frequency requires larger values of q to trap such waves within the filament.

For light waves, $q_{em} = 2\epsilon(n_o/n_c)(\lambda/\lambda_o)^2$ where n_c is the critical density for the laser light. The parameters used throughout this work

are $n_o = 0.1n_c$, $V_T = 0.035c$, $\lambda = 10\lambda_o$ and $v_o = 0.01c$. Then $q_{em} = 20\epsilon$ which can easily be greater than unity implying that the first few eigenstates are trapped within the filament, the remainder being free to propagate in what, for them, is an everywhere underdense plasma. To illustrate this, (Fig (A5.1)(a)) shows the intensity variation across a filament when $\epsilon = 0.15$ for the laser driver or backscattered light (both correspond to an N=0 state as given by the dashed curve) and sidescattered light (corresponding to an N=6 state as given by the solid curve). The figure shows the "filament": the concentrated intensity profile of the laser light, consistent with the density channel (1), and which is used as the driver in the SRS equations. Backscattered light similarly suffers filamentation while sidescattered barely 'sees' the density variation.

Plasma waves, on the other hand, scale to much shorter lengths and therefore have a coupling parameter

$q_{es} = (c^2/3V_T^2)\,q_{em} \approx 344\,\epsilon\,(n_o/n_c)(\lambda/\lambda_o)^2 T_{keV}^{-1}$. This can easily be very large implying strong localization of plasma wave energy at specific points within the filament. Propagation anywhere requires $\omega > \omega_-$, the minimum plama frequency, yet Landau damping implies an upper limit to the frequency $\omega < \omega_+$. Within this range a finite number of eigenstates may be supported, the number being approximately $\sqrt{(q/4)}$. As the filament or cavity deepens successively more plasma waves may be excited (A5.6). (Fig A5.1(b)) displays the intensity profiles for three of the possible 14 plasma wave states supported by a cavity for which $\epsilon = 0.15$. The lowest frequency mode $\omega = \omega_-$ (N=0) is that localized near the density minimum while the highest is $\omega = \omega_+$ (N=13) localized near the density maximum. One intermediate state, N=4, is also shown localized midway up the filament wall.

Of course in an inhomogeneous plasma three-wave interactions may occur at any of the densities present (up to $n_c/4$). In the context of the present periodic system and the consequent discrete set of eigenstates we can have resonant three-wave interactions between a whole series of pairings of light wave and plasma wave eigenstates. In principle then we need to solve three coupled sets of equations of the form (2). In practice, we may simplify the problem by observing that since $q_{es} >> q_{em}$

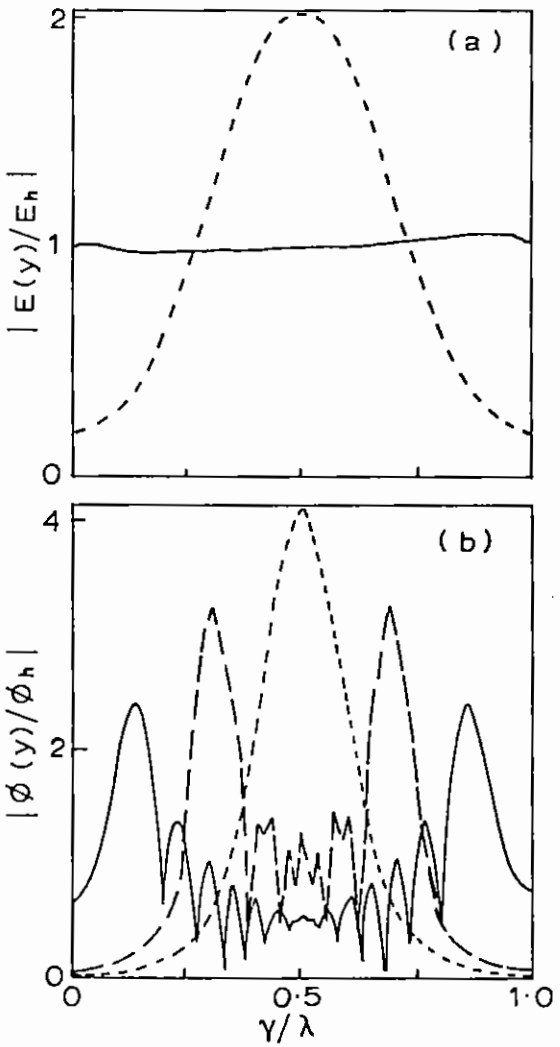

Fig A5.1 Profiles of electric field and potential (normalised to homogeneous values) across a filament for light wave and plasma wave respectively when ε = 0.15. (a) Incident and backscattered light N = 0 (.....); sidescattered light, N = 6 (.....). (b) Plasma wave eigensates N = 0 (....), N = 4 (....) or N = 13 (....).

we may assume, to lowest order, that the light wave intensities are uniform across the filament. Fig A5.2 illustrates the effect of the

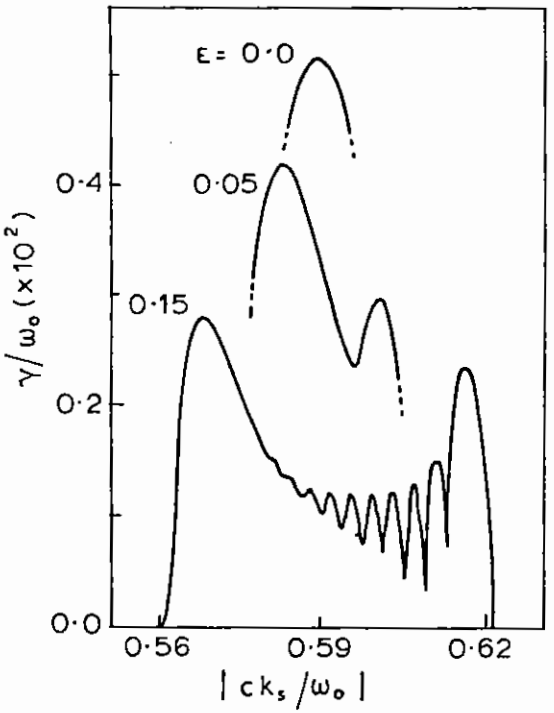

Fig A5.2 The SRS growth rate for backscatter as a function of the scattered light wavenumber assuming light waves of uniform intensity across the filament.

inhomogeneity on the plasma wave alone. When $\varepsilon=0$, the homogeneous growth rate has a maximum growth rate $\gamma_o = kv_o\omega_p/2(\omega\omega_s)^{\frac{1}{2}}$ and band width γ_o. Reduction in growth is rapid until the bandwidth associated with the inhomogeneity $\varepsilon\omega_p \simeq \gamma_o$; subsequently it is rather slower but such that the bandwidth for growth is determined by $\varepsilon\omega_p$ rather than γ_o. This is akin to using bandwidth in the incident laser to reduce growth. A cold plasma theory shows that oscillations exist only at density maximum, $\omega=\omega_+$, and density minimum, $\omega=\omega_-$, in other words only where density gradients are zero. These dominate as (Fig A5.2) shows clearly (ω_+ on the left, ω_- on the right) with growth rates deduced

analytically to be $\gamma_{\pm} = (\sqrt{3}/2)(\varepsilon\omega_p^2/\gamma_o\omega_{\pm})^{-1/3}\gamma_o$ when $\varepsilon\omega_p > \gamma_o$. These expressions reproduce the numerical values to good accuracy. Finite temperature allows states at intermediate frequencies as clearly seen when $\varepsilon = 0.15$ in (Fig A5.2). The frequency separation between peaks can also be deduced analytically to be $\delta\omega \simeq 2KV_T/6\varepsilon$. Each peak in (Fig A5.2) is associated with a given eigenstate, N, which is localized at a specific point within the filament or cavity (cf. Fig A5.1(b)).

Given this strong localization of the plasma wave energy it is straightfoward to anticipate just how the non-uniform light wave intensity profiles will modify (Fig A5.2). Including first only the effects of the filament on the scattered wave, Fig A5.1(a) shows that backscattered light (N=0) is concentrated around the filament bottom. The numerical results show that the resonance at ω_- is enhanced while that at ω_+ is diminished by the factors which would be anticipated from (Fig A5.1(a)). Growth at w_- still shows a reduction with increasing ε, albeit now rather weak, while that at ω_4 is all but suppressed, there being little scattered light wave energy near the density maximum where this resonance occurs.

Finally, including the non-uniform laser intensity profile produces (Fig A5.3) - now all three interacting modes are correctly treated for the profile (1). (Fig A5.3(a) shows the backscatter growth rates showing a further expected strong bias towards the resonance at the filament bottom. For deeper filaments the net growth shows an increase over homogeneous values which continues until the minimum density reaches a values such that Landau damping becomes strong ($k\lambda_D$ locally large) after which it quickly decreases with ε. Finally a stage is reached where Landau damping is so strong that around the density minimum SRS degenerates into stimulated Compton scattering (SCS) and the maximally growing states are those at higher densities (ie localized up the filament wall) where Landau damping is relatively weaker and SRS still occurs. Ultimately, the regions of laser light concentration and plasma wave propagation become mutually exclusive with only SCS remaining.

Growth for sidescatter shows essentially the same features as for

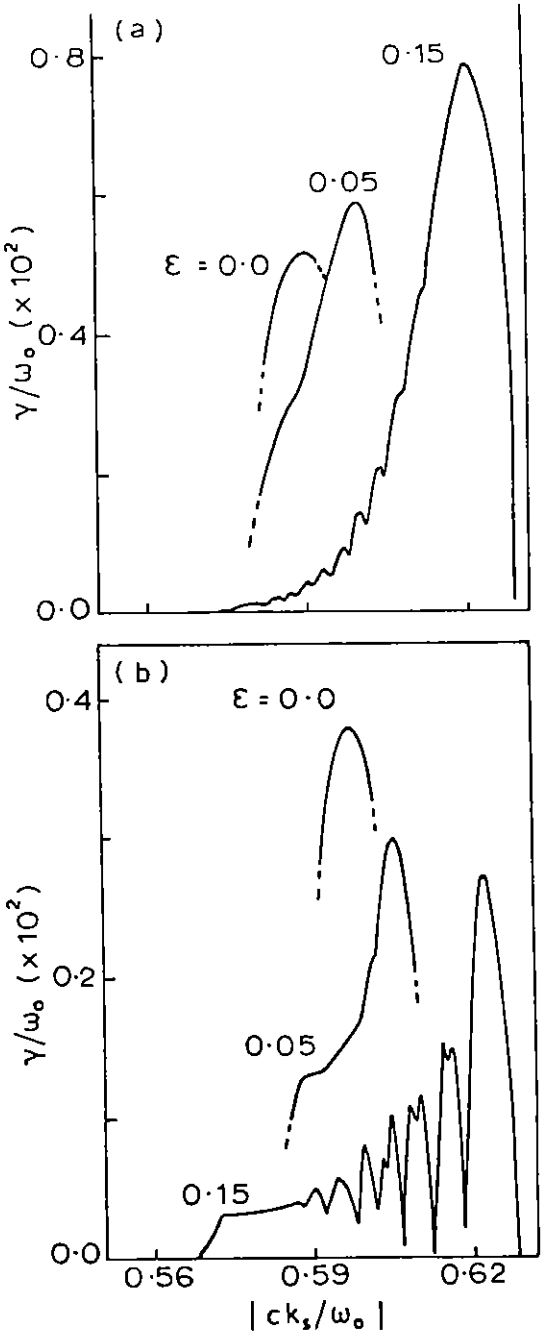

Fig A5.3 The SRS growth rate for (a) backscatter and (b) sidescatter as a function of the scattered light wavenumber including the effects of filamentation on all waves.

backscatter with one exception. The difference is illustrated in (Fig A5.1(a)) showing that sidescattered light (N=6) is barely affected by the filamented profile. Relative to the backscatter case, this means that the enhancement of the resonance at ω_- is correspondingly weaker as is clear from (Fig A5.3(b)). One effect of filamentation, which might potentially signal its presence, is to make SRS backscatter relatively much stronger than sidescatter even then the plasma is sufficiently broad to allow significant lateral gain (A5.4).

In summary this work has shown scattering to be strongly confined to the bottom of filaments. In shallow filaments modest increases in growth result, due mainly to the locally enhanced laser intensity there. The increase is less than might be anticipated since the inhomogeneity reduces growth, through bandwidth effects, by its action on the plasma wave propagation. For deeper filaments, Landau damping at the lower densities present plays the dominant role strongly suppressing growth. Sidescatter exhibits no enhancement over its homogeneous value and is decreased relative to backscatter.

A5.2.2 Filamentation in a flowing Plasma

R G Evans (RAL)

The filamentation of laser light in a plasma may be driven by the ponderomotive force or by the local thermal heating. In either case the pressure is raised in the "hot spots" of the beam resulting in a lower density and an increased refractive index. Since the filamentation process requires the hydrodynamic response of the plasma it is clear that it can be affected by the zero order plasma flow.

The effects of plasma motion transverse to the laser beam have been analysed by Short, Bingham and Williams (A5.7). The plasma hydrodynamic response can be regarded as two counter-propogating pseudo modes and the effect of transverse flow is to move one of these modes closer to its dispersion relation and hence to increase the growth rate of the filamentation. Here we make a simple estimate of the effects of plasma flow parallel to the direction of laser propagation. An idealised problem is considered, namely the steady state response of an

isothermal fluid moving in the x-direction subject to a small external applied pressure (eg the ponderomotive force) Δp_A.

The zero order solution is characterised by the flow velocity v_x and density g, and the perturbed solution is:

$$v_x + v_x \; ; \; v_y \; ; \; \rho + \rho$$

The fluid is assumed to have an ideal gas equation of state so that

$$\Delta p = c^2 \Delta \rho .$$

The linearised continuity, x and y momentum equations are:

$$v_x \frac{\partial \rho}{\partial x} + \rho \frac{\partial v_x}{\partial x} + \rho \frac{\partial v_y}{\partial y} = 0$$

$$\rho v_x \frac{\partial v_x}{\partial x} = - \frac{\partial}{\partial x} (p + p_A)$$

$$\rho v_x \frac{\partial v_y}{\partial x} = - \frac{\partial}{\partial y} (p + p_A)$$

In the normal way we assume that all quantities are periodic in x and y with wave numbers k_x and k_y. Elimination of v_x and v_y then gives the fluid density response as:

$$\frac{(\rho / \rho)}{(p_A / \rho c^2)} = - \frac{k_x + k_y}{k_x + k_y - M^2 k_x}$$

where $M = v_x/c$ and c is the isothermal sound speed.

This simple analysis shows that fundamentally different behaviour can

be expected if the flow Mach number is sufficiently large that $M^2 k_x > k_x + k_y$. In this case the local pressure increase gives rise to a local density increase and there is no filamentation instability. The occurence of finite k_x does not happen with normal laser illumination since it implies modulation of the light intensity along the propagation direction. If however the target is illuminated by two or more coherent laser beams as shown in((Fig A5.4) then there is a standing wave pattern of the required form and qualitatively different filamentation behaviour may be expected if the flow Mach number is large.

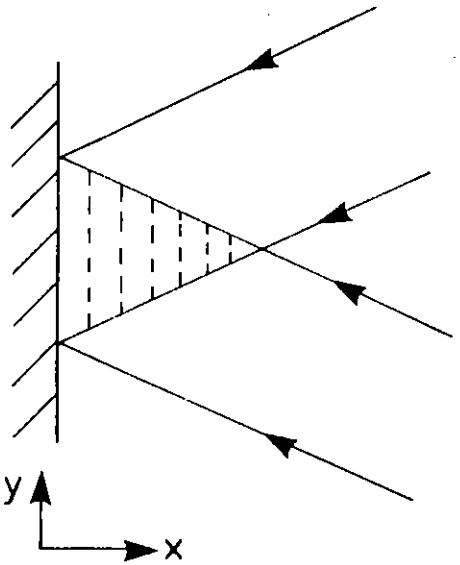

Fig A5.4 Finite k produced by interference of coherent overlapping beams.

A5.2.3 Filamentation in laser produced plasmas

D J Nicholas (RAL) and S G Sajjadi (Lanchester)

A numerical study of beam filamentation in laser produced plasma is presented. This involves the numerical solution of the Schrodinger equation coupled with the thermal transport equations for both ions and electrons. The solution of the resulting equation with non-linear refractive index due to thermal and ponderomotive forces, show self-focusing and a variety of strong aberration effects. Intensity amplification at the final focus is found to be between one and two orders of magnitude greater than the initial beam intensity, governed in general by diffraction and aberration effects within the beam.

The equation for the electric field of the laser in paraxial form is taken

$$\nabla^2 A + 2ik_o \varepsilon_o^{\frac{1}{2}} \frac{\partial}{\partial z} (\varepsilon_o^{\frac{1}{2}} A) + k_o^2 (\varepsilon - \varepsilon_o) A = 0 \qquad (1)$$

where $k_o = (\omega/c)$. This is solved in conjunction with the equations of thermal transport.

For the electrons,

$$C_{V_e} \frac{\partial Te}{\partial t} = \nabla.(k_e \nabla T_e) + K_{ib} A^2 - q_{ei} \qquad (2)$$

For the ions,

$$C_{V_i} \frac{\partial Ti}{\partial t} = \nabla.(k_i \nabla T_i) + q_{ei} \qquad (3)$$

where C_{V_e} and C_{V_i} are the specific heats of the electrons and ions and q_{ei} is the ion electron equipartition rate. K_{ib} is the laser absorption via inverse Bremsstrahlung. Both ponderomotive and thermal self focussing are accounted for.

A5.2.3.1 Numerical Scheme

Equations (1), (2) and (3) can be expressed as following

$$\nabla^2 A + i\,\Psi(z)\,\frac{\partial A}{\partial z} + \zeta(r,z,A,T_e,T_i) = 0 \qquad (4)$$

$$\frac{\partial T_e}{\partial t} - \nabla\cdot\left[k_e(r,z,T_e,T_i)\nabla T_e\right] - \Omega_e(r,z,A,T_e,T_i) = 0 \qquad (5)$$

$$\frac{\partial T_i}{\partial t} - \nabla\cdot\left[k_i(r,z,T_e,T_i)\nabla T_i\right] - \Omega_i(r,z,T_e,T_i) = 0 \qquad (6)$$

Equations (4) - (6) are solved simultaneously, subject to the following initial - boundary conditions.

$$\frac{\partial}{\partial r}A(o,z) = \frac{\partial}{\partial r}A(r_o,z) = 0$$

$$\frac{\partial}{\partial r}T_e(o,z,t) = \frac{\partial}{\partial r}T_e(r_o,z,t) = 0$$

$$\frac{\partial}{\partial r}T_i(o,z,t) = \frac{\partial}{\partial r}T_i(r_o,z,t) = 0$$

$$A(r,o) = \exp(-r^2/r_o^2)$$

$$T_e(r,z,o) = (T_e)_o$$

$$T_i(r,z,o) = (T_i)_o$$

where r_o is the Gaussian radius of the beam. Using the variable-weighted implicit differencing scheme in equation (4), we obtain,

$$\Theta(\nabla^2 A)^{m+1}_{i,j+1} + (1-\Theta)(\nabla^2 A)^{m+1}_{i,j} +$$

$$i\left[\Theta\Psi_{i,j+1} + (1-\Theta)\Psi_{i,j}\right]\left(\frac{\partial A}{\partial z}\right)^{m+1}_{i,j+\frac{1}{2}} +$$

$$\Theta(\zeta^m_{i,j+1}A^{m+1}_{i,j+1}) + (1-\Theta)(\zeta^m_{i,j}A^{m+1}_{i,j}) = 0$$

with $0 \leq \Theta \leq 1$.

A two step alternating-direction implicit method (ADI) is applied to equations (5) and (6), to obtain, first step,

$$(\Delta t)^{-1}(T^{m+\frac{1}{2}}_{i,j,n+1} - T^{o}_{i,j,n}) - \left[\nabla_r(k^m\nabla_r T^m)\right]_{i,j,n+1} -$$

$$\left[\nabla_z(k^m\nabla_z T^{m+\frac{1}{2}})\right]_{i,j,n+1} - \Omega^m_{i,j,n+1} = 0$$

second step,

$$(\Delta t)^{-1}(T^{m+1}_{i,j,n+1} - T^{o}_{i,j,n}) - \left[\nabla_r(k^{m+\frac{1}{2}}T^{m+1})\right]_{i,j,n+1} -$$

$$\left[\nabla_z(k^{m+\frac{1}{2}}T^{m+\frac{1}{2}})\right]_{i,j,n+1} - \Omega^{m+\frac{1}{2}}_{i,j,n+1} = 0$$

where, $\nabla_\eta \equiv \frac{\partial}{\partial\eta}$

A5.2.3.2 Results

Although we have considered problems in both uniform and non-uniform plasmas, we shall limit our discussion here to the latter case. Calculations are carried out at electron temperatures T_e = 0.5, 1.0 and 1.5 keV and at two laser wavelengths of 1.06μm and 0.54μm. The calculations are carried with radial symmetry (r,z) the initial filament being Gaussian in profile given by $I_o(r,o)\exp(-r^2/r_o^2)$ with r_o set at 6.13μm. For example in (Fig A5.5) a Gaussian beam with a peak

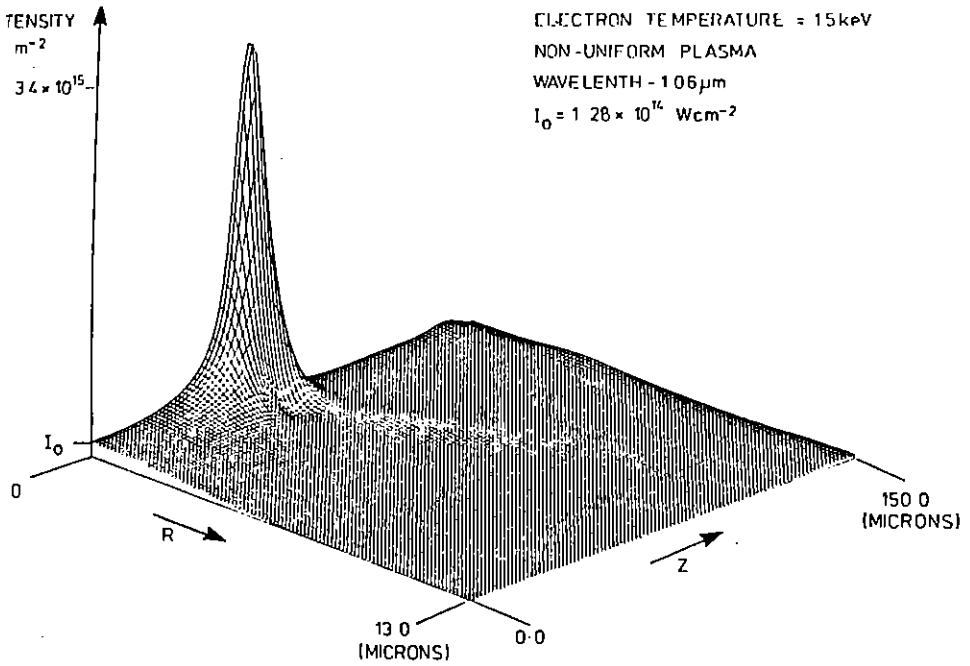

Fig A5.5 Numerical simulation of laser beam self-focusing in a non-uniform plasma at λ = 1.06μ. T_e = 1.5keV, I_0 = 1.28 x 10^{14}Wcm^{-2}. Intensity at first focus = 3.4 x 10^{15}Wcm^{-2}.

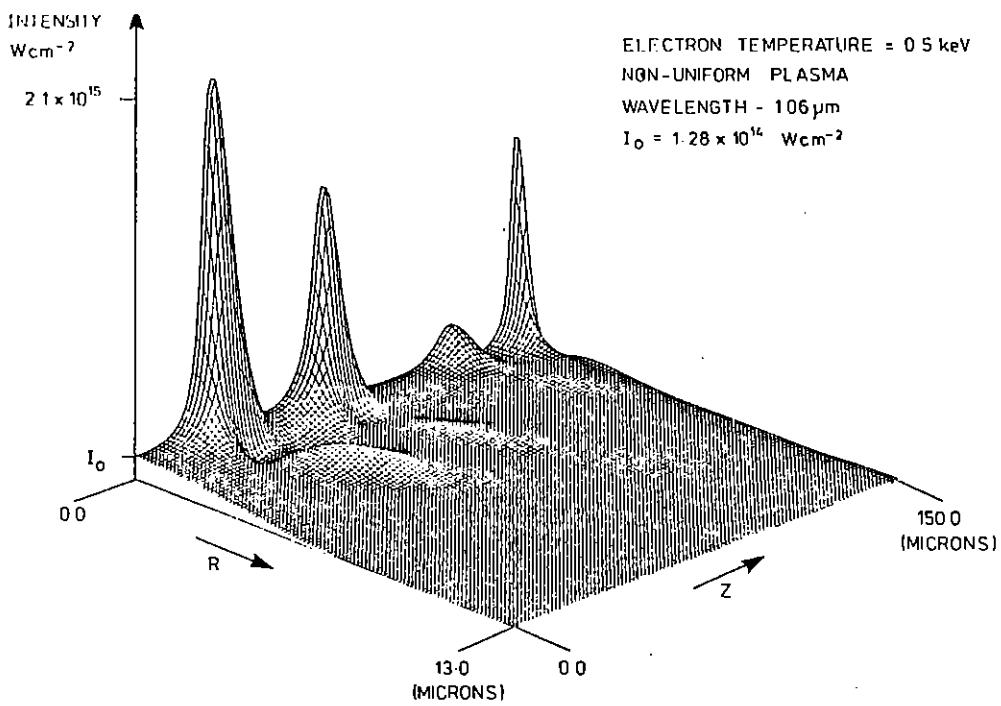

Fig A5.6 As for Fig A5.5 but with T_e = 0.5keV. I_0 = 1.28 x 10^{14}Wcm^{-2}. Intensity at first focus = 2.1 x 10^{15}Wcm^{-2}.

intensity of 1.28 x 10^{14} Wcm^{-2} propagates through a non-uniform plasma with T_e = 1.5 keV. The beam focuses at distance z = 58.2 μm, where the peak intensity on the axis reaches 3.4 x 10^{15} Wcm^{-2}. Successive focii are also weaker.

If the plasma temperature decreases the thermokinetic pressure decreases and the ponderomotive force readily displaces the electrons and the ions. Under such conditions the self-focussing distance decreases. For example with T_e = 0.5 keV, (Fig A5.6), the beam focuses at the distance of 38.1μm and the focus has a lower peak intensity 2.1 x 10^{15}Wcm^{-2} than that shown in (Fig A5.5). However, the beam continues to form a succession of focii in this case the fourth appearing quite near to critical density. In (Fig A5.7) the general dependence of the self-focusing distance Z_{sf} on the initial peak intensity I_o of the filament is shown for various electron temperatures T_e and for the two lasr wavelength 1.06μm and 0.546μm. Also shown are the critical intensities I_c for the process at each plasma temperature.

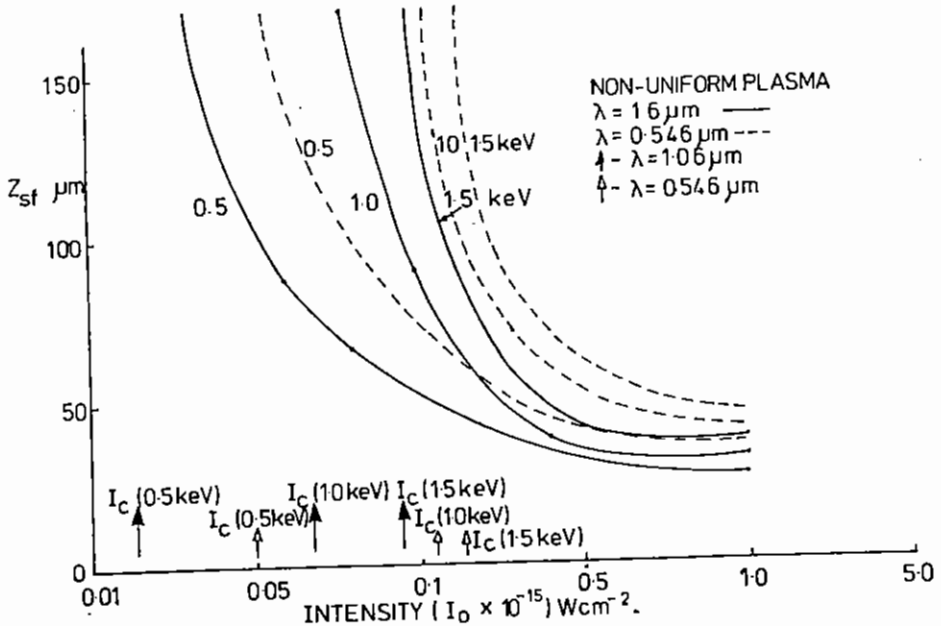

Fig A5.7 Variation in self-focusing distance Z_{sf} with initial filament intensity I_0 for non-uniform plasma. Continuous curves give results for λ = 1.06μm, hatched curves, the results for λ = 0.546μm.

For non-uniform plasma the scaling laws for the threshold intensities depend on local conditions. In the linear region at lower temperature T < 500 eV then

$$I_c \sim 7.5 \times 10^{13} T^{0.63}$$

whilst on the entire temperature range investigated the scaling behaves as T^m where $0.05 < m < 2.5$. This is very much in keeping with the general experimental results where the scaling law was dependent on whether thermal or ponderomotive self-focusing forces were dominant. When the ponderomotive force dominates, the threshold power varies in

approximately linear fashion with temperature. On the other hand when the thermokinetic forces dominate the scaling law behaves as $T^{1.9}$.

Another important factor with these instabilities is their growth rates. Assuming, a spatial growth rate in the form $I = I_0 e^{\alpha z}$ our simulations can readily be used to estimate growth rates. It can be seen that at low intensities and at the start of the filamentation the process is linear with rates of 10%-20% μm^{-1}. However the growth rats quickly become non-linear with final values (in the non-linear regime near the focus) > 73% μm^{-1}. Most of the theory that we have discussed and made comparisions with is applicable in the linear, early stages of the growth of the instability. It would appear that there is a need for additional theoretical study of the instability into its highly non-linear regime.

A5.2.4 Weibel Instability in an ablating plasma

A R Bell and E M Epperlein (Imperial College)

We have reported previously (A5.8) on steady-state ablation from an infinite planar target when the illuminating laser irradiation has a small non-uniformity which is spatially sinusoidal. We solved the perturbation equations for hydrodynamics with magnetic field, including the $\nabla n \times \nabla T$ source, Nernst convection, Righi-Leduc heat flow and collisional diffusion. The thermomagnetic instability (A5.9) is included in these equations and was shown to have a positively stabilising efect, reducing the pressure non-uniformity. In contrast, the Weibel instability (A5.10) is a phase-space phenomenon and is not so included. The Weibel instability has a faster growth rate than the thermo-magnetic instability when both have positive growth rates (A5.11), and in the overdense plasma the thermo-magnetic growth rate is negative. Clearly the Weibel instability is important in any description of 2-D ablation structures and we report here its inclusion in the calculations. The mechanism of the Weibel instability consists of a feedback loop between the magnetic field and the off-diagonal terms of the pressure tensor, and operates in isolation from hydrodynamic processes. In consequence, it can adequately be modelled

by the inclusion of a growth term in the equation for the generation and convection of magnetic field. A kinetic treatment of the collisional Weibel instability is needed, and we use the growth rates calculated (A5.12) for a Lorentz plasma on the assumption that the perturbation wavelength is much smaller than the scalelengths of the zeroth order solution.

In an ablating plasma, the Weibel instability amplifies the magnetic field produced by the grad(n_e)xgrad(T) term as it convects toward the solid. In the present model, the production and amplification of magnetic field is balanced by its convection to the solid where it is dissipated by collisional diffusion, thus allowing a steady state. Our equations exclude the possibility of a perturbation which not only grows in space, but grows exponentially in time. If a temporally growing solution exists, our calculations underestimate the effect of the Weibel instability in an ablating plasma.

Fig (A5.8) plots the perturbed momentum flow when Weibel amplification is included. We give results for Z=10. We multiply the Weibel growth rate γ_W by a factor μ which gives the correct growth rate when μ=1. This enables us to examine the sensitivity of the results to the exact growth rate by making μ larger or smaller than one. Curves a) and c) of Fig (A5.8) give the perturbed momentum flow when μ=1. They differ negligibly from the corresponding curves with Weibel amplification ignored, indicating that the instability is not strong enough to overcome smoothing. Curves b) and d) give the results when Weibel amplification (γ_W) is multiplied by five (μ=5). Instability then dominates at short wavelength leading to a large non-uniformity in momentum flow (pressure) at high density. The sensitivity to μ implies a relatively fine balance between smoothing and instability. The competition is yet more sensitive to changes in the Nernst convection velocity. In the present calculation, the Nernst velocity for convection of magnetic field to high density exceeds the oppositely directed plasma flow velocity be between 40 and 70 percent depending on the Mach number. Thus a 50 percent reduction in the Nernst velocity would be sufficient to reverse the overall convection velocity of magnetic field in part of the plasma, producing a completely different solution. However, such a reduction appears unlikely (A5.13). There

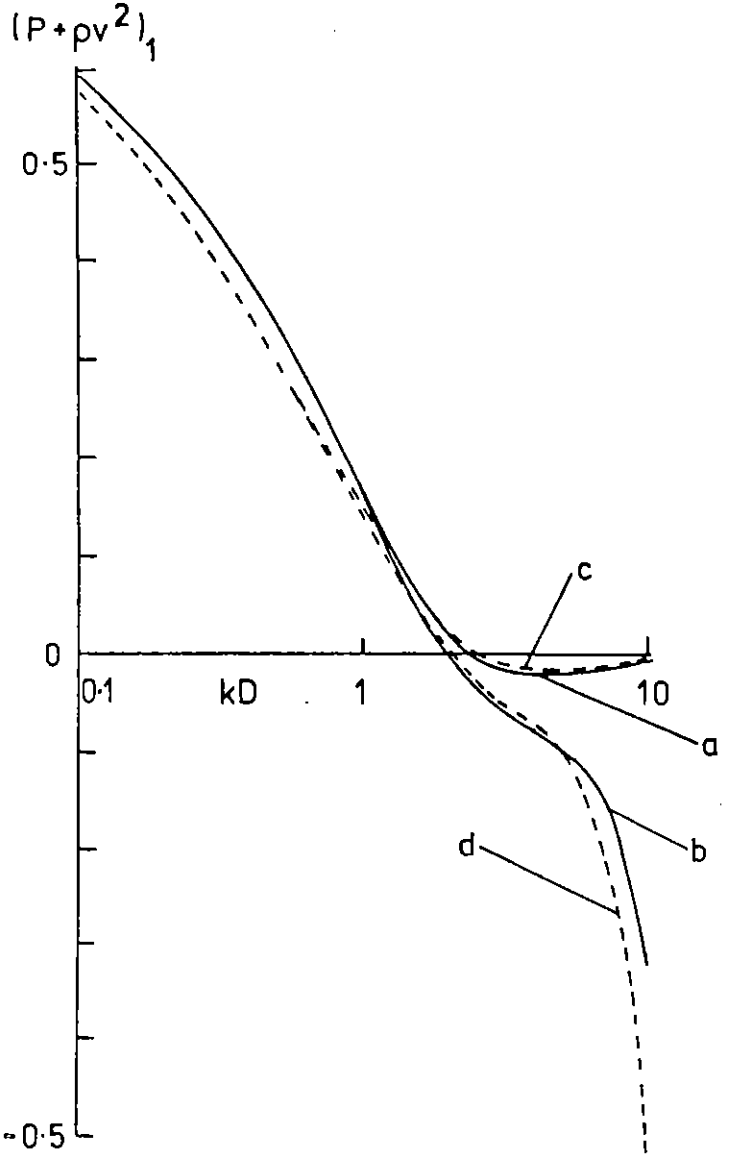

Fig A5.8 A plot of the amplitude of the peturbed momentum flow ($P+\rho v^2$) when Weibel amplification is included. It is plotted as a function of kD where k is the spatial frequency of the perturbation and D is the distance between the critical and solid surfaces.
a) μ=1 at the critical surface b) μ=5 at the critical surface c) μ=1 at high density d) μ=5 at high density. In each case the density at critical is 10^{21} electrons cm^{-3}, the temperature at critical is 5KeV, and Z=10.

is a further complication with respect to convection velocities. Because the Weibel instability consists of a feedback process between the magnetic field and the off-diagonal terms of the pressure tensor, it is important to know the convection velocity of the relevant moment of the electron distribution, which need not be the same as the convection velocity of the magnetic field.

We tentatively conclude that the Weibel instability is not strong enough to overcome the smoothing processes, but we admit that a more complete calculation, particularly through the adoption of non-planar geometry, may conceivably reverse the conclusion.

A5.2.5 Local and non-local treatment of the collisional Weibel instability

E M Epperlein, T H Kho and M G Haines (Imperial College)

A collisional version of the Weibel instability (A5.10) has been investigated by many authors in recent years in the context of ablatively driven laser-plasmas (A5.12, A5.14, A5.15). A limitation of these previous studies has been the assumption of a prescribed equilibrium. In (A5.12), a stability analysis was developed based on Cartesian tensor expansion of the electron Fokker-Planck equation. This was applied to an "equilibrium" composed of drifting hot and cold Maxwellian distribution functions, to mock up the non-linear electron heat flow. It was found that the unstable Weibel mode, driven by the anisotropy in the distribution function caused by the heat flow, can have significant growth rates ($\sim 10^{10} s^{-1}$) occurring at densities above critical.

Here we calculate local Weibel growth rates γ [(A5.12), equation (10)] for a more realistic situation, that of a plasma heated by inverse-Bremsstrahlung.

The distribution function f of the plasma is calculated by means of a time dependent one-dimensional electron Fokker-Planck code (A5.13), which uses the aproximation $f=f_o+v_z f_z/v$ (z being the direction of the heat flow) with the full electron collision operator for f_o and the

angular scattering operator of f_z (an approximation that is expected to be valid for high-Z plasmas) (A5.16). Fixed ions are assumed. The value of f_{zz}, necessary for calculating γ, is obtained from the approximate relation (A5.17)

$$f_{zz} = -\frac{2v}{9\nu}\left[\partial_z f_z - \left(\frac{e}{m}E_z\right)\partial_v (f_z/v)\right]$$

where E_z is the electric field, e is the magnitude of the electron charge, m is the electron mass and $\nu=\left[4\pi n(Z+1)(e^2/m)^2 \ln\Lambda\right]/v^3$ is the electron collision frequency (n being the electron number density, Z the ionic charge and $\ln\Lambda$ the Coulomb logarithm). We find that f_z makes only small contribution towards the total Weibel growth rate.

The simulation is performed for a 100μm overdense plasma slab of z=10, with a background exponential density profile of scale-length 43μm (giving a density jump of ~10) and an initially uniform electron temperature of 200eV. The heating is achieved via inverse-Bremsstrahlung absorption of 1.06μm laser light at critical density, corresponding to an absorbed intensity of $\sim 10^{13} W/cm^2$. Fig (A5.9) shows the profiles of temperature and (Fig A5.10) shows the profiles of heat flow [normalised to the free-streaming heat flow $q_{fs}=nm(T/m)^{3/2}$], at 2, 30 and 60ps.

For a given time in the evolution of the plasma γ is calculated as a functionof the transverse perturbation wavelength λ at every spatial point. The maximum growth rate γ_{max} and respective wavelength λ_{max} are then plotted as functions of space z in (Figs A5.11 and A5.12). These calculations have been repeated for an assumed Maxwellian f_o (at the temperatures and densities shown in (Fig A5.9.1), and f_{zz} based on linear transport (A5.17), namely:

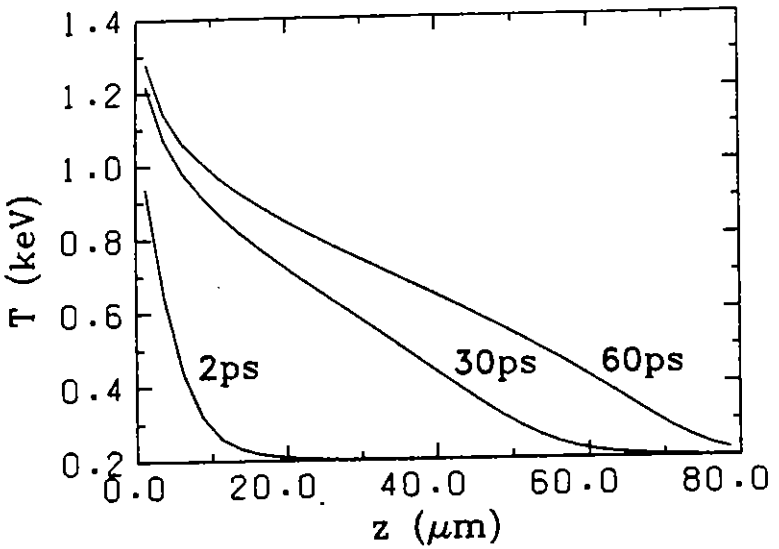

Fig A5.9 Plot of electron temperature T as a function of space z, at different times in the evoluton of the plasma. Initial T = 200eV.

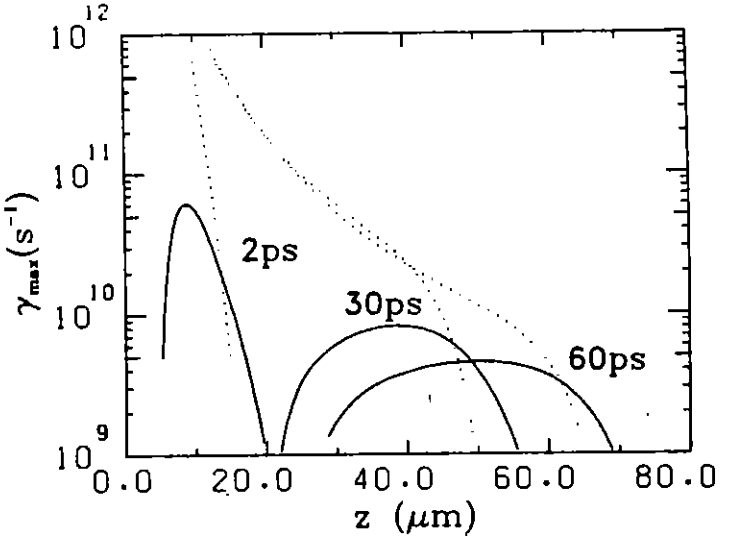

Fig A5.11 Plot of maximum Weibel growth rate γ_{max} as a function of z. Solid and dotted lines are based on (f_0, f_{zz}) and (f_0^m, f_{zz}^m), respectively.

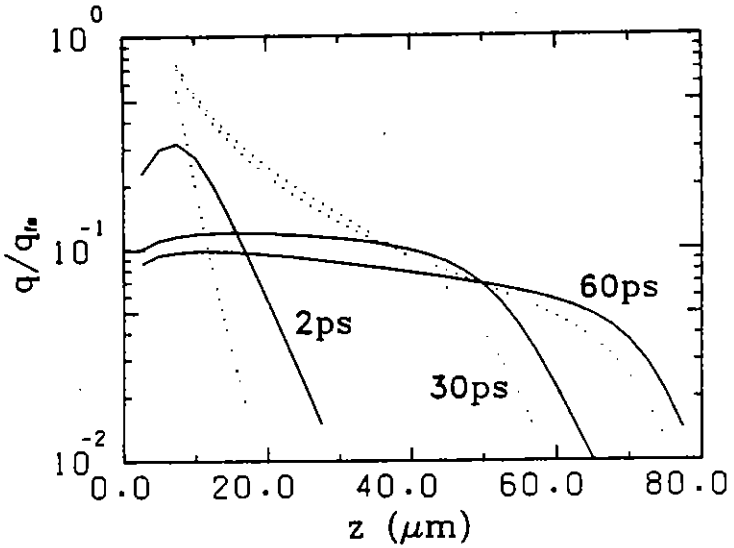

Fig A5.10 Plot of heat flow q in units of q_{fs} as a function of z. Solid and dotted lines are based on f_z and f_z^m, respectively.

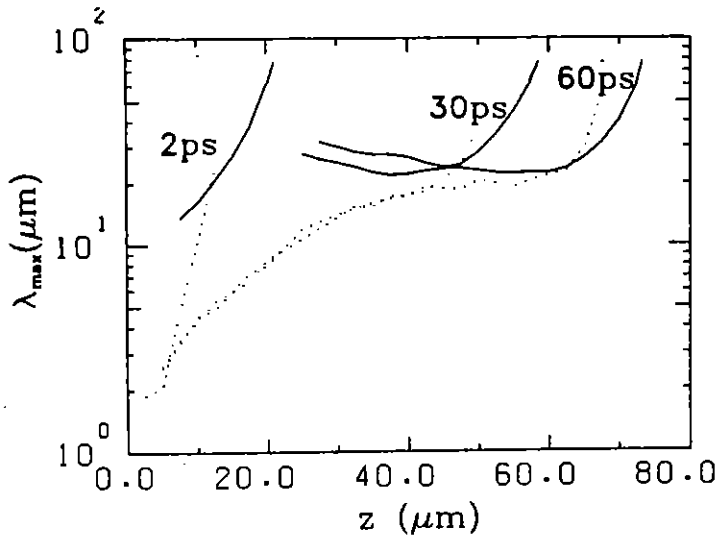

Fig A5.12 Plot of optimum perturbation wavelength λ_{max} as a function of z. Solid and dotted lines are based on (f_0, f_{zz}) and (f_0^m, f_{zz}^m), respectively.

$$f_o = f_o^m = n\left[\frac{m}{2T\pi}\right]^{3/2} \exp\left[-v^2 m/2T\right],$$

$$f_z = f_z^m = \frac{v_r}{v}\left[4\frac{v^2}{v_T^2}\right]\frac{f_o^m}{l_T^2}$$

$$f_{zz} = f_{zz}^m = -\frac{2}{9v^2}\left\{\frac{v^5}{v_T^2} - v^3\left[\frac{5}{2} + \frac{1}{l_n}T\right]\right.$$

$$\left. + \left(4\frac{v^2}{v_T^2}\right)\left[\frac{3}{2}v_T^2 v\left(\frac{5}{2} + \frac{1}{l_n}T\right) + v^3\Delta - v^3\left(5+\frac{1}{l_n}T\right) + \frac{v^5}{v_T^2}\right]\right\}\frac{f_o^m}{l_T^2},$$

where $l_{n,T} = \left[\partial_z \ln(n,T)\right]^{-1}$, $\Delta = (\partial_z^2 T) l_T^2/T$ and $v_T = (2T/m)^{1/2}$.

The new values of γ_{max} and λ_{max} are plotted in (Figs A5.11 and A5.12) dotted curves. We also plot as dotted curves in (Fig A5.10) the new values of heat flow based on f_z^m.

(Fig A5.11) highlights two major defficiencies in the instability calculations based on f_o^m and f_{zz}^m. They overestimate γ_{max} close to critical and underestimate it at higher densities. The first arises as a result of the depletion of the hot electron population relative to the thermal Maxwellian. The second arises from the transport of these relatively collisionless electrons to higher densities, thus giving rise to the appearance of the instability ahead of the bulk of the thermal front. An explanation for both effects comes from the fact that electrons with energies between 9 and 12T provide the main contribution towards γ. At these high energies $f_{zz}/f_o \sim 1$ whereas

$f_{zz}^m/f_o^m \sim 10^2$, thus confirming the breakdown of the linear thermal transport approximation. Such phenomena are equivalent to having "inhibited" heat flow and "pre-heating" (as shown in Fig (A5.11), familiar in the context of laser-heated plasmas (A5.19).

The fact that the instability does not penetrate as far into the cold plasma as the heat front follows from the increased magnetic diffusion rate, which scales as $T^{-3/2}$ (T being the temperature of the thermal electrons).

It is interesting to note that the above local analysis of the Weibel instability predicts asymptotic growth times of the order of 0.5ns and wavelengths of about 20μm, which appears to be in good agreement with experimental observation of plasma jets (A5.2,A5.20,A5.21). There are however severe limitations in the present theoretical treatment, such as the assumption that the instability grows locally in space, the neglect of the ion response and the linear approximation. Of these, the first one is probably the most important as it may directly affect the onset of the Weibel instability. In the past few months we have tackled this problem by numerically solving a perturbed generalized induction equation,

$$\partial_t B + \partial_z\left[(v_i + v_N)B\right] = \partial_z(D_m \partial_z B) - k^2 D_m B + S$$

where v_N is the Nernst velocity (A5.13), v_i is the ion velocity, D_m is the magnetic diffusivity and S is a source term arising from perturbations in the electron stress tensor (or more precisely from perturbations in f_{xz}). The source term is obtained by solving the perturbed kinetic equations for f_x, f_z and f_{xz} and Maxwell's equations, for a given B-field. A simple equilibrium model based on planar ablation has been used to derive the profiles of n, T and v_i (A5.22). The diffusion and source parts of the induction equation are solved half-implicitly and the convective part is solved using FCT (A5.23).

Preliminary results indicated that the instability source is strongest close to the critical surface (yielding maximum local growth rates of the order of $10^9 s^{-1}$). Due to the strong localization of the source,

however, longitudinal diffusive process (ie diffusion of B and f_{xz} in the z-direction) have the effect of reducing the overall growth rate of the plasma relative the maximum predicted local growth rate. With the further inclusion of v_N and v_i, which act to convect the B-field away from the critical surface (A5.22), the source is not strong enough to sustain growth and the plasma becomes stable.

We may envisage other equilibria, based on more strongly driven laser-plasmas, where the source of free energy (in the form of pressure anisotropy) for driving the Weibel instability is much larger. However, our present results based on a classical planar equilibrium indicate that transport effects would tend to drastically reduce the instability, if not kill it altogether.

A5.2.6 Heat Flow Inhibition due to Curvature

S Jorna and L Wood (St Andrews)

We have investigated the effects of geometry on heat flow by solving the one dimensional time dependent Fokker-Planck equation in spherical geometry. Our aim was to quantify the results presented in (A5.24 and A5.25), predicting a reduction in the heating of the cold boundary, in a two boundary heating problem, with increased curvature. The width is kept constant as we vary the radius. The geometry is then described by the aspect ratio (R/ΔR).

We present results for cold and hot boundaries at 1 and 2KeV respectively separated by 12μm. The width of the system is several times the mean free path of the thermal electrons. Fig A5.13 shows the

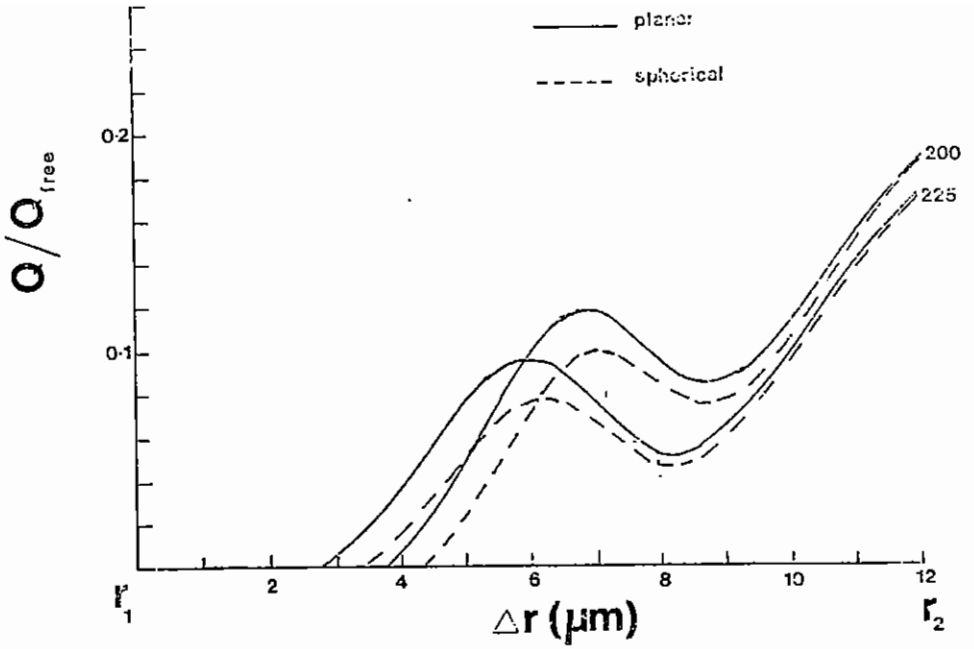

Fig A5.13 Planar and spherical heat flows divided by free streaming heat flows plotted against radial position for times t = 2ps and t = 2.25ps.

calculated heat flow divided by the free streaming heat flow, calculated locally at each radial point, plotted against radial position for an inner radius (R_1) of 1cm (planar) and 40μm at times 2.0 and 2.25ps. Comparing the spherical and planar results we find:

1. A decrease in heat flow of 15-20% for the case with R/ΔR~3.

2. A decrease in penetration due to curvature.

It was found that when the inner radius exceeds 120μm the results corresponded to the planar case.

To quantify the effects of geometry on heat flow we considered a collisionless system with two counterstreaming Maxwellians. Applying the boundary conditions used in the Fokker-Planck calculations with no net flux through the boundaries at R_1 and R_2, the ratio of spherical to planar heat flows is given by

$$\frac{q_{spherical}}{q_{planar}} = \frac{R_1^2}{R_2^2}$$

which predicts a 40% reduction in heat flow for a collisionless system. Collisions slow down the fast heat carrying electron driving the system to a more collisional regime. Our results of 15-20% reduction agree reasonably with the collisionless predictions.

Our Fokker-Planck code now has incorporated the complete Rosenbluth potentials making no assumptions about isotropy of the distribution function. We expect shortly to verify or contradict the commonly made assumption of isotropy in calculating these potentials.

A5.2.7 The influence of self-generated magnetic fields on the Rayleigh -Taylor instability

R G Evans (RAL)

It has long been recognised that the Rayleigh Taylor instability in laser accelerated targets generates large amounts of fluid vorticity (A5.26 and A5.27) and that there should be an accompanying magnetic field. It has been speculated that this self-generated magnetic field might affect the growth rate of the Rayleigh Taylor instability through the j x B force, through the interchange of energy between fluid and magnetic field (A5.28) or via the reduced thermal conductivity if the Hall parameter $\omega\tau$ approaches unity.

Some experimental data on the Rayleigh Taylor growth is available (A5.29 and A5.30) but does not include magnetic field measurements. The available experimental data is consistent with fluid simulations that did not consider the self-generated magnetic field.

The connection between Magnetic Field and Vorticity can be briefly described as follows:

the vorticity ξ in a fluid evolves in a manner which is obtained by taking the curl of the momentum equation and using well known vector identities:

$$\frac{\partial \underline{\xi}}{\partial t} = \text{curl}(\underline{v} \times \underline{\xi}) - \text{curl}\left(\frac{1}{\rho}\nabla p\right) \qquad (1)$$

The evolution of the magnetic field is obtained by using the generalised Ohm's Law and Faraday's Law:

$$\frac{\partial \underline{B}}{\partial t} = \frac{c^2}{4\pi\sigma}\nabla^2\underline{B} + \text{curl}(\underline{v} \times \underline{B}) + \frac{c}{e}\,\text{curl}\left(\frac{1}{n_e}\nabla p_e\right) \qquad (2)$$

The maximum rate of generation of vorticity in the Rayleigh Taylor instability is in the high density, relatively cool material near the ablation surface. The resistivity in this region is not small enough to neglect the magnetic diffusion but if we do so we obtain an upper limit on the magnetic field strength. The similarity of equations (1) and (2) shows that this upper limit on B is simply proportional to the fluid vorticity ξ (A5.27).

In this collisionless limit Mima et al (A5.27) showed that the quantity $(\xi + \omega_{ci})$ is conserved, where the ion cyclotron frequency $\omega_{ci} = eB/m_i c$. This result is obtainable directly by taking the curl of the canonical momentum $(\underline{p} + e\underline{A}/c)$, which is conserved in the absence of dissipation.

If we allow for the small difference in electron pressure and fluid pressure:

$$p = \frac{Z+1}{Z}\,p_e$$

then

$$\underline{B} = -\frac{c}{e}\,\frac{m_i}{Z+1}\,\xi \qquad (3)$$

The importance of the magnetic field in being able to influence the Rayleigh Taylor growth rate through the j x B force can be obtained by comparing the energy in the magnetic field $B^2/8\pi$ with the energy density in the fluid vorticity $\frac{1}{2}\rho v^2$, where $\xi = k \times v$, k is the Rayleigh Taylor wavenumber and v is the perturbation in the fluid velocity (the basic plasma expansion is irrotational).

$$\frac{U_B}{U_\xi} = \frac{(c^2 m_i)k^2}{\omega_p^2 m_e}\,\frac{Z}{(Z+1)^2}$$

c/ω_p is the electron collisionless skin depth, so we see that the fluid and magnetic energies are about equal if the Rayleigh Taylor wavelength λ is of the order of the ion collisionless skin depth. If the ablation surface has a density of $10^{23}\,cm^{-3}$ and $(Z+1)/Z = 1$ then the two energies are equal if $\lambda = 5.5\,Z^{-\frac{1}{2}}\,\mu m$.

It must be remembered that this analysis is an upper limit on B and the magnetic diffusion will reduce B in real plasma. It is still possible to say that if the Rayleigh Taylor wavelength is greater than the above value then the magnetic energy is insufficient to affect the linear Rayleigh Taylor growth. Investigation of the effects of magnetic field on the Rayleigh Taylor growth rate using expensive computational methods should therefore concentrate on wavelengths of a few microns or less. Even though the resistive diffusion reduces the magnitude of the magnetic field, it may influence the Rayleigh Taylor growth by transferring energy from the field maxima (where the vorticity is greatest) to the field nulls (where reconnection is greatest).

In the non-linear regime when the amplitude of the Rayleigh Taylor "spikes" becomes large the $\omega\tau$ reduction in heat flow may significantly affect the hydrodynamics by leading to differential ablation, or the magnetic pressure $B^2/8\pi$ may become comparable to the fluid pressure. The conventional idea of "saturation" of the Rayleigh Taylor modes is

that the amplitude A grows as $A = A_o \exp(\gamma t)$, with $\gamma^2 = kg$. When the acceleration A exceeds the gravity g the spikes are in "free fall" and no longer grow exponentially ie saturation occurs for

$$\gamma^2 A = g \text{ or } kA = 1$$

Since the vorticity $\xi = k \times v$, then when $kA=1$, $\xi_{max} = \gamma$, and the saturated value of the vorticity is numerically equal to the growth rate.

In order to calculate the effects reduced heat flow due to the finite Hall parameter $\omega\tau$ it is necessary to include the resitivity in order to be consistent. The evolution of magnetic field is taken to be:

$$\frac{\partial B}{\partial t} + \frac{k^2 c^2}{4\pi\sigma} B = \frac{c}{e}\,\frac{m_i}{(Z+1)}\,\frac{\partial \xi}{\partial t} \qquad (4)$$

then

$$B_{max} = \frac{\gamma}{\gamma + \frac{k^2 c^2}{4\pi\sigma}}\,\frac{c}{e}\,\frac{m}{(Z+1)}\,\gamma \qquad (5)$$

If the magnetic diffusion is moderately strong ie

$k^2 c^2/4\pi\sigma \gg \gamma = (kg)^{\frac{1}{2}}$, and we write

$$\sigma = \frac{n_e e^2}{m_e \nu_{ei}} \qquad \omega = \frac{eB}{m_e c}$$

then

$$(\omega\tau)_{max} = \frac{g}{k}\tau_{ei}^2\frac{m_i}{m_e}\frac{1}{Z+1}\frac{\omega_p^2}{c^2} \qquad (6)$$

Since τ_{ei} is not constant in the ablation flow it is difficult to make use of this relation. As an order of magnitude take T_e=50eV, $n_e=10^{22}cm^{-3}$ and $g=10^{16}cms^{-2}$. Then $\omega\tau_{max} \simeq 6\lambda$ where λ is the Rayleigh Taylor wavelength in cm. Since wavelengths in the range 5μm - 100μm are expected the Hall parameter ωτ remains small near the ablation surface but may become significant close to the critical density where the temperatures are much higher, but the density and temperature gradients are weaker. The non-linear evolution of vorticity in this region together with Weibel instabilities and Nernst convection due to the large heat flow (A5.31, A5.32) is not amenable to this simple model and needs study using computer modelling. The cases of Rayleigh Taylor instability driven by non-uniform illumination or by target non-uniformity may well behave differently since in the former case there is a source of vorticity in the low density high temperature plasma.

A5.2.8 Inertial and Nernst effects in Ohm's law

M G Haines (Imperial College)

There is currently much interest in the convection and amplification of magnetic fields in laser-produced plasma. Nishiguchi et al (A5.32) have shown, using the linear transport theory of Braginskii (A5.33), that the Nernst effect (the current flow driven perpendicular to a temperature gradient and a magnetic field) can cause the convection of magnetic field. This effect arises only because of the velocity dependence of the collision frequency, as does also the thermoelectric term. The velocity of convection of magnetic field described by the Nernst effect is

$$\underline{V}_T = -\frac{\tau_e}{m_e\Delta}(\beta_1''\chi^2 + \beta_0'')\nabla T_e \simeq \frac{q_e}{3/2 n_e T_e} \qquad (1)$$

where $\chi=\omega_e\tau_e$ the Hall parameter; and β_1'' β_0'' and Δ are defined in Braginskii (A5.33), where ω_e is the electron cyclotron frequency and $\tau_e=\nu^{-1}$ is the electron-ion collision time. The physics behind the Nernst convection is that the magnetic field tends to be frozen more to the hotter electrons that are responsible for the heat flux than to the colder and more collisional electrons through which the magnetic field can more easily diffuse. In laser fusion the heat flux from the critical surface to the ablation surface must be larger than the outward enthalpy flow $\frac{5}{2}n_e kT_e\underline{v}$ associated with the centre-of-mass ablation velocity $\underline{v}$, and therefore any transverse magnetic field will be convected inwards. Furthermore, because the density increases between the critical and ablation surfaces by several orders of magnitude in the case of 1.06μm laser irradiation, there is a resulting large negative value of $\nabla.\underline{V}_T$ and hence an amplification of the magnetic field by flux compression.

Recently Kho and Haines (A5.13) have verified that this phenomenon occurs even under non-linear heat flow conditions when the lowest order isotropic component of the electron disribution departs markedly from a Maxwellian.

That this is not unexpected can be analytically shown from an artificial model of a plasma with a collision frequency ν that is proportional to v^{-2} instead of v^{-3}.

In carrying out this theory it is possible to extend the model further to include electron inertial terms. These are also of current interest in modelling the dynamics of magnetic fields in laser fusion. In a collisionless particle-in-cell code, VENUS, Forslund and Brackbill (A5.34) predict that a self-generated magnetic field just outside the critical surface of an irradiated target rapidly propagates with hot electrons in a transverse direction along the surface of target, and in a layer of thickness a few c/ω_{pe} where c/ω_{pe} is the collisionless skin

depth. Amiranoff et al (A5.35) have aproximately reproduced this effect in a fluid code by including inertial terms in Ohm's law.

Employing the Cartesian tensor expansion of the electron distribution function, f,

$$f = f_0 + \frac{\underline{f}_1 \cdot \underline{v}}{v} + \frac{\underline{\underline{f}}_2 : \underline{vv}}{v^2} + \ldots\ldots \qquad (2)$$

derived by Shkarofsky et al (A5.36), the component of the Fokker-Planck equation describing the evolution of $\underline{f}_1$ for a Lorentz gas in the ion rest frame is

$$\frac{\partial \underline{f}_1}{\partial t} + v\nabla f_0 - \frac{eE}{m_e} \partial_v f_0 - \frac{e}{m_e c} \underline{B} \times \underline{f}_1 = -\nu \underline{f}_1 \qquad (3)$$

where terms in $\underline{\underline{f}}_2$ are ignored. If $\partial \underline{f}_1/\partial t$ is ignored and ν is set equal to $\nu_T v_T^3/v^3$ the transport coefficients of Braginskii, and the corrections recently found by Epperlein and Haines (A5.31), can be found. The main features and trends of having a velocity dependent collision frequency can be derived analytically in a simple, exact expression by artificially writing instead that ν is $\nu_T v_T/v^2$ where $v_T=(2T_e/m_e)^{\frac{1}{2}}$ the thermal speed and ν_T is some main collision frequency. The terms that result from ν being velocity dependent will be slightly larger in magnitude for a real plasma with $\nu \propto v^{-3}$ if f_o is Maxwellian. One merit of this model is that Ohm's law can be derived without any assumptions on f_o, and hence is likely to be valid under extreme conditions of non-linear heat flow or of large inverse bremsstrahlung absorption where Langdon (1980) has shown a $\exp(-v^5/v_T^5)$ velocity dependence of f_o.

Employing the definitions

$$\underline{j} = -\frac{4\pi}{3} e \int_o^\infty dv\, v^3 \underline{f}_1$$

$$\underline{q}_T = \frac{2\pi}{3} m_e \int_o^\infty dv\, v^5 \underline{f}_1 \qquad (5)$$

eq (3) can be multiplied by $\frac{4\pi}{3} v^5$ and integrated $\int_o^\infty dv$ to give

$$\frac{2}{m_e}\frac{\partial \underline{q}_T}{\partial t} + \frac{4\pi}{3}\nabla\int_o^\infty f_o v^6 dv + \frac{20\pi}{3}\frac{e}{m_e}\underline{E}\int_o^\infty f_o v^4 dv + \frac{2e}{m_e^2 c}\underline{q}_T \times \underline{B} = \frac{\nu_T v_T^2}{e}\underline{j} \qquad (6)$$

This is a more general form of Ohm's law, valid for arbitrary f_o. It can be seen that the inertial term involves the total energy flux $\underline{q}_T$ and the effect of magnetic field is through $\underline{q}_T \times \underline{B}$. That this occurs because of the velocity dependence of the collision frequency can be shown by having $\nu=\nu_T$, a constant, instead. Then the moment that yields

$\underline{j}$ is $\int_o^\infty dv \frac{4\pi}{3} v^3 \times$ eq (3), giving

$$-\frac{1}{e}\frac{\partial \underline{j}}{\partial t} + \frac{4\pi}{3}\nabla\int_o^\infty f_o v^4 dv + 4\pi \frac{e}{m_e}\underline{E}\int_o^\infty f_o v^2 dv - \frac{1}{m_e c}\underline{j} \times \underline{B} = \frac{\nu_T \underline{j}}{e}$$

The even moments of f_o can be defined as

$$n_e = 4\pi \int_o^\infty f_o v^2 dv \tag{8}$$

$$\frac{p_e}{m_e} = \frac{1}{2} n_e v_T^2 = \frac{4\pi}{3} \int_o^\infty f_o v^4 dv \tag{9}$$

$$\frac{R}{m_e} = \frac{4\pi}{15} \int_o^\infty f_o v^6 dv \tag{10}$$

so that eq(7) becomes, again in the ion rest frame

$$-\frac{m_e}{ne^2} \frac{\partial \underline{j}}{\partial t} + \frac{1}{n_e} \nabla p_e + \underline{E} - \frac{\underline{j} \times \underline{B}}{n_e e c} = \frac{\underline{j}}{\sigma} \tag{11}$$

where $\sigma = m_e \nu_T/(n_e e^2)$. In contrast eq (6) becomes

$$\frac{2m_e}{5ep_e} \frac{\partial \underline{q}_T}{\partial t} + \frac{m_e}{ep_e} \nabla R + \underline{E} + \frac{2}{5} \frac{\underline{q}_T \times \underline{B}}{p_e c} = \frac{2\nu_T m_e}{5e^2 n_e} \underline{j} \tag{12}$$

Before comparing these results it is clearer if the electron heat flux $\underline{q}_e$, measured in the electron centre-of-mass frame, is employed, ie

$$\underline{q}_e = \underline{q}_T - \frac{5}{4} \frac{m_e v_T^2}{e} \underline{j}$$

where terms in the traceless stress tensor and in j^3 are neglected.

Furthermore if f_o is a Maxwellian the moment R can be expressed as

$$R = p_e^2/(nm_e) \tag{14}$$

Then eq (12) becomes

$$\frac{2m_e}{5ep_e} \frac{\partial \underline{q}_e}{\partial t} - \frac{m_e}{n_e e^2 T_e} \frac{\partial}{\partial t} (T_e \underline{j}) + \frac{\nabla p_e}{n_e} + \frac{\nabla T_e}{e}$$

$$+ \underline{E} - \frac{\underline{j} \times \underline{B}}{n_e e c} + \frac{2\underline{q}_e \times \underline{B}}{5p_e c} = \frac{\underline{j}}{\sigma^1} \tag{15}$$

where σ^1 is $\frac{5}{2}\sigma$.

The effects of including a velocity dependent collision frequency are many: (a) An inertial term in $\partial \underline{q}_e/\partial t$ now appears in eq (15) and the term in $\partial \underline{j}/\partial t$ of eq (11) now is of the form $\partial(T_e \underline{j})/\partial t$: (b) The thermoelectric term, absent in eq (11) is the fourth term in eq (15); and (c) the effect of the Nernst term, which in Braginskii's notation would be $\beta(\underline{b} \times \nabla T_e)/e$ where $\underline{b}$ is the unit vector in the direction of the magnetic field, is shown to describe the advection of magnetic field by a velocity $\underline{V}_T$, as described in eq (1). For a real plasma with $\nu \propto v^{-3}$ this term is a little larger than that given in eq (15). An artificial collision frequency ν proportional to v^{-2} rather than v^{-3} displays in simple closed form the important features of having a velocity dependent collision frequency, principally the occurrence of the thermoelectric effect and the Nernst effect. From eq (12) the magnitude of these terms can be determined also for a non-Maxwellian distribution function as occurs in non-linear heat flow in laser fusion. The Nernst term is also of relevance to magnetic confinement where convection of magnetic perturbations associated with MHD instabilities and magnetic islands will have an additional velocity of convection in, say, the poloidal plane of a tokamak, through the large Righi-Leduc heat flow in the plane of the magnetic surfaces. Finally

the electron inertial terms in Ohm's law now have a $\partial \underline{q}_e / \partial t$ term which might be important during the transient surface propogation of magnetic field and heat flux in long wavelength laser experiments, though it must be remembered that in the ordering, the collisional frequency is assumed to be greater than $\partial/\partial t$.

A5.3 ATOMIC PHYSICS

A5.3.1 The effect of orbital relaxation on transition energies in radiative opacity calculations

S J Rose (RAL)

The calculation of plasma photoabsorption was first of interest in astrophysical studies, particularly in the calculation of stellar structure. In the last few years the opacity of laboratory (particularly laser-produced) plasmas has been of interest. Because of the lack of experimental opacity data (except for cold material), calculated values have to be relied upon. Several excellent papers have appeared in the literature which have reviewed the subject (A5.33-A5.37).

Although some workers (A5.37) use experimental data and data obtained from accurate calculations, many opacity calculations employ a single set of one-electron orbitals for a particular temperature and density which are obtained by solution of the one-electron wave equation in an average-atom potential. However, because each orbital is associated with a single energy, this one-electron picture predicts only one energy for each one-electron transition. In reality, transitions occur between different energy levels of the ions in the plasma and in general many transitions, each occurring at a different energy, involve the same one-electron transition. Average-atom opacity calculations have to be corrected for this. It is possible to consider the transitions occurring between configurations or at a more detailed level, between terms resulting from the configurations. As was first pointed out by Mayer, (A5.38) this splitting of the one-electron transition energy is particularly important for calculation of the Rosseland mean opacity which is very sensitive to windows in the absorption spectrum. The contribution to the Rosseland opacity from a single line below an absorption edge can be considerably different from that of a number of different lines, slightly different from one another in energy, absorbing in roughly the same part of the spectrum. The same effect occurs for absorption edges; instead of one edge for each one-electron energy level, a number of edges slightly different in

energy are found. In order to calculate the contribution to the opacity of the transition between one configuration and another, it is necessary to know both the transition energy and also the probability of the initial configuration occurring in the plasma.

We denote the transition energy involving the one-electron excitation from orbital i to f as $\Delta E^{ex}(i,f)$ and the ionization energy of an electron in orbital i as $\Delta E^{ion}(i)$. If the initial and final configurations are constructed from the same set of orbitals, the excitation and ionization energies are given by

$$\Delta E^{ex}(i,f)=I(f)-I(i)+\sum'_{k(n_k>1)}(n_k-\delta_{ki})\{H(f,k)-H(i,k)\}, \qquad (1)$$

$$\Delta E^{ion}(i)=-I(i)-\sum'_{k(n_k>1)}(n_k-\delta_{ki})H(i,k); \qquad (2)$$

I(a) is the expectation value of the one-electron operator and H(a,b) is the average-of-configuration interaction energy between an electron in shell a and one in b. In average-atom opacity calculations, for a particular temperature and density, a single set of average-atom orbitals is used to evaluate the transition energies $\Delta E^{ex}(i,f)$ and $\Delta E^{ion}(i)$ for each of the different initial configurations occurring in the plasma using Eqs (1) and (2). It is the purpose of this paper to examine, for a specific case, the effects of orbital relaxation which are neglected in average-atom calculations.

There has recently been much experimental interest in photoabsorption spectroscopy of chlorine ions in laser-produced plasmas (A5.39,A5.40). We have therefore considered the examples of 1s-2p and 1s-3p excitation and 1s ionization in chlorine ions with configurations $1s^2 2s^2 2p^n$ (n=0-6) and $1s^2 2s^2 2p^6 3s^2 3p^n$ (n=0-5). Firstly, $\Delta E^{ex}(1s,2p)$, $\Delta E^{ex}(1s,3p)$ and $\Delta E^{ion}(1s)$ are calculated as the difference in energy between average-of-configuration isolated-ion self-consistent-field calculations‡, separately optimised for each initial and each final state (method 1). [‡Although non-relativisitc notation is used throughout, values shown come from relativistic calculations (A5.42) on which an appropriate average has been performed]. This is the most

accurate method of calculations reported here and has been shown to give transition energies within a few eV of experiment (A5.41). For comparison, the excitation and ionization energies from a configuration with n_k electrons in orbital k are calculated (method 2) from Eqs (1) and (2), with the I and H integrals for each transition evaluated from orbitals obtained from average-of-configuration isolated-ion self-consistent-field calculations‡ for the initial configuration involved in the transition. Lastly (method 3) $\Delta E^{ex}(1s,2p)$, $\Delta E^{ex}(1s,3p)$ and $\Delta E^{ion}(1s)$ are calculated from Eqs (1) and (2) for different n_k using a single set of I and H integrals evaluated from orbitals obtained from an average-of-configuration isolated-ion self-consistent-field calculation for a particular initial configuration. Because there are several possible different initial configurations, method 3, unlike methods 1 and 2, allows several different calculations of excitation and ionization energies. An average-atom opacity calculation uses the same procedure as method 3 to calculate the different transition energies except that in an average-atom calculation the orbitals are optimised on some (in general) non-integral ionization stage and the effects of plasma density are included in the calculation. $\Delta E^{ex}(1s,2p)$ and $\Delta E^{ion}(1s)$ calculated by these three methods for initial configurations $1s^2 2s^2 2p^n$ (n=0-6) are shown in Figs (A5.14) and (A5.15). Figs (A5.16) and (A5.17) show $\Delta E^{ex}(1s,3p)$ and $\Delta E^{ion}(1s)$ for initial configurations $1s^2 2s^2 2p^6 3s^2 3p^n$ (n=0-5). There are significant differences between the two methods, which have implications for an average-atom opacity calculation of a chlorine plasma. Comparison of the results of methods 1 and 2 shows that the effect of relaxation caused by removal of the K-shell electron causes an overestimate of the transition energy (in the worst case by 30eV). Secondly, method 3 shows a much larger change in the transition energy with unit change in the ionization stage than is found from methods 1 and 2 (which show approximately the same change). This result suggests that in an average-atom opacity calculation the effect of orbital relaxation between one ionization stage and another is to overestimate (in the worst case of 1s-3p excitation by a factor of three) the distribution of transition energies. Also, comparison of Figs (A5.14) and (A5.16) and of Figs (A5.15) and (A5.17) shows that although the effects of orbital relaxation are not negligible for

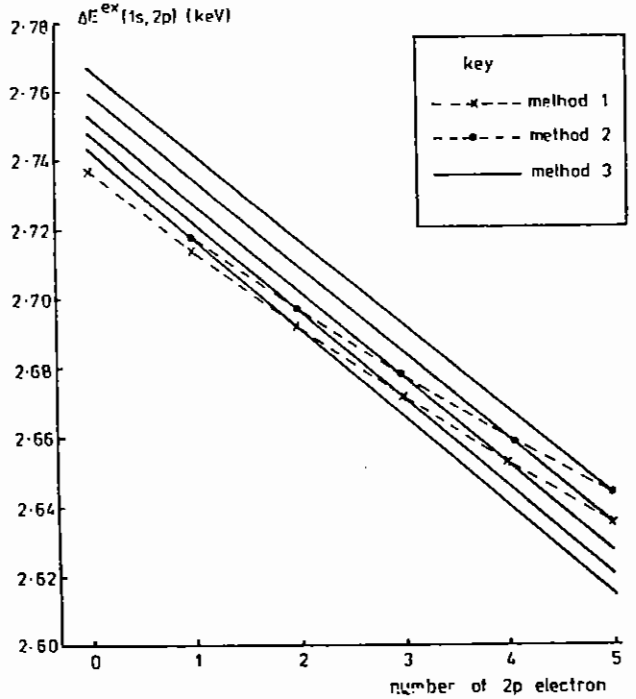

Fig A5.14 Chlorine 1s-2p excitation energies for initial configurations $1s^2 2s^2 2p^n$ (n = 0-5).

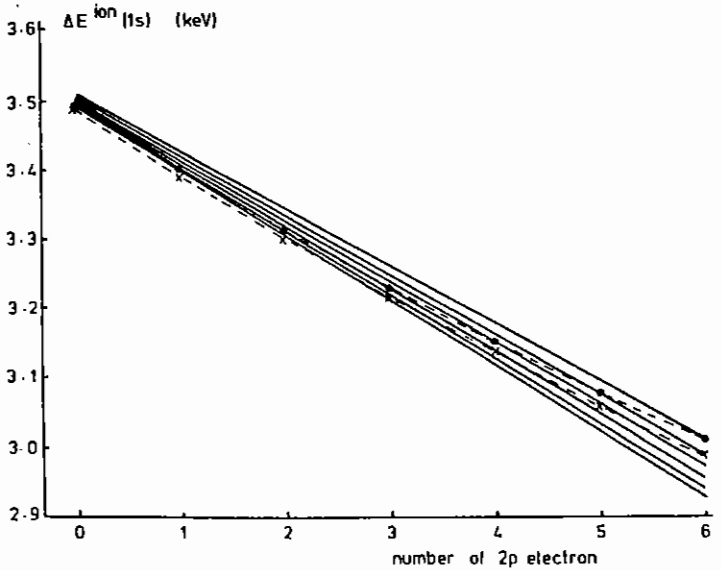

Fig A5.15 Chlorine 1s ionisation energies for initial configurations $1s^2 2s^2 2p^n$ (n = 0-5) (key as in Fig A5.14).

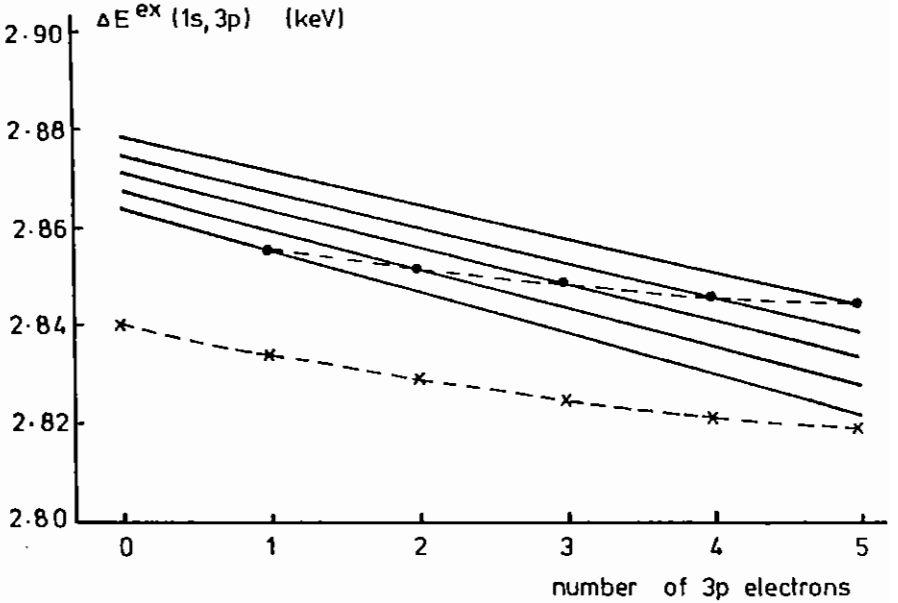

Fig A5.16 Chlorine 1s-3p excitation energies for initial configurations $1s^2 2s^2 2p^6 3s^2 3p^n$ (n = 0-5) (key as in Fig A5.14).

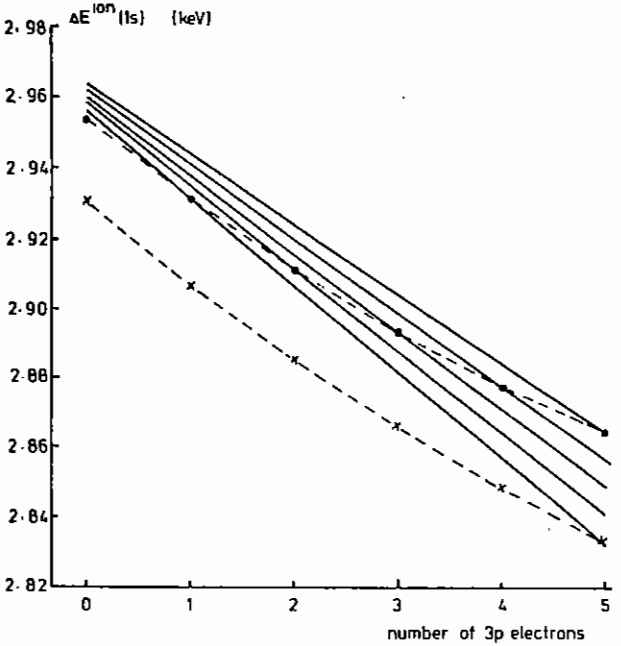

Fig A5.17 Chlorine 1s ionisation energies for initial configurations $1s^2 2s^2 2p^6 3s^2 3p^n$ (n = 0-5) (key as in Fig A5.14).

transitions involving the more highly-ionised open L-shell, the effects are very significant for transitions involving the open M-shell.

We have shown here that the neglect of orbital relaxation in average-atom opacity calculations introduces two categories of errors in the calculation of transition energies. The first results from the difference in the orbitals between the initial and final states of the transition and the second results from the differences in the orbitals between the different ionization states present in the plasma. Instead of performing many separately optimised ionic structure calculations, the computationally less expensive procedure of Liberman and Albritton (A5.43), which has already been used to predict emission spectra, may be the most appropriate method of overcoming the problem of orbital relaxation in average-atom opacity calculations. In addition to affecting transition energies, orbital relaxation will also affect transition oscillator strengths although we do not present calculations of this effect.

It should also be noted that the calculations reported here do not include term-splitting and that the construction of terms from a single set of orbitals neglects the effect of orbital relaxation between one term and another.

A5.3.2 Modelling of gain in the Carbon Fibre XUV laser

M H Key (RAL, G J Pert (Hull)

The production of population inversion and gain on the n = 3 to 2 transition of hydrogenic C^{5+} ions, during adiabatic cooling and recombination of a plasma of C^{6+} ions and electrons, has been extensively modelled for self similar expansion of a plasma cylinder of gaussian density profile and uniform temperature (A5.44) as illustrated in figure (A5.18).

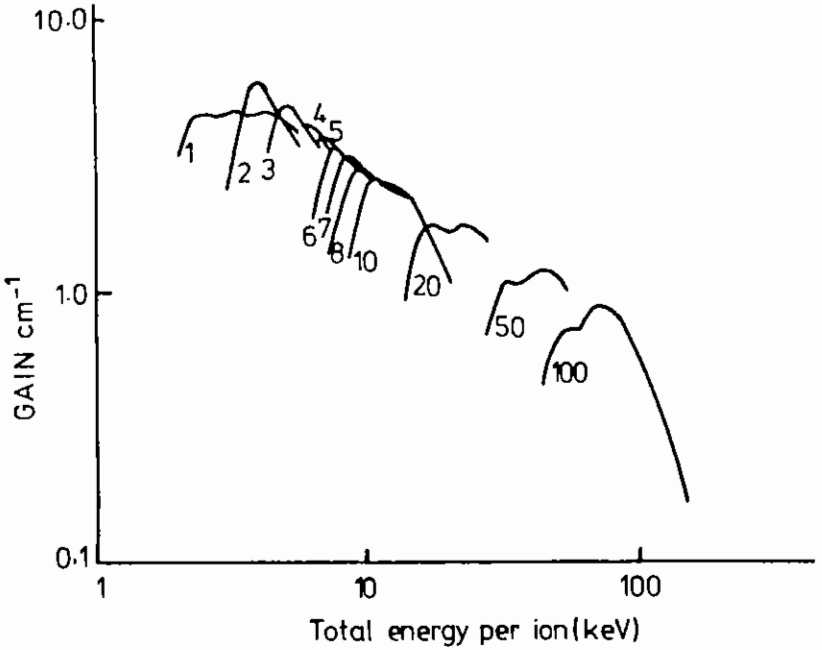

Fig A5.18 Computed variation of gain with initial plasma energy for plasmas expanding from 30 μm initial radius with variable initial density of ions (labelled in units of 10^{19} cm^{-3}) After Ref (A5.54).

Maximum gain is produced when the initial temperature has its lowest value consistent with limiting the build up of ground state C^{5+} population to a level below that which quenches inversion through trapping of n = 2 to 1 radiation and enhancement of n = 2 population. This requirement must be satisfied at the stage where expansion and cooling have moved the collisional (LTE) limit above the n = 3 level allowing 3 to 2 inversion. The smaller the mass of plasma the more rapid the expansion, allowing lower initial temperature and greater n = 3 population density at the LTE limit as indicated by Saha's equation

$$n(3) = 3^2\left[\frac{h^2}{2\pi mkT}\right]^{3/2} \frac{n_e^2}{z} \exp\,(I(3)/kT) \qquad (1)$$

where I(3) is the ionisation potential and n(3) the population density of the n=3 state.

These qualitative statements can be represented quantitatively by an analytic fit to the numerically computed data illustrated in fig (A5.18). The optimum energy density ε is seen to vary with initial radius R and ion density N in the form $\varepsilon \sim (NR)^{3/4}$. The mass per unit length M scales as NR^2 and the expansion time τ_e as R/V_t, where $V_t \sim \varepsilon^{1/2}$ is the thermal velocity. Hence $\varepsilon \sim M^{6/17} \tau^{-6/11}$. Finally, introducing a constant of proportionality from numerical simulations in which τ is the duration of the heating pulse, we can specify the optimum absorbed energy per unit length (A5.45 and A5.46).

$$E = 1.7 \times 10^6\, M^{17/11}\, \tau^{-6/11} \qquad J\ cm^{-1} \qquad (2)$$

The gain depends on the mass and the optimum gain scales over a limited range as $G \sim M^{-17/22}\, \tau^{-8/11}$. On our earlier experimental work we have used this computed optimum energy content Equation (2) and compared it with the computed mass and energy content of plasma produced by laser heating and ablation from a carbon fibre. The latter has involved a complex 1D hydro code representation of this problem (A5.47) and gives results not only for the global plasma mass and energy content but also for the radial variation of plasma parameters as illustrated in fig (A5.19). Optimised conditions were found empirically when the ablated plasma mass and energy matched the requirement for maximum gain as illustrated in figure (A5.20).

This optimisation is only approximate since the actual temperature and density profile is somewhat different from that in the simple self similar model. Moreover the empirical finding of optimised conditions is unhelpful in assessing the importance of experimental variables.

A more helpful approach is to determine the global characteristics

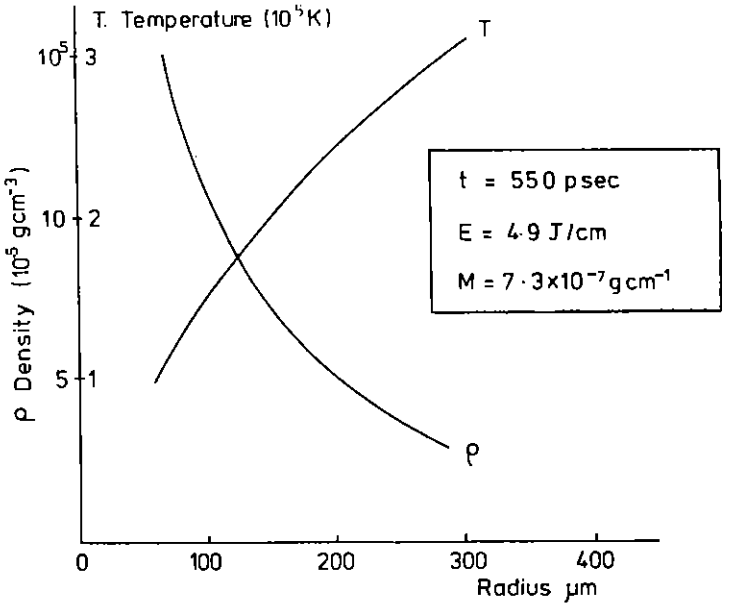

Fig A5.19 Computed radial variation of electron density and temperature at the time of peak amplification for a typical laser irradiated fibre (Hydro-code data G J Pert).

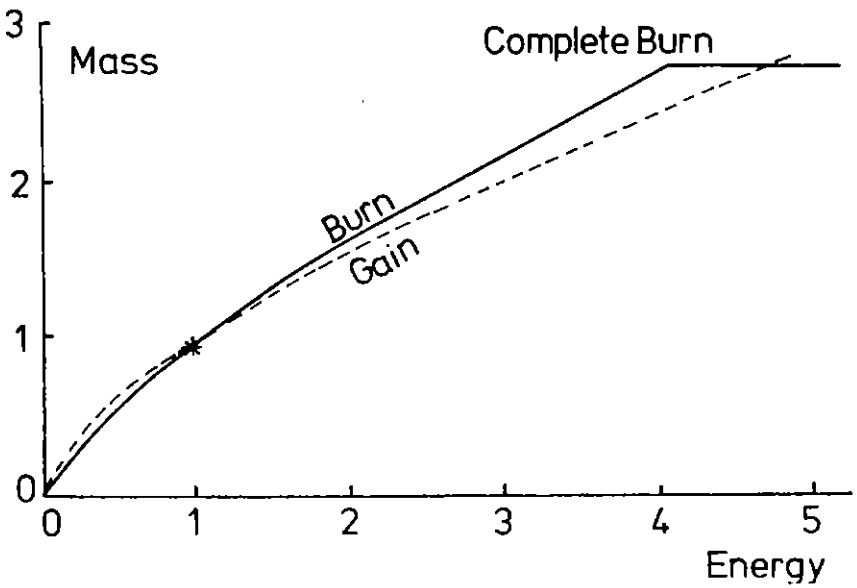

Fig A5.20 Schematic variation of plasma mass with laser energy for irradiated fibres (burn) and optimum mass energy relationship for gain.

(mass and energy content) of the ablated plasma from an analytic model.

Many such models have been developed to treat ablation with different assumptions and regimes of validity (A5.48). A new model of particular relevance to the present problem has recently been developed and is valid for non steady state ablation (appropriate for short pulses) and absorption dominated by inverse Bremsstrahlang (appropriate for low intensities) (A5.48).

This model gives the result:

$$M = 2\times10^{-3}\,\alpha^{-1/3}\,Z^{-1}\,A^{7/8}\,\lambda^{-4/9}\,(\ln\Lambda)^{-2/9}\,r^{2/9}\,E^{5/9}\,\tau^{4/9} \quad \text{gm cm}^{-1} \qquad (3)$$

relating the ablated mass per unit length M to the absorbed energy per unit length E, pulse duration τ, laser wavelength λ, atomic mass A and number Z, fibre radius r and Coulomb logarithim $\ln\Lambda$.

Good agreement in the relevant parameter range is obtained between equation 3 and the results of 1D hydro simulation as illustrated in fig (A5.21), which also shows the optimum E and M for maximum gain from equation (2) and from numerical simulation with the self similar model. The latter two approaches are also in good agreement.

The best matching of ablation and gain requirement occurs at the intersection of the 'burn' and 'gain' characteristics in fig A5.21. For a 5μm fibre and 200 psec laser pulse at λ = 0.53 μm the optimum absorbed energy is approx 5J cm^{-1} giving a gain coefficient of 8 cm^{-1}. Variation of E causes a relatively slow departure from optimised behaviour because increased energy per unit length ablates more mass and more mass requires more energy for optimum gain. A factor of 2 change in E reduces G by about a factor of 2.

The intersection of the 'burn' and 'gain' characteristics can be represented analytically given equations (2) and (3) and we can derive the scaling relationships: for λ = 0.53 μm and carbon fibres,

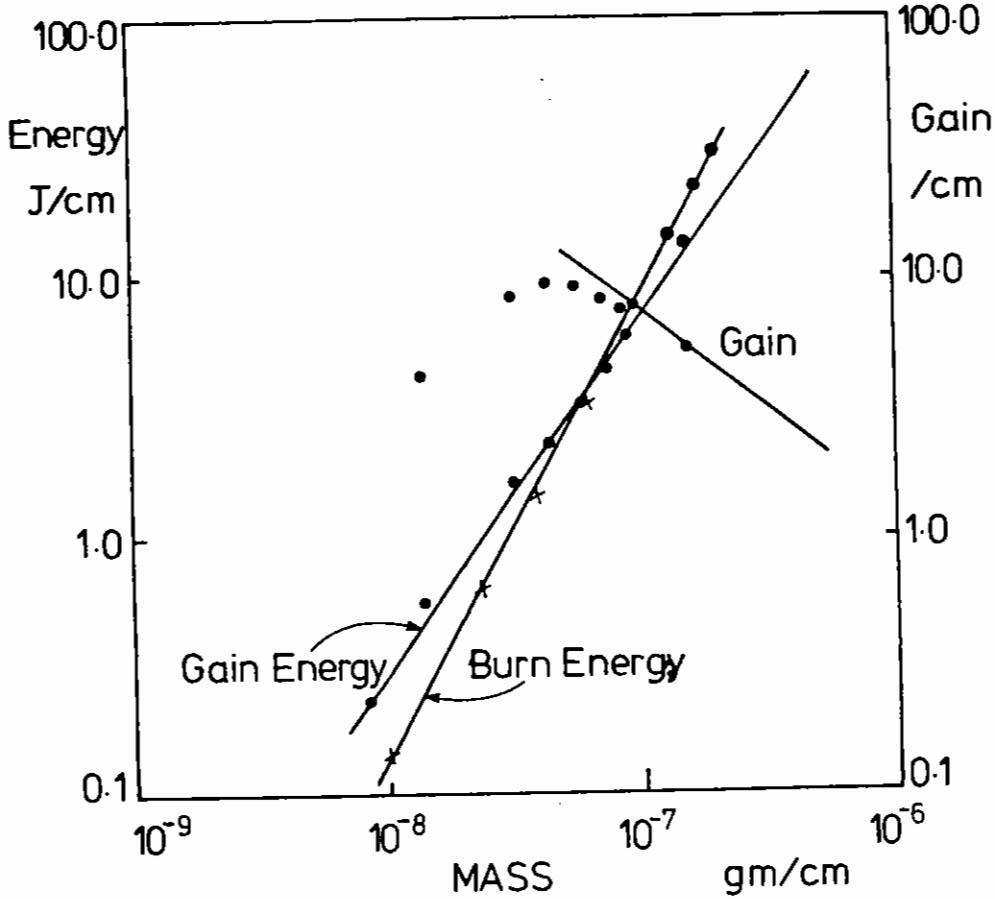

Fig A5.21 Comparison of numerically computed (points) and analytically modelled (lines) plasma formation for 5 μm diameter fibres irradiated with 200 psec pulses at λ = 0.53 μm. Peak gain occurs at the intersection of the burn/gain characteristics.

$$E/1Jcm^{-1} = 1.1 \times 10^{-1}(r/1\ \mu m)^{2.4}(\tau/100\ psec) \quad (4)$$

or

$$M/1gcm^{-1} = 5.3 \times 10^{-9}\ (r/1\ \mu m)^{1.6}(\tau/100\ psec) \quad (5)$$

for the optimum energy per unit length E and the corresponding mass per unit length M.

On the basis of these relationships it was decided to choose experimental parameters, for the work described in section (A4.5) which presented fewer practical problems but remained optimised. Relative to fig (A5.21), thicker fibres were chosen for better stability in long lengths and better absorption fraction when placed in a 25 μm wide line focus, and the pulse duration was reduced accordingly to keep the plasma mass and gain similar. (Equations 4 and 5). Thus fibres with ϕ = 7μm and pulse length of 70psec were chosen. The analysis also suggested that it would be possible to obtain similar gain values without the experimental complication of a prepulse, so this was dispensed with. Results of experiments using these parameters are broadly in agreement and are presented in section (A4.5).

A limitation of the modelling discussed so far is that it does not treat the radial variation of gain by solving both the atomic rate equations and the full hydrodynamic behaviour simultaneously. This is a difficult problem particularly because of the complexity of treatment needed for radiation trapping effects in the general case. Results of such calculations are valuable and allow estimates of the effect of variation of absorbed energy along the length of an irradiated fibre.

Although the expanding plasma contains a range of temperature and density, fig (A5.19), any given fluid element will experience a broadly similar time history of its thermodynamic state. In consequence we may anticipate that different parts of the plasma may give optimum gain at a given time at different radii. Fortunately at times of peak gain both the density and temperature profiles are relatively flat over an annular region ~ 200 μm wide embracing a cold core ~ 20 μm wide.

However the question of axial uniformity is not fully resolved. Preliminary results confirm that the system is quite tolerant in this respect and can tolerate considerable variation without significant loss of gain, but the analysis of the spatial variation of gain still lacks a proper treatment of the crucial L_α re-absorption problem.

The modelling analysis is ongoing in support of the experimental programme.

A5.3.3 Electric Field Effects in GaAs-GaAlAs Quantum Wells and Superlattices

E J Austin (Oxford) and M Jaros (Newcastle)

A number of novel semiconductor devices (A5.49) based on GaAs-GaAlAs quantum well structures have been proposed. The small size (10-500 Å) of these systems leads to the confined carriers in the wells being subjected to very high electric fields. Previous theoretical work (A5.50,A5.51) has nevertheless used 'weak field' techniques (perturbation and variational methods) to study these structures.

In the present work an exact solution of the Schrodinger equation, valid at arbitary field strengths, is obtained for model quantum well systems.

The model used is the envelope function effective mass approximation, in which the rapidly-varying Bloch component of the wavefunction is factored out and the problem reduces to a one-dimensional Schrodinger equation for the slowly-varying envelope function along the layer growth (x) direction, with the quantum well represented as a finite square well:

$$\frac{-h^2}{2m^*}\frac{d^2\psi}{dx^2} + (V_o - eFx)\,\psi = E\psi \quad x \leq a$$

$$\frac{-h^2}{2m^*}\frac{d^2\psi}{dx^2} - eFx\psi = E\psi \quad x > a \quad (1)$$

Here m^* is the carrier effective mass, V_o is the depth of the potential well, F is the magnitude of the electric field, and the well width is 2a.

The effect of the field is to shift the energy levels of the quantum-confined electrons and holes; at the same time, field-induced tunnelling broadens the zero-field bound states into resonances. The solutions of Equation (1) can be obtained as a linear combination of Airy functions; application of the method of phase shift analysis (A5.52,A5.53) allows the positions and widths of the Stark resonances to be obtained.

In addition, the change in the density of states $\Delta\rho$ can be obtained from the phase shift Θ:

$$\Delta\rho = \frac{2}{\pi} \frac{d\Theta(\varepsilon)}{dE} \qquad (2)$$

$\Delta\rho$ can be related to the spectroscopic lineshape for electron-hole recombination transitions (A5.54).

The Stark shifts obtained from this calculation are found (A5.53) to be in agreement with recent (A5.55) experimental results. We also calculate (A5.53) that carrier tunnelling out of the wells is rapid at high fields; this is in agreement with experimental results (A5.56) on the variation of luminescence lifetime with field. Our calculations also demonstrate the importance of nonperturbative effects. At fields of around $4 \times 10^5 Vcm^{-1}$ (which are readily attainable experimentally), large anomalous Stark shifts, extensive carrier tunnelling and the appearance of confined antiresonance states are predicted. These results have implications for hot electron transport in quantum well devices (A5.57) and are being studied further.

Calculations on double wells (A5.58) have demonstrated field-induced carrier localisation and delocalisation effects. This work is currently being extended to larger multiple quantum well and superlattice structures. Of particular interest here is the effect of

the inevitable deviations from perfect geometry present in real systems. Preliminary calculations suggest that carrier localisation induced by irregularities can be counteracted by the application of an electric field; this phenomenon may have important implications for device efficiency.

A5.3.4 Optical Potential Studies of Resonance Levels and Dissociation Processes

E J Austin (Oxford) and G Jolicard (Besancon)

Resonances play an important role in the discussion of collision phenomena, atomic ionization, and molecular dissociation processes. Numerical calculations of resonance energies and widths depend on differentiating the resonance from non-resonance continuum wavefunctions; many of these methods exploit the quasi-bound (localisation) properties of resonance wavefunctions. In the stabilisation method (A5.59,A5.60) the resonance problem is treated in a bound state formalism; the Hamiltonian is diagonalised in the form of discrete, exponentialy decaying functions. The resonance eigenvalues are characterised by remaining essentially unchanged as the basis size varies. In the complex scaling method (A5.61,A5.62,A5.63) a coordinate rotation allows the resonance wavefunction to be obtained in square integrable form. The optical potential calculation described here is to some extent intermediate between the stabilisation and complex-scaling methods.

We consider the model potential

$$U(r) = \frac{1}{2} r^2 \quad , \quad r \leq 0$$
$$\lambda > 0 \qquad (1)$$
$$= \frac{1}{2} r^2 \exp[-\lambda r^2], \; r > 0$$

and modify this potential by the addition of an imaginary optical potential $-iAr^8$. Since $U(r) \to 0$ as $r \to \infty$ the potential Equation (1) supports no bound states. It is anticipated that the resonance states

should be identifiable by their insensitivity to the value of the parameter A, provided that the optical potential is sufficiently distant from the inner potential region.

The use of the optical potential allows bound state techniques to be used, as in a stabilisation calculation. A matrix diagonalisation in a 40-state harmonic oscillator basis was performed. Due to the presence of the imaginary optical potential, the resonance energy is obtained as a complex number $E_0 - i\Gamma/2$, where Γ is the resonance width. As expected, E_0 and Γ show stability over a range of several orders of magnitude of the optical potential A. The values obtained for E_0 and Γ (A5.64) are in agreement with those obtained by the stabilisation method Equation (1).

The optical potential approach provides a simple direct method of calculating resonance positions and widths for this simple model problem. Further studies are necessary to elucidate the precision which can be expected from calculations of this type.

In addition to the study of scattering resonances, it is anticipated that this technique should be relevant to two other types of problem:
(a) Multiphoton ionisation and dissociation processes can be treated in a time-independent formalism by adopting the Floquet (atom+ field) (A5.65) approach. Addition of an optical potential could be used to indentify ionization and dissociation resonances.
(b) Non-linearly coupled oscillators such as the Henon-Heiles system:

$$V(x,y) = x^2 + y^2 + \lambda\,(xy^2 + x^3) \qquad (2)$$

are being intensively studied (A5.66) both as models for dissociating molecules and as examples of quantum non-linear dynamical systems. The potential Equation (2) supports no bound states, but has a large number of quasi-bound (resonance) states. The energies and widths of these states should be calculable using the method described here.

A5.3.5 Atom Data for modelling of neon-like ion systems which are proposed for a soft X-ray laser

P G Burke, K A Berrington, G P Gupta and A E Kingston
(Queen's University, Belfast)

There is consdierable interest in developing a soft x-ray laser. Most of the proposed schemes have relied on high power visible lasers to provide the high energy density needed to produce population inversion against the short radiative lifetimes. Population inversion has been inferred in many experiments but recent experiments at the Lawrence Livermore National Laboratory showed unambiguous strong amplification. Their experiments involved the production and excitation of neon-like selenium in a laser produced plasma about 1cm long and showed gain length products of around 6 on the $2p^5 3p$ to $2p^5 3s$ transition at about 206Å. Considerable gain has also been observed in the isoelectric transition in yttrium so it is clear that other elements are also of interest in this context.

Fig (A5.22) indicates the main features of the inversion process for Se XXV. The ground $2p^6$ state is connected by strong optically allowed transitions to the $2p^5 3s$ states but the transitions from the $2p^5 3p$ to the ground state are very small. These $2p^5 3p$ states are excited by electron excitation from the ground state and radiate to the $2p^5 3s$ states. The theoretical model suggest that the lines at 183, 209 and 206Å should have approximately the same intensities. However, the experimental observations show that the 183 line is very weak. The most sophisticated models of this system by Barbara Whitten of the Lawrence Livermore Laboratory suggest that the observed and predicted intensities of the 183Å line differ by almost an order of magnitude.

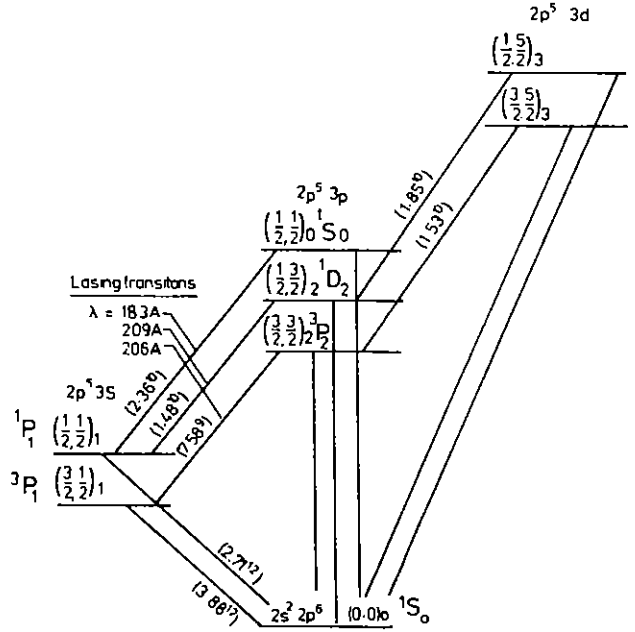

Fig A5.22 Energy levels of Se XXV. The numbers in ( ) are theoretical A values.

It has been suggested that the discrepancy between the observed and theoretical intensities is due to the use of inaccurate atomic data in the modelling. In the Department of Applied Mathematics and Theoretical Physics at Queen's University Belfast we have started a series of calculations on the energy levels, A-values and electron excitation rates of neon-like ions.

Because of the great interest in selenium experiments we have decided to carry out calculations on selenium first. This poses some serious computational problems as to carry out a proper calculation on selenium we should include each of the target states for each J separately. This is a very large calculation and it is indeed one of the largest we have carried out. As an initial calculation we have decided to carry out a calculation in LS coupling which we will transform to give results in JJ coupling.

In this calculation we have used the Hartree Fock 1s2s and 2p orbitals and have used Alan Hibberts's CIV3 code to obtain 3s3p and 3d orbitals. In Table 1 we compare our calculated wavelengths, for some of the important transitions, with the observed wavelengths. There is reasonably good agreement between theory and observations. We also carried out a very large configuration interaction (CI) for these transitions and obtained excellent agreement for two of the transitions

TABLE 1 Calculated wavelengths for Se XXV

Transition	Calculated		Observed
	3s, 3p, 3d	Large CI	Observed
$(2p^5)(3p)\,^1S_o^e - (2p^5)(3s)\,^1P_1^o$	178	181	183
$(2p^5)(3p)\,^1D_2^e - (2p^5)(3s)\,^1P_1^o$	212	210	210
$(2p^5)(3p)\,^3P_1^e - (2p^5)(3s)\,^3P_1^o$	209	206	206

and the difficult 183Å line is only in error by 1%. Using this code we also are able to calculate the Einstein A-values for the transitions in neon-like selenium and in Table 2 we compare present results with results which have been used in the modelling and it is clear that there is reasonably good agreement between the present calculations and the earlier calculations for A-values. The collision calculations are

TABLE 2. Some Calculated A(s^{-1})values for Se XXV

	Present	Earlier Calculations
$(2p^6)^1S_o^e - (2p^5)(3s)^3P_1^o$	3.45 (12)	3.88 (12)
$(2p^6)^1S_o^e - (2p^5)(3s)^1P_1^o$	2.09 (12)	2.71 (12)
$(2p^5)(3s)^3P_1^e - (2p^5)(3p)^1S_o^o$	1.97 (10)	2.05 (10)
$(2p^5)(3s)^1P_1^e - (2p^5)(3p)^1S_o^o$	2.23 (10)	2.36 (10)

now well underway and as we would have expected there is a large amount of resonance structure in the calculated cross section. In Fig (A5.23) we present some initial calculations for transitions from the ground

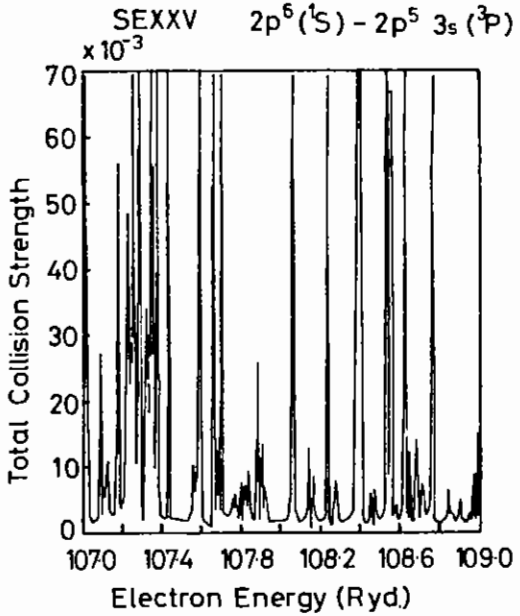

Fig A5.23 Electron excitation collision strength for excitation of the ground state of Se XXV to the first LS excited state.

state in selenium to the first excited state. The very small background of about .002 is in quite good agreement with earlier distorted wave calculations but the large peaks are associated with resonances which are not included in the distorted wave calculations. These results are very preliminary as they are only over a very short energy range and it is difficult to estimate their effect in an integrated Maxwellian rate. Past experience would suggest that this transition the rate could be increased by at least a factor of 2.

A5 References

A5.1 D W Phillion et al, Phys Rev Lett 49, 1405 (1982),
W Seka et al, Phys Fluids 27, 2181 (1984),
R P Drake et al, Phys Rev Lett 53, 1739 (1984).

A5.2 C J Walsh, D M Villeneuve and H A Baldis, Phys Rev Lett 53, 1445, (1984),
H C Barr and G A Gardner, Proc Int Conf on Plasma Phys, Lausanne (ed M Q Tran and M L Sawley) Vol II, 265 (1984).

A5.3 Z Q Lin, O Willi and P T Rumsby, J Phys D 14, L35 (1981),
M J Herbst et al, Phys Rev Lett 46, 328 (1981).

A5.4 R E Turner, D W Phillion, E M Campbell and K G Estabrook, Phys Fluids 26, 579 (1983).

A5.5 P K Kaw, A T Lin and J M Dawson, Phys Fluids 16, 1967 (1973),
D R Nicholson, Phys Fluids, 19, 889 (1976).

A5.6 T Tanikawa, A Y Wong and D L Eggleston, Phys Fluids 27, 1416 (1984).

A5.7 R W Short, R Bingham, E A Williams, Phys Fluids 25, 2302 (1982).

A5.8 Annual Report to the LFC (1983).

A5.9 D A Tidman and R A Shanny, Phys Fluids 17, 1207 (1974).

A5.10 E S Weibel, Phys Rev Lett 2, 83 (1959).

A5.11 E M Epperlein, Report on CECAM Workshop on Heat Flow Instabilities, Orsay, France (1983).

A5.12 E M Epperlein, Plasma Phys and Controlled Fusion 27, 1027 (1985).

A5.13 T H Kho and M G Haines, Phys Rev Lett 55, 825 (1985).

A5.14 T Mochizuki, T Yabe, K Mima, K Yoshikawa, H Azechi, A Kikuchi and C Yamanaka, Jpn J Appl Phys 19, L645 (1980).

A5.15 F F Kamenets, V R Kudashev, V P Lakhin, A B Mikhailovskii and G I Suramlishvili, Sov Phys JETP 59, 62 (1984).

A5.16 J Albritton, Phys Rev Lett 50, 2078 (1983).

A5.17 I P Shkarofsky, T W Johnston and M P Bacynski, The Particle Kinetics of Plasmas (Addison-Wesley, Reading: Mass) (1983).

A5.18 A Ramani and G Laval, Phys Fluids 21, 980 (1978).

A5.19 A R Bell, R G Evans and D J Nicholas, Phys Rev Lett 46, 243 (1980).

A5.20 O Willi, P T Rumsby, O Hooker, A Raven and Z Q Lin, Opt Comm 41, 110 (1982).

A5.21 G Theill and B Meyer, Laser Particle and Beams 3, 51 (1985).

A5.22 W M Manheimer, D G Colombant and J H Gardner, Phys Fluids 25, 1644 (1983).

A5.23 J P Boris and D L Book, J Comp Phys 11, 38 (1973),
S T Zalesak, J Comp Phys 31, 335 (1979).

A5.24 S Jorna and L Wood, Rutherford Appleton Laboratory Central Laser Facility Annual Report (1984).

A5.25 S Jorna and L Wood, CECAM Report on 'Interactions and Transport in Laser-Plasmas', 89-110 (1984).

A5.26 A Hasegawa, M Y Yu, P K Skukla, K H Spatschek, Phys Rev Lett 41, 1656 (1978).
R L McCrory, L Montierth, R L Morse and C P Verdon, Phys Rev Lett 46, 336 (1981).

A5.27 K Mima, T Tajima and J N Leboeuf, Phys Rev Lett 41, 1715 (1978).

A5.28 G J Pert, J Plasma Phys 18, 277 (1977).

A5.29 A J Cole, J D Kilkenny, R G Evans, C J Hooker, P T Rumsby and M H Key, Nature (Phys Sci) 299, 329 (1982).

A5.30 J Grun, M H Emery, S Kacenjar, C B Opal, E A McLean, S P Obenschain, B H Ripin and A Schmitt, Phys Rev Lett 53, 1352 (1984).

A5.31 E M Epperlein and M G Haines (to be published in Phys Fluids) (1986).

A5.32 A Nishiguchi, T Yabe, M G Haines, M Psimopoulos, H Takewaki, Phys Rev Lett 53, 262 (1984).

A5.33 W F Huebner, JQSRT 4, 753 (1964).

A5.34 A Cox, Stars and Stellar Structue, Vol III, ed by L Aller and D McLaughlin, Univ of Chicago Press, Chicago, Ill (1965).

A5.35 T R Carson, D F Mayers and D W N Stibbs, Mon Not R Ast Soc 140, 483 (1968).

A5.36 B F Rozsnyai, JQSRT 27, 211 (1982).

A5.37 W F Huebner, Los Alamos Scientific Laboratory Report, LA-UR-81-2347, Los Alamos, New Mexico (1981).

A5.38 H Mayer, Los Alamos Scientific Laboratory Report, LA-647, Los Alamos, New Mexico (1947).

A5.39 A Auer, R D Cowan, B Yaakobi, O Barnouin and R Epstein, Los Alamos Scientific Laboratory Report, LA-UR-81-2347, Los Alamos, New Mexico (1985).

A5.40 D K Bradley, J D Hares, A Rankin and S J Rose, Rutherford Appleton Laboratory Report, RAL-85-020, Chilton, Didcot, Oxon (1985).

A5.41 N Beatham, I P Grant, B J McKenzie and S J Rose, Physica Scripta 21, 423 (1980).

A5.42 I P Grant, B J McKenzie, P H Norrington, D F Meyers and N C Pyper, Computer Phys Comm 21, 207 (1980).

A5.43 D Liberman and J Albritton, Proc of the 3rd Int Conf on the Radiative Properties of Hot Dense Matter, Williamsburg, Virginia (to be published) (1985).

A5.44 G J Pert, J Phys B 4, 3301 (1976).

A5.45 G J Pert, J Phys B 2, 12, 2067 (1979).

A5.46 G J Pert, Plasma Phys 1, (in press) (1986).

A5.47 G J Pert, Plasma Phys 16, 1051 (1974).

A5.48 M H Key et al, Phys Fluids 26, 2011 (1983).

A5.49 F Capasso, Surf Sci, 142, 513 (1984).

A5.50 G Bastard, E E Mendez, L L Chang and L Esaki, Phys Rev B 28, 3241 (1983).

A5.51 D A B Miller, D S Chemla, T C Damen, A C Gossard, W Weigmann, T H Wood and C A Burras, Phys Rev Lett 53, 2173 (1984).

A5.52 E J Austin and M Jaros, Phys Rev B 31, 5569 (1985).

A5.53 E J Austin and M Jaros, Appl Phys Lett 47, 274 (1985).

A5.54 E J Austin and M Jaros, J Phys C 18, L1091 (1985).

A5.55 C Alibert, S Gaillard, J A Brum, G Bastard P Frijlink and M Erman, Solid State Commun 53, 457 (1985).

A5.56 J A Kash, E E Mendez, L L Chang and L Esaki, Phys Rev B 28, 3241 (1985).

A5.57 M Jaros, E J Austin, D Ninno, M A Gell and K B Wong, Physica B 134, 389 (1985).

A5.58 E J Austin and M Jaros, J Phys C 19, 533 (1986).

A5.59 A U Hazi and H S Taylor, Phys Rev A 1, 1109 (1970).

A5.60 I Eliezer, H S Taylor and J K Williams, J Chem Phys 47, 2165 (1967).

A5.61 J Aguilar and J M Combes, Comm Math Phys 22, 269 (1971).

A5.62 E Baslev and J M Combes, Comm Math Phys 22, 280 (1971).

A5.63 B Simon, Comm Math Phys 27, 1 (1972).

A5.64 G Jolicard and E J Austin, Chem Phys Lett 121, 106 (1985).

A5.65 S-I Chu, Adv Atomic and Molecular Phys 21, 197 (1985).

A5.66 D W Noid, M L Kosykowski and R A Marcus, Ann Rev Phys Chem 32, 267 (1981).

Editors: M Shaw and J Boon

A6 HIGH POWER LASER FACILITY OPERATIONS AND DEVELOPMENT

A6.1 SPRITE

A6.1.1 Sprite Operations

M J Shaw, H T Medhurst, F Kannari and E Hodgson (RAL)

This year has seen the transformation of Sprite from a system largely used for laser R&D to a fully-fledged target-shooting laser with its own dedicated target area. During this reporting period Sprite was operated as an injection-locked unstable resonator providing a single beam of 50ns duration for target irradiation. A total of 696 laser shots were fired, 510 of them were logged as shots on target, the remainder were used for machine testing and diagnostics. Fig A6.1 shows the histogram of laser energy on target. Over three-quarters of the target shots provided more than 80J on target.

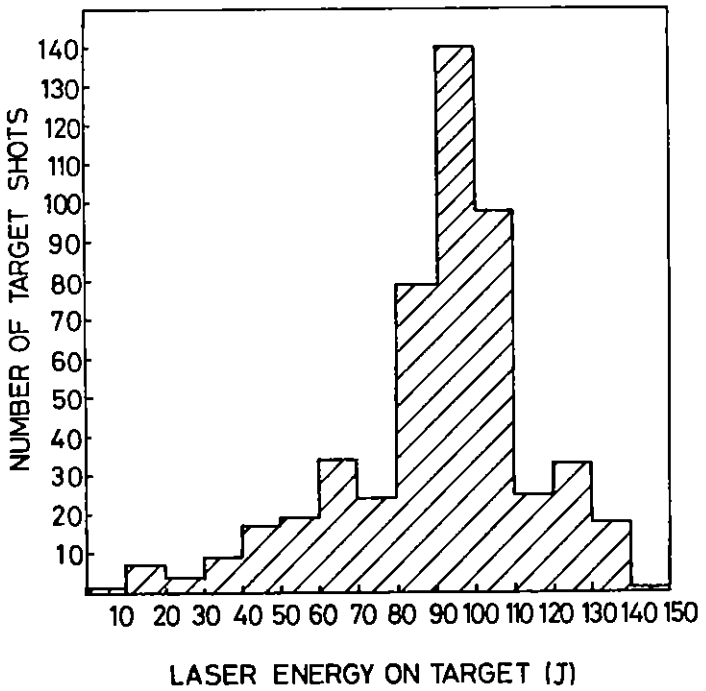

Fig A6.1 Histogram of Sprite target shots as a function of laser energy on target.

During this year there were 78 target shooting days in two periods as shown in Fig A6.2 which gives the histogram of the number of shots per

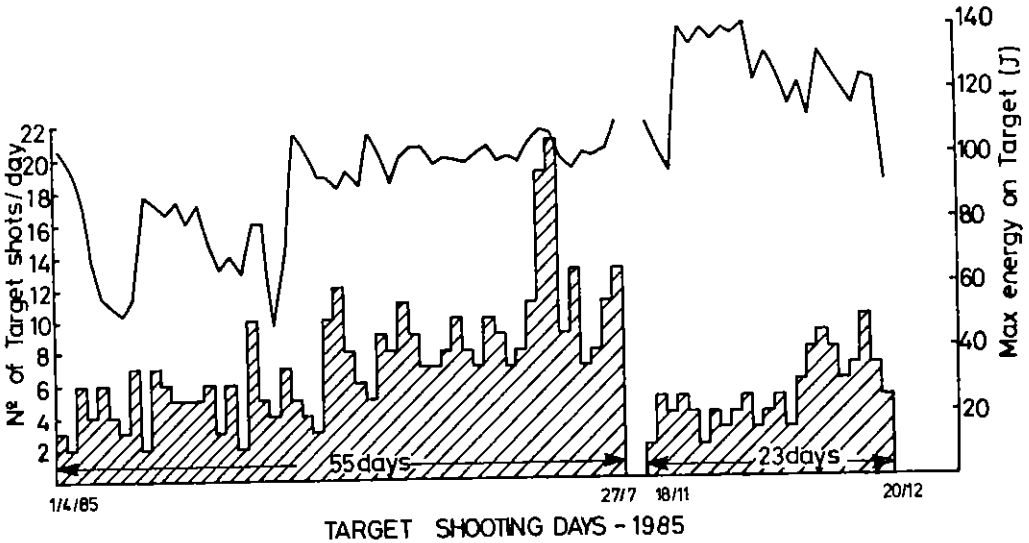

FIg A6.2 Distribution over the year of number of target shots per day (shaded) and maximum laser energy on target.

day together with the maximum energy on target recorded on that day. Since most days called for at least one shot of maximum energy, the latter figure is a good indication of the capability of the laser system. The large improvement in energy in the Autumn was due to the installation of anti-reflection coated windows on the oscillator for the first time and shows the importance of reducing losses and parasitic oscillations in the Sprite cavity. The number of shots per day was mostly limited by turn-around time in the target area. There appears to be no problems in operating the laser with a repetition rate of one shot every 10-15 minutes or so. The laser energy on target was limited by the need to operate the pulsed-power system in a non-self destruct mode which meant that Marx charging voltages of less than 65kV

were used in order to avoid breakdown in the output water lines. At this charging voltage the Marx stores 12.6 kJ thus during the target shooting run in the Autumn the target was being irradiated with better than 1% wall-plug efficiency. With the new output water lines which have since been fitted (see below) operation at up to 75kV should be possible with predicted energies on target being in the region of 175J.

A major new innovation this year has been the installation of a TV frame store system to record both the near and far field laser intensity distribution. This system is described in more detail in section C2.3.

A6.1.2 Sprite Laser Development

M J Shaw, F Kannari, H T Medhurst, D Baker, E Madraszek, J Boon, C Lockett, D Wood and S Hicks (RAL)

This reporting year has seen major improvements to the engineering of the Sprite system both electrically and mechanically and significant progress on the multiplexer system.

The main mechanical work has involved the replacement of the old 4" copper output lines of Sprite with a completely new design of line using 6" dia aluminium tubing and machined aluminium blocks which double as "tee" or elbow sections as shown in Fig A6.3. The new lines

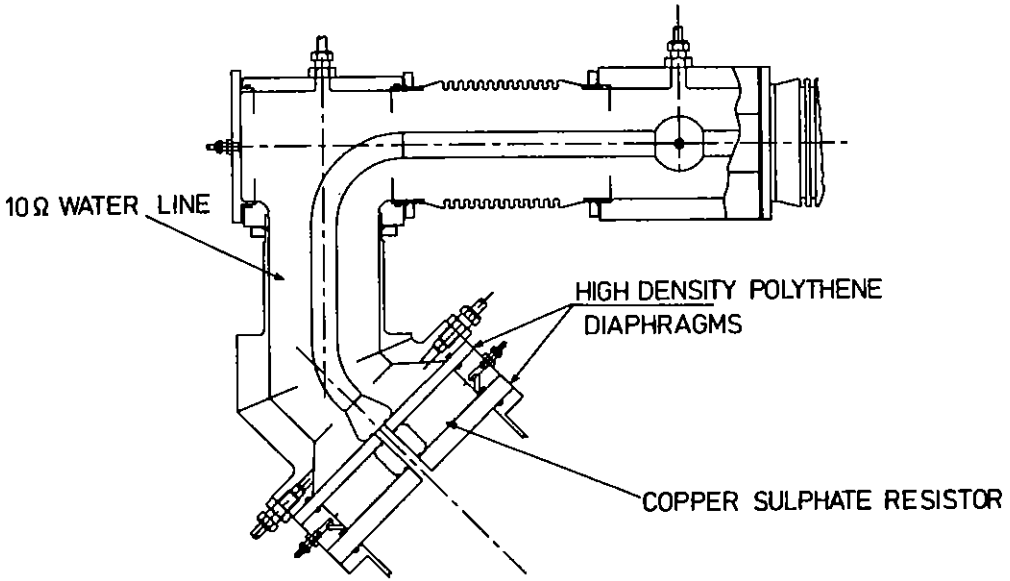

Fig A6.3 New water transmission lines for Sprite.

are very much easier to assemble whilst maintaining concentricity between the inner and outer cylinders. Each line terminates in a 200Ω copper sulphate disc resistor before entering the diode chamber. These resistors serve the dual purpose of voltage monitors and energy dissipating elements to cope with post-pulse. During the main power-pulse the resistors cause a 5% loss in energy at the diode however in the immediate post pulse and before diode closure, the diode impedance goes very high thus residual line energy is preferentially diverted to the resistors. It is hoped that the use of these shunt resistors will help to reduce post-pulse arcing and hence prolong anode foil life.

Another significant improvement to the Sprite system has been the

introduction of a second commercial discharge laser (Lambda Physik EMG 103) as a trigger laser and the development of an entirely new triggering system as shown in Fig A6.4. The Sprite Marx is now

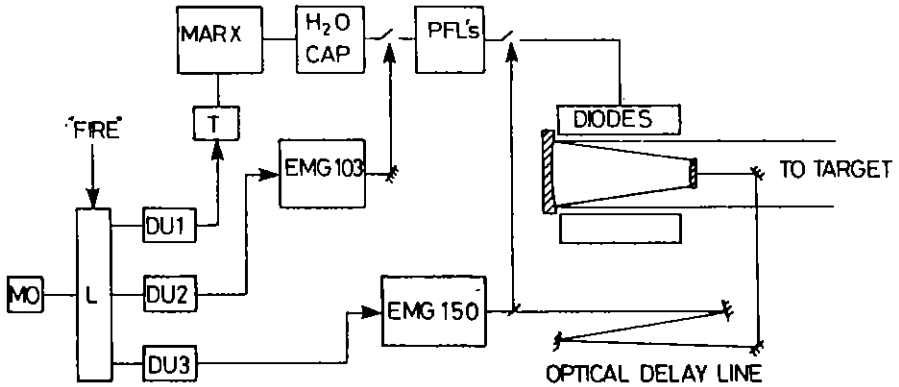

Fig A6.4 New control system for Sprite incorporating digital delay units (DU's) and injection via an optical delay line.

triggered with a magnetically switched pulse transformer as used on Goblin (see last year's annual report). The whole system instead of being slaved to the Marx erection as previously is now command triggerable to within a few nanoseconds. Central to this improvement has been the in-house development of inexpensive digitally programmable delay units (Fig A6.5) which provide pulse delays of 0 - 2,569 ns in 1 ns increments.

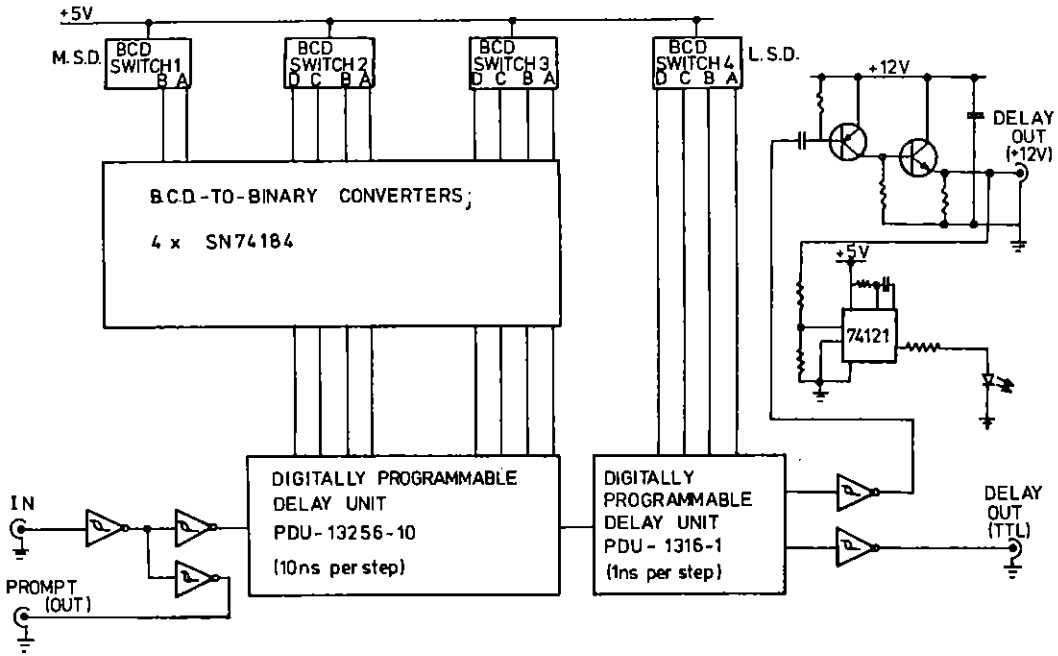

Fig A6.5 Circuit of the digitally programmable delay module.

The operation of the new trigger system is as follows: (see Fig A6.4). A master oscillator, MO sends out a trigger pulse every 1.5 secs and a logic unit, L sends these trigger pulses via delay units DU2 and DU3 to the two discharge lasers. These lasers are set firing a few minutes before the required shot and the delay units are adjusted to give a pre-determined delay betwen the laser outputs. This adjustment is necessary to compensate for the drift in the internal delay in the two discharge lasers. During this time, shutters prevent the laser beams from reaching the spark gaps or injecting the oscillator. When a shot is required the Marx is charged and the fire command given in the usual way. This opens the shutters and the next master oscillator pulse triggers the Marx via DU1 in addition to the two discharge lasers. The most crucial timing sequence, namely that of the injection-locking

pulse, is done purely optically. The same laser pulse from the EMG 150 is split into two beams. One is used to trigger the PFL spark gaps and the other, after approximately 100 ns of optical delay, injects the Sprite unstable resonator. The use of the programmable delay units permits easy optimization of the switching lines of the water capacitor and pulse forming lines for maximum laser output. In use, the main problem with this new system was found to be due to poor beam quality and instability in the optical delay line. In order to overcome this, better thermal insulation has been provided in the oscillator room and an image relaying section has been incorporated into the delay line.

Development of the multiplexer has proceeded throughout the year, however not as smoothly as had been hoped. On the positive side, the vast majority of the engineering work on the multiplexer hardware has been completed and short pulses have been generated in the oscillator room, transferred to the multiplexer room and a series of pulses have been amplified in Goblin (these results are reported more fully in section C2.2). On the negative side however the Lumonics discharge laser purchased as a multiplexer pre-amplifier has been a dissapointment in this application. Gain, beam uniformity and beam quality out of this amplifier have all fallen short of expectations. At the present time it is not clear whether or not this laser can be made to reach the required performance.

As a stop-gap measure, and in order to make the short pulse amplification measurements on Goblin, the Goblin amplifier was used as its own pre-amplifier (ie double-passed twice for each pulse). Output energies of 0.75 J per beam were obtained with saturated gains of about 20 for the final double-pass. This energy should be enough to efficiently extract energy from Sprite in the multiplexed mode. An important addition to Goblin this year has been the incorporation of a magnetic guide field to the electron-beam diode. This field which is approximately 1kG in the laser chamber is produced by a pair of Helmholtz coils which are powered by the discharge of a 1 Farad electrolytic capacitor bank. The time to peak field is 50 ms and the electrolytic bank is set to fire at this interval before the Marx bank. The cost of this installation was essentially zero since capacitor bank, SCR switches and coils were scrap items from previous

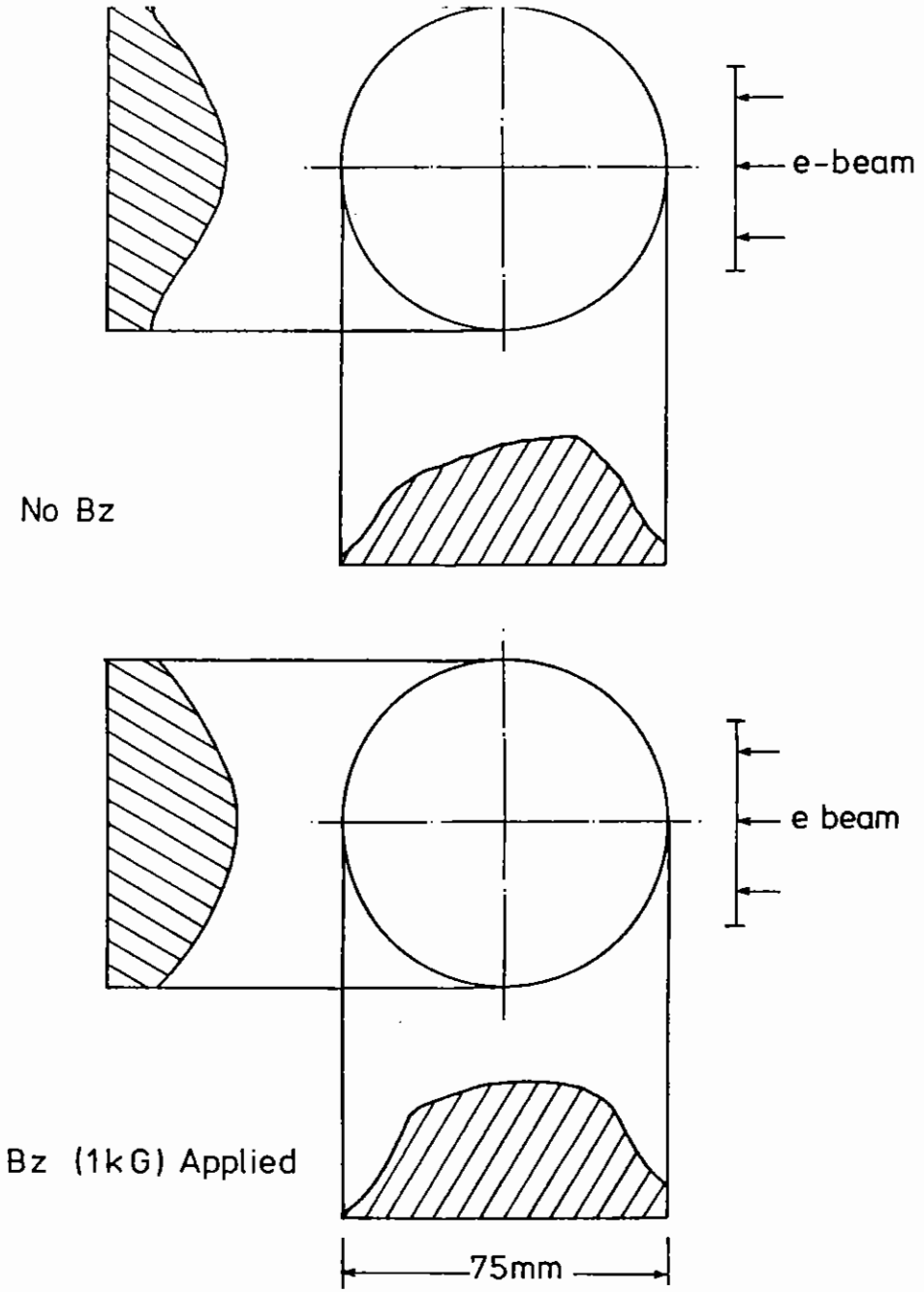

Fig A6.6 Vertical and horizontal beam profiles of the output from Goblin run with a planar resonator both with and without the magnetic guide field (B_z). The profiles were taken with the system described in section C2.3.

experiments. The effect of the field is to both increase the output energy of the laser, and to improve the deposition uniformity especially along the beam direction as can be seen from fig A6.6.

A6.1.3 Sprite Target Area Operations and Development

F O'Neill, I C E Turcu, Y Owadano (RAL)

In last years Annual Report the first target experiments using Sprite were described. These experiments on X-ray generation were carried out using a simple box-type target chamber and only basic plasma diagnostics were employed. The laser beam was focussed onto target using a simple plano-convex fused silica lens.

In the past year the Sprite target area has been significantly up-graded and the redundant six-beam target chamber from VULCAN has been installed as shown in Fig A6.7. The laser beam travels from the

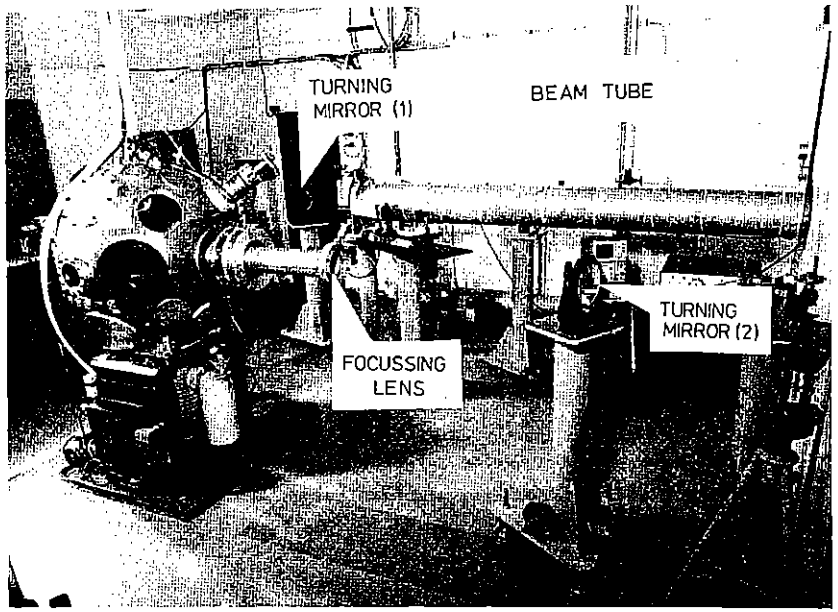

Fig A6.7 Sprite single beam KrF target area.

Sprite laser area in a beam tube and is then directed into the target chamber using two dielectric-coated turning mirrors. The focusing lens forms the input window of the target chamber.

By installing the 6-beam target chamber on Sprite, users are able to use the full range of diagnostics equipment as used in the VULCAN target areas and the Sprite facility is now scheduled for experiments in the same way as the other target areas. Beam focussing onto target has been improved by using a single-aspheric fused silica lens. The sprite laser beam is still converged into the target area (see last years Annual Report) to keep the optics size to a minimum and the effective focussing aperture onto target is f:10.

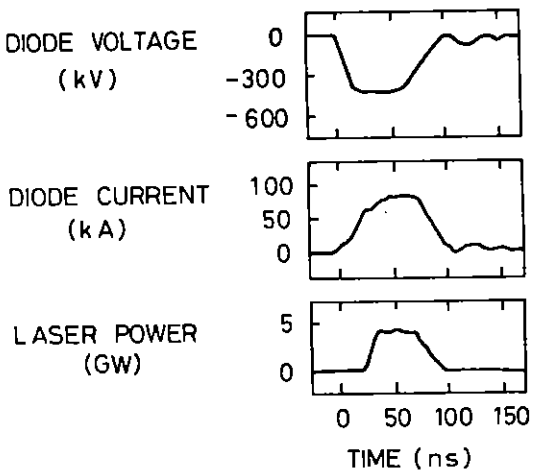

Fig A6.8 Sprite diode voltage, diode current and laser output power versus time.

The laser pulse shape on target is approximately square shaped as shown in Fig A6.8. The intensity profile of the focussed beam in the target plane has been measured by first attenuating the beam and then moving a knife edge through the laser spot on a shot-by-shot basis while measuring the unobscured fraction of the energy with a calorimeter placed behind the focal plane. By assuming a Gaussian beam profile we can deconvolve the intensity profile from the measurements as shown in Fig A6.9. These results show that the laser spot size is ~ 50μm and that half the laser energy on target falls within a circle of 80μm diameter.

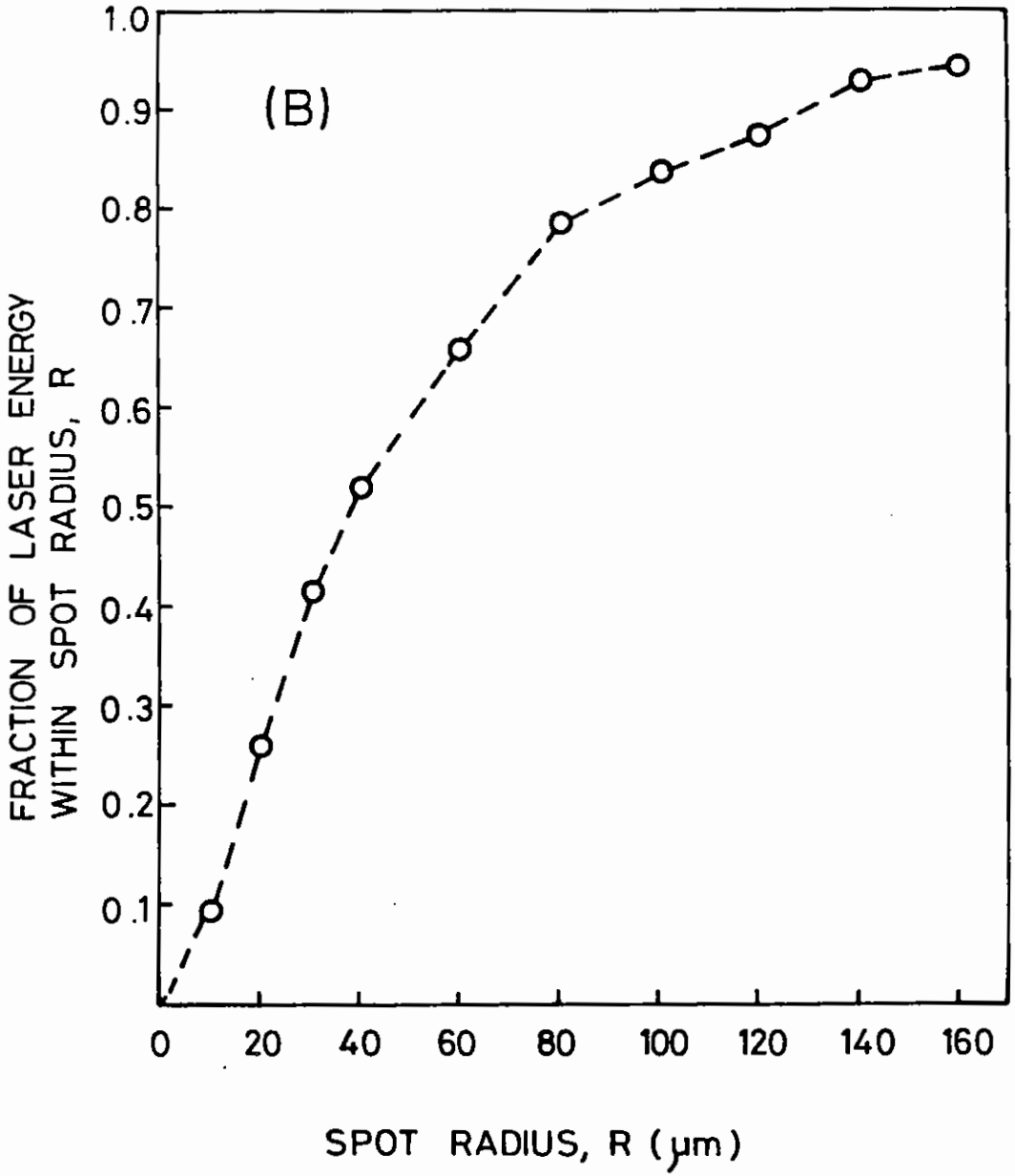

Fig A6.9 (A) Intensity profile of Sprite beam on target. (B) Energy profile on target.

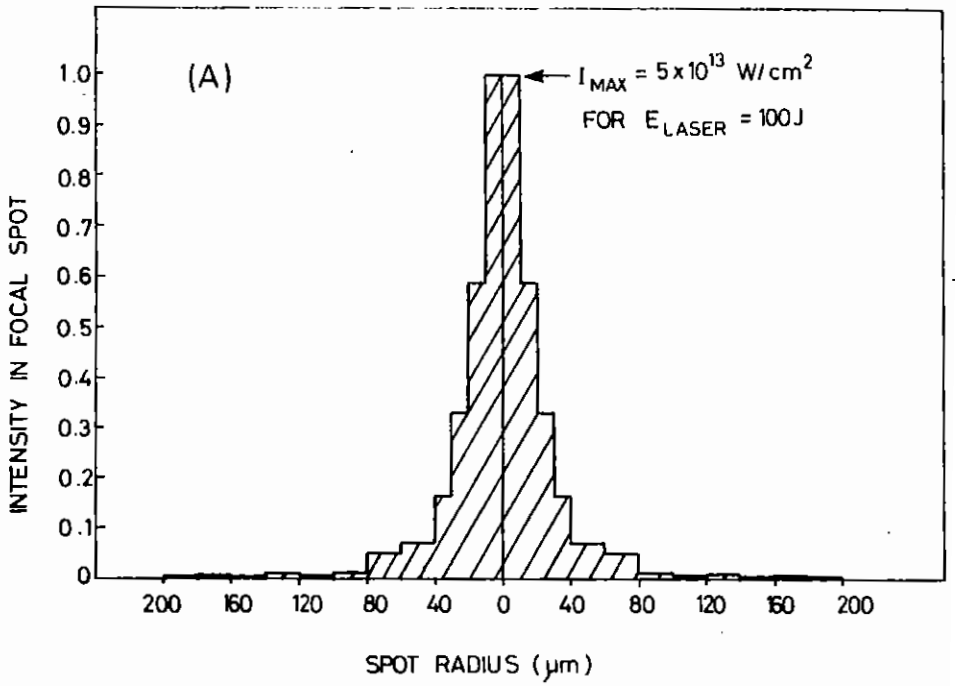

Fig A6.9 (A) Intensity profile of Sprite beam on target. (B) Energy profile on target.

The main KrF beam parameters available on target are summarised below.

Wavelength	249 nm
Energy	140 J
Pulse duration	50 ns
Spot Size at ½ intensity	50 μm
Peak intensity	~ 10^{14} W/cm^2
Shot rate	average 10 shots/day

This performance represents a considerable improvement over last year and user experiments utilizing this new facility are described in Section A4. This target area has also been used for target experiments with a 1J discharge-pumped KrF laser as described in Section C6.

A6.2 VULCAN

A6.2.1 Introduction and Operation Statistics

P T Rumsby (RAL)

This year has seen another major step in the present phase of the glass laser facility upgrade programme with the successful bringing on line in August of the new Target Area East (TAEast).

This area contains a versatile and multi-purpose 6 beam and backlighting target irradiation facility which is particularly suited to work in XUV laser research. Scheduled operations on VULCAN are now carried out in this area and the recently commissioned 12 beam area, TA West with the old 2 beam area (TA2) retained for non-scheduled instrumentation development and test work using one beam only.

Commissioning of a second 6 beam target area served by the laser has involved the construction of a complex remotely controlled beam switchyard area within the laser room. Details of TA East and the new switchyard area given below.

Operation of VULCAN for scheduled experiments has been intensive and reliable with a total of over 3500 shots fired during the year up to March 20th. Almost 1400 main shots involving the full laser system were fired into target areas for experiments during the year with TA West receiving 645, TA East 488 and TA2 257. Shot failure rate due to system faults has remained at below 3%. The usual pattern of 3 or 4 week experimental periods followed by a one week maintenance, development and modification period has been maintained during the year and consequently the laser has been available for operational use for

36 weeks out of 52. During scheduled experimental operation periods the longest period of time when the laser was unavailable for shots was half of one day, caused by an electrical fault.

The flexibility of the glass laser facility has been demonstrated during the year during beat wave experimental runs in June 1985 and January 1986. As discussed in detail in Section C1, these experiments have required major modifications to the oscillator and amplifier configurations in order to produce and amplify pulses of two different wavelengths. Such modifications have been made and removed very successfully in very short periods.

A6.2.2 Probe Beam Developments

C Danson, S Hancock, N Rizvi, P Rumsby (RAL)

Optical probing has always been a major diagnostic technique employed by experimentors, and consequently for some time a small diameter beam has been available for this purpose. The beam was derived from the main laser short pulse amplifier chain by splitting out 50% of the energy after the 16 mm rod amplifier and could operate for extended setting up periods on a 9 second cycle giving a few mj in 100 ps or could deliver up to 50 mj on a 2 minute cycle or on main shots.

The installation of multiple frame diagnostic cameras in the target areas during the year (Section A1.1) has meant that up to 200 mj of energy were needed on main shots and hence the probe beam system has been modified to permit this.

The new scheme now splits out 20% of the beam at a much later stage in the short pulse chain after the 32 mm rod amplifier where the single pulse energy is over 1J. As this pick off point is after a Faraday rotator unit it is not possible for this route to supply high repetition rate, low energy shots for setting up. Consequently the original probe beam split off before the Faraday has been retained and can be selected remotely when required by the laser operator by inserting kinematically locating mirrors. Both output probe beams are collimated and adjusted to be collinear. The time delay between them

is known.

Using this double system energies up to several 100 mj in 100 ps have been delivered for optical probing measurements on main shots while rapid setting times have been retained.

A6.2.3 Computer Control and Data Acquisition

C J Reason, P Gottfeldt, C B Edwards, D A Pepler and B Espey (RAL)

The GEC 4080 computer and its associated CAMAC system has run reliably during the year except for a short time when an earth loop caused pickup problems. The configuration of the 4080 is the same as last year but the CAMAC system has been further expanded. The crate in TA2 which was on the parallel branch has been removed and installed in TAE on the serial branch and a new crate has been installed on the serial branch in the old capacitor room.

A facility for testing complete flashlamp assemblies in disc amplifiers has been installed close to the main capacitor banks. In the past, amplifiers have been assembled with individually pre-tested flashlamps which have occasionally exploded after a few shots in actual operation. To prevent costly damage to laser glass the amplifiers are now subjected to 50 shots prior to glass installation. One of the main capacitor banks has been fitted with a two-way motor driven switch to allow the bank to be connected to the amplifier under test when required. Flashlamp pulses are monitored using current transformers feeding into a specially designed multi-input digitiser. The Eurocrate also houses power supplies and modules for timing, a digital to analogue converter and computer control although it will run as a self contained unit. In operation the digitiser and the two-way switch are controlled and monitored from a CAMAC module in a crate on the fibre optic coupled serial branch. Both PILC and main pulses are read into the computer for checking and graphical output is available if required. Under the control of the main laser program, complete shots can be run to check this amplifier. The laser control program itself is interlocked to prevent shots being fired to the test amplifier during laser shots.

The laser control program (LASR) has been expanded during the year to include new facilities to keep it in line with changes on the laser. Also a start has been made on re-writing entire sections of the program and splitting them into new processes, thus allowing concurrent use of some of the facilities on the laser. The first section to be re-written is the layout diagram using a new colour graphics system. This will allow faster operation and a more rapid response to changes in the laser layout. It is also proposed to re-write the interlock section and the touch screen section.

New data acquisition programs have been written for the experimenters as they are required but the plans to fire shots from the south control room have been shelved because of suggestions that the operation of the laser is becoming more complex and the possibility of experimenters firing their own shots is now thought to be undesirable.

The Falcon computer running in a Hytec housing in the CAMAC system in TAW has had its program blown into PROM and has run reliably. The program in a similar system in TAE is still being developed and is running from RAM. This system is more complex than the one in TAW and various facilities, such as the control of the timing trombones and controlling alignment crosses on the TV screens, have not been included because of memory size constraints. A change in the micropower pascal system is being investigated to use the memory more efficiently to allow these to be included. The 4080 computer now communicates with both Falcons via the CAMAC to arbitrate between them having access to various pieces of common equipment. This has involved temporarily running the TAW system in RAM.

Some of the data acquisition has been distributed to small computers that communicate back to the 4080. A system has been developed in a collaboration between the Division and Essex University Electronics Centre to monitor the beam quality of the laser. This is based on a Syntel computer system consisting of a 6809 CPU board on a G64 backplane bus with up to 15 BT framestores interfaced into it. The software, written in C and called from BASIC, allows beam profiles to be snatched on each shot, processed to determine if the quality of the

beam has deteriorated and the results displayed to the operator in false colour. The programs and data are stored on two floppy discs.

In addition to the above, two systems based on commercially available framestores and Apple computers have been installed. One monitors the laser pulse length from an EEV CCD camera coupled to a streak camera via a fibre optic reducer, and the other measures component optical quality based on fringe information from a Zigo interferometer. A framestore interfaced to an IBM PC has been installed to gather data from the phase conjugation laboratory, and an IBM PC has been installed to collect data on the picosecond laser facility in the LSF.

A6.2.4 Target Areas

A J Cole, R Hawkins, C J Hooker, M H Key, D A Pepler, S Wilcox, P Apte (RAL)

A6.2.4 (a) Target Area West

Target Area West has operated as a twelve beam, symetric irradiation facility for the majority of the reporting period. Conversion to operate at 1.053 μm was successfully carried out for the spherical transport experiment described in section A1.1. The complete wavelength changeover operation, comprising of CW laser and beam expander conversions, more than 50 mirror and splitter changes and main lens spacer changes required one week of "down" time for the target area.

TAWest has also been used to carry out cluster beam experiments, specifically the EXAFS studies of dense plasmas reported in section A3.1. Two cluster schemes have been used. The first, shown in Fig 6.10(a), consists of two opposed sets of three nearest neighbour beams. These beams were run long pulse to irradiate both sides of a foil target. The 50% beam splitters were removed to allow these six beams to be run at the full output energy of the laser. The backlighting beam was operated short pulse to provide an x-ray backlighting source on a separate target.

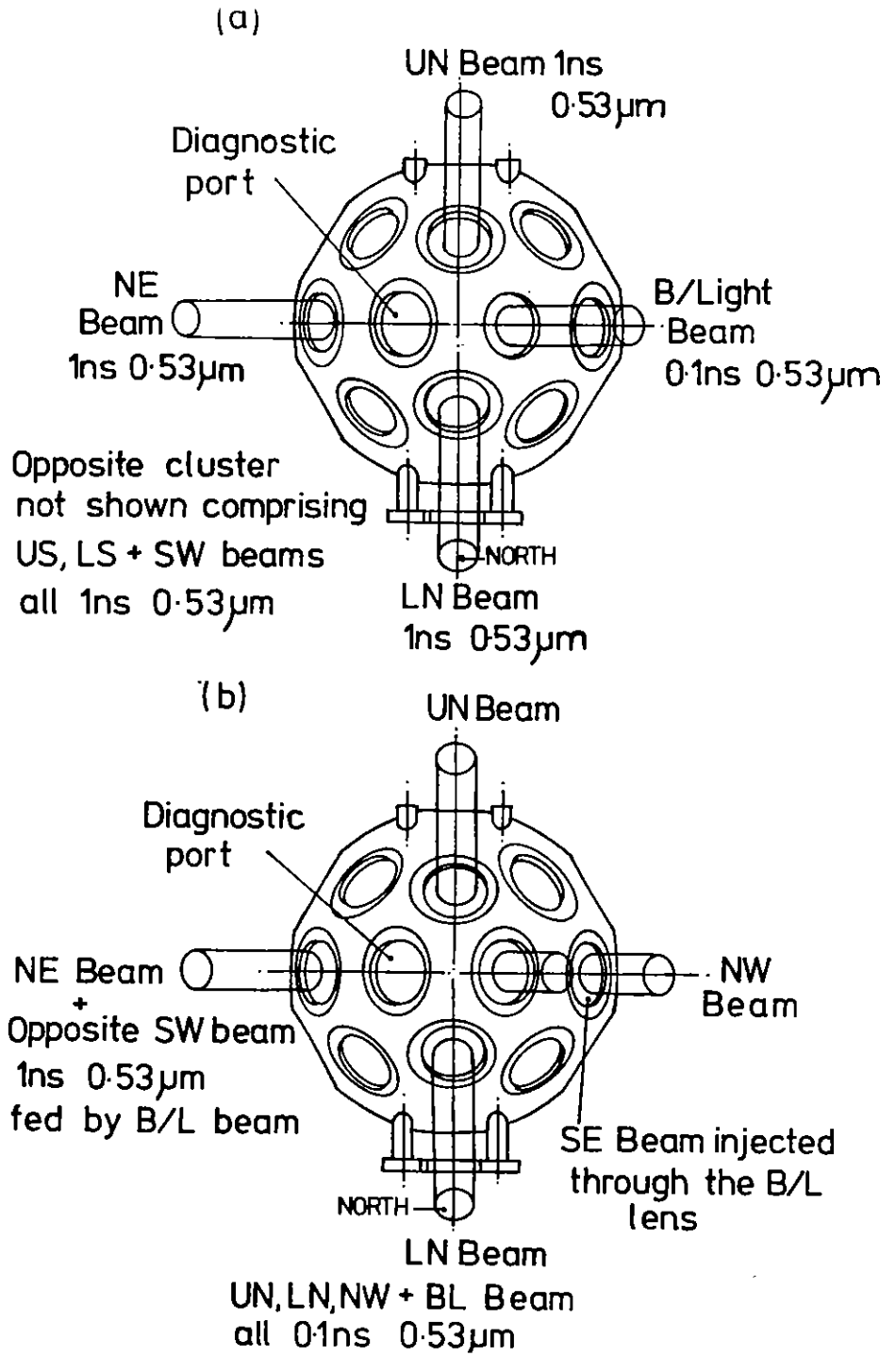

Fig A6.10 Cluster beam arrangements used in Target Area West.

The second cluster arrangement is shown in Fig 6.10(b). In this case four full energy short pulse beams were used to provide a very high brightness x-ray source for x-ray backlighting. These were injected through the backlighting beam lens and the three surrounding nearest neighbour beams are illustrated. The backlighting beam from the laser was operated long pulse and split into two in the target area. These beams were then injected through the NE and SW lenses to irradiate the main foil target.

Both of these cluster beam schemes proved to be successful and will allow TAWest to fulfil a wider role than was originally envisaged.

A6.2.4 (b) TA East

Target Area East was commissioned in September 1985 and has since operated continuously using a range of irradiation geometries. The target area layout and principle beam systems were descibed in last year's report (A6.1). The control system, based on a Falcon micro-computer, is essentially the same as that in TAWest, a description of which can be found in the 1984 annual report (A6.2).

Following several weeks of beam alignment and timing, the first target shot was fired on the 6th October. A spectrum was successfully recorded on a flat-field x-ray grating spectrometer.

The first experiments were studies of x-ray laser schemes and utilised the full flexibility of the TAEast system. Line foci, produced using the optical system designed by Ross and Hodgson (A6.3), of up to 21 mm length have been achived. The longest lengths were obtained by staggering pairs of beams along the length of a fibre target. Double sided illumination of narrow stripes on foil targets have also been successfully achieved.

Target alignment of fibres and stripes is carried out using a novel optical technique described in section C4.4. Further details of these experiments can be found in section A4.5.

Three beam experiments for laser annealing studies have also been

performed. This required the installation of a 200 nsec optical delay line in the target area. In addition, two of the beams were spatially and temporally averaged using segmented mirrors (see section A4.6), to provide a uniform annealing beam on the target. The high degree of accessibility in the TAEast target chamber greatly facilitates this kind of experiment.

The beat wave experiment described in section A1.2 was performed in TAEast. In this case the target chamber itself was not used, the experiment being performed in a "stand-alone" Z pinch system. The large amount of clear space in TAEast allowed this complex experiment to be performed without disturbing the conventional beam line optics. This again demonstrates the highly flexible nature of this target area's facilities.

A6.2.5 Beam Switchyard

C J Hooker, D Riley, W T Toner, S Hancock, P Gottfeldt, R Hawkins

The beam switchyard plays a vital role in the Vulcan system since it controls the way in which beams are fed to Target Areas East and West. The optical layout was designed for complete flexibility, and in fact allows any combination of infra-red and green beams to be fired into either target area. There are also a number of laser diagnostics, such as energy and beam profile monitors. The switchyard is a small enclosure within Laser Area 3, and is intended to be as environmentally stable as possible. There is no air conditioning, to minimise air-currents, and heat sources are excluded from the enclosure. The harmonic generating crystals are used without windows, which requires the humidity to be kept below 40 per cent: this has been achieved by dehumidifying units.

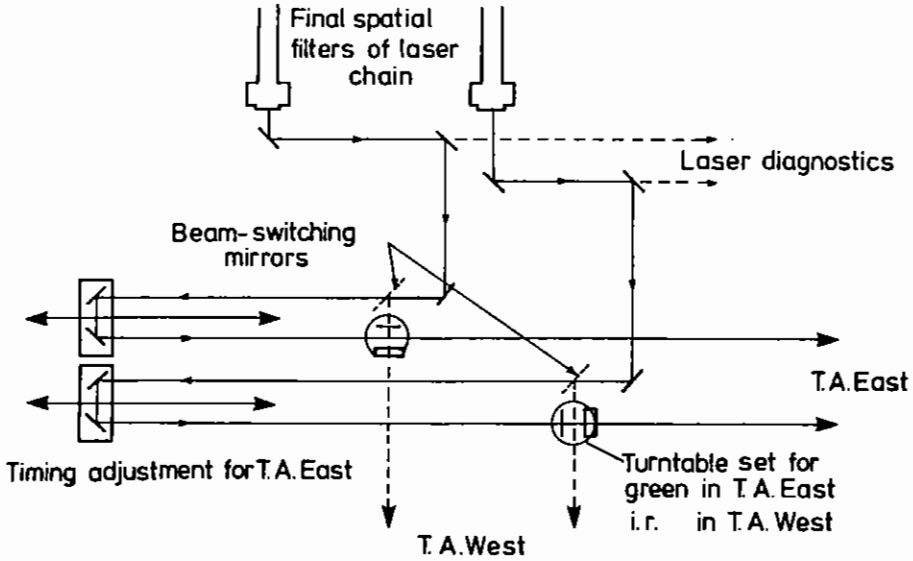

Fig A6.11 Arrangement of beam lines and components in one level of beam switch yard.

Fig A6.11 shows the layout of one level of the area, which handles two beams from Vulcan; there are three levels in all. The most novel feature is the turntables which carry the harmonic-generating crystals and their associated waveplates. Each turntable is centred at the point where the beam paths to TA East and TA West intersect, and allows the crystal to be rotated by 90° so that either area may receive a green beam. The crystal mounting has a tilt mechanism for turning, and the waveplate can be rotated to vary the green energy output; both these adjustments are controlled from the target area computers. If infra-red is required in one area, the turntable is moved to the position that would supply green to the other, and the beam passes between crystal and waveplate.

The switching mirrors move on vertical slides to switch the beams from TA East to TA West. When in place for shots into TA West the mirror mounts rest on 3-point kinematic supports. At present the adjustments of these mirrors are not motorised, although in the final switchyard configuration they will be.

The six beams from Vulcan reach the TA West shutters simultaneously, a necessary condition for compression experiments, since the beam paths inside the area are equal. For TA East, the philosophy of maximum flexibility requires beam-timing to be variable, so each path to TA East in the switchyard includes an adjustable delay with a range of 12 nanoseconds. Each delay-line consists of a pair of mirrors mounted on a carriage, which is driven by a motorised linear slide over a range of nearly 2 metres. The mirrors are not individually adjustable, but a vertical tilt motion on the carriage allows irregularities in the slide movement to be compensated. The slides are controlled from a terminal in TA East via a customised microprocessor system which is independent of the main target area computer.

All other switchyard devices are controlled from the Falcon microcomputers in the target areas, via a common Eurocrate rack in Laser Area 3. The target area programs have been modified so that only one area can gain control of the switchyard at one time. Which area has control is determined by the 4080 in the main control room, and depends on the state of the shutters into the two areas; however, once access has been granted the controlling Falcon cannot be excluded, and retains control until it signals to the 4080 that it has finished. During operations, the crystals and waveplates are left in standard positions; each area makes any required offsets before a shot, then restores the standard position before giving up control.

The switchyard was set up at the same time as TA East, and commissioned during the September 1985 X-ray laser run. A number of teething problems occurred with both hardware and software, but these have largely been overcome, although inexplicable changes of crystal tuning still occur form time to time. For so complex a system, the switchyard performs remarkably well.

A6.3 TARGET PREPARATION

C Brown, B Child, N Prior, P Rumsby, S Taylor, S Whittaker (RAL)

The last year has seen the introduction of a new target irradiation facility on the SPRITE UV laser (A6.1.3) and the commencement of experiments in the new VULCAN multibeam, multipurpose target area T A East (A6.2.4). As a consequence the number and complexity of targets produced by the target preparation group during the year has increased significantly.

Target Area East now provides optics which enable high quality line foci up to 20 mm long to be produced for XUV laser experiments (Section 4.5) and hence a wide variety of targets to support this continuing campaign have been developed and made.

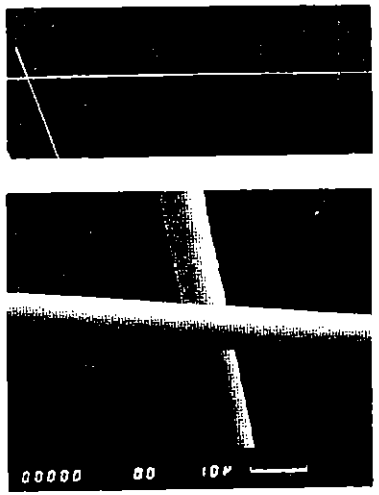

Fig A6.12 S.E.M. photograph of short (3mm) carbon fibre mounted on carbon fibre supports.

For the carbon recombination laser scheme carbon fibres of 7 µm diameter in lengths up to 23 mn have been selected and mounted. Horizontally oriented fibres with lengths up to 12 mm can be mounted at one end only with acceptable bending but beyond this length double ended mounting is needed. Techniques to tension fibres and attach them to carbon fibre supports have been developed successfully. Fig A6.12 shows an SEM photograph of a short (3 mm) fibre mounted in this way. Straight fibres up to 23 mm long are now made routinely.

Mask coating techniques have been developed to enable 50 to 100 µm wide and 21 mm long stripes of various materials to be coated on both thin foil and massive supports for other XUV laser schemes.

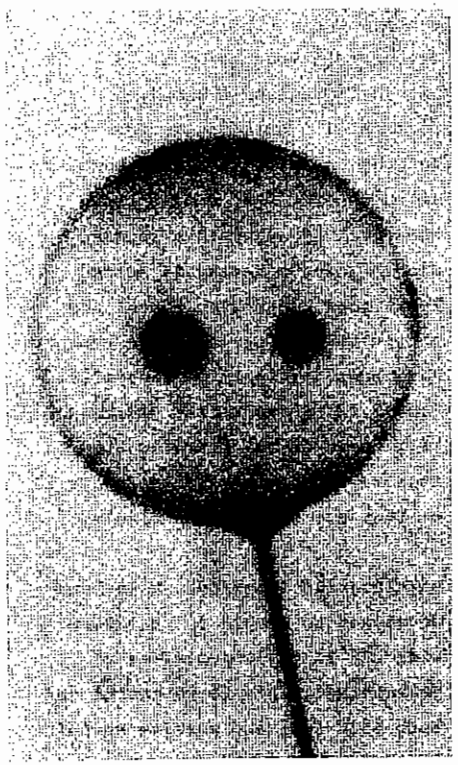

Fig A6.13 Example of glass target with two 30μm Φ aluminium dots.

Transport experiments have required large numbers of multi-layer spherical targets for ablation rate measurements and in addition have necessitated the development of techniques for applying dots and stripes to both spherical and planar targets. Masks have been acquired and equipment built to enable dots of various materials in diameters from 10 μm upwards to be deposited in known positions on microballoon targets. Fig A6.13 shows an example of such a target with two, 30 μm dia 200 nm thick aluminium dots applied to a glass shell target. Polystyrene shells have been coated with one dot of aluminium and the other of SiO positioned to correspond to beam centre and overlap points in the TA West 12 beam chamber. Such targets, when overcoated with parylene N have been used to measure mass ablation uniformity using streaked X ray spectroscopy techniques.

A6 References

A6.1 C Hooker, A Damerell and P Gottfeldt, Annual Report to Laser Facility Committee RAL-85-047 A6.32 (1985).

A6.2 W T Toner et al Annual Report to Laser Facility Committee RAL-84-049 A6.20 (1984).

A6.3 I Ross and E Hodgson J Phys E 18 169 (1985).

SECTION B LASER SUPPORT FACILITY

B LASER SUPPORT FACILITY

Introduction

W T Toner

The Laser Support Facility (LSF) began operations on 1 May 1985 and the reports in this section are an account of its first year's work. The LSF was set up in response to requests from the academic community to expand the scope of the very successful Ultra Violet Radiation Facility (UVRF) and funding was increased by contributions from the subject committees of the Science Board. A Laser Loan Pool was instituted as part of the facility to complement the RAL-based programme and a versatile tunable picosecond laser was added to the RAL-based facilities. The lasers and equipment which previously constituted the UVRF were moved to new Laboratories outfitted for the purpose. The facilities at RAL and in the loan pool are described in more detail in chapter B4.

The new facilities have quickly been put to good use. In addition to fourteen contributions from groups using the excimer and dye lasers taken over from the UVRF, this section contains eight reports of work done using Loan Pool lasers and four reports of experimental work with the picosecond system.

The experiments cover several fields in the three subjects chemistry (B1), biology (B2) and physics (B3). They are selected from proposals made to a panel (the Laser Support Facility Panel) whose members are drawn from the academic community, on the basis of peer-reviewed assessment of scientific merit. Although there is no explicit or directed scientific programme, the nature of the facilities provided results in a degree of coherence of technique and subject matter.

B1 CHEMISTRY

Section Editors J P Hardy/A J Langley

B LASER SUPPORT FACILITY

Introduction

W T Toner

The Laser Support Facility (LSF) began operations on 1 May 1985 and the reports in this section are an account of its first year's work. The LSF was set up in response to requests from the academic community to expand the scope of the very successful Ultra Violet Radiation Facility (UVRF) and funding was increased by contributions from the subject committees of the Science Board. A Laser Loan Pool was instituted as part of the facility to complement the RAL-based programme and a versatile tunable picosecond laser was added to the RAL-based facilities. The lasers and equipment which previously constituted the UVRF were moved to new Laboratories outfitted for the purpose. The facilities at RAL and in the loan pool are described in more detail in chapter B4.

The new facilities have quickly been put to good use. In addition to fourteen contributions from groups using the excimer and dye lasers taken over from the UVRF, this section contains eight reports of work done using Loan Pool lasers and four reports of experimental work with the picosecond system.

The experiments cover several fields in the three subjects chemistry (B1), biology (B2) and physics (B3). They are selected from proposals made to a panel (the Laser Support Facility Panel) whose members are drawn from the academic community, on the basis of peer-reviewed assessment of scientific merit. Although there is no explicit or directed scientific programme, the nature of the facilities provided results in a degree of coherence of technique and subject matter.

B1 CHEMISTRY

B1.1 TIME RESOLVED RESONANCE RAMAN SPECTROSCOPY OF ELECTRONICALLY EXCITED STATES

J N Moore, D Phillips and I McCubbin (The Royal Institution) and R E Hester (University of York)

Sulphonated anthraquinone derivatives

During this year, a study on the resonance Raman spectra of transients from a variety of sulphonated anthraquinone derivatives (Figure B1.1) has been completed. Some details were given in the previous year's report, but for clarity will be given again here.

The pump and probe experimental arrangement (shown in Figure B1.2) permits the recording of well-resolved Raman spectra from transients with decay times in excess of about 30 ns. The reaction scheme, Figure B1.3, which describes the consequences of excitation of a typical anthraquinone, the 2,6-disulphonate derivative, indicates five transient species in this time domain, these being the triplet state, the radical anion, the semiquinone radical and two transients of uncertain structure, labelled B and C in Figure B1.3.

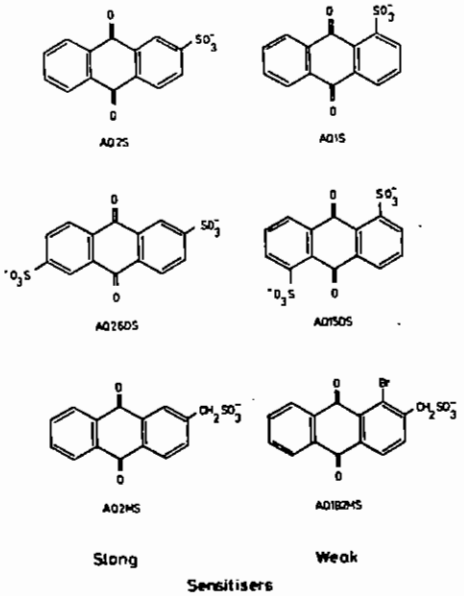

Fig B1.1 Structures of sulphonated anthraquinone derivatives.

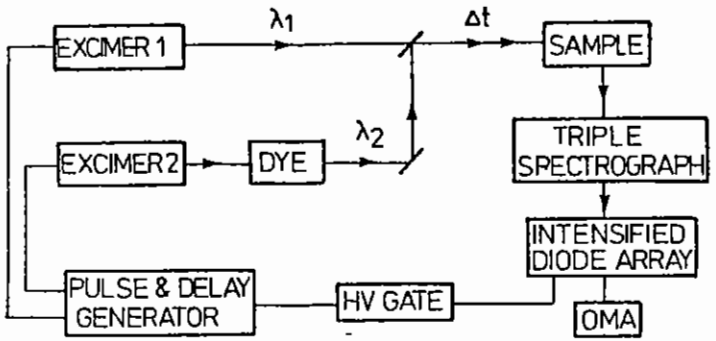

Fig B1.2 Experimental set-up.

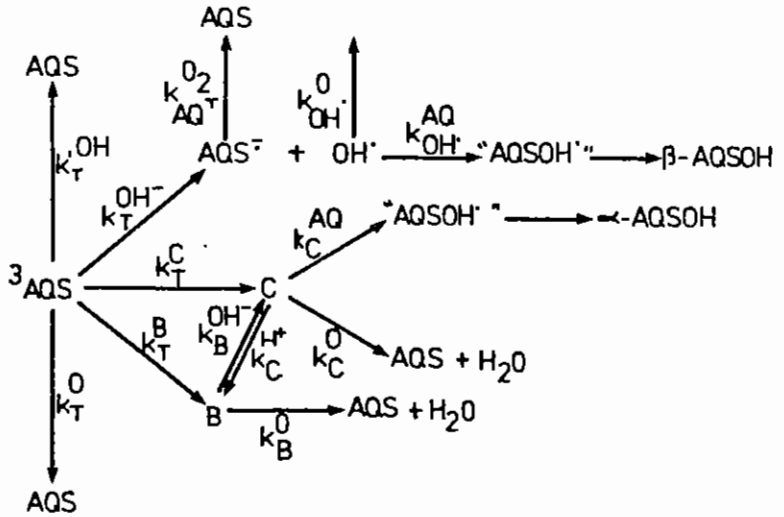

Fig B1.3 Photochemical reaction scheme for AQ26DS.

The work carried out in 1985 has been aimed at obtaining an understanding of the structure of these transients, and their relationship to the other species. The polarisation of Raman spectral bands has been particularly useful in this regard. Figure B1.4 shows a typical polarised spectrum of the transient Raman spectrum of the radical anion, and Figures B1.5 and B1.6 similar spectra for transients B and C, respectively. From these results, the spectra of all five transients of AQ26DS have been assigned as in Table B1.1. It can be seen that the spectra of transients B and C resemble that of the radical anion closely, which indicates they are strong-charge-transfer complexes in which considerable charge transfer from water to

anthraquinone occurs in the ground state. At high probe laser intensities, the spectrum of the transient is lost, that of the radical anion being observed, indicating that photo-excitation of the charge-transfer complexes results in complete electron transfer from water to anthraquinone.

The observation of the band assignable to the C-O stretch confirms the structure of transient C as that with the water molecule attached to the ring (Figure B1.7(a)), whereas this band is absent in transient B, which thus has the water molecule attached via the carbonyl group (Figure B1.7(b)).

Similar studies have been completed upon other 'strong' photosensitizers, AQ2S and AQ2MS. Results are typified in Figure B1.8.

Quite different Raman spectra were obtained for the triplet state of the weak sensitizers AQ15DS and AQ1B2MS, which confirms that in these compounds, the triplet state is $^3\pi\pi^*$ in character rather than $^3n\pi^*$, as in the 'strong' sensitizers.

This study is now concluded, and full papers are currently being written up for publication.

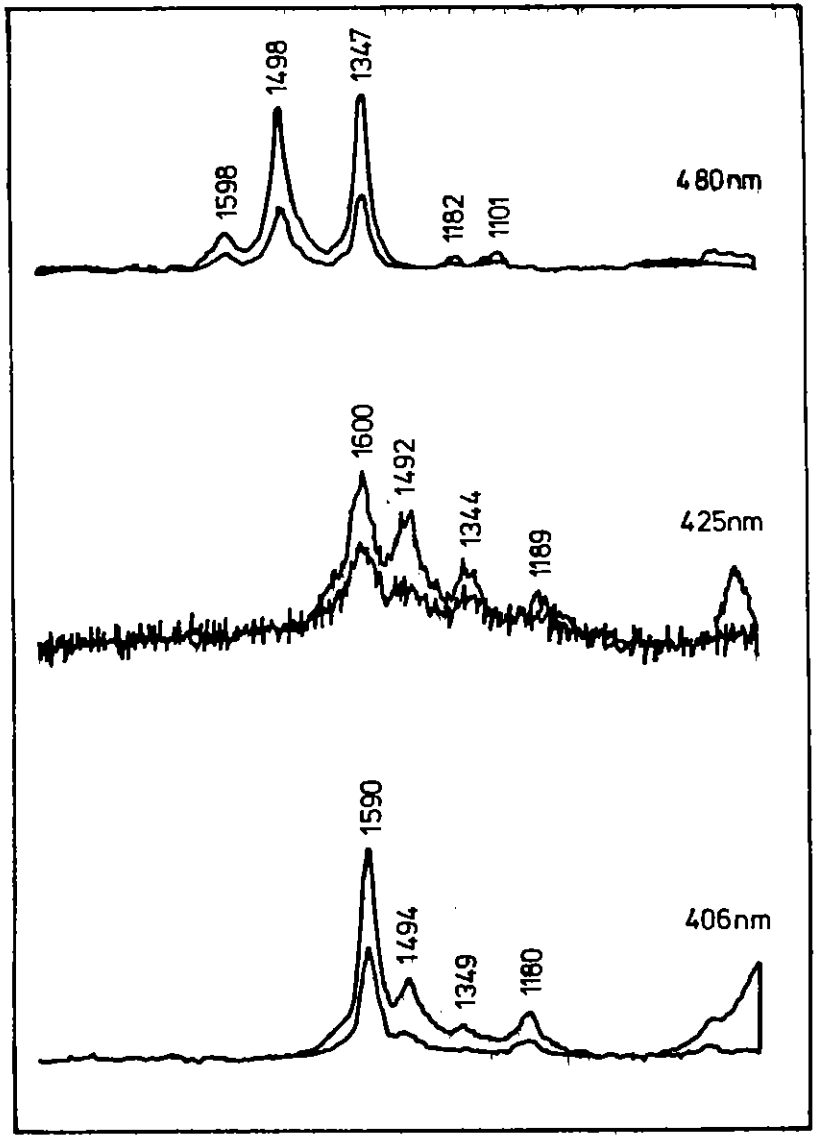

Fig B1.4 Polarised Raman spectra of AQ26DS obtained at several probe laser wavelengths. The bands assigned to AQ26DS are labelled in units of cm^{-1}.

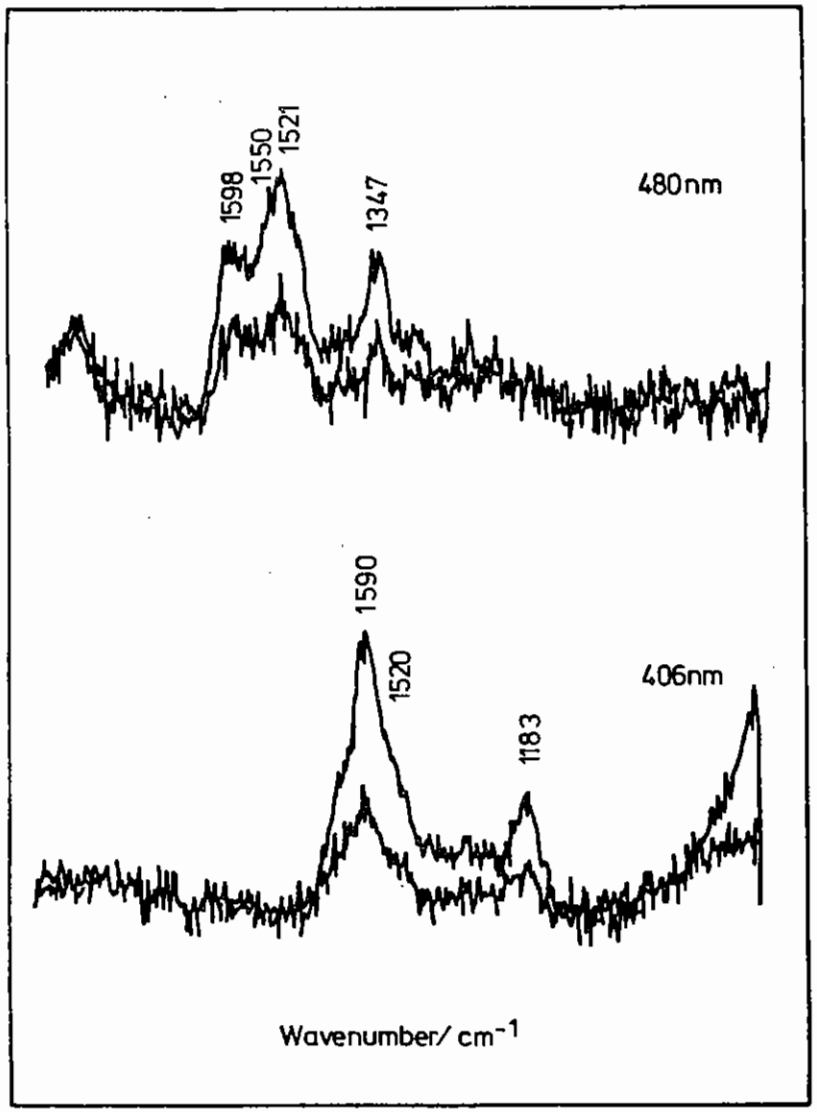

Fig B1.5 Polarised spectra of AQ26DS(B) observed at two probe laser wavelengths at a time delay of 1μs between the pump and probe lasers. Pump laser 351nm. Probe laser used at low irradiance.

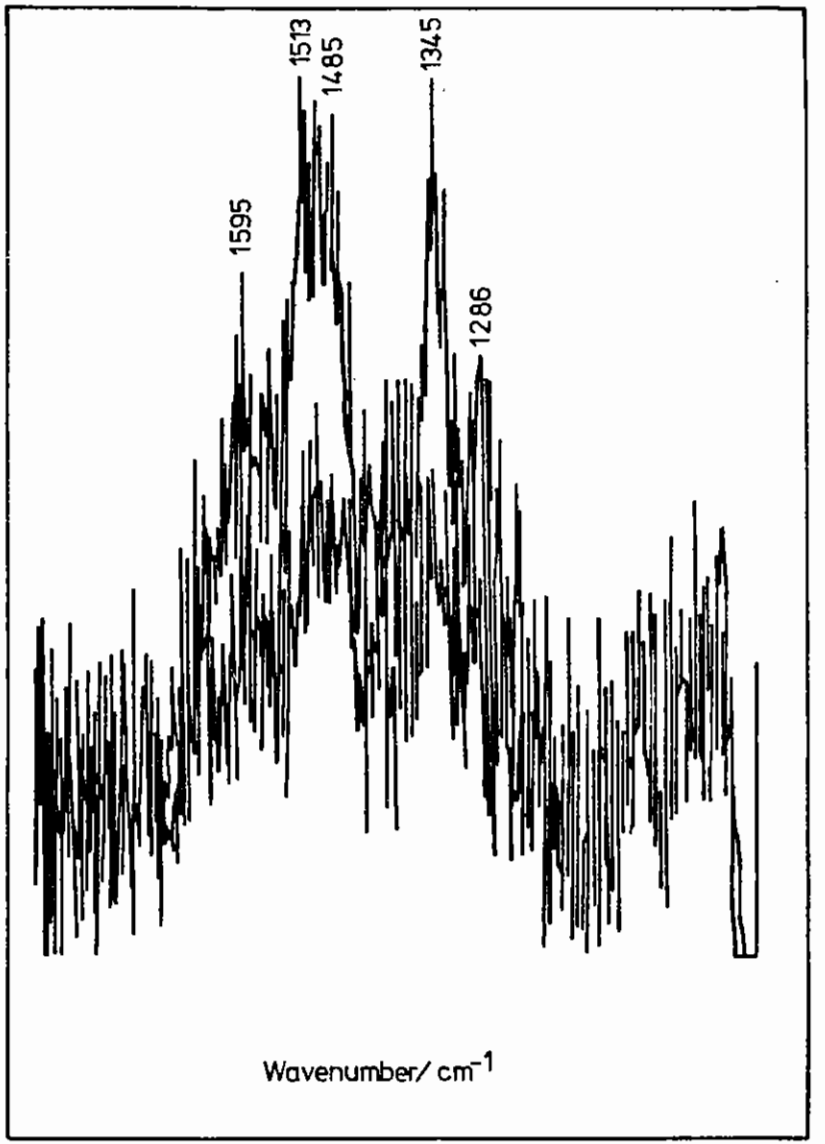

Fig B1.6 Polarised spectra of AQ26DS(C). Observed at a time delay of 400ns between the pump and probe laser. Pump laser 351nm; probe laser 560nm.

(a)

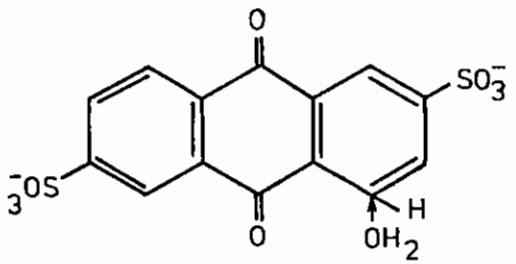

AQ26DS (C)

(b)

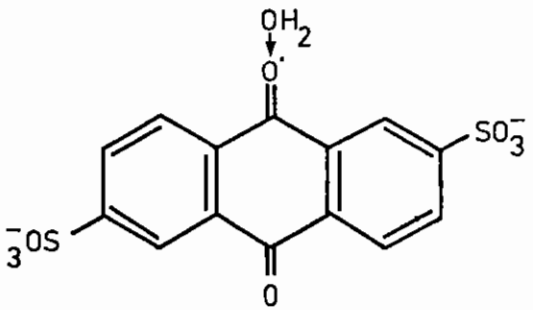

AQ26DS (B)

Fig B1.7 Structures proposed for transients C and B.

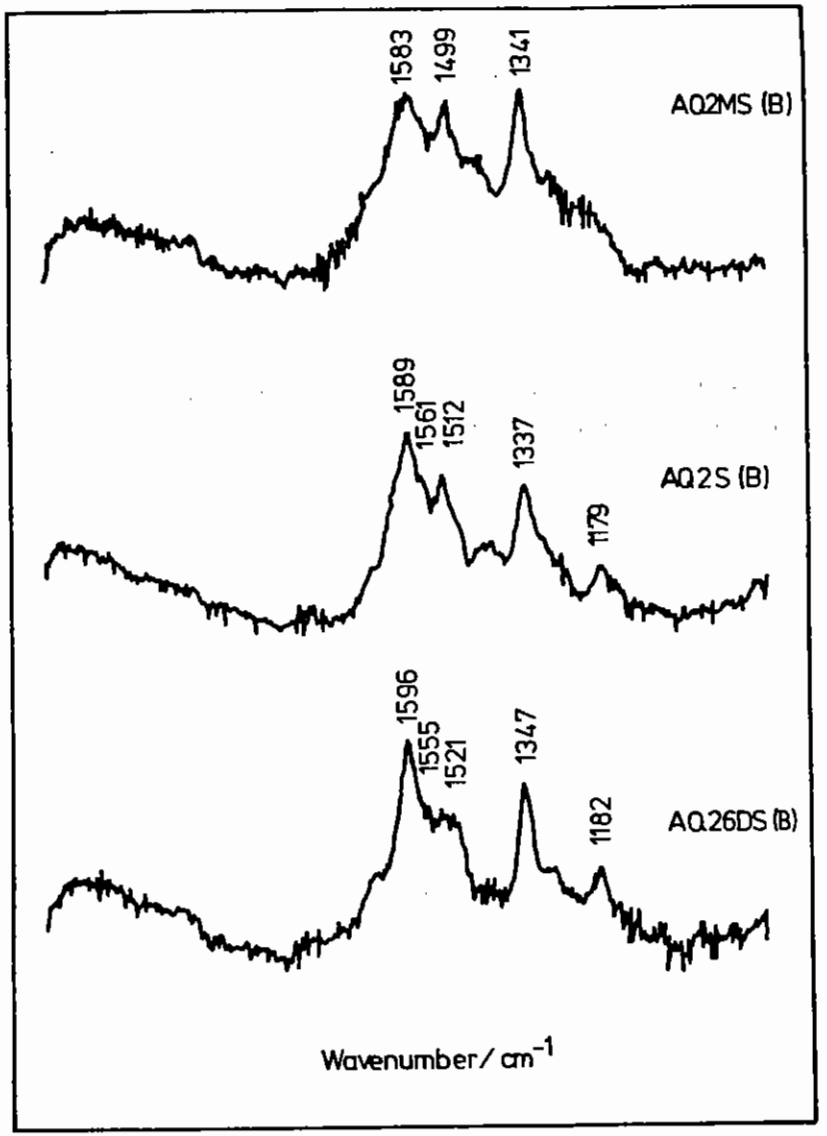

Fig B1.8 Spectra assigned to the transients B for all the "strong" sensitisers. All observed at a time delay of 500ns between the pump and probe lasers. Pump laser 351nm; probe laser 441nm. Bands assigned to B are labelled.

B1.2 SURFACE-ENHANCED RESONANCE RAMAN SPECTROSCOPY

R E Hester, H Virdee and J de Groot
University of York

It is well established that several orders of magnitude enhancement in vibrational Raman band intensities result from adsorption of a wide range of molecules on selected metal surfaces. This enhancement process enables spectra to be obtained with good sensitivity from surface-adsorbed species and has a wide range of potential applications, from the study of heterogeneous catalysis mechanisms to the characterization of molecular species at electrodes. The technique becomes particularly powerful when combined with the additional resonance enhancement which results from excitation of the Raman spectra with radiation of a wavelength which is coincident with a strong vibronic absorption band of the adsorbed molecule. For example, good vibrational Raman spectra have been obtained from cytochrome c in aqeous solutions of nanomolar concentration levels by means of surface-enhanced resonance Raman spectroscopy (SERRS), whereas it is necessary to work with concentrations approaching molar levels in order to obtain spectra of solute molecules without resonance or surface -enhancement effects. Since many chemical and biochemical systems which are of interest to us have their vibronic absorptions in the ultraviolet rather than the visible region, a source of laser radiation which can be tuned through the uv region holds the promise of a powerful and sensitive probe into molecular structure and bonding through the exploitation of SERRS effects.

Previous studies have indicated that SERRS excitation profiles (ie dependence of Raman band intensities on the wavelength of the excitation source) follow closely the shape of an absorption band of the adsorbed species rather than that dictated by the specific metal surface. Thus, athough the SERS effect on silver - the most active of the metals investigated to date - reaches its maximum in the red end of the visible spectrum, the SERRS excitation profile of a dye molecule which absorbs in the blue region also peaks in the blue. It is the aim

of this work to examine the possibility of SERRS in the ultraviolet region. One use would then be to enable us to probe enzyme active sites through the use of colloidal metal dispersions and another study modified electrodes coated with organic polymers.

In the RAL Annual Report for 1985 we described an extensive series of experiments involving adsorption of the model compounds pyridine, NADH and pyrrole on silver and gold aqueous sols. Excitation of resonance Raman spectra (RRS) was observed with suitable ultraviolet laser excitation but no SERS or SERRS effects. In view of these results there seemed little point in going on to experiments with enzymes on metal sols, but we have concentrated our efforts on improving the sensitivity of the Raman instrumentation - as described at greater length in section B2.2 of this report - and on variations of the SERRS experiments with small model compounds. Negative results are often more difficult to evaluate than positive ones: there are usually several possible reasons why a spectrum is not obtained! Nonetheless we are increasingly persuaded that rapid sample degradation under the influence of high peak power laser pulses probably is responsible for the failure of our experiments with silver and gold sols to produce SERR spectra.

We have also done more experiments with surface-modified silver, gold and platinum electrodes. In order to minimize the problem of sample degradation at the point where the (defocused) Raman excitation laser beam impinges on the electrode surface, the electrochemical cell shown as Figure B1.4 in last year's report was redesigned to accommodate a rotating working electrode. Electrode rotation ensured that the laser energy was distributed over an annular ring of sample on its surface in experiments which involved the integration of signals from many laser pulses.

Two types of electrode surface coating have been studied: polypyrrole and thionine. Both of these forms of electrode modifier have yielded good quality SERR spectra with low power cw laser excitation in our York laboratory. In each case the optical absorption properties of the surface coat changes with electrode potential, and thus the oxidation state of the coat, such that ultraviolet laser

Table B1.1

WAVENUMBER/cm^{-1}						ASSIGNMENT
AQ26DS	AQ26DSH	AQ26DS	^{3}AQ26DS	AQ26DS (B)	AQ26DS (C)	
1668	-	1496	-	-	-	b_u(C=O) asym
1669	1606	1347	1210	1347	1345	a_g(C=O) sym
1625	-	1598	1597	1598	1595	b_g(C-C) str
1596	1576	1498	1556	1555	1513	a_g(C-C) str
-	-	-	1490	1521	1485	(C-C) str
-	-	-	-	-	1286	(C-O) str
1177	1177*	1182*	1182*	1180*	-	a_g (C-H) ip bend
-	-	1101	1126	-	-	(C-C) str / (C-C) def

Observed frequencies and assignments of AQ26DS and derived species. Bands indicated with an asterisk are those also observed in the ground-state spectra. Assignments are given for the equivalent AQ26DS C_{2h} mode.

excitation (UVSERRS) could yield further interesting structural information. However, as with the colloidal metal systems reported on above, no SERR spectra have yet been obtained using the pulsed laser systems. Even with average powers well below those used to give good Raman spectra with cw laser excitation, clear indications of rapid sample decomposition in the pulsed laser beam have been found. 1 mJ at 10 Hz gives an average power of only 10 mW, but it has to be remembered that since the EMG 150 excimer laser pulses have a temporal half-width of only ca 5 ns the power within each 1 mJ pulse is in excess of 2×10^5 W. Our experiments appear to indicate that energy dissipation mechanisms for surface-adsorbed species are inadequate to cope with the pulsed laser conditions.

B1.3 RESONANCE RAMAN SPECTROSCOPY OF METAL AND METALLACARBENE COMPLEXES

J J McGarvey, S E J Bell and J Bechara
Dept of Chemistry, Queen's University of Belfast

Introduction

We have continued our studies of the resonance Raman (RR) spectroscopy of copper(I) complexes, $Cu(L)_2^+$, [where L= 2,9-dimethyl-1, 10-phenanthroline (DMP) or 2,9-diphenyl-1,10-phenanthroline(DDP)], with the aim of establishing the nature of the metal-ligand charge-transfer (MLCT) excited states of these photoelectrochemically interesting species. We now have definitive evidence that the excited electron is ligand-localized.

A new line of investigation has also been started, in which RR spectroscopy is being used as a structural probe of photo-generated transients in catalytically important metallacarbene species such as the Fischer complex, $(CO)_5W{=}C(OMe)Ph$ (Figure B1.9).

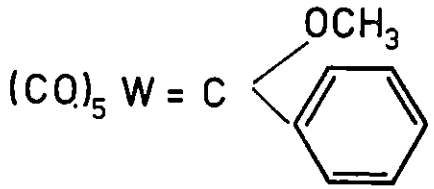

Fig B1.9 Structure of the Fischer complex.

The present report summarises the principal findings for both the copper and tungsten systems.

1. Resonance Raman Spectra of Charge-Transfer Excited States of Copper(I) Complexes

Experimental

Ground state RR spectra of the complexes were generated by means of the Innova Ar^+ laser at 363.8nm. Excited states were populated and probed by dye laser pulses at 360nm and 540nm. In all experiments, solutions of the complexes (ca 10^{-3} mol dm^{-3} in methanol) were argon-purged and flowed through quartz capillary sample tubes. Raman spectra were recorded using the Triplemate spectrograph (1200gr/mm grating) and gated diode array, as described in the 1985 Report.

Results and discussion

As a strategy for establishing the nature of the MLCT excited states, the RR spectra of the $Cu(DPP)_2^+$ complex were compared with those of the mixed-ligand species $[Cu(DMP)(Ph_3P)_2]^+$. (Ph_3P = triphenylphosphine). This complex has a long-lived (τ~300ns in methanol) MLCT excited state in which the transferred electron is necessarily localised on the sole DMP ligand. Ground and excited state RR spectra of this mixed-ligand complex are compared in Figure B1.10. The most striking

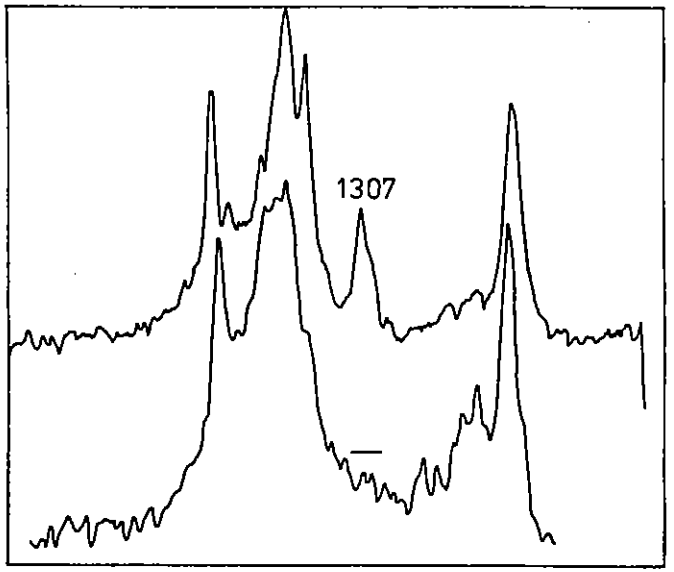

Fig B1.10 Resonance Raman spectra of $[Cu(DMP)(Ph_3P)_2]$ in methanol Upper: Ground state (Ar^+, 363.8nm, 50mW) Lower: Excited state (dye, 360.0nm; pulse energy at sample: 3mJ).

difference between them is that the strong band in the ground state spectrum at 1307 cm^{-1} (attributable to neutral ligand) has disappeared in the excited state spectrum, hence providing a convenient

spectroscopic marker for the conversion of neutral ligand to the radical anion. Figure B1.11 shows RR spectra of $Cu(DDP_2)^+$. In (a), ground state (Ar^+, 363.8nm) and excited state (dye, 360nm) spectra are compared while (b) displays the excited state spectrum generated at a different dye laser excitation wavelength (540nm). The latter spectrum, although dominated by an intense solvent band, shows a strong feature at $1602cm^{-1}$ attributable to the complex, but no peak is observed in the $1300cm^{-1}$ region. We therefore conclude that this is the radical anion Raman spectrum excited in resonance with an intraligand ($\Pi \rightarrow \Pi^*$) transition of the anion. By contrast, the excited state spectrum generated at 360nm under equivalent conditions (ie a large excess of laser photons over absorbing complex molecules in the sampling region, so that the ground state is essentially bleached) does show a relatively strong band at $1316cm^{-1}$ as well as one at $1624cm^{-1}$. The spectrum resembles that of the ground state and must therefore be attributed to neutral ligand vibrational modes, resonantly enhanced through an LMCT transition from neutral ligand to the copper centre, which has a formal charge of +2 in the MLCT excited state. By selective excitation in different absorption bands of the MLCT excited states it is therefore possible to observe resonant Raman modes of both neutral ligand and the radical anion. This provides compelling evidence for a localized formulation of these states: $[Cu^{II}(L)(L^{\bullet -})]^+$. Our results, which are the first of this type reported for d^9-d^{10} transition metal complexes, are a further demonstration of the power of RR spectroscopy for the investigation of redox excited states. Furthermore, the technique could be used as a probe of charge-separated excited states in which longer-lived charge storage might be expected to occur. We intend to address this aspect in future work.

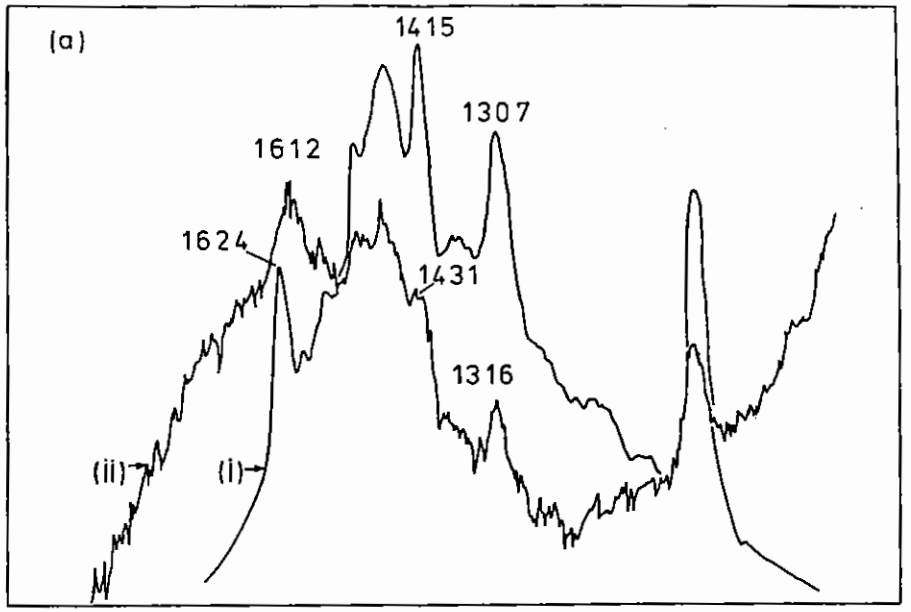

Fig B1.11 (a) (i) ground state (Ar^+, 363.8nm, 100mW)
(ii) excited state (dye, 360nm, 2.5mJ pulse energy)

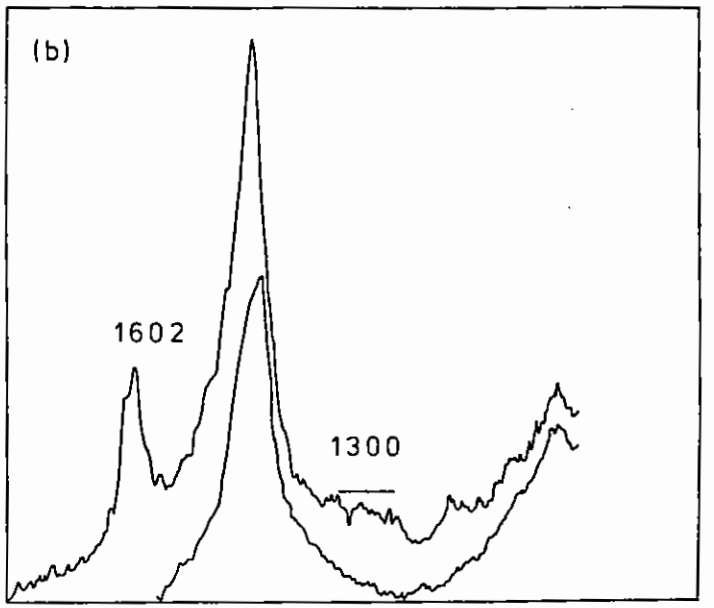

Fig B1.11 (b) excited state (dye, 540nm, 5mJ pulse energy).

2. Metallacarbene Complexes

Metallacarbenes such as the Fischer complex are important in thermally induced catalytic transformations, one example being the ring-opening polymerization of cycloalkenes. In this respect, their photochemical behaviour is of considerable interest because of the possibility of populating both charge-transfer and ligand-field (LF) excited states which may exhibit distinctive reactivity patterns. It is now well established that excitation in the LF bands of the Fischer complex leads to a highly reactive species following photo-induced loss of CO: $(CO)_5W{=}C(OMe)Ph$ - LF excit^n → $(CO)_4W{=}C(OMe)Ph$.

We have now used RR spectroscopy to provide information on the structure of such species.

Preliminary studies of the complex at QUB using a Nd/YAG laser pulse at 355nm and spectrophotometric detection showed the prompt formation of a long-lived transient (τ~10 μs in dichloromethane) with a strong but featureless absorption band in the region of 360nm.

For the RR studies, sample handling and the experimental set-up were similar to those for the copper work. Figure B1.12 shows examples of

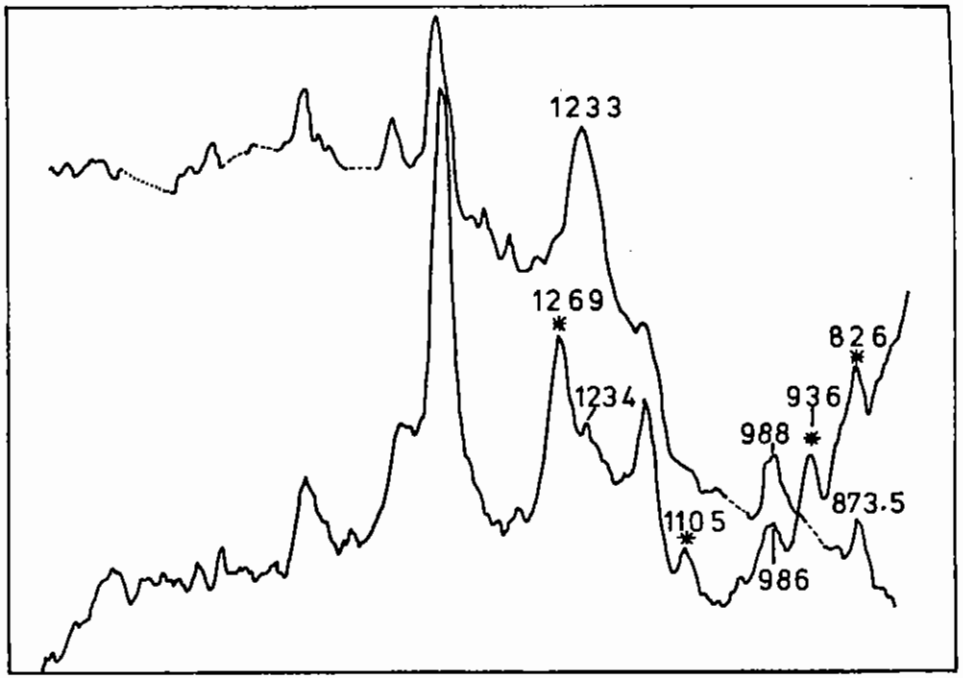

*Fig B1.12 Resonance Raman spectra of $(C)_5$ W=C(OMe)Ph in dichloromethane Upper: Ground state (Ar^+, 363.8nm, 100mW) Lower: Transient species (dye, 360nm, 2.5mJ pulse energy) * denotes transient features.*

the RR spectra obtained. The ground state (λ_{exc} = 363.8nm) shows vibrations characteristic of the carbene ligand since at this wavelength resonance enhancement occurs via a metal→carbene CT transition. Somewhat surprisingly, no features directly attributable to modes of the W=C bond have been observed. In the spectrum generated with the pulsed dye laser source at 360nm, (which creates and then probes the transient), features due to both transient and residual ground state are observed. Several of the (shifted) transient features occur with the same relative intensities as ground state counterparts and must be enhanced via a similar type of transition. The intense absorption band of the transient at 360nm is therefore also assigned to a W---Carbene CT transition.

Analysis of the frequency shifts leads us to tentatively assign a cyclic structure to the transient formed after initial CO loss (Figure B1.13).

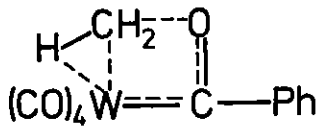

Fig B1.13 Proposed structure for the transient species formed after CO loss.

One mechanistically significant point about the proposed species is that it contains an "agostic" hydrogen, bound both to carbon and to the tungsten centre. The feature at 1105 cm^{-1} which appears in the RR spectrum of the transient is in the region where vibrations due to such an agostic species would be expected to occur. To provide support

for the assignment we are currently studying the RR spectroscopy of the deuterated ($-OCD_3$) complex. These initial results do however indicate that the RR technique is capable of providing information of considerable mechanistic value in these important complexes. Time-resolved Raman studies are also planned.

B1.4 MOLECULAR BEAM STUDIES OF THE GEOMETRY OF OXIDES AND HALIDES OF THE TRANSITION ELEMENTS

I R Beattie, T R Gilson, K Millington and S Firth
Southampton University

A knowledge of the geometry of discrete molecules of the oxides and halides of the transition element is of fundamental importance in valence theory (Ref B1.1) and is necessary for the interpretation of the molecular properties of these species. Because of the high temperatures necessary to vaporise the compounds most conventional physical techniques cannot he applied to determine the geometry of the isolated gas molecule. The approach adopted in the present experiments is to seed the sample into a high pressure (up to ten atmospheres) of a carrier gas (argon for example) followed by isotropic expansion into a rapidly pumped vacuum system operating at about 10^{-2} torr. The resultant free jet expansion containing rotationally cooled molecules is probed by a narrow band tunable dye laser. Examination of the total fluorescence while scanning the dye laser leads to excitation spectra. Ideally each line corresponds to one rovibronic transition. Thus a rotational analysis, coupled with suitable isotopic substitution can lead to both ground and excited states molecular geometries.

During Division Head's Week in January 1986 a complete molecular beam apparatus was transported to the Rutherford Laboratory. The production of a beam of nickel dichloride seeded into argon was successfully accomplished and this was crossed with the dye laser. Several fluorescence spectra were recorded in the region 335-350 nm. These spectra were not run under maximum resolution (because of difficulties with the laser line narrowing etalon), so that clear cut assignments could not be made. However the spectra did show some reproducible fine structure.

It is proposed to make further studies of $NiCl_2$ and also to examine related species such as $FeCl_2$ and $CoCl_2$ which can also be seeded into argon at temperatures of the order of 800^0 C.

B1.5 LASER PHOTOACOUSTIC SPECTROSCOPY OF C-H LOCAL MODES IN CYCLOBUTENE

J E Baggott, D W Law, P D Lightfoot and I M Mills
University of Reading

Introduction

High-energy stretching overtones of X-H bonds (X=C,N,O etc) exhibit local mode behaviour in that their positions and intensities may be understood in terms of a diatomic morse oscillator formalism, in apparent contradiction of our understanding of molecular vibrations in terms of normal modes. This apparent contradiction has been reconciled by the work of Mills and Robiette (Ref B1.2) and we are now in a position to model the vibrational structure of X-H overtones starting from either pure normal mode or pure local mode basis functions provided the necessary coupling matrix elements are included in the Hamiltonian. In the local mode representation the X-H bonds are considered as independent morse oscillators with terms allowing for coupling to any symmetrically equivalent bonds included as off-diagonal elements. Such coupling is most effective at low vibrational excitation (normal modes) but becomes overwhelmed by the effects of morse anharmonicity as the excitation is increased (local modes). Such behaviour has important consequences for vibrational photochemistry (Ref B1.3,B1.4).

As part of a continuing study of the vibrational structure of C-H local modes in cyclobutene (Ref B1.5,B1.6) we have determined photoacoustic spectra of the v=4 overtones of both methylenic and olefinic C-H bonds. The former was determined using pulsed laser techniques at RAL and the latter using intracavity CW dye laser techniques at Reading. Cyclobutene undergoes a ring-opening reaction to form buta-1,3-diene with a low threshold (ca 11300 cm^{-1}) which falls

between the two v=4 overtones. Thus, isomerisation may be induced by excitation of the olefinic v=4 overtone, and kinetic experiments are in progress in our laboratory (Ref B1.7).

Experimental

The intracavity CW dye laser techniques have been described previously (Ref B1.8). Absorption spectra of gas phase cyclobutene in the range 10600 - 11120 cm^{-1} were measured using pulsed laser photoacoustic techniques similar to those used by Perry et al (Ref B1.9). A Lambda Physik EMG 101E XeCl excimer laser was used to pump a FL2002 dye laser IR 140. Output from the dye laser was passed through a non-resonant photoacoustic cell containing a Knowles BT 1759 electret microphone. A sample pressure of 506 Torr was used. Pulse repetition rates were typically 10 Hz. The microphone signals were amplified and detected by a boxcar integrator consisting of an Ortec/Brookdeal model 9415 Linear Gate and model 9425 Scan Delay Generator. Output signals from the boxcar were transferred to an Apple IIe microcomputer via a commercial 12-bit A/D converter. The boxcar gate was usually set on the first acoustic shock wave and the amplitude of this signal was monitored as a function of excitation wavelength.

Results and Discussion

The laser photoacoustic spectra of both methylenic and olefinic v=4 C-H overtones are shown in Figure B1.14. These data have been added

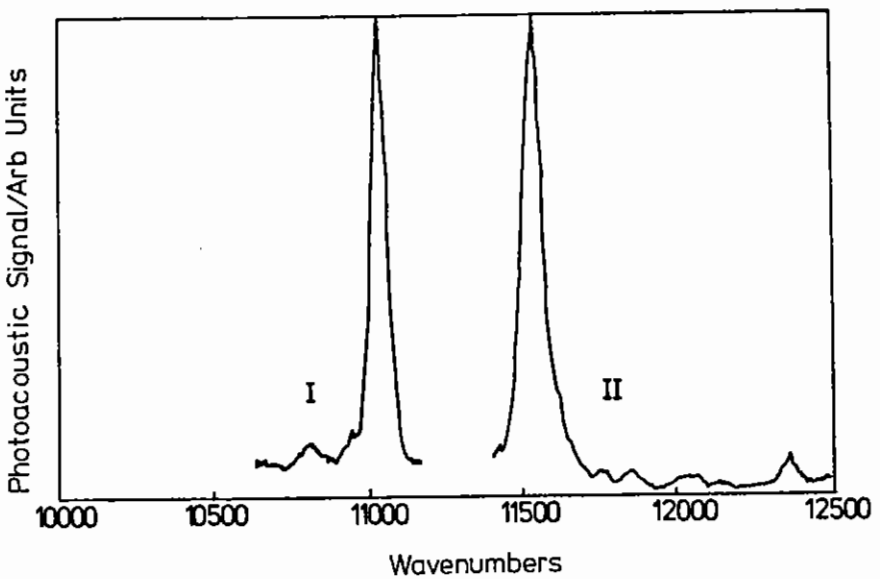

Fig B1.14 Laser photoacoustic spectra of gas-phase cyclobutene in the region of the V = 4 C - I^{-1} stretching overtones, I - determined using pulsed laser techniques, see text, II - determined using intracavity CW laser techniques.

together with similar data on the v=5,6 overtones determined using CW laser photoacoustic spectroscopy (Ref B1.6) to build up a picture of local mode effects in cyclobutene. The band positions have been modelled using two effective vibrational Hamiltonians, one for each type of C-H bond present.

Particularly relevant to the suggestion (Ref B1.3) that local mode behaviour may result in mode-specific photochemical rearrangements, we have analysed our vibrational Hamiltonians in terms of the time-dependent evolution of superposed eigenstates, using a local mode basis (Ref B1.6). Such an analysis allows us to determine the time scale over which coupling to other molecular vibrations causes probability to flow out of the initially populated local mode basis state. We have concluded (Ref B1.6) that the effects of Fermi resonances between the methylenic C-H overtones and states involving ring C-C stretch modes cause rapid loss of specificity (subpicosecond time-scale). The olefinic C-H overtone, on the other hand, shows behaviour characteristic of a 'nearly' pure local mode and we must therefore suggest that coupling between such states and the high density of background vibrational states occurs, but we cannot deduce the relevant time-scale of such coupling from our spectra. The results of kinetic studies (Ref B1.8,B1.10) indicate a picosecond or subpicosecond time-scale. Work on local modes in other polyatomic molecules is in progress.

B1.6 REACTION OF CH_3O and CH_3O_2 RADICAL

M Keiffer, M J Pilling (Oxford University)

Introduction

Reactions in the CH_3/O_2 system are of importance in combustion processes. At the lower temperatures relevant to preignition in internal combustion engines, the reactions proceed through the methyl peroxy radical, although at slightly higher temperatures this radical becomes unstable; indeed the instability of peroxy radicals is thought to be the major source of the negative temperature coefficient observed in the region between the first and second ignition stages in rapidly compressed alkane/oxygen mixtures. Clearly a detailed understanding of reactions in the CH_3/O_2 system is of central importance in this area of combustion chemistry.

We recently demonstrated (Ref B1.11) that previous flash photolysis measurements of the rate constant for reaction (1):-

$$CH_3 + O_2 + M \longrightarrow CH_3O_2 + M \qquad (1)$$

were invalidated by significant contributions from radical/radical reactions, in particular

$$CH_3 + CH_3O_2 \longrightarrow 2\ CH_3O \qquad (2)$$

By working at low radical concentrations we were able to eliminate these effects and so obtain accurate data for k_1. Analysis of data at high radical concentrations enabled estimates of k_2 to be made. The experiments also demonstrated that the reaction:-

$$CH_3O + CH_3O_2 \longrightarrow \text{Products} \qquad (3)$$

is much faster than had been realised. The purpose of the present experiments was to investigate the feasibility of measuring k_3 using flash photolysis coupled with LIF detection (for CH_3O) and absorption spectroscopy for (CH_3O_2).

Basis of Method

The basic approach is to generate CH_3O_2 and CH_3O by 193nm laser flash photolysis of mixtures of acetone, methyl nitrite and oxygen:-

$$CH_3COCH_3 \longrightarrow 2CH_3 + CO$$

$$CH_3 + O_2 \longrightarrow CH_3O_2$$

$$CH_3ONO \longrightarrow CH_3O + NO$$

such that $[CH_3O_2] \gg [CH_3O]$. The CH_3O_2 is then monitored at 254 nm by absorption, averaging the signals over a large number (~2000) of shots, whilst the CH_3O is monitored using a pulse-probe LIF technique at 293nm, the time delay between the pulse and the probe being varied to build up a decay profile for CH_3O simultaneously with that for CH_3O_2.

The method of data analysis is similar to that employed in our experiments on $CH_3 + H$, (Ref B1.12).

Experimental

The experimental system is shown in Fig B1.15. A dichroic mirror was employed to direct the photolysis laser pulse along the absorption axis. The major difficulty was to reduce scattered light from the Xe lamp and the photolysis laser at the fluorescence photomultiplier. The absorption and fluorescence techniques have opposing requirements and much of the week was spent trying various optical arrangements - in the end, satisfactory performance was obtained. Good absorption signals were recorded at 254nm and fluorescence signals for CH_3O were also recorded, albeit very weak ones. Problems were encountered with the doubling crystal and the doubled dye laser output was very low for much of the week, although satisfactory pulse energies were obtained by the end.

Conclusions

The experiment is a complex one and, in the week allocated to us, it was not possible to do more than demonstrate that the experiment is feasible. We have now acquired a CMX4 laser on loan from CEGB and hope now to complete the experiments at Oxford.

B1.7 PHOTOLUMINESCENCE FROM THE $^5D_1$ STATE OF THE EU^{3+} DECATUNGSTATE ANION IN SOLUTION

James R Darwent, Colin D Flint and Phil J O'Grady
Birkbeck College, University of London

Introduction

The luminescence of complexes of the Eu^{3+} ion in crystals, glasses and fluid solutions has been extensively studied. In dilute crystals at low temperatures it is sometimes observed that, in addition to

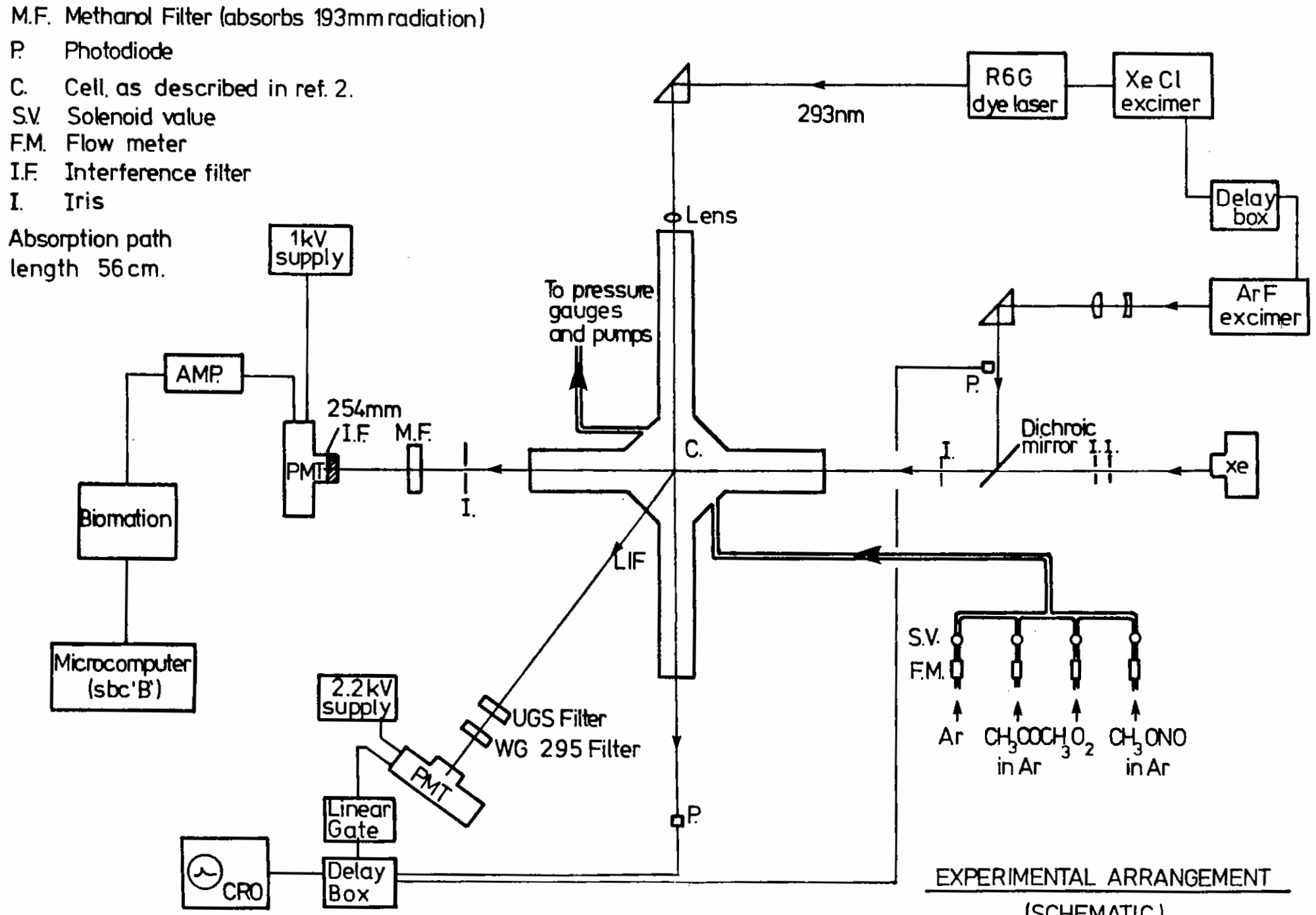

Fig B1.15 Schematic of experimental arrangement.

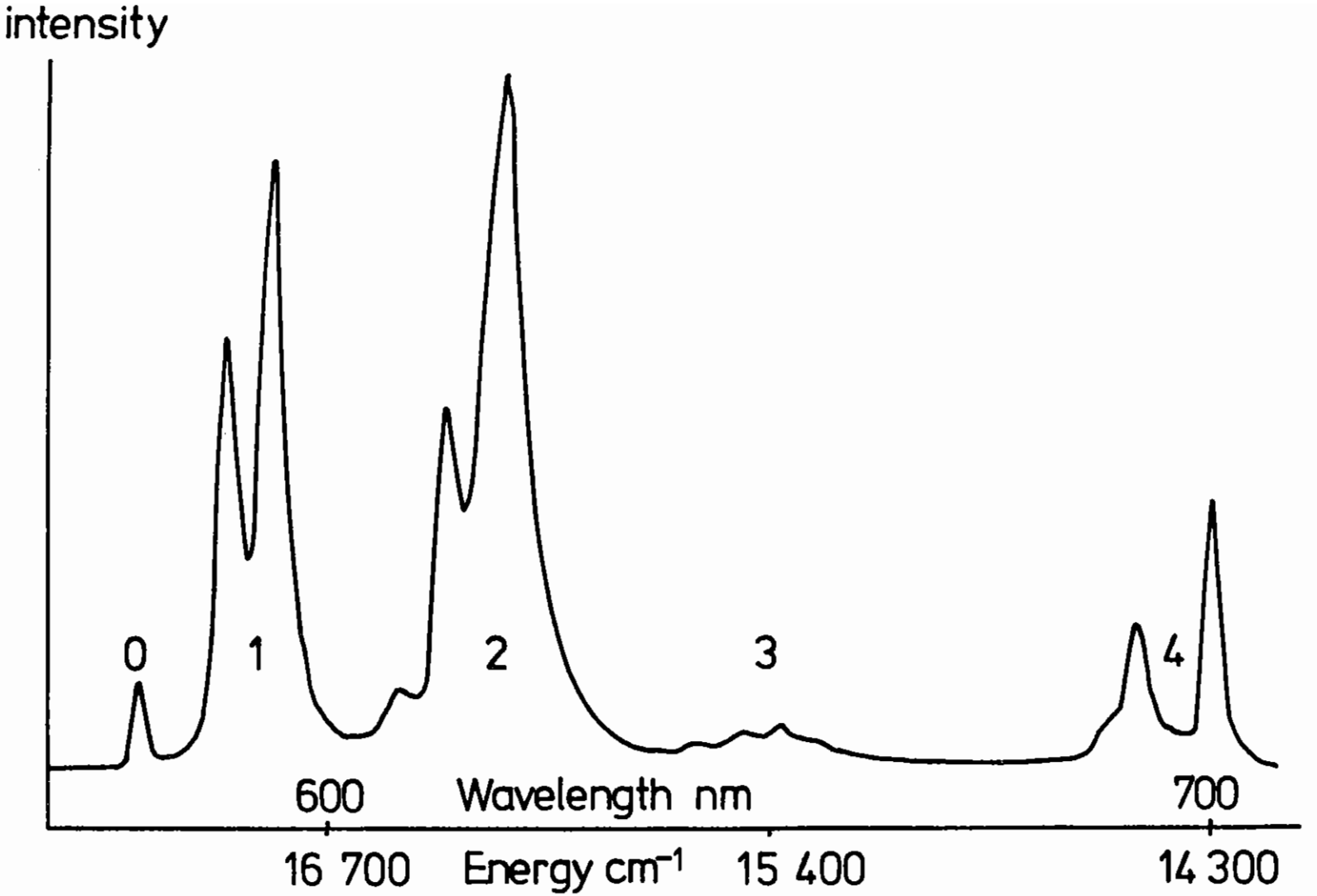

Fig B1.16 Low resolution room temperature emission spectrum of a 0.1 M solution of $EuW_{10}O_{36}^{9-}$ *in* D_2O *excited at 395 nm showing the* $^5D_0 \rightarrow {}^7F_J$ *transitions. The terminal state J values are shown.*

^5D_J(J=1,2,3) states which lie about 1800, 4100 and 7000 cm^{-1} to high energy is detected (Ref B1.13,B1.14). This emission is also occasionally observed in undiluted crystals where interlanthanide coupling is weak (Ref B1.13). As far as we are aware emission from the higher components of the ^5D Russell-Saunders term has never been observed in aqueous solutions and it is arguable that no emission would be expected since these states can relax to the lowest $^5D_0$ level by coupling to a single quantum of a high frequency vibration. Even for Eu^{3+} in YVO_4, where two vibrational quanta are required, the emission from the $^5D_1$ level was not observed although an upper limit of 4% at 4K and << 1% at 77K was placed on its contribution to the total emission (Ref B1.15).

Balzani et al (Ref B1.16) have reported that the $EuW_{10}O_{35}^{9-}$ ion shows intense luminescence in aqueous solution under UV or 394 nm excitation. In the latter case they report the quantum yield in D_2O as 0.5 and the lifetime as 3.7×10^{-3} s. They suggest that this ion may find use as an inorganic photosensitizer. The high value of this quantum yield indicates that the polytungstate ligands are effective in screening the $^5D_0$ state of the Eu^{3+} ion from multiphoton radiationless relaxation by the solvent molecules. It seemed probable therefore that in this species the solvent molecules would also be relatively ineffective in enabling the $^5D_1 \rightarrow {}^5D_0$ radiationless relaxation and that this ion may represent a case where the $^5D_1$ state would be relatively long lived and play an important role in the photophysics of this system.

Experimental

$Na_9EuW_{10}O_{36}\cdot 18H_2O$ was prepared by the method of Peacock and Weakley (Ref B1.17) and dehydrated by standing over silica gel in vacuo. Two laser systems were used for study of the photophysical properties of this ion. The first, which was used for kinetic studies and low resolution spectroscopy consisted of a EMG 150ETS Lamda-Physik Excimer laser operated with KrF producing 100 mJ of 248 nm radiation, together with a 0.2 m monochromator, R928 photomultiplier and a Philips 3305

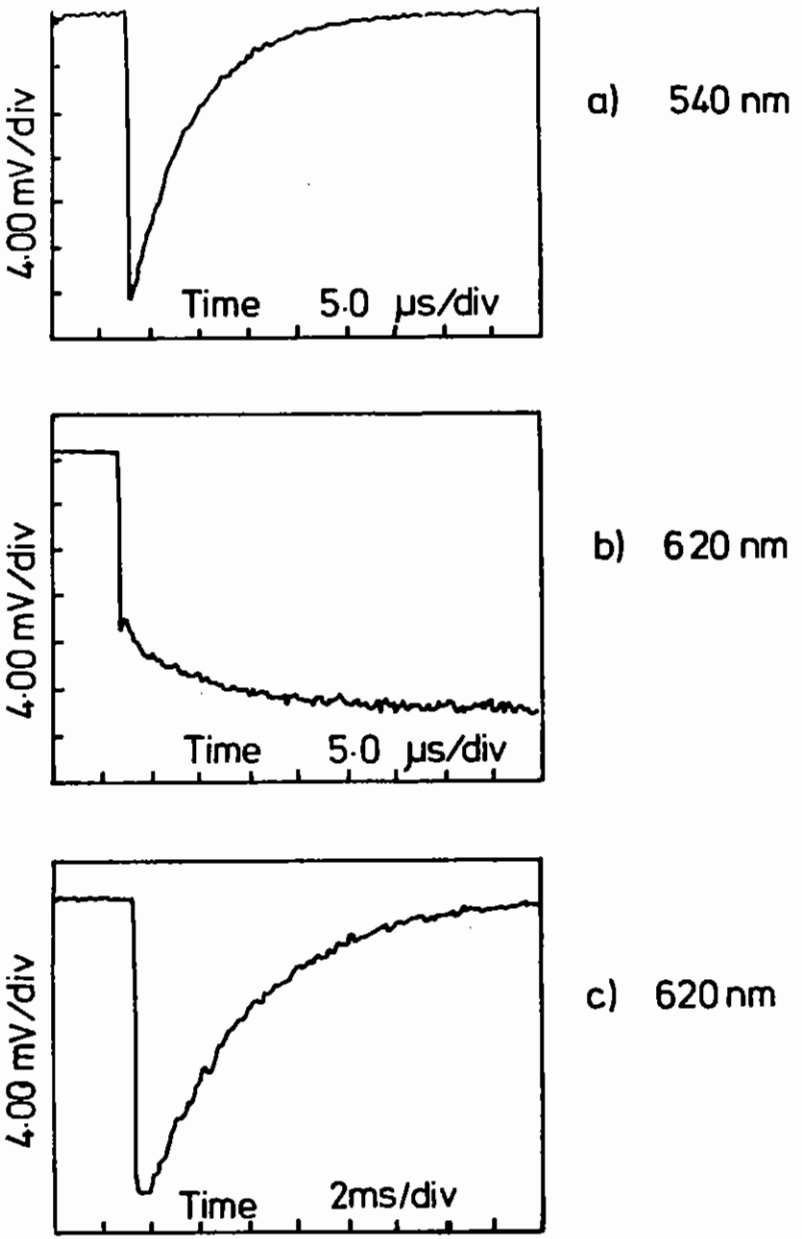

Fig B1.17 The luminescence kinetic behaviour of a 0.1 M solution of $EuW_{10}O_{36}^{9-}$ in D_2O excited at 248 nm, (a) fast decay at 540 nm, (b) fast rise of the emission at 620 nm, and (c) slow decay of the emission at 620 nm.

resolution spectroscopy consisted of a EMG 150ETS Lamda-Physik Excimer laser operated with KrF producing 100 mJ of 248 nm radiation, together with a 0.2 m monochromator, R928 photomultiplier and a Philips 3305 digital oscilloscope interfaced to a microcomputer. The second system consisted of a JK System 2000 Nd:YAG pumped dye laser which with Coumarin 480 and 30 mJ of 365nm pump produced ca 3 mJ of 468 nm radiation at the sample at 10 Hz repetition rate. The radiation was dispersed via a 600mm D460 Monospec monochromator and analysed on a PAR OMA II with an intensified diode array camera which could be gated. The gating pulse was derived from the laser with a fast photodiode which resulted in the gate opening 100 ns after the laser pulse. This prevented stray light from the laser and Raman scattering from distorting the spectra. Between 4 and 1500 laser pulses were used per measurement depending on the gate width employed. Some room temperature, low resolution spectra were measured using a Perkin-Elmer MPF 3 spectrofluorimeter. Low temperature solid state spectra were measured using a CF100 continuous flow liquid helium cryostat.

Results

The room temperature 395 nm excited luminescence spectrum of a 0.1 M solution of $EuW_{10}O_{36}^{9-}$ in D_2O is shown in Fig B1.16. The spectrum is similar to that reported by Balzani et al. Measurement of the luminescence decay curve at room temperature as a 0.1M solution in D_2O with 248 nm excitation and the observation wavelength as the major emission maxima gave an exponential decay with a lifetime of 2.3×10^{-3}s which increases to 3.8×10^{-3}s when the concentration is reduced to less than 10^{-4} M. Under higher time resolution it was clear that this emission had a rise time with a time constant of 7.1×10^{-6} s independent of concentration and that a second emission process with a decay time equal to this rise time gave luminescence at 19 000, 18 650, 18 000 17 100 and 16 030 cm^{-1}. This kinetic behaviour is shown in Fig B1.17. The wavenumbers of these transitions indicates that they arise from a state some 1790 cm^{-1} to high energy of the $^5D_0$ which can only be identified as the $^5D_1$ state of the $EuW_{10}O_{36}^{9-}$ complex.

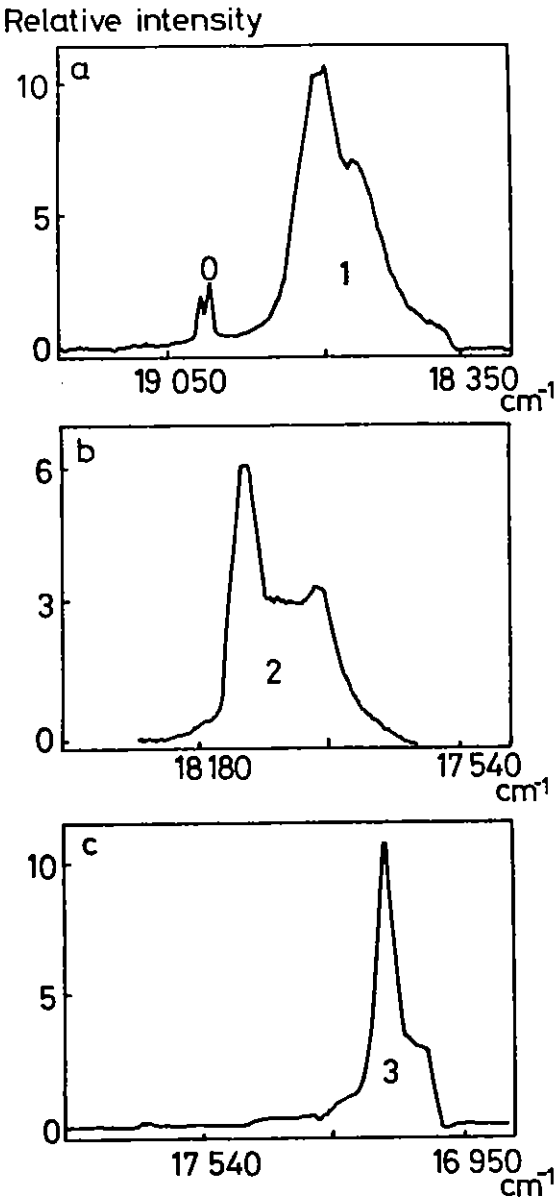

Fig B1.18 High resolution room temperature emission spectrum of a 0.1 M solution of $EuW_{10}O_{36}^{9-}$ in D_2O excited at 467.8 nm, using a 2×10^{-6} s observation window centred at (a) 1.1×10^{-6}s, (b) 7.1×10^{-6} s and (c) 21.1×10^{-6} s after the laser pulse. The half-life of the $^5D_1$ state is 4.9×10^{-6} s. The low energy emission in (a) is due to the $^5D_1 + {}^7F_4$ transition.

The same two emission processes were also observed with excitation into the $^5D_2$ level at 21 375 cm^{-1} and under higher spectral resolution the short-lived emission could be resolved into several components. These spectra were most conveniently obtained by using a 10^{-5} s observation window starting 10^{-7} s after the laser pulse (Fig B1.18). The $^5D_1 \rightarrow {}^7F_3$ emission (17 000 cm^{-1}) lies under the $^5D_0 \rightarrow {}^7F_1$ transition and Fig B1.18c has been obtained by subtracting the long lived emission. This has resulted in some distortion in the wings of the spectrum. The $^5D_1 \rightarrow {}^7F_4$ (16 030 cm^{-1}) is a weak emission in the same region as the strong $^5D_0 \rightarrow {}^7F_2$ transition. It is seen most clearly as a

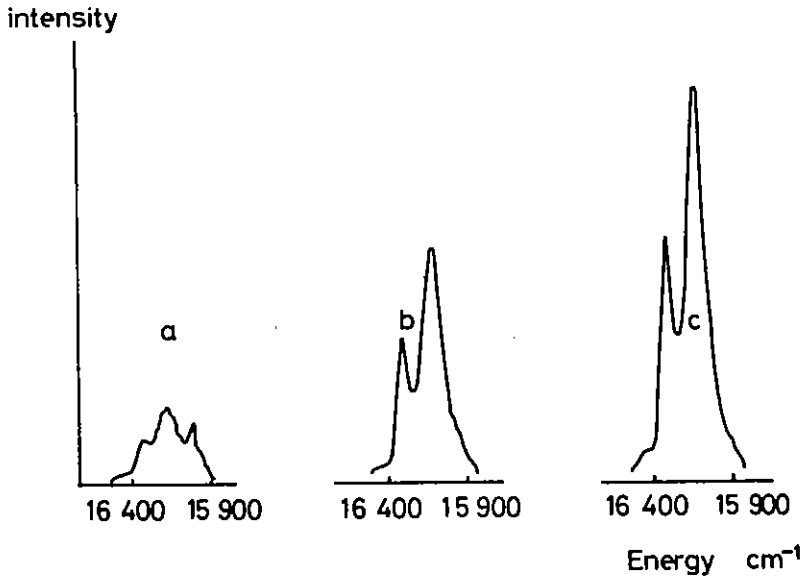

Fig B1.19 Time evolution of the 620 nm emission of a 0.1 M solution of $EuW_{10}O_{36}^{9-}$ in D_2O excited at 467.8 nm, using a 2 x 10^{-6} s observation window centred at (a) 1.1 x 10^{-6} s, (b) 7.1 x 10^{-6} s and (c) 21.1 x 10^{-6} s after the laser pulse. The half-life of the $^5D_1$ state is 4.9 x 10^{-6} s. The low energy emission in (a) is due to the $^5D_1 \rightarrow {}^7F_4$ transition.

low energy line in the first of the time resolved spectra (Fig B1.19). Measurement of the development of the luminescence as a function of time following pumping of the $^5D_2$ state shows that >97% of the population of the $^5D_0$ state is from the $^5D_1$ state rather than directly (Fig B1.19). In contrast pumping into polytungstate bands with 248 nm radiation results in more than 20% direct population of the $^5D_0$ within 100 ns of the laser pulse.

The luminescence and excitation spectra in H_2O are similar with all the main features shifted a few cm^{-1} to lower energy. At low concentrations the $^5D_1$ state has a lifetime of 3.7 x 10^{-6} s increasing to 4.8 x 10^{-6} s at 0.1 M which is equal to the risetime of the $^5D_0$ emission. The lifetime of the $^5D_0$ state also changes from 260 x 10^{-6} s to 1.8 x 10^{-3} s as the concentration is increased.

In this work we have shown that two long lived luminescent states of $EuW_{10}O_{36}^{9-}$ can be observed in aqueous solution at room temperature. Their well established spectroscopic properties and precisely defined energy levels should be well suited for energy transfer studies. If this ion is used as a photosensitizer, as suggested by Balzani et al, then both of these states may be exploited.

B1.8 LASER-INDUCED DESORPTION OF PHYSISORBED ATOMS AND MOLECULES

J P Hardy (RAL)
C J S M Simpson (Oxford University)

Introduction

Laser-induced desorption (LID) of molecules and atoms physisorbed or chemisorbed on surfaces has been used to probe the nature of energy transfer at surface/absorbate interfaces. Desorption may be induced by rapid heating (>10^{10} K/sec) of the surface with a nanosecond laser pulse or by resonant excitation of internal modes of the adsorbate.

Both kinds of experiment have shown that molecules desorb with very low translational energy. For the non-resonant, thermal desorption case, velocity distributions for desorbed species are typically far below the final temperature achieved by the substrate during the laser pulse (Ref B1.18).

This observation has lead to some speculation that for the very fast heating rates induced by a nanosecond laser pulse, the atom or molecule does not fully equilibrate with the surface before desorption occurs. Cold translational temperatures may therefore reflect non-equilibrated rotational, vibrational and translational degrees of freedom.

Alternatively, it has been argued that the overriding constraint on the translational temperature of departing atoms and molecules is the potential well depth that must be overcome before desorption can occur. Depressed translational temperatures are seen in this case as evidence of an adiabatic or near-adiabatic desorption process in which energy transfer from the surface is not fast enough on a nanosecond timescale to replenish the energy used by the desorbing species to overcome the potential well depth (Ref B1.19).

The LID experiments performed at the RAL were a comparative study of the atoms Ar and Xe, and the molecules O_2, CO and H_2O physisorbed on polycrystalline copper. The aim was to clarify the issue of the relative importance of non-equilibrium effects, internal energy tranfer or adiabatic processes during desorption.

Experimental

A polished polycrystalline copper plate was used as the substrate. It was placed in a UHV chamber (base pressure 5×10^{-10} torr) and cooled with liquid He to the 25 to 40K range. Monolayer and multilayer deposition of adsorbates was achieved by introducing via a bleed valve the appropriate gass to a pressure in the 1 to 5×10^{-9} torr range as measured by the quadrupole mass spectrometer (QMS). The probe was cooled steadily until pressure reduction indicated that deposition had occurred.

The Lambda Physik FL2002 dye laser was used to irradiate the surface (585nm, 12ns fwhn, 45° angle of incidence). After aperturing to 1.5mm diameter, the pulse energy at the surface was varied in the range 1 to 3mJ (4-12 MW cm^{-2} peak power). The absorbtivity (ratio of reflected intensity to incident intensity) for the sample for these intensities was .5 to .6.

Desorbed molecules and atoms travelling normal to the surface were detected by the QMS. The ionizer of the QMS was shielded by a liquid N_2 cooled shroud which acted both as a cooled aperture to prevent molecules undergoing collisions with chamber walls from entering the ionization region, and as a shield to reduce radiative heating of the cold surface by the filament. The time of flight (TOF) distance was set at 69mm. Signal from the mass spectrometer was digitized and displayed on an oscilloscope.

Results and discussion

Table B1.2 summarizes the results obtained on the LID experiments. The temperature increase of the Cu substrate resulting from the laser pulse was calculated to be in the region of 200 to 300K (Ref B1.20). The translational temperature for the desorbed species was calculated from the maximum of the observed TOF distribution using

$$T = \frac{d^2}{t^2} \frac{m}{4K}$$

where d is the TOF distance, t is the time corresponding to the maximum in the distribution and m is the mass of the species desorbed.

Figure B1.20 shows a typical fit obtained by using the Maxwell-Boltzmann distribution corresponding to the temperature obtained in this manner.

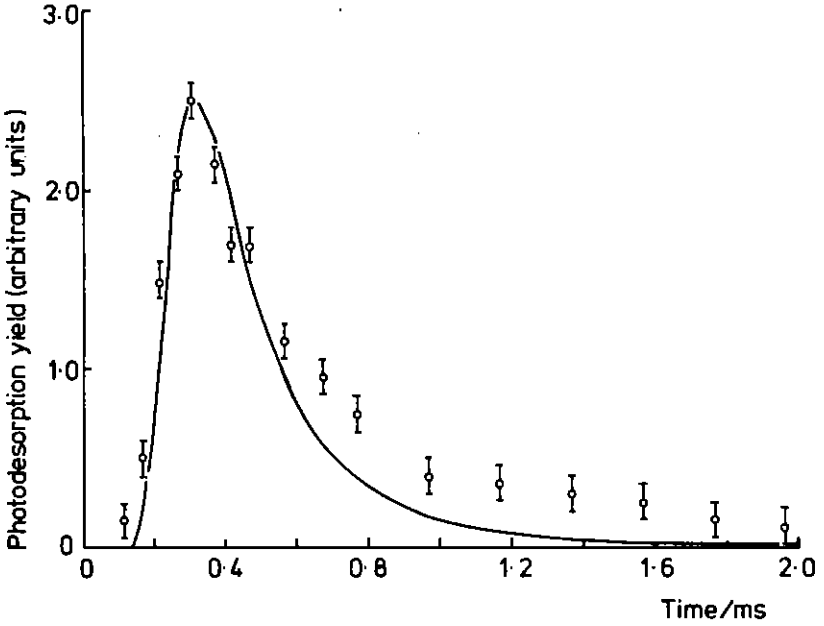

Fig B1.20 Experimental photodesorption yield for Ar multilayers, incident laser intensity 6 MW cm^{-2}. Solid line, Maxwell-Boltzmann distribution for 58K.

All species considered clearly desorb with translational temperatures far below the final temperature of the substrate. For low coverages of O_2 and CO the translational temperature is depressed even relative to the starting temperature. The O_2 data shows that the desorption temperature is very sensitive to coverage, with multilayer coverage resulting in the highest translational temperatures.

Ar and Xe desorbed from multilayers show similar translational temperature suggesting that energy transfer to internal degrees of freedom is not responsible for the cold temperatures observed. In fact, calculations show that even if cooling by collisions was occurring, the observed translational temperature was still lower than the maximum T to R transfer possible.

The desorption of molecules or atoms from multilayers which are transparent for the incident radiation will not be a direct process. The initial and very rapid heating of the Cu substrate and the corresponding monolayer of adsorbate immediately adjacent to it will be transferred at a slower rate through the successive layers until the final layer achieves a sufficient temperature for desorption to occur. The higher translational temperature for atoms or molecules desorbing from multilayers suggest that the process is slowed down sufficiently for the desorbing particle to continue to receive energy from the surface, or its neighbouring energetic adsorbates while it climbs up the potential well before desorbing.

The latent heats of evaporation of Ar, O_2 and Xe are 7.9kJ mol^{-1}, 9.3kJ mol^{-1} and 15.4kJ mol^{-1} respectively and these species desorb with corresponding temperatures of 75, 60 and 57K. These preliminary experiments therefore provide evidence that the deeper the potential well, the more slowly the molecule or atom will depart for a given heating rate.

Further evidence for this contention is also provided by the desorption of H_2O which has been coadsorbed with Ar. H_2O desorbs at a much lower temperature than the surrounding Ar atoms. Thus the lower temperature of the desorbed H_2O is a reflection of the greater binding energy of the H_2O in the Ar lattice compared with Ar itself.

The results of these preliminary experiments provide strong evidence that the major cause of subthermal velocities for atoms or molecules desorbed by nanosecond laser pulses is that the desorbing species leaves the surface faster than energy can be transferred from the surface to the absorbate. That is, on the nanosecond timescale of these experiments, the desorption process is adiabatic or near adiabatic, resulting in low translational and presumably rotational energy in departing molecules. It is not necessary to evoke non-equilibrium heating of the adsorbate to explain results.

Table B1.2

Material Absorbed	Initial Temperature[a]	Desorbed Species Temperature[b]	State of Adsorption
O_2	34	13 ± 3	sub monolayer
O_2	30	47 ± 7	monolayer
O_2	26	60 ± 10	multilayer
CO	30	20 ± 5	monolayer
Ar	25	75 ± 17	multilayer
H_2O	25	24 ± 5	co-adsorbed with Ar
Xe	40	57 ± 15	multilayer

(a) ± 1 K

(b) For description from multilayers the measured temperature depends upon the thickness of the adsorbed layer; the average values of the temperature are given.

These results were obtained using a Cu surface which had not been subjected to any special cleaning procedure. We have just completed some initial work in the same apparatus using a titanium polycrystalline surface which has been cleaned with an Ar atom gun. Ar and CH_4 desorb with similar temperatures, lending further support to the conclusion that internal energy transfer is not responsible for translational cooling. Further work on different cleaned metallic and dielectric surfaces should enable more quantifiable data on the effect of potential well depth on translational temperatures for desorbing particles. It should also be possible to extract information on rates of surface diffusion for weakly bound adsorbates.

B1.9 FLUORESCENCE OF DISSOCIATING MOLECULES

J G Frey (Southampton University)

Attempts were made to observe high overtone Raman/fluorescence emission during the dissociation of iodomethane following excitation at 248nm with the EMG150 line narrowed KrF excimer laser. The molecules are excited to a repulsive state from which emission is very weak owing to the competing non-radiative processes. The emission that does occur provides a considerable amount of information on the structure of the highly excited molecule and the sub-picosecond dynamics of the dissociation, including the details of the nuclear motion during dissociation. The connection between the band intensities and frequencies and the potential energy surface is made with the time-dependent formulation of Raman scattering developed by Heller. The initial excitation transports the ground state wavefunction on to the excited state surface. As it is no longer an eigenstate it will evolve with time, moving out along the potential energy surface towards dissociation. The emission of radiation, governed by Frank-Condon overlap considerations, occurs to higher and higher vibrational levels of the ground state. The long progressions of the ground state vibrational mode that should occur will map out the progress of the wave packet on the excited state surface and thus the progress of the dissociation.

Initially there were some problems with the EMG150 and with the monochrometer which were resolved within the first few days. The laser radiation was then focussed into a simple flow cell. The flow rate and pressure were adjusted so that the viewing region was irradiated (too high a pressure and the radiation would be totally absorbed at the front of the cell). The fluorescence was collected with a simple imaging system and focussed onto the monochromator slit, with the output recorded on the OMA. While some Raman signals from air could be seen, little could be recorded from the iodomethane despite extensive signal averaging.

These test experiments indicate that improved optics are needed to collect a much greater fraction of the emitted radiation. This coupled with a more suitable monochromator should ensure the success of the experiment.

B1.10 PICOSECOND DIFFUSE REFLECTANCE LASER FLASH PHOTOLYSIS

F Wilkinson, C J Willsher and P Leicester (Loughborough University) and M J C Smith (RAL)

Introduction

Flash photolysis has been proved to be an invaluable technique to study primary photoprocesses in a large number of systems (Ref B1.21), and has now been successfully extended by us to include opaque materials by employing as the analysing source light diffusely reflected from a sample in order to monitor transient absorption following pulsed laser excitation (Ref B1.22). By means of nanosecond "Diffuse Reflectance Laser Flash Photolysis" we have successfully studied transients in a wide range of samples, including microcrystalline ketones (Ref B1.23), inorganic phosphors (Ref B1.24), dyed fabrics and polymers (Ref B1.25), doped semiconductors (Ref B1.26) and from a variety of organic molecules adsorbed on or intercalated in oxide substrates (Ref B1.27). The development of picosecond lasers has extended the study of transient absorptions in homogeneous or transparent media to the nanosecond and sub-nanosecond time scales (Ref B1.28), but all such improvements in time resolution have been reported exclusively for

optically transparent systems using transmission flash photolysis. We have now successfully carried out the first ever experiments of "Picosecond Diffuse Reflectance Laser Flash Photolysis" using xanthone adsorbed on silica gel in the form of an opaque white powder. This sample has already been studied by us using nanosecond diffuse reflectance laser flash photolysis and a triplet-triplet absorption centred on 590 nm was easily identified, which makes it an ideal material to pump at 295 nm and probe at 590 nm using wavelengths which are readily available on the picosecond laser RAL. We now show that the growth of the xanthone triplet can be followed by directly measuring the level of the probe beam diffusely reflected from the sample by varying the delay between the pump and probe beams.

Experimental

Generation and detection of the transient absorption was effected by pumping the sample at 295 nm (pulse width = 6 ps, energy = 20 μJ) and probing at 590 nm (energy = 1 μJ), using the Spectra-Physics picosecond laser system at RAL. Light diffusely reflected from the sample was detected by a filtered photodiode, and the signal fed to a Boxcar Integrator and thence to a IBM microcomputer. A second photodiode monitored a portion of the probe beam taken before hitting the sample, in order to correct for shot-to-shot variations. The sample of xanthone contained 11.5 mg of xanthone per 5 g of silica ("Davasil", with a particle radius of 60 Å and surface area of 480 $m^2 g^{-1}$) and was held in a powder holder behind a quartz window. Nearly colinear pump and probe beams were incident normal to the quartz window, with the pump beam about 2 mm in diameter and the probe beam located entirely within the excited area of the sample. A portion of the diffusely reflected probe beam was detected by the photodiode. Figure B1.21 illustrates the basic arrangement for carrying out transient absorption measurements, and the method of extracting information on the transient absorption from the photodiode signals is given below.

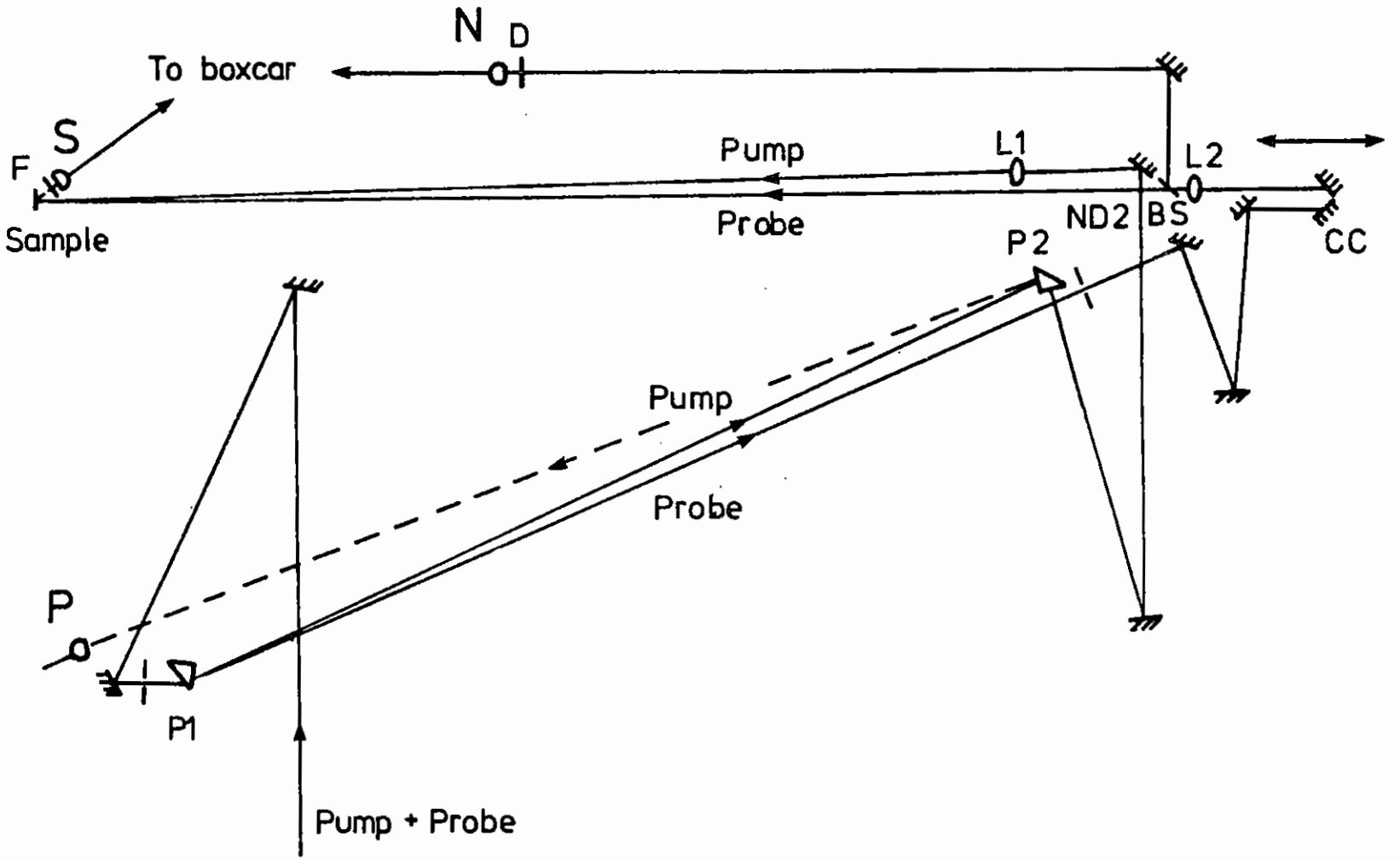

Fig B1.21 Experimental layout, showing prism P1 used to separate the 295nm and 590nm beams, and the movable corner cube CC used to adjust the timing.

The signal detected from S with both pump and probe beams on is:

$$S_{on} = aJ_t^{590} + \beta E + b_1$$

where J_t^{590} is the reflected light modified by transient absorption at the probe wavelength, E is the emission induced by the pump and transmitted to the photodiode by the filter, and b_1 is the background signal. With the pump beam off the signal is:

$$S_{off} = aJ_b^{590} + b_2$$

where J_b^{590} is the reflected light from the background at the probe wavelength, and b_2 is the background signal. Since $R=J/I_o$ (where R is the diffuse reflectance, and I_o is the incident probe intensity), then

$$S_{on} = aR_t^{590}I_o + \beta E + b_1$$

and $S_{off} = aR_b^{590}I_o + b_2$

The signal from the normalisation detector N is:

$$N = \gamma I_o + b_3$$

where b_3 is the background signal from this detector. Baseline offsets (b_1,b_2,b_3) were all small and amounted to less than 5% of the signal from S or N. In addition, negligible emission was detected from the sample when pumping at 295 nm, so the term βE is insignificant in this case.

A plot of S_{on} vs N normalises for shot-to-shot variation and gives;

$$slope_{on} = (S_{on} - b_1)/(N - b_3) = aR_t^{590}/\gamma$$

and similarly for S_{off}:

$$slope_{off} = (S_{off} - b_2)/N - b_3) = aR_b^{590}/\gamma$$

The ratio of transient reflectance to background reflectance is;

$$R_t^{590}/R_b^{590} = slope_{on}/slope_{off}$$

and the transient absorption of the sample is therefore;

$$1-(R_t^{590}/R_b^{590}) = 1 - (slope_{on}/slope_{off}) = \Delta R^{590}/R_b^{590}$$

Results

To record transient absorption (which is, strictly speaking, the relative decrease in diffuse reflectance), signals due to the probe beam alone and due to simultaneous pump and probe were obtained. Each run comprised 100 shots, with normalisation for shot-to-shot variation carried out as described above. Transient absorption following excitation at the pump wave-length reduces the level of the diffusely reflected probe beam. This has been observed for different delays between the pump and probe beams incident on the same area of sample. The results obtained are shown in Figure B1.22. It can be seen that the transient absorption at 590 nm has a rise-time (1/e) of about 200ps, and at later times, up to the maximum delay studied, the intensity of the diffusely reflected probe pulse levels off to a constant value, which represents an 8% absorption of the probe beam. It has been found from nanosecond diffuse reflectance laser flash

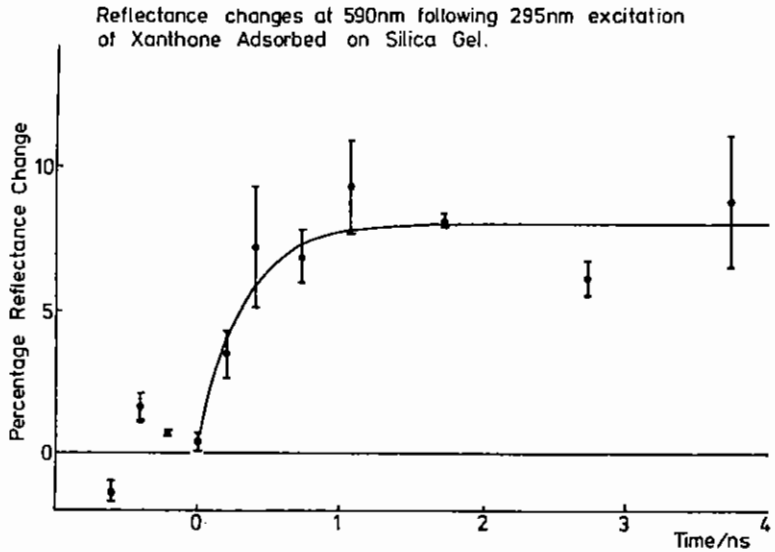

Fig B1.22 Change of diffuse reflectance of xanthone on silica gel as a function of delay between pump and probe beams. Pump wavelength = 295nm, probe wavelength = 590nm.

photolysis of this sample that the transient absorption eventually decays on the microsecond timescale. These results represent the first observation of the growth of an absorption in an opaque sample following picosecond excitation due in this case to the production of the triplet state in xanthone, but spectral information will be required to confirm this assignment.

B1.11 TWO-PHOTON SPECTROSCOPY OF URANYL COMPOUNDS

R G Denning, J R G Thorne and T J Barker (Oxford University)

This report describes the continuation of our study of the elecronic structure of the uranyl ion by two-photon absorption spectroscopy. The background to this study was presented in last year's report. During the year we have extended the study to new compounds, including some with oxygen isotope substitution, and extended the wavelength coverage by using the Facility's Nd:YAG pumped dye laser. This laser has allowed us to work with the first Stokes output of a hydrogen Raman cell giving 1 mJ pulse energies in the spectral region close to 1 micron.

The work on $Cs_2UO_2CL_4$ single crystals is now complete. A description of the electronic structure of the uranlyl ion, which has unusual chemical stability, is the objective of this work. The complexity of the problem is illustrated by the fact that fourteen parity conserving pure electronic transitions are found in the energy range from $20{,}000cm^{-1}$ to $32{,}000\ cm^{-1}$. In addition the higher energy portion of this spectrum shows evidence in one-photon absorption (OPA) of broad intense parity changing transitions. In the face of this complexity the two-photon absorption (TPA) spectrum shows remarkable simplicity. Only the pure electronic transitions and sidebands due to the gerade vibrations are observed in place of the electric dipole vibrationally induced intensity of OPA. In the latter case the polarity of the vibrations lead to a strong dispersion with respect to the photon wave-vector so that the spectrum displays structure which reflects the phonon density of states modulated by the electron-phonon coupling. Such dispersion is completely absent from the electronic origin bands observed in TPA, while the gerade vibrations, which exhibit a higher order polarity, have much smaller dispersion. As a consequence it is possible to measure the true homogeneous width of the origin bands in favourable circumstances.

It is not practicable to present the full analysis of the spectrum here. Instead we pick out four illustrative examples. First we can observe, with a signal to noise ratio of 10:1, transitions in which one quantum of the uranyl symmetric stretching mode is superimposed on a

pure electronic transition in the cation containing the natural abundance of oxygen-17; the cation concentration being 0.075%. This illustrates the remarkable dynamic range over which the experiment can detect sharp features, and has far-reaching consequences for the implications of our study because it has been argued that the analysis of he electronic structure may be flawed if weak electronic transitions have not been detected. With the sensitivity now obtained we are able to make a positive assignment of every spectral feature in the region below 28,000 cm^{-1} at an intensity, throughout the majority of the spectrum, equal to one thousandth of that of the most intense features.

Second, we find that one of the twelve electronic states in the low energy region of the spectrum has a width of 10 cm^{-1} compared with values of less than 1 cm^{-1} for the remainder of the transitions. Using the two-photon polarisations and the changes in the spectrum which occur on oxygen-18 substitution , it is possible to show that this width is due to the rapid relaxation of this state into identifiable vibronic states associated with lower electronic states. The mechanism of the coupling is helpful in determining the one-electron configurations which underlie these transitions.

Third, we observe a distinct progression in the UO_2 rocking mode in which the linear triatomic unit undergoes a symmetric displacement with respect to the plane formed by the four chlorine atoms in such a way as to preserve the two-fold axis in the C_{2h} crystallographic site. We interpret this in terms of a small charge displacement from oxygen to uranium , in the course of the electronic excitation, which modifies the interaction between the oxygen atoms and the cesium ions in neighbouring positions in the lattice.

Finally, we observe two electronic states in the region above 29,000cm^{-1} which provide very strong and broad TPA. This part of the OPA spectrum is completely opaque due to a broad intense parity-allowed transition. Nevertheless the TPA spectrum (Fig B1.23) shows well defined progressions in the UO_2 symmetric stretching mode with frequencies that suggest that they share the same configurational parentage as the low energy transitions. The origins of these

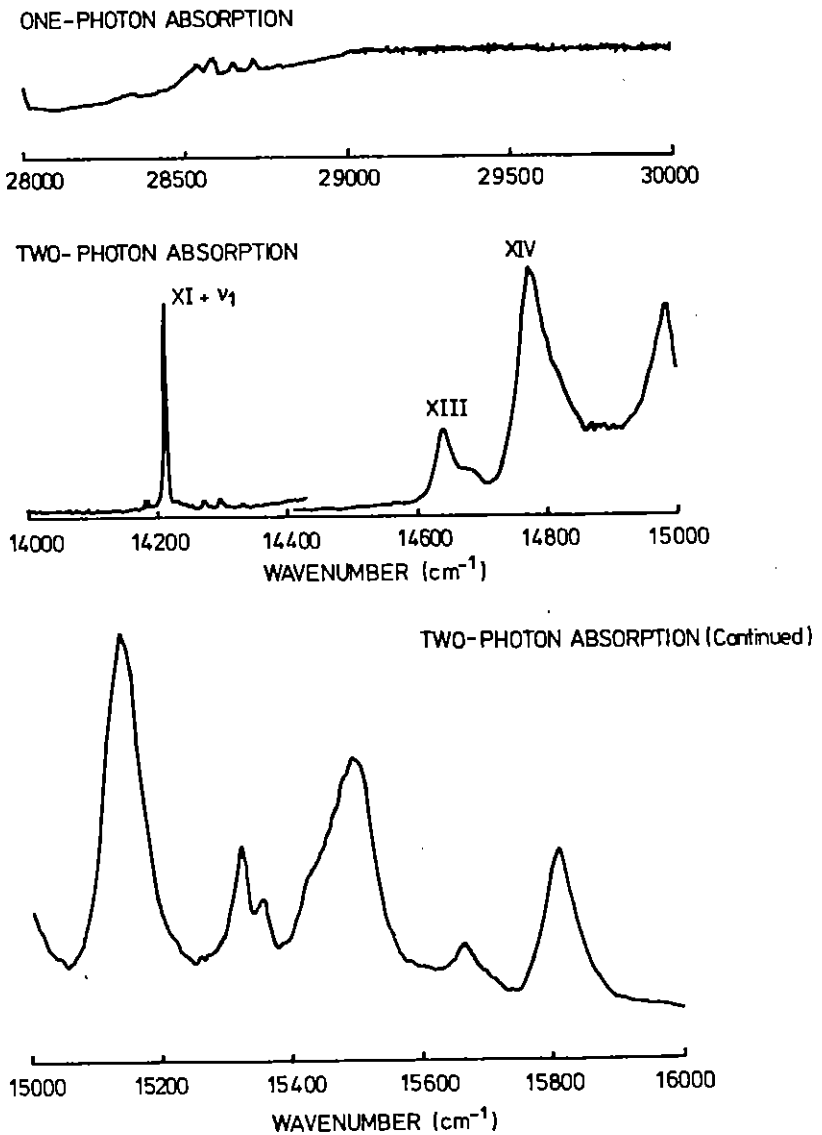

Fig B1.23 One and two-photon absorption spectra of single crystals of $Cs_2UO_2Cl_4$ at 4.2K between 28000 and 32000cm^{-1}.

progressions have the same 10 cm^{-1} positive oxygen-18 isotope shift as the other electronic origins, confirming that the change in the zero point vibrational frequencies is of the same magnitude in all the states. The polarisations of these bands imply that they correspond to an excited state which would have symmetry in the cylindrical ion. This is particularly interesting because our previous theoretical model of the electronic structure predicted (Ref Bl.29) an electronic state with this symmetry in the high energy part of the spectrum, but such a state could not be observed in OPA. Quantitatively our simple parameterisation of the perturbations of the valence electrons failed because this state was predicted to lie at an energy where it should have been observable. With this state now clearly located in TPA it is possible to refine the model. In particular we find that the TPA data is consistent with the predictions of a new ab initio calculation (Ref Bl.30) which includes the change in the core potential when the large relativistic corrections for electrons with low azimuthal quantum numbers are taken into account. The effect is to destabilise those orbitals which have significant f-electron character in relation to the other orbitals. The calculations show that the effect is largest for the configuration which is responsible for the transitions in Figure 1.11.1 and serves to explain the deficiencies of our elementary model.

Finally we have extended our study to include single crystals of $CsUo_2(NO_3)$ and $NaUO_2(CH_3COO)_3$, where the effects of quite different ligand environments can be studied.

We wish to acknowledge support from the SERC and our appreciation for the valuable assistance of Laser Facility staff.

Bl.12 A NEW RADICAL: CCF?

R N Dixon, M J Trenouth and C M Western (University of Bristol)

We report here the observation of a new band at 315 nm which we believe to be the previously unobserved species CCF. It was found by chance in the course of studies on the methoxy radical CH_3O.

Experimental Methods and Results

The experiments were performed in a low pressure (100 m Torr) flow system involving the reaction of fluorine atoms (produced by a microwave discharge in 100 m Torr at a 10% F_2 in He mix) with a few m Torr of various simple organic compounds. The reaction took place in a standard laser induced fluorescence cell with baffle arms and a lens system to collect light onto a photomultiplier. A long pass filter was used to block scattered laser light for total fluorescence excitation spectra; this was replaced with a mono-chromator to obtain dispersed fluorescence spectra. Excitation was achieved with the laser loan pool's JK system 2000 YAG-pumped dye-laser with the output doubled in an INRAD second harmonic generator.

The fluorescence excitation spectrum of the new band is shown in Fig Bl.24; the reaction F. $+CH_3OH$ was used in this case. Despite extensive searches either side of this band no other similar vibrational bands could be seen though features due to CH_3O and CH were observed. In contrast, the dispersed fluorescence spectrum (Fig Bl.25) shows extensive vibrational structure with two vibrational frequencies, 1280cm^{-1} and 1920cm^{-1}.

The band does not correspond to any well known one (Ref Bl.31) so the reaction was varied to aid identification. The reaction F. $+CD_3OD$ gave the same spectrum indicating the absence of H. Both F. + $CH_3CH_2OHCH_3$ and F. $+C_5H_{12}$ gave much stronger, but otherwise indentical signals indicating the absence of O. In contrast, the reaction of air and F. did not give the unknown band implying the compound did contain carbon. Likewise a microwave discharge in pentane only, which is known to give rise to species such as C_2 and C_3 (Ref Bl.32) gave no bands in the region of interest.

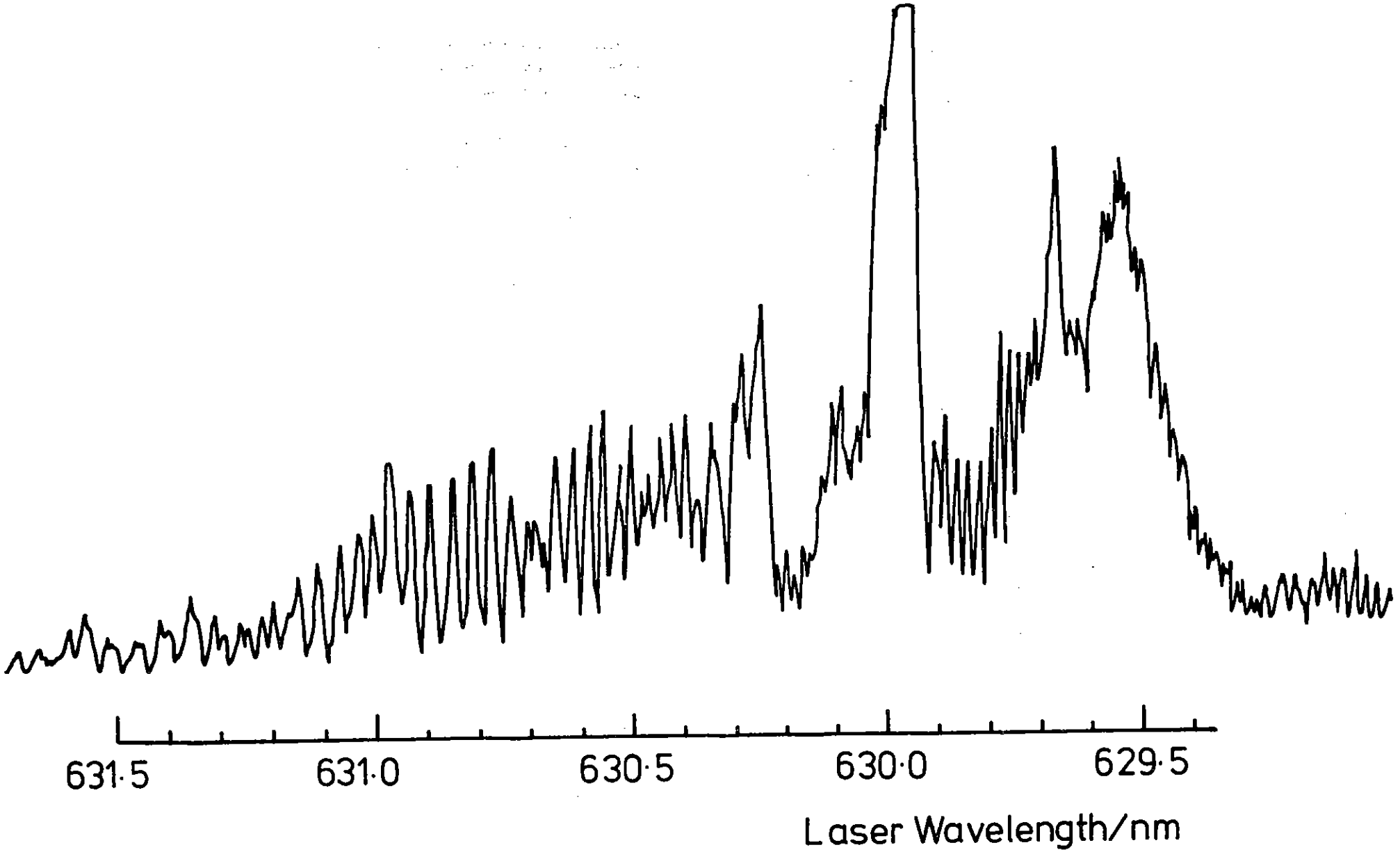

Fig B1.24 Fluorescence excitation spectrum of the new species. The absorption actually takes place at twice the frequency of the laser.

We concluded that the band was due to a compound containing only C and F; however the spectroscopy of the obvious candidates CF (Ref B1.33), CF_2 (Ref B1.34) and CF_3 (Ref B1.35) is reasonably well understood and none show bands corresponding to Fig B1.24. Interestingly the spectrum is not produced by a discharge in CF_4, a source for CF_n, though it is seen if hydrocarbons are added as this is also a source of F.

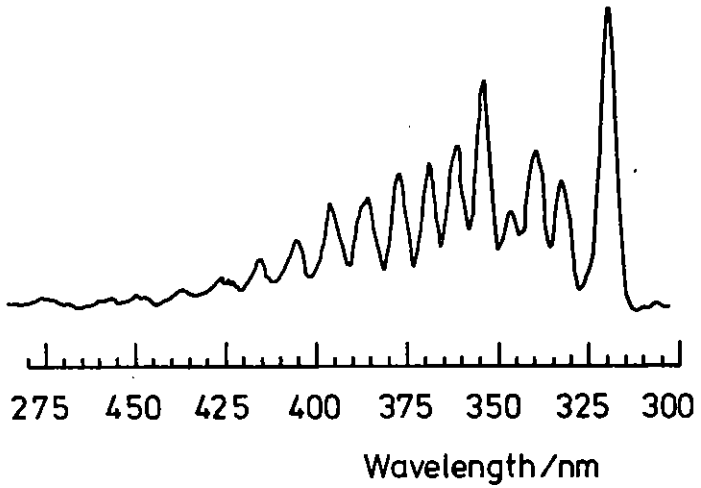

Fig B1.25 Dispersed fluorescence spectrum of the new species. The exciting laser was fixed on the strongest bandhead in the excitation spectrum. The vibrational transitions seen can be assigned to progressions in two frequencies, 1280cm^{-1} and 1920cm^{-1}.

Discussion

The excitation spectrum shows several clear branches which is most typical of an open shell linear molecule. The rotational spacing (<1cm^{-1}) suggests 3 heavy atoms which is consistent with the two vibrational frequencies seen in emission. We therefore propose that the species is the C_2F radical whch has not been seen before. The only

theoretical guidance available is a discrete-variational Xα calculation (Ref B1.36) which unfortunately does not predict an absorption at 315 nm.

A preliminary analysis indicates that neither of the states involved is a Σ state but a reasonable reproduction of the spectrum can be obtained assuming it is a $^2\Delta - {}^2\Pi$ transition. A more detailed analysis is underway and we hope to confirm our assignment with ^{13}C isotopic substitution.

An interesting feature which merits further study using different techniques is the lack of any other vibrational bands. The long progression seen in emission implies that there should be many strong bands seen in absorption so their absence in fluorescence excitation spectra is presumably due to a predissociation which must be strongly dependent on vibrational state.

B1.13 MULTIPHOTON LASER SPECTROSCOPY OF THE $2^1\Sigma^+$ ELECTRONICALLY EXCITED STATE OF HCl

M A Brown, P C Cartwright, P R R Langridge-Smith, K P Lawley, R J Donovan,
Department of Chemistry, University of Edinburgh, West Mains Road, Edinburgh EH9 3JJ

Introduction

The ground electronic state of hydrogen chloride has been investigated in numerous studies, both experimental and theoretical. On the other hand relatively little information is found in the literature on electronically excited states of HCl, even though these states are of considerable interest in connection with their probable importance in laser physics and photochemistry. The expected general pattern for "Rydberg" electronic transitions is not found and it is now clear that mixing between "Rydberg" and "Valence" states is essential for the interpretation of absorption and emission spectra of molecules such as HCl (Refs B1.37-40), HF (Ref B1.41) and Cl_2 (Ref B1.42). In each case

the repulsive inner branch of an intravalence shell ("Ion-pair") state, with a minimum at large inter-nuclear separation, cuts through the entire "Rydberg" state electronic manifold, possessing minima at small bond lengths, and causes various avoided crossings with members of the same symmetry. As a result the otherwise regular pattern of a "Rydberg" family is heavily perturbed, as has been previously observed in high resolution VUV absorption studies, though no real explanation was given (Refs B1.43-4). Recent ab-initio CI calculations on HCl have predicted that the 2 $^{1}\Sigma^{+}$ state is an asymmetric double well potential lying approximately 10.5 eV above the ground state. This potential is believed to arise from the "avoided crossing" of a $^{1}\Sigma^{+}_{R1}\pi + 4p\pi$ "Rydberg"-like origin state and the $B^{1}\Sigma^{+}$ valence $\sigma \rightarrow \sigma^{*}$ "Ion-pair" state (see Figure B1.26).

In view of the exotic nature of these mixed $^{1}\Sigma^{+}$ states we have recently been performing some laser multiphoton spectroscopy on electronically excited HCl. A few of our preliminary results are presented.

Experimental

Two photon excitation of HCl near 10.5 eV requires the production of tunable laser radiation in the region 230-240 nm. This was achieved using non-linear optical frequency doubling and mixing techniques.

A Quantel YG581 Nd^{3+}/YAG laser capable of delivering up to 300 mJ $pulse^{-1}$ of 532 nm radiation at 20 Hz was used to pump a Quantel TDL50 dye laser. The dye laser fundamental (typically 610-630 nm) delivered 60 mJ $pulse^{-1}$ at an estimated bandwidth of 0.08 cm^{-1}. This was then frequency doubled using a KDP crystal, to produce ultraviolet radiation in the region 305-315 nm with typical pulse energies 10-12 mJ $pulse^{-1}$. Finally, this UV laser radiation was mixed in a KDP mixing crystal with residual 1064 nm fundamental radiation (100 mJ $pulse^{-1}$) from the Nd^{3+}/YAG laser. The resulting UV radiation (230-240 nm, 0.8-1 mJ $pulse^{-1}$, 1-1.5 cm^{-1} badwidth) was separated from the fundamental and frequency doubled laser radiation using a Pellin-Broca dispersing

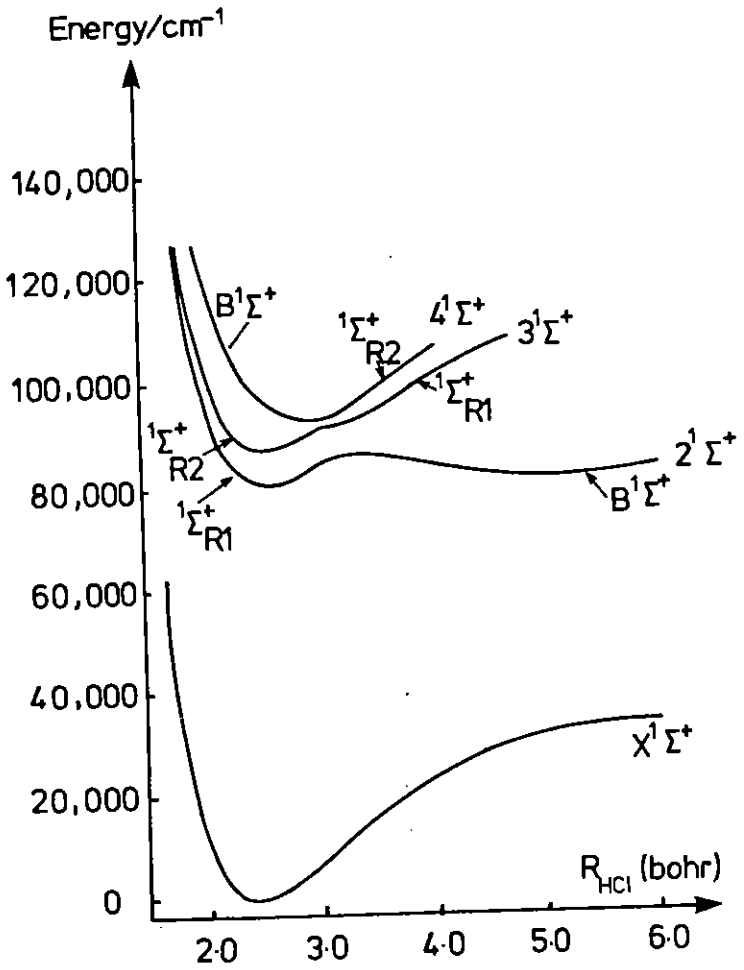

Fig B1.26 Calculated MRD CI potential energy curves for some $^{1}\Sigma^{+}$ states of HCl.

prism, spatially filtered and then passed on to the experiment. "Auto-tracked" angle tuning of the KDP crystals and quartz compensators was accomplished using a photodiode based servo-tracking system which monitored the frequency doubled and mixed ultraviolet laser radiation. Excitation of HCl into the excited electronic states was detected either by multiphoton ionisation or fluorescence techniques.

Results

(a) Multiphoton ionisation spectroscopy

Multiphoton ionisation spectra were recorded both in a static cell and in a supersonic jet expansion of 2-5% HCl in Argon. The latter method allows easier assignment of spectrally congested regions. The pulsed valve used to generate the supersonic molecular beam was an adapted Bosch automobile fuel injector. In both the static cell and molecular beam apparatus the ionic species were collected with a pair of biased parallel nickel plates (bias voltage 90 V) and the resulting current sent to a home-built differential input operational amplifier with variable gain (10^3-10^7 volts amp^{-1}). Spectra were calibrated by simultaneously recording optogalvanic lines from a Fe/neon hollow cathode lamp and fringes from a solid quartz etalon (finesse ~7, FSR = 3.37 cm^{-1}). All the signals were then processed in the usual manner using Stanford Research Systems SR250 gated integrators.

According to the two photon selection rules $\Delta J = 0, \pm 2$ we expect to see O, Q, S branches in the excitation spectrum, with the Q branch ($\Delta J = \Delta\Omega = 0$) being the most intense. A small portion of the recorded spectra is shown in Fig B1.27. Excitation of two vibronic levels is illustrated: one vibronic level being v' = 11 of the "Ion-pair" state and the second being v' = 0 of a $^1\Sigma^+$ "Rydberg"-like state (the H state as assigned by Douglas and Greening (8) which is strongly coupled wit the "Ion-pair" state. Spectroscopically, the extent of this mixing is readily seen by comparison of the relevant "rotational" constants. An unperturbed state of HCl, eg one of $^1\Pi$, $^1\Delta$ symmetry, may be expected to have a B_v value of ~10 cm^{-1} and any vibrational level from the "Ion-pair" state a B_v value of typically ~3 cm^{-1}. However the mixing

of the $^1\Sigma^+$ "Rydberg" state and the "Ion-pair" state is so severe that the resulting rotational constants (6.6cm^{-1} and 4.3cm^{-1} for the respective "Rydberg" and "Ion-pair" vibronic levels) are indicative of the mixed character of the states. The extent of this "Rydberg" - "Ion-pair" mixing is more clearly illustrated using fluorescence spectroscopy.

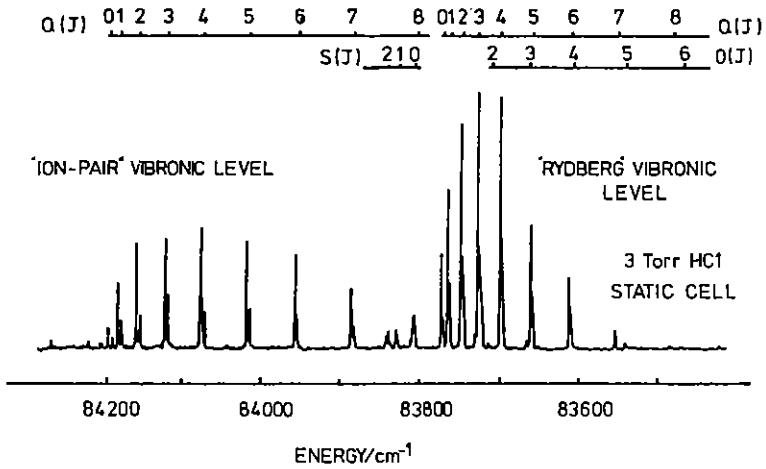

Fig B1.27 (2+1) Multiphoton ionisation spectrum of electronically excited HCl (3 torr HCl, static cell).

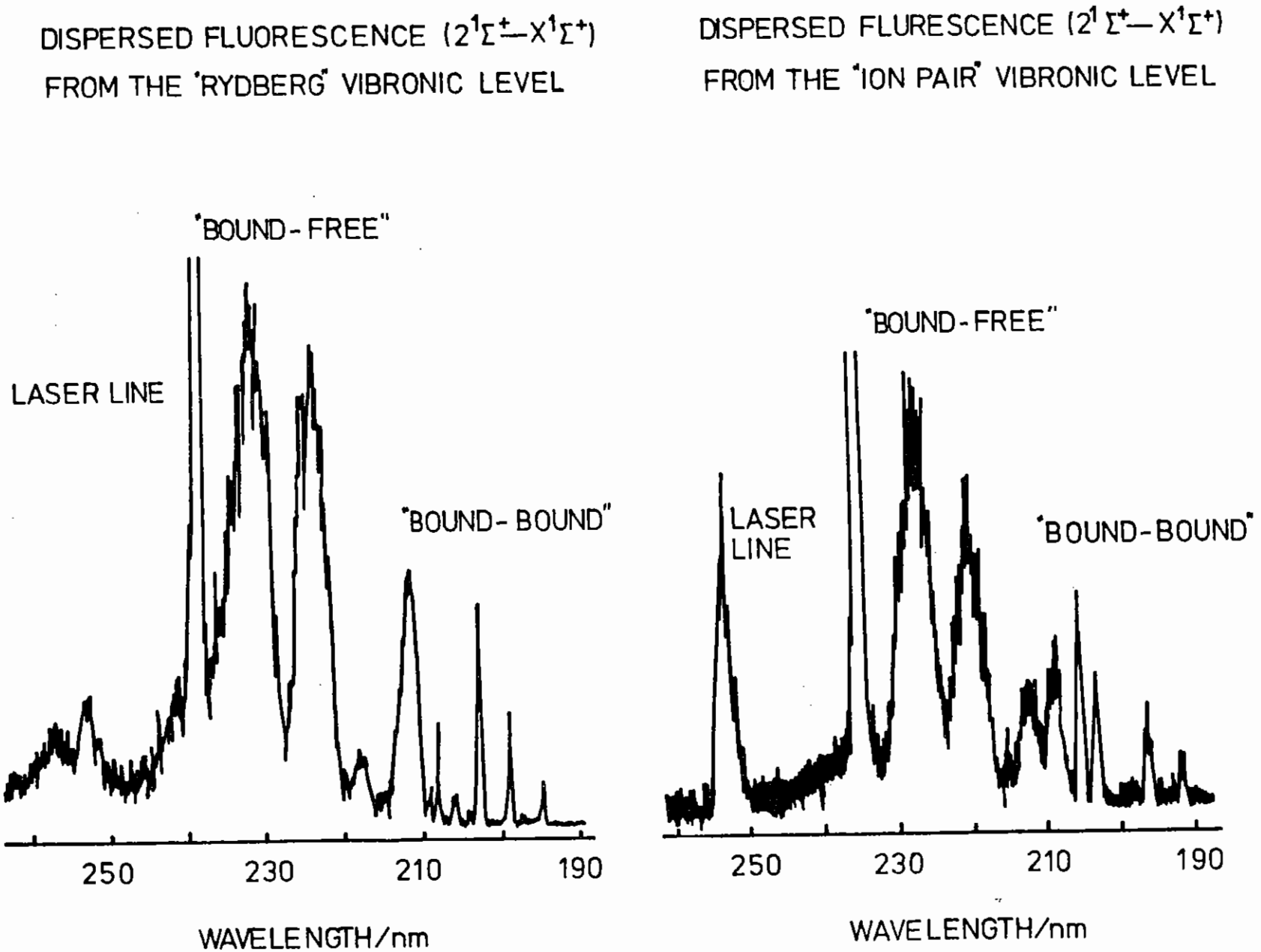

Fig B1.28 Dispersed fluorescence spectra obtained by two photon excitation at Q(3) of the respective "Rydberg" and "Ion-pair" vibronic levels (3 torr HCl).

(b) Fluorescence spectroscopy

Both fluorescence excitation and dispersed fluorescence spectra were obtained. In the dispersed emission spectra the molecular fluorescence was imaged (f/1.5 collection optics), etendue matched through a Jobin Yvon HRS 2 (0.6 m, f/7) monochromator and detected by a Hamamatsu R928 photomultiplier tube. Following two photon excitation at Q(3) of the respective "Ion-pair" and "Rydberg" vibronic levels dispersed fluorescence spectra were recorded (see Figure B1.28). Both these spectra show characteristic fluorescence from the outer "Ion-pair" well of the $2^1\Sigma^+$ state to both highly excited bound levels and to the vibrational continuum of the ground state, thus confirming further the strong mixing of the "Ion-pair" and $^1\Sigma^+$ "Rydberg" states. The bound-bound portion of the spectrum will of course extend well into the vacuum ultra-violet. Instrumental limitations precluded any study of fluorescence to wavelengths shorter than 190 nm.

(c) Reactive properties of the 2 $^1\Sigma^+$ state

Relaxation and reactive properties of excited electronic states of HCl are of interest, particularly reactions with noble gases, ie Xe, Kr, leading to the formation of exciplex monohalides. These processes may be of importance in understanding the kinetics of the discharge plasmas in commercial excimer lasers, eg XeCl (308 nm), KrCl (222 nm), (which use HCl primarily as the Cl-containing fuel).

Following excitation of HCl into the $2^1\Sigma^+$ state in the prescence of Xe, XeCl* $B^2\Sigma^+ \rightarrow X^2\Sigma^+$ (~308 nm) chemi-luminescence was observed (see Fig B1.29). The XeCl excitation spectra followed that of the HCl excitation strongly suggesting that the excited HCl molecular state is primarily responsible for the chemi-luminescent reaction. Thus we believe that the HCl molecules can be prepared in a rotationally state selected manner on excited electronic surfaces and their kinetic properties studied.

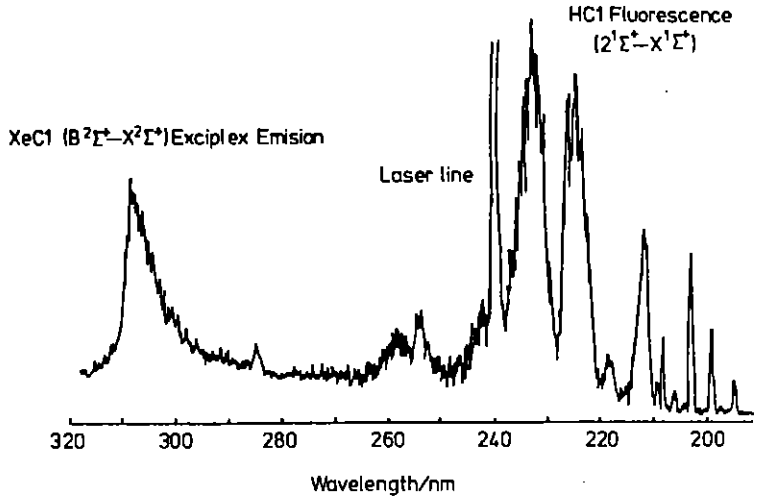

Fig B1.29 XeCL($B^2\Sigma^+ \rightarrow X^2\Sigma^+$) Exciplex emission following electronic excitation of HCl (3 torr) in the presence of xenon (20 torr).

Conclusion

We have conclusively shown that using multiphoton spectroscopic techniques the theoretically predicted "Rydberg" - "Valence" mixing in electronically excited HCl can be studied in detail. We are currently involved in further experimental and theoretical studies of this interesting problem.

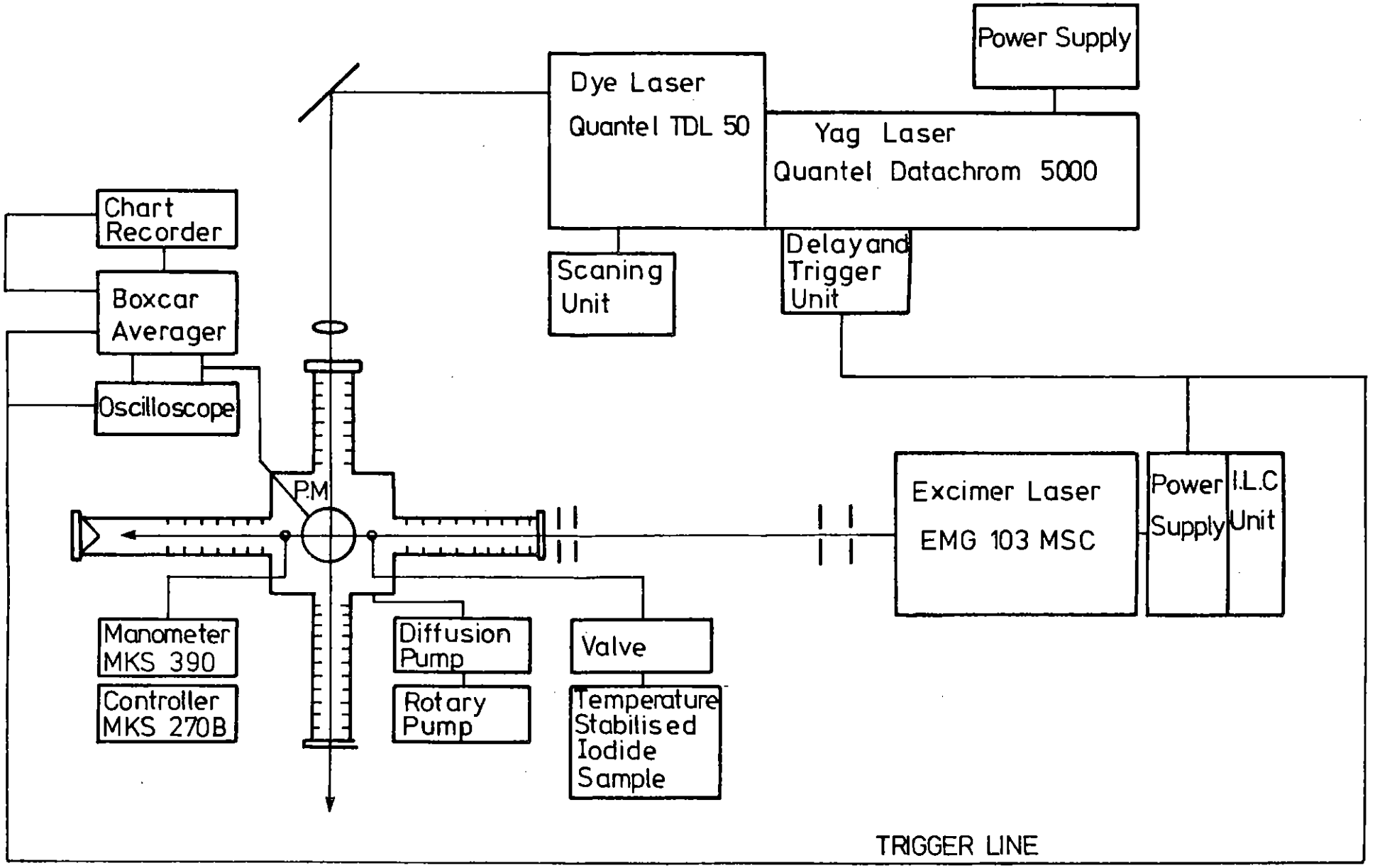

Fig B1.30 Experimental layout.

B1.14 MEASUREMENT OF THE RELATIVE POPULATIONS OF $I^*(^2P_{1/2})$ AND $I(^2P_{3/2})$ PRODUCED BY THE PHOTODISSOCIATION OF ALKYL IODIDES

P A Gorry, P M Hughes, D Raybone, T M Watkinson and J C Whitehead
(Manchester University)

In these experiments, we are using a novel two-photon laser-induced fluorescence method to determine the branching ratio for the formation of iodine atoms in their ground and excited states following UV photolysis of some alkyl iodides

$$RI \xrightarrow{h\nu} R + I(^2P_{3/2})$$

$$\rightarrow R + I^*(^2P_{1/2}).$$

The experimental arrangement is shown in Fig B1.30. A low pressure (30-40 m Torr) of the alkyl iodides is photodissociated by the 248 nm output of an excimer laser (20 s^{-1}, 50 mJ/cm^2). After a delay of 100-200 ns, the iodide atoms were detected using the focussed output of the loaned Datachrome 5000 YAG-pumped dye laser (0.5 mJ pulse energy). This laser scans over a pair of two-photon absorption lines ($^2D_{5/2} \leftarrow {}^2P_{3/2}$ for I and $^2D_{3/2} \leftarrow {}^2P_{1/2}$ for I^*) at 304.7 and 306.7 nm respectively. These excited atomic states fluoresce twice emitting first an IR photon and then a VUV photon in the range 158-206 nm. The VUV fluorescence was then detected using a solar blind photomultiplier which efficiently discriminated against light from both the photolysis and probe lasers. By scanning over the two absorption lines, two laser-induced fluorescence peaks are observed whose relative intensities depend on the quantum yield for I^* production ($\phi = I^*/(I + I^*)$). The molecule CH_3I whose quantum yield at 248 nm is well known ($\phi = 0.76$) was used as a calibrant. Typical data is shown in figure B1.31 for photolysis of CH_3I and C_2H_5I. There is a small degree of dissociation of these molecules by the probe laser at ~300nm which is corrected for when determining the peak ratios following photolysis.

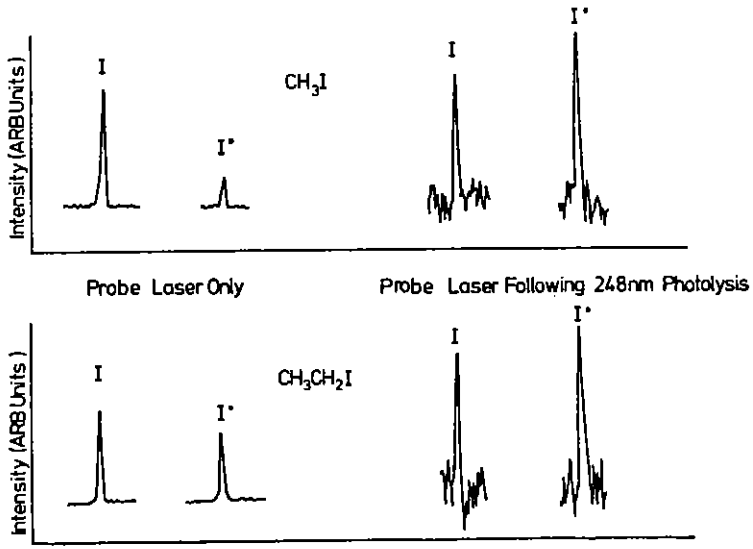

Fig B1.31 Photolysis of CH_3I and C_2H_5I.

During the period of the loan, we have studied photolysis of CH_3I, CH_2I_2, C_2H_5I, allyl iodide and C_3F_7I and we plan to extend the work to other iodides and to the detection of Br^*/Br yields from the photolysis of various bromides in an analogous manner. This data will be used to extend and interpret the measurement of photofragment translational energy distributions for such molecules made in this laboratory.

B1.15 PHOTODISSOCIATION DYNAMICS OF NO-CONTAINING MOLECULES

M R S McCoustra, J A Dyer and J Pfab, Department of Chemistry, Heriot-Watt University

This report covers work carried out with the JK 2000 Nd-YAG/dye laser at Heriot-Watt University during two loan periods of two months. The work is part of an SERC supported research project concerned with the photodissociation dynamics and spectroscopy of polyatomic NO-containing molecules.

Introduction

The photodissociation of gaseous polyatomic NO-containing compounds is of importance in atmospheric photochemistry and photodissociation lasers. The quantum states of the nascent NO photofragment in its electronic ground state are probed readily by laser induced fluorescence (LIF) permitting these nitrosocompounds to be used as bench mark examples for photochemistry in the near-uv and visible and the dynamics of selectively energised molecules (Refs B1.45-49). In addition a wide variety of polyatomic molecules of this type exists making it possible to study systematically the relationship between dissociation dynamics, spectroscopic and structural properties of the parent molecules.

The aim of this investigation is to characterise the quantum state distribution of nascent NO from the photodissociation of a range of nitroso-compounds and to measure energy partitioning among the photofragments and rates of radiative and non-radiative processes following electronic excitation. Our method is based on the use of pulsed laser dissociation in conjunction with delayed two-photon LIF probing of the NO fragment in the low pressure vapour or a supersonic expansion cooled jet. A substantial amount of data has been collected on the predissociation of $CC\ell F_2NO$ and several other C-nitroso-compounds in the 560 to 720 nm range. The 355 nm dissociation of jet-cooled methyl nitrite, t-butyl nitrite and dimethylnitrosamine has also been studied.

Experimental

The JK 2000 YAG pumped dye laser provided the pulsed beam for photolysis in the visible while an excimer pumped dye laser (Lambda Physics EMG 50 and FL 2002) was used for probing of NO by the two-photon LIF technique. The two collinearly aligned beams were focussed into the centre of the cell as shown in Fig B1.32 or the

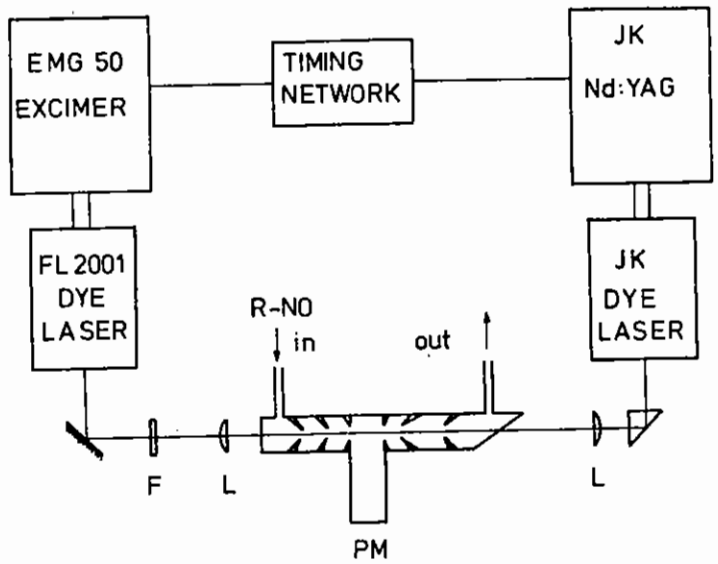

Fig B1.32 Arrangement used for pulsed dissociation-probe experiments of C-nitroso-compounds in the gas phase at 300K.

expansion chamber employed for nozzle-cooling. Fluorescence from the γ-bands of NO was viewed at right angle and imaged onto a filtered and apertured solar blind photomultiplier. The signal was processed by a transient recorder (Transiac 2001) or gated integrator and averaged by an IBM-PC or boxcar averager. The room temperature experiments used flowing vapour of about 100 mTorr while jet-cooling was performed with a commercial pulsed solenoid valve. Mixtures containing 1 to 10% by

volume of the nitroso-compound in Ar were expanded through a 0.5 mm orifice and photolysed 5 mm downstream. The stagnation pressure ranged from 100 to 500 Torr with the background vacuum being maintained below 10^{-4} Torr. The opening of the pulsed valve and firing of the two synchronised lasers was controlled by an analog multiple delay generator in conjunction with a crystal controlled master oscillator that was operated at a repetition rate of 10 Hz. The minimum delay of 40 ns used was dictated by the combined electronic jitter of the systems. Fluorescence excitation spectra and decay times of jet-cooled $CClF_2NO$ were obtained using the JK-2000 laser system for excitation in the red by monitoring emission in the near-ir with a red sensitive photomultiplier.

Results and discussion

The photolysis of $CClF_2NO$, 2-chloro-2-nitrosopropane and several other halogenated C-nitroso-compounds at 300K was found to produce predominantly NO(v=0) throughout the 560-690 nm range of their n,π^* transitions. The proportion of nascent NO(v=1) is very small but increases at short wavelength where a competing two-photon dissociation becomes important leading to a non-linear increase of NO yield with photolysis pulse power. The rotational population distributions of the nascent NO conform well to a statistical model.

State-selective photolysis of jet-cooled $CClF_2NO$ was performed at a number of wavelengths corresponding to well defined narrow features in the single-photon LIF excitation spectrum of the cold parent. Competition between molecular fluorescence and photodissociation occurs from the electronic origin at 14187 cm^{-1} up to roughly 15000 cm^{-1} where fluorescence becomes weak due to rapid dissociation. Fig B1.33 shows photofragment yield spectra that are not corrected for the variation of dye out-put with wavelength. These spectra were obtained by monitoring the production of $NO(^2\pi_{\frac{1}{2}}, v=0)$ with the probe laser fixed to the P_{11} head of the γ (0,0) band while scanning the photolysis laser through the absorption of the nozzle-cooled parent. The LIF spectrum

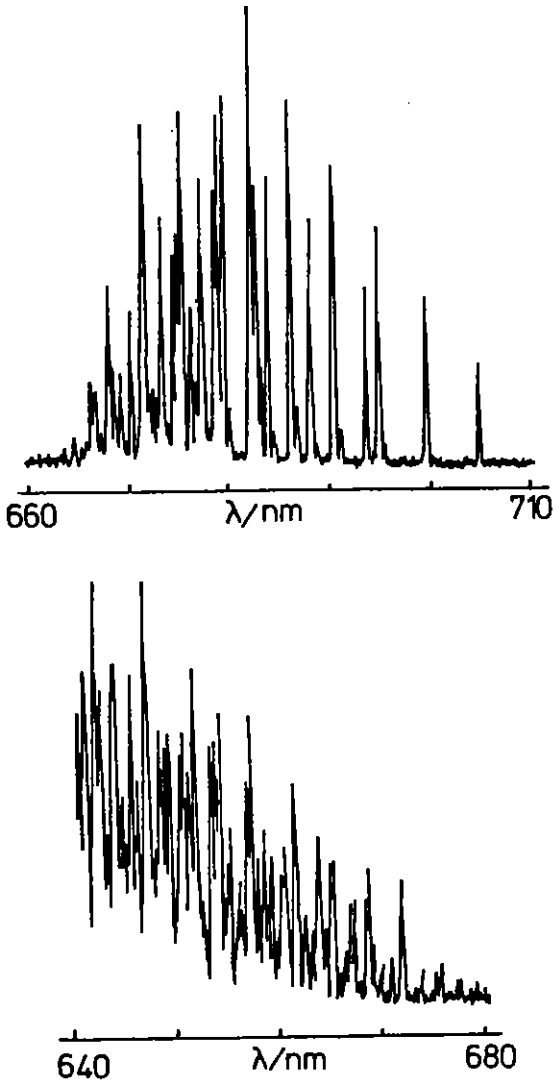

Fig B1.33 NO fragment yield spectra of jet-cooled $CClF_2NO$.

of NO(v=0) with the dissociation laser tuned to the 646.6 nm feature is shown in Fig B1.34. Variation of the delay between dissociation and probe laser provided the appearance time of the NO fragment for all major absorption features at low energy including the origin of the system (fig B1.35).

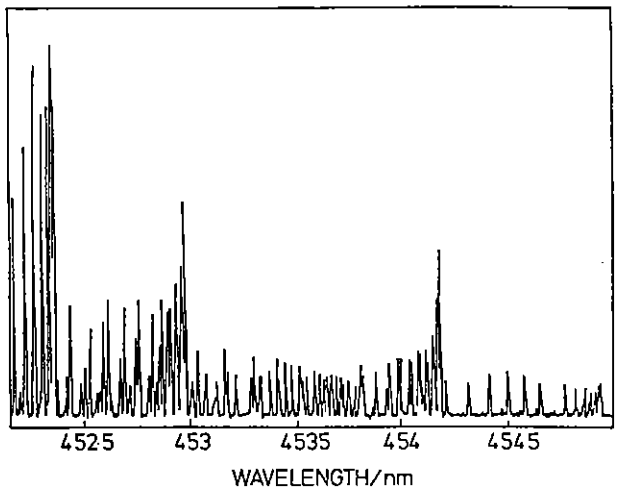

Fig B1.34 Two-photon LIF spectrum of NO(v=0) from the state-selective photolysis of jet-cooled CF_2ClNO at 646.6nm.

The last week of the loan period was used for exploratory work on the 355 nm dissociation dynamics of jet-cooled alkyl nitrites and nitrosamines. Two-photon LIF spectra of nascent NO(v=0, 1,2 and 3) were recorded readily with excellent S/N. Fig B1.36 shows as a representative example part of the spectrum of nascent NO(v=2) from the photolysis of cold t-BuONO. In all cases examined the dissociation was prompt showing the typical characteristics of an impact dominated process with extensive rotational and vibrational excitation of the NO fragment.

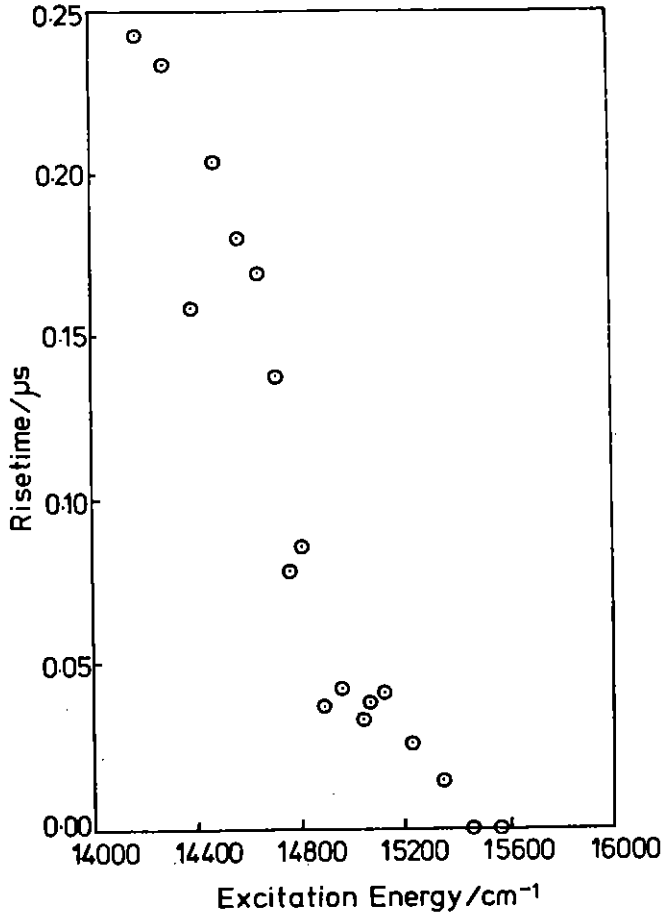

Fig B1.35 Plot of NO fragment appearance time as a function of excitation energy used in the photolysis of jet-cooled CF_2ClNO.

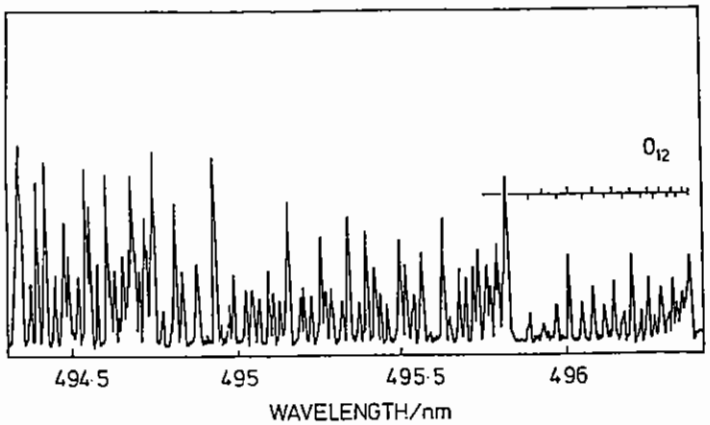

Fig B1.36 Two-photon LIF spectrum of NO(v=2) from the 355nm photolysis of jet-cooled t-BuONO.

Conclusions

The experiments described here were successful and a large amount of results has been collected. Their evaluation is in progress and will take some time, but a few of the major conclusions can be summarised already. $CC\ell F_2NO$ and the other C-nitroso-compounds studied predissociate to NO(v=0) almost exclusively following excitation in their n,π^* bands in the visible. The quantum state distribution of NO is statistical and intramolecular energy randomisation appears to precede the rupture of the C-N bond. The photo-dissociation of the O- and N-nitroso-compounds in the near-uv in contrast appears to be prompt with impact dominated partitioning of the excess energy among the fragments. These molecules are clearly excellent candidates for future detailed studies of the photophysics and dynamics of complex molecules.

B1 References

B1.1 For a review of structures in this area see M C Drake and G M Rosenblatt, J Electrochem Soc, 1979, 126, 1389.

B1.2 I M Mills and A G Robiette, Mol Phys, 56, 743 (1985).

B1.3 B R Henry, Acc Chem Res, 10, 207 (1977).

B1.4 F F Crim, Annu Rev Phys Chem, 35, 657 (1984).

B1.5 J E Baggott, H J Clase and I M Mills, Spectrochim Acta Part A, in press.

B1.6 J E Baggott, D W Law, P D Lightfoot and I M Mills, J Chem Phys, submitted.

B1.7 J E Baggott and D W Law, in progress.

B1.8 J E Baggott, Chem Phys Lett, 119, 47 (1985).

B1.9 J W Perry, D J Moll, A Kuppermann and A H Zewail, J Chem Phys, 82, 1195 (1985).

B1.10 J M Jasinski, J K Frisoli and C B Moore, J Chem Phys, 79, 1312 (1983).

B1.11 M J Pilling and M J C Smith, J Phys Chem, 1985, 89, 4713.

B1.12 M Brouard, M T MacPherson, M J Pilling, J M Tulloch and A P Williamson, Chem Phys Letters, 1985, 113, 413.

B1.13 C D Flint, F L Stewart-Darling, Mol Phys 1981, 44, 61.

B1.14 H-D Amberger, Z Phys Chem 1981, 109, 125.

B1.15 C Brecher, H Samelson, A Lempicki, in W C Nieuwport, G Blasse, A Bril, "Optical Properties of Ions in Crystals" Eds H M Crosswhite and H W Moos Interscience New York 1967.

B1.16 R Ballardini, Q G Mulazzani, M Ventura, F Bolletta, V Balzani, Inorg Chem, 1984, 23, 300.

B1.17 R D Peacock, T J R Weakley, J Chem Soc(A), 836, 1937.

B1.18 D Burgess Jr, R Viswanathan, I Hussla, P C Stair and Ei Weitz, J Chem Phys 79 (1983) 5200.

B1.19 R R Lucchese and J C Tully, J Chem Phys 81 (1984) 6313.

B1.20 J F Ready, Effects of High Power Laser Radiation, Academic Press, New York (1971).

B1.21 G Porter and M A West, in "Techniques of Organic Chemistry", Vol VIII, Wiley-Interscience, New York, 1974, Chapter X and R V Bensasson, E J Land and T G Truscott, "Flash Photolysis and Pulse Radiolysis", Pergamon, Oxford, 1983.

B1.22 C J Willsher, J Photochem, 28, (1985) 229.

B1.23 F Wilkinson and C J Willsher, Chem Phys Lett, 104, (1984) 272; Appl Spectrosc 38, (1984) 897.

B1.24 F Wilkinson and C J Willsher: J Lumin 33 (1985) 189.

B1.25 F Wilkinson, C J Willsher and R B Pritchard; Eur Poly J 21, (1985) 333.

B1.26 F Wilkinson, C J Wilsher, J Pouliquen, D Fichou, P Valat and J Kossanly: submitted to J Photochem.

B1.27 F Wilkinson, C J Willsher, D Oelkrug and S Uhl, in preparation; F Wilkinson, C J Willsher, L J Johnston, H L Casal and J C Scaiano, Can J Chem, in press.

B1.28 B I Greene, R M Hochstrasser and R B Weisman, J Chem Phys 70 (1979) 1247; M P Irvine, R J Harrison, M A Strahand and G S Beddard, Ber Bunsenges Phys Chem 89, (1985) 226.

B1.29 R G Denning, T R Snellgrove and D R Woodwark, Mol Phys, 37, 1109, (1979).

B1.30 R L DeKock, E J Baerends, F M Boerriger and J G Snijders, Chem Phys Lett, 105, 308, (1984).

B1.31 R W B Pearse and A G Gaydon, The Identification of Molecular Spectra, Chapman and Hall, 1976.

B1.32 Von K H Holman, W Lange and H Gg Wagner, Ber Bunsenges, Physik Chem 75, 121 (1971).

B1.33 T L Porter, D E Mann and N Acquista, J Mol Spec 16, 228 (1965).

B1.34 F J Comes and D A Ramsay, J Mol Spec 113, 495 (1985).

B1.35 M SUto and L C Lee, J Chem Phys 83, 89 (1984).

B1.36 G L Gutser and T S Zyubina, Chem Phys 83, 89 (1984).

B1.37 M Bettendorff, S D Peyerinhoff and R J Buenker, Chem Phys, 66, (1982), 261-279.

B1.38 D M Hirst and M F Guest, Mol Phys, 41, (1980), 6, 1483-1491.

B1.39 E F van Dishoek, M C van Hemert and A Dalgaro, J Chem Phys, 77, (1982), 7, 3693-3702.

B1.40 W J Stevens and M Krauss, J Chem Phys, 77 (1982), 3, 1368-1372.

B1.41 M Bettendorf, R J Buenker, S D Peyerimhoff and J Romelt, Z Phys A, 304 (1982), 125-135.

B1.42 S D Peyerimhoff and R J Buenker, Chem Phys, 57 (1981), 279.

B1.43 D S Ginter, M L Ginter and S G Tilford, J Mol Spectrosc, 90 (1981) 177.

B1.44 A E Douglas and F R Greening, Can J Phys, 57 (1979), 1650-1661.

B1.45 J P Simons, J Phys Chem 88, 1287 (1984).

Bl.46 H Zacharias, K H Welge et al, J Chem Phys 74, 218 (1981).

Bl.47 R Vasudev, R N Zare and R N Dixon, J Chem Phys 80, 4863 (1984).

Bl.48 J Pfab, J Hafer and W Krieger, J Chem Phys, 78, 266 (1983).

Bl.49 I Nadler, J Pfab, H Reisler and C Wittig, J Chem Phys 81, 653 (1984).

Section Editor: M J C Smith

B2 BIOLOGY

B2.1 ULTRA-VIOLET RESONANCE RAMAN SPECTROSCOPY OF SPECIFIC COVALENT ENZYME REACTION INTERMEDIATES

P J Tonge, R Chittock and C W Wharton (Birmingham)
R E Hester (York)

Since our pioneering observation last year of the first vibrational spectrum of a natural covalent enzyme intermediate (B2.1-3) we have devoted considerable attention to improving the quality of our spectra, preparation of the acylenzyme and studies of model compounds. Our observations have stimulated competitive work in the US (B2.4).

Optimisation of Spectra

The original spectra, samples of which were published in the Report last year, were characterised by poor resolution of the aromatic features which were expected to be present. Despite very thorough analysis of the Triplemate spectrometer optics and careful study of model compounds the reason for the poor resolution at the low wavenumber end of the spectrum (1400cm^{-1} and below) has not been established. The sensitivity of the diode array system has been improved fourfold by fitting of a cylindrical lens which corrects for vertical astigmatism and matches the image height to the array height. This has allowed better quality spectra to be obtained.

Aromatic features of protein and substrates normally appear near to 1610cm^{-1} (B2.5), however in our spectra, which are obtained by using 248nm radiation, the main spectral feature of the enzyme is seen near to 1640cm^{-1} and of the substrate near to 1670cm^{-1}. These frequencies are characteristic of the 'amide I' bands of proteins and peptides (ie the protein backbone and the substrate (Acytyl-L-Phe-gly OMe) amide links). Although our observation of apparent amide vibrations,

presumably by pre-resonance enhancement, differs from most recent work in other laboratories (see above), there is a report in the literature of observations similar to our own using 257nm excitation (B2.6). All other measurements have been made at 240nm or lower wavelengths so it is possible, although unlikely, that the results may be explained by the 8nm difference in wavelength of the exciting light.

Model Studies

A wide range of thiolesters that represent progressively complete models of Ac-L-Phe-gly-Papain have been synthesised and studied by means of FTIR and RR spectroscopy. All of these compounds show strong RR features between 1670cm^{-1} and 1690cm^{-1}.
N-acetyl-gly thioethyl ester and N-acetyl-L-Phe-gly thioethyl ester show broader bands than does ethyl thiolacetate since the amide appears to contribute to the thiolester carbonyl vibration feature.

Notably, all model compounds show higher frequencies for Vc=o in acetonitrile than in H_2O (or ^2H_2O). In most compounds Vc=o is 1688 ± 2cm^{-1} although in N-Ac-L-Phe-gly thioethyl ester, the most complete model it is 1680cm^{-1}. Similarly in H_2O or ^2H_2O the frequency is 1677 ± 2cm^{-1}.

The acylenzyme Vc=o was observed at 1690cm^{-1} thus we may propose that the active centre environment is less polar than water being similar to that of acetonitrile. The dielectric constant of acetonitile is 37.5 which compares with a value of 32 for the enzyme active centre determined by probing the active centre with fluorphores which are sensitive to their environment (C W Wharton, unpublished results). Certainly we can say on the basis of these results that there is no evidence for hydrogen bonding. Thus we may propose that interaction between the carbonyl oxygen and the amide hydrogens of the oxyanion hole is not detectable (B2.7).

The UV spectrum of an acyl-enzyme

It has been shown (B2.8) that very highly specific acylpeptides such as Boc-p-iodophenylalanyl-L-citrulline (Boc-PiP-Cit) are capable of reversibly acylating the enzyme at pH4. We have prepared this acylenzyme and have determined the UV difference spectrum with respect to unacylated enzyme. The difference spectrum is shown in Fig B2.1. The absorption maximum is seen to occur at 239nm, red-shiffed some 7-9nm relative to simple thiolesters.

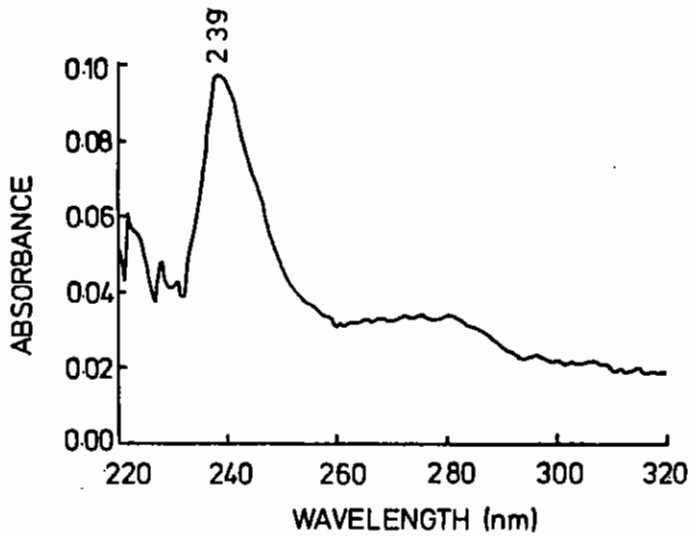

Fig B2.1 Ultra-violet difference spectrum of the acylenzyme Boc-PiP-Cit-papain at pH 4.0 The instrument (LKB) was zeroed before addition of DTT to the sample cuvette to activate the enzyme. The reference cuvette contained inactive enzyme plus acylating agent. The enzyme was calculated to be 98% acylated and has a concentration of 0.18 mM.

Resonance tuning

This observation encouraged us to attempt to use laser radiation at 239nm in order to better exploit the resonance condition. The excimer-pumped dye laser was used to give 478nm light which was then frequency doubled to 239nm. Despite much effort only a few tens of μJoules could be obtained per pulse; this proved insufficient to obtain Raman spectra.

Very recently Bajdor et al, (B2.4) in Peticolas' laboratory (Eugene, Oregon, USA) have used a YAG pumped dye laser, doubling and anti-stokes Raman shifting to give 239nm emission. They have used a vertical sample tube in which a small hole is drilled and into which the laser pulses are fed. This, together with flow-mixing, allows focusing into the sample and permits high quality spectra to be obtained using a scanning double monochromator. The acylenzyme N-Acetyl-glycly-L-lysine-Papain has been prepared by continuous mixing.

A very clear band which is absent in the substrate and free enzyme appears at 1678cm^{-1}. This frequency is similar to that expected in water and indicates some hydrogen bonding given that we have shown that the dielectric constant in the active center is ca. 30. The lower frequency seen here may be the result of a more specific interaction with the enzyme since the catalytic rate is higher for this substrate.

We have attempted to observe the Vc=o of Boc-PiP-Cit-papain at pH4. We have not seen a peak in this region and, since we have shown that acylenzyme is present (see above), are forced to conclude that Vc=o is shifted to lower frequency to an extent that leads to its obscuration by the very large pre-resonance amide I band. Thus there is negative evidence that the interaction may be strong in this extremely specific acylenzyme.

Preliminary studies of glyceraldehyde-3-phosphate dehydrogenase (GAPDH) NAD^+ and NADH

Fig B2.2 shows the RR spectrum of NAD^+ using 248nm excitation. The three main bands arise form the adenine portion of the molecule while the small feature at $1674cm^{-1}$ is at the frequency seen in FTIR for the amide side-chain of the nicotinamide ring. The noise level is rather high and the featureless (checked by shifting the Triplemate wavelength) region at the RHS of Fig B2.2 is dominated by differential diode sensitivity. A spectrum of NADH of similar quality has been obtained.

GAPDH is supplied in a form which has three of four NAD^+ molecules bound to it per enzyme molecule. We have obtained RR spectra of the protein in order to compare the spectra of the bound nucleotides with those in free solution. Further work is needed to provide spectra of sufficient quality.

The OSMA OMA system

The intensified diode array which forms part of this system was purchased using funds allocated in conjunction with the grant that supports this work. Initial studies have shown that the diode elements show a much more closely-matched light sensitivity than the PARC system and that the dark noise level is low. At present the light sensitivity of the system is rather low but this is, in part, due to the absence of the cylindrical focusing lens. The computing facilities and ease of use of the system as a whole seem excellent.

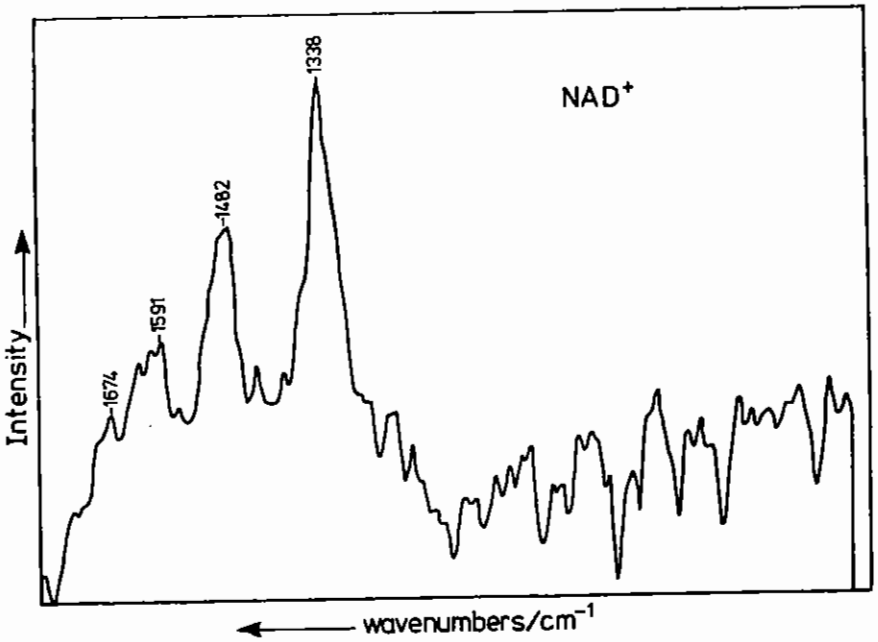

Fig B2.2 Resonance Raman spectrum of Nicotinamide adenine dinucleotide (NAD^+) using 248 nm radiation. $[NAD^+] = 250\mu M$ in H_2O. Spectrum is the result of accumulating 2000 scans followed by smoothing.

B2.2 ULTRA-VIOLET RESONANCE RAMAN SPECTRA OF AMINOACIDS AND PROTEINS

R E Hester, J De Groot and B Stewart (University of York)

The aim of this programme is to obtain resonance Raman spectra of proteins under conditions which will enable specific structural features to be probed with good sensitivity and selectivity. By tuning the laser excitation wavelength to coincidence with a strong vibronic absorption band of a molecule the vibrational Raman bands associated with the chromophoric part of that molecule may be enhanced by several orders of magnitude. Thus, for a protein like hemoglobin, it is well established that Raman spectroscopy with visible laser excitation

yields much information of the structure and bonding in the metalloporphyrin prosthetic group while those vibrational modes associated with the polypeptide chains remain "quiet". This selectivity serves to simplify the observed spectra in a useful way, but obviously it also obscures much that is of interest. Hemoglobin and other protein molecules contain other chromophoric groups which become active only with ultraviolet excitation. Of particular interest are those aminoacid residues which contain aromatic groups, eg tyrosine, tryptophan and phenylalanine, and the $-CO.NH_2-$peptide group which forms the basic repeat unit in the polypeptide chains. A technique which can selectively probe the vibrational modes of these groups by the simple means of tuning the excitation wavelength to coincidence with each chromophore in turn and thus generating its specific Raman bands could be a very powerful tool indeed for studying protein structure and conformation in solution.

As a preliminary stage in achieving our objective of generating UV resonance Raman spectra of proteins, we first are studying a number of model compounds including the simple aromatic aminoacides and N-dimethylacetamide, which serves as a model for the peptide link. The most direct way of obtaining laser radiation at a wavelength suitable for resonance with the peptide absorption band at ca. 190nm appeared to be from a line-narrowed ArF excimer system at 193nm. Due to the intrinsically small spectral bandwidths (ca. 10-20cm^{-1} typically) associated with Raman-active vibrational modes, the normal broad band output (ca. 80cm^{-1}) of an excimer laser is unsuitable for Raman spectroscopy. Our previous experiments with the Lambda Physik EMG150 laser operated in line-narrowed mode with KrF at 249nm gave a spectral bandwidth of ca. 0.2cm^{-1} and temporal bandwidth of ca. 5ns. With single pulse energies of ca. 3mJ and a pulse repetition rate of 10Hz multichannel Raman spectra of standard solvents (water, ethanol, cyclohexane) were obtained in real time with the Spex Triplemate spectrometer and EG and G OMA-2 intensified diode array detector system. Integration of ca. 1000 pulses of scattered light typically are required to give reasonable quality spectra of solute at the 1M concentration level or resonance Raman spectra of solutes at ca. 10^{-4}M. Individual pulse energies higher than ca. 3mJ result in the generation of non-linear effects or even sample degradation. On changing from KrF

to ArF we found the laser performance was unreliable in terms of its pulse-to-pulse stability. Our pulse monitor indicated that the line-narrowing of the laser output was erratic and, although this was more difficult to determine with the available diagnostic facilities, there was evidence that even when operating regularly with narrowed pulses the wavelength of the pulses varied within the natural gain profile of ArF. Since the Raman experiments require integration of large numbers of pulses, the net result of this wavelength instability was an effective broadening of the Raman bands to such a degree that the spectra were unobservable. We concluded that further laser design development and improvement in diagnostics are required before Raman spectroscopy can be done successfully with ArF 193nm excitation.

In addition to the problems of laser instability at 193nm we also encountered difficulties due to the very poor optical throughput of the Spex Triplemate spectrometer in the short-wavelength ultraviolet region. Due to its design characteristics being determined primarily by the need to minimise the transmission of stray light, the spectrometer has a large number of optical surfaces, including three holographic diffraction gratings. We spent a considerable amount of time in measuring the spectral sensitivity variations and absolute throughput of the instrument before coming to the conclusion that the performance was particularly poor at wavelengths below ca. 250nm and that for this reason we should substitute a single grating spectrograph for the Triplemate for the short-wavelength Raman experiments. A Hilger Monospec instrument was available and was adapted for this purpose to fit to the Spex UVISIR sample compartment and the PARC 1420 diode array detector assembly. A cylindrical lens also was fitted to the detector mounting flange in order to concentrate the Raman output on to the small (2.5mm high) array. The substantial improvement in throughput achieved with this single grating spectrograph is, of course, somewhat offset by a deterioration in stray light rejection and our preliminary trials with this system have revealed a number of stray light artifacts which may interfere with the Raman spectra.

In addition to the use of an ArF excimer as the excitation source for these experiments with aminoacids and proteins, two further possibilities exist and are being explored. First, since the line-narrowed output of the EMG150 KrF laser is known to be reliably reproducible and of high pulse energy, its wavelength can be shifted from 249nm to short wavelengths by use of a high pressure hydrogen cell in which stimulated Raman effects occur. From 15mJ pulses at 249nm we have produced 3mJ pulses of hydrogen (6 bar pressure) anti-Stokes radiation at 224.8nm and have used these as a Raman excitation source in our experiments. Solvent spectra have been generated with a makeshift assembly being used to separate the 224.8nm radiation from the 249nm and other Stokes and anti-Stokes lines from the hydrogen cell, but we found these also to be contaminated with relatively strong and sharp H_2 rotation lines, most notably at 524cm^{-1} shifted form the 224.8nm excitation lines. We plan to improve this experimental arrangement so as to generate Raman spectra also with the 2nd and 3rd anti-Stokes H_2 lines at 205.6nm and 189.4nm as excitation sources. The other possible means of generating laser radiation in the short wavelength ultraviolet region is through frequency multiplying the output of an excimer-pumped dye laser. For this purpose it is not necessary to use a line-narrowed excimer since the dye action itself limits the spectral bandwidth. The continuous tuning of wavelength afforded by this route is of obvious interest in the selective resonance enhancement of vibrational modes of individual aromatic aminoacid residues in a protein chain, but it suffers from the disadvantage that the crystals available limit tuning to 217nm. However, further stimulated Raman shifting of the frequency-doubled dye laser output is possible and we are exploring this route to tunable excitation Raman spectroscopy in the shortest wavelength ultraviolet region.

B2.3 LASER-INDUCED PHOTODYNAMIC TRAPPING OF SINGLE STRAND BREAKS IN MAMMALIAN DNA

C W Wharton (Birmingham), R A Meldrum and S Shall (Sussex) and D R Trentham NIMR (MRC, Mill Hill)

Introduction

Cellular DNA may be damaged by ionising radiation (single and double strand breaks), UV light (pyrimidine dimer formation) and mutagens which react chemically with bases in DNA (B2.9, B2.10). Depending on the dose of damaging agent the cell may recover by DNA repair, be mutagenised or transformed, or be killed. An important form of repair is excision repair during which a piece of DNA which contains the damage is excised and replaced by resynthesis of the patch using the intact strand as former. This process involves four stages namely: incision (not necesary for direct strand breaks) polymerisation of the new strand, excision of the damaged strand and finally ligation (joining) of the new DNA strand to the original strand at the distal end of the patch (B2.9).

Breaks in DNA, transient or otherwise occur as a result of a wide range of biological phenomena including differentiation and oncogene activation which can lead to cellular transformation and carcinogenesis. The natural lifetime of breaks can cover a wide range from hours (UV damage) to seconds or less (some X-ray induced breaks) (B2.11). A number of methods are available for the study of break development and/or accumulation but all suffer from a number of disadvantages such as the need to use several powerful cellular inhibitors in order that damage repair may be seen against the general replication (cell division) background. Available methods are very time consuming and laborious although some are sensitive and accurate but none can provide information on the timescale of seconds or less in which many repair processes are expected to occur.

The concept of laser induced photolytic release of a break-trapping agent is novel in this context although it has been employed to very good effect in studies of muscle contraction using 'caged'-ATP (B2.12).

Here the diffusional barrier to access of ATP which limits kinetic studies of contraction is obviated by prior loading of the muscle cells with caged-ATP followed by photoactivation to release ATP.

We have synthesised caged-dideoxynucleotide triphosphates which are used with permeabilised cells. The photoreleased ^{32}P-labelled dideoxynucleotide triphosphates are inhibitors of DNA polymerase β which is an important (probably predominant) enzyme in excision (patch) repair (B2.13, B2.14). The nucleotide causes inhibition of polymerisation by being incorporated as a chain stopper into the repair patch, while the α-^{32}P at high specific activity can be used to measure the extent of such incoporation.

The kinetics of DNA repair may be followed by arranging that laser photoactivation of the trapping reagent occurs at a fixed time interval after a damaging event. Thus in the work described here, which refers to preliminary feasibility studies, a pulse of 248nm radiation is followed by photoactivation of trapping agent by using 351nm laser irradiation. Many of the fundamental features of the method have been validated and are described below.

Results

Synthesis and photolysis of caged reagents

Caged phosphate

For initial studies O-nitrophenyl-2-ethyl phosphate (caged phosphate) was synthesised in 27% yield by using the method of McCray et al, (B2.12). Trial photoactivation experiments were performed using the EMG 150 (XeF laser) which emits at 351nm. Considerable attention was given to beam enlargement and shaping such that the 10cm^2 area of a 3.5cm diameter culture plate was evenly illuminated. Removal of the hole in the centre of the beam was achieved by off-axis oscillator

injection into the amplifier. The beam was enlarged and squared (from its rectangular shape) followed by magnification. The four lenses plus a turning prism which was required in order to permit horizontal illumination of the culture plates resulted in a large loss of power; typically from 90mJ at the laser to 20mJ at the target.

Photolytic experiments showed that 0.3mM inorganic phosphate was released per Joule of light absorbed, which converts to a quantum efficiency of 62% in good agreement with the literature value of 60% (B2.15). The absorbance of caged phosphate (and other nucleotides) is quite low at 351nm (ε = 410) so it was considered that multipassing the laser beam might be used to reduce the number of pulses (20-100) required to liberate 250μM phosphate (nucleotide triphosphate) needed in trapping experiments. A three pass scheme using mirrors gave a 1.5-fold increase in photoyield but was greatly restricted by the 30% absorption of the incident light by the base of the polystyrene culture dishes. Since it will eventually be necessary to achieve photoactivation as above in a single pulse, non-absorbent culture dishes and multi-passing will clearly be required as will a significant increase in laser output power and optical efficiency.

Caged dideoxynucleotide triphosphates

Following preliminary experiments with caged phosphate caged dideoxythylmidine triphosphate (c-ddTTP) was synthesised in collaboration with Dr D R Trentham, NIMR, Mill Hill. Recently a new (unpublished) synthesis of caged nucleotide triphosphates has been devised, which obviates many of the difficulties of the previous (B2.16) very complex synthesis. The new method involves a direct reaction between a diazonium derivative of the cage and the nucleotide triphosphate. c-ddTTPb was synthesised in 80% yield (previously ≤ 25%) and purified by using preparative HPLC (C-8 column). The purified compound (4 mg) was shown to photolyse quantitatively to give ddTTP with a 58% quantum yield. Although ddTTP labelled with ^{32}P in the α position would be the ideal trapping agent for UV-induced excision repair (thymidine dimer exicision) α-^{32}P ddTTP is not commercially

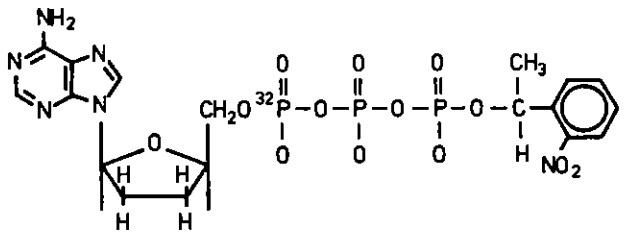

(I)

Fig B2.3

available as yet. Thus we have prepared the adenine analogue α-^{32}P-c-ddATP (Fig B2.3) by using the radiolabelled material at a specific activity of 5000 Ci/mmole as well as unlabelled material on the milligram scale. The ^{32}P-labelled material was synthesised on the 250μCi scale using acetate buffer at pH 4 to give a 40% yield. Fig B2.4 shows the HPLC elution diagram of material which had previously been purified by preparative HPLC following isotope dilution with cold c-ddATP. It is seen that 96% of the ^{32}P resides in the two peaks that relate to the diastereoisomers of c-ddATP.

Partial photolysis of c-ddATP (diluted with cold material, Fig B2.4) results in ^{32}P as well as optical absorbance (260nm, nucleotide) appearing quantitatively at the elution volume (3-6 ml) of ddATP.

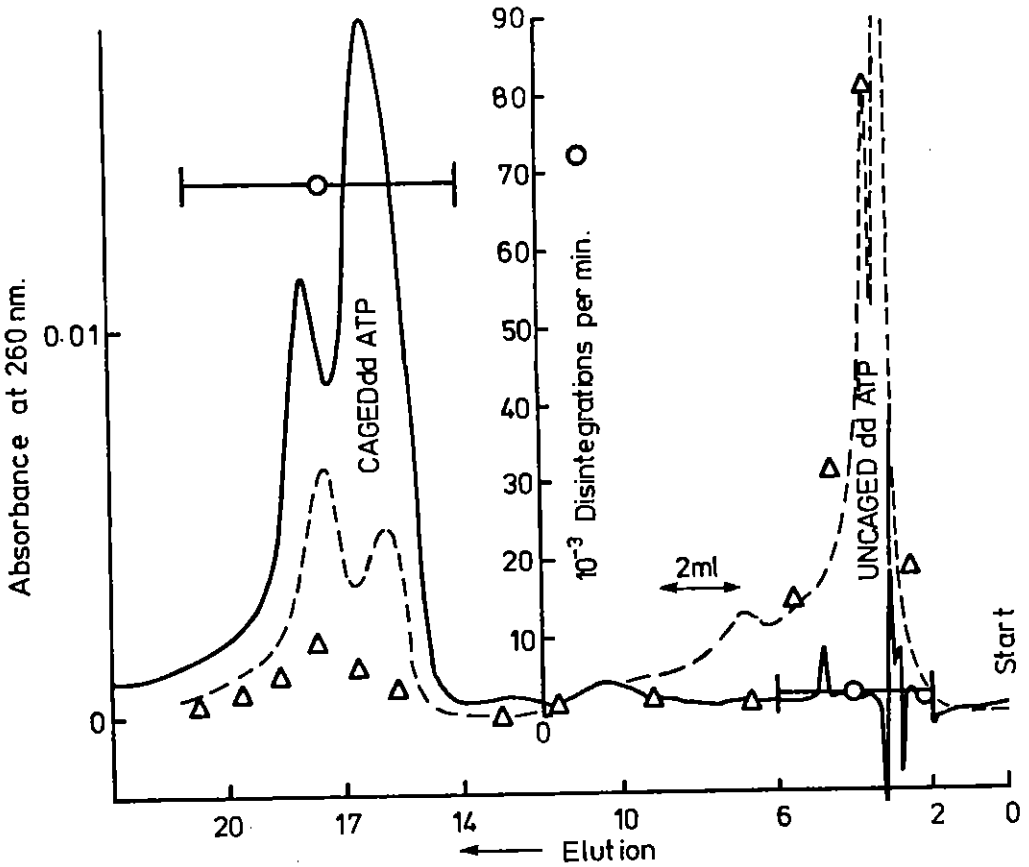

Fig B2.4 Analytical high pressure liquid chromatography of caged α-^{32p} dideoxyadenine triphosphate Chromatography was performed on a 3.9 mm x 30 cm C-8 μBondapak column which was eluted at a rate of 1 ml min^{-1} with 25% methanol: 10 mM phosphate pH 5.2, 10 μL of 2.3mM ddATP was mixed with 10 μL α ^{32p} c-ddATP for HPLC, 10 μL being applied. 1 ml samples were counted for ^{32p} using a Triton scintillation mix. Circles; radioactivity of bulked fractions prior to photolysis (96%α-^{32p} c-ddATP). Triangles; Radioactivity after 20 min photolysis at 366 nm using a low power UV lamp. Dotted line; A_{260} after photolysis.

Photolysis of caged dideoxynucleotide triphosphates

Earlier photolysis experiments with caged phosphate showed that a new absorption centred on 310nm developed consequent upon photolysis. This absorption difference ($\Delta\varepsilon$ = 2230) can be used to quantitate photolysis as shown in Fig B2.5. This shows that photolysis is a first order phenomenon in which 1.1mM ddATP is released per Joule absorbed (the culture dish was placed on a mirror).

Irradiation of c-ddATP with light at 248nm did not release ddATP, this is ascribed to strong protective nucleotide absorption since caged phosphate was previously shown by us to photolyse at this wavelength with a quantum yield of 58%.

Caged arabinosylcytosine triphosphate

The dideoxy materials described above are directed at the β-polymerase which has been supposed to be predominant in excision repair. Arabinosylcytosine triphosphate (araCTP) is an α (replication) polymerase inhibitor which has been reported to be at least transiently incorporated as a chain stopper. In order that our range of inhibitors should be as complete as possible c-araCTP was synthesised in 80% yield using the diazonium method. This compound was shown to be photolysed with the same parameters as c-ddATP and was used as prepared (80% pure) in some biological experiments.

High pressure liquid chromatography

This was in general very successful but some tailing occured when picomolar quantities of very high specific activity ^{32}P material were run. Accordingly this material (200μCi) was diluted with 12.4 nmoles of cold c-ddATP before the main preparative run to eliminate tailing. The final material, 96% pure, had a specific activity of 33 Ci/nmole on

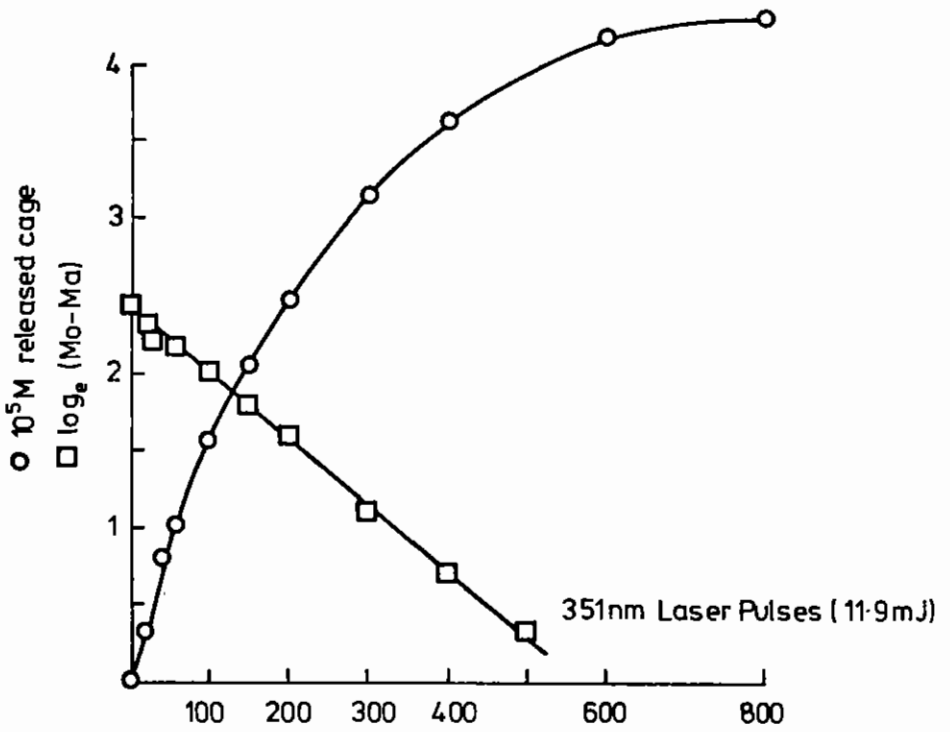

Fig B2.5 Photolysis of c-ddATP using 351 nm (XeF) excimer laser radiation (11.9 mJ pulse^{-1}). Circles; $\Delta A_{310\ nm}$ converted to molar photolysis by using $\Delta\varepsilon$ = 2230 M^{-1} cm^{-1}. Squares: Log plot which shows the first order nature of the photolysis. Concentration of c-ddATP was 2.3 x 10^{-5} M in a 3.5 cm diameter culture dish as a 3 mm layer. The culture dish was placed on a mirror for irradiation.

our arrival at RAL. Regrettably despite great success in all of the syntheses this specific activity was too low for direct labelling experiments with DNA. It is clearly necessary to be able to run the HPLC using picomolar quantities so that isotope dilution will not be needed.

Experiments with cells

The effect of laser irradiation on DNA synthesis

It was first necessary to establish that 351nm UV irradiation did not damage DNA. Petri-dishes each containing a monolayer of about 10^6 AA8 Chinese Hamster ovary fibroblasts were subjected to doses of 0 to 110kJ/m^2 351nm UV irradiation from the Xenon fluoride excimer laser. The radiation was delivered as 10ns pulses at 10Hz. In order to provide a comparison, cells were subjected to 248nm UV irradiation which is known to cause considerable damage in the form of pyrimidine dimers to DNA. Cells received doses of radiation between 0 and 10 J/cm^2 in the form of 10ns pulses (1-40) from the Krypton fluoride laser. The growth medium was removed from the cells to avoid absorption of the UV light by proteins and the cells were irradiated in phosphate buffered saline. Fresh growth medium was reapplied after irradiation and the cells incubated at 37°C for 24 hours with 1.0μCi/ml^3 H-TdR to measure DNA synthesis.

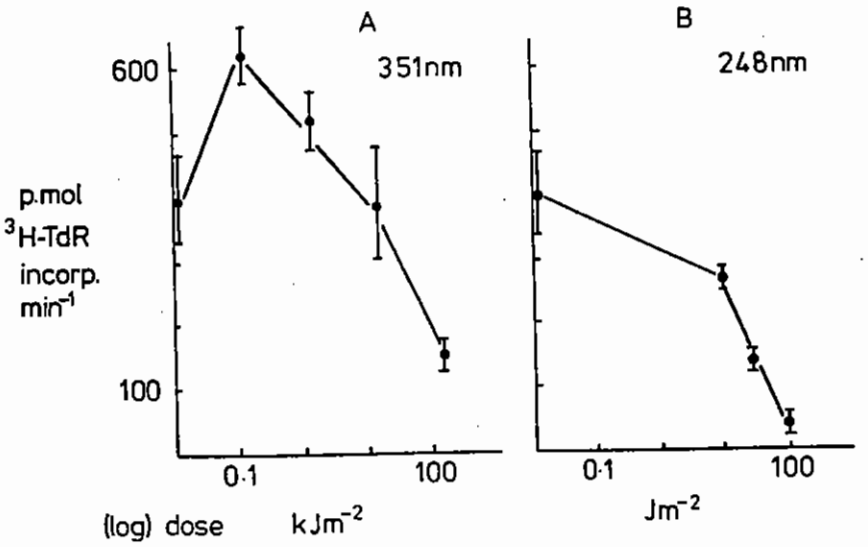

Fig B2.6 Irradiation of 10 cm^2 monolayer AA8 fibroblasts with 351 nm and 248 nm UV light. Incorporation of ^{3}H-Tdr during 24 incubation after irradiation.

It can be seen from Fig B2.6A that there is some enhancement of DNA synthesis over 24 hours after doses of 0.1 and 1.1kJ/m^2 of 351nm irradiation. DNA synthesis in 24 hours after doses higher than 11kJ/m^2 of 351nm is reduced showing that these levels of irradiation are damaging to the cells. The dose used for optimum photo-activation of 'caged' ddTTP and ddATP is ca. 1kJ/m^2. It remains to be investigated if breaks are induced in the DNA immediately after irradiation with doses which enhance synthesis of DNA as this might complicate the application of the break trapping technique. Fig B2.6B shows the severe damaging effect of 248nm wavelength UV irradiation.

Permeabilisation of cells

To introduce a dideoxy triphosphate molecule into cells it is usually necessary to permeabilise the cells. Several methods of permeabilising and resealing cells have been tried and the most successful to date is a method which employs hypotonic shock to permeabilise the cells which are then resealed by making the medium isotonic (B2.17). The integrity of the cell physiology is best maintained after this process by addition of serum to the isotonic medium. However it was found by assessment with thin layer chromatography that there was about 16% breakdown by serum enzymes of the thymidine triphosphate (TTP) to thymidine which would not be phosphorylated or incorporated into the DNA of permeabilised cells but would be incorporated into unpermeabilised cells. It also appeared that unpermeabilised HL60 leukaemia cells incorporated thymidine triphosphate to a small extent. These cells may allow some entry of the triphosphates through their unpermeabilitised membrane or they may have enzymes on the surface of their membranes which break down the thymidine triphosphate to thymidine monophosphate and thymidine. From comparative results with AA8 fibroblasts it seems that these characteristics may vary with cell type. It was confirmed by the nucleoid sedimentation technique that permeabilisation of cells did not introduce breaks in the DNA.

Chain termination during repair of UV-induced damage

The principle of dideoxythymidine (ddT) acting as a terminator of DNA chain elongation in mammalian cells was well demonstrated. Cytosine arabinoside (ara-C) was used to inhibit DNA α polymerase which is mostly involved in cell replication DNA synthesis. Dideoxythymidine is incorporated into DNA by β polymerase which is principally involved in DNA repair synthesis. In cells where replication synthesis was inhibited by ara-C, incorporation of ^{3}H-TdR into DNA repair synthesis, induced by 248nm UV damage, was inhibited by dideoxythymidine.

Experiments which examined the effect of ddT on replication DNA synthesis showed different involvement of α and β DNA polymerase in different cell types. Dideoxythymidine reduced incorporation of ^{3}H TdR into DNA synthesis in HL60 leukaemia cells but did not reduce

incorporation into DNA replication synthesis in AA8 fibroblasts suggesting that β polymerase as well as α polymerase is involved in HL60 cell replication synthesis, but only α polymerase is involved in AA8 fibroblast replication synthesis.

Inhibition which results from photoactivation of caged araCTP

It has been demonstrated that photoactivated caged-araCTP affects incorporation of ^{3}H-TTP into DNA synthesis in permeabilised cells either by competitive inhibition of DNA polymase α or by direct incorporation into DNA (B2.18). AA8 fibroblasts and HL60 cells were permeabilised, 'caged' ara-CTP was introduced into the cells with ^{3}H-TTP, the cells resealed in isotonic medium and the 'caged' ara-CTP activated by 351nm irradiation. Cells were then incubated at 37°C for one hour. In both cell types photoactivation of the caged molecule reduced the incoporation of ^{3}H-TTP as might be expected (Fig B2.7). It was previously shown that the presence of an inactivated caged molecule was not toxic to permeabilised or intact cells by measuring ^{3}H-TTP and ^{3}H-Tdr uptake after one hour or 24 hours incubation of the cells with the 'caged' compound.

Incorporation of ^{32}P into DNA

Permeabilised cells (AA8) incubated with α ^{32}P ddATP showed no uptake of ^{32}P in the absence of UV irradiation. After 20Jm^{-2} 248nm light 50 fmole ddATP/10^{9} cells were incorporated. Bleomycin, an anticancer drug, inhibited this incorporation.

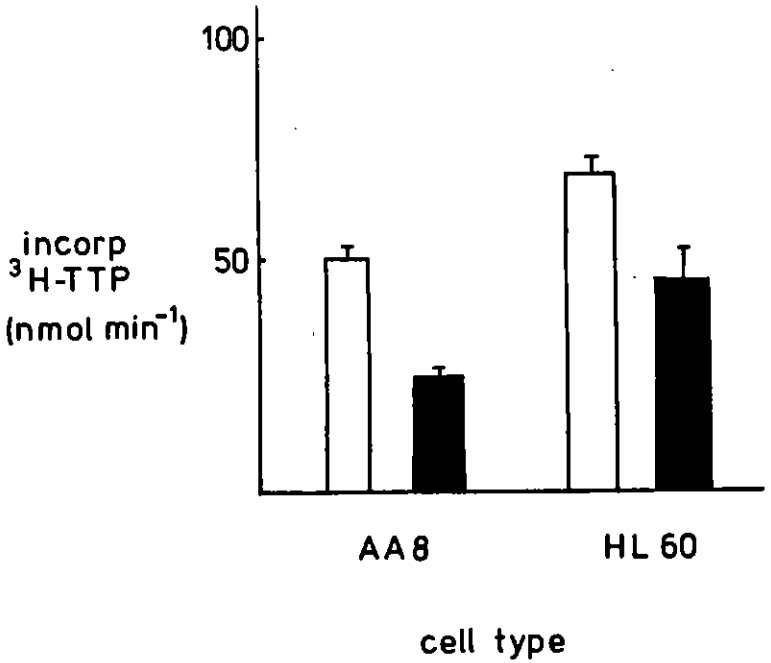

Fig B2.7 The effect of photoreleased arabinosylcytosine triphosphate on HL60 and AAD DNA synthesis. Unfilled bars - no photoactivation. Filled bars - 1 kJ/m^2 351 irradiation.

CONCLUSIONS AND FUTURE WORK

As a result of the experiments we have performed so far we have shown that ^{32}P is incorporated into DNA during damage repair and that caged nucleotide triphosphate photorelease (from C-araCTP) caused α polymerase inhibition. Thus each aspect of the method has been validated in separate experiments. Although the experiments with C-α^{32}P ddATP were unsuccessful owing to the specific activity being too low (33 Ci/mmole) we confidently expect that when material at 5000 ci/mmole is available we will be able to observe direct ^{32}P incorporation from C-α^{32p} ddATP and that the method will be fully verified.

At present, work is in progress to improve permeabilisation and resealing of cells to produce optimum incorporation of released 'caged' radiolabelled triphosphate molecules. All existing techniques employ large molecules such as sugar or proteins in the buffers which may absorb some of the UV light. It is necessary to modify the techniques without unduly disturbing the cell physiology. Partial success has now been achieved using rapid permeabilisation by low concentrations of ATP^{4-} in alkaline buffer (B2.19).

Cell culture facilites were kindly made available by the MRC Radiobiology Unit, Harwell, but it was unavoidable when performing experiments at RAL that cells were not maintained in 5% CO_2/air during incubation periods. The quality of results will be greatly improved when gassed incubation conditions are available where the experiments are performed.

B2.4 INVESTIGATIONS OF FAST ABSORPTION CHANGES IN PHOTOSYSTEM 1

E H Evans, R Sparrow, L Tramontini and R G Brown
(Lancashire Polytechnic, Preston)
I N Ross, M J C Smith and W T Toner (RAL)

A flash spectrometer has been developed which is able to detect small absorption changes of the order of 1% in the picosecond time regime. Standard deviations of the order of ± 0.3% are routinely observed. Pulses of 5psec FWHM are generated by a Nd/YAG pumped dye laser and are amplified by a second dye laser. Absorption changes have been monitored by the pump-probe technique. The 5ps pulse at 585nm is split to provide the pump (excitation) pulse (1.5 x 10^{15} photons cm^{-2}) and the probe pulse at 705nm (~ 10^{13} photons cm^2) by Raman shifting in ethanol. A variable time delay was introduced between the pump and

probe pulses with a totally internally reflecting prism on a moveable mount. The absorption change for a given delay between the pump and probe pulses was typically the average of 100 separate flashes. In each experiment 200 flashes were used to alternately excite the sample and measure a base-line by chopping the pump pulse. The equipment is described in more detail in Sections B4.2 and B4.3.

Preliminary experiments have been performed on a photosystem 1 preparation from the cyanobacterium Chlorogloea Fritschii. This was chosen because it has been well-characterised (B2.20) and would be anticipated to exhibit absorption bleaching of the order of a few per cent. The sample contained 100μg ml^{-1} chlorophyll and a chlorophyll/P700 ratio approximately 80.

The sample was found to be stable for at least several thousand flashes, as monitored by a reproducible absorption change at a given delay as a function of the number of flashes used to excite the sample.

705nm is the absorption maximum of the PS1 reaction centre chlorophyll (P700) and absorption at this wavelength undergoes a slight bleaching following the pump pulse. The observed time-profile of the bleaching is shown in Fig B2.8. A rise-time of the same order as the width of the excitation pulse is observed but the return of the absorption at 705nm is at least biphasic. The observed profile is remarkably similar to results presented by Il'ina et al (B2.21) for a PS1 in beans in the presence of the reductant tetramethyl-p-phenylene diamine but where they assume P-700 has all been photo-oxidised (Fig B2.9). Their interpretation may therefore be open to question. This absorption was attributed to the tail of the absorption peak of the antennae pigments, but without measuring the full absorption spectrum of the species we observe, we are unable to attribute it at present. Further experiments to obtain these absorption spectra are to be performed in the near future.

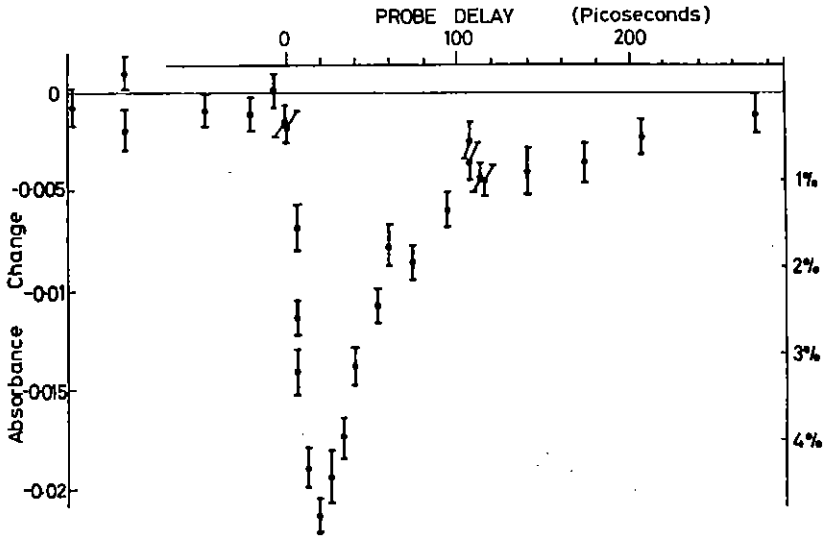

Fig B2.8 Absorption changes at 705 nm following 585 nm excitation of Photosystem I.

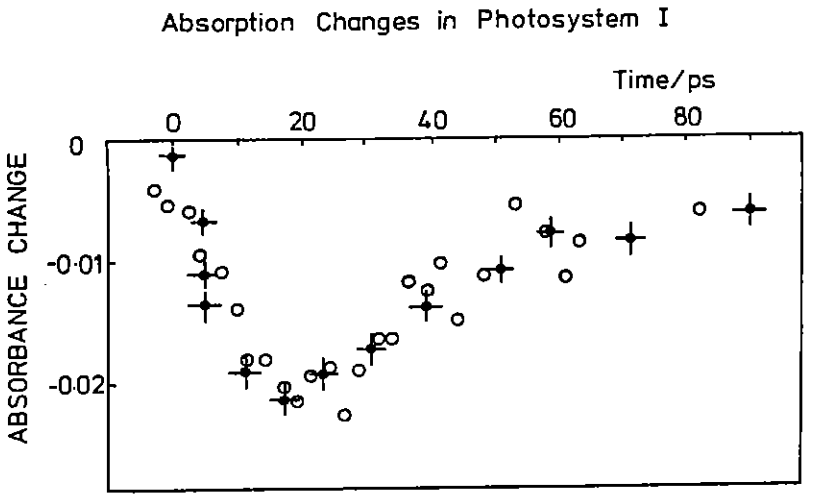

Fig B2.9 Absorption changes in Photosystem I.
0 Il'ina et al. (Ref B2.21)
Excitation pulse: 650 nm, 10^{15} photons/cm^2, 25 ps 300 μg/ml Chl, Chl/p700 = 60; 2 mm path length.
Absorption monitored at 704 nm under saturating 633 nm light.

+ This work
Excitation pulse: 585 nm, 1.5 x 10^{15} photons/cm^2, 5 ps 80 μg/ml Chl, Chl/p700 = 80, 1 cm path length
Absorption monitored at 706 nm under room light.

B2.5 TIME RESOLVED FLUORESCENCE STUDIES ON 1,4-DI-2-(5-PHENYLOXAZOLYL) BENZENE (POPOP)

A D B Waldman and J J Holbrook (University of Bristol)
A J Langley (RAL)

Introduction

Time-resolved fluorescence emission anisotropy studies have allowed both the internal motions and isotropic rotational diffusion of proteins in solution to be measured on the nanosecond timescale (B2.22, B2.23). However, the comparatively long times required for data acquisition using the time-correlated single-photon counting method (B2.24) limits these studies to systems at chemical equilibrium.

Here, an attempt is made to use a streak camera to resolve the fluorescence intensity and anisotropy in time following a single, intense pulse of exciting light of 5-10ps duration. If such 'single-shot' fluorescence decay measurements can be made, the properties of species which exist only transiently in the progress of many biochemical reactions (which take place on the ms timescale) may be probed by triggering the laser at a known time after the reaction is started by mixing two solutions together in a stopped-flow device. Moreover, use of a streak camera and ultra-short light pulses also allows measurements of rotational motions to be made in the time range 10-100ps.

We describe preliminary studies of fluorescence in the compound POPOP (which is widely used as a fluorescent standard (B2.25)) in order to characterise the detection system and assess the viability of making fluorescence intensity and anisotropy decay measurements using this technique.

A schematic diagram of the experimental configuration is shown in B2.10.

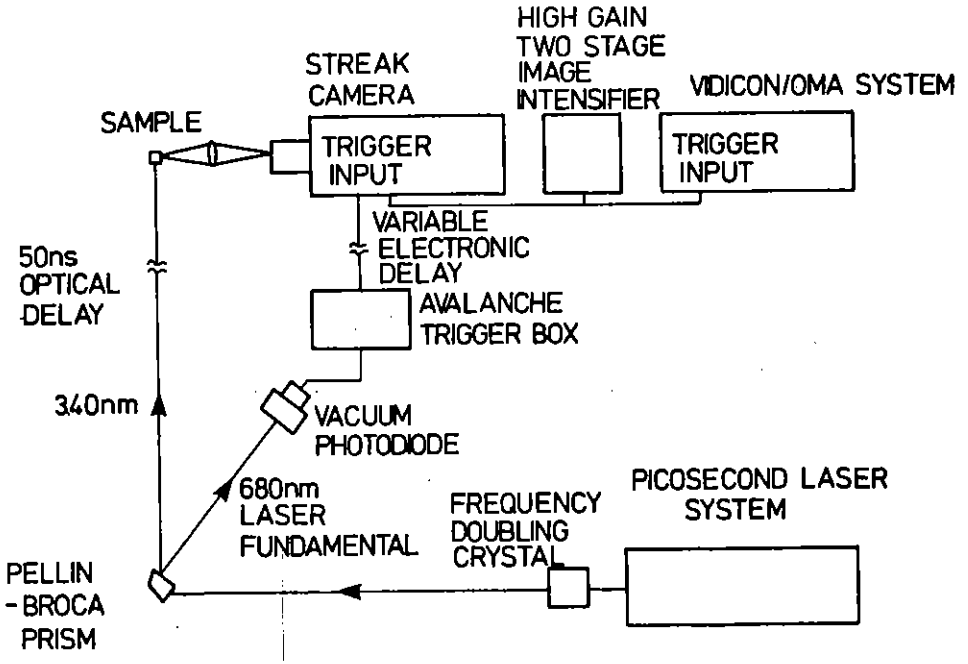

Fig B2.10 Instrumental configuration for time-resolved fluoreescence decay measurements.

Results

The low signal to noise ratio of the fluorescence decays observed in single-shot experiments precludes accurate lifetime measurement but are consistent with an excited state lifetime of 1-1.5ns (see Fig B2.11). This is in broad agreement with the two lifetime of POPOP determined using other methods (B2.25). Although the data obtained to date is too noisy to allow reliable determination of the rotational correlation time of the dye molecule in solution, improvements in the efficiency of the collection optics and the use of a more sensitive detector with greater dynamic range to monitor the streak image may enable fluorescence intensity and anisotropy decays to be measured accurately on a single-shot basis.

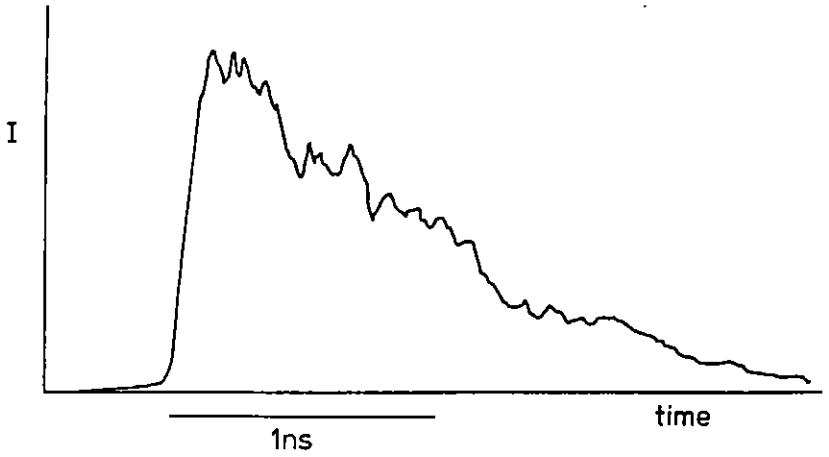

Fig B2.11 The decay in fluorescence intensity (I) from 1,4-Di-2-(5-phenyloxazolyl) benzene (POPOP) (20μm solution in cyclhexane) following a single pulse of exciting light at 340nm.

B2.6 INVESTIGATIONS OF PHOTOSYNTHETIC PROCESSES

Y E Atkinson, M C W Evans, R C Ford, J H A Nugent
(University College London)

Introduction

We have used the loan pool JK2000 (ns-pulsed) Nd:YAG and dye laser system to bring about photochemical reactions in biological samples prepared from photosynthetic organisms.

(i) Laser-induced turnover of the water oxidation system in higher plants (as detected by electron paramagnetic resonance spectrometry - epr)

(ii) Laser-induced turnover of the primary electron donor in the two plant photosynthetic multi-protein membrane complexes which are termed Photosystem 2 and Photosystem 1.

Results

(i) The photosynthetic oxidation of water ($2H_2O \rightarrow O_2 + 4H^+ + 4e^-$) is a process which requires the accumulation of four oxidising equivalents in an enzyme whose active site is thought to contain 4 manganese atoms. A multi-line epr signal can be observed after the accumulation of 2 oxidising equivalents which may arise from a binuclear manganese complex (see Fig B2.12).

The very high intensity of the 532nm light from the Nd:YAG laser allowed us to study the turnover of the water-oxidising enzyme in the very concentrated samples which are required for epr spectroscopy.

Further work on the lineshape and saturation properties of the multi-line signal may advance the present understanding of the environment and structure of the water oxidation system.

(ii) We also used the high energy of the dye laser to determine the light-intensity dependence of P700 photo-chemistry in samples of Photosystem 1 which had been irradiated with various doses of 16MeV X-rays as part of a project investigating the size of the Photosystem 1 complex. The samples used in this project have lost part of their light-harvesting function, and it was important to determine their light saturation behaviour. Using the YAG-pumped dye laser we were able to show the light-harvesting function (as a ratio of Photosystem 1 activity) was unaffected by the doses used.

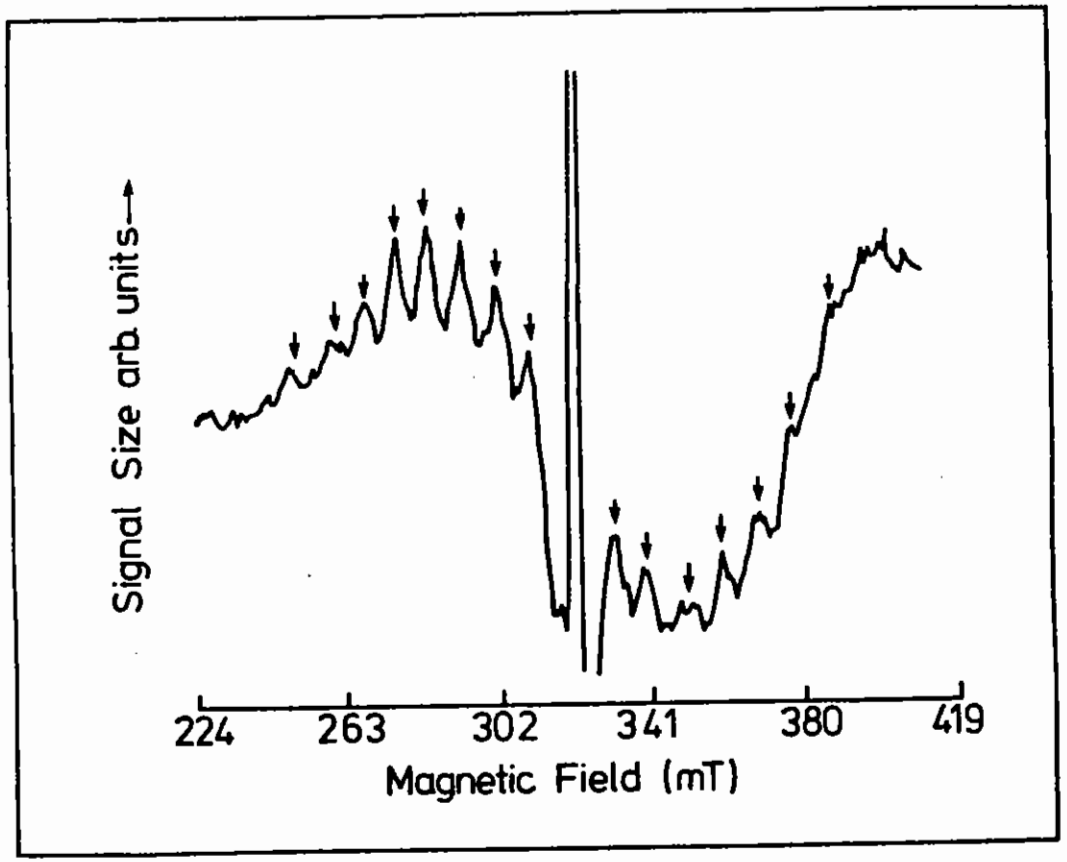

Fig B2.12 Multi-line epr spectrum of the oxygen-evolving system in Photosystem 2 from pea (plus 2 mM p-phenylbenzoquinone) after one 532 nm light pulse from the Nd-YAG laser. Epr conditions: Power 50 mW; modulation amplitude 2 mT; temperature 8K; microwave frequency 9.05 GHz.

References

B2.1 P J Tonge, C W Wharton, R J Szawelski, P M Killough and R E Hester, Biochem Soc Trans 13, 930-931 (1985)

B2.2 P J Tonge, C W Wharton, R J Szawelski, P M Killough and R E Hester, "Spectroscopy of Bilogical Molecules", Eds A J P Alix, L Bernard and M Manfait, Wiley, London

B2.3 C W Wharton, Biochem J, 233, 25-36 (1986)

B2.4 K Bajdor, W L Peticolas, C W Wharton and R E Hester, J Raman Spec submitted for publication (1986).

B2.5 C R Johnson, M Ludwig, S O'Donnel and S A Asher, J Amer Chem Soc, 106, 5008-5010 (1984)

B2.6 I Harada, Y Sugarawa, H Matsuuva and T Shimanouchi, J Raman Spec, 4, 91-98 (1975).

B2.7 B Asboth and L Polar, Biochemistry, 22, 117-122 (1983).

B2.8 M Smolarksy, Biochemistry, 19, 478-484 (1980).

B2.9 P C Hanawalt, P K Cooper, A K Ganesan and A S Smith, Ann Rev Biochem, 48, 783-836 (1979).

B2.10 A Collins, C S Downes and R T Johnson, "DNA repair and its inhibition", IRL Press, Oxford (1984)

B2.11 P E Bryant, R Warring and G Ahnstrom, Mutuation Research, 131, 19-26 (1984)

B2.12 J A McCray, L Herbette, T Kihara and D R Trentham, Proc Natl Acad Sci (USA), 77, 7237-7241 (1980)

B2.13 E Wist, Biochim Biophys Acta, 562, 62-69 (1979)

B2.14 J Waser, U Hubscher, C C Kuenzle and S Spadari, Eur J Biochem, 97, 361-368 (1979)

B2.15 J H Kaplan, B Forbush and J F Hoffman, Biochemistry, 17, 1929-1936 (1978)

B2.16 M A Ferenczi, E Homsher and D R Trentham, J Physiol, 352, 575-599 (1984)

B2.17 P Reinhard, M Burkhalter and J R Gautschi, Biochim Biophys Acta, 474, 500-511 (1977)

B2.18 S Yoshida, Y Machiko and S Masaki, Biochim Biophys Acta, 477, 144-150 (1977)

B2.19 B D Gomperts, Nature, 306, 64-66 (1983)

B2.20 E H Evans, and C A Pullin, Biochim J, 196, 489-493 (1981)

B2.21 M D Il'ina, V V Krasauskas, R J Rotomkis and A Yu Borisov, Biochem Biophys Acta, 767, 501 (1984)

B2.22 I Munro, I Pecht and L Stryer, PNAS (USA) 76, 56-60 (1979).

B2.23 R B Cundall, R E Dale, "Time-Resolved Spectroscopy in Biochemistry and Biology", Plenum Press, New York and London.

B2.24 P H Lami, G Pfeffer and G Laustriat, Le Journal de Physique 27, 398-404 (1966).

B2.25 R A Lampert, L A Chewter, D Phillips, D N O'Connor, A J Roberts, S R Meech, Anal Chem 55, 68-73 (1983).

B3 PHYSICS

Section Editor: J Szechi

B3 PHYSICS

B3.1 ABSORPTION LINEPROFILE MEASUREMENTS OF HEII BALMER (1640A) IN A DENSE Z-PINCH PLASMA

J P Marangos, K G H Baldwin*, D D Burgess
Imperial College, London SW7

* Now at ANU, Canberra, Australia

An absorption experiment has been performed with the aim of studying the lineprofile and lineshift of the HeII n=2 to n=3 transition, in a dense ($N_e > 10^{24} m^{-3}$) z-pinch plasma. This work employed tunable coherent VUV radiation generated by stimulated anti-Stokes Raman scattering of 3600A laser radiation in H_2 gas. The laser radiation was produced by the FL2002 dye laser pumped by an EMG201 MSC (loaned for the period of the experiment by M C Gower).

Previous work (Ref B3.1) on this technique had confirmed that intensities high enough to compete against background plasma emission (10^{10} photons per pulse) could be produced, thus making this a suitable source of radiation for an absorption experiment in the dense plasma.

The plasma employed was formed in a z-pinch discharge specifically designed to generate dense cool plasmas for work on the effects of strong coupling and high density on spectral lineshapes and shifts (Ref B3.2). This plasma has been diagnosed by interferometric and linewidth measurements and found to have an electron density of $10^{24} m^{-3}$ and a temperature of 3.3eV (Ref B3.3). Absorption measurements were made in both wings of the line. A comparison of the absorption data obtained (figure B3.1) in this experiment with the results of previous emission studies of the 1640A line in the plasma enabled an estimate of the total absorption coefficient of the line to be made. This was used to estimate the n=2 level population and the temperature of the plasma which was found to be 3.4eV in good agreement with the temperature diagnosed by other techniques. Measurement of the continuum opacity was used to calculate the electron density of the plasma and this compared well to the values measured by other techniques.

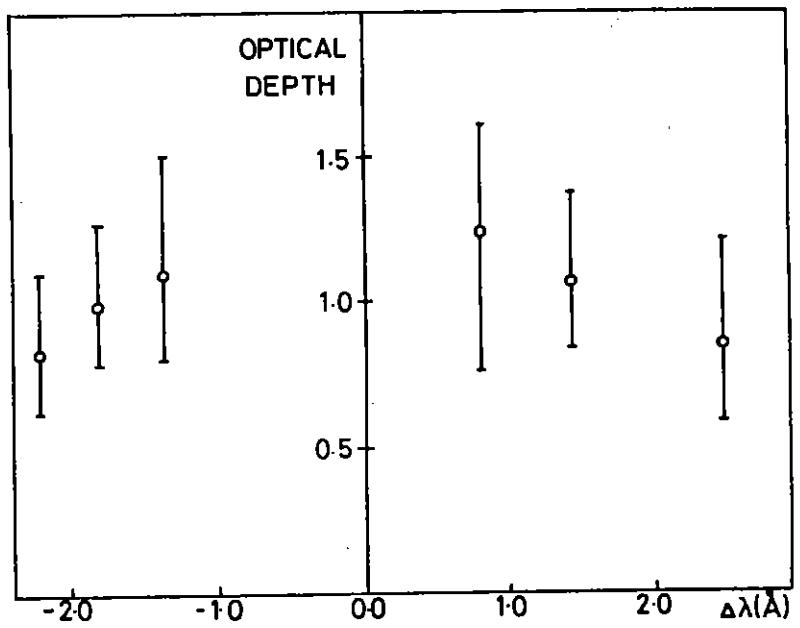

Fig B3.1 Optical depth vs Δλ.

The feasibility of performing high resolution lineshape and lineshift measurements on this line has been demonstrated. The entire lineprofile should be resolvable at a linecentre optical depth of 4 when the UV optics and generation system have been further optimised and a monitor of the probe radiation has been developed.

B3.2 THE APPLICATION OF AN IMPROVED UP-CONVERTED VUV SOURCE TO RADIATION TRANSFER IN ATOMIC HYDRODGEN

C D Heryet and R C M Learner (Imperial College)

The aim of this investigation is the use of tunable frequency-tripled laser radiation for the study of fundamental processes involving atomic hydrogen in the 122nm region. The primary interest is in the propagation of radiation (absorption, scattering, trapping, quenching, etc) over a wide range of atomic number densities and detuning frequencies.

A PTFE-coated cell suitable for the containment of atomic hydrogen at the necessary large atomic number densities has already been tested and preliminary results suggest that the production and containment are now sufficiently well understood to reach the ultimate target of 10^{12}–10^{16} atoms per cm^3, corresponding to line centre opacities ranging from less than one to 10^4.

The experiment is shown schematically in Figure B3.2. The function of the VUV monochromator is the removal of radiation at the fundamental (ie untripled) frequency. A well-diagnosed experimental configuration was established in earlier work. Close to line centre, the interest is not so much in the line shape but in the time-dependence of the laser pulse shape. The first time-resolved data were obtained in the period of this report.

Preliminary results on radiation trapping were unfortunately masked by instrumental effects associated with the atomic hydrogen source, which were not identified until near the end of the experimental period and further scheduled time will be needed to complete the project.

In association with the diagnosis of the atomic hydrogen source problems, significant improvements were achieved in the output of the frequency-tripled laser. The existing arrangement was found to be capable of operation over the entire region from 119nm to 130nm, with an output always in excess of 10^7 photons, and with no change in the optical arrangement. Improved conversion efficiency could, of course,

have been achieved by mixing noble gases, but this was not necessary in this experiment and so the speed and convenience of spectral scanning with a single gas were maintained. Finally, it was found that the output power in the 121 to 123nm region was enhanced by up to two orders of magnitude if the tripling cell is filled with krypton but contaminated by trace impurities of xenon. The impurity level was around 10 parts per million, and so well below the proportion usually mixed with krypton to improve phase-matching over a selected narrow region of the spectrum. The enhancement was achieved under a variety of operating conditions and, although further study is required, the technique is clearly simple and useful. The results are shown as dotted curves in fig B3.3.

B3.3 193 NM LASER PHOTODISSOCIATION OF NOCl – INITIAL VIBRATIONAL DISTRIBUTION AND RELAXATION

I T F Gillan, D J Denvir, D G Cunningham, H F J Cormican, I Duncan, W D McGrath and T Morrow (The Queen's University of Belfast).

Introduction

During the past year our programme (Ref B3.4) on possible stimulated anti-Stoke's Raman (SASR) up-conversion in inverted highly vibrationally excited molecules concentrated on elucidation of the fundamental photophysical and photochemical processes which occur on 193 nm laser photodissociation of nitrosyl chloride NOCl and obtaining the essential experience and parameters required to optimise the system for subsequent investigation of possible laser frequency up-conversion.

The early work on the photodissociation dynamics and photochemical reactions of the NOCl system has been reviewed in several publications (Refs B3.5-8). The formation of highly vibrationally excited NO (ie NO‡) on direct flash photodissociation of NOCl was first observed by Basco and Norrish (Ref B3.5), who proposed the process(1). The production of NO‡ via a slow subsequent reaction (2) (k_2 = 5.4 x 10^{-12} cm^3 $molecule^{-1}$ s^{-1}) was proposed by Grimley and Houston (Ref B3.6) in order to explain an observed slow build-up in infra-red flourescence intensity after laser photodissociation of

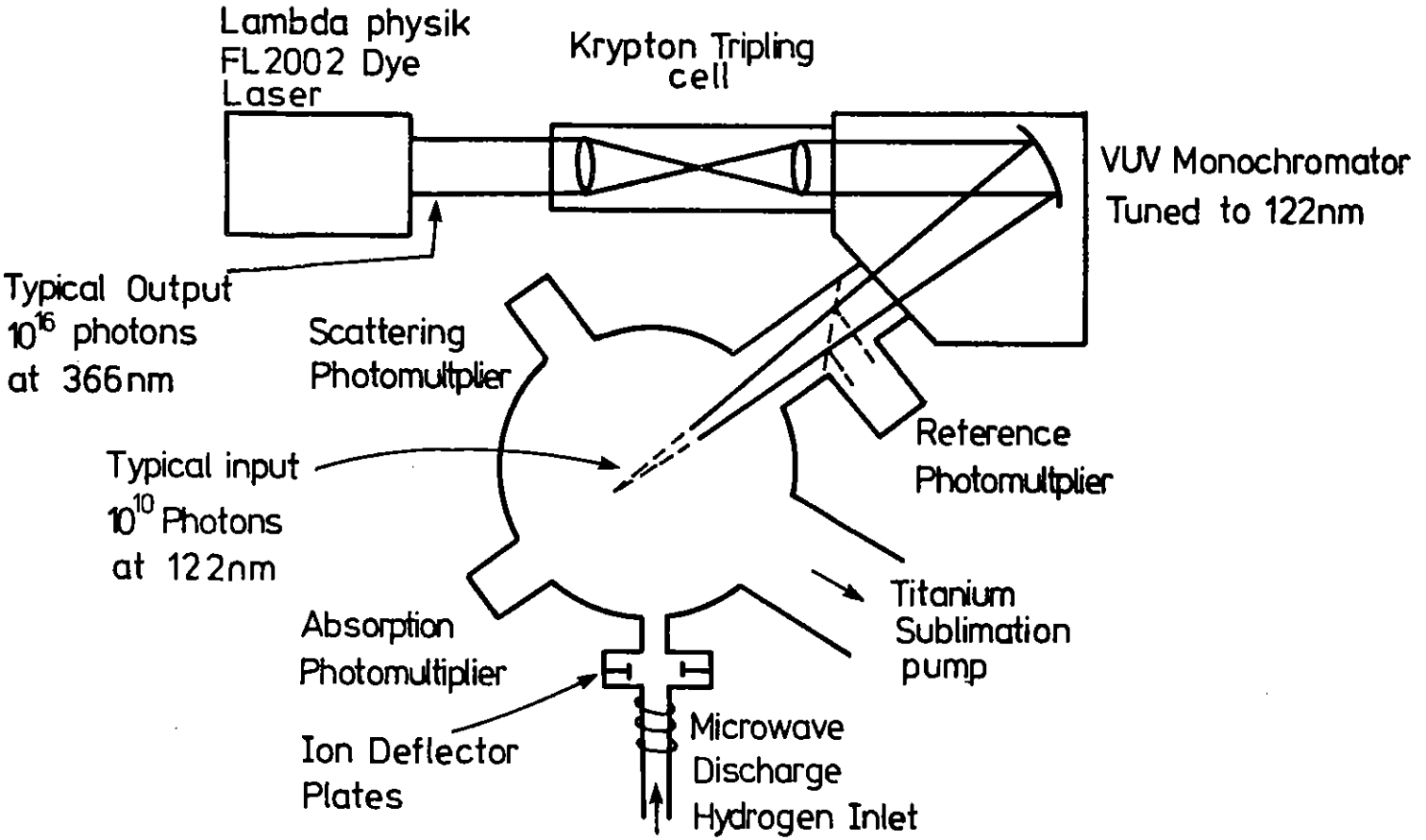

Fig B3.2 Experimental lay-out.

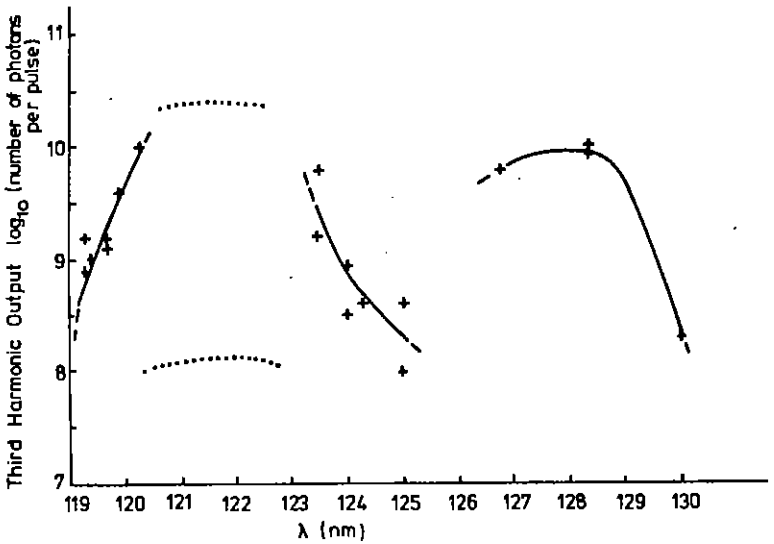

Fig B3.3 Third Harmonic Output obtained.

NOCl.

$$NOCl \xrightarrow{h\nu} NO^{\ddagger} + Cl \qquad (1)$$

$$Cl + NOCl \longrightarrow NO \text{ (or } NO^{\ddagger}) + Cl_2 \text{ (or } Cl_2^{\ddagger}) \qquad (2)$$

The translational energy distribution of the photofragments (ie NO‡ and Cl resulting from 193 nm laser photodissociation of NOCl was obtained by Werner, Wunderer and Walther (Ref B3.9) using the unambiguous time-of-flight spectroscopy technique. They interpreted their results on the basis of the NO‡ formed in (1) having initially a narrow vibrational distribution (v'' ≈ 10–18) strongly peaked at v'' =14.

The initial vibrational population distribution of the NO‡ ($X.^2\pi$) formed in (1) has been investigated for several photodissociation laser wavelengths (viz 193, 249, 308 and 337 nm) by Moser, Weitz and Schatz (Ref B3.8) using time-resolved infra-red emission as the diagnostic technique. Their vibrational distributions were deconvoluted from the initial emission intensities (at ~ 1 μs after the laser pulse) isolated using a variable interference filter whose band-pass overlapped ~ 3-4 vibrational emission bands. Their results for 193 nm photodissociation of NOCl indicate a broad initial vibrational distribution (v'' = 1-18) with a maxima in the v'' = 8-10 region. The authors assume rapid (< 1 μs) rotational thermalisation under their pressure conditions (0.05-0.3 Torr NOCl) and that reaction (2) is too slow to contribute appreciably to the NO‡ yield at short times (~ 1 μs) after the laser pulse. The work of Sudbϕ and Loy (Ref B3.10) however indicates rotational thermalisation times of the order of 10 μs (at 0.05 Torr) to 1.5 μs (at 0.3 Torr).

Recent work (Ref B3.11) of the present authors has confirmed that reaction (2) is considerably faster (ie k_2 = (3.0 - 7.0) x 10^{-11} cm^3 $molecule^{-1}$ s^{-1})(Refs B3.12-13) than proposed by Grimley and Houston (Ref B3.6) and leads predominantly to formation of vibrationally excited Cl_2 (ie $Cl_2^{\ddagger}$) and NO in its ground vibrational state. The $Cl_2^{\ddagger}$ subsequently undergoes vibrational energy transfer (k_T = 1.9 x 10^{-12} cm^3 $molecule^{-1}$ s^{-1}) with residual NOCl to produce

NOCl‡. Although the vibrational energy transfer from Cl_2‡ to NOCl might be expected to selectively populate the v_2 mode of NOCl‡, population of several lower vibrational levels of the v_1 mode by inter-mode transfer from v_2 and also by near-resonant vibrational energy transfer from NO‡ would be expected. The slow vibrational energy transfer from Cl_2‡ leads to the build up of NOCl‡ (v_1 mode) infra-red fluorescence, observed by Grimley and Houston (Ref B3.6) and wrongly attributed to NO‡ formed directly in reaction (2). The failure of the latter authors to distinguish between NO‡ and NOCl‡ (v_1 mode) fluorescence may be attributed to the relatively low spectral resolution obtainable using the infra-red fluorescence technique. The formation of NOCl‡ in partially photodissociated mixtures leads to intense transient NOCl‡ absorption over the 200–300 nm region.

In the experiments reported below, the laser induced fluorescence technique was used to determine the initial vibrational distribution and the subsequent vibrational relaxation kinetics following 193 nm laser photodissociation of NOCl. The initial vibrational distribution determines the maximum frequency up-conversions and gains attainable in the SASR process (Ref B3.4). The influence of input ArF laser power and added buffer gases on the laser potential of the NOCl photodissociation system are also discussed in detail.

Experimental

The basic experimental configuration used was similar to that described previously (Ref B3.4). The NOCl (in excess He buffer) was photodissociated in a flowing gas cell using the EMG 150 ArF laser. The nascent NO‡ was probed by tuning the time delayed dye laser pulse into resonance with appropriate vib-rotational lines in either the β- or γ-systems of NO and monitoring the subsequent laser induced fluorescence from either the $B.^2\pi$ or $A.^2\Sigma^+$ states respectively.

The complete β/γ fluorescence spectra were recorded on the intensified diode array (OMA) system and the digitised OMA output was fed directly to an Apple microcomputer which integrated the area under a selected (v' → v'') fluorescence band. As previously (Ref B3.4), the microcomputer provided signal averaging over a number (~ 5–50) of

photodissociation events, provided direct correction for shot-shot variations in the dye laser output and also controlled the tuning steps of the dye laser and the firing sequence of the photodissociation and probe lasers. The averaged fluorescence signal as a function of the dye laser input wavelength provided an excitation (absorption) spectrum of the NO‡ ($A.^2\Sigma^+ \rightarrow X.^2\pi$ or $B.^2\pi \rightarrow X.^2\pi$) vibrational band under investigation.

A typical excitation (absorption) spectrum of the NO($B.^2\pi$. v' = 0 → $X.^2\pi$. v'' = 10) band, recorded 150 ns after 193 nm laser photodissociation of NOCl, and the recorded spectrum of the corresponding NO($B.^2\pi$. v' = 0 → $X.^2\pi$) laser induced fluorescence are shown in figure B3.4.

Results

Since the tuning range of any one dye generally only overlapped a limited number (2–3) of adjacent v' → v'' bands, the initial vibrational energy distribution of the nascent NO‡ was obtained by measuring the ratios of the relative fluorescence excitation spectra obtained following dye laser excitation in adjacent (v' → v'' and v' → v'' + 1) bands of the β and γ systems. The ratios of the relative vibrational populations, given in Table B3.1, were obtained from the ratios of the fluorescence excitation spectra after correction for the relative absorbed dye laser energies.

The integrated absorption cross section σ_A of a single elect-vib-rotational line is related to the oscillator strength f(J', J'') by the expression (Ref B3.14)

$$\sigma_A = \int_{J',J''} \sigma \, dv = \frac{\pi e^2}{mc^2} \cdot f(J', J'') \cdot N_{J''}/N_{TOT} \qquad (3)$$

where $N_{J''}/N_{TOT}$ is the fractional population in that absorbing rotational level. The oscillator strength f(J',J'') is related (Ref B3.14) to the band oscillator strength f(v', v'') by

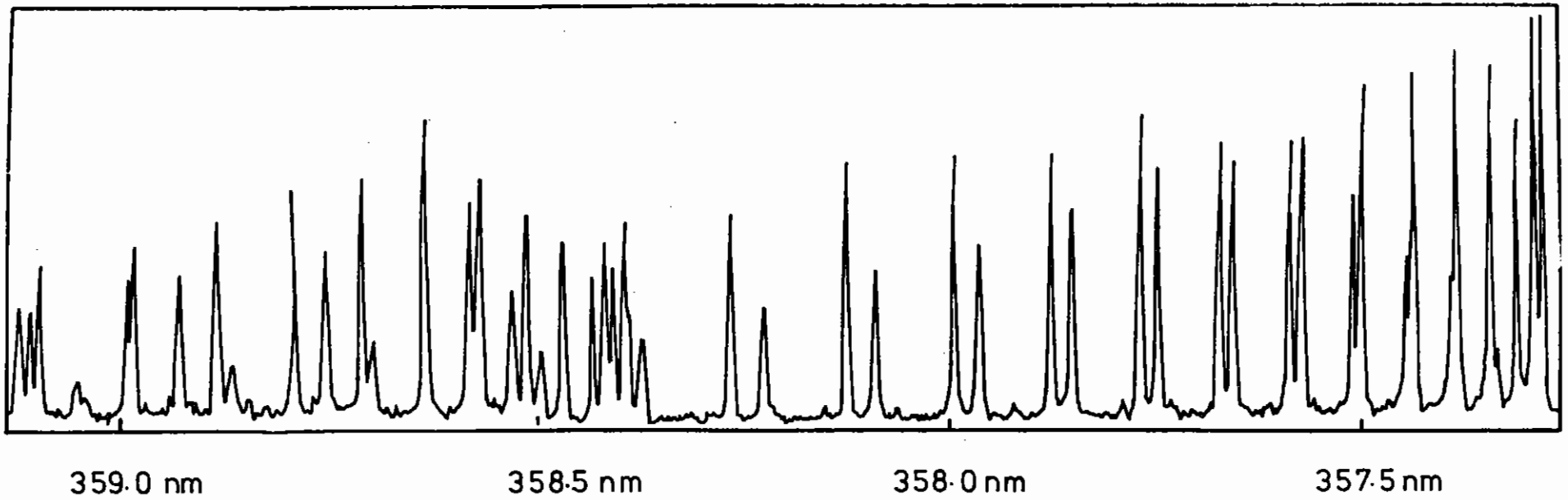

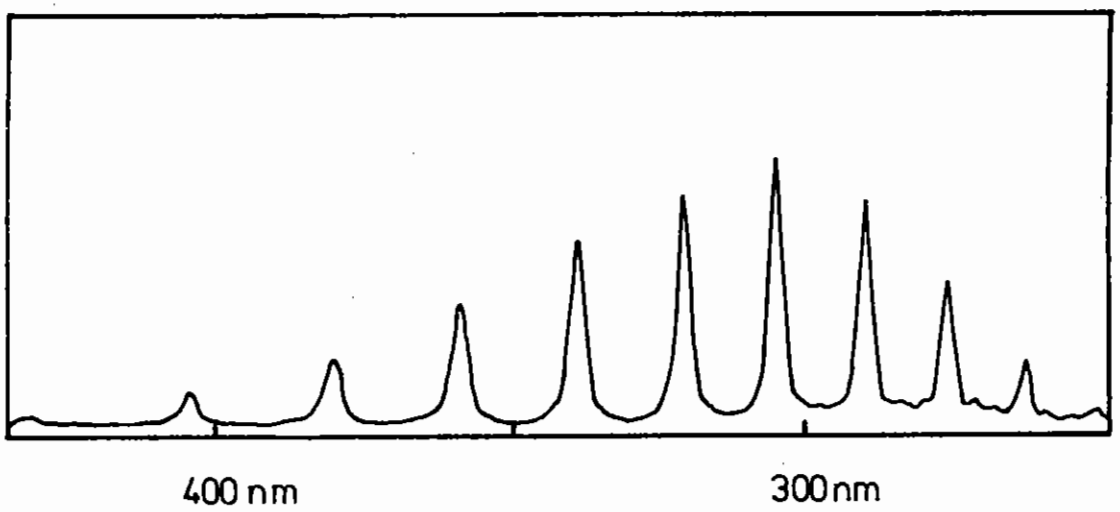

Fig B3.4 (a) Typical excitation spectrum of NO β(0,10) band recorded 150 ns after 193 nm photo-dissociation of 0.2 Torr NOCl in 760 Torr He and (b) the corresponding β emission spectrum (uncorrected for detector response).

$$f(J', J'') \propto f(v', v'')S_{J', J''}/(2J'' + 1) \qquad (4)$$

where $S_{J', J''}$ is the HONL-LONDON factor for the appropriate (J'-J'') transition.

Since the terms $N_{J''}/N_{TOT}$ and $S_{J', J''}/(2J'' + 1)$ in expression (3) and (4) are essentially constant for corresponding elect-vib-rotational lines in adjacent (v' + v'', v' + v'' + 1) absorption bands, the corresponding relative absorbed dye laser energies are determined predominantly by the ratio of the oscillator strengths f(v', v'')/f(v', v'' + 1). The oscillator strengths f(v', v'') used were either taken from the paper by Ory (Ref B3.15) or calculated from the Franck-Condon factors given by Nicholls (Ref B3.16). The ratio of the laser induced fluorescence intensities for excitation in adjacent (v' + v'', v' + v'' + 1) bands was obtained as an average over several (4-25) corresponding rotational lines in the adjacent (v' + v'') bands.

All results in Table B3.1 were obtained on 193 nm photodissociation of 0.2 Torr NOCl in 760 Torr helium using a laser energy density of ~ 50 mJ/cm^2 incident on the gas cell. The use of low NOCl pressures minimised self-quenching of the β/γ fluorescence whilst the high buffer gas pressure facilitated rapid (< 50 ns) rotational and translational thermalisation of the photodissociated mixtures to approximately room temperature.

TABLE B3.1

Experimentally determined ratios of the initial vibrational populations in various v" levels of NO(X.$^2\pi$)

Population Ratios (v" +n)/v"	Value
5/4	1.58 ± 0.29
6/5	1.98 ± 0.36
7/5	7.80 ± 1.43
7/6	3.15 ± 0.58
8/7	0.78 ± 0.14
9/8	0.98 ± 0.18
10/7	1.41 ± 0.11
13/10	0.48 ± 0.12
13/12	0.68 ± 0.18
13/11	0.67 ± 0.17
14/12	0.55 ± 0.14
14/11	0.35 ± 0.09

The photodissociated mixture was probed adjacent to the ArF laser entrance window by the apertured (diameter ~ 1 mm) dye laser beam which was delayed to ~ 150 ns after the ArF pulse. All NO‡ spectra recorded under the latter conditions were observed to be rotationally cold and, under the conditions used, the laser induced fluorescence intensity was a linear function of the probe dye laser pulse energy.

Under such conditions we assume essentially total photodissociation of the NOCl close to the ArF laser entrance window and that the ArF laser does not appreciably perturb the initial vibrational distribution of the nascent NO‡. The validity of these assumptions was investigated in considerable detail for our experimental conditions. The bleaching curve (ie % transmission versus incident laser energy density) obtained for the ArF laser incident on a 1 cm long sample containing 1 Torr NOCl (in 760 Torr helium) showed excellent agreement with a simple computer simulation of the bleaching process. The latter indicates % NOCl photodissociations > 90% under the experimental conditions used to

obtain the ratios in Table B3.1. The initial populations monitored in the NO‡ ($X.^2\pi$) v'' = 7, 9 and 14 levels were independent of the incident ArF laser energy density over the range 30-100 mJ/cm^2 indicating the absence of appreciable perturbation of the initial vibrational population distribution by the ArF photodissociation laser under our experimental conditions.

Individual measurements of the v''/(v'' + n) population ratios were subject to relatively large random errors due to the inherent difficulty in maintaining constant excitation and detection geometry during a prolonged experimental period. These errors were largest when the second harmonic of the dye laser was used as the excitation source due to reduced excitation intensity and slight 'beam walk' on wavelength tuning. For results obtained under the latter (worst) conditions a plot of relative deviation from the mean value versus frequency of deviation approximated to a normal error distribution curve with an average relative deviation $\delta = 0.26$. The latter figure was therefore used as an estimate of the precision of any individual measurement of the population ratio and where N measurements were averaged the errors reported in Table B3.1 are given as $\delta/\sqrt{N}$.. For ratios obtained using the dye laser fundamental (ie v''> 10) this procedure somewhat over estimates the probable errors.
The initial vibrational distribution, shown in figure B3.5, was obtained from the ratios in Table B3.1 and is normalised to unity for v'' = 4. The large probable errors, represented by the error bars in figure B3.5 arise from accumulation of errors due to multiplication of the population ratios in Table B3.1. The populations in the NO($X.^2\pi$) (v'' = 0) and (v'' = 1) levels were observed, as reported previously (Ref B3.4), to build up after the photodissociation pulse from negligibly small initial values.

The subsequent kinetics of the vibrational populations in the NO‡ ($X.^2\pi$ v'' = 0, 1, 5, 7 and 9) were investigated during the current experiments and previously (Ref B3.4). Levels with v'' ≤ 5 showed a rapid initial build up of population, followed by a subsequent decay, whilst for v'' ≥ 7 the populations were observed to decay from their initial values with approximately exponential dependences. The lifetime τ_D of the (v'' = 9) level as a function of NO‡ pressure (ie

initial NOCl pressure) was investigated in detail for various initial NOCl pressures in the range 0.25 - 20 Torr. The individual temporal dependences of the NO‡ (v'' = 9) number densities, n(t), at all initial NOCl pressures were observed to fit an exponential decay process of the form $n(t) = n(0)e^{-t}/\tau_D$ over the time range investigated (ie t = 0 to $t > 1.5\ \tau_D$). The rate constant (ie $1/\tau_D$) for the decay process was a linear function of the initial NOCl pressure (ie total initial NO‡ number density) for initial NOCl pressures in the range 0.25 - 5.0 Torr. The rate constant k_Q for the quenching of the NO‡ ($X.^2\pi$. v'' = 9) by NO‡, derived from the slope of the linear plot of τ_D^{-1} versus initial NOCl pressure was $(6.5 \pm 0.6) \times 10^{-12}$ cm^3 molecule^{-1} s^{-1}. Increase in initial NOCl pressure above 5 Torr resulted in a progressively marked reduction in τ_D (to ~ 23 ns at 20 Torr NOCl) and increased deviation from the linar dependence of τ_D^{-1} on initial NOCl pressure. The latter deviation was attributed to additional rapid vibrational quenching either by undissociated NOCl, remaining after the ArF laser pulse at these high initial NOCl pressures, or by ground state NO formed by the subsequent reaction (2).

DISCUSSION

(a) Energy partitioning among NOCl photo-fragments

The intial vibrational distribution, shown in figure B3.5, is similar in general shape but somewhat narrower than the distribution obtained by Moser et al (Ref B3.8) using the infra-red fluorescence technique. The v'' = 4 - 14 levels are all initially highly inverted with respect to the lower v'' < 4 levels with the maximum inversions occurring for the levels v'' = 8 - 10 with respect to v'' = 0, 1.

Of the maximum energy available, ie 4.83 eV (= $h\nu - D_o$), for partition between the photofragments (ie NO and Cl) on 193 nm photodissociation of NOCl the distribution in figure B3.5 indicates that the average vibrational energy per NO molecule, $\bar{E}_v$, is 2.22 ± 0.10 eV. The translational energy distributions (of NO and Cl) measured by Werner et al (Ref B3.9) indicate that the average total translational energy $\bar{E}_{tot}$

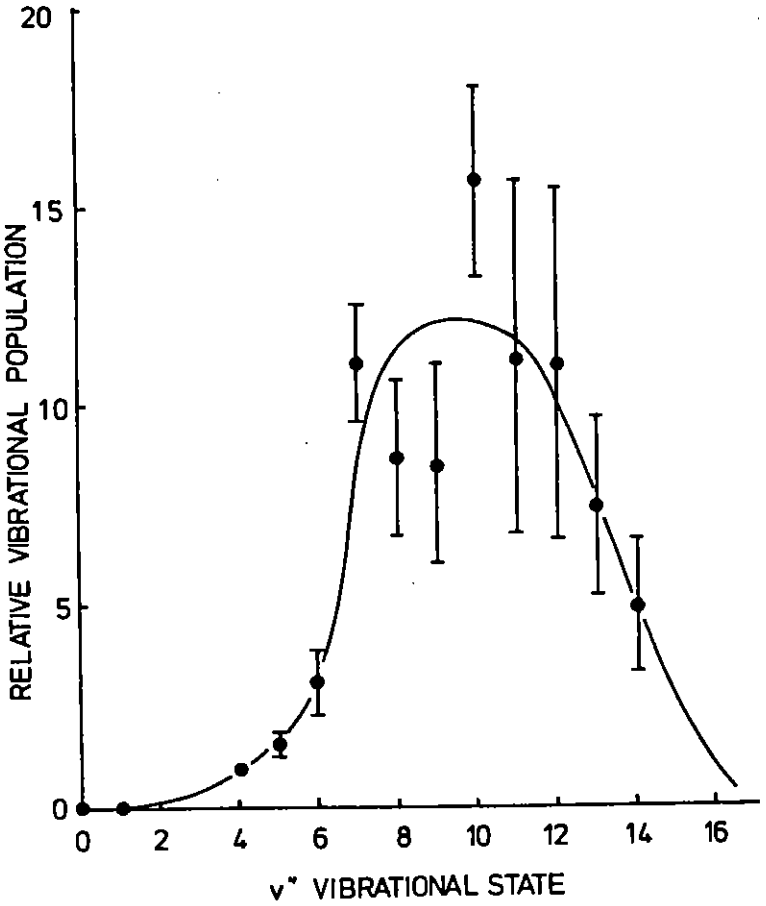

Fig B3.5 The NO‡ vibrational population distribution observed 150 ns after 193 nm photodissociation of 0.2 Torr NOCl in 760 TOrr He. The populations are normalised with respect to the v" = 4 level.

of both fragments is 1.47 eV and the average excitation available for distribution between vibration (ie $\bar{E}_V$) and rotation (ie $\bar{E}_R$) of the NO fragment is therefore 3.36 eV. The average initial rotational excitation of the NO molecule is therefore $\bar{E}_R$ = 1.14 eV, an energy which would be equivalent to an initial rotational temperature of ~ 13,200 K at thermal equilibrium. The initial rotational population distribution, like the initial vibrational and translational distributions, may however be far from a thermally equilibrated population distribution. Assuming that the average total initial translational energy $\bar{E}_{tot}$ is equally partitioned between the NO and Cl photofragments then the average translational energy $\bar{E}_T$ per molecule is 0.735 eV corresponding to a translational temperature of ~ 5700 K at thermal equilibrium.

Under our experimental conditions, where NOCl was photodissociated in the presence of a large excess of helium, the photofragments are rapidly (< 50 ns) rotationally and translationally cooled to room temperature, whilst the vibrational equilibrium is relatively slow (> 10 μs). In the absence of excess inert gas, the photodissociated system would still equilibrate rotationally and translationally relatively quickly (in ~ 1 μs at 0.2 Torr) but to a high equilibrated translational and rotational temperature of ~ 7600 K. Under the latter conditions, the maximum population per rotational level is a factor of ~ 7 lower than in the presence of buffer gas and the Doppler width of each rotational line is increased by a factor of 5, leading to a corresponding reduction of the absorption cross-section by the same factor. The intensity of laser induced fluorescence (or maximum population in a single rotational level of the upper electronic state) attainable on excitation of the NO‡ ($X.^2\pi$) by the dye laser in the absence of inert buffer gas would be a factor of 35 lower (neglecting dye laser bandwidth effects) than that observed in the presence of excess buffer gas. Several experimental attempts to observe laser induced fluorescence from NO‡ in the absence of buffer gas failed to produce detectable signals in agreement with the above conclusions. It also seems likely that in the absence of inert gas the broad-band 193 nm ArF laser output will couple into various rotationally hot

vibrational bands (eg $\gamma(3,0)$, $\beta(7,0)$, $\gamma'(0,5)$, $\varepsilon(5,7)$, $\gamma'(3,9)$) and considerably perturb the energy distribution of the photofragments. The latter conclusion is supported by the observation of intense β and γ fluorescences when only the ArF laser was incident on NOCl in the absence of buffer gas.

(b) Laser potential of NOCl photodissociation system

The object of the current programme (Ref B3.4) is to utilise the inverted highly vibrationally excited NO‡ for laser frequency up-conversion either via the SASR process or by direct optical pumping to produce population inversions in the higher (A, B, C, D) electronic states of NO. From the considerations discussed in (a), the initial partitioning of the available energy between vibration, rotation and translation of the photofragments is now well understood and the maximum population per inverted vib-rotational level is obtained in the presence of excess buffer gas when the system is rapidly equilibrated rotationally and translationally to ~ room temperature.

Under the latter conditions, the fraction of the total population of any one vibrational level in one vib-rotational level is a maximum of ~ 0.05 for the rotational levels (J'' = 5.5 - 9.5) in the $X.^2\pi_{\frac{1}{2}}$ splitting of NO‡. Direct optical pumping, using the dye laser, of such selected rotational levels in the higher inverted vibrational levels (eg $A.^2\Sigma^+.(v' = 2) \leftarrow X.^2\pi_{\frac{1}{2}}$ (v'' = 8) or $A.^2\Sigma^+.(v' = 3) \leftarrow X.^2\pi_{\frac{1}{2}}(v'' = 9)$) before significant vibrational relaxation has occurred (ie < 1 μs) will produce population inversion between the excited levels of the $A.^2\Sigma$ state and the corresponding levels of the lower $X.^2\pi$ (v'' = 0–4) states. The $A.^2\Sigma^+(v' = 2,3)$ levels have a radiative lifetime of ~ 200 ns and the stmulated emission cross-sections for $A.^2\Sigma^+(v' = 2) \rightarrow X.^2\pi(v'' = 0)$ and $A.^2\Sigma^+(v' = 3) \rightarrow X.^2\pi(v'' = 1)$ emissions at 205 and 203 nm respectively are ~ 5×10^{-17} cm^2. Burrows et al (Ref B3.17) obtained laser action on the comparable $A.^2\Sigma^+(v' = 0) \rightarrow X.^2\pi$ (v'' = 1,2) transitions at 237 and 248 nm by direct longitudinal pumping on the $\vartheta(0,0)$ transition at low (0.2 Torr) pressure of NO in the absence of inert buffer gas.

In the NOCl photodissociation system, the excess buffer gas required to

obtain rapid rotational/translational equilibration to ~ room temperature will also cause some rotational redistribution within the lower and upper levels involved in the optical pumping process. The rotational quenching rate constants currently available suggest that rotational relaxation into the lower pumped rotational level of the $X.^2\pi_{\frac{1}{2}}(v'' = 8,9)$ state should at least partially compensate for the detrimental rotational redistribution within the upper $A.^2\Sigma^+$ lasing level.

The main limitation on the population inversions (and gains) attainable from the optically pumped laser schemes proposed above is the NO‡ ($X.^2\pi$, v'' = 8,9) number density, determined solely by the maximum pressure (and length) of NOCl which can be completely photodissociated using presently available ArF laser output energies of ~ 200 mJ/pulse. The latter maximum photodissociation energy limits our maximum inversion to ~ 10^{15} molecules cm^{-3} per elect-vib-rotational level in a 10 cm gain length. Burrows et al (Ref B3.17) observed laser action for corresponding inversion densities of (0.2 - 9) x 10^{15} molecules cm^{-3} (optimum gain at (3.5 - 7.0) x 10^{14} molecules cm^{-3}) in a gain length of ~ 94 cms. Under high reflectivity resonant cavity conditions the gain length would be relatively unimportant.

As for the optically pumped laser, the maximum up-converted gain attainable by the stimulated electronic Raman scattering (SERS) process is also limited by the presently available ArF laser output energies of ~ 200 mJ/pulse. It is usual to assume that for SERS, starting from spontaneous Raman 'noise', the SERS threshold will be reached for $g_R l = 30$, where g_R is the Raman gain coefficient and l the length of the Raman medium. In practice, an SERS signal may be detectable for much lower values of $g_R l$, particularly when the SERS medium is used as an anti-Stokes Raman amplifier. For a typical up-conversion scheme involving near resonance ($\Delta\nu = 0.5$ cm^{-1}) dye laser pumping of a single elect-vib-rotational line of the $A^2\Sigma^+(v' = 3) \leftarrow X^2\pi_{\frac{1}{2}}(v'' = 9)$ band, under the optimum inversion conditions described above, the estimated $g_R l$ values for the upconverted transitions $A^2\Sigma^+(v' = 3) \rightarrow X.^2\pi(v'' = 0,1)$ are ~ 5 for an input dye laser pump power density of ~ 10^8 W/cm^2.

B3 References

B3.1 K G H Baldwin, J P Marangos, M C Gower and D D Burgess, Optics Communications, 52, p351-354.

B3.2 K G H Baldwin, University of London PhD Thesis (1983).

B3.3 J P Marangos, University of London PhD Thesis (1986).

B3.4 I T F Gillan, D J Denvir, J Bechara, H F J Cormican, I Duncan, W D McGrath and T Morrow, Rutherford Appleton Laboratory Laser Division Annual Report, Report No RAL-85-047, Sec B3.4, B53 (1985).

B3.5 N Basco and R G W Norrish, Proc Roy Soc A268, 291 (1962).

B3.6 A J Grimley and P L Houston, J Chem Phys 72, 1471 (1980).

B3.7 G E Busch and K R Wilson, J Chem Phys 56, 3655 (1972).

B3.8 M D Moser, E Weitz and G C Schatz, J Chem Phys 78, 757 (1983).

B3.9 L Werner, B Wunderer and H Walther, Chem Phys 60, 109 (1981).

B3.10 A S Sudbo and M M T Loy, J Chem Phys 76, 3646 (1982).

B3.11 J Bechara, T Morrow and W D McGrath, Chem Phys Lett, 122, 605 (1985).

B3.12 M A A Clyne and H W Cruse, J Chem Soc Faraday Trans II, 68, 1281 (1972).

B3.13 D Kita and D H Steadman, J Chem Soc Faraday Trans II, 78, 1249 (1972).

B3.14 S Cieslik and M Nicolet, Planet Space Sci 21 925, (1973).

B3.15 H A Ory, J Chem Phys 40, 562 (1964).

B3.16 R W Nicholls, Nat Bur Stand J Res A68, 535 (1964).

B3.17 M D Burrows, S L Baughcum and R C Oldenborg, Appl Phys Lett 46, 22 (1985).

Section Editor: W T Toner

B4 LASER SUPPORT FACILITY OPERATIONS AND DEVELOPMENT

B4.1 INTRODUCTION

J Hardy, J Szechi, W T Toner, (RAL)

The Laser Support Facility began RAL-based operations in its new laboratory space at the beginning of May 1985. The layout of the facility is shown in Fig 1. Shuttered beam ports connect all four laser laboratories and cable patch panels can be used for signal interconnection so that any laser may be synchronised and used with any other. For example, UV picosecond laser pulses have been amplifed in both excimer lasers (Sections B4.2 and C3.3). The laboratories are all fully provided with the gas and power connections to run additional lasers if required; both the JK YAG-pumped dye laser and the Oxford KX1F excimer laser have been used for short periods in Lab B (Sections B1.7 and B2.3). A separate sample preparation laboratory, equipped with basic facilities, is also now in use. The Loan Pool facilities are discussed in Section B4.4.

Fifty six scheduled experiments by twenty nine user groups were carried out during the period of this report. The time was allocated approximtely 70% to chemistry and 15% to each of physics and biology supported projects, and this is reflected in the contributions to this report.

Both excimer lasers were refurbished in Germany at the beginning of the period and have operated reliably for most of the year, although problems with the EMG150 thyratrons have occured recently. An etalon has been purchased and is now used to monitor the performance of the line-narrowed KrF laser (the EMG150ETS) during experimental runs, and this laser has also been run line-narrowed as both an XeF and an ArF laser, although the latter is not entirely satisfactory. Several mJ at 225 nm and 206 nm have been obtained by Raman shifting the line-narrowed 248 nm laser in hydrogen.

The F12002E excimer pumped dye laser has been used with a frequency tripling cell to generate light at 120 nm with improved efficiency (Section B3.2). Some measurements were also made to establish the near infra-red capabilities of this laser using a Raman cell with a

capillary tube waveguide. The EMG101E was used to pump the dye sulforhodamine 101 at 652 nm to give hydrogen Stokes lines at 895, 1420 and 2480 nm. With 14 mJ at 652 nm, 1.5 mJ at first Stokes and 0.5 mJ of second Stokes were observed. Although the third anti-Stokes line at 360 nm could be seen, the available detection system was not sensitive enough to observe the 0.1 to 0.2 mJ of the third Stokes which we believe was present. In optimum conditions, 14 mJ of fundamental should be capable of generating 0.5 mJ of the third Stokes.

The effective throughput of the Triplemate spectrometer has been improved by a factor of about 2.5 by the incorporation of a cylindrical lens to match the output spectrum to the height of the elements in the diode array.

The most notable changes in the equipment in 1985 are the addition of the Picosecond laser system and its diagnostics (Sections B4.2 and B4.3) and the acquisition of a new gateable intensified diode array and controller, the OSMA system by Spectroscopy Instruments Limited. The EMG101E excimer laser and the FL2002 dye laser will become part of the loan pool equipment in May 1986 and will be replaced with a higher power excimer laser (the Lumonics HX460) pumping a Lambda Physik FL3002. The HX460 has been delivered. It is rated to produce 30 Watts average power and to run either as a 200 mJ maximum pulse energy laser at high repetition rate or to deliver up to 400 mJ/pulse at a lower repetition rate. In the high pulse energy configuration it may be used to pump two independently tunable dye lasers. A list of equipment available for use at the laboratory from May 1986 is given in Table 1.

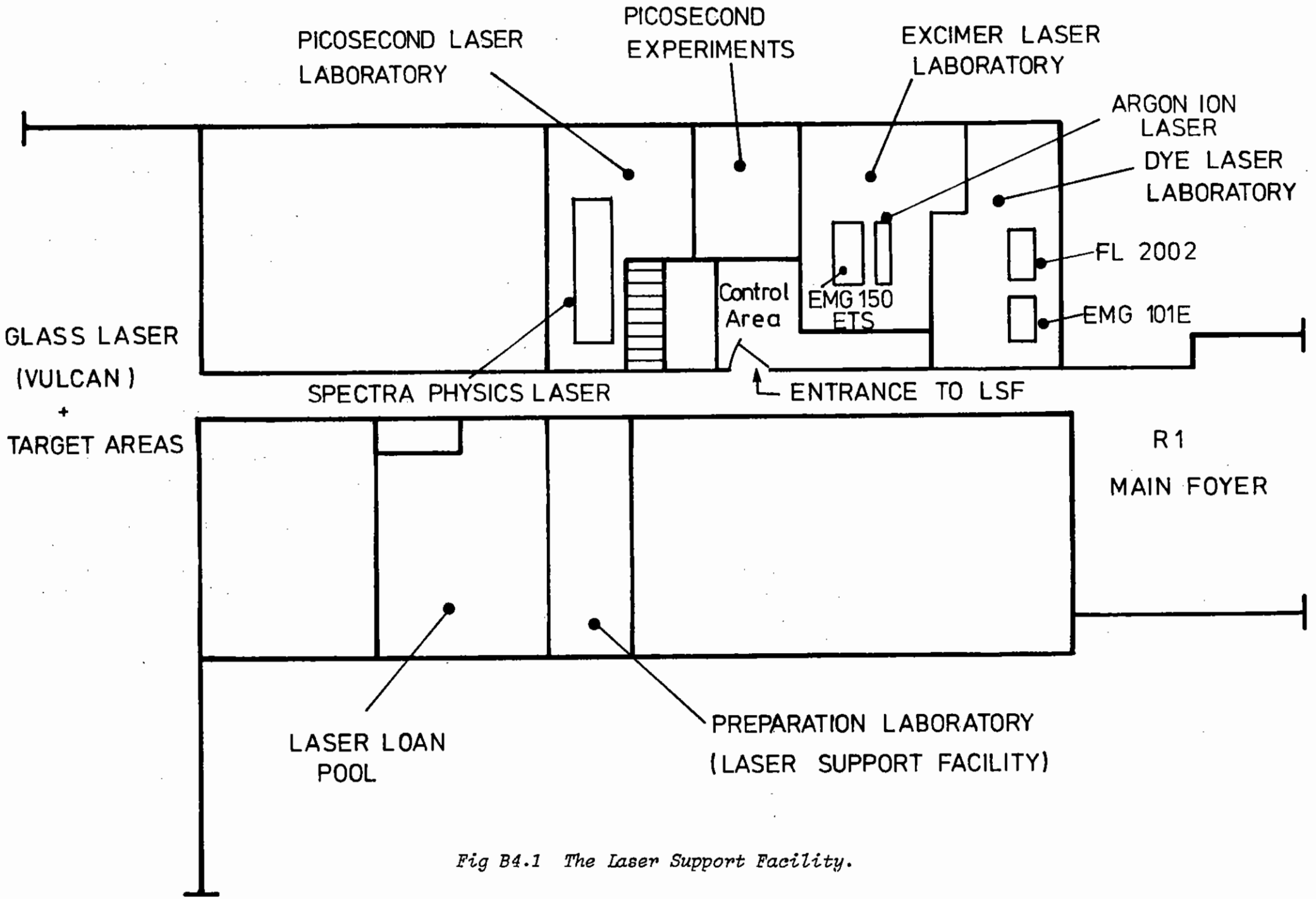

Fig B4.1 The Laser Support Facility.

TABLE I

Table I: List of RAL-based lasers and equipment from May 1986

1. Scheduled Lasers

RL1: Pulsed Dye Laser System. Output tunable from VUV to Infra-red.

(a) Pump Laser: Lumonics HX 460. Normally operates at 308 nm in two configurations (i) up to 200 mJ/pulse at up to 200Hz or (ii) up to 400 mJ/pulse at up to 80Hz. 30 watts max average power.

(b) Dye Laser: Lambda Physik. FL32002. Etalon, doubling with autotracking, Raman shifting, and frequency tripling options.

c) Second Dye Laser: Two independently tunable beams available by adding Loan Laser LL6.

RL2: High Energy Excimer Laser

(a) Excimer Laser: Lambda Physik EMG 150ETS. Operates at 193, 248, 351 nm. Injection locked line narrowed option. Up to 750 mJ/pulse at 10Hz (248 nm). Raman Shifter.

(b) Tunable dye output available using Loan Laser LL6.

RL3: Continuous Wave Ion Laser

Coherent Innova 90-5 (UV) CW Argon Ion Laser.

RL4: Picosecond Laser System

(a) Pump Laser: Spectra Physics CW modelocked YAG model 3460. Frequency doubling.

(b) Dye Laser: Spectra Physics Sync-Pumped 375 dye laser (80 mW at 82 MHz, 3 psec).

(c) Optional Cavity Dumper.

(d)* Amplifier Pump: Quanta-Ray DCR2 Q-Switched Nd-YAG 10 Hz; 2 nSec; .8J; Doubling + tripling.

(e) Dye Amplifier: Quanta-Ray PDA (1 mJ at 10 Hz 3 ps with R6G) Doubling. Mixing, doubling and mixing with YAG. Raman shifting output + continuum available. 308 and 248 nm outputs can be amplified in RL1 and RL2.

2. Auxillary Equipment

RD1 OMAII Intensified Diode Array, gateable
RD2 OMAII SIT Vidicon with UV scintillator
RD3 OSMA-SI Intensified Diode Array, gateable
RD4 SPEX 1877 Triplemate Spectrometer
RD5 Monospec 0.6 m grating spectrometer
RD6 Low dispersion spectrograph
RD7 Minuteman UV spectrograph
RD8 CW-pulsed Xe arc lamp
RD9 Tracor Northern signal processor
RD10 Biomation transient record, various photodiodes, calorimeters and oscilloscopes. A fast oscilloscope may not always be available. Calibration spectral lamps including a deuterium lamp are available.

3. Picosecond Diagnostic Equipment

PD1 Scanning Autocorrelator
PD2 *Fast Sampling Oscilloscope and fast photodiode
PD3 *Delli-Delti S-25 Streak Camera (2 ps limiting resolution) Synchroscan option. PD3 can be coupled to the RD2 OMA.
PD4 SRS Gated Integrators, computer interface. PD4 is usually used with PD5 computer.
PD5 IBM PC XT370
PD6 Camac Crate interfaced to PD5
PD7 *LeCroy qVt pulse height analyser interfaced to PD6. Various photodiodes and calorimeters; some NIM and CAMAC plug-ins.

4. Preparation Laboratory

This is a 25 m^2 laboratory with formica topped benches, activated filter fume hood, chemical balance, pH meter, freezer, test tube centrifuge and spectrophotometer. It is freely available to all users doing experiments at the laboratory. Basic dark room facilities are also available and there are two Joyce-Lobel microdensitometers.

Notes

1. Items marked * are the property of other groups at the CLF. They are usually but not always available to LSF users.

2. Access is also sometimes possible to equipment (eg Oxford Lasers excimer (1Hz), JK2000 oscillator (10Hz), S1 streak camera)) belonging to other groups in the Division.

B4.2 THE LSF PICOSECOND LASER SYSTEM

J R M Barr, I N Ross, W T Toner

The LSF picosecond laser system shown in figure B4.2 consists of a frequency doubled modelocked Nd:YAG laser (Spectra Physics Series 3000) which provides a continuous train of <120ps pusles at 82MHz repetition rate with up to 7.5W average power at 1.064μm. Frequency doubling to 532nm in potassium tytanyl phosphate (KTP) yields up to 750mW in <85ps pulses. This source is used to sychronously pump a dye laser (Spectra Physics 375B) which operates over the wavelength region 560nm to 680nm at an average power of 80mW. The repetition rate is 82 MHz and the pulse energy is ~1nJ. The pulse length varies slightly through the spectral region due to the bandwidth of available wavelength selectors and is typically 2.5ps (560nm-630nm, two plate birefringent filter) or 3.5ps (610nm-680nm tuning wedge). In the latter case the pulse is not transform limited.

Amplification of single pulses at 10Hz repetition rate is achieved using a pulsed dye amplifier (PDA, Quanta Ray) pumped by a Q-switched frequency doubled Nd:YAG laser (DCR-2A, Quanta Ray, 0.8J at 1.064μm). The gain of the amplifier chain is typically $5x10^5$-10^6 giving an output of 0.5mj-1mj. The background amplified spontaneous emission is <5% but in some wavelength regions it may be reduced by appropriate spectral filtering. Pulse to pulse energy fluctuations are currently ~23% RMS and efforts are being made to reduce this.

Efficient frequency doubling of the amplified pulses with conversion efficiencies in the region of 7-10% is possible using KD^*P crystals. The wavelength range 280nm to 340nm may be generated with pulse energies of ~50μJ. It is possible to frequency double the output of the synchronously pumped dye laser directly and an average power of 0.35mW has been demonstrated from a 100mW pump at 585nm. The residual

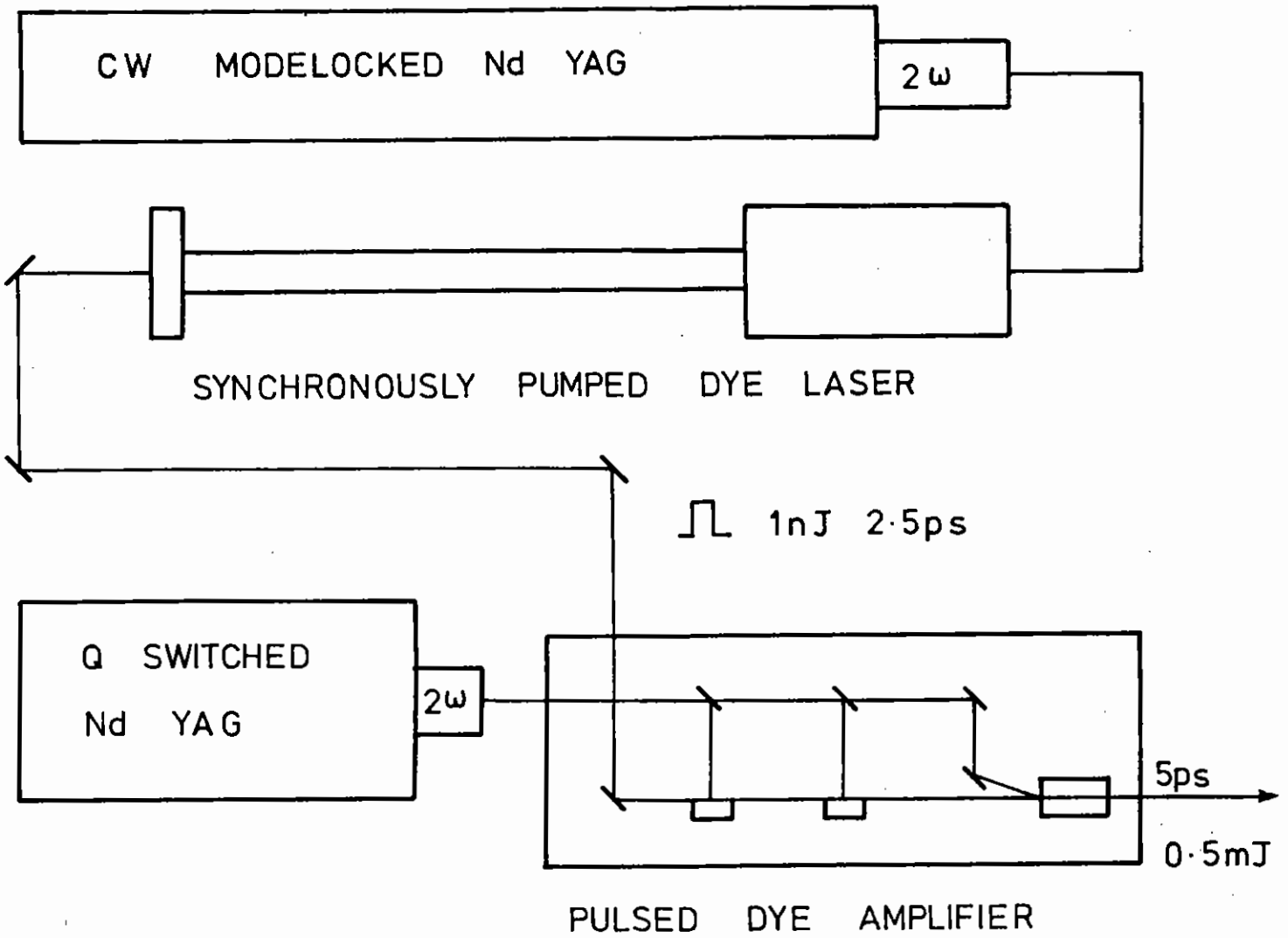

Fig B4.2 The Picosecond Laser System.

1.064μm output from the DCR2 has been mixed with the amplified dye pulses to give ~15μJ per pulse in the 363nm to 415nm range and after mixing with the doubled dye pulses gives ~5μJ in the 245nm to 257nm range. Amplification in excimer amplifiers at 308nm and 248nm has been demonstrated. A continuum has been demonstrated.

Further details of these extensions to the operating range of the laser are given in sections C3.1, C3.2, and C3.3 of this report.

Various pieces of diagnostic equipment are available. A rotating block autocorrelator enables real time measurements of the pulse length of the synchronous dye laser to be made. A fast diode (rise time ~30ps) and sampling scope are also available.

During the eight months since the installation of the picosecond laser the system has performed very reliably with minimal maintenance apart from routine adjustments. Only one flashlamp change on the modelocked Nd:YAG laser has been required despite a typical useage of 35-40hrs per week.

B4.3. A DETECTION SYSTEM FOR KINETIC MEASUREMENTS OF SMALL ABSORPTION CHANGES ON PICOSECOND TIMESCALES

M J C Smith and W T Toner (RAL)

Introduction

Absorption changes following excitation of a sample have been widely used to study ultrafast processes in physics, chemistry and biology. The combination of the tunable output of the picosecond dye laser (section B4.2) with Raman shifting, second harmonic or continuum generation provides a highly versatile system for generating excitation and probing pulse at separate wavelengths. A sensitive detection system is required since the excitation pulse energies and

hence induced absorption changes are limited and since the excitation intensity must be kept below the level at which non-linear effects or photochemical degradation of the sample set in. Attention must be paid to the large shot to shot variations which are inevitable when pump or probe beams are generated by non-linear processes.

Optical System

Figure B4.3 shows a schematic diagram of the detective system employed in a typical experiment where a sample is excited at 585nm and monitored through its absorption at 705nm as a function of delay between pump and probe pulses. The output of the pulsed dye amplifier is split. 30% of the beam forms the excitation pulse and passes through a chopper and a variable delay line consisting of a corner cube prism mounted on a translating slide. The remainder of the beam is focused into a cell containing ethanol to generate the probe beam by stimulated Raman scattering. After passing through optical filters, a spatial filter and a polariser, the probe beam is recombined with the pump beam by reflection off the surface of a wedged quartz flat. Light transmitted by the sample at the probe wavelength is detected by one of a pair of photodiodes constituting a difference detector. The second photodiode of the difference detector detects light reflected from the second surface of the quartz flat, proportional to the probe intensity incident on the sample. A probe monitor (PIN Silicon photodiode) and a pump monitor (vacuum photodiode) are employed for shot-by-shot normalisation of the difference detector signal as discussed below.

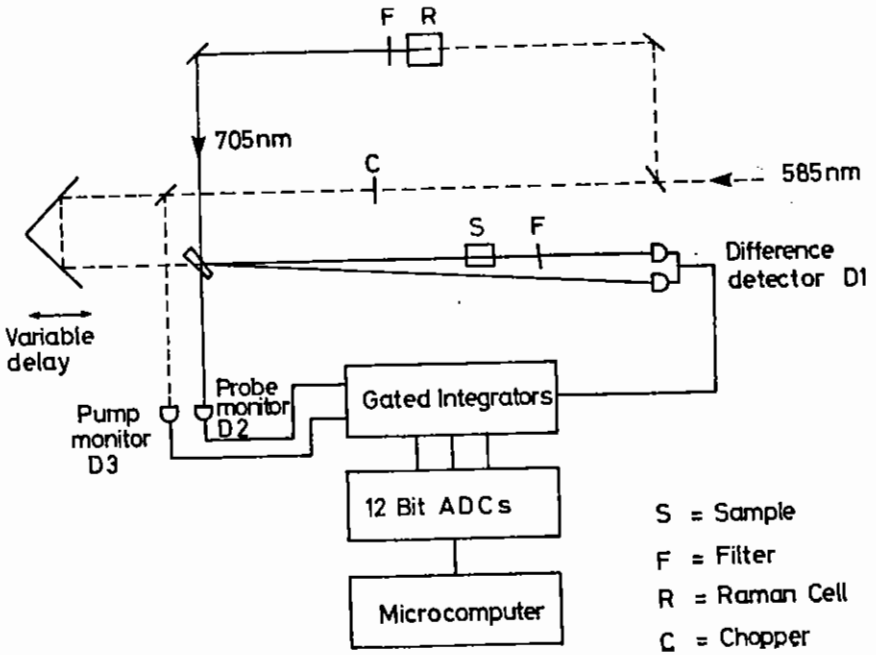

Fig B4.3 Picosecond transient absorption detection system.

Signal Processing

The difference detector was based on the design of Polland and Zinth (Ref B4.1) and consists of two reverse-biased Hamamatsu S1723-02 PIN silicon photocells operating so that the voltage induced by light incident on one detector is opposed by that induced by light incident on the other. The net voltage produced which is proportional to the difference in the two light levels is passed through an ac coupled unity gain amplifier and terminated into a 50Ω load.

Signals from the difference detector, the probe monitor and the pump monitor are passed to Stanford Research Systems SR250 gated integrators and the integrated signals during the gate period are digitised and stored by an SR245 computer interface. An IBM PC XT reads and analyses the data.

Data Processing

In a typical experiment, shot-to-shot variations in the pump intensity are typically in excess of 20% and in the probe intensity, typically 30%-40%. A simple average of the difference signal is not appropriate if the absorption changes are small.

The signal from the difference detector when the pump beam is on may be expressed in terms of the incident and transmitted light intensities as

$$D_{on} = \alpha I_o - \beta I_t + b \qquad (1)$$

where α and β are constants determined by the sensitivities of the respective channels of the detector and b is a baseline offset. When the pump beam is blocked by the chopper (alternate shots) the difference signal is

$$D_{off} = \alpha I_o - \beta I_o + b \qquad (2)$$

A method of analysis is described below which is appropriate when the baseline offsets in equations (1) and (2) are known to be identical (ie when the pump beam alone has been shown to produce no signal on the difference detector from for example fluorescence).

Fluctuations in I_o from shot to shot were eliminated by employing a probe monitor for normalisation which produces a signal proportional to the incident intensity

$$N = \gamma I_o$$

Figure B4.4 shows a plot of the difference signal against the

normalisation signal in a bleaching experiment. The pump off data define a baseline shown in the upper part of the figure. The data obtained with the pump on are more scattered as a result of shot to shot variations in pump intensity.

A normalised absorption change is determined from the data according to the equation

$$DA = (\gamma/\beta)\ (P_o/P)\ (D_{on} - D_{off}(N))/N$$

$D_{off}(N)$ is represented by the linear least squares fit of D_{off} vs N. The absorption change is normalised to a standard pump intensity, P_o and the results averaged. The calibration factor (γ/β) is determined from measurements on a quartz flat of known transmission.

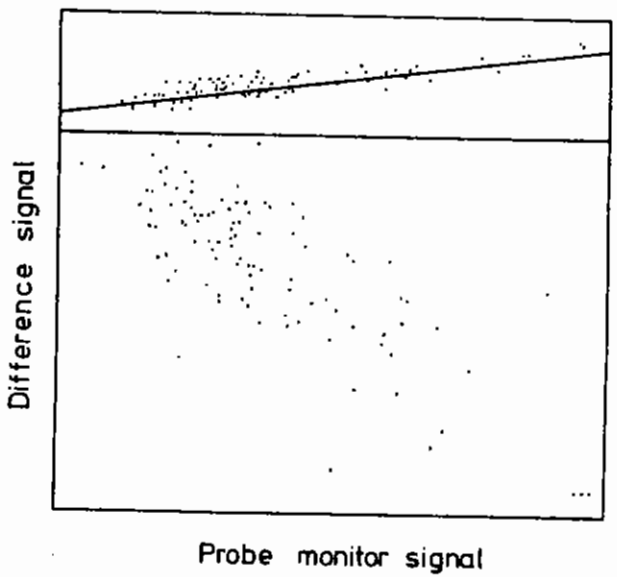

Fig B4.4 Plot of the difference detector signal against probe monitor signal with pump off (upper line) and pump on (lower line).

Performance

Typical performance of the detection system described yields single shot standard deviations corresponding to 1% absorption changes. By averaging over 100 shots a precision of 0.1% absorption change has been achieved. Time resolution in kinetic studies is at present approximately equal to the laser pulse width (5ps) and is limited by manual positioning of the optical delay.

Results obtained using the detection system are presented in sections B1.10 and B2.4. Good agreement is found between kinetic measurements described here and those of previous studies. In figure B2.9 absorption changes observed in photosystem I on timescales less than 100ps are shown to agree closely with those obtained by Il'ina et al

(Ref B4.2). On longer timescales similarly good agreement is found with published results. Figure B4.5 shows absorption changes measured at 705nm in the dye methyl DOTC following excitation at 585nm. The 1/e time of the decay is 1.2ns in agreement with the lifetime of the S_1 state of the analogous carbocyanine dye ethyl DOTC (τ = 1.2ns) (Ref B4.3).

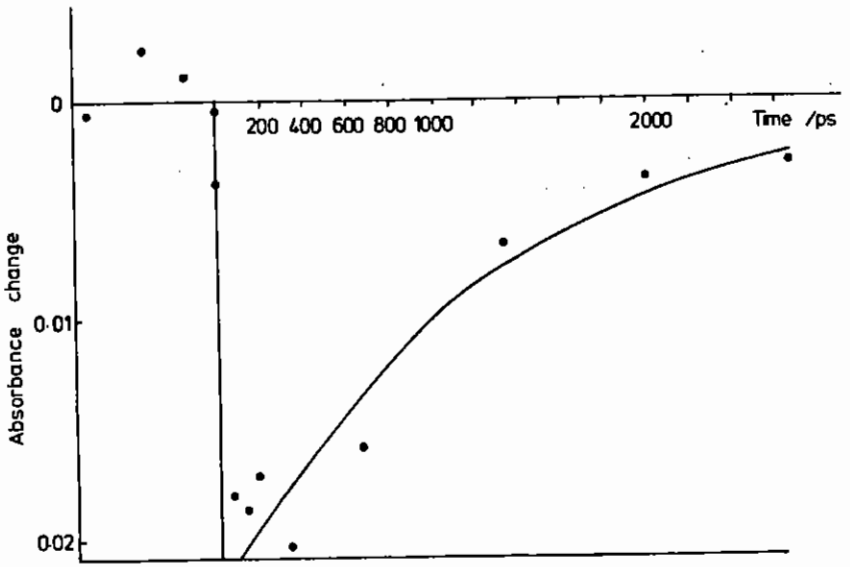

Fig B4.5 Absorbance changes at 705 nm following 585 nm excitation of methyl DOTC.

In its present state of development the precision of the detection system described here is comparable to that of previous designs. Gadonas et al (Ref B4.4) were able to measure absorption changes in the range 0.05% to 0.2% with 200 to 1000 laser shots. Further improvement of the detection system described here is possible. A precision of 0.01% on absorption measurements has been achieved (Ref B4.1).

B4.4 STREAK CAMERA DIAGNOSTICS

J R M Barr, G L Hogg, A J Langley, W T Toner (RAL)
A Waldman (Bristol), R Phillips, Z Sobiesierski (Exeter)

A streak camera-vidicon system was commissioned during the year and is now being used in experiments on fluorescence decay anisotropy and amorphous semiconductor luminescence. The camera is a Dellistrique DS-3 with an S25 tube fibre-optically coupled to two stages of 18mm channel plate intensification. It is currently set up with the fibre optic coupling to give a x 2 reduction and thus a wide time window at moderate time resolution. The lens used to image the streak slit onto the photocathode is a UV doublet lens whose modulation transfer function is shown in fig B4.6. An f1.4 camera lens is available for high resolution work in the visible.

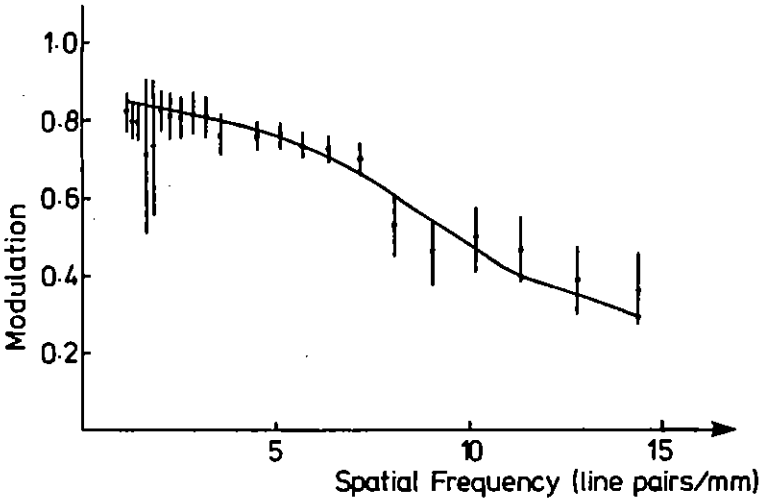

Fig B4.6 Modulation Transfer Function of UV doublet lens.

The output of the image intensifier is imaged with an f1 copying lens onto an EG and G OMAII SIT vidicon at X1.5 reduction.

Most system measurements have been made at 10Hz in the repetitive triggering mode using an ITT vacuum photodiode to produce a fast rising trigger pulse. The OMA has been run asynchronously at 14Hz to accumulate data over several hundred to several thousand shots.

The absolute sensitivity of the system at a wavelength of 630nm was measured to be .07 OMA counts per photon at an intensifier gain of 9000. When photocathode quantum efficiency is taken into account this is equivalent to approximately 5 counts per primary photoelectron and

this is of the same order as the OMA noise in a single scan of the seven channels over which the signal is spread. Higher gain (up to x60,000) is available.

The static resolution of the system is 7 OMA channels FWHM corresponding to 1.4% of the time window or 38psec on the fastest streak speed currently available. In repetitive triggering this broadens to 11 channels FWHM 60psec) in exposures of a few hundred pulses due to a combination of trigger jitter and dynamic resolution broadening. Longer exposures give slightly worse resolution. Figure B4.7(a) is a 3000 scan (2100 laser pulse) exposure to scattered picosecond laser light (~2.5 psec pulse width) and shows a 13 channel width at half maximum. Dark current background is highly reproducible and can be subtracted. Figure 2(b) is the sum of 25 successive multi shot exposures in which the optical delay has been changed by 100psec between each exposure. Dark current background has been subtracted. The variation of system sensitivity over the streak window is illustrated in figure 2(c). The small scale structure does not represent a real local variation in sensitivity but is the result of the finite steps in optical delay between successive equal intensity exposures. Dark current background has again been subtracted.

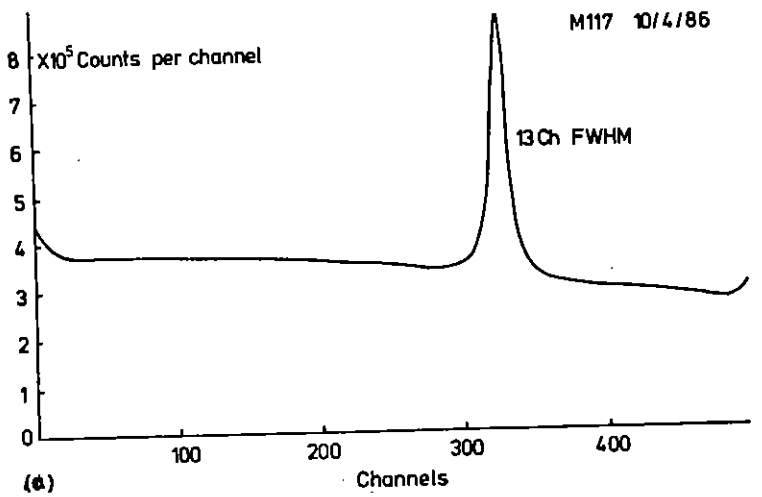

Fig B4.7(a) Temporal resolution of streak camera - OMA system.

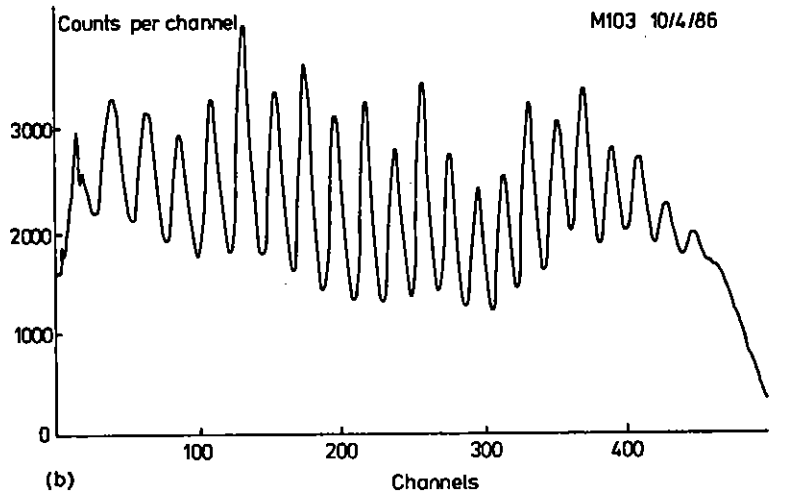

Fig B4.7(b) Streak rate linearity: successive peaks are 100ps apart in time.

A luminescence decay curve from amorphous phosphorus at 4 kelvins resulting from a 3000 scan exposure is shown in figure B4.8. Scattered laser light at 630nm was eliminated by two cut-on filters with edges at 665 and 695 nm. Dark current has been subtracted but no corrections for sensitivity and sweep rate variations have been made. Amorphous semi conductor luminescence extends to the millisecond time scale and the small scale structure which apparently precedes the onset of luminescence is due to an incorrect adjustment of the flyback blanking circuit and a slight over-subtraction of the resulting parasitic signal which is localised to this region of the screen.

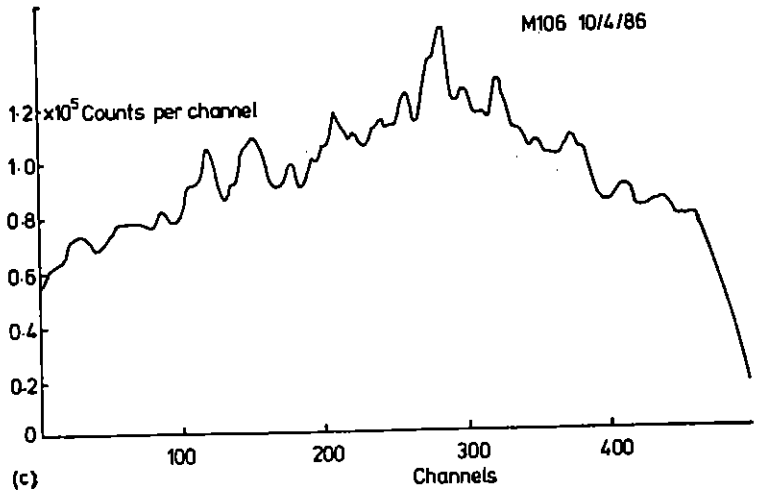

Fig B4.7(c) Variation of sensitivity across time window.

Preliminary measurements in single shot operation show a factor of ~2 improvement in time resolution. An example of a fluorescence decay curve of POPOP excited at 340nm can be found in section B2.5 (Fig B2.11). This is uncorrected for sensitivity and streak rate variations and the background subtraction in this case does not include fixed pattern noise from the streak camera.

The present ad-hoc use of the OMAII gives synchronisation problems in single shot experiments and a system to enable single shot laser, streak camera and OMA operation for stopped flow experiments is being developed.

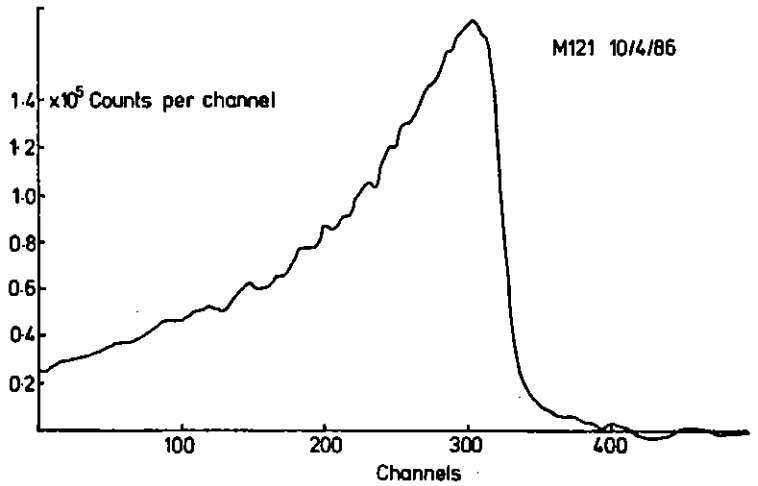

Fig B4.8 Luminescence decay curve of amorphous phosphorus.

B4.5 LASER LOAN POOL

A J Langley and W T Toner

The LSF Laser Loan Pool was set up to cater for users whose experimental equipment cannot be moved to RAL or whose other commitments prevent them carrying out experimental programmes away from home. In the first year of operation the loan stock consisted of two pulsed tunable dye laser systems (JK 2000 and Quantel Datachrome) and a total of 10 loans were made. Scientific results are presented in sections B1.7, B1.11 to B1.15 and B2.6. More lasers are now being delivered and the equipment available for loan in 1986 is listed in Table B4.2.

Applications for loans are treated in the same manner as proposals to use the RAL-based facilities: they are peer reviewed, ranked according to scientific merit by the LSF Panel and scheduled by the LSF Scheduling committee. Loans are presently restricted to a maximum duration of three months on any one occasion but users with approved programmes of work may apply for more than one loan per annum.

LSF staff visit the host laboratory prior to the loan to identify any difficulties likely to arise. The laser is transported by RAL and LSF staff assist users to set it up in their laboratory and to give any training in its use that may be required. Safe installation and use of the laser is the responsibility of the host laboratory. The host institution is also responsible for loss or damage (fire,accident, etc) and third party claims while the equipment is on their premises. At the end of the loan period LSF staff arrange for the laser to be collected.

Maintenance and repair is carried out in the field by LSF staff or by equipment manufacturers at the expense of the LSF. Experience in the first year of operation has been that these arrangments work well. The relatively simple JK laser has given few problems. There have been a number of teething problems with the more sophisticated Quantel system

which is equipped with a full range of doubling, mixing and Raman shifting options but manufacturers have cooperated well in making quick repairs under warranty at laboratories as far apart as Edinburgh and Southampton.

Lasers are intensively used on loan as users are scheduling their work to make maximum use of the short loan period. Although some of the loans are to groups with little laser equipment of their own, most are to experimental groups with extensive equipment they wish to supplement in order to explore a new wavelength or power range or to perform multi-laser experiments.

Table B4.2 List of Loan Pool Laser and Equipment from May 1986

1: Lasers

A: Pulsed Dye Lasers with output tunable from UV to IR.

LL1(a) Pump Laser JK2000 Pulsed Nd-YAG laser (Doubled + tripled) 0.5J at 106nm, 10Hz.

(b) Dye Laser JK2000 Dye laser 0.1cm^{-1} line width. 10mJ at 580nm.

LL2(a) Pump Laser Quantel Datachrome 5000 Pulsed Nd-YAG laser (Doubled + Tripled) 0.7J at 1064nm, 20Hz.

(b) Dye laser Quantel Datachrome dye laser system with full range of doubling + mixing options and autotracking. 0.08cm^{-1} line width. 60mJ at 560nm.

LL3(a) Pump laser JK Hyperyag 750 Pulsed Nd:YAG laser (Doubled + Tripled) .78J at 1064nm, 20Hz.

(b) Dye laser Quanta-Ray PDL dye laser and WEX wavelength extender with full range of doubling and mixing options and autotracking.

LL4(a) Pump laser Lambda Physik EMG101 Excimer Laser (Chlorides) 6.5 watts avge power, 40Hz.

(b) Dye laser Lambda Physik FL3002 dye laser with doubling crystals + computer controlled scanning.

LL5 Dye Laser FL2002 with excimer pumping optics.

B: Continuous Wave Laser

LL6(a) Pump laser Spectraphysics 2025 UV CW Ar Ion laser 5 watts vis/.4 watts UV Single line + single frequency options.

(b) Dye laser Spectraphysics 375 Dye Laser.

2: Diagnostics

LD1 Imacon 500 S-20 Streak Camera. Film redout.

LD2 2 gated integrators (SR250), 1 Fast Sampler (SR255), 1 Computer Interface (SR245), 1 Analogue processor (SR235), 1 Gate Scanner (SR200).

Editor: P T Rumsby

C LASER RESEARCH AND DEVELOPMENT

Introduction

In order to support its various operational programmes and keep its facilities at the forefront of laser technology the CLF carries out a wide variety of laser research and development work. This work is discussed in this section which reports the development that has taken place during the year in the areas of Nd glass lasers, KrF gas lasers and picosecond laser systems. Novel developments that have taken place in the areas of optical coatings, lens design and manufacture and high quality line focus production are also reported. In addition new X-ray instrumentation developments and novel work on the use of low power, high repetition rate excimer lasers for plasma and X-ray production are discussed.

Section editor: C B Edwards

C1.1 OSCILLATOR DEVELOPMENT

C Danson, C Edwards, R Wyatt (RAL)

Most developments in this area during the past reporting year have been concerned with the generation of appropriate synchronised pulses to drive the Vulcan system during the scheduled 'Beat Wave' campaign. The main requirements for this experiment were the generation of two synchronous laser pulses of 200 ps duration at wavelengths of 1.053 μm and 1.064 μm to drive the beat-wave, with an auxilliary 2ns pulse for Thomson scattering diagnostics.

The oscillator systems were built 'off-line' to facilitate development in parallel with normal operations, the output being injected into the main systems for test purposes as required.

The initial investigations were performed with a novel oscillator employing both YAG and YLF within a common cavity as shown in Fig C1.1. The design was of the acoustically modelocked and Q-switched type (Ref C1.1) which enabled the oscillator output to be synchronised reliably with the other laser components. The critical issues which were investigated were the synchronism of the output pulses at the ten ps. level, the reproducibility of the energy ratio between the two wavelengths, and the longer term stability of the cavity.

In order to achieve synchronisation of the Q-switch envelopes, it was necessary to match the build-up time of the cavity at both wavelengths. YAG has a larger stimulated emission cross section than YLF, and the build-up times were adjusted by varying the pumping levels of each rod independently. Dichroic output couplers were employed to introduce a wavelength dependent loss into the cavity but were found to be less convenient than tuning the pumping rate.

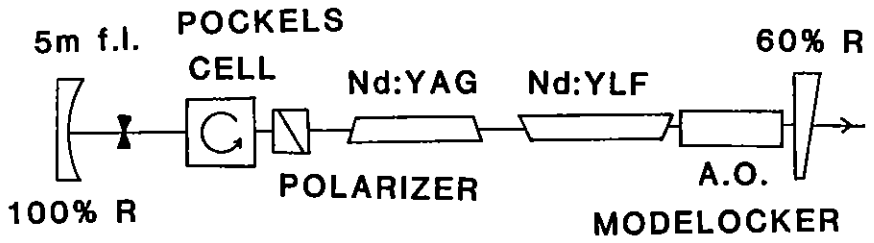

"HYDRA"
BEAT-WAVE OSCILLATOR

Fig C1.1

Though the net dispersion in the cavity was calculated to be neglible, it was found difficult to achieve stable modelocking at both wavelengths simultaneously. This was certainly due in part to adverse environmental effects, and possibly due to gain competition within the YAG rod on the 1.052μm line.

The most serious problem associated with this cavity concerned the synchronism of the modelocked pulses, which was observed to vary between pulses making servo-compensation impossible. Fig C1.2 shows a streak record of such a mistimed output.

STREAKED-SPECTROMETER OUTPUT OF THE 'HYDRA' OSCILLATOR

Fig C1.2

Despite these problems the oscillator was used to drive the VULCAN facility in a series of tests designed to evaluate gain reconfigurations necessary to provide the required drive for the Beat Wave experiments. During this period most of the hardware problems that would be encountered when converting the system to two wavelength operation were revealed.

In order to improve reliability, major modifications were made to the oscillator systems at this stage. The revised design consisted of two independent oscillator cavities with common control electronics for synchronisation, as shown in Fig C1.3.

DUAL WAVELENGTH OSCILLATOR

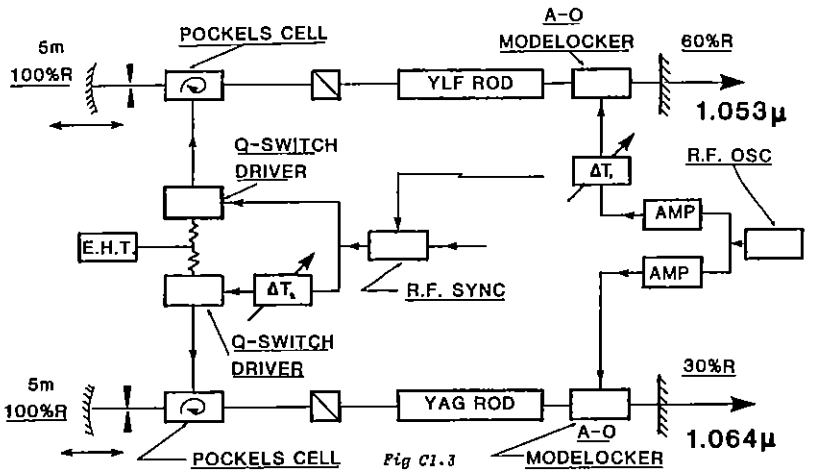

Fig C1.3

The oscillator consisted of a matched pair of acousto-optic modelockers driven from the same r.f. generator. The delay (T_1) was provided by means of cables and a telescopic r.f. line stretcher giving continuous variation of phase between the two r.f. signals. By this means the position of one laser pulse within its cavity could be adjusted relative to the other pulse enabling the pulses to be made synchronous with respect to the point of injection into the rod amplifier chain.

To ensure that the two short pulses occurred at the appropriate time relative to the long pulse oscillator output and the various optical and electronic gates elsewhere in the system, the electro-optic Q-switches were triggered from the same source, synchronised to the phase of the mode-locking r.f. The delay (T_2) could be placed in either line, allowing for differences between the Q-switch build up times.

OSCILLATOR OUTPUT STREAKS

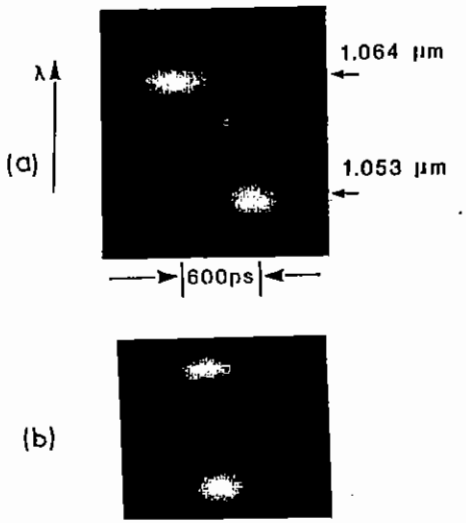

Fig C1.4

To demonstrate the effect of the relative phasing of the modelockers, Fig C1.4(a) shows a streaked spectrometer record of the oscillator output. A known delay has been introduced by means of the r.f. line stretcher, and the resulting desynchronisation between the two wavelength outputs is clearly shown. Fig C1.4(b) shows the output of the system with the delays adjusted appropriately to give synchronised output. The long term stability of the two oscillators was found to be excellent.

C1.2 LASER MODIFICATIONS FOR BEAT-WAVE EXPERIMENTS

C Danson, C Edwards, D Rodkiss, R Wyatt (RAL)

Beat-wave experiments (section A1.2) were scheduled between routine operational periods on VULCAN. A period of one week, both before and after, the experiment was allowed for system preparation; therefore it was necessary to ensure that any modifications were reversible in the short term.

The oscillator presented the least problems, in terms of disruption, as it was assembled separate from the main system until required. The

oscillator output is then relayed to a point, before the switchout and pre-amplifier, where it is injected into the system, using a pair of decoupling mirrors.

LASER GLASS GAIN CHARACTERISTICS

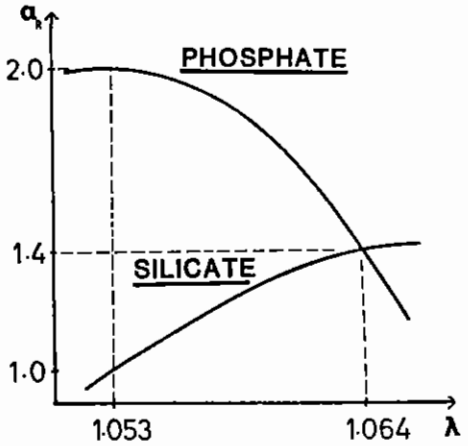

Fig C1.5

The system normally operates with two synchronised Nd:YLF oscillators. Their outputs are passed through amplifier chains which consist of a series of rod amplifiers followed by disc amplifiers. The amplifying medium is Nd doped phosphate glass, the fluorescence of peak which is matched well with the 1.053μm YLF line, but has a much reduced gain coefficient for the 1.064μm YAG line. Consequently if the two Beat-Wave oscillator pulses were to be injected into an unmodified amplifier chain the YLF output would be 10^4 times more intense than the YAG output. If selected phosphate glass rods were removed and replaced with silicate glass rods, whose fluorescence peak lies close to the 1.064μm YAG line (Fig C1.5), then it is possible to balance the energies of the two wavelengths at the system output. The staging of the laser system for the Beat-Wave experiment is shown in Fig C1.6, together with the gains available at the two wavelengths. This configuration produces about 80 Joules at each wavelength, limited by damage to the output stages of the laser.

In addition to the Beat-Wave pulses a synchronous long pulse is required, 2ns in duration, with an energy of about 80 Joules. This is then frequency doubled to 0.53μm and used in the Thompson scattering diagnostics. A fraction of the Beat-Wave energy is coupled out of the system after the 32mm diameter rod and directed to the target area

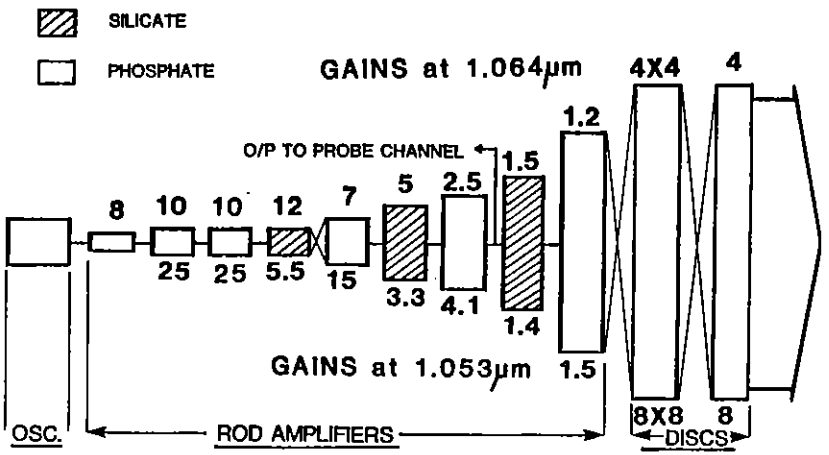

Fig C1.6

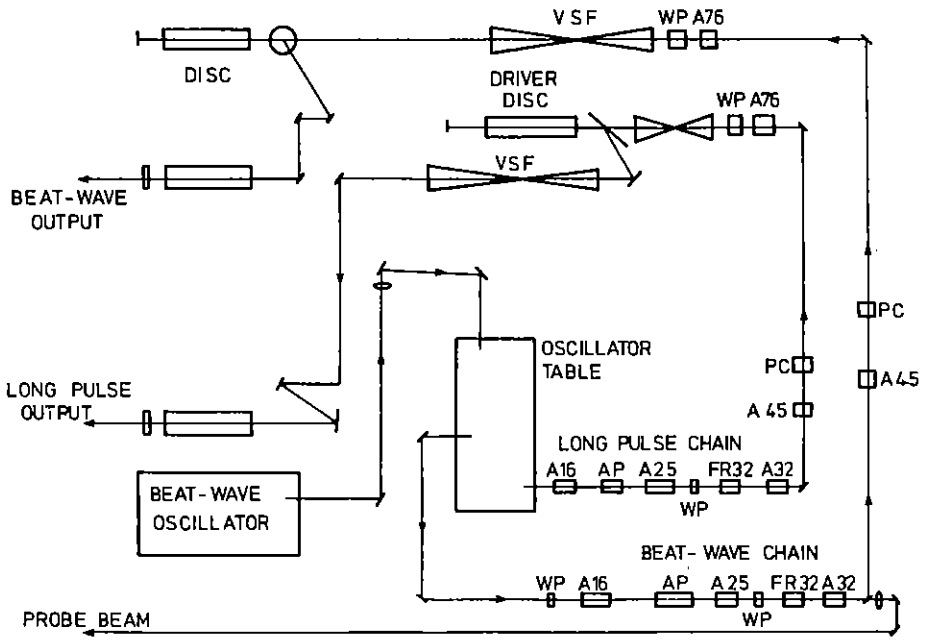

VULCAN GLASS LASER SYSTEM FOR THE BEAT-WAVE EXPERIMENT

Fig C1.7

where it could be used for Raman-Nath scattering. Fig C1.7 shows a schematic lay-out of the VULCAN system configured for the Beat-Wave experiment.

C1.3 HOT OPERATIONS TESTS

C Danson, C Edwards, R Wyatt (RAL)

One possible approach to any future upgrade in energy available to experimenters from the VULCAN facility is the operation procedures due to the requirements of improved beam quality control to avoid laser damage of optical components. In order to investigate fully the constraints of such 'hot operations' experimental time was scheduled in November 1985. The opportunity was also taken to make measurements of damage threshold of surfaces treated by the neutral solution and colloidal silica processes.

There were three main aims of the study. Firstly it was required to assess the operational feasibility of running high fluence laser shots, secondly to identify the limiting component in such operations, and thirdly to make experimental measurements of disc amplifier gain saturation. To this end one of the six output beam lines was configured such that the disc amplifier could be run well into saturation when the output energy would be in excess of 350J with peak laser fluences of 7J cm^{-2}.

KDP doubling crystals damaged at a fluence of 4J cm^{-2} in broad agreement with the measurements made by other laboratories. These particular crystals were operating without index matching fluid and without windows, but since they were designed originally for fluid-filled operation, the crystal surfaces were not particularly well polished. It is believed that if crystals designed for such bare operation were tested the damage threshold might be somewhat higher. Nevertheless it is now accepted by most laboratories that the doubling crystals have the limiting damage fluence, and that routine operations should be restricted to below 5J cm^{-2}.

A most disturbing aspect of the tests was the poor performance of some laser glass which was found to damage at less than 5J cm^{-2}. This is believed to be due to platinum inclusions within the bulk of the glass. This problem has been observed principally by the Livermore group at comparable fluence, and the output stages of any future 'hot' system would certainly need the improved platinum free glass that is now becoming available.

Neutral solution processed vacuum spatial filter lenses, colloidal silica test plates, and samples of dielectric coated mirrors were found to have a damage level well above the maximum attainable of 7J cm^{-2}, and will not be the dominant constraint in an upgraded laser. In addition, the colloidal silica anti-reflection coatings were found to have a reflectivity less than one half of one per cent, and hence represent an extremely cost effective innovation. The only problem of such treated components is the useful life in operation due to contamination by hydrocarbons. An extended life-test is planned to address this issue.

The saturation measurements on the disc amplifier gave a net gain of 4.5 at an input energy of 80 Joules. This measurement will be useful in the design of the output stages of the upgraded laser, and for comparison with the new design of amplifier at present under test.

In conclusion, it was found that a maximum fluence limit exists at about 5J cm^{-2} due to crystal damage. At higher levels, the time required to obtain sufficiently smooth beam profiles on a day to day operational basis would be prohibitive, apart from considerations of target cleanliness. However if the laser aperture were better filled, with improvements to conversion efficiency and with attention to lost energy due to Fresnel losses, then a significant upgrade in energy would be possible at the existing aperture and with existing optical component technology.

Several series of shots were run through various components up to the maximum of of 350J and useful data was obtained under all 3 areas of study. Further tests to evaluate the feasibility of such an upgrade scheme are planned for late 1986.

Reference

C1.1 D J Kuizenga, 'Short pulse oscillator development for the Nd:glass laser fusion systems', IEEE J of QE Vol QE17 No 9 Sept 1981.

Section editor: M J Shaw

C2 HIGH POWER GAS LASERS

Introduction

M J Shaw (RAL)

With the establishment of SPRITE as a routine laser-target shooting facility, the main development aim has been, and remains, to increase the power available on target from the present few GW by compressing the pulselength from 50 ns into the nanosecond region or less.

Multiplexing, ie the extraction of energy from an amplifier on a number of separate identifiable beams, is the preferred means of achieving this aim. The use of Raman amplifiers as an efficient method of combining these beams and improving beam quality is a natural adjunct to the multiplexing technique. In this section we report on the laser R & D effort in this direction over the past year.

Section C2.1 presents briefly the results of a very detailed series of experiments to investigate the benefits of using high krypton concentrations in KrF lasers. Section C2.2 gives preliminary results of our first multiplexing amplifier experiments using the Goblin laser. These are really quite exciting in that they indicate that energy extraction on multiple short pulses can be highly efficient. We can thus consider leap-frogging over our previous expectations for the SPRITE multiplexer, which was initially to provide 8 ns pulses on target, to much shorter pulses, in the 10 to 100 ps range, which hopefully will be available on target in early 1987.

Beam quality remains the important question however, and the remainder of this Section is devoted to this topic. In C2.3 we describe the development of a TV/computer system for measurement of UV laser beam profiles and in C2.4 and C2.5 we report on our continuing Raman work which includes both theoretical studies and experimentatal development. Ultimately we feel that the beam combining and beam quality improvement aspects of Raman amplifiers will be necessary in future high power gas laser systems.

C2.1 PARAMETRIC STUDY OF E-BEAM PUMPED KrF LASERS WITH Kr-RICH MIXTURES

F Kannari (RAL)

Since the discovery of the KrF laser in 1975, the factors which determine its efficiency have been actively studied both experimentally and theoretically (C2.1 + C2.5) under various pumping conditions. Although the maximum intrinsic efficiency of around 10% is attainable at appropriate pumping conditions (the estimated intrinsic efficiency of SPRITE is approximately 8% with the injection locked unstable cavity), further improvement is still an important issue for achieving an overall ICF driver efficiency in excess of 5%. Recently oscillator performance has been investigated in Ar-free mixtures at pressures of around one atmosphere (C2.6 - C2.8). The results of theoretical kinetic simulation indicate that the Kr-rich mixture can achieve a higher intrinsic efficiency due to increased KrF formation efficiency and higher extraction efficiency. To date, oscillator experiments have not been able to demonstrate the theoretically predicted improvement in intrinsic efficiency at high Kr concentration. We have analysed the fundamental parameters to understand the KrF^* formation and the energy extraction processes by combining experimental measurements with theoretical calculations as a function of Kr concentration.

During this experiment, the Goblin laser which was developed as a pre-amplifier in the Sprite multiplexing system was used as an oscillator. Fig C2.1 shows a schematic view of the electron-beam diode and the laser cell. In order to measure the intrinsic laser efficiency precisely, we have eliminated the unextracted laser volume by inserting an aluminium spacer within the laser cell. Consequently, the $2.5^W \times 2.5^H \times 40^L$ cm^3 laser volume is pumped by a 450-kV, 75-kA, 120-ns (FWHM) electron-beam. The excitation rate is 1.4MW/cm^3 for 1 atm Kr gas.

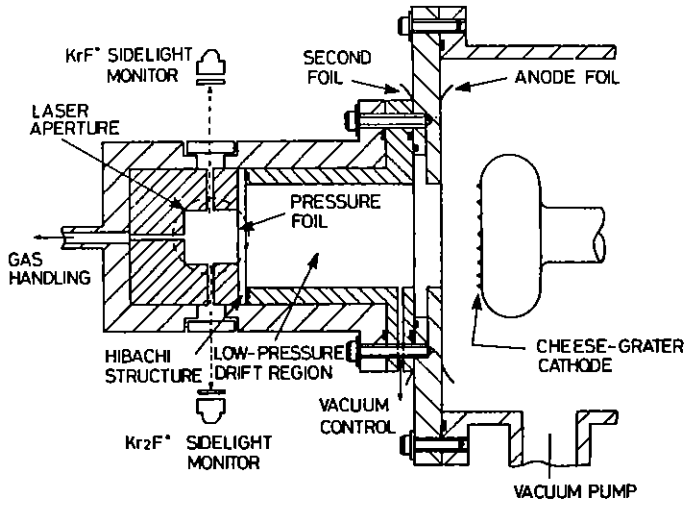

Fig C2.1 Cross-sectional view of the electron gun, electron drift region and laser aperture.

We have measured the sidelight depletion of $KrF^*(B-X)$ by the intracavity flux to determine the rate constants for vibrational relaxation of KrF^* by Kr and Ar. The finite vibrational relaxation process decreases the fraction of accessible KrF^* to stimulated emission and also the value of gain-to-loss ratio resulting in the decrease of energy and efficiency. These effects are significant for conditions with short KrF^* lifetime such as laser mixtures at high Kr conectration. The vibrational relaxation rates obtained are 4×10^{-11} and $5 \times 10^{-11} cm^3 s^{-1}$ for Ar and Kr, respectively. The fraction of $KrF^*(B-X)$ sidelight depletion $(N_0-N)/N_0$ also indicates the efficiency with which lasing photons remove the energy stored in the $KrF^*(B)$ state. Since in the limit of infinitely fast vibrational relaxation this efficiency is given by $(I/I_s)/(1+I/I_s)$, where I and I_s are an intracavity intensity and a saturation intensity, respectively, the reduction factor due to the finite vibrational rate is about $(1-1/\beta)$, where $\beta = 1 + \Theta_V(\tau_D/\tau_V)$. The quantities τ_D, and τ_V are the characteristic times for collisional deactivation including spontaneous emission, and vibrational relaxation, respectively and Θ_V is the Boltzmann factor for the accessible vibrational level.

The dependence of $(1-1/\beta)$ on the total gas pressure is shown in Figure C2.2 for two kinds of laser gas mixture. In the case of Ar-free mixtures (solid curves) the efficiency of stimulated emission decreases as the total pressure increases above 1 atm since the lifetime of $KrF^*(B,C)$ decreases faster than the vibrational relaxation time. The reduction factor $(1-1/\beta)$for Ar-free mixtures is always smaller than those of Ar-rich mixtures (10% Kr; dotted curves) at the same total pressure.

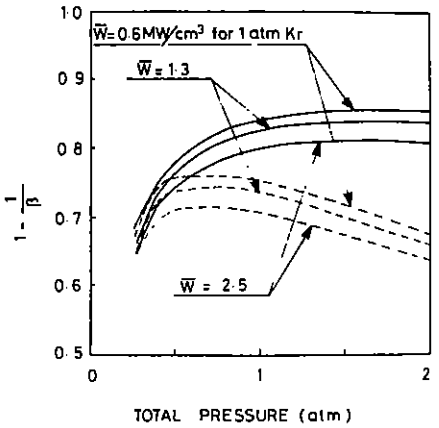

Fig C2.2 The reduction factor $(1-1/\beta)$ of the stimulated emission efficiency for two kinds of laser mixtures.

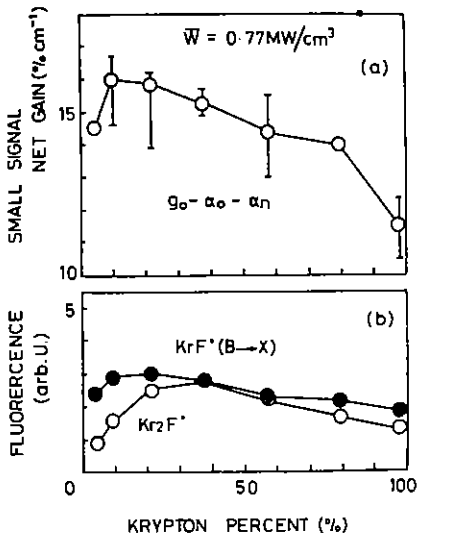

Fig C2.3 Plots of measured small-signal -net gain (a) and sidelight fluorescences without lasing (b).

We have also measured the net small-signal gain ($g_o - \alpha_o - \alpha_n$), where g_o is the small-signal gain, α_o is the saturable loss and α_n is the non-saturable loss. Using these measured parameters together with the calculated values of saturation intensity and g_o/α_o, we have estimated the KrF^* formation and extraction efficiencies by employing a steady-state analysis including the finite vibrational relaxation process. These calculations were compared with measurements of intrinsic efficiency as a function of Kr concentration.

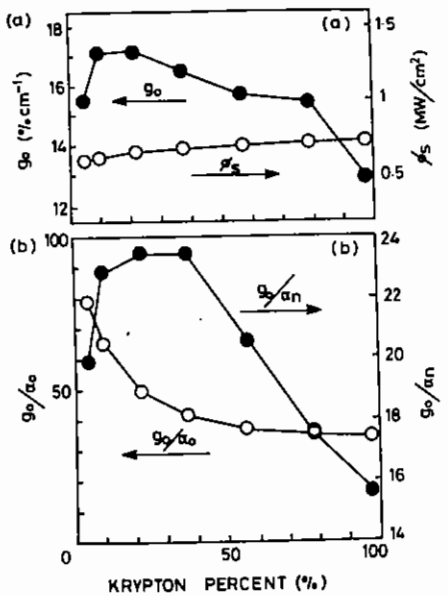

Fig C2.4 Plots of estimated small signal gain and saturation intensity (a), and gain-to-loss ratio (b).

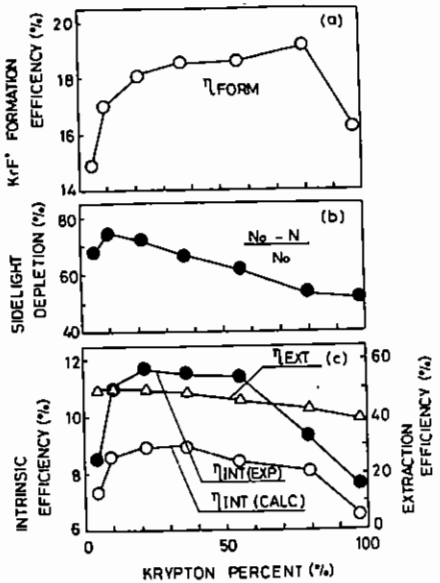

Fig C2.5 Plots of estimated formation efficiency (a), measured sidelight depletion at optimum output coupling (b) and estimated intrinsic and extraction efficiencies (c).

The results of one series of experiments are shown in Figures C2.3-C2.5. In these experiments the electron-beam deposition energy was kept constant and equivalent to 793 Torr of pure Ar. The constant excitation rate was estimated to be 0.77MW/cm^3.

The results of the calculation of local extraction efficiency using the parameters shown in Figure C2.4 are also plotted in Figure C2.5(c). The product of the formation efficiency in Figure C2.5(a) and this extraction efficiency shown in Figure C2.5(c). Although the absolute value of the calculated intrinsic efficiency is smaller than the experimental measurement, the relative trend with Kr concentration is reproduced well. We can interpret the data on intrinsic efficiency as follows. The increase of the intrinsic efficiency at low Kr concentration may be attributed to the increase in formation efficiency because the extraction efficiency does not change in this region. As the Kr fraction is increased, the extraction efficiency starts to decrease due to the effect of finite vibrational relaxation and three-body quenching by Kr and this competes with the increase of formation efficiency. At high Kr concentration, the increase in non-saturable absorption decreases the extraction efficiency still more. The sudden decrease in formation efficiency at 99% Kr is reflected in an equally sudden decrease in intrinsic efficiency.

In the case of high Kr concentration mixtures, the total pressure seems to be important in order to obtain the best compromise between the three-body ion-ion formation reactions, vibrational relaxation and the three-body collisional quenching rates. We have measured the intrinsic efficiencies as a function of total pressure for Kr concentrations of 10, 50 and 99.7%. The results are plotted in Figure C2.6 as a function of the corresponding deposition energy. The efficiencies of 50 and 99.7%-Kr mixtures show some improvement at total pressures of around 1 atm. The 50%-Kr mixture shows comparable efficiencies to that of 10% Kr except at total pressures of over 850 Torr. The efficiencies of 99.7% Kr mixture are between 8 and 9% and lower than the case of 10 and 50% Kr throughout the pressure range.

The formation channel of Kr_2F^* and its photo-dissociation by KrF laser photons were also investigated by measurement of the sidelight depletion of Kr_2F^*. We have obtained new results indicating that the direct formation from Kr_2^* is the most important formation channel of Kr_2F^* for pressures of around 1 atm. Because only that Kr_2F^* formed by the KrF^* quenching channel can act as a saturable absorber, the

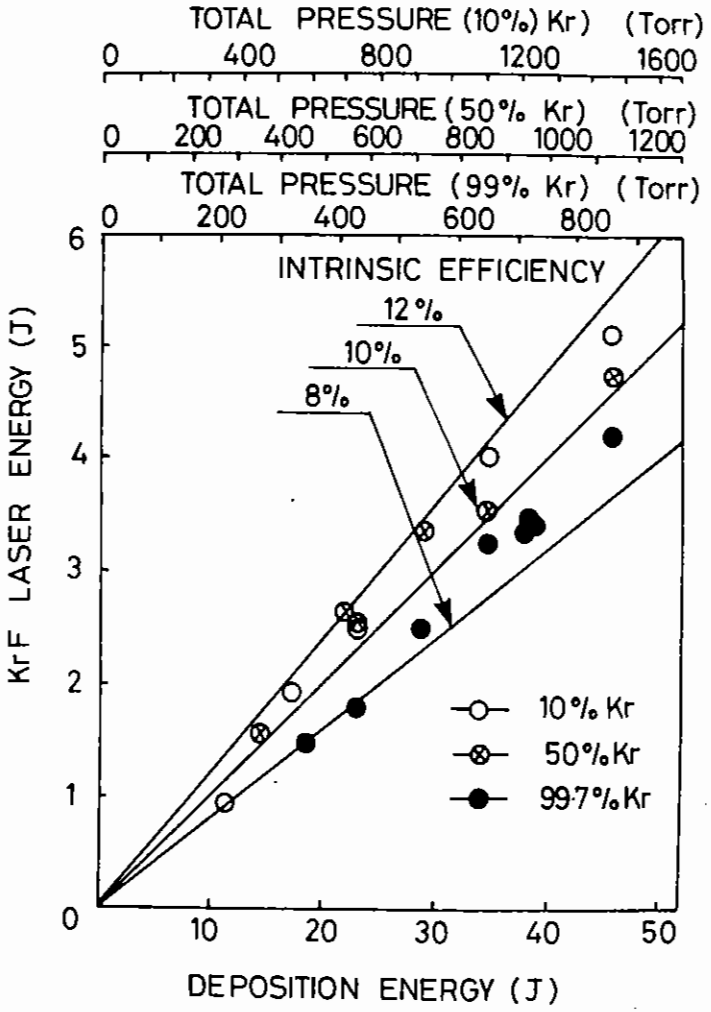

Fig C2.6 Laser output energy as a function of deposition energy for 10, 50 and 99.7% Kr mixtures. The solid lines are lines of constant intrinsic efficiency.

improvement of the energy extraction efficiency by the photo-dissociation effect of Kr_2F^* at high intracavity flux will be less than that of early predictions (C2.9). Since the effect of finite vibrational relaxation is significant at high excitation rate due to electron quenching, the operation at high excitation rate to achieve high intracavity flux and to increase the photo-dissociation of Kr_2F^* is not promising.

In conclusion the large increase in intrinsic efficiency previously predicted for Kr-rich operation of the e-beam-pumped KrF laser has not been realized in this study. However in attempting to track down the reasons for this, we have obtained a much better understanding of the complex processes which determine the operation of this laser system. For Kr-rich operation at low pressure, the main processes which control efficiency are:-

i) three-body ion-ion recombination
ii) three-body collisional quenching of KrF^*
iii) vibrational relaxation of KrF^* and
iv) production of Kr_2F^* absorbers via a non-saturable channel.

The three-body ion-ion recombination process seriously limits the formation efficiency of KrF^* at pressures below one atmosphere (760 Torr). The vibrational relaxation rates of KrF^* in collision with Ar and Kr have been measured and found to be $4 \times 10^{-11} cm^3 s^{-1}$ and $5 \times 10^{-11} cm^3 s^{-1}$ respectively. This latter relaxation rate is insufficiently large to compete with increased three-body collisional quenching of KrF^* at high Kr concentrations. The net result of this is that the stimulated emission efficiency is always less in Kr-rich mixtures than in Ar-rich mixtures.

C2.2 KrF SHORT PULSE PRODUCTION AND AMPLIFICATION

F Kannari, S Hicks, E Hodgson, C Hooker, I Ross and M Shaw (RAL)

In this Section we present the first results of multiple short pulse amplification in a KrF laser medium.

C2.2.1 Short Pulse Production

The interim configuration uses a Pockels cell to slice out a short KrF pulse from a longer 25ns pulse produced by the Lambda Physik EMG 150 injection-locked oscillator. A novel optical switch is used to slice out the short pulse. As shown in Fig C2.7 this comprises a single Pockels cell switched by a vacuum photodiode. The single switching operation is initiated by the input beam and returns the applied half wave-voltage V_1 to zero. When this occurs the photons in the region between the Pockels cell (PC) and the retro-mirror (M) are switched out on the polariser (P). Compared to the normal Pockels cell system employing a polariser and analyser, the requirement on the high-voltage driver is simplified so that no pulseforming line is necessary. Also the pulse width of the switched-out beam can be easily changed by adjusting the optical delay between the Pockels cell and the retro-mirror.

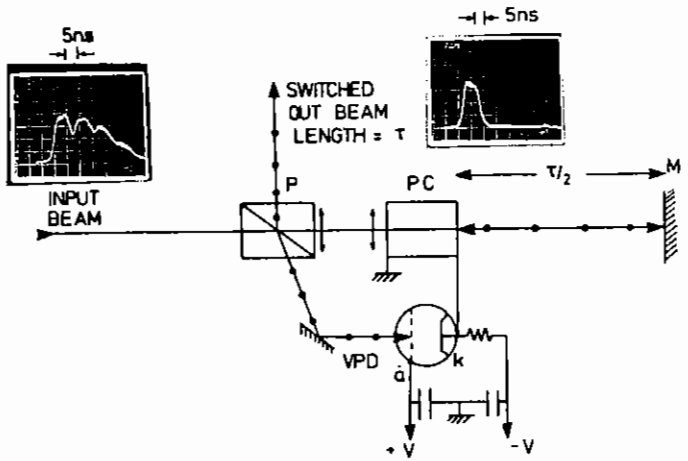

Fig C2.7 System used to switch-out a short pulse from the 25 ns KrF oscillator pulse. The Pockels cell (PC) is pulsed directly from half-wave to full-wave voltage using a vacuum photodiode (VPD) as a switch.

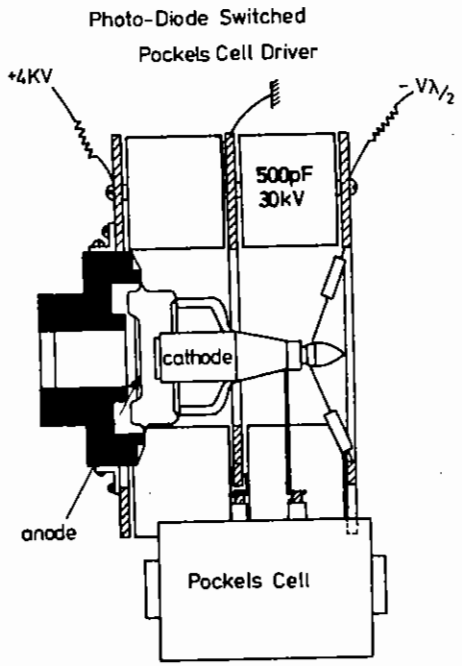

Fig C2.8 Cross-section through vacuum photodiode (ITL TF 1850) switch showing low inductance arrangement of capacitors and resistors and connection to Pockels cell.

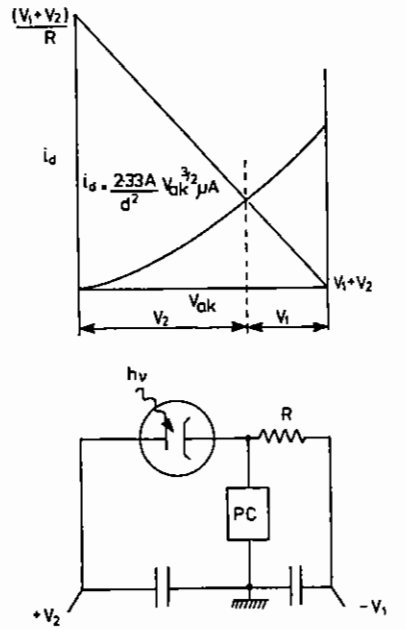

Fig C2.9 Space-charge limited diode current and the resistor load line give the voltage swing across the Pockels cell. This is independent of light input and made equal to tne half-wave voltage by adjustment of V_2.

A schematic cross-section of the Pockels cell driver is shown in Fig C2.8. Before an incident pulse arrives at the photodiode, the voltage on the electrode of Pockels cell is statically kept at $-V_{\lambda/2}$ by the capacitors C1 and C2 which are coaxially arranged around photodiode to reduce inductance. Because the value of current in the photodiode with sufficient input light (> 1kW) is determined by the Child-Langmuir law, the current is a function of only the Anode-Cathode size and the applied voltage. As shown in Fig C2.9 the value of the resistor R and V_2 can be chosen such that the voltage swing on the Pockels cell is exactly equal to the half-wave voltage. The system will also operate from a single polarity supply (in fact most of our measurements were made that way) in which case V_1 is $+V_{\lambda/2}$ and the same voltage swing switches the Pockels cell to the full wave voltage, V_λ. In practice V_1 and V_2 were varied to obtain the best contrast ratio on the short pulse switched out. The response time of photodiode is simply determined by the transit time spread of the photo-electrons across the A-K gap which is very small (< 1ns). The risetime of the voltage pulse is limited by the stray capacitance in the circuit due to the value of R (about 50Ω) and is approximately 3ns (10%-90%). A higher positive charging voltage V_2 can reduce the value of R resulting in a faster risetime, however this would eventually be limited by the maximum insulation voltage in the photodiode. Since no cable timing is required a vacuum diode suffices to switch the high impedance Pockels cell and maintenance-free high repetition-rate operation is achieved.

At the present, the efficiency of this system is limited by an unexpected absorption in the coating of the polariser. The transmission of P-polarisation beam in the polariser set at 63° angle is 67%. The transmission of the Pockels cell is 74%. Consequently, the output energy of an 8ns pulse is about 20mJ which is about 10% of the incident long pulse energy. In the case of short-pulse generation, a high contrast ratio especially in the pre-pulse region is essential because the pre-pulse always experiences small signal gain in the pre-amplifier which results in a further degradation in the contrast ratio. Therefore, we have adjusted the timing of switching the Pockels

cell so that the leading edge of the long pulse is switched out. Consequently the contrast ratio measured at the entrance to the Goblin pre-amplifier is better than 100:1.

C2.2.2 Multiplexed Short Pulse Amplification

The switched-out pulse from the oscillator is transferred from the oscillator room to the multiplexer room using a 12m long evacuated beam pipe which also serves as a spatial filter and image relaying stage. This also magnifies the beam up from 10 x 10mm^2 to 20 x 20mm^2. As originally intended the single pulse was to have been split into four beams which were to be amplified in a uniform beam discharge pre-amplifier (Lumonics Hyperex 420). Unfortunately difficulties were experienced with this system in terms of achieving the desired gain and beam quality so it was decided to utilise the long gain time of Goblin (100ns) and use it as its own pre-amplifier. The input beam was split into three beams separated by 10ns each of which is amplified twice by a double pass through the Goblin gain medium as shown in Figure C2.10.

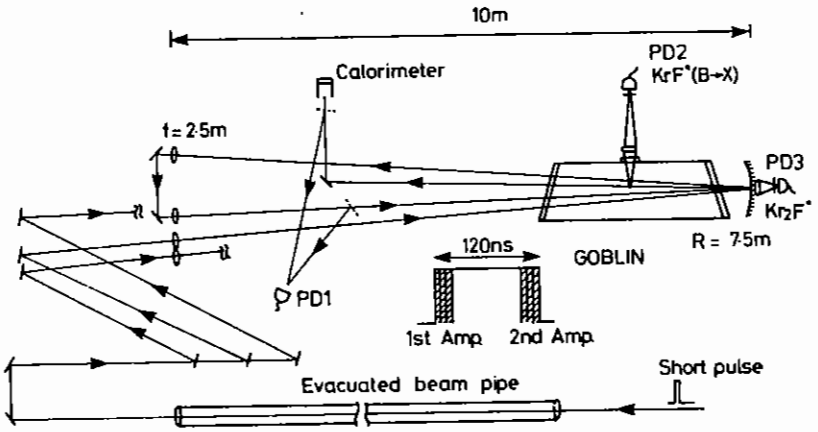

Fig C2.10 Experimental arrangement for multiplexed amplification in Goblin. Each beam double-passes the amplifier twice.

On the second double-pass the three beams are separated by 12ns. Diagnostics are done on the second beam which is typical of a multiplexed beam in that it is preceded and followed by other pulses. A photodiode measures the input and output pulse intensities as a function of time for the second double-pass where the amplifier is saturated. A Scientech volume absorbing calorimeter measures the output energy. The depletion of KrF^* and Kr_2F^* sidelight are also measured. The optical arrangement of the multiplexer has an array of positive lenses which expand the beam from its initial 20mm diameter to 60mm diameter to fill the Goblin pumped volume after passing through a pinhole plate at the focus. A 7.5m ROC mirror reconverges the amplified beam to the pinhole plane. In these measurements the diagnostics were performed on the output beam before it reached the focus on its second double-pass. Due to the long delay down the

multi-beam pipe it was not possible to start to saturate the laser medium until near the end of the pumping pulse. This is a non-ideal situation since the build-up of parasitic oscillations and/or absorbing impurities could affect the results. Thus the mesurements taken here represent worst-case conditions.

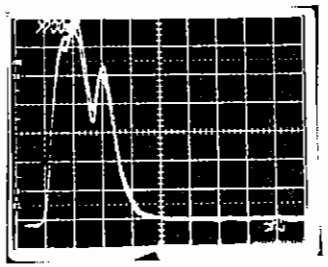

12-ns - input beam
5ns/div

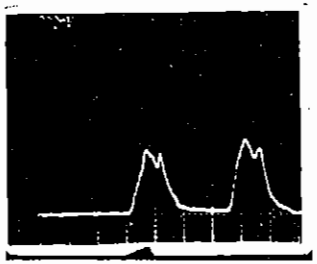

Typical input & output beams for the second amplification
10ns/div

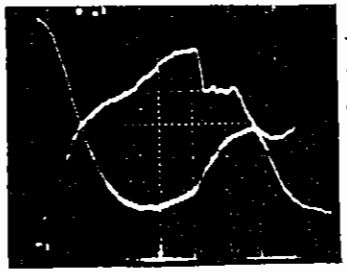

Typical sidelight waveforms of KrF^*(lower) & Kr_2F^*(upper)
20ns/div

Fig C2.11 Pulse shapes in the Goblin multiplexed amplifier with a 12 ns input pulse. Pulse separation = 12 ns.

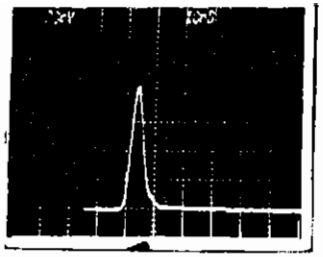

5-ns input beam
10ns/div

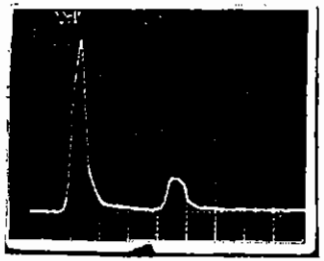

Typical input and output beams for the second amplification
10ns/div

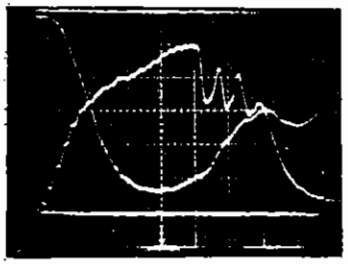

Typical sidelight waveforms KrF*(lower) and Kr_2F^*(upper)
20ns/div

Fig C2.12 Pulse shapes in the Goblin multiplexed amplifier with a 5 ns input pulse. Pulse separation = 12 ns.

Two sets of results were obtained for input pulse lengths of 5ns and 12ns respectively. The majority of data were taken with an atmospheric pressure gas mix of $Ar/Kr/F_2$ = 487/228/2.3 (Torr). Some data were also obtained with the same ratio mixture at 1.5 atm total pressure. Typical oscilloscope traces are shown in Figs C2.11 (12ns pulses) and C2.12 (5ns pulses) which show respectively the input pulse shape, the pulse shapes after the first and second amplification, and the depletion of sidelight. In the second trace the relative amplitudes of the input and output pulses are not to scale. The maximum saturated output energy obtained was about 700mJ for both the 12ns and 5ns pulses. This was a somewhat unexpected result and implies that the shorter pulse was extracting energy from the amplifier more efficiently than the long pulse. The difference between the two cases, seen clearly in C2.11 and C2.12, is that when the pulse is of 5ns duration

the amplifier gain has 7ns between pulses to re-pump and as is well known (C2.10) the extraction efficiency of a storage medium depends strongly on the gain. This difference in gain is seen clearly in Fig C2.13 which shows how the gain saturates as a function of input intensity for the two different pulse lengths.

We have analysed this data initially in terms of a simple Franz-Nodvik (C2.11) model modified to take account of re-pumping. In this case the saturated gain is given by

$$G = (F_s/F_{in})\ln\left(G_0\exp(F_{in}/F_s) - G_0 + 1\right)$$

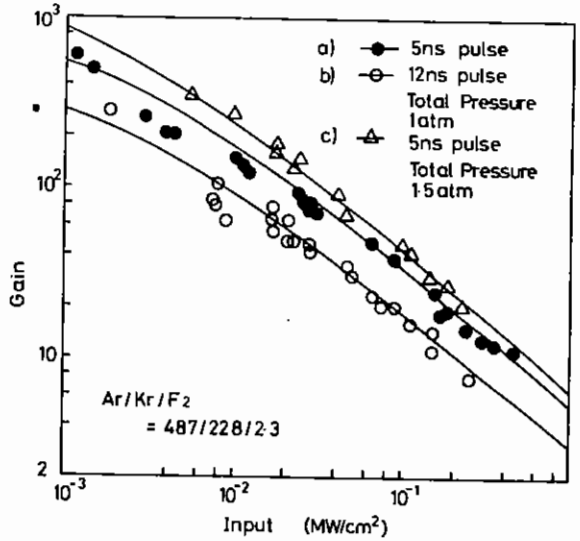

Fig C2.13 Gain as a function of input intensity for 5 and 12 ns pulses at 1 atm and 5 ns pulses at 1.5 atm.

where G_0 is the small signal gain (ie. $\exp(g_o l)$), F_{in} is the input fluence (Jcm^{-2}) and F_s is the saturation fluence:

$$F_s = \frac{h\nu}{\sigma}(1 + \tau_p/\tau^*)$$

where τ_p is the pulse length and τ^* is the KrF^* lifetime. Thus the saturation fluence is a function of pulse length and tends to $I_s\tau_p$ for long pulses (I_s = saturation intensity) and to $h\nu/\sigma$ for short pulses. In Fig C2.13 the 1 atm data is fitted with $G_0 = 800$ and $E_s = 3.5mJ\ cm^{-2}$ for the 5ns pulse and $G_0 = 400$ and $E_s = 4.5mJ\ cm^{-2}$ for the 12ns pulse. At 1.5 atm both the gain and saturation energy are increased to $G_0 = 1500$ and $E_s = 4mJ\ cm^{-2}$ for the 5ns pulse. Using the data described in Section C2.1 we would expect G_0 to be ≈ 400 for a single pass and E_s to be $4.3mJ/cm^2$ for the 5ns pulse. Our results should however refer to double-pass values and the small signal gain should clearly be a lot higher. One effect reducing gain is the non-saturation of Kr_2F^* absorbers. As can be seen from Figs C2.11 and C2.12 the decay time of Kr_2F^* is long ($\approx$ 40ns) and thus substantial absorption remains during the extraction time of the measured pulse. A fuller analysis of these results needs to take account of absorption in the laser medium as well as the transient nature of the problem where the pulse length, storage time and medium transit time are all of the same order.

These results are very encouraging for the future of the Sprite multiplexer. We have demonstrated a saturated output energy from Goblin which should be adequate to efficiently extract Sprite. In addition we have shown that higher power pulses can be obtained by allowing the gain to re-pump between pulses and that little or no penalty in terms of efficiency is incurred in this mode of operation. Previous measurements (C2.12, C2.13) have shown that a KrF laser medium can be efficiently extracted with pulses of very short duration ($\sim$ 10ps). This fact coupled with the results presented here strongly support the possibility of building very high power, short pulse KrF lasers based on multiplexed e-beam-pumped amplifiers like Goblin and Sprite.

C2.3 KrF LASER BEAM DIAGNOSTICS USING A COMPUTER CONTROLLED VIDEO FRAME STORE

S Clark, I Laidler, D Emmony (Loughborough University)
B Omar (Portsmouth Polytechnic)
D Hollis (Sheffield University)
M Shaw (RAL)

During the past year Sprite beam diagnostics have been considerably improved by the introduction of a TV camera and video frame store system. This system provides digital storage of a TV frame which is typically a 2D intensity distribution of the laser beam in either the near or far field.

The equipment used is shown in Fig C2.14 and the experimental set-up to diagnose the Sprite beam is shown in Fig C2.15. The whole beam having passed through a 99% reflectivity turning mirror is further attentuated by a fused silica beam splitter and an NO_2 absorption cell (C2.30). An exactly equivalent lens to the target chamber lens brings the beam to a focus. At the equivalent target plane (in the near or far field) is placed a thin (150μm) glass fluorescer which converts the 249nm UV light into the visible with a high degree of linearity (see below). The fluorescence distribution is imaged by a lens onto a CCD image sensor (EEV P4310) having 385 x 288 pixels on a 22μm spacing. Either standard camera lenses or microscope objectives are used depending on the spot size. The camera produces a standard 625 line TV picture and a laser pulse occurring at any time other than in a fly-back period is recorded, stored on the CCD array and readout during the next frame period. This storage feature of the CCD device means that the camera can run asynchronously to the laser firing and still have a greater than 95% chance of capturing a frame. On command of a trigger signal indicating firing of the laser, the desired frame is read into the frame store. The frame store is a commercially available unit, the Eltime Image III with slight hardware modifications so that both the controlling computer and an external trigger signal can initiate a frame snatch.

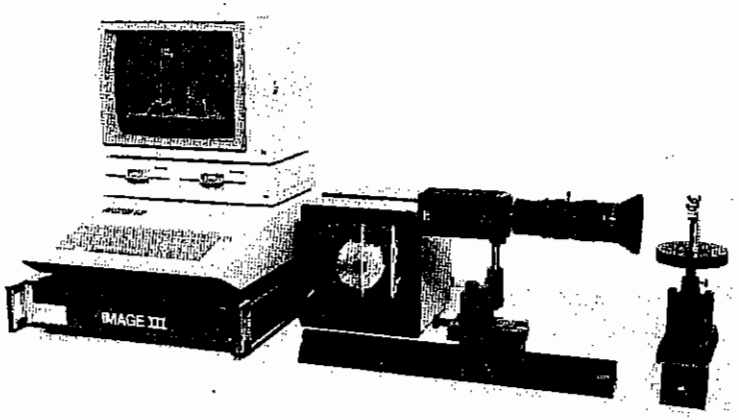

Fig C2.14 TV camera, frame store and computer used for laser beam profiling.

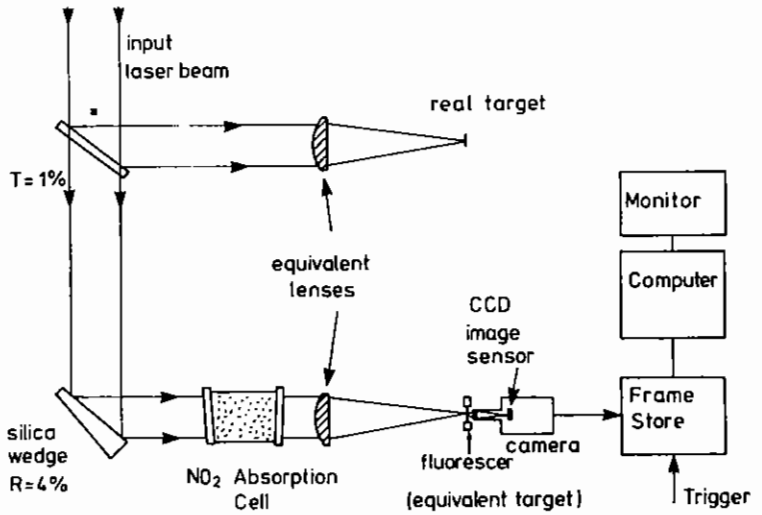

Fig C2.15 Optical set-up to measure the SPRITE beam profile.

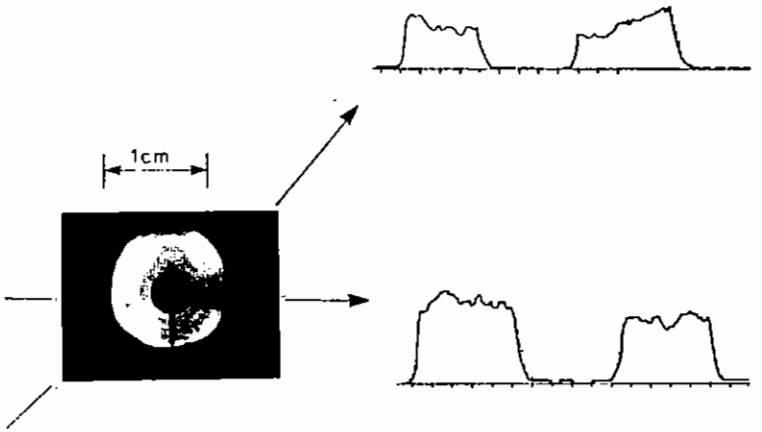

Fig C2.16 Typical near-filed intensity distribution from SPRITE showing intensity profiles in horizontal and 45⁰ directions.

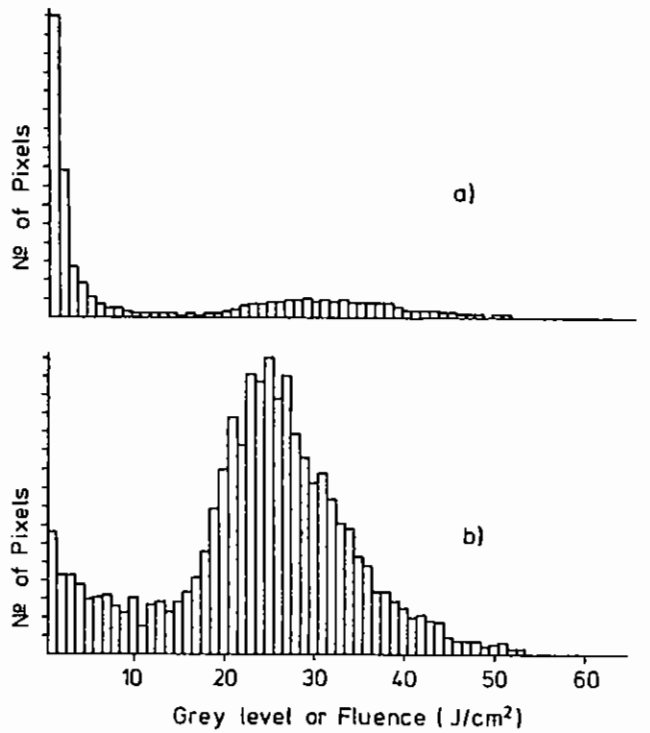

Fig C2.17 Histogram of laser fluence (grey-level) a) with background b) with background removed.

The store is set up to hold two pictures each 256 x 512 pixels simultaneously in memory each with 64 levels of intensity resolution (greylevels). The incoming data is digitised and stored in the frame store memory in a grid format so that any point in the picture can be addressed using cartesian type co-ordinate addressing.

An Apple IIe computer is used to control the system and it is this which makes the system particularly powerful and versatile.

A suite of programs was written to perform the following tasks.

a) Acquisition, storage and display of data.
b) Image processing.
c) Intensity profiling in X, Y and Θ directions.
d) Radially averaged profiling.
e) Numerical integration.
f) Statistical analysis.

By using options e and f it is possible to calibrate an image in absolute units and so obtain the fluence (J/cm^2) at any point in the image. Option f will also give such parameters as average fluence, fluence per intensity level recorded and standard deviation of fluence.

The profiling programme allows the user to select the location of the profile and whether it is a line profile or a radial profile and produces graphs of recorded intensity versus position along the profile.

The image processing routines include removal of background (dark level) noise, image enhancement and a routine to display the difference (in intensity levels) between two frames. There are also routines to store an image on disc for future referencing and processing.

Fig C2.16 shows a typical focussed near field intensity distribution from the Sprite unstable resonator and two intensity profiles through the beam pattern. In Fig C2.17 we show typical histograms of the laser fluence. In a) the background is not subtracted showing that in this

case the majority of the picture was dark. In b) the background is excluded and the histogram gives a good indication of the variation of fluence in the laser beam. In nearly all cases the most likely fluence was close to the average fluence and also the peak fluence was typically only 2x the average fluence.

The key element in this system is the fluorescer which converts the image from the UV into the visible for the camera to record. Most of the work so far has been done using borosilicate glass (pyrex) as the image converter, since its linearity was found to be good and its conversion efficiency was good enough for this purpose. Furthermore pyrex is readily available in very thin form (microscope cover slides which allows a microscope objective to focus on the fluorescence, which occurs within a few μm of the front surface of the slide, from behind the back surface of the slide.

The question arises however for other applications whether specially doped glasses would be good linear converters of UV light but have much more sensitivity than pyrex and be better matched to the spectral response of the CCD image sensor. To this end we have investigated a number of different doped glasses and we have looked at the fluorescence yield, time response, spectral response and linearity.

Dopants of lead, tin and copper have been tried and Fig C2.18 shows that a very significant increase in the fluorescence signal can be achieved over undoped glass. The time response of the fluorescence is in general quite complex with no single decay time dominating. In general however glasses are unsuitable as fast fluorescers which will follow the time response of a short laser pulse. However in imaging this is not important since it is the integrated fluorescence which is recorded (ie the area under the curves in Fig C2.18) and in this respect lead dopants clearly give the highest fluorescence yields. This result is confirmed if one looks at the spectral response as shown in Fig C2.19. These results were taken on a spectrophotometer with a calibrated spectral response using Hg 254 nm as the exciting line. The advantage of lead dopants is not so strong if one considers the spectal sensitivity of the CCD image sensor which in the non- intensified

versions is much more sensitive in the red than in the blue. In this case tin dopants look promising. For maximum sensitivity, the combination of a lead-glass fluorescer and an image-intensified CCD device would be best.

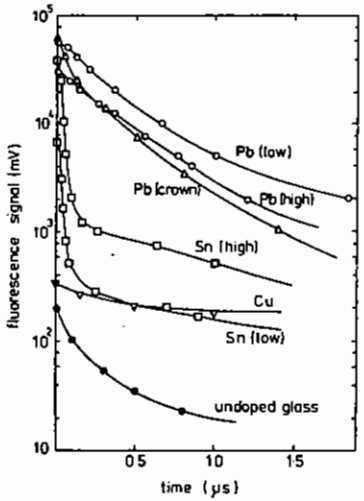

Fig C2.18 Relative fluorescence power as a function of time for various glasses irradiated with a KrF laser pulse at about 1mJ cm^{2}.

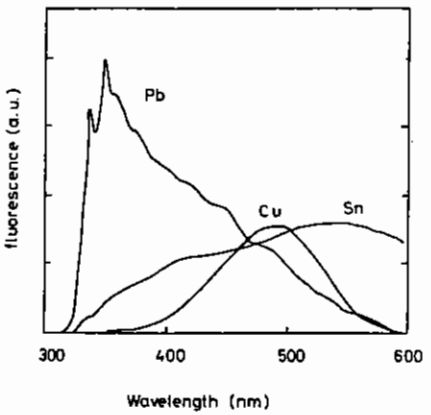

Fig C2.19 Relative spectral response of lead, copper and tin doped glasses excited by 254 nm Hg lamp. Curves have been corrected for spectral response of spectrometer and photomultiplier.

The linearity of the various doped glasses is shown in Figs C2.20 and C2.21. Here the influence of doping concentration is apparant. Curiously the concentration effects the linearity differently with different dopants eg high doped tin and low doped lead both show significant non-linearity. However it should be noted that between 100μJ and 10mJ/cm^{2} all of the glasses are adequately linear for a 6 bit frame store. For ultra-linearity over a very wide range lead crown glass appears to be a very good image converter.

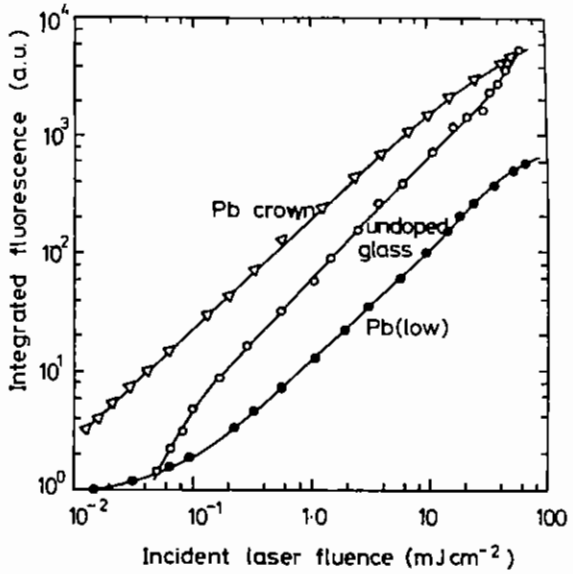

Fig C2.20 Linearity of fluorescence energy with incident laser fluence for undoped and lead doped glasses.

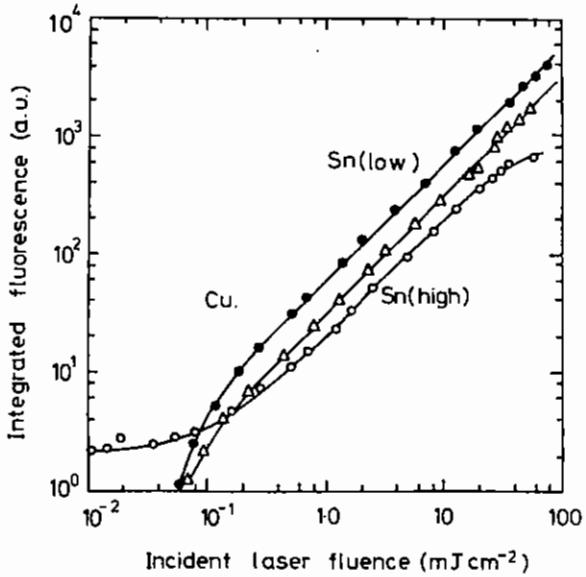

Fig C2.21 Linearity of fluorescence energy with incidence laser fluence for copper and tin doped glasses.

C2.4 THEORY OF RAMAN AMPLIFICATION WITH BROAD-BAND PUMPING

J P Partanen (RAL)

Raman amplification experiments with Sprite described in last years annual report revealed some interesting results when the pump laser linewidth is much broader than the linewidth of the Raman scatterer, ie the inverse of dephasing time the molecular excitation wave responsible for scattering. In the past year we have clarified the theory of forward Raman amplification which is needed for pulse compression of the Sprite laser. Forward Raman amplification will be used to combine short pulselength beams from the multiplexed Sprite to a single short pulselength Stokes beam.

Using Maxwell's equations and the damped harmonic oscillator equation for the Raman scattering molecules we can derive the coupling equations for the pump and the Stokes electric field amplitudes E_p and E_s, respectively, and the vibration wave amplitude q_v(C2.15):-

$$\frac{dE_p}{dz} = i \frac{\omega_p}{\omega_s} C_1 q_v E_s \qquad (1)$$

$$\frac{dE_s}{dz} = i C_1 q_v^* E_p \qquad (2)$$

$$q_v = i C_2 E_p E_s^* \qquad (3)$$

where ω_p and ω_s are angular frequencies of the pump and the Stokes waves, respectively, and C_1 and C_2 are constants. Fig C2.22 shows the relationship for the pump, the Stokes and the vibration wavevectors for two slightly different frequency pump waves in a non dispersive medium. As can be seen, the vibration wavevector is the same for both pump waves. Therefore with a broad-band multi-mode pump a single vibration wave can scatter energy form each of the pump modes to the corresponding Stokes mode and we get the coupling equations (C2.15)

$$\frac{dE_{pn}}{dz} = i \frac{\omega_p}{\omega_s} C_1 q_v E_{sn} \qquad (4)$$

$$\frac{dE_{sn}}{dz} = i C_1 q_v^* E_{pn} \qquad (5)$$

$$q_v = i C_2 \sum_n E_{pn} E_{sn}^* \qquad (6)$$

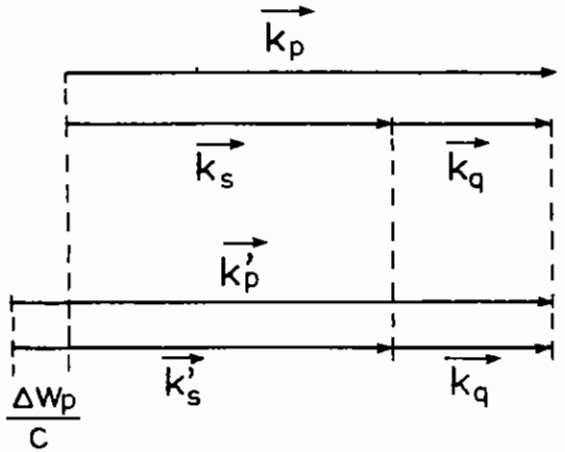

Fig C2.22 Wavevector relationship for the pump, with Stokes and the vibration waves for two slightly different frequency pump beams.

The vibration wave is driven by the beat-waves produced by each pump mode with the corresponding Stokes mode. Fig C2.23 illustrates the growth of the vibration wave amplitude in the complex plane. It is assumed that all the beat-wave amplitudes $E_{pn} E_{sn}^*$ have the same magnitude but random phases. From Eqs (4)-(6) it can be deduced (C2.15) that all the beat-waves grow in the direction of the sum of them in the complex plane as shown in Fig C2.23(b) and after a certain

interaction length all the beat-waves are in the same phase (Fig C2.23 (c)) At the entrance of Raman amplifier where this phase locking occurs it can normally be assumed that the effects of the interaction on the pump modes is negligible. Under this assumption we get from Eqs (5), (6) that the vibration wave amplitude has an exponential growth

$$q_v(z) = q_1(0) \exp\left(\tfrac{1}{2}\,\gamma\, I_p z\right) \qquad (7)$$

where I_p is the total pump intensity $\left(I_p = \tfrac{1}{2}\,\Sigma\left|E_{pn}\right|^2\right)$ and γ is the Stokes beam gain coefficient with

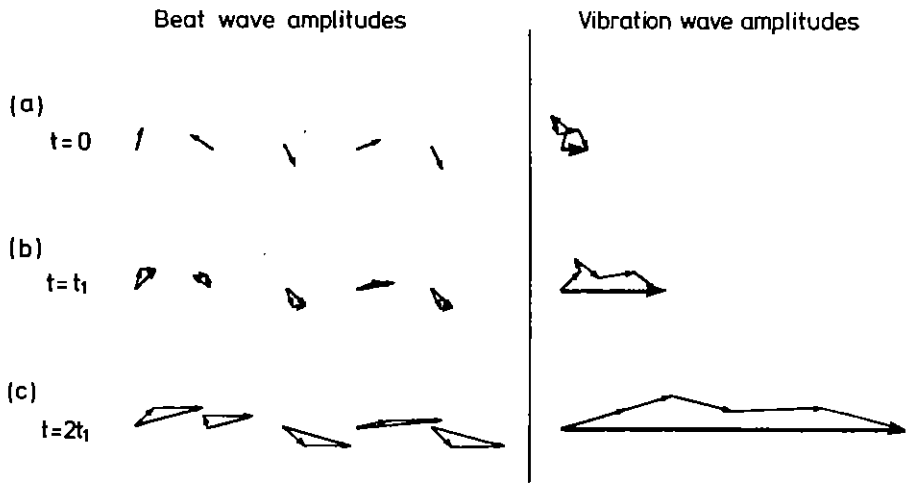

Fig C2.23 The growth of the vibration wave amplitude and the beat wave amplitude which drives it in a broadband-pumped Raman amplifier. The vectors are drawn in the complex plane.

monochromatic pumping $\left(I_s = I_s(0)\exp(\gamma I_p z)\right)$. Applying (7) to (5) we get an equation for the Stokes mode amplitudes which can be solved to lead to the expression

$$I_s(z) = I_s(0) + \frac{\left|q_v(0)\right|^2}{4C_2{}^2}\left[\exp(\gamma I_p z) - 1\right] \qquad (8)$$

for the Stokes beam intensity with broad-band pumping. If the beat waves are non correlated at the entrance of the Raman amplifier we get an estimate for their complex sum (in Eq (6)) using random walk theory:

$$\sum_N E_{pn}\, E_{sn}{}^* = \frac{1}{N^{\frac{1}{2}}} \exp(i\phi) \sum_N \left|E_{pn}\right|\left|E_{sn}\right| \qquad (9)$$

where N is the number of modes and ϕ gives the phase of the sum vector. Assuming top hat profiles for the pump and Stokes beams we get an expression for the initial vibration wave amplitude $\left|q_v(0)\right|$ and that leads to the Stokes beam intensity expression

$$I_s(z) = I_s(0) + \frac{I_s(0)}{N}\left[\exp(\gamma I_p z) - 1\right] \qquad (10)$$

The expression (10) shows that the Stokes beam growth rate is the same with broad-band pumping as with monochromatic pumping after an initial interaction which is required for phase-locking. The interaction length required for phase locking depends on the number of modes, ie. the linewidth of the pump beam. In Fig 3 we show our small signal gain Raman amplfier experiments with two pump linewidths and the asymptotes of the theoretical expression (10) (C2.16). After the phase-locking has occurred the growth and the pump depletion is the same with broad-band pumping as with single mode pumping in a dispersionless medium.

The Stokes beam grows from spontaneously Raman scattered photons in a Raman generator. As soon as the Stokes beam is sufficiently strong to establish a vibration wave all the Stokes photons created are going to be in the right phase. Therefore the threshold for Stokes beam formation in a forward Raman generator does not depend on the pump linewidth.

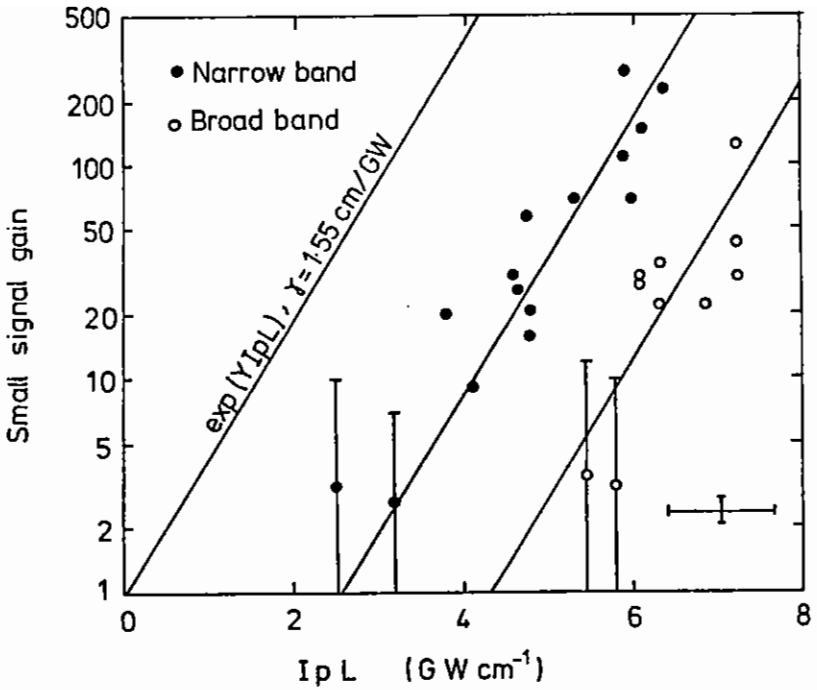

Fig C2.24 Small signal gain measurement with a hydrogen Raman amplifier. Solid points are with pump laser linewidth 0.07 cm^{-1} and open points with linewidth 0.7 cm^{-1}. Solid lines are from Eqn (10) with N = 20 and N = 200 respectively.

The effect of dispersion on the Stokes beam amplification is that beat-waves from different mode pairs have a slightly different wavevector. This causes the beat-wave amplitudes to rotate in the complex plane from the sum vector direction when the beams propagate as shown in Fig C2.25. From C2.25(b) we see that if the gain is not sufficiently high the vibration wave amplitude decreases and there is no Stokes signal gain. With high gain the Stokes beam grows as it does without dispersion. A criterion for the growth of the Stokes beam comes from the requirement that the gain must be high within the dephasing length, $\gamma I_p \ell_d \geq 1$. $\left(\ell_d = \left[\Delta\omega_p \left(1/v_p - 1/v_s\right)\right]^{-1}\right.$, Ref (C2.15). Using Fig C2.25 we have illustrated the interesting result that the Stokes beam grows in a dispersive medium if the pump intensity is higher than a critical intensity given by

$$I_c = \frac{\Delta\omega_p}{\gamma}\left(\frac{1}{v_p} - \frac{1}{v_s}\right) \qquad (11)$$

where $\Delta\omega_p$ is the pump beam linewidth and v_p and v_s are pump and Stokes beam group velocities, respectively. Using approximate solutions of the coupling equations (2) and (3) Akhmanov et al (C2.17) first discovered the critical intensity with a definition slightly differing from Eq (11). It has been verified experimentally many times.

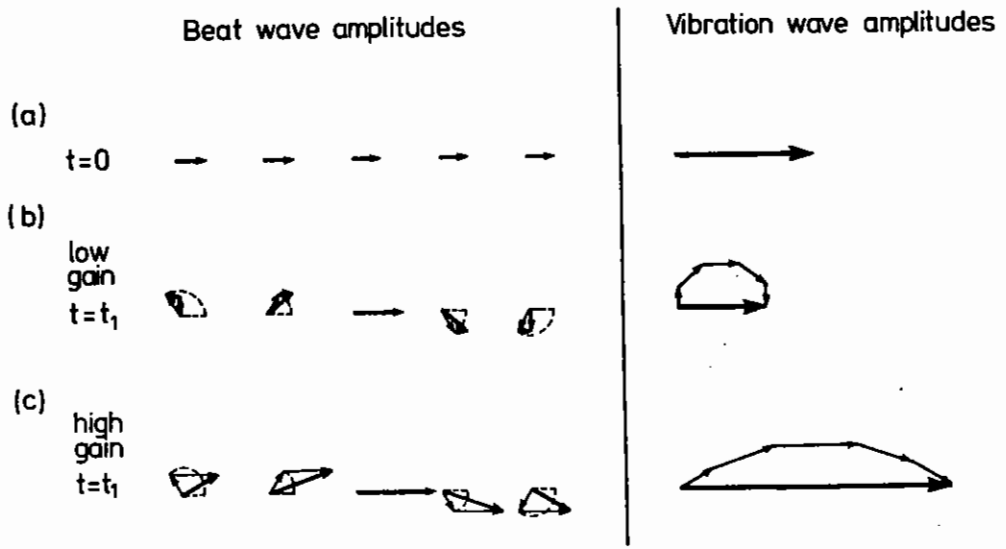

Fig C2.25 The effect of dispersion on the growth of the vibration wave amplitude with low (b) and high (c) gain. Dispersion causes the rotation of the beat wave amplitudes in the complex plane as the pump and Stokes beams propogate.

C2.5 DEVELOPMENT OF A NARROW LINE KrF OSCILLATOR

J P Partanen, G M Davis and M J Shaw (RAL)

As explained in the previous section the growth of the Stokes beam in the Raman amplifier depends on the linewidth of the pump laser even if the dispersion is not strong. With high dispersion like in liquid Raman amplifiers, the effect can be very dramatic. We have started to develop a narrower linewidth KrF oscillator. In the last year we have studied the line narrowing of KrF lasers. We are also building a small scale electron-beam-pumped KrF laser to provide a long excitation of the laser medium. Longer pulselength provides many round trips in the oscillator cavity which makes the line narrowing easier.

C2.5.1 Line Narrowing of KrF Laser with a Multipass Grating Interferometer

The bandwidth of a free-running KrF laser is about 90 cm^{-1}. The line narrowing apparatus in a typical 1 m long oscillator cavity must have a finesse of the order of 10^4 to have only one single longitudinal mode oscillating. The narrowest operational KrF laser cavities have had about 10 longitudinal modes. If the line narrowing is done only by intercavity Fabry-Perot etalons the number of etalons needed for single mode operation is 3 or 4. Another approach is to use a grating or a set of prisms for coarse and etalons for fine line narrowing. In both of these methods thick Fabry-Perot etalons are slightly tilted inside the laser cavity to avoid broad-band feedback by reflection. Walk-off of the beam inside the thick tilted etalon introduces losses and a reduction of the finesse. These walk-off problems can be avoided by using a multipass grating interferometer, MGI.

In an MGI the grating is used in its second order Littrow configuration. Then the first order diffracted radiation is travelling normal to the grating surface. When a mirror is aligned parallel to the grating as shown in Fig C2.26 the interference of the beams

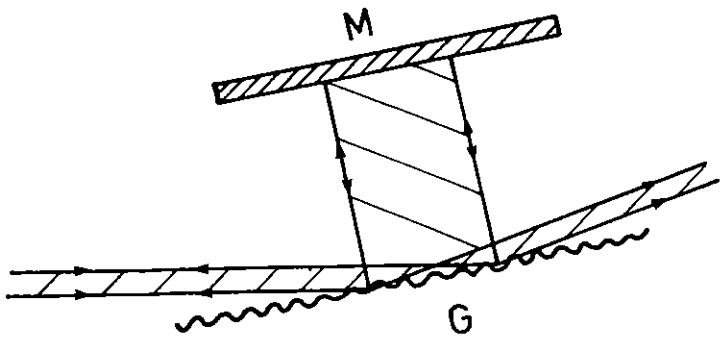

Fig C2.26 The Multipass Grating Interferometer (MGI).

travelling between the grating and the mirror causes the back reflected beam to have a similar wavelength dependence as the transmission function of a Fabry-Perot etalon (C2.18). For the free spectral range of an MGI we have an expression

$$\Delta \bar{\nu}_f = \frac{1}{2d} \qquad (1)$$

where d is the distance between the grating and the mirror and for the finesse

$$F = \frac{\pi (R_m E_n^0)^{\frac{1}{4}}}{1 - (R_m E_n^0)^{\frac{1}{2}}} \qquad (2)$$

where R_m is the reflectivity of the mirror and E_n^0 is the zero order diffraction efficiency of the grating with normal incidence. Although the Littrow diffraction has low efficiency the peak reflectivity of an MGI can be high in the same way as a high reflectivity Fabry-Perot etalon can have high a peak transmission. In addition to this etalon effect, the Littrow grating in an MGI is used for course line narrowing with the resolution

$$\delta \bar{\nu}_g = \frac{1}{2w \tan\theta} \qquad (3)$$

where w is the width of the beam and θ is the angle of the incoming beam to the normal of the grating surface.

We used the cavity shown in Fig C2.27 to experimentally study the line

narrowing of KrF laser with an MGI. The grating available for

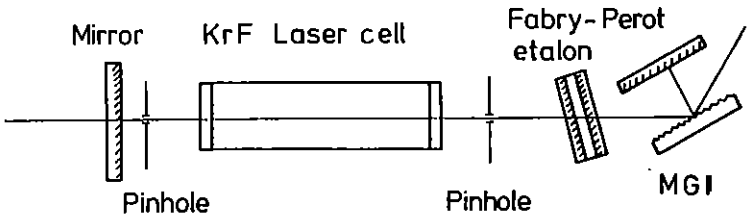

Fig C2.27 Narrow line KrF laser oscillator employing the MGI. The output beam is taken from the output coupler to the left.

experiments was a 3500 grooves/mm holographic grating for which the second order Littrow angle is 61°. The resolution of the grating itself with 0.6 mm apertures is 5 cm^{-1} (Eq (3)). For further line narrowing an etalon must have a free spectral range of 2.5 cm^{-1} or more. Therefore the thickness of the etalon must be less than 2 mm. A slight tilt in an intracavity Fabry-Perot etalon which is only a few times thicker than the width of the beam does not cause any serious walk-off problems. Therefore we could use an extra 1.5 mm air spaced etalon (Fig C2.27) with finesse of 15 to achieve more line narrowing. The effect of this etalon reduces the linewidth to 0.2 cm^{-1}. The final line narrowing is done by the MGI. The distance between the grating and the mirror was 2.5 cm giving a free spectral range of 0.2 cm^{-1} (Eq (1)). We measured the zero order diffraction efficiency of the grating with normal incidence to be about 40 % and the mirror used in the MGI

had a high reflectivity (> 98 %). From Eq (2) we get that the finesse of the MGI is about 7 leading to an expected linewidth of the oscillator cavity of 0.03 cm^{-1}.

Fig C2.28 Fabry Perot interferometer taken of the laser output with an etalon of 0.11 cm^{-1} FSR.

We studied the linewidth of the laser beam by letting the output which is taken through the 95 % mirror at the other end of the cavity go through an expanding lens and a diagnostic Fabry-Perot etalon. The etalon used was a 3 cm thick quartz etalon with high reflectivity coatings in both ends giving a free spectral range of 0.11 cm^{-1}. Fig C2.28 shows a photograph of fringes produced by this etalon. Judging from the figure and more recent measurements with a photodiode array we get that the linewidth of the cavity is about 0.03 cm^{-1}. Fringes appeared only after very careful alignment of the mirror in the MGI to be parallel with the grating surface. The alignment was done with the help of a HeNe laser though the dielectric high reflectivity mirror. With other other diagnostic etalons we checked that the linewidth of the cavity was of the order of 0.2 cm^{-1} without the alignment of the MGI mirror and 5 cm^{-1} with the Littrow grating along.

C2.5.2 Long Pulse KrF Oscillator

The maximum achievable excitation time in discharge pumped KrF lasers is about 40ns due to collapse of the discharge. This limits the number of roundtrips in an oscillator cavity to less than 10 which is not sufficient to establish a good cavity mode. In an electron beam excited KrF laser the pulse length is determined by the length of the electron beam and can be made much longer.

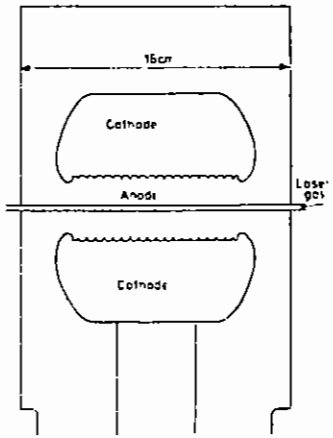

Fig C2.29 The co-axial electron beam diode designed for the long pulse KrF oscillator.

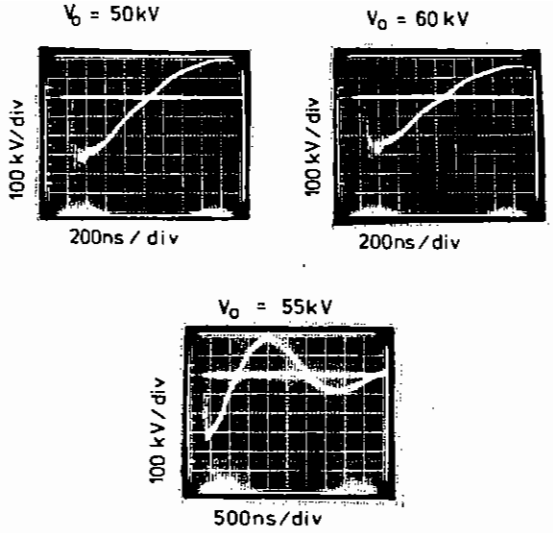

Fig C.31 Output from the pulse-transformer into an 85Ω load resistor.

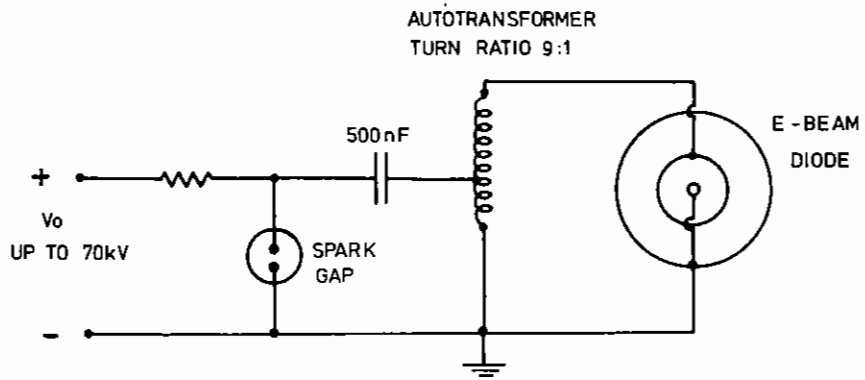

Fig C2.30 Circuit of the transformer driven e-beam generator.

In the long pulse KrF oscillator under construction at RAL we have designed the electron beam to have 150-200ns pulse length. One design aim was to make the electron beam diode as short as possible to increase the number of roundtrips. However, the diode must tolerate about 250 kV cathode voltage, which is needed for the electrons to penetrate through the anode foil from vacuum to the laser gas. The design was carried out using the computer code PE2D(C2.19) which can be used to calculate equipotential contours of electrodes with complicated shapes. The shape of the diode is shown in Fig C2.29. For uniform illumination the laser gas is inside an anode tube surrounded by a coaxial cathode.

The voltage (~ 250kV) and the current (~ 3kA) for the electron beam diode are provided from a pulse transformer. The high voltage circuit is shown in Fig C2.30. Because there is no high voltage capacitor or pulse-forming line in the secondary circuit it is very important to have a low inductance primary circuit. We have constructed the primary circuit using wide copper sheet conductors and a rail spark gap. Replacing the electron beam diode with a corresponding 85 Ω copper sulphate resistor, we have tested the pulse transformer circuit. High voltage pulse wave forms are shown in Fig C2.31. We can deduce that the voltage gain of the pulse transformer to 85 Ω load is about 5.

The long pulse KrF oscillator will be tested during the Summer 1986.

References

C2.1 C B Edwards, F O'Neill and M J Shaw, Appl Phys Lett 36, 617 (1980)

C2.2 ibid, 38, 843 (1981)

C2.3 M J Shaw, Appl Phys, B30, 5 (1983)

C2.4 C B Edwards and F O'Neill, Laser and Particle Beams, 1, 81 (1983)

C2.5 F Kannari, A Suda, M Obara and T Fujioka, IEEE J Quantum Electron, QU-19, 232 (1983)

C2.6 ibid, Appl Phys Lett, 45, 305 (1984)

C2.7 E T Salesky and W D Kimma, Appl Phys Lett, 46, 927 (1985)

C2.8 A Suda, M Obara and T Fujioka, Appl Phys Lett, 45, 1165 (1984)

C2.9 M Tanimota, A Yaoita, I Okuda and Y Owadano, Jpn J Appl Phys 24, L311 (1985)

C2.10 A E Siegman, J Appl Phys 35, 460 (1964)

C2.11 L M Franz and J S Nodvik, J Appl Phys 34, 2346 (1963)

C2.12 K T V Gratan, M H R Hutchinson and K J Thomas, Optics Comm 39, 303 (1981)

C2.13 S Szatmari and F P Schaefer App Phys B33, 219, (1984)

C2.14 E Armandillo, A J Kearsley and C E Webb, J Phys E 15, 177 (1982)

C2.15 J P Partanen and M J Shaw, "High power forward Raman amplifiers employing low pressure gases in lightguides - I Theory and Applications", submitted to J Opt Soc Am B (1986)

C2.16 M J Shaw, J P Partanen, Y Owadano, I N Ross, E Hodgson, C B Edwards and F O'Neill, "High power forward Raman amplifiers employing low pressure gases in lightguides - II Experiments", submitted to J Opt Soc Am B (1986).

C2.17 S A Akhmanov, Yu E Dyakov and L I Pavlov, "Statistical phenomena in Raman scattering stimulated by a broad-band pump", Sov Phys JETP, 39, 249-256 (1975).

C2.18 J P Partanen "A multipass grating interferometer applied to line narrowing in excimer lasers" - to be published.

C2.19 C S Biddlecombe, C B Edwards and M J Shaw Proc IEE 129A, 337 (1982)

C3 PICOSECOND LASERS

Section editor: I N Ross

C3 PICOSECOND LASERS

C3.1 IMPROVEMENTS IN PICOSECOND LASER PERFORMANCE

J Barr, I N Ross

The picosecond laser system described in section B4.2 has performed reliably since installation. However a number of areas requiring development and improvement have been identified.

The beam quality of the un-modified pulse dye amplifier (PDA) was found to be limited by the PDA spatial filtering and beam expanding optics after the second amplifier. Removal of these optics has led to a much improved beam quality without loss in output energy and only a small increase in the level of amplified spontaneous emission. Figure C3.1 shows the farfield performance after modification and this demonstrates that the peak intensity at the focus is within a factor of 2 of being diffraction limited.

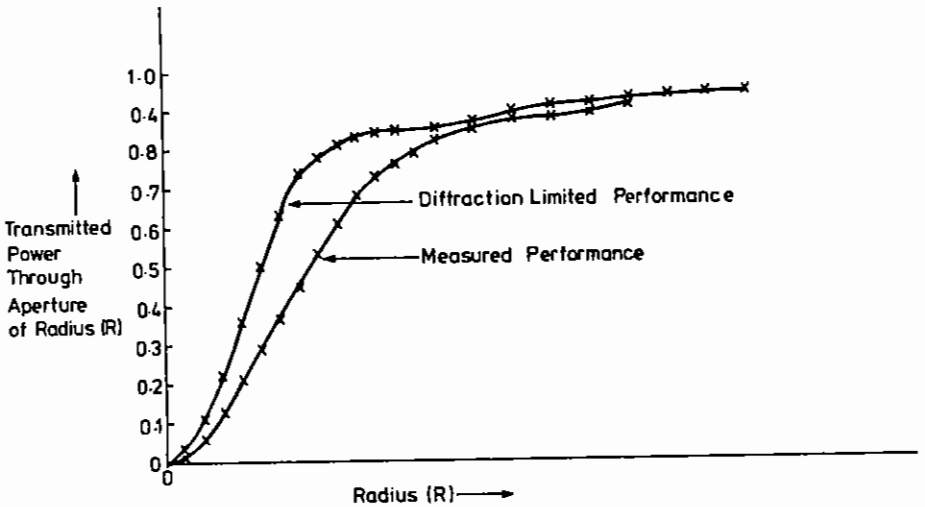

C3.1 Far field performance of the modified picosecond dye laser.

The pulse to pulse fluctuations were larger than expected (30%-50%). These are attributed to mode beating effects in the Q switched Nd:YAG laser and to beam pointing instabilities arising from the pumped dye cells. A pinhole after the first stage has been enlarged to 200μm which reduced the pulse to pulse fluctuations to 15-25%. Control of the ASE has been retained by adjusting the pump energy delivered to each stage. Typical ASE levels are $<5\%$. Further improvements in pulse to pulse fluctuations are expected by reducing the influence of the mode beating in the Nd:YAG laser by adjusting the polarisation and delay of the light pumping each stage.

Transform limited pulses have been obtained over the tuning range of the synchronously pumped dye laser. Previously transform limited pulses were only obtained using the two plate birefringent filter which became increasingly lossy for $\lambda > 610$nm. A tuning wedge was used to tune the laser in this region and gave non-transform limited pulses of 4ps duration. By using a pellicle transform limited pulses were obtained at 630nm with a pulse length of 2.2ps assuming a single sided exponential pulse shape. Figure C3.2 shows the autocorrelation trace which has a half width of 4.4ps. The pellicle was constructed in house out of optical grade melinex of nominal thickness 25μm.

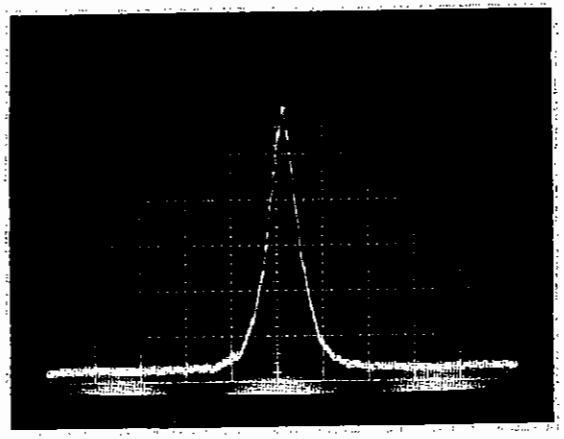

C3.2 Autocorrelation trace at 630 nm showing transform limited performance. The time scale was 6.25 ps/div.

C3.2 EXTENDING THE WAVELENGTH RANGE

J R M Barr, I N Ross, W T Toner

A variety of methods have been used to generate wavelengths for use in picosecond experiments. The processes that have been investigated involve frequency mixing, stimulated Raman generation and continuum generation. The main features of the picosecond laser system are summarised in section B4.2. Figure C3.3 shows typical energy values that have been generated at various wavelengths and the approximate tuning range of the laser using each technique.

C3.2.1 Frequency Mixing

The residual 1.064μm light from the Q switched Nd:YAG contains up to 200mJ in a 2ns pulse corresponding to a peak power of 100MW which is comparable to the peak power of an amplified pulse. Sum frequency mixing of the amplified dye output with 1.064μm is an attractive method of generating additional wavelengths. The wavelength region 366nm to 415nm can be reached directly and mixing after doubling the dye laser output covers 222nm to 258nm. This process was tested using two KDP crystals borrowed from the Laser Loan Pool. A simple non colinear geometry with a 5^{o} crossing angle was adopted. Typical spot sizes of ~3mm in diameter were used. Approximately 15μJ at 400nm was generated from ~400μJ at 650nm and ~100mJ at 1.064μm. Mixing after doubling was tested using the same geometry and yielded ~4-8μJ at 248nm from ~40μJ at 324nm. This wavelength is of considerable interest since it corresponds to the KrF laser wavelength and has been used to provide picosecond pulses for amplification in a KrF amplifier as described in section C3.3.

C3.2.2 Raman Generation

Stimulated Raman scattering in liquids and gases has also been used to provide additional wavelength coverage. Ethanol with a Stokes shift of 2921cm^{-1} has been used to generate probe wavelengths in experiments. Typically 350μJ at 585nm generates 30-35μJ at 705nm in a cell of 40mm path length. The pump light (radius 3mm) was focused by a 20cm focal length lens into the cell giving a 1.4 x diffraction limited spot size of 33μm. The first and second anti-Stokes were also visible in the form of rings. Increasing the intensity by a factor of 2-4 leads to breakdown in the liquid which was readily heard due to the acoustic shock. Slight spectral broadening was also noted but unlike continuum generation in H_2O it was very weak and the spectrum dominated by Stokes and anti-Stokes generation. From the experimental point of view stimulated Raman generation in liquids causes problems since the transmitted beam quality is poor due to thermal and non-linear processes in the focal region. Spatial filtering is necessary to provide a useable beam. However any pointing instablities caused by

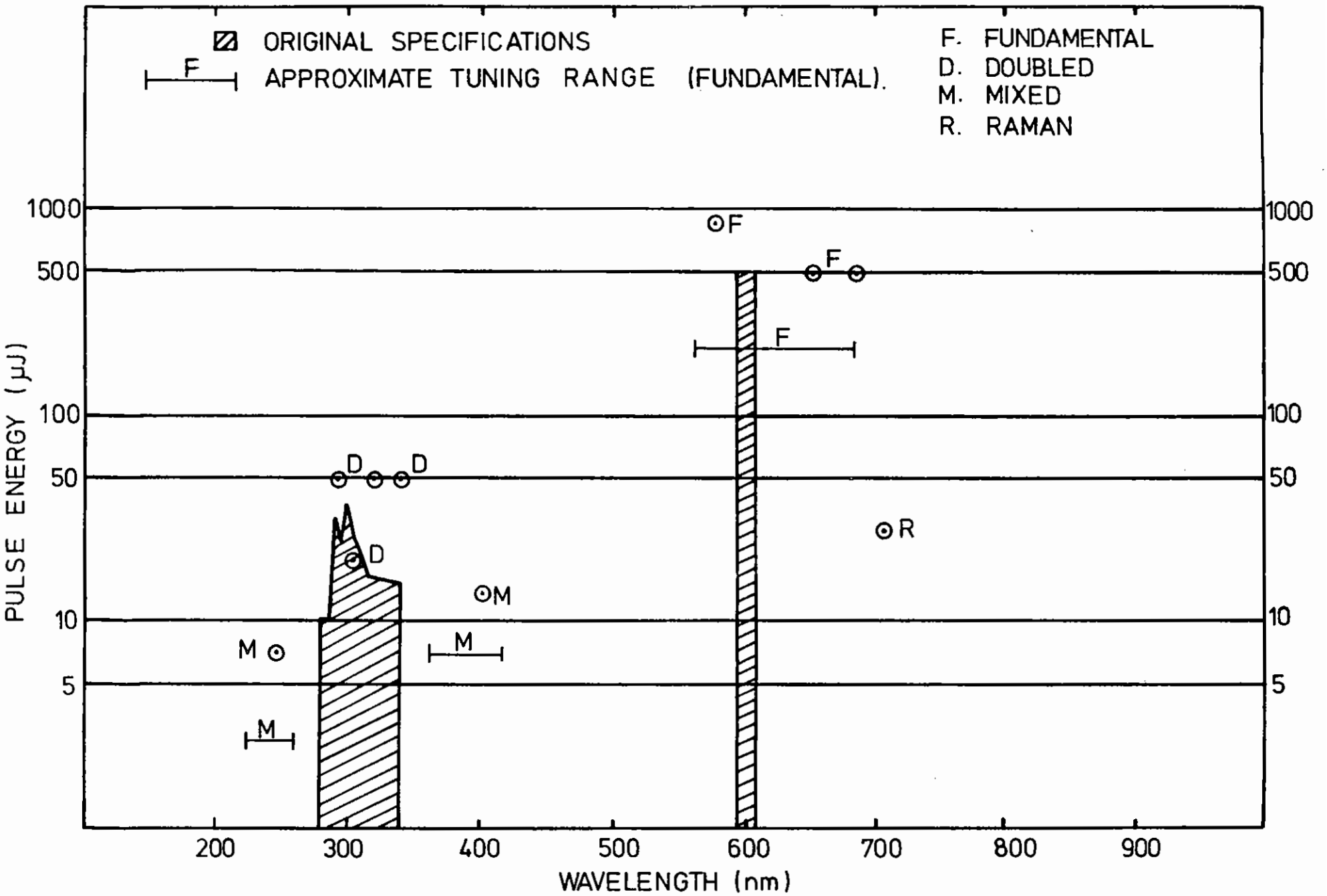

C3.3 Wavelengths and energies available from the picosecond laser.

the liquid can increase pulse to pulse fluctuations due to aperturing by the pinhole. The pulse to pulse fluctuations are about twice the level of those in the fundamental and are typically in the range 30-50%.

In view of the beam quality problems of Raman generation in liquids, H_2 was briefly tested as a Raman medium. H_2 is attractive because it has a large Stokes shift of 4155cm^{-1}. H_2 was prepared in a 1.56m long high pressure cell at 20 atmospheres. The pump radiation was focused using a 1m focal length lens to a ~170μm radius spot. Typically 600μJ was input giving approximately 3-5μJ at 814nm, a conversion of 0.5-0.8%. There was evidence that some 1st anti-Stokes at 485nm was generated. The results indicate that unless conversion can be increased by operating at a higher pressure (~30 atmospheres) or by increasing the power density that H_2 is not a promising medium for picosecond Raman shifting. It is intended that methane will be tested since it has a higher gain than H_2 for picosecond pulses.

C3.2.3 Continuum Generation

The main features of continuum generation in H_2O have been studied experimentally. The picosecond pulses were focused into the centre of a 4cm long cell filled with analar grade water using a 10cm lens. Typically 700μJ at 585nm was used giving a conversion into the continuum of 10%. The main features are shown in Figure C3.4 and were recorded by filtering the continuum using a J.Y. H20 UV spectrometer and detected using a vacuum photodiode with an S1 cathode. The spectrum was not corrected either for the monochromator transmission or the diode sensitivity. The dip at 485nm is due to inverse Raman scattering at the 1st anti-Stokes wavelength in water. The enhancement at 730nm is related to the 1st Stokes but the peak occurs at shorter wavelengths than expected (744nm) due to the reduction in monochromator transmission as 800nm is approached. The spatial properties of the continuum are similar to the input light but with approximately twice the divergence and provides a beam quality that may easily be used in experiments. The pulse to pulse fluctuations of the input were 30% while the fluctuations of the continuum were about 20%. However

reducing the input energy by ~x2 increased the continuum fluctuations until they were comparable with the input laser.

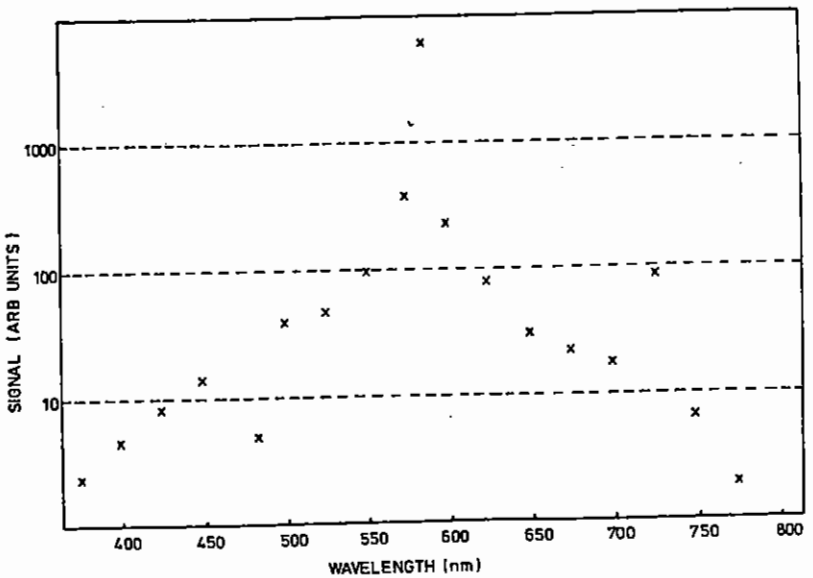

C3.4 Continuum generation in water using the picosecond laser.

C3.3 AMPLIFICATION OF PICOSECOND PULSES IN EXCIMER LASERS

J R M Barr, I N Ross, W T Toner

One of the limitations of the present picosecond laser system is the low pulse energy available in the UV (<50μJ). There is experimental and theoretical interest in the behaviour of atoms exposed to the extremely large electric fields produced by UV fields in excess of 10^{15}Wcm^{-2} (C3.1). An attractive method for reaching these intensities is to amplify picosecond UV pulses in rare gas halide excimer

amplifiers which can exhibit small signal gains up to 700 in XeCl (2) and 2 x 10^4 in KrF (C3.3,4). A recent experiment indicates that up to 10mJ cm^{-2} can be extracted from a KrF amplifier using sub-picosecond pulses (C3.4). It is anticipated that the 500cm^2 aperture of Sprite will enable up to 5J to be generated in a picosecond pulse. Feasibility tests of amplification in XeCl and KrF have been made and the results are briefly described here.

The generation of the 308nm and 248nm picosecond pulses are described in sections B4.2 and C3.2 respectively. Typically 10μJ at 308nm and 5μJ at 248nm were available. Synchronisation between the picosecond lasers and the excimer amplifiers can be ± 2ns in principle but is normally limited by the excimer amplifier timing jitter. The excimer amplifiers were standard Lambda Physik excimer lasers with the mirrors removed and 5^o optics installed.

The preliminary measurements indicate that even with a non optimised system reasonable results can be achieved. At the time of the test the EMG101 (XeCl) typically generated 1mJ of amplified spontaneous emission which was less than expected (>10mJ). As a result the observed small signal gains were small ~10-20 for a single pass and ~100 for a double pass with spatial filtering. An improvement by at least a factor of 10 is expected with a better gas mix. The amplifier section of an EMG 150was used for 248nm amplification in KrF. Typical single pass gains were ~400 with an average of 300μJ per pulse measured on a mean power calorimeter. Optimisation is expected to increase the amplified energy to some tens of millijoules after a second pass.

C3 References

C3.1 K Boyer, H Egger, T Luk, H Pummer, C K Rhodes, J Opt Soc Am, B1, 3 (1984).

C3.2 P Corkum, R S Taylor, IEEE J Quant Elect, QE18, 1962 (1982).

C3.3 S Szatmeri, F P Schafer, Appl Phys B33 219 (1984).

C3.4 A P Schwarzenbch, T S Luk, I A McIntyre, V Johann, A McPherson, K Boyer, C K Rhodes, submitted to Optics Lett.

C4 OPTICS

Section editor: I N Ross

C4 OPTICS

C4.1 COLLOIDAL SILICA ANTIREFLECTION COATINGS

I N Ross, F O'Neill

C4.1.1 Introduction

Considerable inefficiency is incurred in all the RAL laser facilities as a result of the lack of a good high damage threshold antireflection coating. As much as 30% of the laser output is lost to Fresnel reflections before reaching the target. Uncoated components include focussing lenses, blast shields, target chamber windows and harmonic crystals (which are now operated freestanding).

A promising new antireflection coating has recently been developed at LLNL (Lawrence Livermore National Laboratory) (C4.1) consisting of colloidal silica spun or dipped onto the optical component. The process is quick, simple and inexpensive. The coating has excellent properties with low reflectivity, broad bandwidth and high damage threshold, and although very fragile it can be cleaned off and the surface recoated without reprofiling. The coating is particularly effective, in comparison with alternatives, in the ultraviolet at the excimer laser wavelengths.

Work has been carried out over the last six months to generate this coating technology at Rutherford and considerable progress has been made in producing a variety of antireflection coatings and in investigating their performance.

C4.1.2 Review of Programme

1) Spun Coatings

All spun coatings have been generated on a commercial photoresist spinner modified to run at the slow speeds required for the colloidal silica process (350 - 400 r.p.m.). This spinner is not designed for spinning components greater than approximately Ø 75 mm and we have in consequence designed and are building a larger scale spinner to enable us to coat components up to 300 mm in diameter. This coating facility

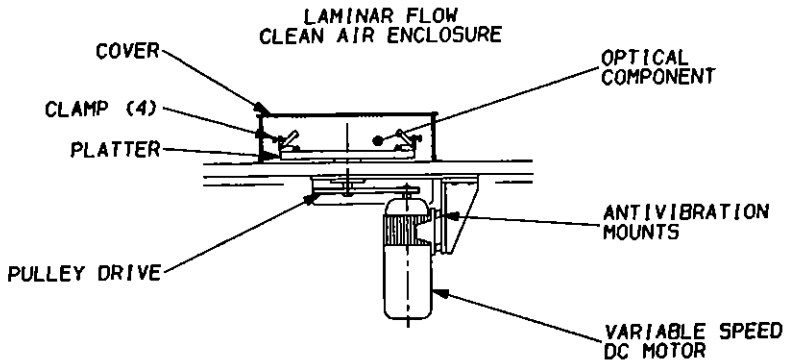

C4.1 Spin coating facility.

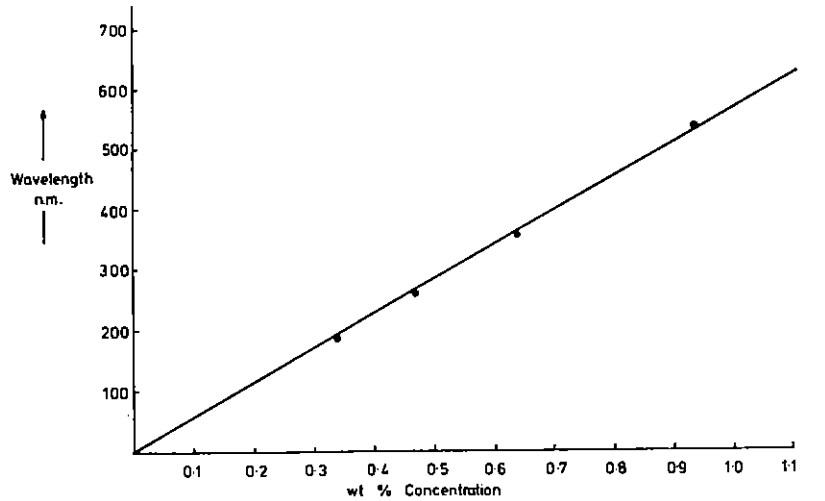

C4.2 Colloidal silica coatings. Wavelength of minimum reflectivity against concentration of colloidal silica solution.

is shown in Figure C4.1.

A large number of coatings have been spun under a variety of conditions and for a variety of wavelengths. We have established the conditions required for good uniform defect-free coatings. At a fixed spin speed we have established the curve for wavelength of minimum reflection (λ min) against concentration of the colloidal silica solution. (Figure C4.2). Coatings have been successfully spun onto glass, fused silica and KDP crystals.

ii) Dip Coatings

Preliminary work towards producing good dip coatings is in progress. This process is necessary for components such as prisms and cubes which have a shape not amenable to spinning and which require coating on several faces. Dip coatings may also be advisable for very small components (less than 30 mm). Figure C4.3 shows a dip tank being used. The component remains fixed while the liquid surface is lowered by opening a constant flow tap. The shape of tank ensures a constant rate of fall of the liquid surface.

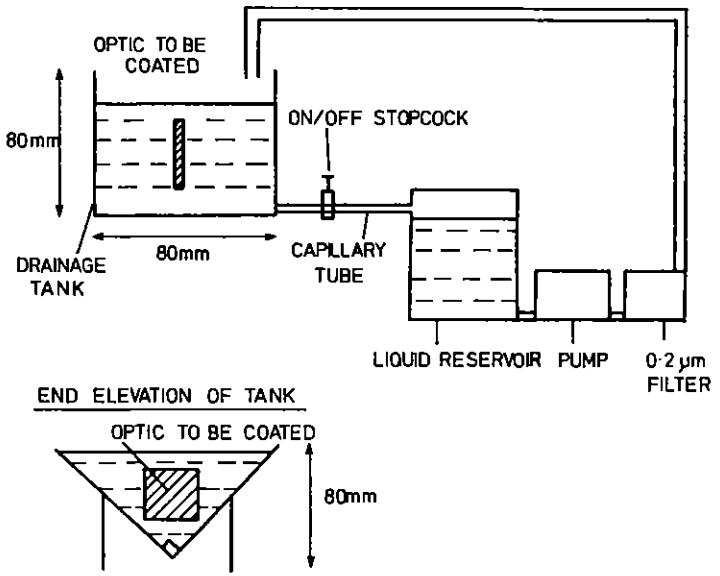

C4.3 Drip coating facility.

iii) Colloidal silica solution

A suspension in ethyl alcohol is used. It has been prepared from tetra ethyl ortho silicate by a base hydrolysis process as specified by LLNL. Once prepared the suspension has been shown to have a shelf life of many months. Elimination of contamination from the ethyl silicate has been shown to improve the laser damage resistant of the coating in the ultraviolet and this is carried out by distillation.

iv) Measurements

A number of measurements have been carried out to test the performance of the colloidal silica coatings:

a) A UV-VIS spectrophotometer measuring the coating transmission, together with spot measurements of reflectivity using laser sources, is used to establish the residual reflectivity and wavelength dependence of the coatings.

b) Laser damage thresholds have been measured at a wavelength of 1.05 μm in the glass laser damage facility. Damage thresholds in the ultraviolet have been measured in the excimer laser damage facility at the Loughborough University.

c) Survival tests have been carried out for coatings left in different laboratory environments and in different vacuum chambers.

d) Two procedures have been tested for removing colloidal silica coatings prior to recoating. One used a very weak solution of HF to etch away the coating, while the other employed a fine polishing compound to polish off the coating without destroying the surface quality of the substrate.

v) Overcoating

A number of components with colloidal silica antireflection coatings have been overcoated with a second dielectric layer by e-beam evaporation. This has a number of potential advantages.

a) the combined coating is far less fragile and can be cleaned in the normal way.

b) a half-wave layer results in excellent antireflection properties with broader bandwidth and perhaps higher damage level than a conventional two layer coating.

c) the overcoating can 'seal' the porous surface of the colloidal silica and perhaps prevent the substrate being affected by a hostile environment (eg. fluorine atmosphere or high humidity).

d) the uniquely low effective refractive index of the colloidal

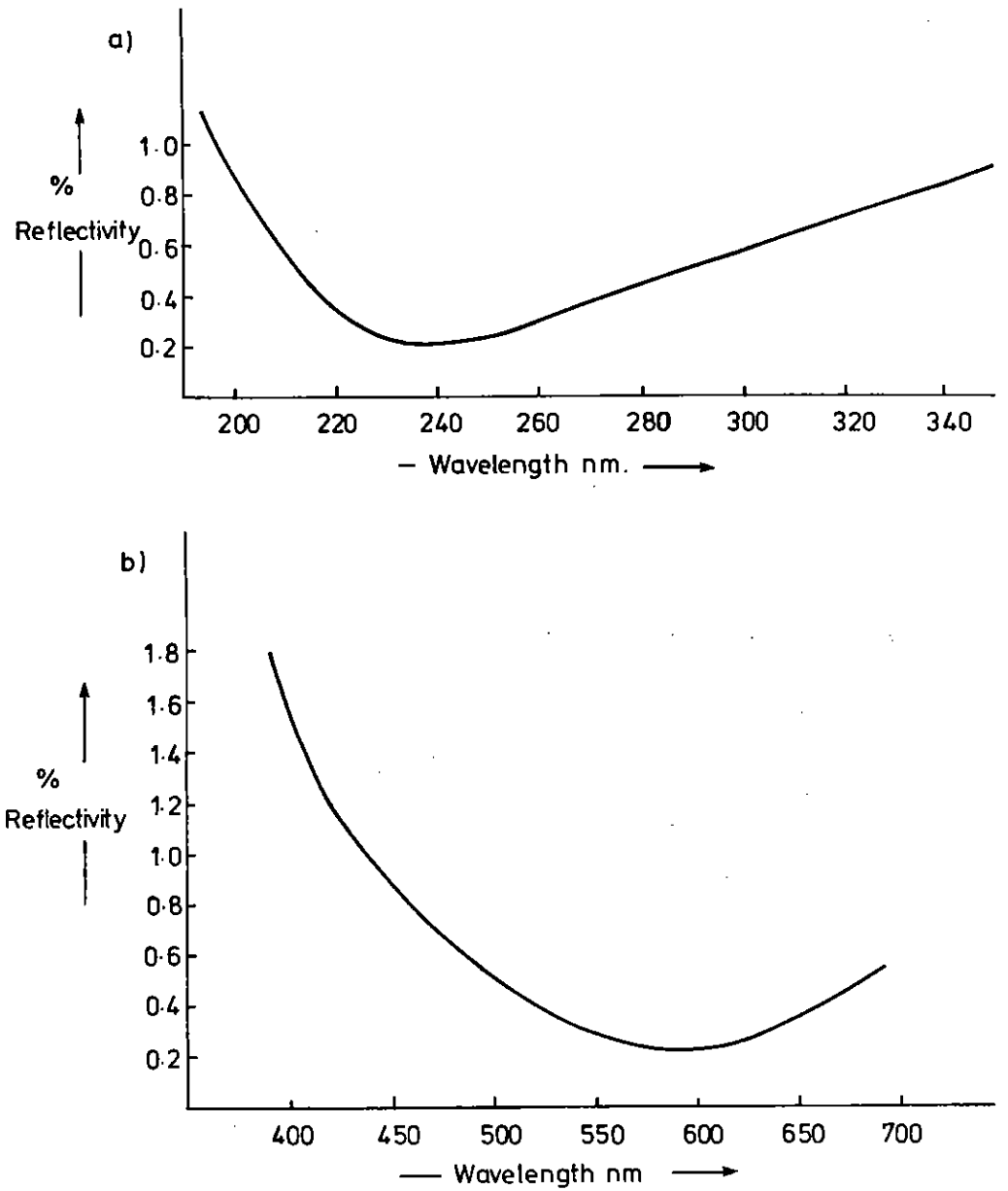

C4.4 Performance of colloidal silica anti reflection coatings
(a) λ/4 overcoat with Zn Se for 0^{o} incidence
(b) λ/2 overcoat with Al_2O_3.

	Single Shot Damage Threshold @ 1.05 μm J/cm^2	
(1) Uncoated glass surface	> 25 J/cm^2	
(2) Colloidal silica a/r coating on glass	20 J/cm^2	
(3) Uncoated KDP	13 J/cm^2	
(4) Colloidal silica a/r coating on KDP	10 J/cm^2	
(5) Colloidal silica a/r coating on glass (after 6 months)	20 J/cm^2	
(6) Colloidal silica a/r coating on glass + λ/2 e Al_2O_3 overcoating	5 J/cm^2	
(7) Tec Optics Ltd HR multilayer on glass	20 J/cm^2	

All colloidal silica coatings used distilled ethyl silicate except (5).

Table C4.1 Damage threshold measurements on various coatings and substrates.

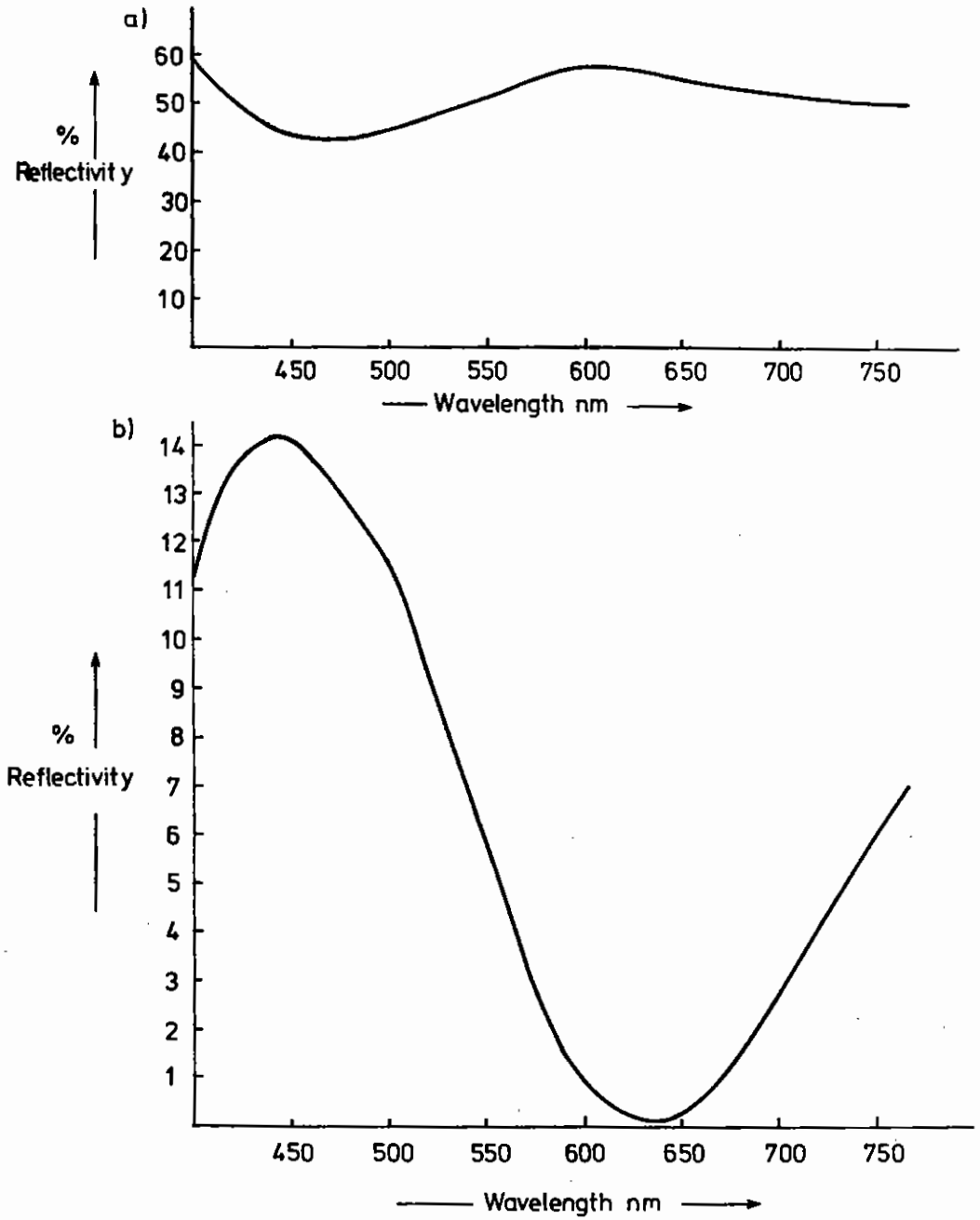

C4.5 Performance of overcoated colloidal silica coatings
(a) λ/2 overcoat with Zn Se for 0° incidence
(b) λ/2 overcoat with Al_2O_3.

silica layer coupled to a high index overcoat can give very high reflectivities even for a two layer coating.

Results

Figure C4.4 shows the spectral reflectivity curve of two plates coated on both sides with concentration to give λ min = 250 nm and 630 nm respectively. All coatings fabricated to date have given reflectivities at λ min between 0.1 and 0.3% per surface.

Table C4.1 gives damage threshold data for different coatings and at two wavelengths using undistilled and distilled ethyl silicate raw material. 1.05 μm damage thresholds of colloidal silica coatings were most satisfactory, and did not appear to drop for coatings made several months earlier using undistilled chemicals.

The performance of coatings in a normal laboratory environment did not seem to undergo any aging process over at least a six month period. However they do seem to be subject to contamination perhaps due to oil vapour when inserted into vacuum systems. Cleaner vacuum systems will be necessary before these coatings can be used in the target chambers.

Using both techniques of coating removal, dilute HF solution and fine polishing compound, good quality bare surfaces and good performance recoating on fused silica has been demonstrated. Following four coating/removal cycles a subsequent coating was still performing well. It is noted that the HF etch process should only be used with fused silica substrates since it will appreciable etch other substrate materials during the coating removal.
Figure C4.5 shows the performance of two overcoated colloidal silica coatings The Al_2O_3 half-wave overcoating gave an exceptionally low residual reflectivity of 0.1% per surface. The second example designed for high reflectivity gave 56% for the two layer coating at normal incidence.

C4.2 SINGLET ASPHERIC FOCUSING LENS

D J Nicholas (RAL)

The requirement is for a robust focusing lens operating in the ~kJ energy range and over the wavelength region of $250 < \lambda < 1060$ nm. The lens should have a minimum number of optical surfaces to reduce the energy loss due to Fresnel reflection. Currently the aspheric lenses take the form of a doublet (C4.2) whose component separation is adjusted to the operating wavelength. The energy loss due to the insertion of this lens in the system is ~20%. We describe here the design of an aspheric singlet lens in which the stigmatic focusing at one wavelength is balanced against the sphero-chromatic aberration at another. The result is a singlet lens, with a perturbed aspheric surface, capable of operating over the entire wavelength range required. The principle of the design is as follows: Seidel transverse ray aberrations of order i, $T^{(i)}$ can be made to vanish (C4.3) choosing the aspheric coefficients such that:

$$a_{i+1} = \frac{n'u'T^{(i)}}{(i+1)y^{i+1}\Delta n}$$

where the meaning of the symbols are given in Figure C4.6.

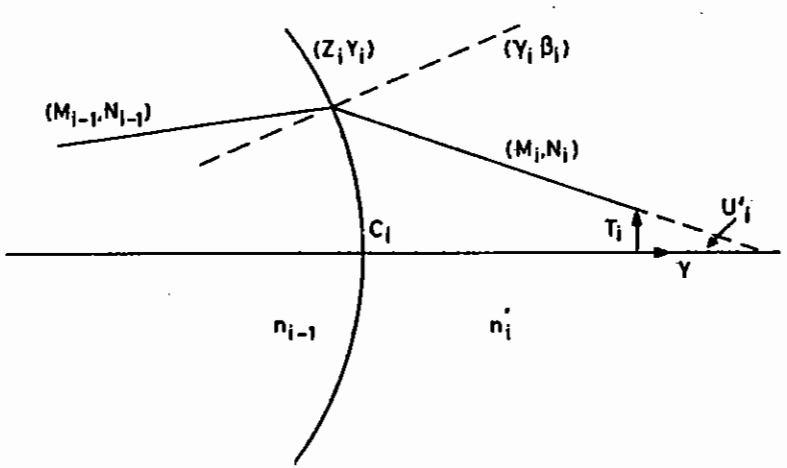

C4.6 Nomenclature adopted.

In the present design the coefficients a_i are chosen so as to minimize the set of partial derivatives $\partial T_J/\partial ai$ in an iterative manner between two selected wavelengths, minimizing $T_J(\lambda_1\lambda_2)$ within the set of 2N linear equations

$$-T_J(\lambda_1\lambda_2) = \sum_{i=1}^{N} \frac{\partial T_J(\lambda_1\lambda_2)}{\partial a_i}.\Delta a_i, \quad J = 1,2 \qquad (C4.1)$$

C4.2.1 Analysis

The general analysis (based on Aldis' theorem[C4.4]) is a formalism adopted in ray-trace procedures in which the total transverse aberration for a system of K optical surfaces is written as

$$n_K u_K N_K T_i = B_i\{Y_i(N_i-N_{i-1})-Z_i(M_i-M_{i-1})\} + \frac{y_i fy_i}{2}(n_iN_i-n_{i-1}N_{i-1}) \qquad (C4.2)$$

where B_i is the refraction invariant and $fy_i = \partial f_i/\partial y_i$. To proceed with the analysis an expression is required which relates the variables in Equation (C4.2), for each surface, with the coefficients a_i of the aspheric. This is accomplished by writing each variable as a power series in the normalized pupil radius ρ such that each variable $R_i = \sum R_i^J \rho^J$.

Equation (C4.2) then yields

$$n_K u_K \{\sum_{J=0,2,4,.} N_K^{(J)}\rho^J\}\{\sum T_i^{(J)}\rho^{(J)}\} = B_i\{\sum_{J=1,3,5,.} Y_i^{(J)}\rho^J\}\{\sum_{J=0,2,4,..} (N_i^{(J)}-N_{i-1}^{(J)})\rho^J\}$$
$$-B_i\{\sum_{J=1,3,5,.} Z_i^{(J)}\rho^J\}\{\sum_{J=0,2,4,..} (M_i^{(J)}-M_{i-1}^{(J)})\rho^J\}$$
$$+\frac{yi}{2}\{\sum_{J=1,3,5,.} \xi_{Yi}^{(J)}\rho^J\}\{\sum_{J=0,2,4,.} (n_iN_i^{(J)}-n_{i-1}N_{i-1}^{(J)})\rho^J\} \qquad (C4.3)$$

This equation is supplemented by similar relationships derived from the transfer and surface equations, that is

$$\{\sum_{J=1,3,5,.} (Y_i^{(J)} - Y_{i-1}^{(J)})\rho^J\}\{\sum_{J=0,2,4,.} N_{i-1}^{(J)}\rho^J\} = \{\sum_{J=1,3,5,.} M_{i-1}^{(J)}\rho^J\}\{\sum_{J} (Z_i^{(J)} - Z_{i-1}^{(J)})\rho^J\}$$

$$+ d_{i-1}\sum_{J=1,3,5,.} M_{i-1}^{(J)}\rho^J$$

and

$$\{\sum_{J=1,3,.} (n_i M_i^{(J)} - n_{i-1}M_{i-1}^{(J)})\rho^J\}\{\sum_{J=0,2,4.} Y_i^{(J)}\rho^J\} =$$

$$\{\sum_{J=0,2,4,.} (n_i N_i^{(J)} - n_{i-1}N_{i-1}^{(J)})\rho^J\}\{\sum_{J=1,3,5,.} \beta_i^{(J)}\rho^J\}$$

respectively. Finally, to find the term N_i^{q+1}, use is made of the relationship

$$N_i^2 = 1 - M_i^2$$

giving

$$\{\sum_{J=0,2,4,.} N_i^{(J)}\rho^J\}^2 = 1 - \{\sum_{J=1,3,5.} M_i^{(J)}\rho^J\}^2$$

Comparing terms of order q + 1 yields the required equations for the aspheric surface and gradient

$$Z_i^{(q+1)} = \sum_{J=2,4,6,.}^{q+1} A_{Ji}(Y_i^J)^{(q+1)}$$

and

$$Z_{Yi}^{(q)} = \sum_{J=2,4,6,.}^{q+1} JA_{Ji}(Y_i^{J-1})^{(q)}$$

This series terminates at $(Y_i^{q+1})^{q+1}$, powers greater than (q+1) do not contain terms of order (q+1).

Only one aspheric is required to correct spherical aberration, the ith say. Now if $T^{(q)}$ is the aberration present when $a_{q+1i}=0$ and $T_r^{(q)}$ is the required value for the complete system then,

$$n_K M_K^{(1)} T^{(q)} + (q+1)a_{q+1i}(n_i - n_{i-1})Y^{(1)q+1} = n_K M_K^{(1)} T_r^{(q)}.$$

Hence,

$$a_{q+1i} = \frac{n_K M_K^{(1)}(T_r^{(q)} - T^{(q)})}{(q+1)(n_i - n_{i-1})Y_i^{(1)q+1}}$$

To satisfy the constant optical path condition we must have, $T_r^{(q)} = 0$, otherwise an aspheric can be designed which selectively aberrates the system or minimizes the aberration at more than one wavelength. Initially all the a_{Ji} should be set to zero. Each is evaluated in turn from the relationship above. After calculating each a_{q+1i} it is necessary to recalculate quantities of order q before proceeding to the next term, because some of them are changed by the new value of a_{q+1i}. Once this is done it will be unnecessary to repeat i again since terms of this order are unaffected by changes in higher order variables yet to be calculated. This procedure is carried out iteratively at two selected wavelength say λ_1 and λ_2. Analytically this is equivalent to minimizing the Jacobian $J(\lambda_1 \lambda_2)$ where

$$J_{1J}(\lambda_1 \lambda_2) = \begin{vmatrix} \frac{\partial T_1(\lambda_1 \lambda_2)}{\partial a_1} & \cdots & \frac{\partial T_1(\lambda_1 \lambda_2)}{\partial a_1} \\ \vdots & & \\ \frac{\partial T_J(\lambda_1 \lambda_2)}{\partial a_1} & \cdots & \frac{\partial T_J(\lambda_1 \lambda_2)}{\partial a_1} \end{vmatrix}$$

The procedure is quite general and could be extended to more than two wavelengths and for more than one aspheric surface.

C4.2.2 Practical design application

We shall consider the design of broadband, or multi-wavelength aspheric singlet lenses based on the above analysis. In order to simplify the discussion, a plano-convex aspheric lens will be considered, although the theory is quite general and any shape factor could be discussed. Also, a glass with a low dispersion, such as fused silica will be chosen. First, the performance of a singlet lens which satisfies Fermat's theorem at one wavelength only, that is $T_r^{(q)} = 0$, will be examined (hereafter referred to as a Fermat lens). The lens is designed at a wavelength of 546 (λ_1) (from practical considerations of manufacture) and its performance investigated over the wavelength range of interest $300 < \lambda > 1000$nm. Figure C4.7 shows the fractional spherical aberration as a function of wavelength.

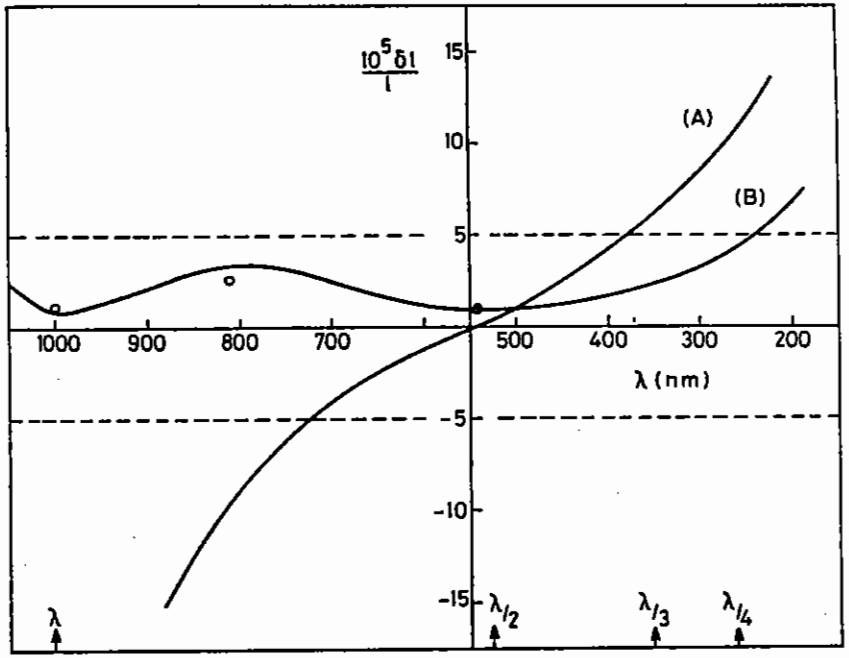

C4.7 Optical performance of an F/2.5 lens
Curve (A); a conventional Fermat aspheric lens
Curve (B); the new perturbed aspheric lens
Also shown (o) are three interferometric measurements of the len's performance.

An optical focusing system containing spherical aberration will produce intensity variation in the vicinity of the focus which may be estimated as follows. If $(Ip+\Delta Ip)/Ip$ is the intensity ratio of the marginal and paraxial rays at the entrance pupil of a lens of back focal length ℓ; $(Io+\Delta Io)/Io$ the ratio at the equivalent target plane a distance Δ from the paraxial focus and $d\ell$ is the spherical aberration content of the lens, then

$$\frac{\Delta Ip}{Ip} = \frac{\Delta}{\ell} \frac{\Delta Io}{Io}$$

Current estimates set the required target illumination uniformity at better than 10%, so $\Delta Io/Io$ 0.1. Also $\Delta Ip/Ip$ $2d\ell/\ell$ so that

$$\frac{d\ell}{\ell} < .05\,\frac{\Delta}{\ell}$$

For a target of 200 μm diameter illuminated by an F/2.5 lens $\Delta/\ell \sim 10^{-3}$ and $d\ell/\ell < 5.10^{-5}$. Figure C4.7 gives the fractional spherical aberration content of two F/2.5 aspheric lenses operating over a range wavelengths. Curve A is that of a conventional Fermat aspheric showing that, essentially, it operates at its design wavelength only. Curve B is that for a lense based on the present anaylsis with optimizing wavelengths selected at 546 nm and 1054 nm. The lens is now zonal but has a useful performance range covering the fundamental and first two harmonics of the neodymium-glass laser.

A singlet F/2.5 lens, based on this principle has been manufactured and tested at several wavelengths using both Zygo and Twyman-Green interferometers. The experimentally measured performance of the lens is also shown in Figure C4.7. The interferograms from which these results were derived is shown in Figure C4.8.

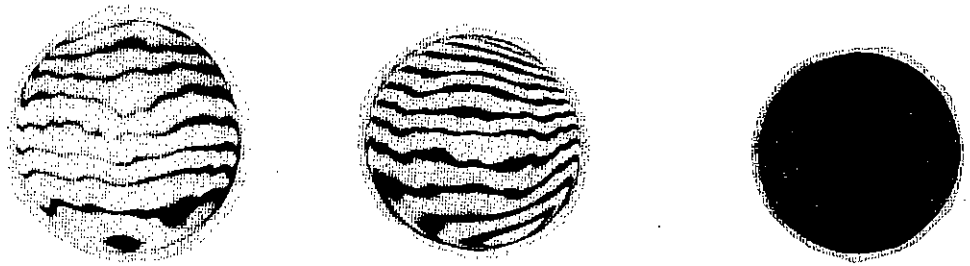

C4.8 Interferograms for the F/2.5 aspheric singlet. (a) and (b); Twyman Green interferometer (c); Zygo interferometer.

A casual glance at the interferograms will show that the lens operates within an error of λ/4 over the entire wavelength range. It is hoped to retest these measurements at a wavelength of 249nm when the facilities become available.

C4.3 NEW LINE FOCUS OPTICAL DESIGNS

I N Ross

The requirements of the x-ray laser programme have led to a number of optical designs for generating high-quality high-aspect-ratio line foci. One of these is already in use and has been described (C4.5).

A number of other possible designs have been investigated and two of these, both offering some advantages over the established scheme, are presented here.

Figure C4.9 shows the two alternative designs. It can be seen that they satisfy the same criterion for giving diffraction-limited transverse resolution in the line focus, since primary focus, line focus and centres of curvature are colinear. Similarly they are restricted to provide normal incidence illumination of targets. Both designs use refracting optics with spherical surfaces and no coatings (unless antireflection coatings are required) and are, in consequence relatively inexpensive. Both geometrics are simpler and more compact than the mirror geometry and a particularly useful feature of scheme A is the coincidence of the line focus and primary focus (virtual).

Scheme A enables a point focus experiment to be converted into a line focus experiment simply by inserting the curved plate without moving the target and target diagnostics. A further useful feature is the ability to adjust the length of line focus by changing the tilt angle of the plate. For polarized light a tilt at the Brewster angle is convenient in order to eliminate surface losses without the use of coatings. Approximate expressions have been evaluated to provide simple estimates for both the length of the line focus (L) and the peak intensity (I) on the curved plate. These are:-

$$L \approx \frac{0.27\ t\ \tan^2 \alpha}{F}\left[1 + \frac{6\ t\ \alpha^2}{R}\right] \text{ mm}$$

$$I \approx \frac{E\ F^2\ \tan \alpha}{3.4 \times 10^{-3} R^2} \text{ J/cm}^2$$

where symbols are giving by Figure C4.9.
E = incident energy
linear dimensions are in mm.

As an example a glass plate of thickness 30 mm, radius 500 mm and inserted at Brewster angle gives a line focus length of 9 mm for an F/2.5 beam, and the peak intensity on the plate is E/90 joules/cm^2. This scheme requires fairly large and thick pieces of glass if very long foci are required at reasonable intensities at the plate.

Scheme B (Figure C4.9) shows a modification to enable longer line foci to be achieved. The curved plate is now wedged and the surfaces no longer have a common centre of curvature. As an example a plate with radii approximately 300 mm and wedge angle of 20^0 with its output face normal to the output beam gives a line focus of length 13 mm for a peak intensity on the plate of E/120 joules/cm^2.

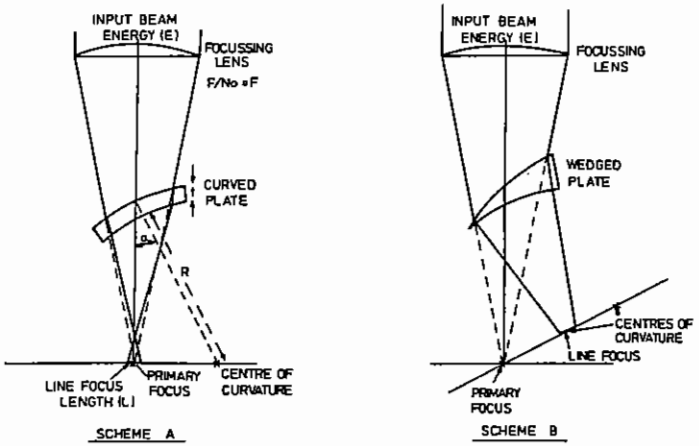

C4.9 Line focus designs using refractive optics.

C4.4 TA East Target Positioning Microscope

C J Hooker, D Riley

With the start-up of TA East for experiments on X-ray laser schemes, it was evident that a new and more accurate method of positioning line-focus targets was needed. In previous experiments using carbon fibres up to 7mm long, two 100x microscope systems were used to project images of the target onto screens, where reference marks defined a unique position in the chamber. There are two reasons why this scheme would not work in TA East.

Firstly, the new time-resolving x-ray spectrometer (section C5.1), which is used as the principal on-axis diagnostic, requires greater accuracy of target positioning to ensure that the target axis points

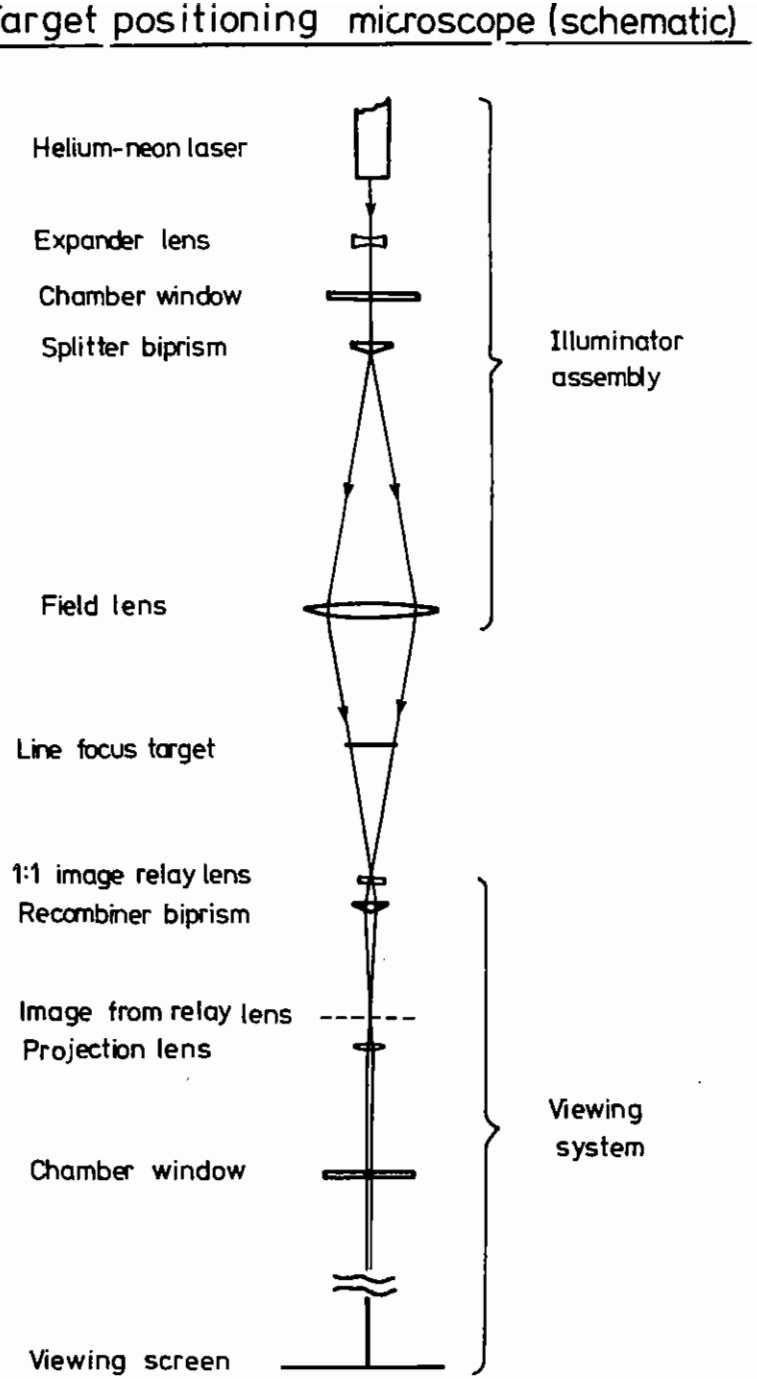

C4.10 Target positioning microscope (schematic).

into the entrance aperture. When the spectrometer is used with a slit on the Rowland circle, to give the best spectral resolution, calculations indicate that the target must be positioned to ± 6 microns at either end of a 7mm fibre: this is the highest accuracy required. For comfortable viewing the allowable error must be magnified to at least 1mm on a viewing screen, thus a magnification of about 200x is necessary.

Secondly, the maximum length of line foci available in TA East is 21mm, and the target viewing system must be able to accommodate this. At 200x magnification, however, the image of a 21mm target is more than 4 metres long: not the most convenient size for viewing. There would also be problems illuminating targets of this size evenly.

The solution lies in the fact that the line focus produced by the Ross-type lens/mirror optics in TA East is a perfect straight line, and the targets are assumed to be straight as well. With this assumption, there is no need to image the entire length of the target: two well-separated points imaged at high magnification would permit accurate positioning. Even so, the existing microscope systems were felt to be unsuitable, mainly because their size would prevent them being moved close together to view the shorter targets. After some experimenting, a split-field microscope was developed, shown schematically in Figure C4.10.
A helium-neon beam is split by a Fresnel biprism into two beams which diverge to a field lens. This lens, which is set to image the splitting point onto the relay lens, causes the beams to reconverge, and to illuminate two points on the target, which is half-way between the field and relay lenses. The separation of these points can be changed by using a different biprism angle, thus different lengths of target can be accommodated. Since the field lens is used at unit magnification, the two beams would normally be focused at the target, and to prevent this an expander lens is used before the split to give illuminated regions about 1mm wide.

The relay lens is a microscope objective of 75mm focal length, used at unit magnification, which forms an image of the target for the projection lens to throw, this time at high magnification, onto a

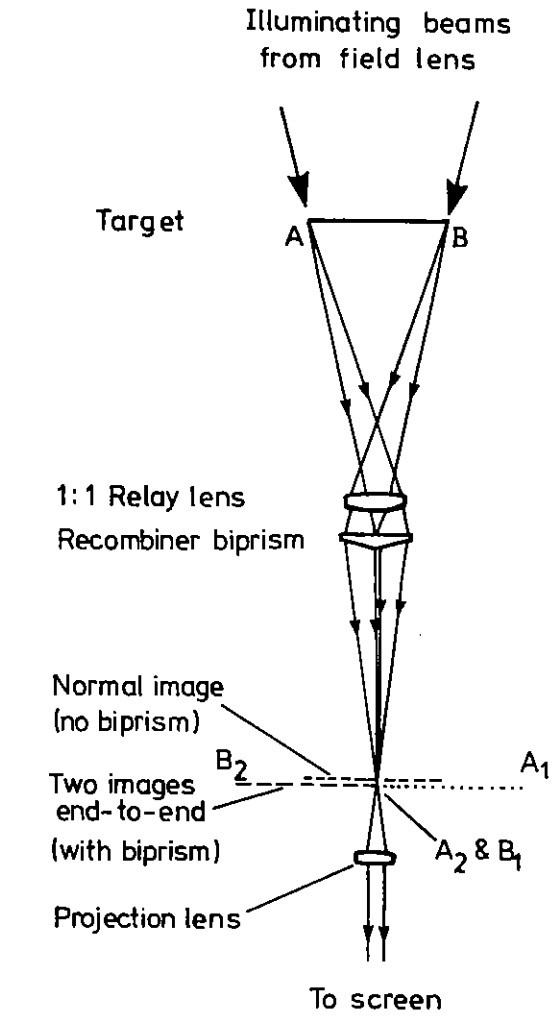

(a) Target microscope viewing system

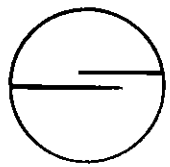

(b) Not aligned

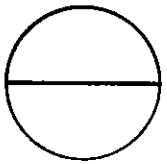

(c) Correctly aligned

C4.11 Operation of positioning microscope.

viewing screen (figure C4.11(a)). Immediately behind the relay lens, however, is the second biprism. This splits the image into two parts which, with a proper choice of prism angle, are separated by a distance equal to the target length. The two images of the illuminated parts of the target, one formed via each half of the biprism, are thus brought together for projection, and at 200 x magnification the final image is only about 40cm in extent.

The appearance of the image is shown in Figure C4.11(b) and (c). When the target is wrongly tilted the image appears broken, and when correctly aligned the image is continuous; with careful inspection this condition can be judged very precisely. As before, two complete systems are used, with their axes roughly orthogonal, to define the target position uniquely. Tests with carbon fibres of known diameter have shown that the required accuracy is easily achieved.

To set up the microscopes for an experiment, a surveying level is used to define a horizontal North-South line through the chamber centre. Two fine V-notches on adjustable mounts, on either side of the chamber, are adjusted to lie on this line, and a 25 micron wire is then stretched between them to serve as an alignment target. The splitter biprism is rotated around the microscope axis until the two beams are bisected by the wire, then the prism and field lens are adjusted to their nominal distances from the wire. The viewing side is set up by first focusing the wire's image on the screen, using an adjustment on the projection lens holder, and then rotating the second biprism until the image appears unbroken. This rotation is the most critical adjustment in the system, since the target axis will always be exactly perpendicular to the roof line of the biprism. Once set, the biprism is locked in position, and reference marks can be drawn on the screen to define the transverse position of the target.

When both microscopes have been set up, the wire is removed. To position a target, the operator first adjusts the tilt movements on the target mount until both microscopes give continuous images, and then uses the translation movements to position the images simultaneously on the reference marks. This sequence is repeated until the alignment is exact. To define the axial position of the target, one end is centred

in one of the illumination beams, and a further reference mark shows where the image of that end should lie on the screen.

These devices have been used successfully in two runs in TA East, and have proved stable and easy to use. Two sets of biprisms, for 7mm and 21mm targets, were obtained, but in practice the 7mm set has been used for all target sizes without loss of precision. Since none of the components comes closer to the target than 150mm, they take up relatively little solid angle, and deposition of target material on the optics is slight. One final feature is that removing only the biprisms converts the system into a conventional microscope for positioning other kinds of targets.

References

C4.1 Wilder, J G Appl Opt 23 1448 (1984)
C4.2 Nicholas, D. J., Pataky, C. and Welford, W. T., App. Opt. 17, 3368, (1978).
C4.3 Nicholas, D. J., Optica Acta 31, 1069, (1984).
C4.4 Cox, A., A system of optical design, Focal Press *b-70).
C4.5 Ross, I N, Hodgson, E M, J Phys E Sci Instrum 18 169 (1985).

C5 INSTRUMENTATION

Section editor: A Ridgeley

C5 INSTRUMENTATION

C5.1 FLAT FIELD SPECTROMETER

G Kiehn (Oxford University), O Willi (Imperial College), A Dammerell, M H Key (RAL)

A novel time resolved XUV grazing incidence spectrograph has been constructed in conjunction with the X-ray laser programme. This configuration utilizes the focal properties of the concave grating to provide 1D spatial imaging. The spectral line profile is a 1D spatial profile of the plasma source. Thus, the instrument simultaneously resolves spectral, temporal, and 1D spatial information. Because the verification of lasing and the optimisation of the mechanisms involved are more easily realised using time resolved spectroscopy, this instrument incorporates a flat focal plane to facilitate coupling to a streak camera for time resolution. Various spectra in the 50Å to 300Å have been obtained.

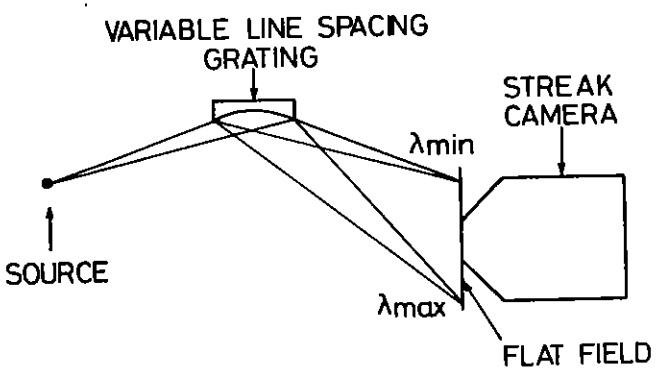

Fig C5.1 Schematic of the Flat Field Spectrograph.

A schematic of the instrument is shown in figure C5.1. A gold coated, concave grating (supplied by Hitachi (C5.1) is used at an angle of incidence of 87 degrees. The grating has a nominal line spacing of 1200 lines per mm, but this spacing varies from 1015 1/mm to 1449 1/mm across the grating surface. It is this variable line spacing which results in focussing in a plane for wavelengths between 50Å and 300Å. The grating is blazed at 3.2 degrees for high first order efficiency over the flat-field wavelength range (C5.2) and has a 5.6 m radius of curvature.

An ultrafast streak camera (supplied by Kentech) is coupled to the flat focal field to provide temporal resolution. The streak camera gives up to 20ps temporal resolution over a 100Å wavelength window within the 50Å-300Å flat field region. Moving the streak camera along the flat

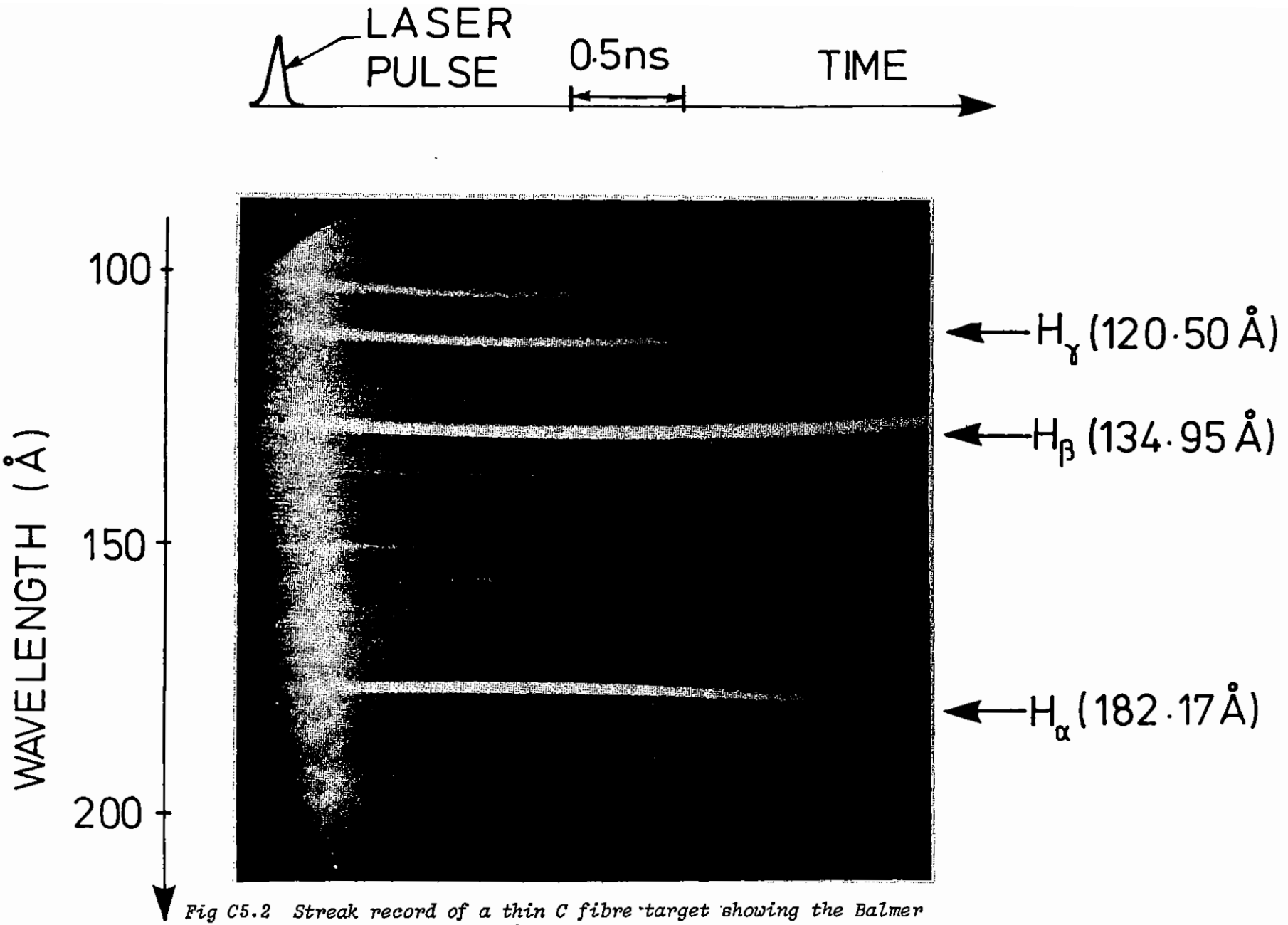

Fig C5.2 Streak record of a thin C fibre target showing the Balmer series of carbon.

The spectrograph was used without an entrance slit, the plasma source being set on the Rowland circle of the instrument.

Figure C5.2 shows a spectrum taken by irradiating a 7μm thick carbon fibre with two opposing line foci. The irradiance on target was 10^{13} W/cm^2 of green laser light. The Balmer series of carbon are clearly seen.

The spectral resolution of the spectrograph in the slitless configuration is source size limited and found to be approximately 1Å. A streak speed of 125 ps/mm was used to obtain 250ps temporal resolution over a 3.5 ns time window for this shot.

Figure C5.3 shows a microdensitometer trace of this spectrum. The intensity of the carbon Balmer spectrum and the minimal higher order contributions agree with published efficiencies for the grating. An overall efficiency of 3% for the spectrograph has been estimated by combining the efficiencies of the grating and the streak camera (C5.3). The spectrograph has demonstrated sufficient sensitivity to record single shot time resolved spectra while simultaneously filtering the input signal for diagnostic purposes.

The following characteristics of the instrument make it ideally suited for the study of laser produced plasmas.

(i) It has a convenient geometry for inserting into a target chamber.
ii) The single component optical system makes it easy to align.
iii) The flat field makes it easy to couple to a streak camera.
(iv) The variable spaced rulings give a reduction in ghost images.

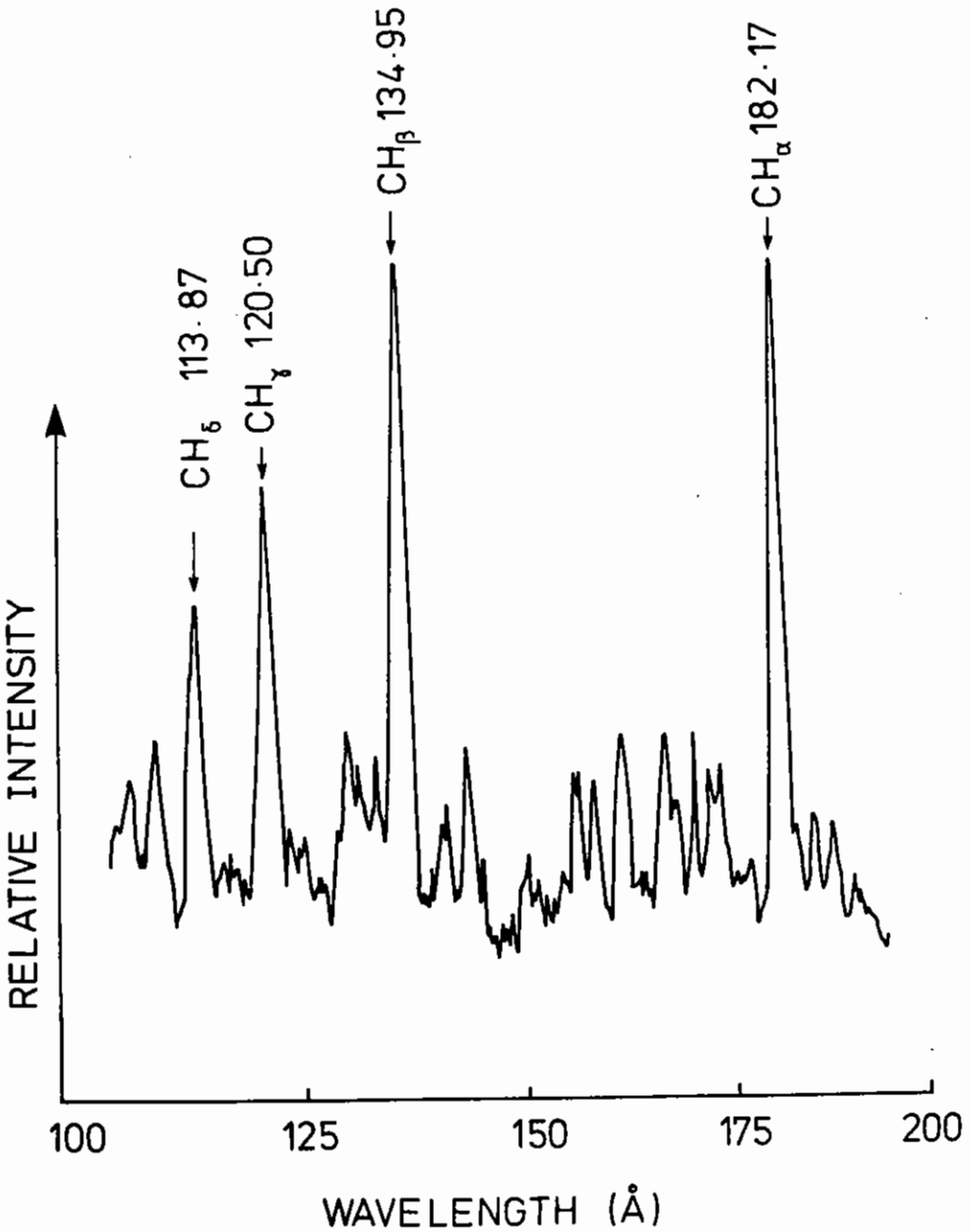

Fig C5.3 Microdensitometer trace of the C fibre streak record taken at t = 600 ps after the input laser beam.

140A. The camera is illustrated in fig (C5.4), which also shows the pinhole array.

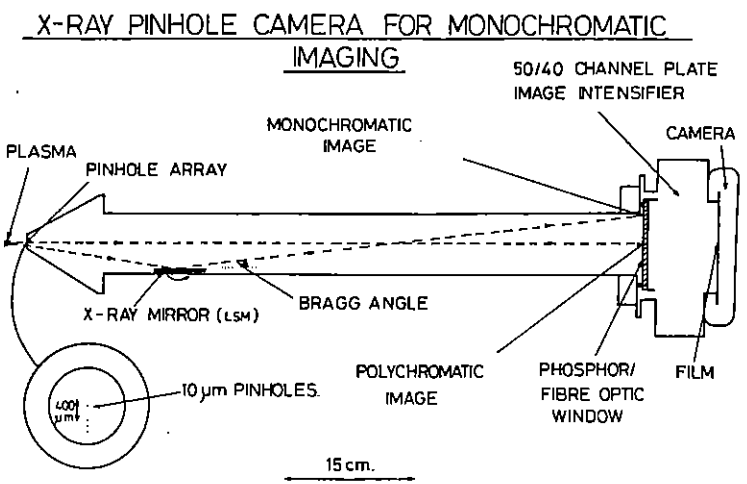

Fig C5.4 Layout of the monochromatic X-ray pinhole camera.

The advantages of using a multi-layer mirror over a crystal are:

(i) it has a high integrated reflectivity thus giving a brighter image

(ii) it has a low dispersion which when used with a broad M-band emitter will give a quasi-continuum feature

(iii) its ideal 2D spacing allows for a very compact instrument.

The pinholes are arranged so that there is a normal polychromatic image and a monochromatic image. Three pinholes are used so as to facilitate the alignment of the diffracted image. The angle of incidence on to

the mirror is adjustable from 2^0 to 4^0 giving a wavelength range of 5-10Å.

An experiment to test the spatial resolution of the instrument has been conducted in the TA2 target chamber. Gold was chosen as a suitable target material because of its broad M-band spectrum at around 5-6Å.

The mirror angle was set by placing an edge in the pinhole mount that block direct X-rays but allowed in indirect X-rays reflected off the mirror. The mirror angle was then adjusted to position the M-band emission in the centre of the field of view as illustrated in fig C5.5.

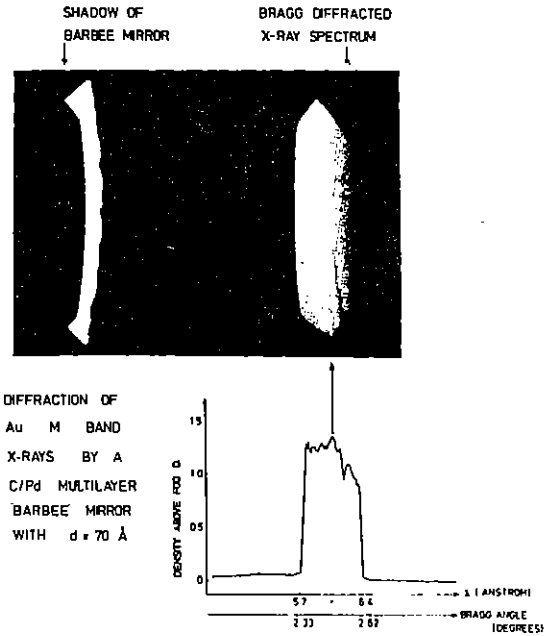

Fig C5.5 Board M-band Au spectrum.

The edge was then replaced by the pinhole array. The pinholes were 10± 1μm in diameter and covered by a 25μm thick beryllium filter. Fig C5.6 shows the targets which consisted of a row of gold microdots laid on a mylar substrate. The microdots were either 10μm or 20μm square separated by 10μm or 20μm spaces. The target was irradicated in a 100μm diameter focal spot with a 10J, 1nsec laser pulse of 0.53μm wavelength. Fig. C5.7 shows the polychromatic image which contains continuum radiation. Fig. C5.8 shows the monochromatic image without a contribution from continuum. Note the improved contrast of the monochromatic image.

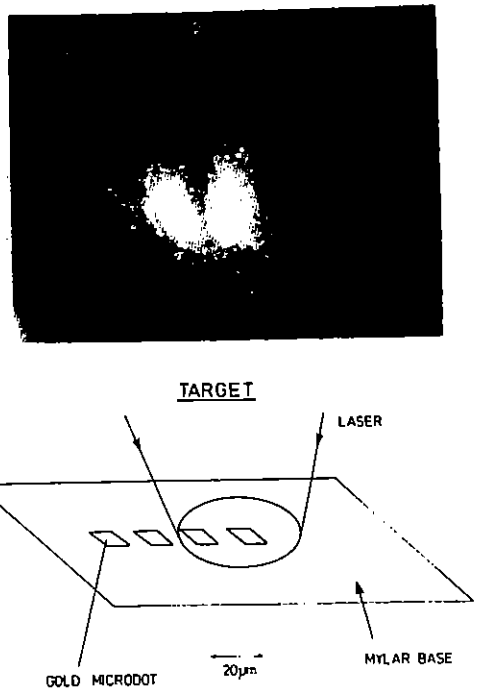

Fig C5.6 Illustration of the target design .

The resolution of a pinhole camera is determined by the relation

$$D > a\left(1 + \frac{1}{M}\right)$$

where D is the minimum resolvable feature of the plasma and a is the diameter of the pinhole.

By irradiating different sized targets the above relationship was verified for the multilayer pinhole camera.

C5.3 TARGET AREA 2 AS AN INSTRUMENTAL DEVELOPMENT AREA

A Ridgeley (RAL)

Since closing down as a facility experimental area in April 1985, TA2 has been re-commissioned as a subsidiary target area. The original TA2 target chamber has been left intact and an optical system has been set up which can accept the backlighting beam into the chamber. The system operates with the second harmonic (0.53μm) and shares the TAE green argon ion alignment laser. The alignment system operates by taking 10% of the argon ion laser output through a beam stop in the dividing wall between TA2 and TAE. The beam stop is operated from TAE for safety reasons and to ensure TAE has priority in use of facilities. It is planned to have a second (infra-red) beam operating at low energies only (<5J) but at a faster repetition rate (~5 mins) and with greater availability. This facility should be useful for the development of VUV instrumentation for example.

TA2 has zero priority in allocation of VULCAN laser shots. This means that shots can only be directed into TA2 if neither TAE nor TAW are imminently ready for a shot or if one of these areas is not using the backlighting. In other words TA2 must not interfere with the running of scheduled experiments in the other target areas. These inclusion conditions mean that potential users of TA2 should assume that a reasonable repetition rate for shots into TA2 exists only at the setting up period in the other target areas.

It is envisaged that TA2 will be used mainly for the testing of new instruments and diagnostic techniques. Users of this facility to date include Y Mikhailov of the Lebedev Institute who used the TA2 system to test his arrangement to use spherically curved crystals as a reflection microscope (C5.4) and B Fraenkel of the Hebrew University of Jerusalem who has conducted experiments into his double diffraction technique (C5.5).

MICRODENSITOMETER RECORDING

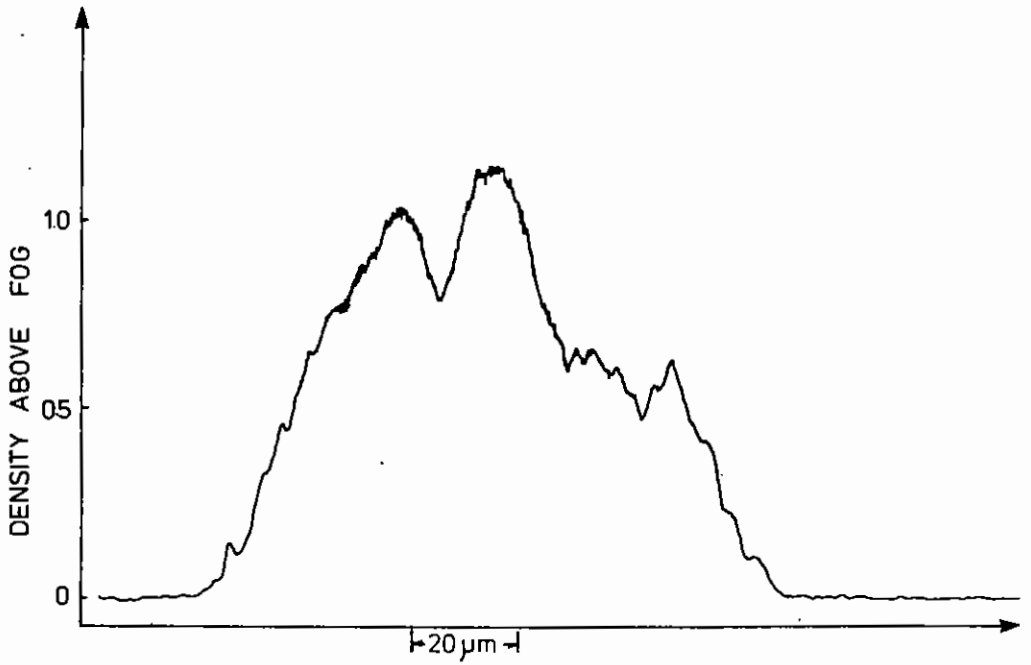

Fig C5.7 Polychromatic X-ray image.

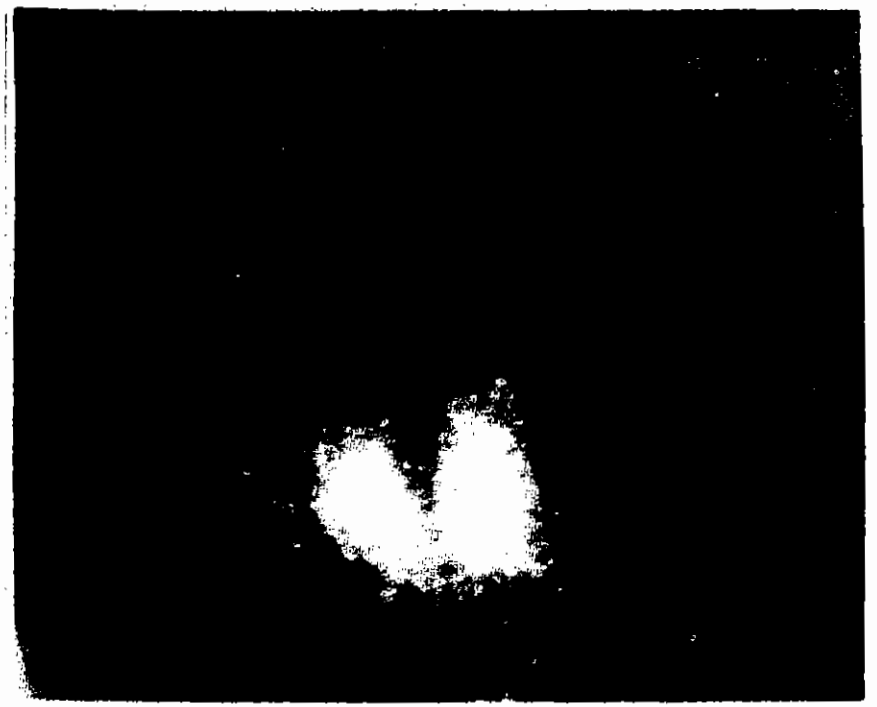

MICRODENSITOMETER RECORDING

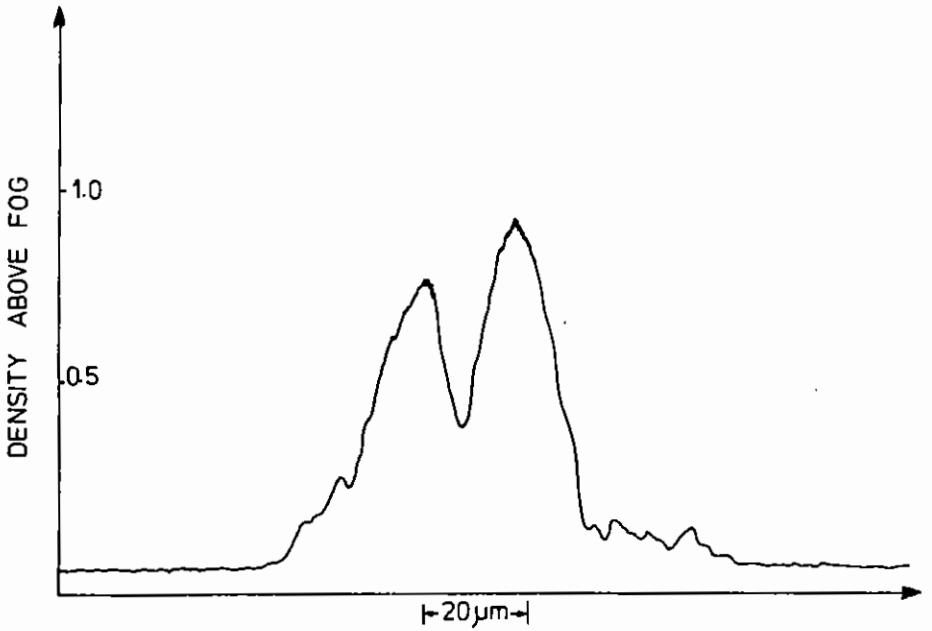

Fig C5.8 Monochromatic X-ray image from the LSM.

References

C5.1 T Kita, T Harade, N Nakano, H Kuroda, Appl Opt, 22, 512 (1983)

C5.2 J Edelstein, M C Hettrick, S Mrowski, P Jelinsky, and C Martin, Appl Opt 19, 3267 (1984)

C5.3 Lawrence Livermore National Laboratory, 1983 Annual Report, 5-29

C5.4 Belyner L M, Gil'ing a. B., Miknilov Yu. A, Piking S A, Skinglor G V, Faenor a. Ya., Fedator S. I., Sov J Quantum Electronics 6 (9) 1 1121-2, 1976

C5.5 Fraenkel B S App. Phys. Lett. 41, (3) 1 234, 1982

Section editor: F O'Neill

C6 LASER-PLASMA GENERATION USING LOW ENERGY KrF LASERS

C6.1 INTRODUCTION

F O'Neill (RAL)

A large part of the user activity at the Central Laser Facility now concerns the use of high brightness soft x-ray sources on VULCAN and Sprite for studies in various areas such as x-ray diffraction, EXAFS and x-ray microscopy. The number of these applications has grown rapidly in recent years and the latest work has been described in section A4 of this report. In this reporting year we have also begun to use low power KrF lasers for generating laser-plasma x-ray sources. The aim of this work has been to assess the potential of such systems as future high average power, quasi-CW, x-ray sources to be made available to users either at the CLF or at their own Universities through the Laser Support Facility.

It is anticipated that these quasi-CW laser-plasma x-ray sources could in some cases compete with storage ring sources especially in those experiments that require the simultaneous use of laser pulses and x-ray pulses. These high power laser-plasma x-ray sources would also be immensley valuable for instrument calibration work associated with the activities of the high power VULCAN and Sprite facilities at the CLF. A high average power laser-plasma source would also be relevant for some industrial applications particularly x-ray lithography and as a fast sputtering source for producing coatings of refractory metals.

The idea of using low energy, high repetition rate lasers as drivers for laser-plasma x-ray sources is not a new one but previous proposals (C6.1) have concentrated on the use of Nd:YAG solid state laser systems. The investigations reported here are different in that they concern the use of discharge excited KrF laser systems for laser-plasma generation. We believe that the use of these systems represents a radically new approach to high repetition rate laser-plasma research. The advantages of the KrF laser as compared to for example the Nd:YAG laser for this application can be listed as follows:-

(1) KrF is a high efficiency gaseous laser system

(2) High repetition rate (> 100 Hz) in a diffraction limited output beam can be achieved.

(3) Short laser wavelength of 249 nm converts more efficiently to soft x-rays.

(4) 100 W lasers commercially available now with potential for > 1 KW in future.

In the following sections are described some preliminary work on the generation and application of low energy KrF laser-plasma soft x-ray sources. Based on this work it seems highly likely that these laser-plasma sources will have an application in future work at the CLF.

C6.2 A LOW ENERGY KrF LASER PLASMA SOURCE FOR X-RAY MICROSCOPY

F O'Neill, Y Owadano, I C E Turcu, E Madrazek (RAL), A G Michette, C Hills, A M Rogoyski (King's College)

In Section A4 of this Annual Report the successful use of high power pulsed laser-plasma sources for soft x-ray contact microscopy of both wet and dried biological material was reported. The lasers used in those experiments were the VULCAN and Sprite systems. VULCAN is a Nd:glass laser giving about 100J of energy per beam at a wavelength of 1053 nm, or about 30J of frequency doubled radiation, in a 1 ns pulse every 20 minutes or so. Sprite is a KrF excimer laser giving about 100J of radiation at a wavelength of 249 nm in a 50 ns pulse with a similar repetition rate. When the laser energy is focused to a small spot (< 300μm diameter) on a target, a plasma is formed which emits soft x-rays in both continuum and line spectra. Typically the emitted x-ray energy in the spectral range 2.3 - 4.4nm over all angles is a few joules. The 2.3 - 4.4nm spectral range is called the "water window" and best contrast is achieved by using x-rays in this range for x-ray

microscopy. The recording medium used in these experiments was a copolymer resist PMMA-MAA, consisting of poly (methylmethacrylate) and methacrylic acid. At the x-ray wavelengths predominant in the spectrum from a carbon target (around 2 - 4nm) this resist required an exposure of about 10mJ/cm^2, which could be achieved by positioning the specimen, in contact with the resist, about 50 mm from the target at an angle of about 50^0 to the incoming laser beam. There was difficulty in these experiments in controlling the exposure, and hence the development procedure, because of the variability of the incident laser energy.

Smaller pulsed lasers, with about 1J per pulse, can have much better energy stability from pulse to pulse, leading to more constant exposure. They are also much cheaper and easier to operate than the higher power lasers, and therefore more suitable for individual laboratories. By moving the specimen chamber closer to the target, and reducing the angle, it is still possible in principle to achieve the necessary level of exposure in a single pulse. This can, however, result in damage to the specimen chamber window (possibly breaking it) and to the resist, caused by debris and radiation from the target. Alternative ways of obtaining suitable exposures with low power sources would include the use of more sensitive resists and the inclusion of x-ray focusing optics.

In this section we report on the use, for contact x-ray microscopy, of a KrF excimer laser with 600 mJ per pulse. Various target to specimen distances were used, with both PMMA-MAA and EBR-9 resists, the latter a very sensitive resist used in electron beam lithography.

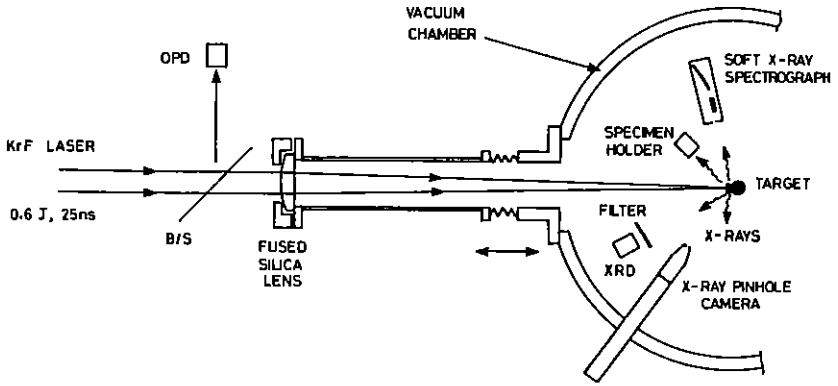

Fig C6.1 Experimental arrangement for X-ray microscopy experiment.

The experimental arrangement for this work is shown in figure C6.1. A Lambda-Physik EMG150 KrF laser, with an injection locked unstable resonator cavity, was used. The output beam was diffraction-limited with dimensions 10 x 25 mm, and each 25 ns long pulse gave 600 mJ of radiation on target at a wavelength of 249 nm. The beam was focused onto a pre-aligned target using a fused silica lens of focal length 125 cm and the intensity on target is estimated to be $< 10^{12}$ W/cm^2 in a spot size ~ 50 - 100 µm. The laser could be pulsed at 1 - 2 Hz but in the experiments reported here single pulses were used for the exposures, except for taking the carbon target spectra for which several pulses were used. The x-ray output was monitored by a pinhole camera, a soft x-ray diode (XRD, figure C6.2a), and a spectrograph. By use of suitable filters the XRD output allowed estimates of the total intensity in particular energy ranges to be obtained, as indicated in

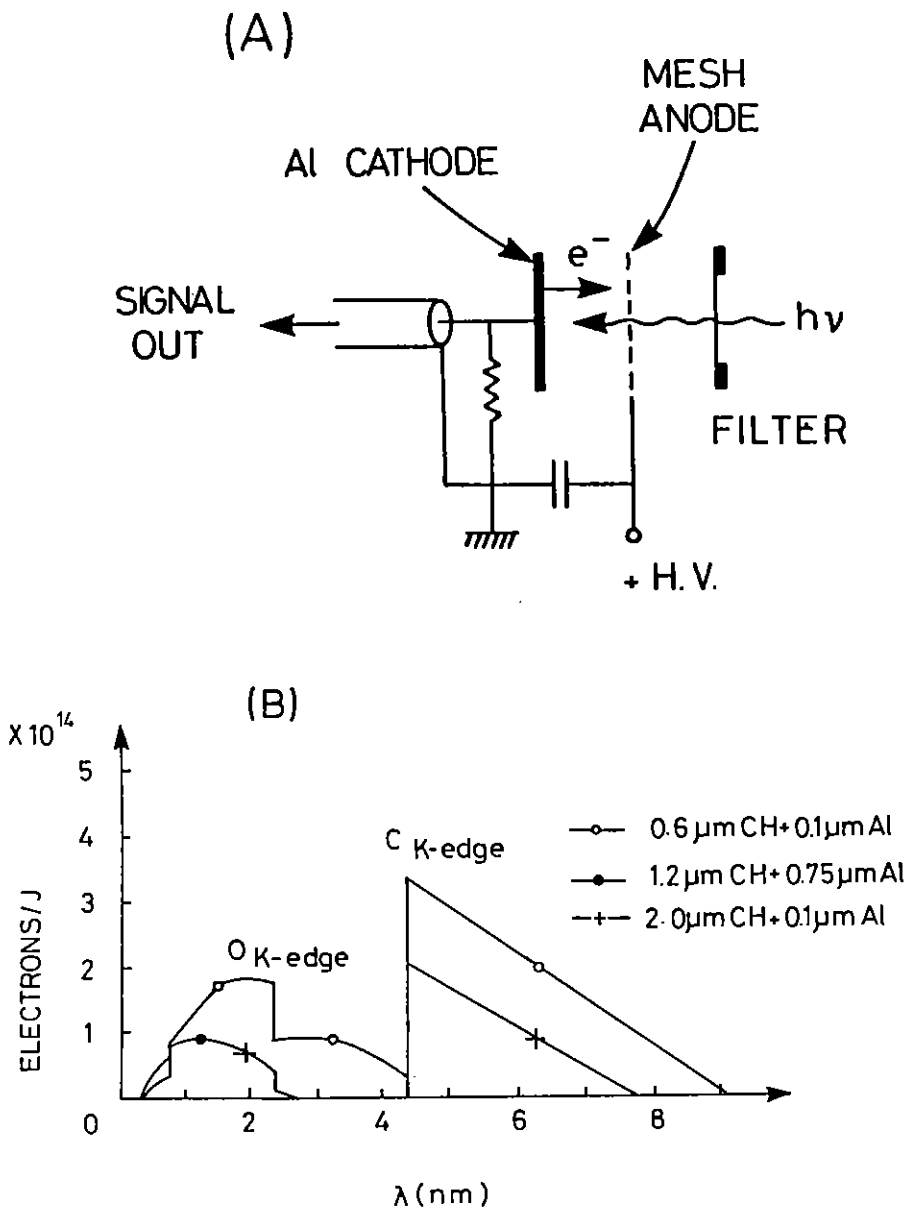

Fig C6.2 (a) Soft X-ray diode
(b) X-ray diode sensitivity.

figure C6.2b. In order to allow the specimen to be positioned closer to the target, a specimen chamber design different to that for previous experiments was used. This is shown in figure C6.3. For images of

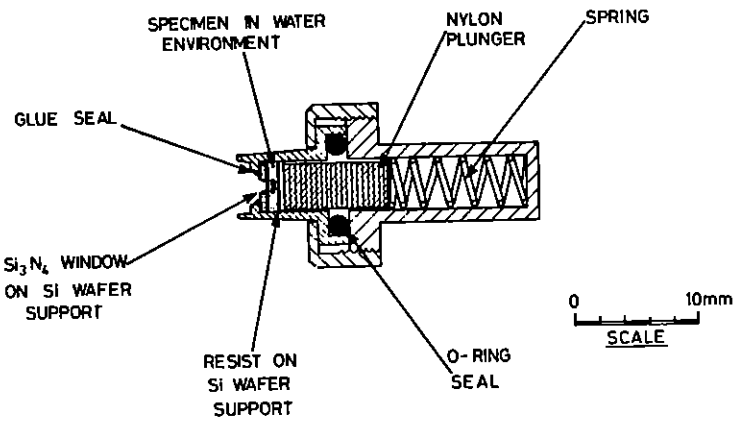

Fig C6.3 Details of compact specimen chamber.

hydrated specimens, a small amount of quick drying insulating varnish was used to seal round the silicon nitride window, in order to maintain the specimen environment when the target vacuum chamber was evacuated. Although it was not necessary to have a high vacuum in order to allow x-ray image formation, the path length of soft x-rays in air at atmospheric pressure being several millimetres, a vacuum of about 5×10^{-5} torr was needed to prevent electrical breakdown of the x-ray diode.

Targets of carbon and brass were used in these experiments. The x-ray diode measurements show that, at an angle of 45^0 to the laser beam, the soft x-ray energy per pulse in the water window was about 1.4 mJ per steradian for carbon targets and about 8 mJ per steradian for brass targets for estimated irradiances on target of about $0.3 - 1.0 \times 10^{12}$ W/cm^2. The x-rays were concentrated in a pulse (figure C6.4b) approximately the same length as the laser pulse (figure C6.4a). For carbon targets the x-ray spectrum (figure C6.5) obtained using eight laser pulses, shows lines at wavelengths of 4.02 nm (strongest), 3.50 nm and 3.37 nm, due to, respectively, the $1s^2$ - 1s2p and $1s^2$ - 1s3p lines in C V (helium-like ions) and the Lyman-α line in C VI (hydrogen-like ions). The level of the trace between the lines is consistent with microdensitometer noise. From the relative intensities of the C V lines and C VI lines, and assuming coronal equilibrium, the electron temperature of the emitting region is calculated to be 63eV, while a pinhole camera image shows the size of the region to be about 100μm (figure C6.4c). For brass targets, more continuum emission was obtained, most of this being in the useful, for x-ray microscopy, water-window wavelength range.

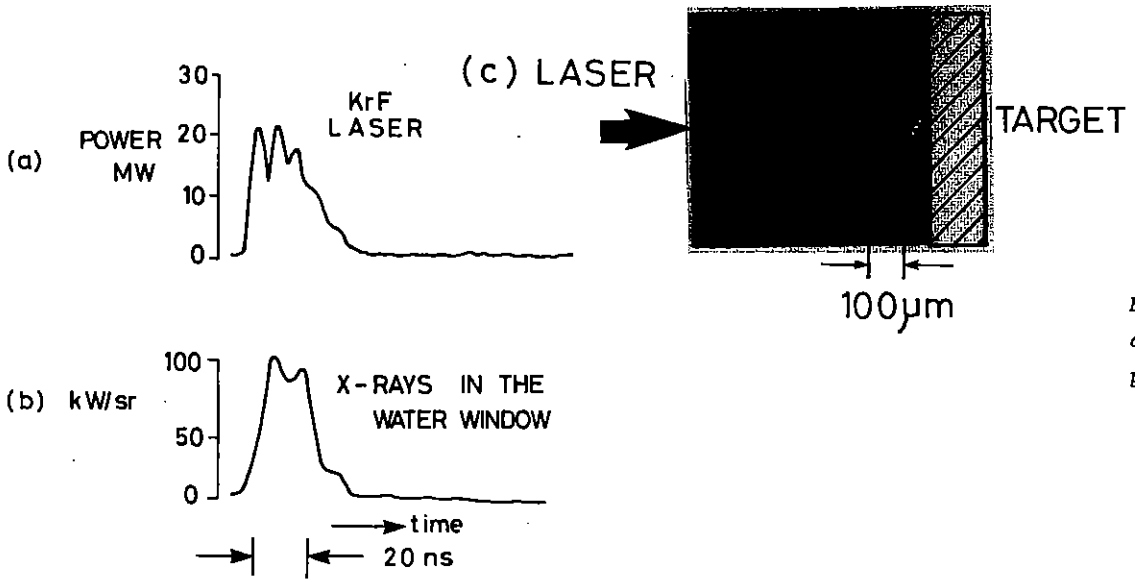

Fig C6.4 (a) Time profile of KrF laser pulse
(b) Time profile of corresponding X-ray pulse from carbon target.
(c) X-ray pinhole camera photograph of the plasma formed with a carbon target.

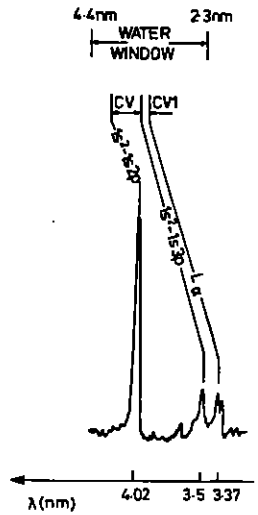

Fig C6.5 Microdensitometer trace of X-ray spectrum from laser-produced plasma using a carbon target.

Single shot x-ray exposures were made on PMMA-MAA and EBR-9 resists in the specimen chamber shown in Fig A6.3. In all cases, it proved simple to obtain exposures of electron microscope grids as test objects, Although no systematic biological study was carried out in these experiments, several types of material were imaged in order to try and assess the potential of the low power laser as a source for contact x-ray microscopy. The specimens included air-dried and wet blood, algae, foxglove epidermal hairs, fatty spreads, flagellae, and tissue cultures. In order to obtain good exposures of these specimens, it was necessary when using carbon targets and PMMA-MAA resist to move the specimen chamber to within 10 mm of the target. Because of the specimen plus resist thickness, typically about 1.5μm, the resolution was still limited at this distance by diffraction (to about 80 nm for a wavelength of 4 nm) rather than penumbral blurring. The proximity of

the specimen chamber to the target almost invariably led to the silicon nitride window being destroyed, which could have allowed the resist to be exposed by scattered ultraviolet radiation in the KrF laser experiments. That this was not so was checked by making exposures using a 6 mm thick CaF_2 window instead of the normal 0.1 μm thick Si_3N_4 window on the specimen cell. This CaF_2 window is transparent to UV radiation down to 140 mm but is opaque to soft x-rays. The resist then remained unexposed. To prevent window destruction, the specimen chamber was moved further away and a ten times more sensitive resist, EBR-9, was used. Although it proved possible to obtain images in this way, they showed very little range of contrast. Clearly some compromise is needed, i.e. a resist mid-way in sensitivity between PMMA-MAA and EBR-9 which still allows imaging without window breakage. An optical micrograph of a biological image in a developed resist is shown in figure C6.6. This shows an image of cyanidium algae which are

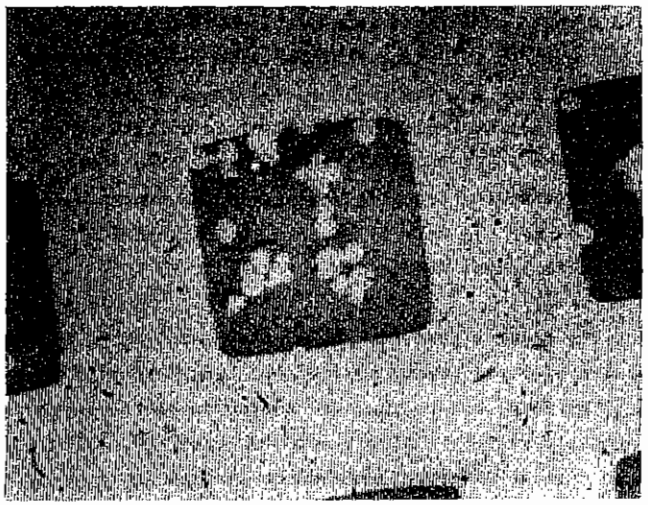

Fig C6.6 X-ray contact image of Cyanidium algae.

typically 5 μm in diameter, imaged in EBR-9 resist. The lack of fine detail in the image is not due to an inherent poor resolution but is either because of the poor range of contrast possible with this resist or due to a real lack of structure in the dried samples.

In conclusion therefore it has been demonstrated that a laser-plasma source generated by a low energy (<1J) KrF laser can emit soft x-rays with sufficient intensity to make images of biological specimens in x-ray resist in single pulses.

Some further developments, for example in the choice of more suitable resists, in the investigation of a wider range of target materials, and in the use of x-ray focusing optics are needed before the evaluation of these sources for soft x-ray contact microscopy can be completed.

C6.3 A REPETITIVE LASER PLASMA SOURCE FOR X-RAY LITHOGRAPHY

F O'Neill, M C Gower, I C E Turcu, Y Owadano (RAL).

X-ray lithography is a promising technology for the productuion of VLSI microelectronic circuits on Si wafers with sub-0.5 μm features using proximity printing. For wavelengths of <1 nm synchrotron radiation or electron bombardment x-ray sources can be used in conjunction with gold on Si, polyimide, or boron nitride substrate masks. Plasmas produced by Z-pinches and ultra-high power Nd:glass lasers are also being investigated as potential sources for x-ray lithography. Recently it has been shown (C6.1, C6.2) that soft x-rays between 4.4 and 8.0 nm generated by a high-repetition-rate 1.06μm Nd:YAG laser-produced plasma can also be used for lithography when using polyimide masks. Such masks have a transmissive window on the long-wavelength side of the carbon K-edge at 4.4 nm.

It is well known (C6.3-C6.5) from previous work with high power systems that soft x-rays can be generated more efficiently from plasmas produced by a KrF laser at 249 nm rather than a Nd laser at 1.06 μm. The purpose of the work described here was to demonstrate that this improved performance could also be achieved using a low-energy commercially available 249 nm KrF laser (Lambda Physik EMG 150ES). The

data reported here represents a major improvement over the work described in Ref C6.2 because the KrF laser-plasma source appears to be a factor of 100 brighter than the Nd:YAG laser-plasma source. The experimental setup is shown in Fig C6.7. The laser, which has already

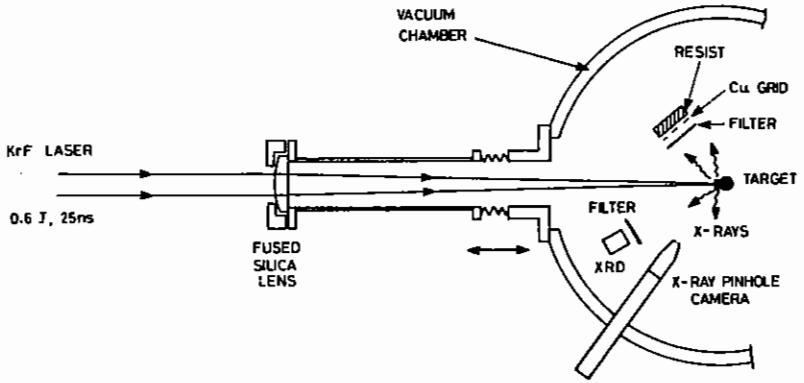

Fig C6.7 Experimental arrangement for X-ray lithography experiments.

been described in Section C6.2, is focused onto metal targets using an aspheric fused silica lens of 125 cm focal length. In Figure C6.8 (c) we show an x-ray pinhole camera picture on Kodak 101-01 film of the 160 μm diameter plasma produced on target by the 0.6 J, 25 ns laser pulse shown in figure C6.8(a). Microdensitometer traces of the exposed (calibrated) film were used to measure the size of the plasma. Accurate focusing was not necessary to obtain x-ray output from the target because the depth of focus of the lens is approximately ±1.5 mm. The laser was run at a 1 Hz repetition rate. Targets consisted of 0.2 - 1 mm diam solid rods placed in the focal plane of the lens, and various materials were tested including C, Al, Fe, Cu brass, Mo, Ta and

W. X-ray signals from the laser-plasma [Figure C6.8(b)] were detected through a 2 μm Mylar filter using an x-ray diode (XRD) with a bare Al cathode pointing at the target at 45^0 to the laser axis at a distance of 7 cm. C and Al targets gave very low x-ray signals. Mo, Ta, and W targets gave the highest signals of about equal amplitude, while Fe, Cu, and brass were ~30% less. W was chosen as the best target material for the present experiments because it gave a high x-ray output which remained constant for many laser shots onto the same spot on target.

The absolute x-ray yield shown in Figure C6.8(b) was calculated from the known sensitivity of the XRD and the estimated transmission of the Mylar filter in the 4.4 - 8.0 nm wavelength region (C6.7).

Using the XRD data presented above we estimate that a KrF laser-plasma source generated by using a commercially available 100 W KrF laser would produce an x-ray output of 0.37 W/sr, which is comparable to the highest intensity achieved from rotating anode electron bombardment sources. We expected that much higher x-ray output could be obtained by focussing the laser to a tighter spot on target using a shorter focal length focussing lens. The laser-plasma source has some additional attractive features. The source size is smaller when viewed over the full 2π emitting solid angle, and resists are more sensitive to longer wavelength x-rays.

We believe that the results presented here represent a major advance in the development of laser-plasma sources for long wavelength x-ray lithography applications, and we suggest that an exposure system based on commercially available high-repetition-rate KrF laser technology could surpass electron bombardment sources in terms of brightness and wafer throughput and would be considerably cheaper and more compact than synchrotron systems.

This laser plasma source has been used for some preliminary work on the exposure of x-ray resists. As an example of such an exposure we show in Figure C6.9 an x-ray image of a fine gold grating mask printed by x-ray proximity printing at a gap of 12 μm into EBR -9

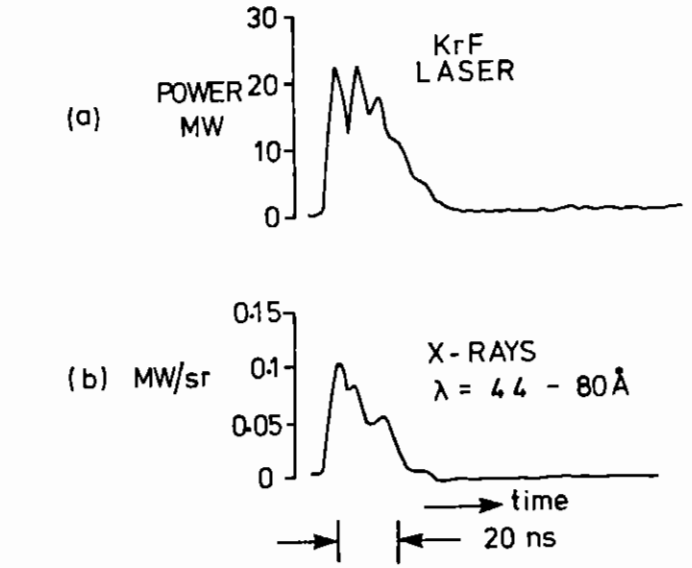

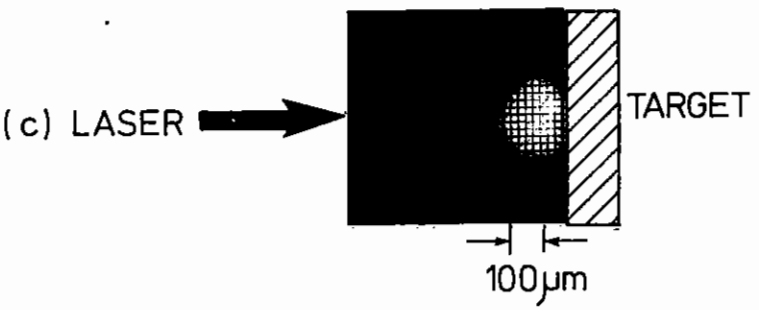

Fig C6.8 (a) KrF laser pulse
(b) 4.4 -8.0 nm X-ray pulse from W plasma
(c) X-ray pinhole camera picture of plasma

resist. These images were very easy to produce and suggest that this type of source will find immediate application in the field of x-ray lithography.

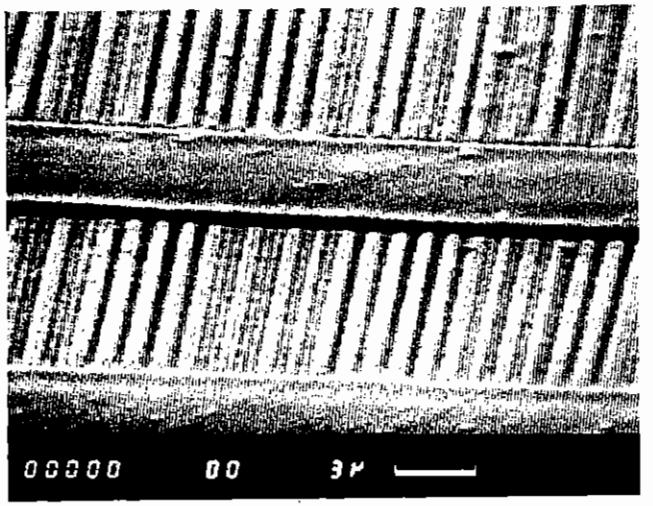

Fig C6.9 Image of fine Au grating mask printed into EBR-9 resist by X-ray proximity printing at a mask-resist gap = 12 μm. Mask and resist were protected from target debris by a 1.2 μm Parylene filter.

C6.4 POTENTIAL HIGH REPETITION RATE XUV SOURCES

F O'Neill, M H Key (RAL)

Synchrotron radiation sources are commonly used for scientific studies which require high fluxes of monochromatic XUV radiation. Typical applications are in photoelectron spectroscopy, surface and interface studies, x-ray microscopy (scanning and contact) and VUV spectroscopy.

For these applications it is sometimes necessary to utilise the tunability and polarisation properties of the XUV beam from the synchrotron.

It is interesting to compare the properties of available synchrotron sources with the potential properties of thermal laser-plasma sources generated by high repetition rate KrF lasers to assess if these laser sources will have any impact in areas now dominated by synchrotrons. In Section A4 of this report a number of experiments were described which utilize high power single shot X-ray sources on the VULCAN and Sprite lasers and in Sections C6.2 and C6.3 above we have presented preliminary work using low energy repetitive laser-plasma sources. With all of these sources the XUV output is achieved by focussing the laser beam to very high intensity (10^{11} W/cm^2) on target. The target material in the focal volume is thus heated to temperatures ~ 10^5-10^6 °K at which temperature the plasma radiates strongly in the XUV region of the spectrum.

In figure C6.10 we compare the single pulse brightness of laser plasma thermal sources with a single pulse from the SRS bending magnet at the SERC Daresbury Laboratory. The upper curves represent a comparison of black-body theory with experiment for two laser-plasma sources generated by low energy lasers as reported in the literature (C6.8, C6.9). The theoretical black-body curves for kT = 27eV and kT = 112 eV have been calculated using the expression:-

$$L_\nu = 2 \times 10^{-3} \frac{\nu^3}{c^2} \left[\frac{1}{\exp(h\nu/kT) - 1}\right] \text{ photons cm}^{-2}\ \text{s}^{-1}\ \text{sr}^{-1} \text{ in } \frac{\Delta\nu}{\nu} = 10^{-3}$$

The data point taken with the KrF laser used a comparatively low intensity of ≈5×10^{11}W/cm^2 on target thus giving a low effective black-body temperature of 27 eV. The 4ω Nd:Glass experimental points utilised a higher intensity of 2.4×10^{13} W/cm^2 on target which gives a higher effective temperature of 112eV and shorter wavelength radiation output to ~ 1 KeV. We expect that the KrF laser can achieve a similar performance to the 4ω Nd:Glass laser by the use of shorter pulses and

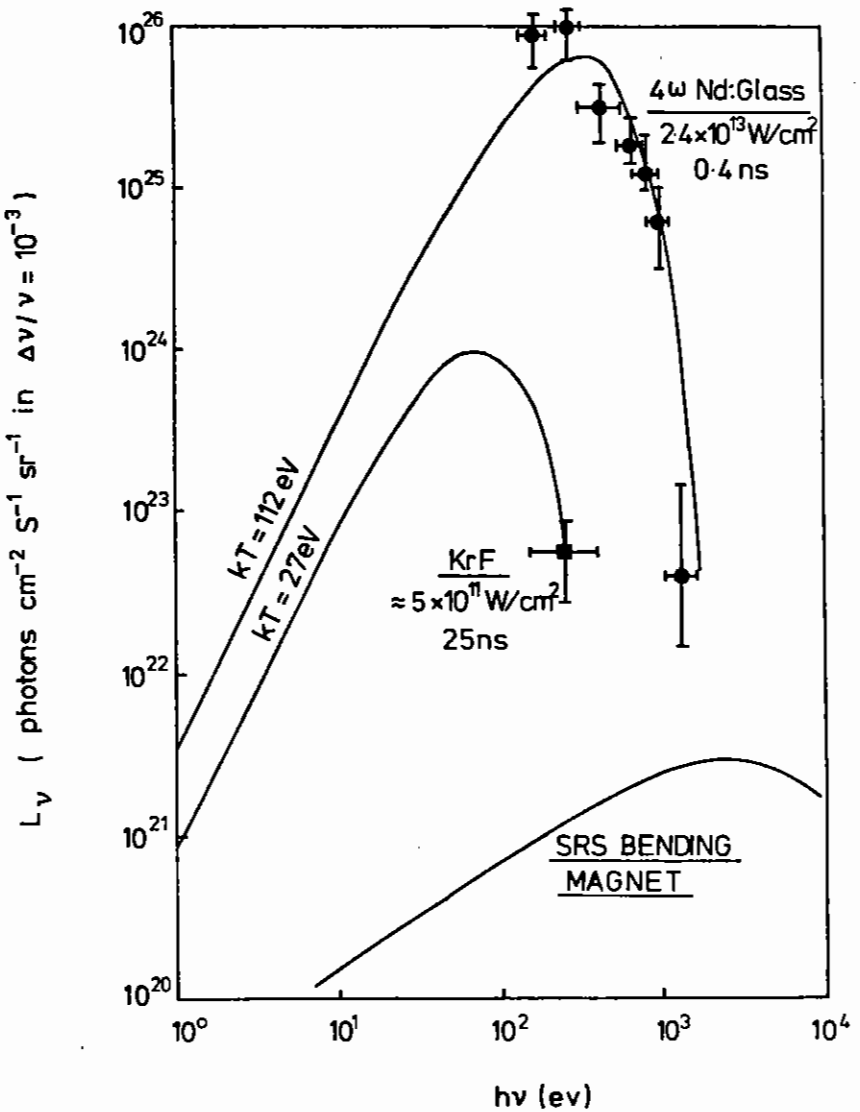

Fig C6.10 Comparison of single pulse brightness of laser-plasma thermal XUV sources with the synchrotron radiation source at Daresbury Laboratory.

tighter focussing on target. It is worth noting that the experimental data taken with the 4ω Nd:glass laser represents a conversion efficienty from laser light to XUV (spectrally integrated) of ≈ 80%.

From figure C6.10 we see that the single pulse brightness of the laser source is five orders of magnitude greater than the single pulse from the synchrotron. When one compares the average brightness of the sources there is very little difference however because the SRS can operate at a pulse repetition frequency of 5×10^8 Hz whereas the laser source can only pulse at $< 10^3$ Hz. The laser source would however be much less expensive to construct and operate and the higher single pulse brightness could be utilised for the increasing number of multi-source experiments which use laser pulses to prepare samples and XUV sources as probes.

It must be said however that the SRS bending magnet source brightness depicted in Fig C.10 represents only what is available from an existing source. A future synchrotron source especially tailored to XUV operation and incorporating undulators could provide 4 - 5 orders of magnitude greater output that the present SRS ring. Such a machine would however be expensive. The laser source described above also has the potential for orders of magnitude improvement by the use of multiple lasers of higher repetition rate (> 10 KHz) and by target optimisation. The small physical size of the laser source also allows the use of compact instruments which view a large solid angle and give a high XUV flux throughput.

From the above discussion we see therefore that thermal plasma sources of high repetition rate generated by KrF lasers could potentially perform as well as storage ring sources but at a much reduced capital cost. Before such laser-plasma systems can be applied to a wide range of scientific studies there are a number of technological problem areas that have to be addressed.

(i) Ablated material

When the laser beam is focussed onto target material is "burnt"

off by ablation during the laser pulse and by shock-wave effects after the pulse. This means that a rapidly renewable target has to be used on a continuous feed and the ablated material would have to be prevented from reaching the laser focussing optics and XUV dispersing optics. This problem will be soluble by using minimum mass thin foil targets to avoid material spall by shock waves and by using electrostatic deflectors and mechanical shutters to stop fast moving plasma and slow moving macroscopic particles from reaching the optics.

(ii) Polarisation

The radiation output from a storage ring source is polarised whereas the radiation from a laser plasma source is likely to be unpolarised. It seems feasible that by using multilayer coated XUV relay optics at angles of incidence ~ 45^0 it will be possible to polarise the radiation from a laser-plasma source.

(iii) UHV Compatibility

Much of the work using XUV sources especially in surface science required UHV conditions of cleanliness. At first sight it would appear that a laser-plasma source which will generate large quantities of debris will be incompatible with UHV requirements. We believe that the techniques described in (i) above will minimise the debris problem. Also since the laser-plasma source is essentially a point source of size < 100 μm it should be possible to use XUV optics to relay the radiation through differentially pumped chambers and/or thin windows separated by pinholes into a suitably clean environment compatible with UHV operations.

In figure C6.11 and C6.12 we show some details of a conceptual high

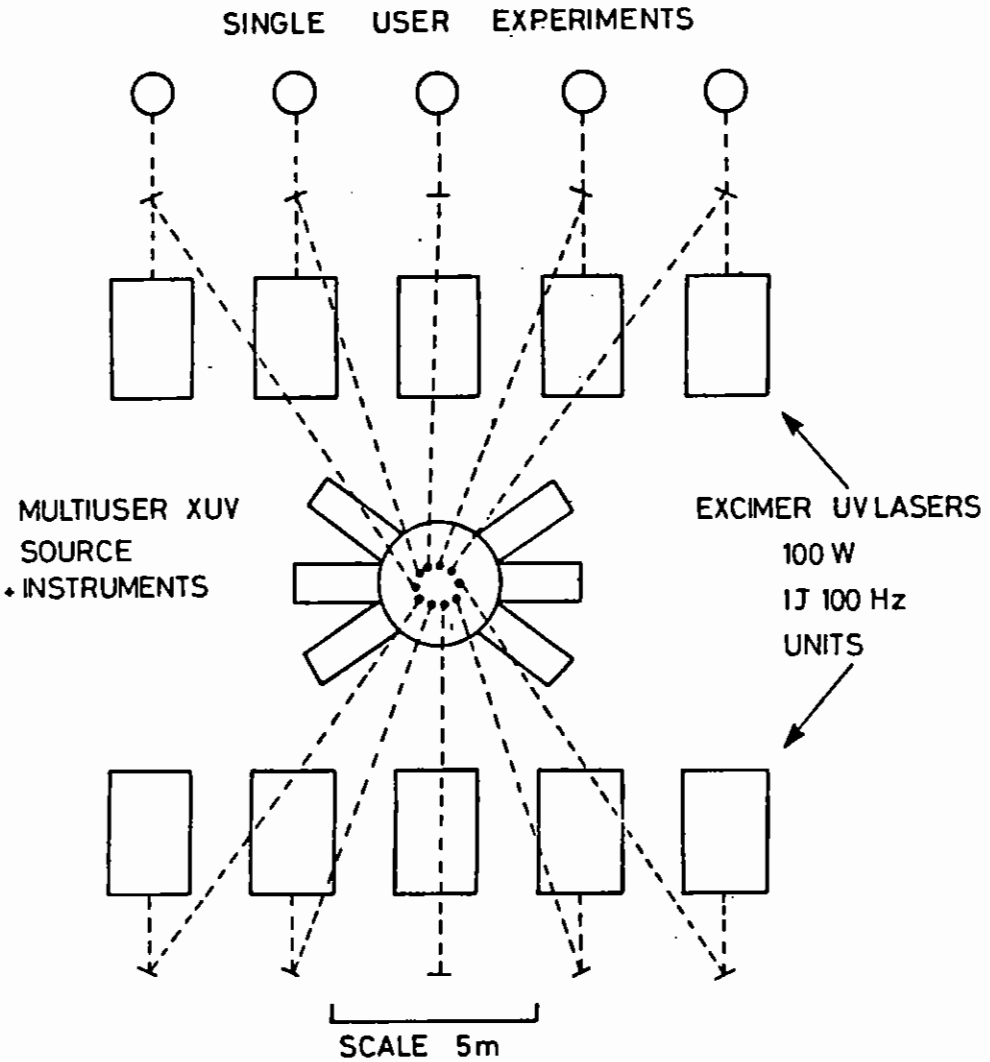

Fig C6.11 Conceptual layout of laser-plasma XUV facility based on 10 KrF laser modules.

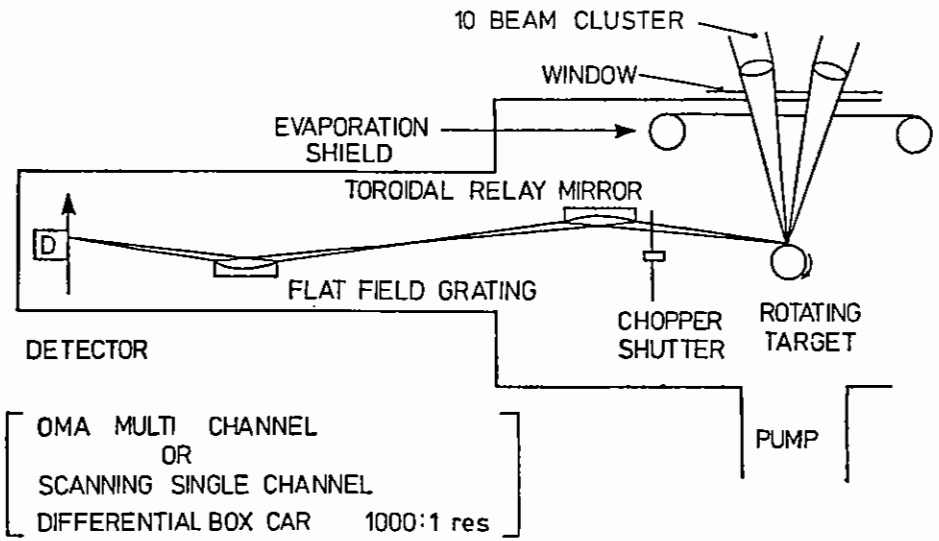

Fig C6.12 Conceptual design of monochromator beam-line for use on XUV facility shown in Fig C6.11.

power laser-plasma XUV source generated by ten independently triggered commercial KrF lasers. At present each laser module could operate at a power of 100 W and a repetition rate of 100 Hz. The operation of this system could be extremely flexible. For example the lasers could be sequentially triggered to give an effective power on target of 1 KW at 1 KHz repetition rate. Another possibility would be to synchronise all lasers in one 10J pulse on target which would generate a very suitable x-ray source for pulsed x-ray diffraction, EXAFS or x-ray microscopy applications as described in Section A4 of this report. Finally the lasers could be grouped into two pulses of 5J each with variable time spacing from nanoseconds to seconds to allow time resolved x-ray measurements of the "pump-and-probe" type.

The machine shown in figures C6.11 and C6.12 is very attractive since it uses commercial lasers already available. It is worth noting that much higher KrF laser powers will be available in the future because the gaseous laser medium lends itself to this type of development. It is expected that 1 - 10 KW lasers will eventually become available thus leading to the development of extremely powerful x-ray sources.

REFERENCES

C6.1 D J Nagel, C M Brown, M C Peckerar, M L Ginter, J A Robinson, T J McIlrath and P K Carroll, Appl Opt 23, 1428 (1984).

C6.2 P Gohil, H Kapoor, D Ma, M C Peckerar, T J McIlrath and M L Ginter, Appl Opt 24, 2024 (1985).

C6.3 Y Matsumoto, M J Shaw, F O'Neill, J P Partanen, M H Key, R Eason, I N Ross, E M Hodgson and Y Sakagami, Appl Phys Lett 46, 28 (1985).

C6.4 P D Gupta, R Popil, R Fedosejevs, A A Offenberger, D Salzmann and C E Capjack, Appl Phys Lett 48, 103 (1986).

C6.5 B Yaakobi, P Bourke, Y Conturie, J Delettrez, J M Forsyth, R D Frankel, L H Golman, R L McCrory, W Seka, J M Soures, A J Burek and R E Deslattes, Opt Commun 38, 196 (1981).

C6.6 D L Matthews, E M Campbell, N M Ceglio, G Hermes, R Kauffman, L Koppell, R Lee, K Manes, V Rupert, V W Slivinsky, R Turner and F Ze, J Appl Phys 54, 4260 (1983).

C6.7 R H Day, P Lee, E B Saloman and D J Nagel, J Appl Phys 52, 6975 (1981).

C6.8 R Kodama, K Okada, N Ikeda, M Minea, K A Tanaka, T Mochizuki and C Yamanaka, J Appl Phys (accepted for publication).

C6.9 F O'Neill, M C Gower, I C E Turcu and Y Owadano, Appl Opt 25, 464 (1986).

D CENTRAL LASER FACILITY PUBLICATIONS April 1985 - March 1986

D1 JOURNALS AND BOOKS

V Aboites, T P Hughes, E M Goldrick, S Sim, S Kartunnan, R G Evans
3/2 harmonic emission from thin foils
Phys Fluids, 28, 8 2555 (1985)

E J Austin, M Jaros
Electronic structure of an isolated GaAs-GaAlAs quantum well in a strong electric field
Phys Rev B 31, 5569 (1985)

E J Austin, M Jaros
Electric field-induced shifts and lifetimes in GaAS-GaAlAs quantum wells
Appl Phys Lett, 47, 274 (1985)

E J Austin, M Jaros
Electric field effects on electron-hold recombination lifetimes in GaAs-GaAlAs quantum wells
J Phys C, 18, L1091 (1985)

J R M Barr, J M Girkin, A I Ferguson, G P Barwood, P Gill, W R C Rowley, R C Thompson
Interferometric Frequency Measurements of $^{130}Te_2$ transitions at 486nm
Opt Comm, 54, 217 (1985)

J R M Barr, J M Girkin, J M Tolchard, A I Ferguson
Interferometric Measurement of the $1S_{\frac{1}{2}}$-$2S_{\frac{1}{2}}$ Transition Frequency in Atomic Hydrogen
Phys Rev Lett, 56, 580 (1986)

R A Beaman, A N Davies, A J Langley and W J Jones
Concentration modulated absorption spectroscopy II. Temporal variation of gain.
Chemical Physics, 101, 127 (1986)

J Bechara, D G Cunningham, D J Denvir, I T F Gillan, T Morrow and W D McGrath
UV Photodissociation of NOCl - stimulated processes and vibrationally inverted products
Optica Acta (1986) (in press)

J Bechara, T Morrow and W D McGrath
The Flash Photodissociation of Nitrosyl Chloride: Vibrational Energy-Transfer Processes
Chem Phys Lett, 122, 605 (1985)

A R Bell
Non-Spitzer heat flow in a steadily ablating laser produced plasma
Phys Fluids, 28, 2007 (1985)

T J M Boyd, G A Gardner and R Rankin
Finite Larmor radius effects in stimulated Raman scattering
Phys of Fluids, 28, 1193 (1985)

P C Cheng, R Feder, D M Shinozski, K H Tan, R W Eason, A Michette, R J Rosser
Soft X-ray contact microscopy
Nucl Instr and Methods in Phys Research (in press)

R Corbett, C Lewis, E Robertson, S Saadat, P Cunningham, A Cole, E Turcu, M Key and S Rose
Laser driven compression of CH shell targets and the effects of increasing aspect ratio
Lasers and Particle Beams (1986) (in press)

D G Cunningham, H F J Cormican, D J Denvir, I Duncan and T Morrow
Raman, collision-induced and weakly bound exciplex lasers in atomic thallium - noble-gas mixtures
Optica Acta (1986) (in press)

R W Eason, D K Bradley, J D Hares, P J Dobson
Laser-reflexafs: Reflection EXAFS spectra using a laser-produced plasma X-ray source
Appl Phys Letts, 47, 442 (1985)

R W Eason, P C Cheng, R Feder, A G Michette, R J Rosser, F O'Neill, Y Owadano, P T Rumsby, M J Shaw, I C E Turcu
Laser X-ray Microscopy
Optica Acta (1986) (in press)

R G Evans
Radiation cooling instabilities in laser driven ablation
Plasma Phys and Controlled Fusion, 27, 751 (1985)

R G Evans
Non uniform illumination of laser targets
Lasers and Particle Beams, 33, 273 (1985)

R G Evans
The Basic Physics of Laser Fusion
Canad J Phys (in press)

R G Evans
Laser Generation of Ultra High Pressure
Plasma Phys and Controlled Fusion, 28, 157 (1986)

M C Gower
Dynamic Holograms from Crystals
Nature, 316, 12 (1985)

J P Hardy
A Time-Resolved Resonance Raman Investigation of the Effect of Triyptophan-Modification on Photocycling Efficiency and Chromophore Conformation in Bacteriohodopain
in 'Time Resolved Raman Spectroscopy' Eds G Atkinson and D Phillips, Gordon and Breach (in press)

J P Hardy, P A Cox, G E Ewing and C J Simpson
EELS of methane physisorbed on NaCl (100)
J Elec Spect Related Phenomena (in press)

J P Hardy, R Stables, G E Ewing and C J Simpson
Thermodynamic measurements of adsorption of Xe and CO on NaCl (100)
Surface Science, 159, L474 (1985)

G Jolicard, E J Austin
Optical Potential Stabilisation Method for Predicting Resonance Levels
Chem Phys Lett, 121, 106 (1985)

M H Key
Highlights of laser fusion related research
Nuc Fus, 25, 1351 (1985)

M H Key
Laboratory Production of X-ray Lasers
Nature, 316, 314 (1985)

T H Kho
Relaxation of a system of charged particles
Phys Rev A, 32, 666 (1985)

A J Langley, R A Beaman, J Baron, A N Davies, W J Jones
Concentration-modulated absorption spectroscopy
Opt Letts, 10, 327 (1985)

A J Langley, R A Beaman, A N Davies and W J Jones
Concentration-modulated absorption spectroscopy I
Chem Phys, 101, 117 (1986)

J G Lunney
Soft X-ray laser action using resonant photo-excitation of autoionising states of lithium-like ions
Optics Comms, 53, 235

J G Lunney
Waveguiding in soft x-ray laser experiments
Appl Phys Letts, 48, 891 (1986)

J G Lunney, J D Hares, P Dobson, S D Tabatabaei, R W Eason
Time resolved X-ray diffraction from silicon during pulsed laser annealing
Appl Phys Letts (in press)

M T Macpherson, M J Pilling, M J C Smith
Determination of the absorption cross-section for CH_3 at 216.36nm and the absolute rate constant for methyl radical recombination over the temperature range 296-577K
J Phys Chem, 89, 2268 (1985)

A G Michette, P C Cheng, R W Eason, R Feder, F O'Neill, Y Owadano, R J Rosser, P T Rumsby, M J Shaw
Soft X-ray contact microscopy using laser-produced plasma sources
J Phys D, 19, 363 (1986)

F O'Neill, M Gower, I Turcu and Y Owadano
X-ray lithography using a KrF laser-plasma source
Appl Opt, 25, 464 (1986)

M J Pilling, M J C Smith
A laser flash photolysis study of the reaction $CH_3 + O_2 \rightarrow CH_3O_2$ at 298K
J Phys Chem, 89, 4713 (1985)

R Rankin and T J M Boyd
Kinetic Theory of Stimulated Raman Scttering from a Magnetised Plasma
Phys of Fluids, 28, 3380 (1985)

S J Rose
The calculation of line coincidences in helium-like ions using the multiconfiguation Dirac-Fock method
J Quant Spectrosc Radiat Transfer, 33, 603 (1985)

S J Rose
Some aspects of dense plasma physics
in 'Spectral Line Shapes' vol 3 ed F Rostas Walter de Gruyter Berlin (1985)

R Rosser, K G Baldwin, R Feder, D Bassett, A Cole, R Eason
Soft X-ray contact microscopy with nanosecond exposure times
J Microscopy 138, 311, (1985)

P T Rumsby
Laser produed plasmas as intense X-ray sources for microscopy at the CLF
J Microscopy 138, 245 (1985)

A M C Smout, R W Eason, M C Gower
Regular Oscillations and self-pulsating in self-pumped $BaTiO_3$
Optics Communications (in press)

P J Tonge, C W Wharton, R J Szawelski, P M Killough and R E Hester
Ultraviolet resonance Raman Spectroscopy of a highly specific acyl-papain
Biochem Soc Trans 13, 930 (1985)

P J Tonge, C W Wharton, R J Szawelski, P M Killough and R E Hester
Spectroscopy of Biological Molecules
Eds A J P Alix, L Bernard and M Manfait, Wiley and Sons, Chichester. UK, p 410-412 (1985)

J S Wark, J D Kilkenby, A J Cole, M H Key and P T Rumsby
Observations of the Rayleigh-Taylor instability on laser imploded microballoons
Appl Phys Lett 48, 969 (1986)

C W Wharton
Infra-red and Raman spectroscopic studies of enzyme structure and function
Biochem J 233, 25 (1986)

O Willi and P H Y Lee
Filamentation of an annular laser beam in a short wavelength laser produced plasma
Optics Comms 55, 120 (1985)

D2 PUBLISHED CONFERENCE PROCEEDINGS AND REPORTS

a) Published Conference Proceedings

E J Austin
Electric field effects on the electronic structure and spectra of GaAs-GaAlAs quantum wells
IOP Solid State Physcis Conf Reading 1985

C N Danson et al
The SERC beat-wave project
Proc 1st Int Topical Conf on Lasers in Science Dallas 1985 Ed W Stwalley (in press)

R G Evans
Efficiency factors in the beat wave accelerator
Proc 2nd Conf on lasers for particle acceleration
AIP Conf Proc no 82 Jan 1985

J M Giskin, J R M Barr, A I Ferguson, G P Barwood, P Gill, W R C Rowley and R C Thompson
Laser Spectroscopy VII, Eds T W Marsh and Y R Shen, Springer Verlag (1985)
Interferometric Frequency Measurements of $^{130}Te_2$ transitions in the region of Balmer β line of hydrogen and deuterium.

M C Gower
Excimer lasers in photolithography
Invited paper in Procs of the 2nd Int Conf on lasers in manufacturing Birmingham Ed M F Kimmitt (IFS Publication Ltd, 1985)

M Jaros et al
Hot carrier recombination in GaAs-GaAlAs quantum wells and superlattices
4th Int Conf on hot electrons in semiconductors Innsbruck 1985 Physia B 134 389 (1985)

F Kannari et al
A magnetic switch driven high voltage trigger generator
Proc V IEEE Pulsed Power Conf Washington DC 1985 (in press)

M H Key
Energy transport in laser produced plasmas
Proc XVII Int Conf in Phenomena in Ionised Gases, (in press) J Bakos Z Sorki Eds 1985

M H Key
Laser produced plasmas - the hottest topic in the Laboratory
Discourse at the Royal Institution Dec 1985 (in press)

S J Rose
The calculation of the opacity of hot dense plasmas
Procs 2nd Int Conf on the radiative properties of hot dense matter World Scientific (in press)

S J Rose
The calculation of the opacity of low-Z materials
Invited paper at 3rd Int Conf on the radiative properties of hot dense matter Williamsburg 1985

W T Toner et al
Fusion related experiments at the Central Laser Facility
Proc 12th European Condf on Contr Fusion and Plasma Physics, Budapest, 1985 (Plasma Physics and Controlled Fusion) (in press)

IOP 12th Annual Conf on Plasma Physics Glasgow 1985:

A R Bell, E M Epperlein
Smoothing and instability with magnetic fields in a non uniformly laser irradiated plasma target

P Choi et al
Collisionless shocks in laser produced plasma

Proc 29th Scottish Universities Summer School in Physics, St Andrews

SUSSP Publication, University of Edinburgh, (1985)

R G Evans
Plasma simulation using fluid and particle codes

M H Key
Compression and Hydrodynamics

M H Key
Introduction to the physics and applications of laser-produced plasmas

F O'Neill
Rare gas halide lasers

7th Int Workshop on laser interaction and related plasma phenomena, Monterey, California USA 1985

D Bassett et al
Rayleigh-Taylor; energy transport and implosion studies using the RAL 12-beam spherical target irradiation facility

M H Key et al
Generation and application of intense X-ray sources using KrF and Nd:glass lasers

S J Rose
The analysis of colliding shock experiments

S J Rose
Aspects of the atomic physics of X-ray lasers

22

b) Reports

C N Danson, C B Edwards and R W W Wyatt
The Vulcan pulse generating system.
RAL Report 84-124

R Bingham and W B Mori
Some non-linear processes relevant to the Beat Wave Accelerator,
RAL Report 85-105

D K Bradley, J Hares, A Rankin and S J Rose
The analysis of colliding shock experiments
RAL Report 85-020

S J Rose
The calculation of the opacity of Hot Dense Plasmas
RAL Report 85-022

R G Evans
The Basic Physics of Laser Fusion
RAL Report 85-060

R D Cowan, B C Fawcett, I P Grant and S J Rose
Classic Multiconfiguration-Dirac-Fock and
Hartree-Fock-Relativistic methods integrated into a programme package for the RAL IBM Mainframe with Automatic Comparative Output
RAL Report 85-098

A Ridgeley
A report on the Mapping of the DIDSY sensor responses as a function of micro meteorite impact positions on the Giotto bumper shield
RAL Report 85-108

F O'Neill
Rare gas halide lasers
RAL Report 85-116

R Bingham, R A Cairns, A E Dangor, R G Evans and C J McKinstrie
Saturation of Plasma Beat Waves by Collisional Dumping
RAL Report 86-030

D3 UNPUBLISHED CONFERENCE PROCEEDINGS

Proc 13th Int Conf on solid state nuclear track detectors Rome 1985

P M Evans, A P Fews, W T Toner
Energy loss of charged nuclear particles in hot plasma

P M Evans, A P Fews, W T Toner
Measurements of Rayleigh-Taylor instability in laser accelerated foils

17th European Conf on Laser Interaction with Matter (XVII ECLIM) Rome 1985:

J Corbett et al
Laser-driven compression of CH shell targets and the effect of increasing aspect ratio

R G Evans
Magnetic fields generated by the Rayleigh-Taylor Instability

M H Key et al
Initial experiments with a novel facility for X-ray laser research

G P Kiehn
Time resolved spectrograph for X-ray laser research

D J Nicholas
Numerical simulations of the filamentation instability

F O'Neill et al
X-ray generation using KrF laser irradiation of carbon targets

Conf on Lasers and Electrooptics, Baltimore, USA, 1985

C N Danson et al
The use of the Vulcan high power laser facility for the generation and diagnosis of beat-waves in a low density plasma

M C Gower
High resolution photolithographic image projection using a self-pumped $BaTiO_3$ phase conjugate mirror

F O'Neill et al
Laser plasma studies using ahigh power 249 nm KrF laser

M J Shaw et al
A high power KrF laser pumped Raman amplifier

Seventh Nat Quantum Electr Conf Malvern UK: IOP (Sept 1985)

J B M Barr, J M Girkin, J M Tolchard and A I Ferguson
Generation of intense narrow band 243 nm radiation and its application to two photon Dappler free spectroscopy of the hydrogen 1s-2s transition.

J Bechara, I T F Gillan, D J Denvir, T Morrow and W D McGrath
UV photodissociation of NOCl - stimulated processes in vibrationally inverted products.

D G Cunningham, H F J Cormican, I Duncan and T Morrow
Raman and collisional-induced lasers

C N Danson, C B Edwards, R W W Wyatt
The use of the Vulcan high power laser facility for the generation and diagnosis of beat-waves in a low density plasma

G M Davis, M C Gower
Experimental study of the dependence of the phase conjugate properties of stimulated Brillouin scattering (SBS) as a function

of laser coherence length

R W Eason, P C Cheng, R Feder, A Michette, R J Rosser, F O'Neill, Y Owadano, P Rumsby and M Shaw
Laser X-ray microscopy

R W Eason, A C Smout and M C Gower
Oscillatory behaviour and regular self-pulsing in self-pumped photorefractive Barium Titanate

R W Eason, D K Bradley, J D Hares, A J Rankin, S D Tabatabaei
Laser-reflEXAFS, and its applications to surface studies

M J Shaw
High power Raman amplifiers

PART II

PART II THE APPLICATION OF UV LASERS TO MICROCIRCUIT FABRICATION

PART II THE APPLICATION OF UV LASERS TO MICROCIRCUIT FABRICATION

1. Introduction

P T Rumsby (RAL)

This part of the Laser Division Annual report covers the work carried out by Laser Division staff on topics related to the laboratory project on the 'Application of UV lasers to microcircuit fabrication'.

This project is equally funded by the Engineering Board of the SERC and the Department of Trade and Industry and is aimed at determining what impact high power UV excimer lasers can make on the lithography of microcircuits. The project has been operating since November 1983 and involves a collaborative effort between the Laser and Technology Divisions at RAL. Only the Laser Division Work is reported here.

The aim of the programme is to develop new lensless methods for performing high resolution, high throughput lithography using a variety of novel imaging systems based on lapsed or real time holography (or phase conjugation). Brief preliminary details of some of the projects started were presented in last year's report and considerable progress has been made during the year on these and other new ideas. However because the main objective of the project is to pass the results of the research to UK companies for exploitation and as much of the work is at present subject to patent action no additional details of this work are presented here.

During the year basic research has been carried out on photorefraction in different materials. Section 2 reports details of work performed on self pumped phase conjugate emission from $BaTiO_3$ in the visible region which attempts to understand better the mechanisms leading to phase conjugate emission in this material. Section 3 gives preliminary details of a programme that has been started to investigate degeneration four wave mixing by photorefraction in the near IR in the important III-V materials.

UV laser photoablation studies have continued in an attempt to understand better the mechanisms leading to ablative decomposition of polymers. Ablation studies carried out using the simple polymer polyacetylene are given in Section 4a while Section 4b gives details of time resolved studies of the ablation of PMMA films.

Where wet development is carried out the exposure behaviour of resists at fluences up to that required for ablation is of major importance since exposure times can be dramatically reduced by using UV lasers rather than lamps so long as reciprocity failure is not severe. Work performed to understand the intensity dependent photochemical changes that occur in resists which could lead to reciprocity failure is reported in Section 5.

Finally in Section 6 we report some preliminary results of work that has been started to use excimer lasers to generate X-rays which are used for proximity lithography. It is hoped that this programme will lead to the development of a laser based quasi CW X-ray source that is much brighter than an electron beam source and considerably smaller and cheaper than a synchrotron source.

2. Physics of self-pumped phase conjugate emission from $BaTiO_3$ crystals

(a) Regular oscillations and self-pulsating in self-pumped $BaTiO_3$

A M C Smout, R W Eason (University of Essex)
M C Gower (RAL)

Introduction

Of the various photorefractive crystals currently available, perhaps the most interesting is $BaTiO_3$, which because of its very large electro-optic coefficients allows highly efficient two beam coupling to occur (1,2), and phase conjugate mirrors (PCMs) exhibiting gains of 10^4% have been constructed using this material (2). One of the most

important appliations of $BaTiO_3$ is as a self-pumped phase conjugate mirror (SPPCM) (3). In this configuration, no external components other than the $BaTiO_3$ crystal are required to produce a phase conjugate (PC) replica of an input beam, and no external pumping of the crystal is needed.

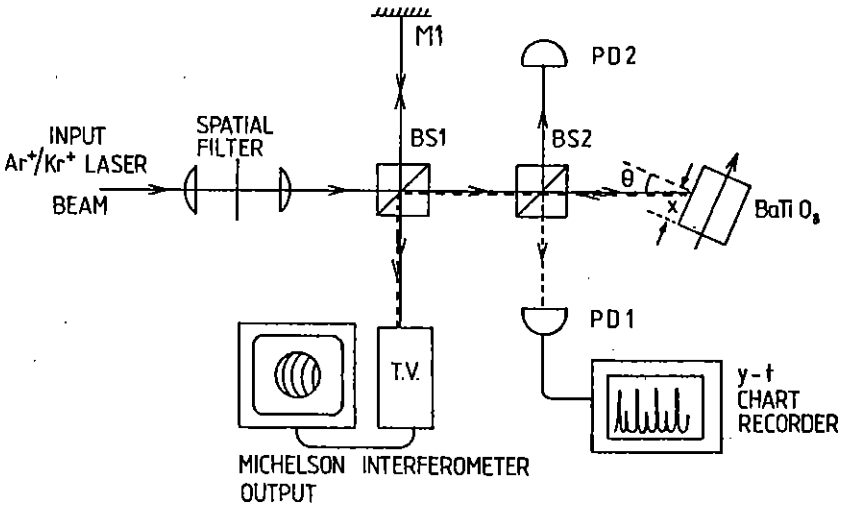

Fig 1 Experimental set-up.

We report here on a configuration for self-pumping in which the reflectivity, and hence the intensity of the PC output beam, is seen to undergo regular self-pulsating. Both the period and character of these pulsations are seen to be dependent on the transverse position and angle of incidence of the input beam with respect to the crystal. The pulsations are accompanied by transient frequency shifts between the incident and PC beams of ± a few Hz.

The experimental arrangement used to observe the self-pulsating is shown in Fig 1. The laser sources used in this work were a Coherent Radiation model CR500K Kr^+ laser, operating in multi-longitudinal mode at power levels of up to ~ 100mW, and a single mode Innova model 90-5 Ar^+ laser which gave powers up to 1W. The pulsations have been observed using all the lines available from λ = 454 to 560nm.

The observations used two different $BaTiO_3$ crystals (from the same original boule). The dimensions of both crystals are approximately 5 x 5 x $5mm^3$. Each crystal had been electrically poled into a single ferromagnetic domain prior to the experiments. The crystal was mounted on a stand allowing controlled rotation and horizontal displacement so that the effect of beam input position (x) and angle (θ) could be determined. Maximum steady state reflectivity was found to be 37% at 40°, uncorrected for Fresnel losses. The incident beam was polarised so as to be an extraordinary ray.

The first beamsplitter BS1 in Fig 1 forms part of a Michelson interferometer, with the mirror M1 as one arm, and the $BaTiO_3$ sample the other. Neutral density (ND) filters are used to correct for the lower intensity of the output from the SPPCM arm. The two beams are adjusted to yield a slight angular mismatch resulting in a linear interference fringe pattern, which is viewed by a TV camera. Any frequency shift between the two beams therefore becomes apparent by the lateral motion of the fringe pattern.

The second beamsplitter BS2 allows the intensity of the PC output wave and the incident wave to be measured simultaneously by photodiodes PD1 and PD2, the outputs from which are connected to a Y/t chart recorder to enable time dependent characteristics to be measured. PD1 is also interfaced to a computer to facilitate the measurement of the period of large numbers of pulsations, and hence calculate mean and standard deviation values.

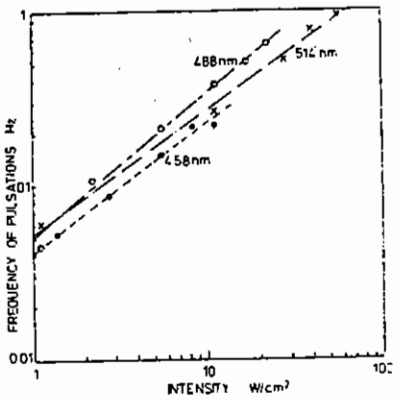

Fig 2 Log-log plot of intensity vs. frequency of pulsation for $BaTiO_3$ driven by the Ar^+ ion laser. The best fit straight line has slope ~ 0.8.

With the apparatus arranged as in Fig 1 and the crystal orientated so that $\theta \sim 5°$ and $x \sim 1mm$, the output at PD1 was seen to behave in a periodic or self-pulsating manner the period of which was dependent on the laser intensity. A log-log plot of the intensity dependance of the period of pulsation is shown in Fig 2, and the slope of the best fit line shown in ~ 0.8. These pulsations were accompanied by the appearance of a new corner cube reflection mechanism as shown in Fig 3(a): an extra pair of beams were seen to make a critical angle reflection of ~ 25° ($n_e = 2.424$) off the exit face of the crystal, subsequently achieving a corner cube reflection in the top left hand corner of the crystal. Fig 3 also shows the sequence of formation of these beams:

3(b) Initially the PC output is zero, and no self-pumping is evident.

3(c) The SPPCM starts to build up, with the left hand corner cube reflection starting fractionally before the usual right hand one.

3(d) At the maximum reflectivity of the pulsation, both self-pumped channels are operating simultaneously.

3(e) The PC output fades rapidly, along with the internal beams, and the crystal returns to its initial state.

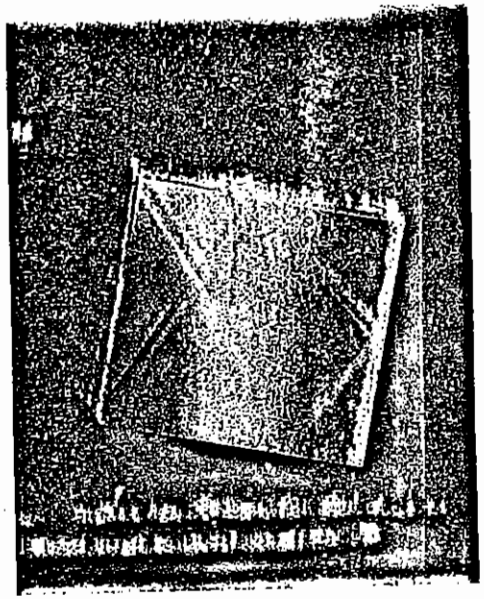

Fig 3(a) Photograph showing the internal beam interaction geometry. Note the additional corner cube reflection resulting from a critical angle reflection at the output face of the crystal.

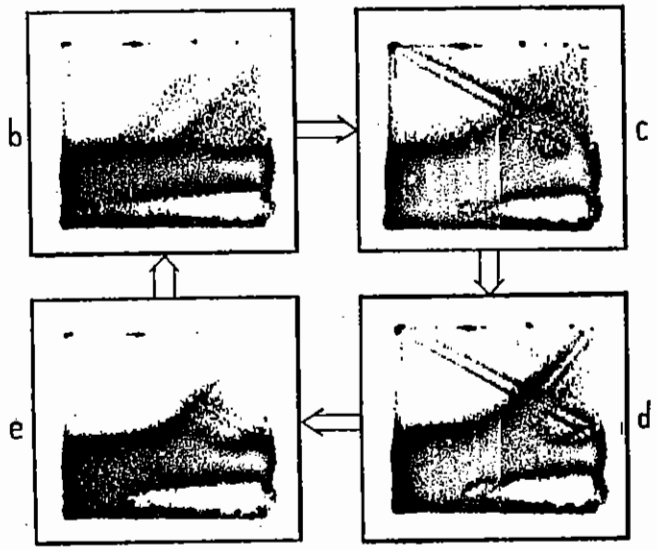

Fig 3(b-e) Sequence of four photographs showing the evolution of the internal beams during a pulsation (exposure time ~ .5s per frame, total pulsation during ~ 15s).

The character and period of these self-pulsations was markedly dependant on the transverse position (x) on the crystal of the incident gaussian beam. Fig 4 shows the wide range of pulsation characteristics

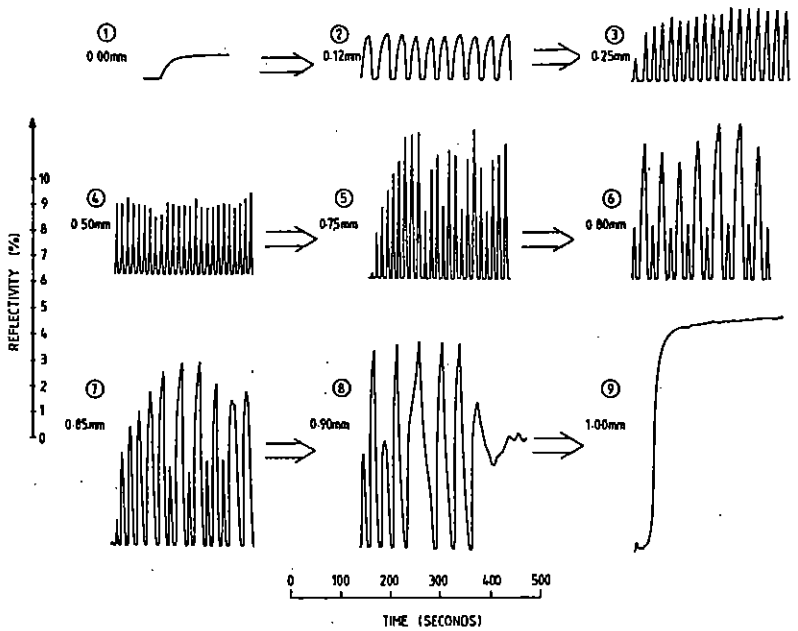

Fig 4 Diagram showing the variation in pulsating behaviour of the PC output as the displacement (x) of the incident beam is altered θ = 5 deg.

observed over ~ 1mm range of x. At x = 0 mm the beam (diameter ~ 1.5 mm) was positioned so as to lie almost entirely within the crystal, grazing the bottom edge, and all subsequent values of x were measured relative to this position. A steady state reflectivity of a fairly low value (~ 1%) was observed at x = 0 mm, but on translating the beam further towards the centre of the crystal, self-pulsating behaviour was seen, the period of which became shorter and more regular until a maximum value was reached at x ~ .5mm. Beyond this point the period started to become less well defined until at x ~ .8 mm alternate amplitude behaviour was observed, a state that appeared to be stable,

lasting for at least an hour. At x ~ .9 mm chaotic behaviour resulted, and further increases in x caused a return to a steady state reflectivity, but at a higher level (~ 10%) and with this left hand corner cube reflection no longer present. Note that at values of x > .95 mm it became geometrically impossible to achieve a critical angle reflection that would intercept the top left hand corner, given the physical dimensions of the crystal with which these readings were taken.

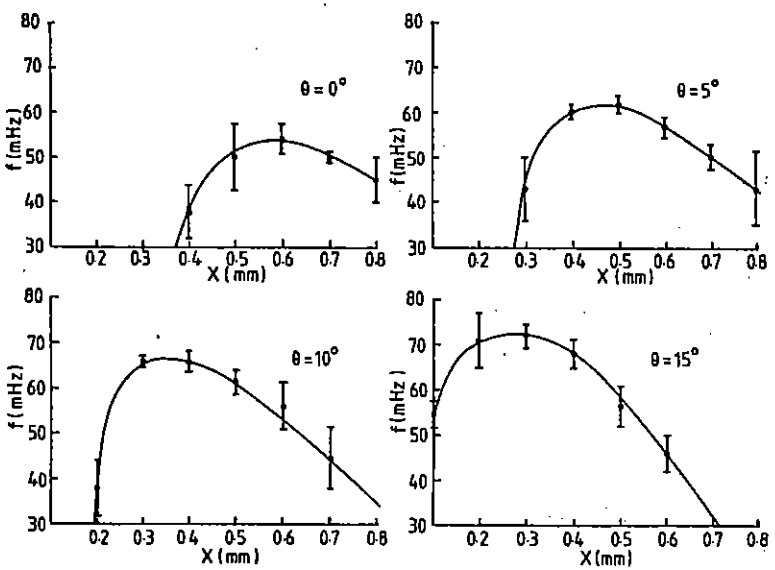

Fig 5 Plot of pulsation frequency vs. crystal orientation. The error bars represent the standard deviation in the point taken over ~ 100 measurements of individual pulsation periods.

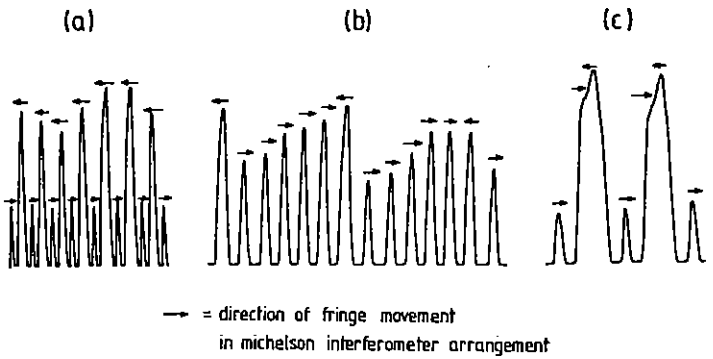

Fig 6(a) Diagram showing the direction of fringe movement in the Michelson interferometer during representative sequences of pulsations. Note that in the alternate amplitude case, the direction of fringe motion alternates also.

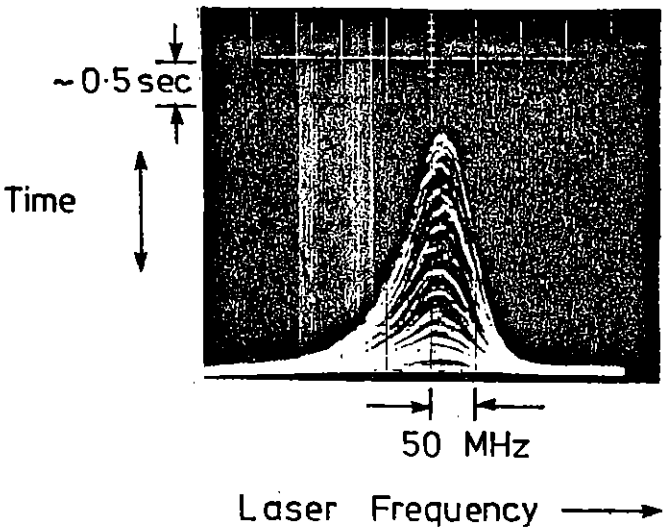

Fig 6(b) Output of scanning Fabry-Perot interferometer analysing the frequency of the PC output during a pulsation period. Note that there is no evidence of mode hopping. The source used was an Ar^+ laser operating in single longitudinal and transverse modes.

Fig. 5 shows the frequency of pulsation as a function of x for various values of θ, with the error bars representing the standard deviation of the mean value for ~ 100 peaks. For $\theta > 40^0$ the critical angle reflection was again impossible, and no pulsating behaviour could be observed over the whole range of x values.

When the Michelson interferometer was used, the following effects were observed. For steady state reflectivity conditions, a static fringe pattern was seen, in contrast to the observation (4). During the self-pulsating behaviour, as the reflectivity increased from zero a static fringe system was again observed building up in intensity as the reflectivity reached its peak. As the reflectivity dropped however, the fringes were seen to begin to move laterally to the left or right, indicating a frequency shift of ± a few Hz. The direction of the fringe movement, and thus the sign of the frequency shift, was not random, but followed a set pattern for most of the modes of pulsation shown in Fig. 4. An example of this is shown in Fig. 6(a).

One possible explanation for this pulsating behaviour might be due to feedback from the $BaTiO_3$ crystal to the laser resonator, causing changes in the longitudinal mode structure as observed (5). This would result in the grating inside the crystal being erased and a new one formed appropriate to the new laser frequency, and hence the PC reflectivity would appear to pulsate. Although it is not clear what effect this would have on a multi longitudinal mode laser, a scanning Fabry-Perot interferometer was used with the TEM_{00} single longitudinal mode Ar^+ laser to examine the PC output. Fig 6(b) shows the pulsating PC output recorded by numerous scans of the interferometer during a single pulsation. It can be seen that single mode operation was not perturbed and that mode-hopping, reported (5), did not take place. Indeed, no hopping or sweeping of modes was seen during the course of thousands of pulsations (the longitudinal mode spacing of the laser was 132MHz and as seen from Fig 6(b) any shift in frequency of the PC beam during a pulsation was < 10 MHz).

It is instructive to make a comparison between the behaviour seen here and that reported in (4). The pulsations we observed were not sinusoidal, and were stable for several hours without need for the enhanced feedback technique described (4)(painting the crystal c-faces with Tippex). Another difference is that during stable pulsing the authors of (4) reported a continuously moving fringe pattern, i.e. a constant frequency shift between the phase conjugate and incident beams, whereas we have always observed a transient shift. While this constant frequency offset has been observed by several authors (6, 7) for a SPPCM operating in a steady state, the difference between the results here and those reported in (4) might suggest that a different mechanism is responsible for the two observed effects. Also, we have observed novel pulsating behaviour where successive peaks have alternating amplitudes (Fig 4), a state which is stable for over an hour (the longest period of measurement).

Although we have been unable to reproduce the results of (4) for our $BaTiO_3$ crystals in air, we have also carried out experiments with the crystal immersed in an index matching fluid (of refractive index 1.42), and have observed an effect we believe to be similar to one described in Reference 4, namely sinusoidal oscillations leading to period doubling and chaos after several minutes. However the oscillations observed using an index matching fluid appear as a maximum perturbation of ~ 20% on the PC output, which never extinguishes completely, unlike the pulsing behaviour we have described previously.

Pulsations could be produced by the beating between different PC beams arising from DFWM and stimulated scattering. However, we do not believe this to be the case since during the dark periods of the pulsations no filamentary structure, usually a prerequisite for self-pumped PC emission, is observed in the crystal. For beating to occur between two waves, both waves must be present at all times, which appears not to be the case. Furthermore, stimulated scattering theories cannot predict the positive frequency shifts observed here (at $I \sim 5W/cm^2$ then Lam (8) predicts a shift of ~ -4Hz, while Chang and Hellwarth (9) predict a shift of < -0.05Hz).

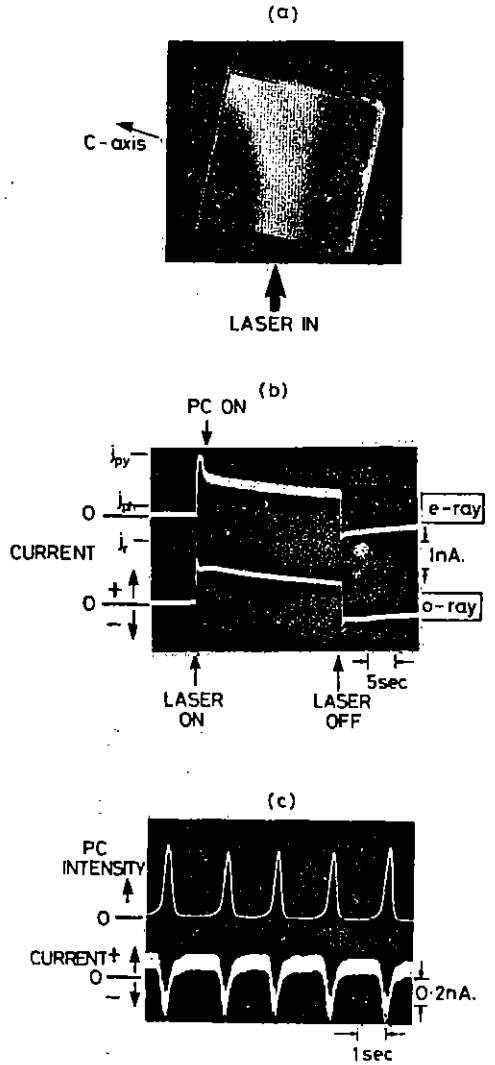

Fig 7(a) Photograph of self-pumped $BaTiO_3$ crystal showing internal beams.

Fig 7(b) Short circuit current observed when the e and o-polarised laser beam is blocked and unblocked. j_{py}, j_{ph} and j_R are the pyroelectric, photovoltaic and reverse (pyroelectric) current densities, respectively.

Fig 7(c) Spontaneous pulsations of PC emission and short circuit pyroelectric current observed when the pump beam enters the crystal on the RHS of centre.

One explanation for this pulsating behaviour is discussed in (10) and in the next section. It might be that there is an additional stationary fringe pattern set up between the PC and pump beams or the second set of beams (see Figs 3b-e) which make a transient corner cube reflection. Charge migration can then occur from one set of gratings to the next and if there is insufficient time to rewrite the original gratings, then a reduction in P.C. emission will occur and the whole process collapse. Emission could then build up again and the cycle repeat itself.

In conclusion then we have observed spontaneous pulsating of the PC emission arising from self-pumped $BaTiO_3$ crystals. Further work is in progress to try to clearly identify the mechanism responsible.

(b) Photoinduced voltages and frequency shifts in a self-pumped phase conjugating $BaTiO_3$ crystal.

M C Gower (RAL)

Phase conjugate mirrors (PCM's) which employ the photorefractive effect in single domain crystals of barium titanate (1-3) are currently of great interest. However, the detailed mechanisms of photorefraction in $BaTiO_3$ which cause effects such as the ~1Hz frequency shift in the self-pumped phase conjugate emission (6,7), are still not fully understood. Here we report measurements on intrinsic and photoinduced voltages which arise in such self-pumped crystals.

A 5.5 mm cube poled single domain crystal of $BaTiO_3$ was pumped in the self-pumping configuration shown in Fig 7(a) using a multimode 1W CW Ar^+ laser at 488 nm. Voltage and current measurements along the c-axis of the crystal were made using silver paint electrodes and appropriate meters. Since the resistivity of our $BaTiO_3$ crystal was found to be $\sim 7 \times 10^{11}\Omega$-cm, an oscilloscope (Tektronix model 5113 dual beam storage with a 5A22N differential amplifier) or a voltmeter (Keithley 155 Null microvoltmeter) which had input impedances < 100 MΩ, were used to make short circuit measurements. The crystal was then found to behave as though a source of constant current. On the other hand, open circuit voltage measurements were made using a Keithley 620C

electrometer which had an internal impedance $> 10^{14}\Omega$. The temperature of the crystal could be controlled by suspending it in silicon oil and heating the container. With the 1.5 mm diameter laser beam entering the crystal, the induced short circuit currents shown in Fig 7(b) were observed for pump beam polarisations in the same (e-ray) and orthogonal (o-ray) planes to the c-axis of the crystal. Unblocking of the laser causes a current to flow in the positive c-axis direction with a rise time of ~ 200 μsec as determined by the capacitance of the crystal (~ 20pF) and its associated circuit. This current then slowly decreases by an order of magnitude to a steady state value. In the case of an e-ray pump wave there is a rapid decrease of ~ 30% when the phase conjugate emission builds up to a value comparable to the pump intensity. This self-pumped emission, not observed for an o-ray pump wave, is accompanied by the familiar beam fanning and corner cube reflection (3) shown in Fig 7(a). Other beams which develop by two-beam coupling are also shown in this photograph. Blocking the laser beam causes the current to rapidly reverse to a magnitude similar to that which it had when the laser was unblocked. Similar time variations of the open circuit voltage across the crystal were observed with peak values reaching 100V. Photoinduced currents with similar characteristics were first noticed in $BaTiO_3$ 30 years ago (11) in a study of the pyroelectric effect.

The pyroelectric current density, j_{py}, arises from a change in the polarisation, P, of a crystal of thickness d due to a change in its temperature, T, and is zero in thermal equilibrium (11):

$$j_{py} = \frac{dP}{dt} = \left(\frac{dP}{dT}_T\right)\frac{dT}{dt} \simeq \frac{\alpha}{\rho_0 C_p}\left(\frac{dP}{dT}_T\right) I \qquad (1)$$

for small αd, where I, α, ρ_0, and C_p are the laser intensity, absorption coefficient, density, and specific heat of $BaTiO_3$, respectively.

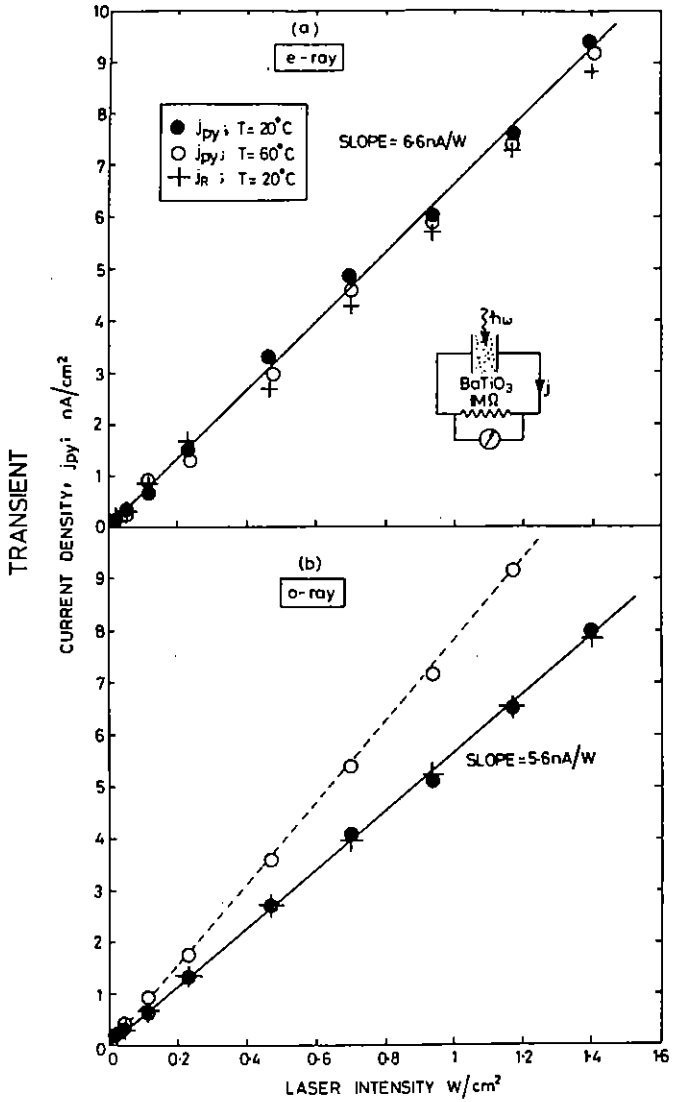

Fig 8 Intensity dependence of the short circuit transient pyroelectric current densities when unblocking, j_{py}, and blocking j_R, the laser for both (a) e-polarised and (b) o-polarised light. Measurements of j_{py} are also shown for a crystal temperature of 60°C.

Using an expanded laser beam of 7 mm diameter to fill the entrance face of the crystal, in Fig 8 we show measurements of the linear relationship between the transient short circuit pyroelectric current density and the laser intensity for both e and o-ray polarisations of the incident beam. The slopes measured in this figure agree well with values estimated using Eq(1) with ρ_0=6 gm/cm^3, C_p = 0.5J/gm/^{0}C and $\left(\frac{dP}{dT}\right)_{20^0C}$ = 2 x 10^{-8} coulomb/cm^2/^{0}C (11) and measured values of α^e = 1.2 cm^{-1} and α^0 = 2.0 cm^{-1}. Since the decay times of the currents during light and dark phases are similar (~ 30 sec) and insensitive to the laser intensity, we concur with Chynoweth (11) that crystal cooling, rather than space charge build up, is responsible for the equal and opposite current observed when the laser is blocked. From Figs 8(a) and 7(b), we see that when the e-ray pump is being depleted by PC emission the crystal appears to equilibrate at slightly lower temperatures. $\left(\frac{dP}{dT}\right)_T$ in Eq (1) is a function of temperature, and going from 20^{0}C to 60^{0}C should double the pyroelectric current (11).

Although as shown in Fig 8(b), with the crystal at 60^{0}C a 35% increase in initial current was observed for the o-polarisation, somewhat suprisingly no increase was observed for e-polarised light.

In Fig 9 we show measurements of the steady-state short circuit currents and open circuit voltages. Such steady state currents are due to an intrinsic photovoltaic voltage in the crystal caused by a local charge assymmetry of the lattice at the acceptor and trapping sites (12-14) of the holes responsible for charge migration in $BaTiO_3$. To our knowledge, photovoltaic fields have not been observed before in $BaTiO_3$ except at temperatures above the Curie temperature of ~ 130^{0}C (12). The short circuit photovoltaic current density is given by:

$$j_{ph} = \frac{eL_{ph}}{\hbar\omega}\alpha I = pI \qquad (2)$$

where L_{ph} is a mean effective drift length along the polar axis of the

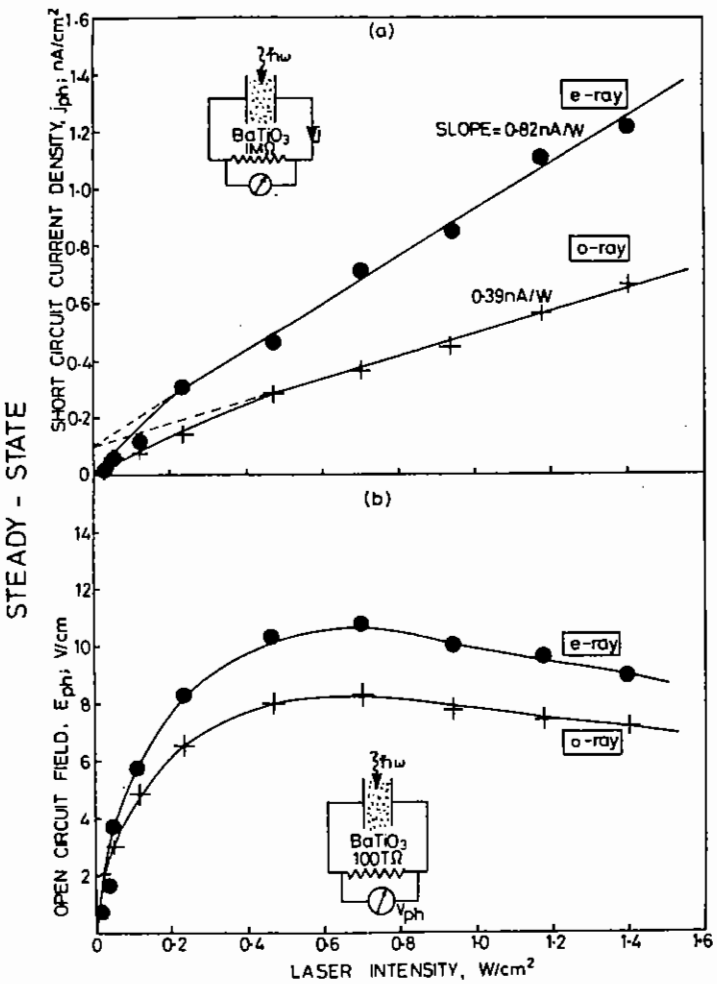

Fig 9 Intensity dependence of the steady-state (a) short circuit photovoltaic current density and (b) the open circuit photovoltaic field for both e and o-polarised pump beams measured 10 mins after unblocking the laser.

holes in the valence band. From the slopes of the graphs in Fig 9(a) the photovoltaic constants for each polarisation were p^e = 0.82nA/W and p^0 = 0.39nA/W which are about an order of magnitude smaller than values measured in iron doped $LiNbO_3$ (13).

The open circuit steady-state voltage is given by the photovoltaic field (15):

$$E_{ph} = \frac{p\,I}{\sigma} \qquad (3)$$

where the total conductivity, σ, is the sum of the dark and photoconductivities, $(\sigma_d + \sigma_p)$. Hence for intensities such that $\sigma_p \gg \sigma_d$, E_{ph} saturates and we obtain:

$$\sigma_p \simeq \frac{pI}{E_{ph}^{sat}} \qquad (4)$$

From Fig 9(b) the photovoltaic saturated fields E_{ph}^{sat} = 10V/cm and 8V/cm, which are four orders or magnitude smaller than in $LiNbO_3$ (13). Eq (4) gives values of $\sigma_p^e = 0.82 \times 10^{-10} I$ and $\sigma_p^o = 0.49 \times 10^{-10} I(\Omega\text{-cm})^{-1}$ when I is in W/cm². Although the presence of an intrinsic photovoltaic field in $BaTiO_3$ will produce a phase shift, ϕ_g, between the light interference pattern and the recorded refractive index hologram which is not 90^0, for the small fields measured this variation would only be noticeably at extremely small beam crossing angles, θ, - for example with $\theta = 1^0$ and a trap density of $6 \times 10^{16}\,cm^{-3}$, we estimate (15) $\phi_g \simeq 86^0$.

The conductivity was also obtained by connecting a 74V battery across the crystal and measuring the current in the circuit. These conductivity measurements are shown in Fig 10(a) and can be summarised by $\sigma_d = 1.5 \times 10^{-12}(\Omega\text{-cm})^{-1}$ and $\sigma_p^e = 1.2 \times 10^{-10} I$; $\sigma_p^o = 0.82 \times 10^{-10} I(\Omega\text{-cm})^{-1}$. These values for σ_p are in good agreement with the saturated photovoltaic field measurements.

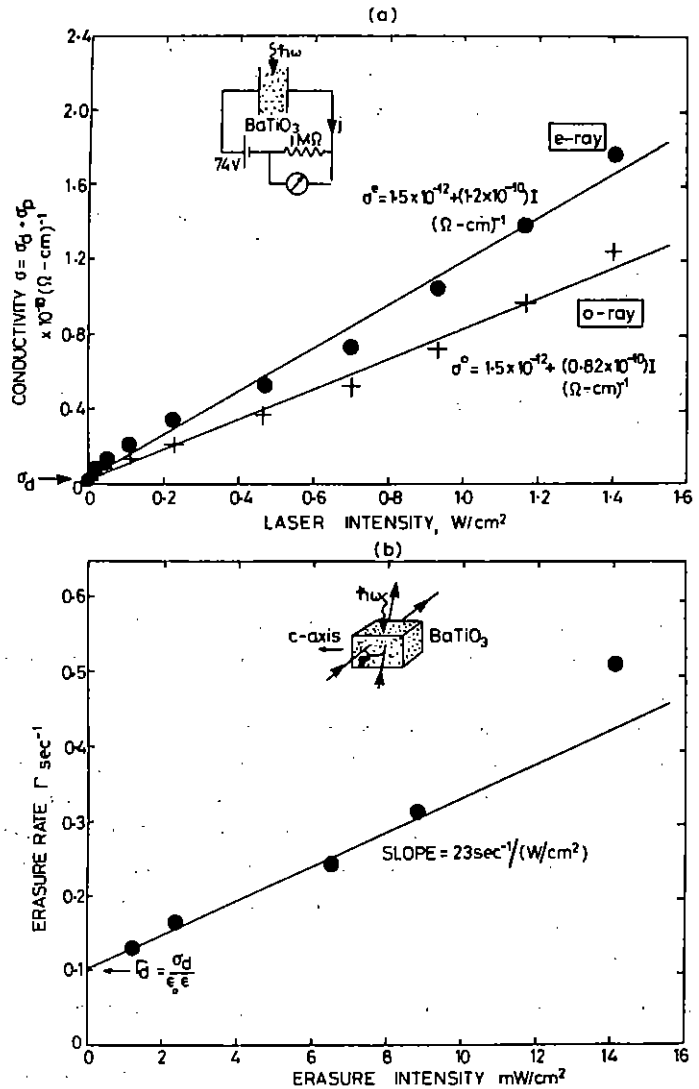

Fig 10(a) Crystal conductivity obtained from resistivity measurements versus laser intensity for e and o-polarised light.

Fig 10(b) Decay rate of two-beam coupling versus erasure light intensity for a crossing angle θ=90. The intensities of the intersecting beams were ~ 1.2 mW/cm².

PULSATIONS AND GRATING MOVEMENT

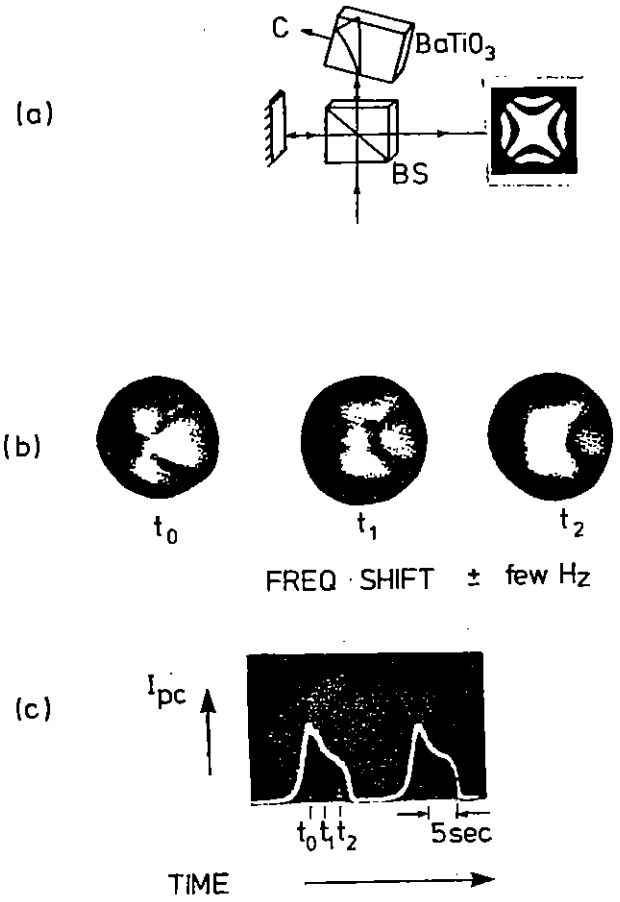

Fig 11 Interference fringes produced by interference of the pump and PC beams produced by the set-up shown in (a). The fringes are similar to those produced by a astigmatic lens and begin to move out of or into the centre at the peak of the pulsation as shown in (b) and (c).

A third method used to estimate the conductivity was by measuring the photoerasure rate of gratings stored in the crystal (2, 16). Two relatively weak e-polarised beams were arranged so as to intersect in the crystal transverse to the c-axis. The decay rate, Γ, of two-beam coupling was measured as one of the incident beams was blocked. The results are shown in Fig 10(b) as the irradiance of a more intense uniform erasure beam entering the crystal from above is increased. From the intercept of this graph and using the relationship:

$$\sigma_d = \varepsilon_o \varepsilon \Gamma_d \qquad (5)$$

where the dielectric constant (1), $\varepsilon = 168$, we find $\sigma_d = 1.5 \times 10^{-12} (\Omega\text{-cm})^{-1}$.

By varying the crossing angle and measuring the slopes of graphs similar to Fig 10(b), the photoconductivity can be estimated (2, 16) from the intercept of a graph of slope vs $\sin^2 (\theta/2)$. This method gives a value

$$\sigma_p^e \sim 3 \times 10^{-10} \; I \; (\Omega\text{-cm})^{-1}$$

which, considering that the grating decay rate is known to have a nonlinear dependence on erasure intensity (16), can be regarded as remarkably good agreement with the saturated photovoltaic field and resistivity measurements.

When the (unexpanded) pump beam enters the crystal to the right of centre of the face shown in Fig 7(a), then the PC emission and open circuit pyroelectric current undergo spontaneous regular pulsations (17) (see Section 2 above) as shown in Fig 7(c). By interfering the PC beam with the pump beam and observing the fringes produced (see Fig 11(a)), the holographic grating was found to be stationary until the peak of each pulsation. As shown in Fig 11(b), at the peak the fringes (similar to those produced by an astigmatic lens) began to move and accelerate creating either positive or negative frequency shifts of a few Hz to the PC beam. Trapped charge carriers are unlikely to become untrapped by the photoinduced fields measured in this work. Indeed, the pulsation and fringe characteristics were unaffected when comparable fields were applied externally to the crystal. Since the

grating is observed to begin to move at the time of maximium PC emission, the movement causing the pulsations may possibly be induced by the stationary fringe pattern in the crystal set up between the interference of the pump and PC beams. When the PC beam and pump intensities become comparable then these fringes reach a maximum modulation and may then cause charge migration away from the gratings produced by self-pumped four-wave mixing processes. If the gratings cannot be rewritten sufficiently rapidly then this movement would then lead to a reduction in the PC emission which in turn would reduce the intensity of the interference fringes. The process could then repeat itself. In contrast to the work reported (6 and 7), very little fringe movement or frequency shift ($< 10^{-2}$Hz) was observed for steady-state PC emission (pump entering the middle or LHS, of the face shown in Fig 7(a)). Such small shifts as were observed probably arose from thermal instabilities to our interferometric setup since they were of a similar magnitude when the PCM was substituted by a conventional mirror.

3. Degenerate four-wave mixing at 1.0 μm by photorefraction in GaAs crystals

P Hribek (Czech Technical University of Prague) and M C Gower (RAL)

GaAs and other III-V materials show great promise for a number of non-linear optical applications in optical data processing at wavelengths in the near infra-red, especially for these which demand a high speed of response and sensitivity of the material. Degenerate four-wave mixing at 1.06μm has recently been observed using photorefractive processes in GaAs by Glass et al (18) and Klein(19).

Crystals of GaAs are noncentrosymmetric cubic with a single non-vanishing electro-optic tensor component $r_{41} = 1.43$pm/V. They are characterised by a large electron mobility ($\sim 5.8 \times 10^3 \text{cm}^2/\text{V.sec}$). Using the set-up shown in Fig 12 we have made grating efficiency

GRATING EFFICIENCY MEASUREMENT

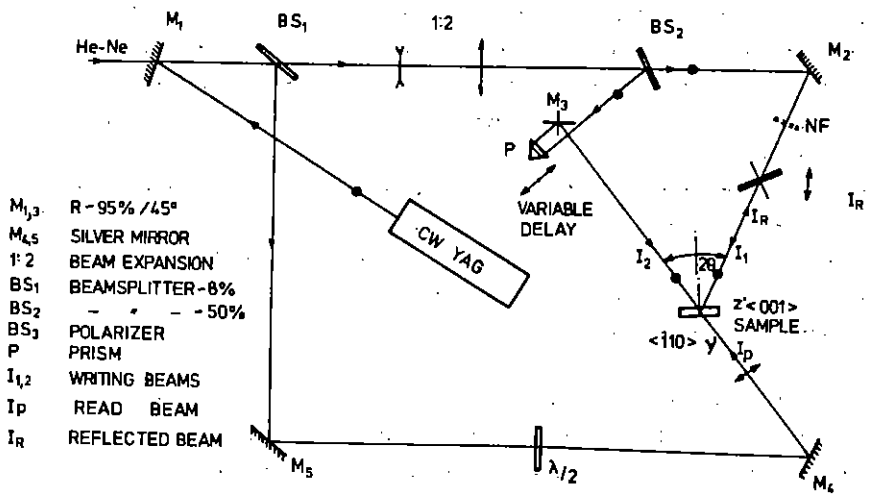

Fig 12 Experimental geometry for diffraction efficiency measurements in GaAs.

measurements using a CW Nd:YAG laser at 1.06μm. The grating diffraction efficiency, η, is defined (see Fig 13) as:

$$\eta = I_4/I_3 = \frac{\text{diffracted wave}}{\text{undiffracted background wave}}$$

With no external field supplied to the crystal (open circuit) so that diffusion processes dominate the movement of electrons, and, as is the case for Cr doped GaAs, the maximum space charge field, E_q >> diffusion field, E_T, then it can be shown that for I_1, I_2, << I_3 then:

$$\eta = \frac{\beta}{(1+\beta)^2}(\delta E_T \ell)^2 \, e^{\frac{-\alpha\ell}{\cos\theta}} \qquad (6)$$

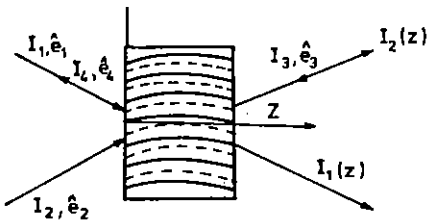

——— Light intensity maxima

---- Minimum change of refractive index

Fig 13 Beam interaction geometry for diffraction efficiency calculation.

where $\delta = \frac{\pi n_o^3 r_{41}}{\lambda \cos\theta}$, $\beta = I_1/I_2$ and α is the absorption coefficient at the laser wavelength of the crystal of length ℓ. Thus to maximise η, we must obtain maximum modulation of the fringes (first term in Eq 6) by making $I_1 = I_2$ ($\beta = 1$). On the other hand, the spacing of the fringes should be kept to a minimum, (ie large beam interaction angle, θ) so that E_T and δ can be made as large as possible. For our GaAs crystal with ℓ = 0.03cm, and $\alpha = 2.7\text{cm}^{-1}$, θ = 15° then from Eq (6) we calculate

$$\eta \sim 4.6 \times 10^{-7}$$

Using a TEM_{00}, CW, Nd:YAG with a power of ~ 50mW, a coherence length > 1cm and the experimental arrangement shown in Fig 12 with beams $I_1 = I_2 = 0.5\text{W/cm}^2$ vertically and $I_p \sim 50\text{mW/cm}^2$ horizontally polarised, then we measured a diffraction efficiency of ~ 5×10^{-7}, in good agreement with the calculation above as obtained form Eq (6).

We are currently investigating the phase conjugation and image processing properties of GaAs at 1.06μm. We would like to thank the British Council for the award of a travel bursary to P Hribek throughout the duration of this work.

4. Excimer laser photoablation studies

(a) Photoablation of plasma polymerised polyactylene films

M Golombok, M C Gower, S J Kirby and P T Rumsby (RAL)

When far ultraviolet light is incident on certain organic polymers etching takes place without thermal phase changes occurring on the etched material (20, 21). This phenomenon of photoablation has attracted attention due to its potential application for self development in microcircuit lithography. There has been considerable speculation on the mechanism for ablative decomposition. Currently, bond scission is a favoured mechanism. The problem with analysing photoablation products is that many of the polymers of interest (eg PMMA and PET) contain oxygen, nitrogen or halogens, which confuse the analysis of the plume (22).

It is therefore of interest to study photoablation on the simplest organic homopolymer. However, we have found that photoablation of the simplest polymer, polyethylene, is very inefficient (23). We now report studies on its conjugated analogue polyacetylene.

Because polyacetylenes are insoluble in organic solvents it is not possible to use the spinning and evaporation techniques usually used for preparing thin resist films. The usual technique for synthesis of polyacetylenes involves a heterogeneous catalytic process in a rare gas atmosphere (24, 25). A less well known technique uses a microwave discharge glow polymerisation of acetylene gas at low pressures (26, 27). This was the method we selected for several reasons. Because only acetylene is present in this particular synthetic process there is little chance of contamination - an important factor since even trace amounts of other materials can greatly alter the properties of the polyacetylenes which are semiconductors (28). The plasma discharge technique also yields films in the micron regime of interest for photolithography. Finally polyacetylene films prepared by this technique are less liable to be attached by the air.

The discharge polymerisation was carried out in a Technics plasma exciton 300-1 discharge apparatus The rf oscillator was tuned to a power of 150W at 13.56MHz. The polymer was formed on a glass plate substrate. Since polyacetylene films prepared by this technique have thus far received little attention, it was necessary to characterise the thin layers so as to assess their suitability for photoablation.

Variation of pressure conditions greatly alters the film quality. There are three possible regimes for the discharge pressure: (1) static regime where the chamber is filled to a certain pressure, the flow lines closed and the discharge initiated, (2) flow regime, where a constant flow is set prior to discharge (3) flow regime, where the gas flow is set constant during discharge. Regimes (1) and (2) give very low pressures due to removal of acetylene through the polymerisation process (see Fig 14). In (2) deposition is very slow (typically less

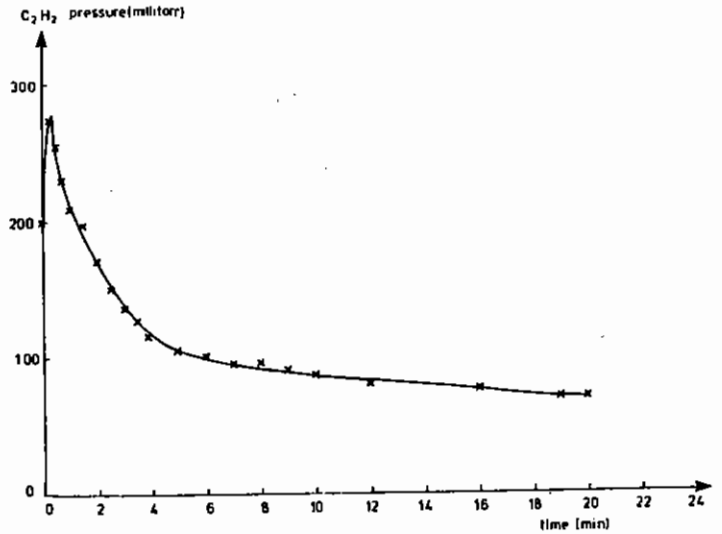

Fig 14 Pressure of acetylene in radio frequency plasma glow discharge, where steady flow at pressure 200 m torr set before discharge, frequency 13.56 Mhz, power 150W.

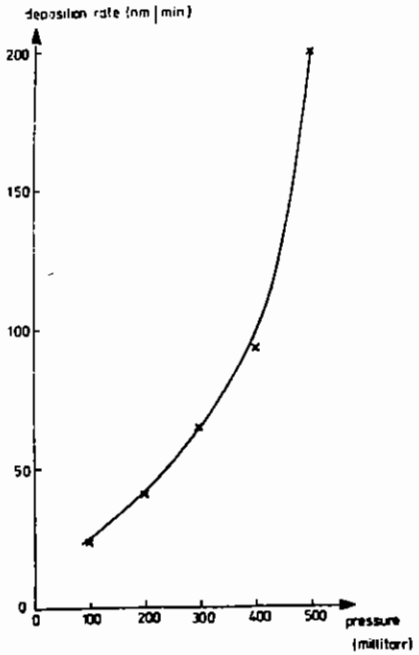

Fig 15 Deposition rate of polyacetylene on glass vs equilibrium discharge gas pressure

than 10nm/min). (3) was found to yield satisfactory results providing a low pressure was maintained. Fig 15 shows mean deposition rates for constant pressure during discharge. As shown by the easily observed interference fringes at higher pressures (> 300mTorr), the films were powdery and not uniform . In a typical run the chamber was pumped down to 150mTorr, flooded with acetylene and re-evacuated to 200mTorr. When the plasma discharge is switched on, the pressure drops to around 50mTorr and the flow of acetylene is adjusted to maintain a pressure of 200mTorr during discharge. A discharge time of 40 minutes gave a clear strong film of about 1.67µm thickness. Because of the extended Π conjugation in these films the polymer chains are susceptible to air attack (29, 30). This is observed as a cracking and warping in the film which occurs after around 24 hours. The films were therefore ablated immediately after deposition and coated with gold.

The film thickness was measured by a Sloan Dektak stylus or in the case of thin and ablated films, by coating with gold and counting the fringes arising from interference between the reflection form the top and bottom of an etch.

The ablation studies were performed using an Oxford Lasers KX2 excimer laser at the ArF wavelength 193nm. The output of 175mJ/cm^2 was focused or expanded depending on the fluence required. The pulse duration was 20ns. A submillimetre grid was used for contact printing

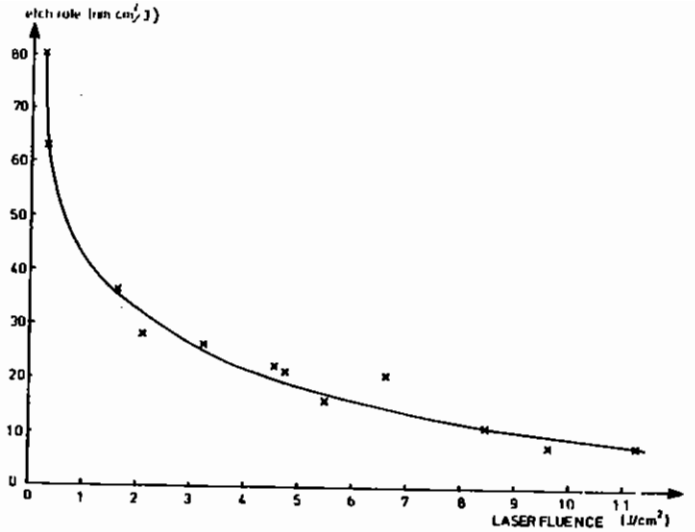

Fig 16 Single shot etch rate ArF (193 nm) laser on 1.67 µm thick polyacetylene films.

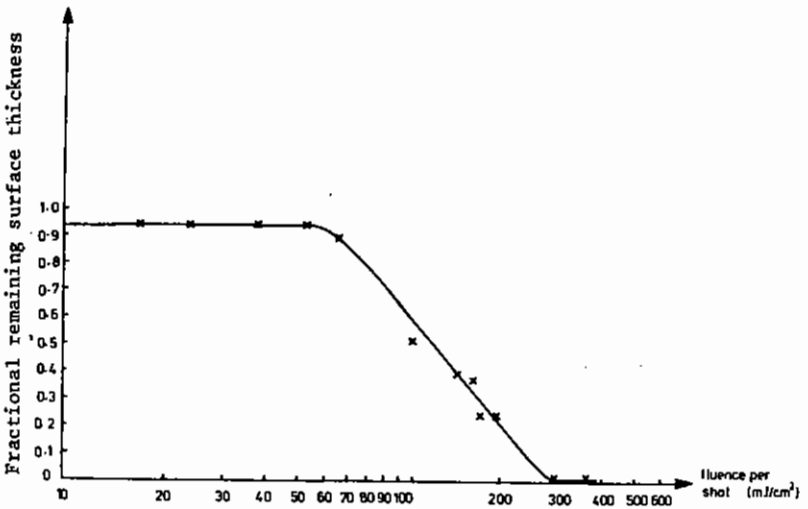

Fig 17 Polyacetylene normalised film thickness remaining after direct etching as a function of single shot fluence. Number of shots = 25. Film thickness = 1.67 µm. Resist : polyacetylene. Wavelength 193 nm.

to establish etch depth and an electron beam etched chrome on quartz mask for contact etching of micron characteristics which were later studied on an electron microscope.

Although a range of single shot fluences up to 1J/cm^2 were incident on the film, it was found that the maximum possible etch depth for a single pulse was .17μm for thicknesses ranging from .2μm to 3.2μm layers. Above fluences of 700mJ/cm^2, melting is observed resulting in a loss of straight line contour at an edge vertex.

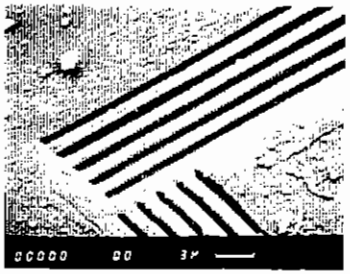

(a)

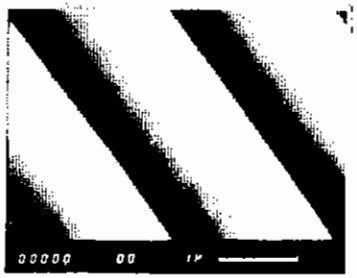

(b)

Fig 18 Scanning Electron Micrograph pictures of 1 μm lines etched by direct contact print on polyacetylene films. Fluence per shot 175mJ/cm^2, 25 pulses.

The etch rate appeared to be independent of film thickness. Fig 16 shows single shot etch areas as a function of fluence. The etching efficiency drops to half its maximum value at 200mJ/cm^2 and levels out at around .10nm cm^2/J. Figs 17 and 18 show results for 25 shot direct etching using a range of fluences on 1.67μm polyacetylene films. Two standard parameters derived from such measurements (31) are the resist contrast γ, and sensitivity Q_0. We find for polycetylene films, $\gamma = 5$ and $Q_0 = 270$mJ/cm^2 shot. This compares with values of $\gamma = 6$ and $Q_0 = 80$mJ/cm^2 measured for direct etching of thin films of PMMA at a laser wavelength of 193 mm (32).

Using a Princeton Applied Research (PAR) Model 1225, 0.2m polychromator in conjunction with an OMA2 optical multichannel analyser and a Model 1254 vidicon detector, spectra of the plume emission in a vacuum above the ablation site were recorded. A survey spectrum is shown in Fig 19. The most prominent bands in the region 300-600nm are due to the C_2 Swan system and the CH A-X

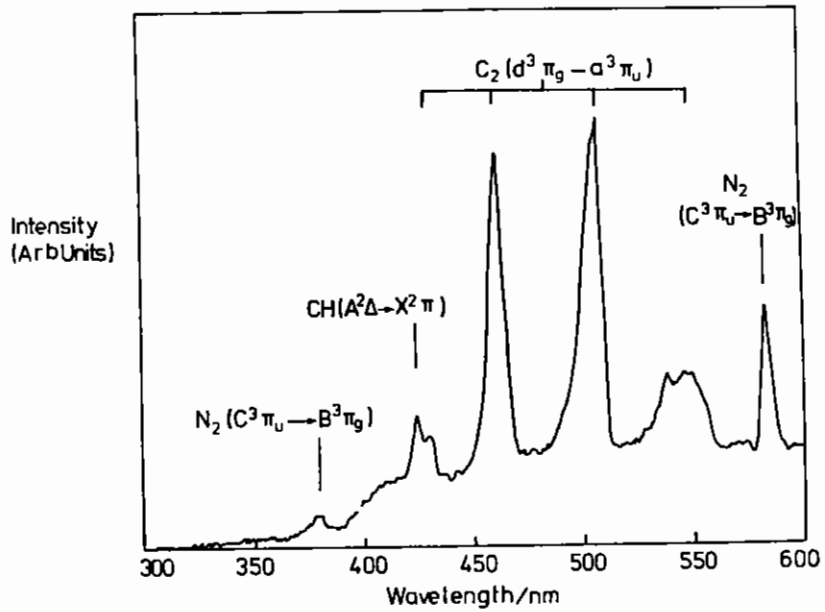

Fig 19 Survey emission from plume during 193 nm laser ablation of polyacetylene film.

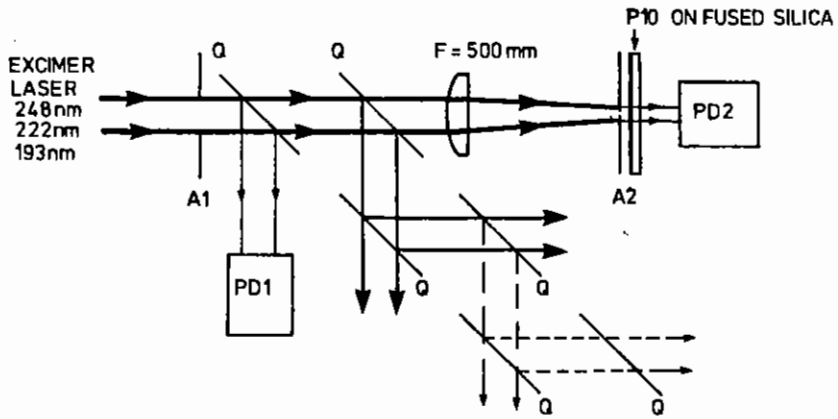

Fig 20 Experimental arrangement for absorption measurements with the excimer laser. Fast photodiodes PD1, PD2, 1mm diameter aperture A2, quartz plates Q, beam defining aperture A1.

transition at 431 nm. As first pointed out in work on the emission spectra of the plume from PMMA (22), these band systems are characteristic of the emission from low temperature flames. Further spectroscopic analysis is currently underway. We note the fact that the required total fluences in this study are considerably higher than those reported for photoablation of other polymeric materials (32). This may be attributed to the Π bonding structure and the resulting higher absorption cross-section. Consequently the distinction between photochemical and thermal pathways which result in ablation will be less marked than in saturated polymer chains. However, the simplicity of structure and ease of fabrication make further study of this material of interest. We note in this regard, photothermal studies of the related diacetylenes (33). Finally, rather than insulating polymers the polyacetylenes are of great interest as organic semiconductors so that using negative etching to provide finely resolved narrow conducting strips above an insulating substrate would be of considerable interest for future study.

(b) Time Resolved Studies of PMMA Ablation

G M Davis and M C Gower (RAL)

There have been many reports (32, 34) in recent years on the ablative photodecomposition (APD) of polymeric material following exposure by the short wavelength high peak powers available with excimer lasers. Several of these studies have indicated that the polymer is ablated on a timescale comparable to the laser pulse length of ~ 15ns (35-37). There is some evidence that the ablating plume (38) shields the polymer from the latter part of the laser pulse resulting in a reduction of the amount of material ablated per shot.

An Oxford laser Model KX2 excimer laser was used in this study. The gas mixture was changed depending on the wavelength required. The experimental apparatus is shown in Fig 20. Two fast calibrated photodiodes PD1 and PD2 were used to monitor the incident and transmitted pulse shapes. Aperture A1 was designed to restrict the beam to a size small enough to enter detector PD1.

A 50cm focal length lens was used to increase the fluence incident on the polymer above that available directly from the laser. To decrease the fluence either a diverging lens or the reflection from a sequence of fused silica plates was used. A 1mm diameter aperture A2 selected a reasonably uniform portion of the beam to illuminate the polymer film. At high fluences this was more difficult to achieve due to non-uniformities in the laser output and there was a 50% variation in the fluence over the irradiated area.

Isofine electron beam resist P10 (PMMA), was spun onto fused silica substrates to a thickness of 0.6µm-0.7µm. The thickness of each sample was measured using an interference microscope. The resist was not pre-baked prior to the exposure but the samples were left ~ 3 days before use (studies using pre-baked samples produced qualitatively similar results.)

The PMMA-coated silica surface was positioned ~ 1mm-2mm from aperture A2 in Fig 20. Initial studies showed that when etching occurred at a fluence close to the ablation threshold at 193nm a substantial fraction of the transmitted light was diffracted by the aperture. To enable the detector PD2 to collect all the diffracted light the distance between the substrate and front surface of PD2 was made as small as possible (< 3-4cm).

In order to avoid saturation of the photodiode detectors, diffusers were used directly in front of the photodiodes. For each wavelength and intensity the signals from PD2 and PD1 were monitored simultaneously. The ratio of these signals was recorded for both

uncoated and coated substrates placed after aperture A2. Assuming that the decrease in transmission due to Fresnel reflections was the same in both cases, a value for the transmission of the PMMA film was deduced.

For laser wavelengths at 193 nm (ArF), 222nm (KrCl) and 249 nm (KrF) the transmission of multiple pulse exposures of the PMMA layer was studied for a range of intensities above and below the ablation threshold. Measurements from photographs of the oscilloscope traces of the photodiodes signals enabled the time evolution of the transmission to be studied within the temporal resolution determined by the 3.5ns risetime of the Tektronix Model 466 storage oscilloscopes.

As the intensity was raised the resist underwent a series of changes which were qualitatively similar for each of the wavelengths studied. At intensities near the threshold for ablation the resist began to etch very slowly. The removal of resist was confirmed by optical and electron microscopy of freestanding ~ 30μm mask exposures at these intensities. We have defined the threshold of ablation as that value of peak intensity (I_T) sufficient to etch the ~ 0.66μm layer in ~ 40 laser pulses. By comparison, after exposing the resist to ~ 60 laser pulses at ~ $^2/_3$ of I_T only the outline with no gross etching of the irradiated region could be seen in the resist with only a small amount of debris deposited in diffraction rings around the edges. The gradual accumulation of ablated debris deposited on the resist causes scatter of subsequent pulses. This scatter by debris is responsible for the observed steady decrease in transmission for intensities just below threshold. At still lower intensities no evidence of any etching could be seen even after 60 pulses. The transmittance of the laser measured at intensities less than $^1/_5$ to $^1/_{10}$ of the threshold intensity was the same as the small-signal value as measured by a spectrophotometer and a lamp source.

Fig 21 shows the temporal variation of the transmittance for the first and second laser pulse at wavelengths of 193nm (ArF), 222nm (KrCl) and 249nm (KrF). At the intensity values near threshold used to obtain the data shown in Fig 21(a) about 10 laser pulses were required to remove most of the PMMA layer at each of the three

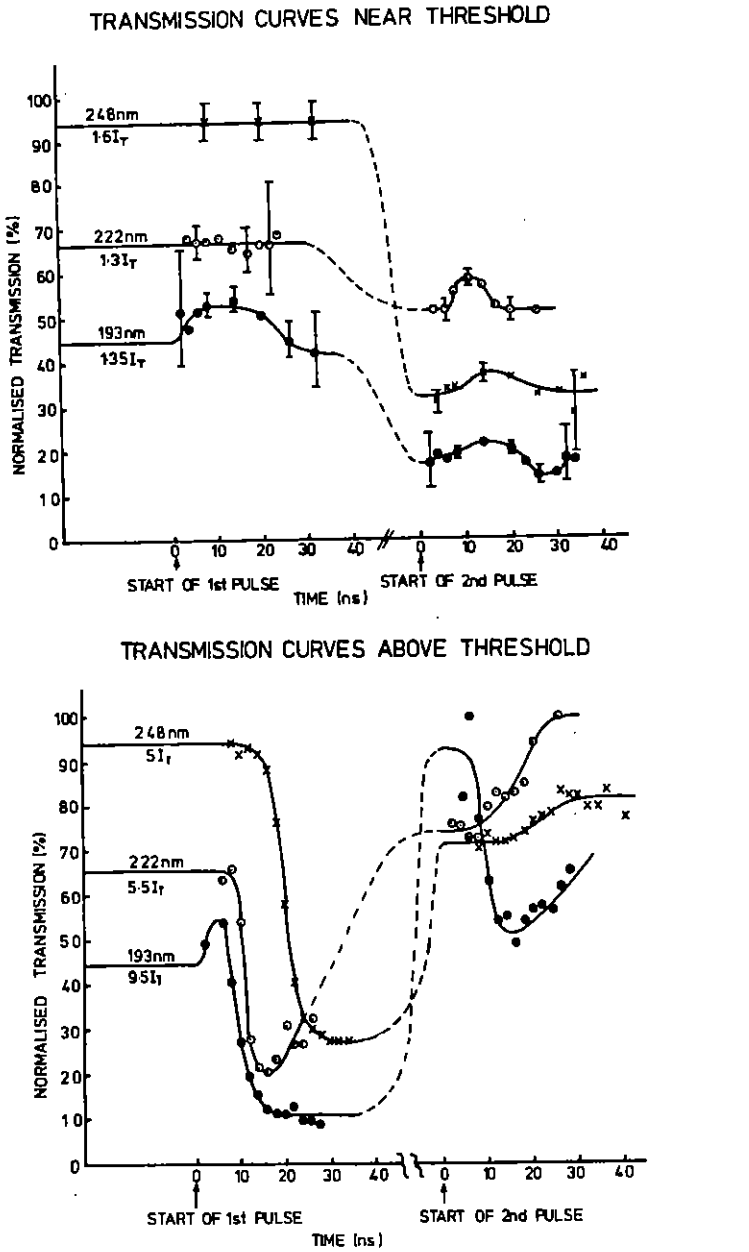

Fig 21 Temporal transmission measurements of P10 resist during the first and second laser pulses at 248, 222 and 193 nm.

(a) Intensity near to ablation threshold.

(b) Intensity several times the ablation threshold.

wavelengths. The value of transmission prior to the first laser pulse corresponds to the average small signal transmission measured with low intensity (< 0.4MW/cm^2) laser pulses or extrapolated from spectrophotometer measurements. In the intensity regime near threshold there was negligible variation in the transmittance during the laser pulses at 248 and 222nm. However, at 193nm there is a small initial rise in transmission of the sample which is probably due to a small quantity of resist being removed at the beginning of the first pulse. During the latter stages of the 193nm laser pulse a slight decrease in transmission is seen. Probably as a result of scattering of the incident laser by ablating material. Since less resist is removed per pulse at 222nm and 248nm, the transmission was unchanged at these wavelengths. PMMA is more transparent and scattering by ablated material is less at the longer wavelengths.

As shown in Fig 21(a) for all wavelengths a discrete jump between the transmission at the end of the first laser pulse and the transmission at the start of the second pulse was observed. This we attribute primiarily to light scattering from the debris deposited on the surface by the first pulse. Scanning electron micrographs confirm that at all wavelengths a large amount of debris is deposited both in and around the exposed area. The slight rise in transmission during the second pulse at each wavelength is thought to be due to removal of this debris.

At fluences several times higher than threshold as shown in Fig 21(b) a rapid decrease in transmission occurs. We attribute this behaviour to light scattering from material ejected by the initial part of the pulse causing a reduction in intensity on the resist to values below threshold for ablation during the latter stages of the pulse. Material largely ceases to be removed during the latter part of the pulse while at even later times as the plume disperses the transmission begins to rise. Again there is a discrete change in transmission between the end of the first pulse and start of the second. However in contrast to the behaviour observed using fluences near threshold there is now a larger transmission at the start of the second pulse. Electron micrographs of the ablated surface and surrounding regions show that there is less debris deposited on resist surfaces than at lower

fluences. Hence at these higher fluences there will be fewer light scattering centres resulting in an apparent increase in the transmission of the sample at the beginning of the second pulse.

At the intensities used to obtain the data in Fig 21(b) most of the resist is removed by a single laser pulse at both 222 and 248nm. The amount of material removed during the second pulse is insufficient to cause a decrease in transmission due to scattering. Instead the combination of resist and debris removal cause an increase in the transmission during the pulse. However at a wavelength of 193nm the absorption in the resist is much greater than at longer wavelengths and the scattering by the ablating plume is likely to be larger so that even at 16 times the ablation threshold intensity only about half of the resist was found to be removed in a single pulse. Hence, as can be seen in Fig 21(b) transmission of the second laser pulse at 193nm follows a similar trend to that of the first pulse.

The maximum slopes of transmission curves similiar to those shown in Fig 21 were found to increase with increasing laser intensity for all those wavelengths investigated. The larger etching rates observed at higher fluences will produce a greater density of material in the pulse which will increasingly scatter the light during the latter stages of the pulse. A change in the size of the particles in the plume at higher fluences may also alter the scattering properties of the plume.

Apart from the absolute value of intensities needed to effect the same degree of ablation, the overall ablation characteristics of PMMA which we have described show little dependence on the irradiating wavelength. To illustrate this the number of pulses required to remove most of the resist was measured at each wavelength as a function of the laser intensity normalised to its ablation threshold value I_T. The results are shown in Fig 22. As can be seen from this figure the only

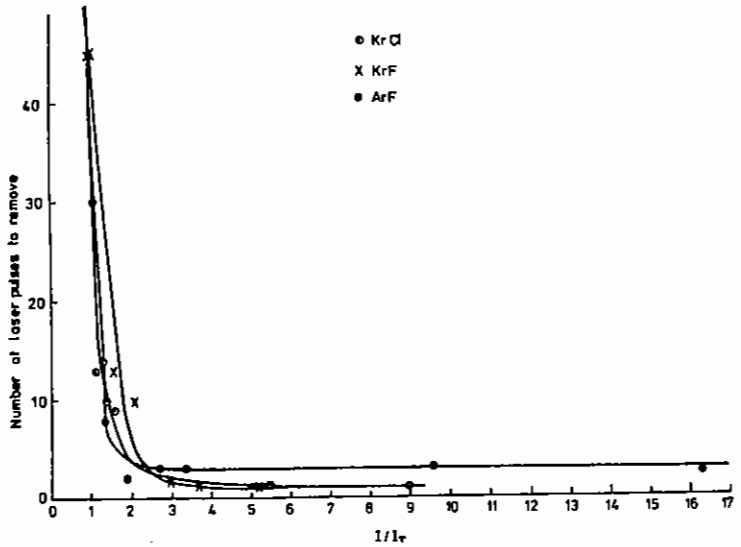

Fig 22 Number of laser pulses required to remove the P10 resist film verses laser intensity normalised to the ablation threshold.

appreciable distinction between the ablation rates is the relatively large asymptotic value approached at high normalised intensities of the ArF laser source.

In contrast to common practice, we have characterised the threshold for ablation in terms of the peak laser intensity rather than its energy fluence. The ablation phenomenon is only observed when a large number of photons are absorbed and effect bond scission in a sufficiently short period of time. A threshold for this effect characterised by a laser intensity is therefore more appropriate. Since it is only those photons which are absorbed in the polymer which can cause bond scission, in comparing the ablation characteristics at different wavelengths it is more meaningful to compare the ratio of the threshold intensity to the absorption depth, ie the parameter $I_T\alpha$ which we call the ablation power density. Table 1 shows measurements of the threshold intensity I_T, absorption depth $^1/_\alpha$, and ablation power density for P10 resist as a function of the ablating laser wavelength.

λ (nm)	Ablation Threshold Intensity I_T (MW/cm^2)	Absorption Depth $1/_\alpha$ (μm)	Ablation Power Density $I_T\alpha$ (GW/cm^3)
248	11	11.0	10
222	5	1.56	32
193	3	0.72	42

TABLE 1

These measurements show that the ablation power density decreases as the laser wavelength increases. Therefore, fewer absorbed photons per unit volume are required to cause ablation at longer wavelengths than at shorter wavelengths. If the ablation mechanism were purely a thermal rather than a photochemical process then $I_T\alpha$ should be similar for each wavelength. On the other hand, if photochemical bond scission were solely responsible for ablation then the ablation power density should decrease at short wavelengths since in this UV spectral region the quantum efficiency for bond breakage is generally larger for shorter wavelengths. Since the opposite trend is observed, we conclude that different reaction pathways are involved in ablation and that the predominent process causing ablation depends on the laser wavelength. A similar conclusion was recently reached by Srinivasan and Braren (39).

5. Excimer laser lithography: intensity-dependent resist damage

G M Davis and M C Gower (RAL)

There has recently been considerable interest in the use of excimer lasers as light sources for high resolution lithography (40-43). One of the potential advantages of using commercially available excimer lasers as light sources is that they produce much higher average powers (up to 100W) than conventional lamp sources. Provided that there is no reciprocity failure in the response of the photoresists exposure times can be greatly reduced by use of an excimer laser source. However the short duration (~10-20ns) pulses of high peak intensity (up to 50MW/cm^2) that are typical of excimer lasers may result in intensity-dependent photochemical changes which might produce a reciprocity failure of the sensitivity of response of the resist.

Reciprocity failure is not necessarily undesirable and may even enhance the resolution (44, 45). However, if resist sensitivity is sacrificed to such an extent so as to negate the higher power produced by the laser source, then the use of an excimer laser is no longer so attractive.

The study of reciprocity failure in photoresists when exposed to excimer laser light has to date received surprisingly little attention. The most detailed investigations have been made using an XeCl laser to expose resists at a wavelength of 308nm (46, 47). Compared to the value measured at low (~ mW/cm^2) intensities with the 313nm line from an Xe-Hg lamp, these studies showed a maximum loss of sensitivity of only a factor of three for peak laser intensities up to 2.4MW/cm^2 when exposing Shipley AZ2400 and two IBM experimental resists. However, experiments by Kawamura et al (48, 49) using a KrF excimer to expose PMMA/benzoin resist at 249nm showed strong increase in etch depth with peak intensity for a given integrated fluence on the resist and suggested substantial reciprocity failure in the resist.

In the work reported here we have examined one of the possible causes of reciprocity failure namely the intensity dependence of the absorption coefficient of the resist. When assessing the suitability of a resist for use at a particular irradiating wavelength one of the important parameters to assess is the absorption coefficient at that wavelength. Lin (50, 51) has pointed out that an absorption coefficient $> 2.5\mu m^{-1}$ is too high to produce etches with steep wall angles while an absorption coefficient $< 0.05\mu m^{-1}$ typically results in low sensitivity of exposure. Furthermore, it is well known (50, 52, 53) that the absorption coefficient of some resists varies with the degree of exposure. For example, exposing a 0.8μm layer of PMMA for two minutes with a Xe-Hg lamp estimated to deliver ~ 168mJ/cm^2 in the spectral range 200-260nm, reduced its transmission at 200nm by ~ 11% (50). This "photodyeing" is dependent on the total energy fluence received and similar effects can be expected for low peak intensity exposures by excimer laser sources. To our knowledge the only experimental evidence of this effect is by White et al (54) who showed that exposures of 0.1μm thick films of PMMA to seven thousand 0.1mJ, 10ns pulses of an F_2 laser at 157nm, resulted in a 77% decrease in transmission.

In addition to these low intensity changes, using higher peak laser intensities to expose resists may result in intensity dependent changes in the absorption coefficient. Recently Sheats (45) observed intensity dependent photobleaching of strongly absorbing PMMA/acridine films (absorption depth of < 0.09μm) following single pulse exposures of 3 - 4MW/cm^2 at 248nm.

In our experiments we have investigated whether similar effects are observed for Shipley AZ2400, Isofine e-beam resists P10 (PMMA) and PM20, resists. These resists are suitable for use at one or more of the excimer laser wavelengths at 248, 222 or 193nm. Thin 0.5-1.5μm thick layers of resist were spun onto fused silica substrates and the transmission of these samples relative to an uncoated substrate were measured using an LKB Ultrospec UV/VIS spectrophotometer Model 4050.

An Oxford Lasers Model KX2 excimer laser operating on either KrF (248nm), KrCl (222nm) or ArF (193nm) was used for the relative transmission measurements at high (0.01-100MW/cm^2) peak intensities. Vacuum photodiodes were used to simultaneously monitor the transmitted and incident laser pulses. Reflections from a succession of fused silica beamsplitters were used to vary the peak intensity incident upon the photoresist. A 50cm focal length lens was used to focus the laser beam so that high incident peak intensities could be obtained by placing the substrate at varying distances from the lens.

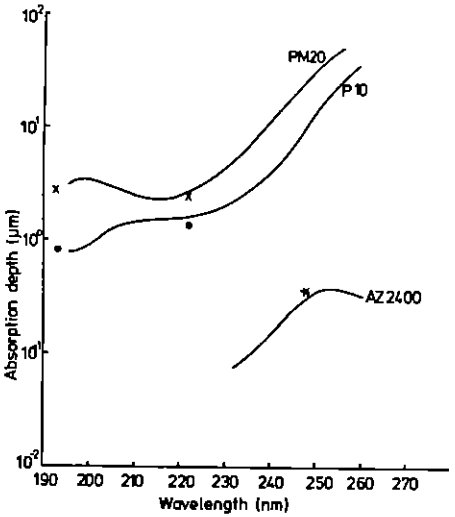

Fig 23 Measured small and large signal absorption depths of PM20, P10 and AZ2400 resists as a function of wavelength.

Fig 23 shows curves of the small signal absorption depth as measured with the spectrophotometer in the spectral range 196 to 260 nm. Also shown in this figure are values of the absorption depth measured with the laser operating at 193, 222 and 248 nm. Table 2, column A records the peak laser intensities used for these measurements. For wavelengths shorter than 232nm the intensity transmitted by the ~ 0.5μm thick layer of AZ2400 was below the detection limit of the

spectrophotometer so that for this spectral region the absorption depth is ≤ 0.08μm. On the other hand no accurate laser measurements of absorption depth were made at 248nm for P10 and PM20 since thin films of these resists were too transmitting at this wavelength. For those resists and wavelengths where measurements could be made there was no significant difference between the spectrophotometer and laser-measured values of absorption depth. These results therefore show no evidence of reciprocity failure in the response of the resists upon exposure to pulsed excimer light.

However at fluences (Table 2, Column B) higher than those used to record the laser measurements for Fig 23 (Column A), the exposed region could be seen after 60 laser shots. The nature of the mark made by the laser was not investigated in detail but appeared to be damage to the resist. A further increase in the intensity caused direct etching of the resist. Column C (Table 2) records the peak intensities required to etch > 90% of the film in 40 laser shots. At even higher single pulse peak intensities (Table 2, Column D) rapid ablation of the resists in ~ 2-4 laser shots was observed. This process, sometimes called ablative photodecomposition (20), has been used as a dry etch

RESIST	λ(nm)	A(MW/cm^2)	B(MW/cm^2)	C(MW/cm^2)	D(MW/cm^2)
P10	193	0.40	1.8	3.2	8.1
	222	0.017	1.4	5.2	9.4
	248	--	5.4	11	27
PM20	193	0.40	1.8	3.7	19
	222	0.017	1.5	6.8	29
	248	--	14	38	107
AZ2400	193	—	0.4	1.8	19
	222	—	1.1	2.9	25
	248	0.038	0.57	4.6	39

A: Intensities used for absorption measurements.

B: Intensities at which the exposed area was visible after 60 laser pulses.

C: Intensities sufficient to etch > 90% of the resist film in 40 laser pulses.

D: Intensities at which ablative photodecomposition was observed.

TABLE 2

technique for the fabrication of fine lines in several organic resists such as Shipley AZ2400 (55), PMMA (55) and PM20 (32).

We conclude that if conventional wet development is the desired fabrication process then the peak incident laser intensity should not exceed that at which damage is observed. The shortest exposure time per unit area for each resist can then be obtained from Table 2. For example, our experiments have shown that about 60 laser pulses at

248nm each of ~ 3mJ/cm^2 and 9ns (FWHM) duration were sufficient to cause complete etching of a 1μm thick layer of AZ2400 resist following a one minute development in a 1:4 solution of Shipley AZ2401 developer:water. Using a KrF excimer laser with the maximum repetition rate commercially available (500pps), we can deduce the minimum exposure time required to deliver the integrated dose of 180mJ/cm^2 necessary for exposure to the bottom of the resist layer. The damage threshold of AZ2400 at 248nm is ~ 0.5MW/cm^2 (Table 2, Column B) which restricts the single shot fluence to < 10mJ/cm^2 for laser pulses of 20 ns (FWHM) duration. This results in a minimum exposure time of ~ 36msec. The maximum area that can be exposed in 36msec is then limited to about 20cm^2 by the single pulse laser energy of 200mJ. It is interesting to compare this result with the minimum exposure time that can be achieved for the same area using a deep UV Xe-Hg lamp. Using a Canon Proximity Mask Aligner Model PLA-521FA that provides illumination in the spectral range 200-270 nm, exposure times of about 380msec have been reported for 1 μm thick layers of AZ2400. Hence exposure with this lamp source takes about an order of magnitude longer than would exposure using a high repetition rate KrF excimer laser source.

We conclude that the minimum exposure time that it is possible to achieve with an excimer laser operating at a wavelegth of 248, 222 or 193nm is set by the ablation damage threshold to the resist. However, the low powers of conventional lamp sources at these wavelengths (a few tens of mW's/nm at 250 nm) ensure that a substantial reduction in exposure time can still be achieved by replacing the lamp in a lithographic machine by an excimer laser. If the wafer fabrication rate is limited primarily by exposure time the use of an excimer laser light source could result in a significant increase in the wafer throughput of the machine.

6. X-Ray Lithography using a KrF Laser Plasma Source

M C Gower and F O'Neill (RAL)

In the semiconductor industry it is generally accepted that lithography using 10 or 5 to 1 optical step and repeat machines will satisfy the bulk of the requirements of the industry in the short term. These requirements might provide critical circuit dimensions as small as 0.7μm to 0.5μm over stepped fields of several square centimetres. It is also generally agreed that as device geometries shrink further, the industry will eventually be forced to use X-ray lithography in a proximity mode of printing. The short wavelengths of X-rays allow diffraction effects to be minimised (the resolution for proximity printing of a mask onto a wafer which is a distance d away is $\sqrt{\lambda d/2}$. X-ray lithography can also be used over larger fields than can be reproduced by an optical stepper and is of potential interest for wafer scale integration of devices. Indeed use is currently made of X-ray lithography in the fabricating of bubble memories where the requirement is for very high resolution on a single layer of photoresist with minimum overlay accuracy.

Although X-ray lithography can offer higher resolution without the depth of focus and dust problems which optical projection schemes suffer, many technological developments are still needed before X-ray lithography becomes the workhorse of the industry. Not the least of these developments must be in mask fabrication. Since the proximity printing technique is inherently 1:1, high resolution masks must be made on strong, stable transparent membranes of deposited materials such as gold which are opaque to the X-ray source. To date, films of polyimide and boron nitride have been used as substrates. Sensitive resists which have a large stopping power for the X-rays while being relatively insensitive to the dry etch process must also be fabricated. Finally, before anything else, efficient high brightness sources of X-rays need to be developed. Electron bombardment sources can produce fluxes on the wafer of ~ 0.1-0.2mW/cm^2 but are characterised by large (~ few mm) spot sizes which are incongruous with producing very small

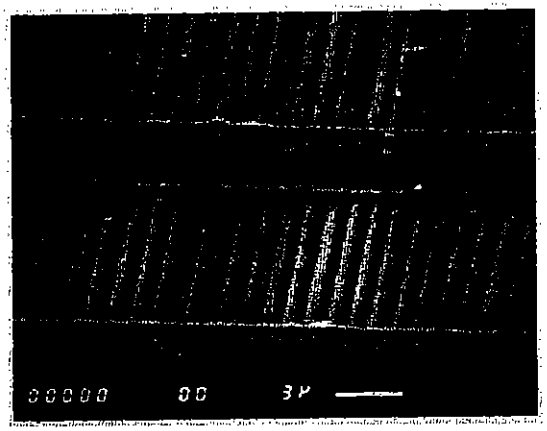

Fig 24 Scanning electron micrograph (SEM) of exposure in EBR-9 resist using a free standing gold mask and an EMG 210E KrF laser source.

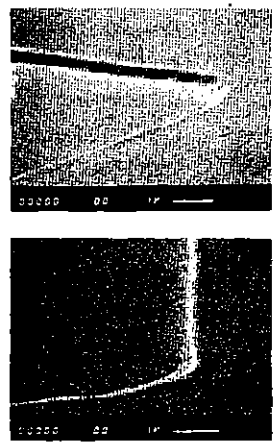

Fig 25 SEM of exposure in P(MMA-MA) resist using a free standing Copper mask and an EMG 150ES KrF laser source.

(< 0.5μm) critical dimensions on the chip. On the other hand, synchrotron sources can produce fluxes of 10-20mW/cm^2 at the mask. However at a capital cost of several million dollars these sources are extremely expensive and are relatively unreliable. Furthermore production is halted on all exposure systems simultaneously, should the synchrotron malfunction for any reason. Laser produced plasma sources appear more promising. The laser is relatively inexpensive and can be remote from the clean room and the aligner.

We have carried out exposures using the X-rays from a plasma produced by a low energy commerically available excimer laser. In Fig 24 we show a scanning electron micrograph of 0.5 μm lines and spaces of the image recorded in EBR-9 photoresist of a gold grating mask proximity printed using a 12 μm gap between mask and resist. This image was recorded using pulses of focussed radiation from a 1J, 20Hz, 249 nm

commercially available KrF laser (Lambda-Physik EMG 210E). Shorter exposure times requiring fewer laser pulses can be achieved using a similar laser which is injection locked to improve its spatial coherence. In Fig 25 we show a photograph of an exposure recorded using 100 pulses of a 600 mJ injection locked KrF laser (Lambda-Physik EMG 150ES). With a high repetition rate (500Hz) version of this laser we estimate average fluxes of ~ 1mW/cm^2 can be delivered to the mask. This is produced by a point source and represents an order of magnitude improvement over the brightness of bombardment sources. Further details of this work can be found in Section C6.3 of this annual report and in Ref 56.

REFERENCES

1. P Gunter, Phys Rept, 93, 199 (1982).

2. J Feinberg, D Heiman, A R Tanguay Jr and R W Hellwarth, J Appl Phys, 51, 1297 (1980).

3. J Feinberg, Opt Lett, 5, 519 (1980).

4. P Gunter, E Voit, M Z Zha and J Albers, Opt Comm, 55, 210 (1985).

5. F C Jahoda, P G Weber and J Feinberg, Opt Lett, 9, 362 (1984).

6. J Feinberg and G D Bacher, Opt Lett, 9, 420 (1984).

7. K R MacDonald and J Feinberg, Phys Rev Letts, 55, 821 (1985).

8. J F Lam, Appl Phys Letts, 46, 909 (1985).

9. T Y Chang and R W Hellwarth, Opt Lett, 10, 408 (1985).

10. M C Gower, Optics Letts, (June 1986).

11. A G Chynoweth, J Appl Phys, 27, 78 (1956).

12. A G Chynoweth, Phys Rev, 102, 705 (1956).

13. A M Glass, D von der Linde and T J Negran, Appl Phys Letts, 25, 233 (1974).

14. D von er Linde and A M Glass, Appl Phys, 8, 85 (1975).

15. N V Kukhtarev, V B Markov, S G Odulov, M S Soskin and V L Vinetskii, Ferroelectrics, 22, 949 (1979).

16. S Ducharme and J Feinberg, J Appl Phys, 56, 839 (1984).

17. A M C Smout, R W Eason and M C Gower, Optics Comm. in press.

18. A M Glass et al, Appl Phys Letts, 44, 948 (1984).

19. M B Klein, Opt Letts, 9, 350 (1984).

20. R Srinivasan and V Mayne-Banton, Appl Phys Lett, 41, 576 (1982).

21. R Srinivasan and W J Leigh, J Am Chem Soc, 104, 6784 (1982).

22. G M C Davis, M C Gower, C Fotakis, T Efthimiopoulos and P Argyrakis, Appl Phys A, 36, 27 (1985).

23. M C Gower, private communication.

24. J Chien, Polyacetylene: Chemistry, Physics and Material Science (Academic Press, 1984).

25. T Ito, H Shirakawa and S Ikeda, J Polym Sci, 12, 11 (1974).

26. F J Vastola and J P Wightman, J Appl Chem, 14, 69 (1964).

27. A Moshonov and Y Avny, J Appl Polym Sci, 25, 771 (1980).

28. H Shirakawa et al, JCS Chem Comm, 305 (1977).

29. J L Bredas, R Silbey, D S Boudreaux and R R Chance, J Am Chem Soc, 105, 6555 (1983).

30. A Matsui and K Nakamur, Japan J Appl Phys, 6, 1468 (1967).

31. N D Wittles in Fine Line Lithography, ed R Newman (North Holland 1980).

32. G M Davis et al, in Microcircuit Engineering 83 ed H Ahmed, J R A Cleaver and G A C Jones (Academic Press 1983).

33. M V Basilevsky, G N Geramisov and S J Petrochenko, Chem Phys, 97, 331 (1985).

34. R Srinivasan and V Mayne-Banton, Appl Phys Lett, 41, 576 (1982).

35. P E Dyer and R Srinivasan, Appl Phys Lett, 48, 445 (1986).

36. G Koren, J T Yeh, J Appl Phys, 56, 2120 (1984).

37. G M Davis, M C Gower, C Fotakis, T Efthimiopoulos and P Argyrakis, Appl Phys, A36, 27 (1985).

38. B Braren and R Srinivasan, J Vac Sci Technol, B3, 913 (1985).

39. R Srinivasan and B Braren, J Polymer Sci (Chem) in press.

40. K Jain, C G Willson and B J Lin, IEEE Electron Device Lett, EDL-3, 53 (1982)

41. K Jain, C G Willson and B J Lin, IBM J Res Develop, 26, 151 (1982).

42. Y Kawamura, K Toyoda and S Namba, J Appl Phys, 53, 6489 (1982).

43. H G Craighead, J C White, R E Howard, L D Jackel, R E Behringer, J E Sweeney and R W Epworth, J Vac Sci Tech, B1, 1186 (1983).

44. D J Ehrlich and J Y Tsao, Appl Phys Lett, 44, 267(1984).

45. J R Sheats, Appl Phys Lett, 44, 1016, (1984).

46. K Jain, S Rice and B J Lin, Polymer Engineering and Science, 23, 1019 (1983).

47. S Rice and K Jain, IEEE Trans Electron Devices, ED-31, 1 (1984).

48. Y Kawamura, K Toyoda and S Namba, Appl Phys Lett, 40 374 (1982).

49. Y Kawamura, Y Itagaki, K Toyoda and S Namba, AIP Conference Proceedings No 100, 288, EdC K Rhodes, H Egger and H Pummer, American Institute of Physics, (1983).

50. B J Lin in Fine Line Lithography, Ed R Newman, North-Holland (1980)

51. B J Lin, J Vac Sci Technol, 12, 1317, (1975).

52. R B Fox, C G Isaacs and S Stokes, J Poly Sci, Part A, 1, 1079 (1963).

53. F H Dill, W P Hornberger, P S Hauge, J M Shaw, IEEE Trans Electron Devices, ED-22, 445 (1975).

54. J C White, H G Craighead, R E Howard, L D Jackel, R E Behringer and R W Epworth, D Henderson and J E Sweeny, Appl Phys Lett, 44, 22, (1984).

55. S Rice and K Jain, Appl Phys A33, 195 (1984).

56. F O'Neill, M C Gower, I C E Turcu and Y Owadano, Appl Optics, 25, 464 (1986).

ACKNOWLEDGEMENTS

Much effort has gone into the production of the report. Thanks are due to all the University contributors who (almost) met the manuscript deadline and to the section editors for their liaison work with University users and proof reading.

The brunt of the labour in coordinating the work, drawing diagrams and producing wordprocessor text was carried out by Nic Allen, Jan Smith, Chris Ayling, Clare Schröder and Wendy Ferguson, to whom many thanks are due. Reproduction of the report was by the RAL Reprographics Section.

M H Key